Friction modelling requirements and implementation in railway freight vehicle dynamic simulations

A thesis submitted in partial fulfilment of the requirements of the University of Huddersfield for the degree of doctor of philosophy

Institute of Railway Research

July 2020

By David Downes

Supervisor Dr Philip Shackleton

Abstract

The highly nonlinear characteristics of dry friction damped suspension components used in railway freight vehicles increases the modelling challenges in Multibody Simulations (MBS) software packages such as VAMPIRE, SIMPACK and ADAMS VI-RAIL. These system nonlinearities then lead to lower confidence levels in modelling methodologies and therefore, more uncertainty in the simulation results produced by these models.

The main reasons for the low confidence levels associated with friction modelling methodologies in the context of railway freight vehicles, are due to the lack of reliable test data to validate the friction models used in the primary/secondary suspension. Therefore, there is an industry requirement to better understand the in service/maintenance requirements of these components, first from a testing perspective and then from a modelling one. Once this current gap in knowledge and understanding is bridged, the results generated from the simulation models could then be used in the future to replace on-track/laboratory testing, which would bring significant cost benefits to the rail freight industry.

The work presented in this thesis reviews the current friction testing and modelling methodologies as well as the simplifying assumptions that are implemented in commercial MBS software packages. The most common friction model that is used in railway vehicle MBS for example, is the Coulomb model of dry friction. This model however, is not capable of describing stick-slip behaviour, pre-sliding displacements or the viscoelastic effects of friction surfaces when they start to yield under extreme loading conditions. The Coulomb friction model also has a discontinuity in the vicinity of zero velocity, which can cause numerical issues in MBS as the friction force in this region, is non-differentiable. To handle the discontinuity, a variety of regularisation methods are generally implemented in the Coulomb model which are further discussed in the literature review.

The impact of these regularisation methods on the validity of MBS results however are currently not fully understood or justified, as these tend to be mathematical smoothing functions that are not actually related to the mechanical properties of the friction surfaces. Therefore, to better understand the limitations of the Coulomb friction model and its application, as well as the different regularisation methods that are implemented in freight vehicle secondary suspension friction models, several scale model benchmark tests have been carried out on a variety of rail industry standard secondary suspension wear liner components.

The critical modelling parameters that are required to develop a comprehensive/optimised freight vehicle secondary suspension friction model were then calculated from the benchmark test data. These parameters include the torsional stiffness and damping properties of the centre plate/wear liner components, as well as the Coefficient of Friction (COF) values and frequency signatures of the secondary suspension system.

From this research, three novel secondary suspension friction models are proposed that have been developed to work in conjunction with the SIMPACK software package via the co-simulation functionality. These models include the novel local/global friction models, which are used together in MBS to describe the hysteresis and frequency responses of the centre plate/wear liner components as well as increases in these parameters as a function of time and the number of running cycles.

Acknowledgements

Nomenclature

The mathematical symbols and units used throughout this thesis are listed below.

m = Mass (kg)

I = Inertia (kg.m²)

r = Position vector (m)

x, s = Translational displacement (m)

$\dot{x}_1, \dot{x}_2, V$ = Translational velocity (m/s)

$\ddot{x}_1, \ddot{x}_2, a$ = Translational acceleration (m/s²)

θ = Angular displacement (rad)

$\dot{\theta}_1, \dot{\theta}_2, \omega$ = Angular velocity (rad/s)

ω_n = Natural frequency (rad/s)

$\ddot{\theta}_1, \ddot{\theta}_2$ = Angular acceleration (rad/s²)

F = Applied force (N)

F$_f$ or **T** = Friction force (N)

M = Applied moment (Nm)

τ$_f$, T_{cp} = Frictional torque (Nm)

T_c = Coulomb frictional torque (Nm)

T_{brk} = Breakout frictional torque (Nm)

$T_{brk-\omega_{th}}$ = Breakout torque at the velocity threshold (Nm)

c_v = Transition coefficient (s/rad)

ω_{th} = Velocity threshold limit (rads/s)

K = Translational stiffness coefficient (N/m)

K_τ = Torsional stiffness coefficient (Nm/rad)

K_w = Bogie warp stiffness (Nm/rad)

C = Translational damping coefficient (Ns/m)

C_τ = Torsional damping coefficient (Nms/rad)

σ_0 = Bristle contact stiffness (N/m)

σ_1 = Bristle damping coefficient (Ns/m)

σ_2 = Viscous damping coefficient (Ns/m)

z = Average deflection of the bristle (m)

$g(\dot{\mathbf{x}})$ = Stribeck effect (N)

v_s = Stribeck velocity (m/s)

j = Stribeck shape factor (j = 2 is commonly used)

u = Initial velocity (m/s)

t = Time (s)

Table of Contents

List of figures

List of tables

1. Introduction

The transportation of freight by rail is suggested to be one the greenest modes of transport in comparison to road, sea and air (Stichel, Orlova, Hecht, & Iwnicki, 2015). The major challenges that the railway freight industry are currently facing however are the capacity constraints, reliability issues and operating costs. These factors in particular mean that infrastructure managers and freight operating companies have to use the restrictive network space effectively without impacting on the network safety or efficiency (MacMahon, 2014) and (Allen, Perez, & Hatt, 2007).

The main reasons for the focused research efforts concerning railway freight vehicle dynamics during the last decade in particular are due to a modal shift driven by commercial and governmental influences stemming from the changing industrial markets around the world, as well as road congestion and air pollution. In the United Kingdom (UK) for example, the government is setting ambitious targets to reduce the net carbon emissions of the nation to zero by 2050. Increasing the levels of rail freight therefore, is seen as part of the solution to achieving these targets (Iwnicki, Stichel, Orlova, & Hecht, 2015) and (Baraniuk, 2018).

In response to these world-wide concerns, the UK rail freight industry is starting to plan and prepare for a potential shift in large volumes of freight from road to rail that could take place in the near future. This transition however poses a number of significant engineering challenges to the rail industry in order to make it successful and effective.

The capacity constraints due to the out-dated network infrastructure is one of the major concerns that needs to addressed. Upgrading the current network to accommodate more freight/passenger services is one option, but the most expensive and inconvenient overall. Whereas the cheaper option, is to increase the axle loads and operating speeds of the vehicles currently in service as well as new vehicles being introduced to the industry. However, this option would involve a significant amount of research effort and revisions of the relevant testing and vehicle acceptance standards. It could also lead to shorter vehicle/track maintenance cycles and therefore, higher operating costs for infrastructure mangers and freight operating companies.

To better understand the impact on vehicle-track interaction, maintenance costs and vehicle performance under more demanding operating conditions; Computer-Aided-Design (CAD) and Multibody Simulations (MBS) software packages have been used extensively in several feasibility studies to design new state-of-the-art rolling stock and infrastructure components in order to cope with demands of the modern railway environment, see for example (Iwnicki, Stichel, Orlova, & Hecht, 2015), (Allen, Perez, & Hatt, 2008), (Ekberg, Ulianov, Dewan, Mortimer, & Jackson, 2013), (Chamaret, Dahraoui, Frugier, Henry, & Le Moal, 2016), (Shackleton, 2015) (Benzin, Johnsson, Stichel, Orlova, & Iwnicki, 2015).

The majority of solutions proposed in these works however, still remain in the conceptual stages apart from one idea, the Sustrail high speed freight vehicle. The reasons why some of the other ideas have not been taken forward by the rail industry, are mainly due to the lack of extensive field/laboratory test data for validating MBS freight vehicle models, so the confidence levels in these models remains low. Also, from a simulation perspective, using simplified friction models with many uncertainties can introduce non-physical effects into the MBS model which can then lead to the wrong conclusions being drawn from the simulation analyses if the simplifying assumptions are not fully understood (Bogojevic & Lucanin, 2014) and (Bruni, Vinolas, Berg, Polach, & Stichel, 2011).

The negative impact to the freight industry as a result of the uncertainties associated with the current friction modelling methodologies applied to freight vehicle MBS models are the longer development

times for new vehicle designs and the costs associated with on-track/laboratory testing. Freight vehicles with novel suspensions for example, have to demonstrate compliance with Regional (e.g. Railway Group Standards (RGS)) and International standards using laboratory/on-track tests. Whereas for passenger vehicles with linear coil springs and hydraulic dampers, results from virtual acceptance tests using validated vehicle models can be used in place of physical tests to demonstrate compliance with the relevant standards.

The gauging methods currently applied to rail vehicles with novel suspension systems during the initial design stages of the manufacturing process, have also been analysed recently and are suggested to be stifling innovation, as well as the potential growth of the rail freight industry. The static gauging method for example, as (Allen, Hatt, & Perez, 2007) explains, was developed before the dawn of computers and the commercialisation of sophisticated MBS and gauging software codes (RSSB, 2013), (Johnson, 2006), (O`Neil, 2007)

The verification of freight vehicle friction models through rigorous physical testing and analysis is therefore, fundamental to gain a better understanding of the simplifying assumptions used in MBS computer codes, yet to date this remains an under-researched field. The scale model laboratory tests and validation procedures presented in this thesis, provides all of the critical modelling parameters and benchmark test data that is needed to develop material specific friction models for freight vehicle suspension components. The new knowledge and understanding gained from this study, could also be used by the rail industry to optimise maintenance schedules and practices, as well as to develop gauging and testing standards optimised for the 21st century rail industry. The following sections discuss the aims and objectives of this research.

1.1. Thesis aims

The main aim of this research is to gain a better understanding of freight vehicle secondary suspension systems and the dry friction damping mechanisms employed in those systems. These aims are explained in points 1 – 6 below:

1) Develop a better understanding of the dynamic behaviour of a freight vehicle secondary suspension system throughout its life-cycle.

2) Design a novel laboratory test-rig to investigate and quantify the friction characteristics of a secondary suspension system using industry standard wear liner materials and the X-Factor vehicle acceptance testing methodology.

3) Identify the main sources of the developing nonlinearities in the secondary suspension and review the current modelling methodologies that are used in Multibody Simulations (MBS) to model, or alternatively, not used to model these effects.

4) Develop a local/global analysis friction modelling methodology that is capable of describing the real-world stick-slip behaviour and evolutionary friction characteristics of different secondary suspension wear liner components.

5) Validate the secondary suspension friction models against the laboratory test data.

6) Implement the validated friction models into a complete rail vehicle model developed in SIMPACK using the MATSIM co-simulation interface. Compare the responses of the validated friction models against the standard models available in SIMPACK and quantify the differences in results.

1.2. Thesis objectives

The specific objectives that were carried out in order to achieve the aims of this research work are discussed in points 1 – 10 below:

1) Review the academic/industrial research work undertaken on friction damped rail vehicles during the last 20-years and document the simplifying assumptions that are used in the testing and modelling methodologies.

2) Collaborate with freight vehicle maintenance depots to obtain the relevant geometric/operating parameters for modelling freight bogies, but also, to better understand the mechanisms causing the secondary suspension failure modes.

3) Implement a scaling strategy that permits the full scale forces and contact stresses to be investigated on a 1:7 scale model centre plate component under laboratory test conditions.

4) Build a simple model of the centre plate system in MATLAB/SIMULINK and compare the responses of this model against the friction models discussed in the literature survey.

5) Use the MATLAB/SIMULINK centre plate model to investigate the dynamic characteristics of the system under the tare, part-laden and laden loading conditions using the range of rotational velocities specified for the X-Factor vehicle acceptance test procedure.

6) Collaborate with industry suppliers to obtain wear liner components that are actually used in freight vehicle suspension systems. This requirement will improve the accuracy of the laboratory tests results and add more value to the research.

7) Measure the mass properties of the wear liner samples and the surface roughness profiles of the centre plates/wear liners in a pre/post-test analyses in order to quantify the wear rates of these components.

8) Carry out several rotational benchmarking tests on the Instron fatigue testing machine under 1:7 scale centre plate loads that are representative of the real world tare, part-laden and laden operating conditions.

9) Post-process the laboratory test data in order to obtain the critical system parameters for the different centre plate/wear liner samples. These parameters included the normal load and contact pressures, as well as the effective stiffness and damping properties of these components. The natural frequencies, frictional torque responses and the Coefficient`s of Friction will also be quantified from the laboratory test results.

10) Validate the 1:7 scale centre plate friction models using the laboratory test data as well as the tolerances for measurement/simulation matching errors specified in the Railway Group Standard, GM/RC2641.

1.3. Research methodology and thesis structure

The research methodology used to investigate and quantify the dynamics of the centre plate system is shown in Figure 1.1. The friction characteristics of the centre plate/wear liner components (such as the Coefficient`s of Friction (COF), the evolution in the COF parameters over time, the torsional contact stiffnesses, natural frequencies and the viscous damping properties of these components for example) are central to this research. The key analysis techniques that have been used throughout this work to develop a better understanding of the wear liner friction characteristics, are also shown around the periphery.

The first stage of this research included an in-depth literature review of the friction testing and modelling methodologies that are used in MBS to describe dry friction suspension components. The

findings from this review are discussed in chapter 2. Laboratory tests were then carried out on a 1:7 scale centre plate system to generate new benchmark data for a range of different wear liner materials. The third stage involved post-processing the test data to obtain the COF values, torsional stiffness coefficients and natural frequencies for the wear liner samples. The fourth element of this research work involved calculating the X-Factor values from the benchmark test parameters. The results from the laboratory testing are discussed in chapter 5.

The fifth element of the research work involved building an equivalent dynamic model of the 1:7 scale centre plate system in MATLAB/SIMULINK. The behaviour of this model was then investigated using the COF, stiffness and damping parameters that were pre-calculated from the laboratory test data. After completing these simulations, the responses of the secondary suspension friction models were then validated using the frictional energy measurements from specific test cases. The simulation results are discussed in chapter 6.

The MATLAB/SIMULINK centre plate/wear liner friction models were also developed to carry out co-simulations with SIMPACK for the final part of this research work. These component models could then be incorporated into a complete SIMPACK vehicle model in the future. The simulation results from the secondary suspension friction models however, have led to a better understanding of the different simplifying assumptions used in MBS friction modelling methodologies and how these impact on the accuracy of the model predictions, as well as the computational times of the simulations. These findings are discussed in chapters 4, 6 and 7.
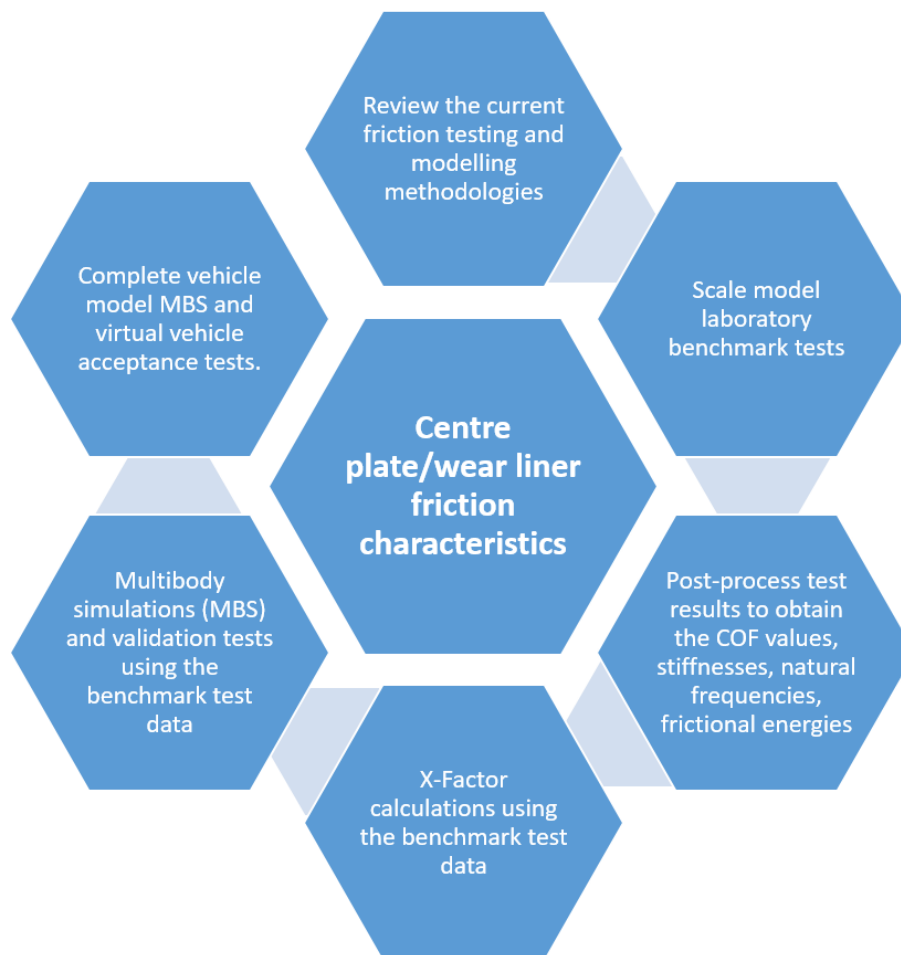
Figure 1.1: Key elements of the friction testing and modelling research methodology.

2. Literature review

2.1. Introduction

The literature review in the following sections discusses the basic designs of Y25 and three-piece bogies as well as the differences in the suspension arrangements and the friction damping mechanisms. The on-going research efforts into freight vehicle dynamics and state of the art modelling methodologies are also reviewed, as well as the relevant field/laboratory tests that are used to validate these modelling and analysis methods. The findings from this review will then be used to identify the current gaps in knowledge surrounding freight vehicle dynamics and also, any areas where improvements can then be implemented.

2.2. Y25 bogie design

The Y25 bogie is used throughout Europe and is designed to run at 100 km/h with a 25 tonne (t) axle load, or at 120 km/h with a 20 t axle load (Adtranz, 2000). This bogie can be set-up to accommodate different types of wagons including coal hoppers, oil tankers and flatbed wagons for carrying shipping containers. Figure 2.1 shows a simulation model of a Y25 bogie as well as a close-up of the primary suspension components.

The main components in the primary suspension are the axle boxes which are connected to the wheelsets via cylindrical-roller bearings. The nested in-board/out-board tare and laden coil springs then connect the axle boxes to a rigid H-shaped bogie frame. The in-board tare springs however, are connected via the spring cap, connecting pins and Lenoir links which transfers the load from the springs to the pusher.

The clearances between the tare/laden springs in the vertical direction then gives rise to a non-linear stiffness characteristic. The suspension characteristics are also non-linear in the longitudinal and lateral directions due to the inclination of the Lenoir links and the 4 mm of longitudinal clearance between the spring cap/pusher as well as the $\pm$ 10 mm of lateral clearance between the axle boxes/bogie frame (Boronenko & Orlova, 2006) and (Bruni, Vinolas, Berg, Polach, & Stichel, 2011).
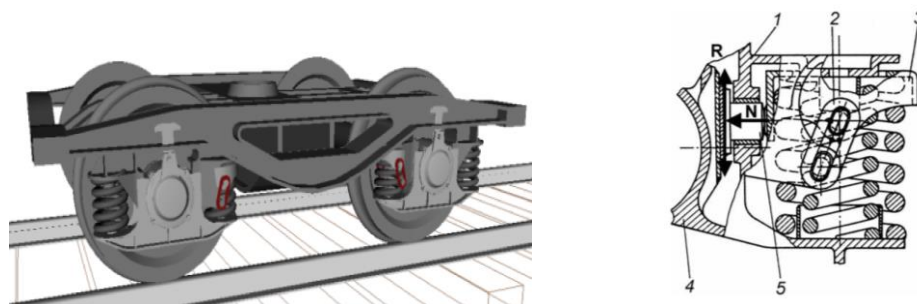
Figure 2.1: (Left) Y25 freight bogie (Kovalev, et al., 2009). (Right) Load-dependent friction damping system: (1) Bogie frame, (2) Lenoir link, (3) Spring cap, (4) Axle box and (5) Pusher/Piston (Hecht, 2007).

The primary suspension is then damped by dry friction in the vertical and lateral directions via the friction surfaces on the axle boxes/bogie frame and pushers. The friction forces in this system however, are dependent on the vertical load supported by the inboard tare springs only. Due to the inclination of the Lenoir links, a component of the vertical force is transmitted to the friction surfaces which increases in proportion to the axle load (Evans & Rogers, 1998) and (Bruni, Vinolas, Berg, Polach, & Stichel, 2011).

The secondary suspension arrangement as can be seen in Figure 2.2, comprises of a spherical centre bowl and two elastic side bearers. The centre bowl component allows yawing, pitching and rolling motions and provides friction damping in these directions as well. Whereas translational motions in the horizontal plane are constrained. The two elastic side bearers support a load of approximately 16 kN each and provide additional roll stiffness and damping to the yawing motions. These components have six Degrees-of-Freedom (DOF) within the vertical and longitudinal clearance limits which are seen to be 12 mm and $\pm$ 1 mm respectively, see Figure 2.3 (Evans & Rogers, 1998).

The steel surfaces on the secondary suspension components are then lined with low friction polymer or composite wear liners before connecting the wagon body to the bogie. The main function of the wear liner is to reduce the bogie rotational resistance by preventing steel-on-steel contact and also, to prolong the useful service life of the suspension components.
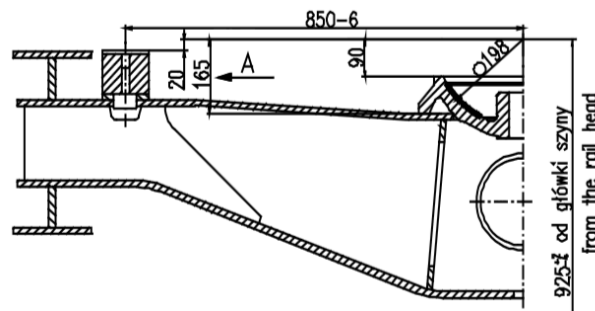
Figure 2.2: Y25 secondary suspension system showing the positions of the side bearers relative to the centre pivot/bowl (Adtranz, 2000).
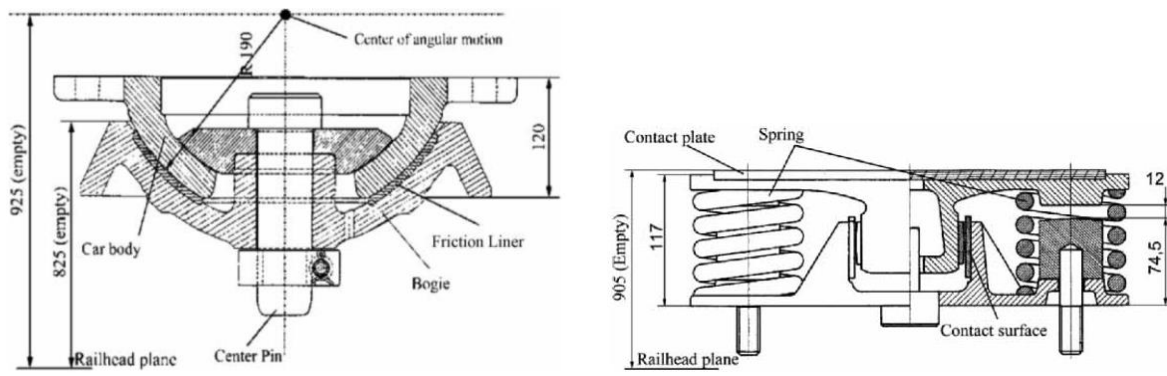
Figure 2.3: (Left) Centre bowl/pivot dimensions. (Right) Elastic side bearer dimensions and clearances (Allen, Perez, & Hatt, 2008).

2.3. Three-piece bogie design

The three-piece bogie is more popular in countries such as China, Russia, Australia, South Africa, Sweden and North America. This design speed of this vehicle is 120 km/h under a 25 tonne (t) axle load, but can be up to 30 – 32.5 t per axle although not at this speed, which is the case on some iron ore freight lines in Sweden and North America, see for example (Fergusson , Frohling, & Klopper, 2008) or (Tournay, 2011). Appendix A contains a diagram of the master/slave freight train arrangement and a description of the geometric/operating parameters.

The basic design includes two cast steel side frames which are connected to the wheelsets via the horn guides, bearing adapters and elastomeric shear pads. The shear pads have a high stiffness and provide a small amount of flexibility as well as friction damping between the wheelsets/horn guides in the

longitudinal/lateral directions. This arrangement however, leads to a higher un-sprung mass in comparison to the Y25 bogie and therefore, larger forces at the wheel/rail contacts, see Figure 2.4.

The tare and laden nested spring groups at each end of the bolster also have clearances in the vertical direction and provide the connection between side frames/bolster. The relative motions between these components are then damped in the vertical and lateral directions by the friction wedges and wear plates on the side frames/bolster, see Figure 2.5. Wedge suspensions and components are also reviewed in (Wu, Cole, Spiryagin, & Sun, 2014) and (Ashtiani, 2017).

The friction damping in three-piece bogie suspension can be either constant or variable depending on the type of vehicle. The Barber S-2 wedge system for example, supplies a constant normal force to the friction surfaces on bolster/side frames under any load. The wedge in this system as can be seen in Figure 2.5, sits on a pre-loaded control spring which is separated from tare/laden spring nests by the pockets in the bolster. The wedge in the Ride Control system on the other hand, sits directly on top of the side spring and therefore, supplies a variable normal force to the friction surfaces, which increases in proportion to the vertical load supported by the tare/laden spring nests (Amsted Rail Company, 2014).
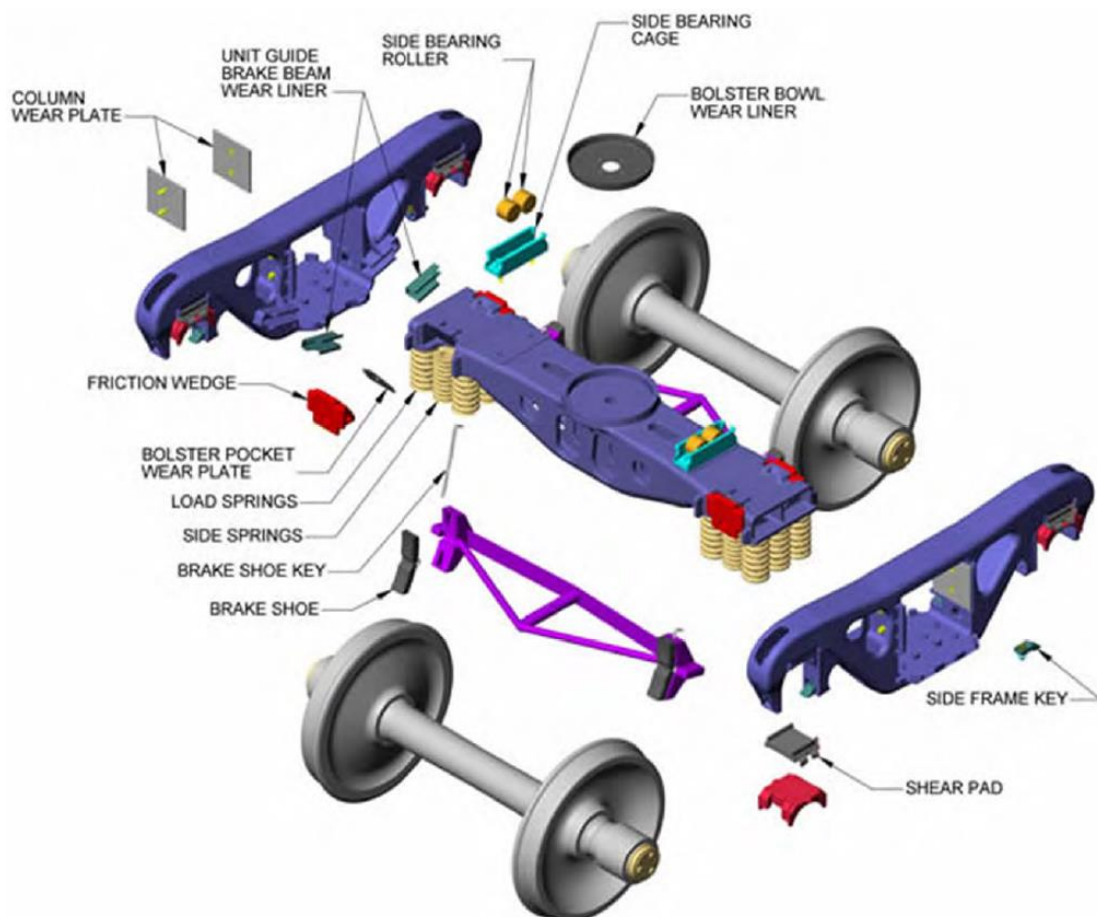
Figure 2.4: Barber S-2 three-piece bogie (Wolf, 2013).
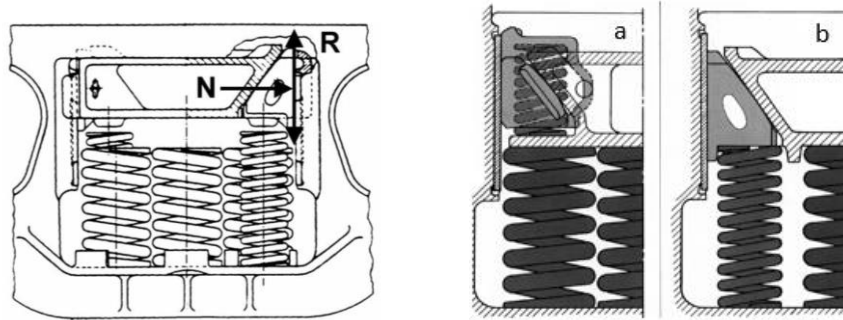
Figure 2.5: (Left) Three-piece bogie spring nests and friction wedges (Hecht, 2007). (Right) Barber S-2 wedge system (a) and the Ride Control wedge system (b) (Wolf, 2013).

The secondary suspension comprises of a flat circular centre plate and wear liner that provides friction damping to the translational and yawing motions in the horizontal plane. Under unfavourable running conditions however, rim contact can take place between the wagon body/bolster centre plates which can lead to high contact pressures and accelerated levels of wear and damage to the suspension components, see Figure 2.6. The side bearers on the three-piece bogie can be either Constant Contact Side-Bearers (CCSB), CCSB with rollers or side bearers with clearances that only come into contact with the wagon body slide plates during curving (Olshevskiya, Yang, & Kima, 2015) and (Boronenko & Orlova, 2006).

The CCSB blocks however can have a negative influence on the running dynamics of the vehicle if they are not properly maintained. These components as can be seen (Figure 2.6 (Right)), can start to work loose from their retaining boxes, which can then lead to higher levels of bogie rotational resistance, bogie crabbing on curve entry/exits as well as increased levels of wheel-squeal and tracking issues, see for example (Tickell, Downing, & Jacobsen, 2004) and (RAIB, 2007). The following section discusses freight vehicle maintenance issues and running costs.
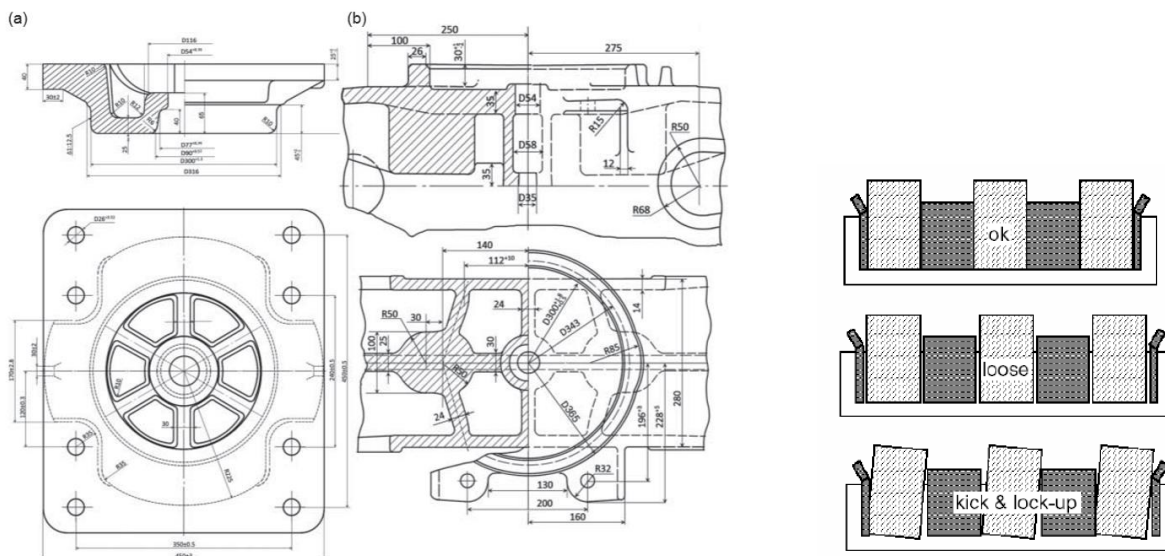
Figure 2.6: (Left) Three-piece bogie centre plate dimensions (Olshevskiy, Kim, & Yang, 2015). (Right) Stucki CCSB arrangement (Tickell, Downing, & Jacobsen, 2004).

2.4. Freight vehicle maintenance issues and running costs

Freight vehicles operate in harsh environments and carry a variety of bulk goods over long distances including coal, iron ore and industrial waste products. To reduce the maintenance costs throughout the vehicle life-cycle (30 – 36 years), rolling stock designers use dry friction dampers in the suspension components due to their simple design, low cost and easy maintenance. (Boronenko & Orlova, 2006) and (Kohli, 2013).

The moving parts in the primary, central and secondary suspensions however, wear out over time as well as suffer from catastrophic failures in service. These parts then have to be replaced during routine as well as scheduled maintenance procedures to ensure the bogie performance remains within the acceptable limits for the vehicle`s homologation. Maintenance issues and the running costs associated with freight vehicles therefore, have to be carefully managed and controlled by freight operating companies as these factors have a significant influence on the operational reliability of the fleet and the profit margins of the company (Tournay & Wu, 2011).

The maintenance costs of three-piece bogie were also studied as part of the Association of American Railroads (AAR) Strategic Research Initiatives Program (Tournay, 2011). The aim of this work was to better understand the roots causes of unpredictable maintenance issues and wheelset life under high axle loads (32.5-tonne). This analysis suggested that the average costs of wheelset replacements per year were more than $800 million and the average life of a wheelset was shown to range from less than 300,000 kilometres (km) to more than 1.2 million km.

The main causes of wheelset replacements were also quantified and shown to be attributed to tread damage (67%), wear (27%) and other causes (6%). Thermal Mechanical Shelling (TMS) and wheel flats were classified as the tread damage mechanisms leading to High Impact Wheels (HIW). Whereas replacements due to wear mechanisms, included wheelsets with asymmetric flange and tread wear.

TMS was suggested to have been caused by unreleased handbrakes as well as high traction forces during curving due to low bogie warp stiffness. High angles of attack of the leading wheelsets in curves also caused crack bands to form around the wheel tread tape line. Whereas, the asymmetry of the brake rigging forces and the position of the brake block relative to the wheel tread as well as the abrasiveness of the blocks, were suggested to be causing the asymmetric wheel wear and poor wheelset/bogie tracking behaviour (Tournay, 2011). The design specifications and loading parameters of a two-unit freight train are shown in Appendix A (Stichel, Jonsson, & Nia, 2014).

Several design improvements were then proposed to reduce High Impact Wheels (HIW) on the North American rail networks. These included optimising the clearances and stiffness characteristics of the axle box constraints and reconfiguring the brake rigging system to provide even braking forces. An alternative brake block shape to mitigate the development asymmetric flange wear and high contact conicities was also suggested, as well as cross anchors and body coupled linkages to increase the warp stiffness of the bogie under heavy axle loads (Tournay, 2011).

Further research by (Kalay, French, & Tournay, 2011) also looked into the safety and economic benefits of introducing more bogie condition monitoring systems and wayside detectors along the North American rail network. This work was carried out as part of the Advanced Technology Safety Initiative (ATSI) approach to freight vehicle maintenance. This automated system works by collecting vehicle performance data from various condition monitoring systems along the route which is then post-processed and compared to the performance limits set by the American Association of Railroads (AAR).

Vehicles that are near to or exceeding these performance thresholds are brought to the attention of the owner who is then given a finite window of opportunity to carry out proactive maintenance measures in order to prevent further damage to the infrastructure. The final conclusions to this

research were that the implementation of the ATSI in North America had led to a significant reduction in accidents rates caused by broken rails/wheels, bogie hunting and bearing failures. The estimated net savings in equipment costs during 2008 due to the implementation of more condition monitoring systems along the network were suggested to be in the region of $227 million (Kalay, French, & Tournay, 2011).

The last set of costs to consider are those associated with track access charges. In the UK for example, freight vehicles with heavy axle loads and novel suspensions, incur higher Variable Usage Charges (VUC) in comparison to more track friendly vehicles, see for example (NetworkRail, 2019). The following section discusses the gauging methodologies applied to railway freight vehicles.

2.5. Railway vehicle gauging methodologies

Railway vehicles are designed and built to a maximum loading gauge that is vehicle specific, whereas the infrastructure buildings, tunnels and platforms are built to a minimum structure gauge. A clearance is then included between the two gauges that allows different types of vehicles to pass safely through the network. These clearances provide safety margins due to unknown factors and also take into account the swaying and overthrow motions of the vehicle during curving (RSSB, 2013).

Since the inception of railways in the United Kingdom (UK) nearly 200-years ago, freight and passenger vehicles have become progressively larger as well as faster and in the case of passenger trains, more comfortable. This has led to a reduction in the original design clearances over the decades due to modern passenger vehicles with air suspensions and tilting mechanisms occupying larger kinematic envelopes in comparison to their predecessors (Johnson D. M., 2006) and (RSSB, 2013).

The gauging methodologies that are applied to passenger and freight vehicles in the UK however, are different. The design dimensions of passenger coaches are described by the C series gauges and freight wagons by the W series. The C1 and W5 gauges for example, are hand calculated using static gauges and fixed clearances. This method was then updated in 1951 to the geometric gauge which took the suspension movements into account. The geometric gauge allocated 100 mm of clearance for the vehicle moving on the suspension and 50 mm for track alignment errors, giving a total clearance of 150 mm (Johnson D. , 2006) and (RSSB, 2013).

Air suspensions were then introduced to passenger vehicles from the 1970`s onwards to try and improve passenger comfort on poor quality track. The softer suspensions however, led to larger kinematic envelopes which exceeded the safety clearances specified by the static gauging methods. On review, rail engineers identified that the clearances specified by the static gauges were overly conservative and that the network space could be used more effectively by taking the actual kinematic envelope of the vehicle into account. This gauging method however, is based on quasi-static hand calculations which are not well suited to describing the dynamics of freight vehicles with many strong nonlinearities due to the friction damped suspension (Allen, Perez, & Hatt, 2008) and (Johnson D. M., 2006).

With the advances in computer based Multibody Simulations (MBS) tools over the last two decades however, rail engineers have started to develop more scientific based approaches to gauging. The dynamic gauging method uses MBS to generate the vehicle motions over specific track files which are saved into a spreadsheet. The gauging calculations for different network routes are then carried out using specific software such as CLEARROUTE or D-GAUGE which can compare the simulated vehicle movement to the position of the measured infrastructure (Allen, Perez, & Hatt, 2008).

In the research work of (Allen, Perez, & Hatt, 2008), a dynamic gauging analysis was carried out on a full non-linear vehicle model of a Y25 bogie that was developed in VAMPIRE. This model was then

validated against test data using equivalent sway test simulations with the vehicle model in the tare and laden loading conditions. In the tare condition, the agreement between the measurements/simulation results for the bottom corners of the wagon body was good, but not as good for the top corner. Whereas in the laden condition, the agreement was good for the top corner and not as good for the bottom corner (Allen, Perez, & Hatt, 2008).

Dynamic simulations were then carried out on the validated vehicle model using P10 worn wheel profiles to investigate the vehicle model response as a function of speed to track irregularities and curves with different levels of cant. The gauging calculations were then carried out in accordance with the GN/LR0002 document, Guidance on VAMPIRE, to derive the kinematic envelope data for post-processing in CLEARROUTE. This software used the mean values and standard deviations of the lateral, vertical and roll displacements of the wagon body, bogies and wheelsets to calculate the clearances (Allen, Perez, & Hatt, 2008).

The dynamic gauging results were then compared to the W10 static gauge for curved and straight sections of track, see Figure 2.7 (Left). The dynamic gauge can be seen, clearly suggests that more clearance could be used up on freight routes. This was also shown to be the case in a tight tunnel, as can be seen from the results on the right. However, it was also mentioned that the validation process was extremely challenging due to a lack of reliable freight vehicle modelling methodologies, incomplete test data and parameter uncertainty relating to the coefficients of friction for the suspension components. A more detailed discussion on the different types of gauging methods used in the UK as well as Europe can be found in (Johnson D. M., 2006). The following section discusses railway vehicle dynamic simulations.
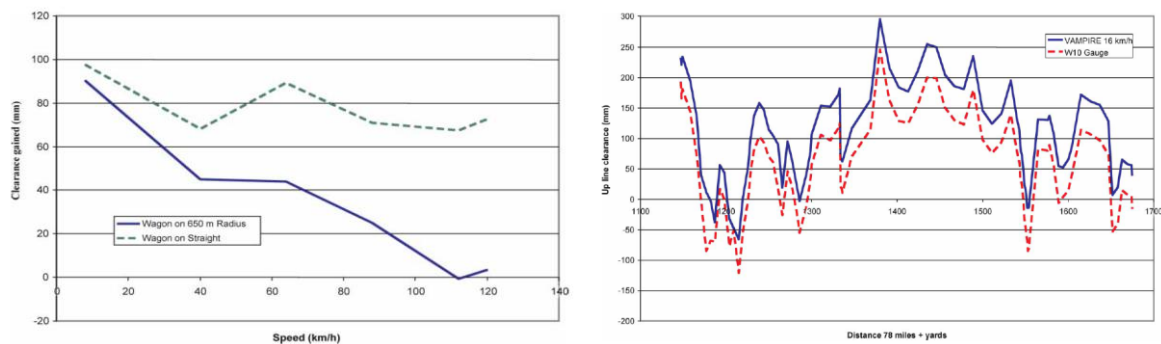
Figure 2.7: Dynamic gauging versus W10 static method. (Left) Clearances gained by the dynamic gauging method. (Right) Clearances in a tight tunnel (Allen, Perez, & Hatt, 2008).

2.6. Railway vehicle dynamic simulations

The analysis of railway vehicle dynamics using Multibody Simulation (MBS) software packages such as VAMPIRE, SIMPACK, ADAMS and MATLAB now plays an important role in vehicle/infrastructure design processes, virtual vehicle acceptance tests, dynamic gauging studies and accident investigations. These software packages are also used by the rail industry as a cheaper and faster alternative to prototype/field testing (Berg & Evans, 2009).

The basic mathematical frame work to develop the equations of motion for the vehicle-track system in the MBS environment, are generally developed using Newton`s second law of motion given in Equation (2.1) This second order differential equation is then solved iteratively using time stepping integration techniques. An equivalent form of (2.1) can also be applied to develop the equations of motion for rotating systems. It should also be pointed out that Lagrangian or Hamiltonian mechanics

are also used in numerical routines by some engineers to analyse complex dynamic systems (Shackleton, 2009) and (Berg & Evans, 2009).

$$\mathbf{F} = m\ddot{\mathbf{x}} + c\dot{\mathbf{x}} + k\mathbf{x} \qquad\qquad (2.1)$$

The equation of motion given in (2.1), states that the vector sum of the externally applied forces $\mathbf{F}$, are equal to the sum of the reactive forces, which are internal to the system. These forces are the mass, damping and stiffness of the system, which are labelled as m, c and k respectively. Whereas the acceleration, velocity and displacement vectors, are labelled as $\ddot{\mathbf{x}}$, $\dot{\mathbf{x}}$ and $\mathbf{x}$. Numerical models of the vehicle-track system are then developed using rigid as well as flexible bodies to represent the mass of the wheelsets, bogie frame and car body. These bodies are then connected together using different combinations of massless force elements to describe the damping and stiffness characteristics of the suspension (Meriam & Kraige, 2012).

The nonlinearities in the suspensions such as the friction force characteristics and the clearances between the tare/laden springs and axle boxes/bogie frame, are then modelled using constraints and either pre-defined or user-defined force elements. The Degrees of Freedom (DOF) for each body in the vehicle model are then prescribed by the user before running and validating the model. The MBS packages discussed above however, all make simplifying assumptions in the mathematical formulations to reduce the solution times which leads to uncertainties/errors into the models. These then need to be fully understood and justified using engineering judgement and experience before implementing any physical actions based on the simulation results.

In the simulation benchmarking exercise carried out by (Iwnicki, 1999) for example, the modelling methodologies and performance of five rail vehicle MBS packages were compared and reviewed (VAMPIRE, NUCARS, SIMPACK, GENSYS, ADAMS-RAIL). The dynamic behaviour of two simplified vehicle models including a passenger coach with two bogies and a laden two-axle freight vehicle with load dependent friction damping, were then simulated on four different track cases using quasi-static and transient analysis techniques.

The results from this study compared the Eigen values of the rigid body masses, the derailment ratios, wheel/rail contact forces, contact angles, simulation times and the positions of the rigid bodies relative to the track reference frame. Although there was a good agreement between the majority of results produced from all five packages, the largest differences in performance were for the contact angles and solution times. The times for the first test case simulations on the passenger vehicle for example, were shown to range between 62 – 3591 seconds (Iwnicki, 1999).

The main conclusions from this work were that further research was required to better understand the small differences in the contact patch parameters of different MBS packages as well as the friction modelling methodologies. It was also recommended that benchmarking exercises should be continuous processes in order to keep pace with the latest developments in MBS software packages. The following sections discuss the different modelling methodologies and force element combinations that are used to describe the dynamics of the primary and secondary suspension components (Iwnicki, 1999).

2.7. Primary suspension models

Primary suspension models are developed using different combinations of springs, viscous dampers, clearances and friction elements. An in-depth review of the modelling methodologies used by different researchers to describe rail vehicle suspension components was undertaken by (Bruni, Vinolas, Berg, Polach, & Stichel, 2011). This work focused on the issue of modelling uncertainties due

to a lack of test data, accurate vehicle parameters and unclear modelling procedures. The models that apply to freight vehicle suspensions will be discussed further throughout this section.

The friction characteristics of the primary/central suspensions of the Y25 and three-piece bogies can be modelled using a variety of different methods. These include the Coulomb model of dry friction which is the most popular overall and is available in all Multibody Simulations (MBS) software packages, see Equation (2.2). The Coulomb friction force vector $\mathbf{F_c}$, is proportional to the normal force, N and the Coefficient of Friction (COF), μ. The instantaneous friction force of the Coulomb model however, is non-differentiable in the vicinity of zero velocity which can lead to numerical issues if these discontinuities are not handled correctly, see Figure 2.8 (Bruni, Vinolas, Berg, Polach, & Stichel, 2011).

$$\mathbf{F_c} = \mu.N \tag{2.2}$$
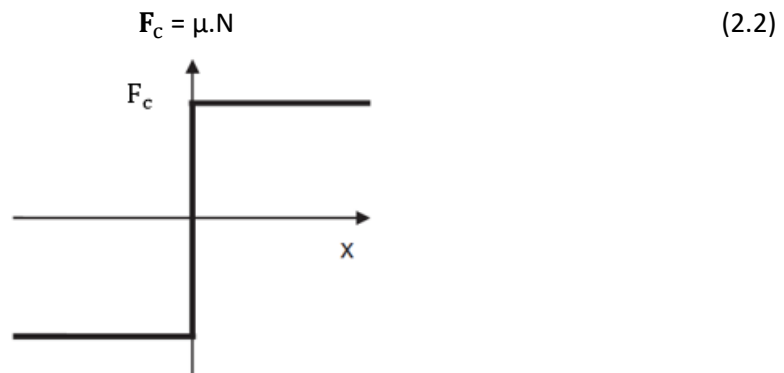
Figure 2.8: Force characteristic of the St Venant/Coulomb dry friction element (Bruni, Vinolas, Berg, Polach, & Stichel, 2011).

The numerical difficulties associated with the Coulomb model however, can be minimised by connecting a coil spring k_s, in series with a friction element, see Figure 2.9. This force element combination produces the force-displacement characteristics shown in Figure 2.10, which is in closer agreement with measurements obtained from laboratory tests (Moore, 1975), (Sextro, 2002), (Jonsson & Stichel, 2009), (Tanaka, Iida, Iida, Suzuki, & Watanabe, 2016), (Ruderman & Bertram, 2011) and (Dahl, 1968).

The solid model of dry friction that was developed by (Dahl, 1968) for example, established a relationship between the pre-sliding behaviours that were observed during laboratory tests and the mechanical properties of ductile/brittle materials, see Figures 2.11. From these stress/strain relationships, it can be seen that the friction force comprises of two components. These components are the breakaway/stiction force, which is related to the ultimate stress that can be supported by the asperity junctions in contact. Whereas the Coulomb force, is related to the rupture stress of the asperity junctions, which is slightly lower (Dahl, 1968).
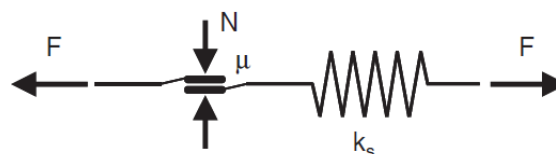
Figure 2.9: St Venant/spring element connected in series (Bruni, Vinolas, Berg, Polach, & Stichel, 2011).
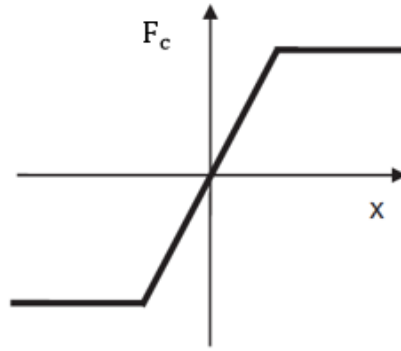
Figure 2.10: Force-displacement curve for Coulomb friction element connected in series with a linear coil spring (Bruni, Vinolas, Berg, Polach, & Stichel, 2011).
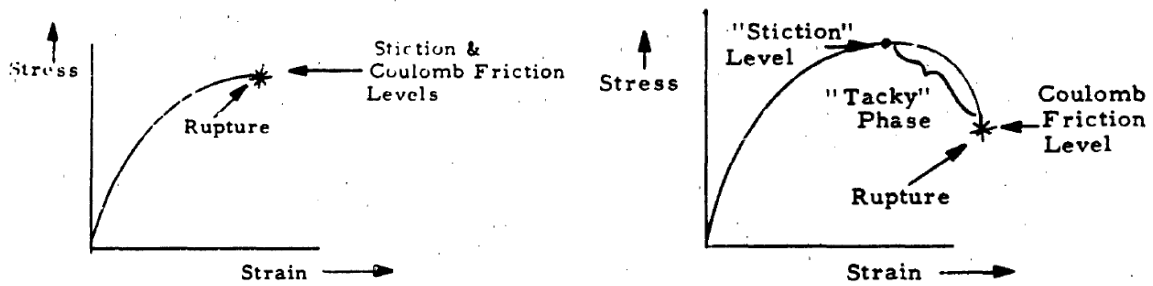
Figure 2.11: (Left) Stress-strain curve for a brittle material. (Right) Stress-strain curve for a ductile material (Dahl, 1968).

The characteristics of the friction model are then prescribed using the piece-wise approximation given in Equation (2.3). The friction force $\mathbf{F_f}$ taking into account the pre-sliding displacements, is either equal to the applied force $\mathbf{F}$ when this parameter is less than the pre-calculated Coulomb force $\mathbf{F_c}$. Whereas, if the applied force is equal to or greater than the Coulomb force, the friction force $\mathbf{F_f}$ is constant and equal to $\mathbf{F_c} \cdot \left(\frac{v}{|v|}\right)$. The friction force is then calculated and updated during each step of the MBS and substituted into the equation of motion given in Equation (2.4).

$$\mathbf{F_f} = \begin{cases} \mathbf{F} & \text{if } \mathbf{F} < \mathbf{F_c} \\ \mathbf{F_c} \cdot \left(\frac{v}{|v|}\right) & \text{elseif } \mathbf{F} \geq \mathbf{F_c} \end{cases} \tag{2.3}$$

$$\mathbf{F} = m\ddot{x} + c\dot{x} + kx + \mathbf{F_f} \tag{2.4}$$

To model the effects of a load dependent friction force, the normal axis of the friction element can be coupled to another force element, such as spring and viscous damper arranged in parallel, see picture (a) in Figure 2.12. The COF characteristics of the exponential and static-dynamic friction models are also shown in picture (b), which are available in some MBS packages, but are challenging to validate without specific test data. This limitation also applies to the regularisation functions shown in (c), which were used by (Bosso, Gugliotta, & Soma, 2000) to describe the two-dimensional friction damping in the primary suspension of the Y25 bogie. For a detailed discussion on the different regularisation methods, see (Wriggers, 2006).
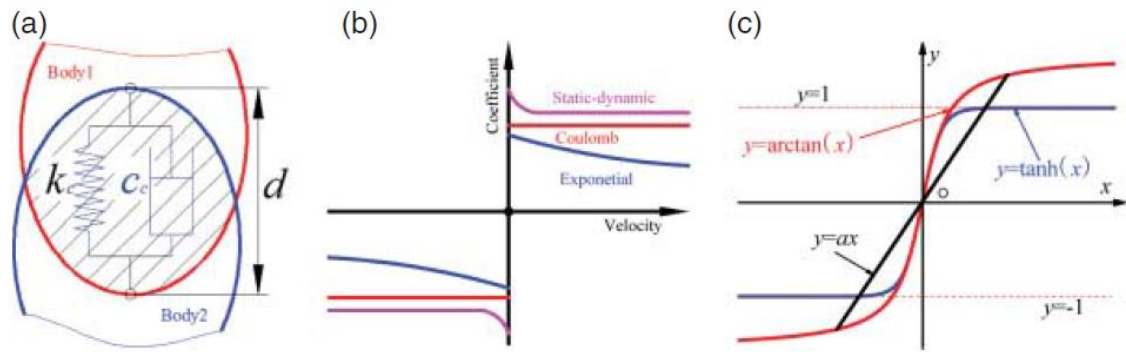
Figure 2.12: (a) Dynamic normal contact model. (b) Different friction models. (c) Regularisation functions (Wu, Cole, Spiryagin, & Sun, 2014).

In the work of (Piotrowski, 2010), a non-smooth rheological friction model was developed to describe the damping forces in the Y25 primary suspension, see Figure 2.13. The theory behind this model was then validated using MBS and the simple two-degree-of-freedom mass-spring oscillator shown in Figure 2.14. The smoothing influence on dry friction when exposed to medium frequency dither in the x and y directions was then investigated. Dither excitations in the context of freight vehicles for example, are generated by the surface irregularities at the wheel/rail interfaces during rolling contact. The frequency of these excitations under normal operating conditions, is then suggested to be several times higher than the bounce mode of the wheelset (Piotrowski, 2010).

The displacement responses of the mass-spring oscillator shown in Figure 2.15, were carried out with the dither amplitude and forcing frequency in the x-direction, set to 0.6 mm and 127 Hz respectively. Whereas in the y-direction, these parameters were set to zero, the dither therefore, is one-dimensional and co-linear with the x-axis. From these responses, it could be seen that the friction damping in the x and y directions when dither is applied to the model is significantly lower, but more so in the x direction. Also, when dither is not applied, there is a Non-Zero Residual Displacement (NZRD) in the x-direction when the mass stops moving. Dither and the smoothing influence this has on the Y25 suspension however, does not normally get taken into account in rail vehicle MBS (Piotrowski, 2010).
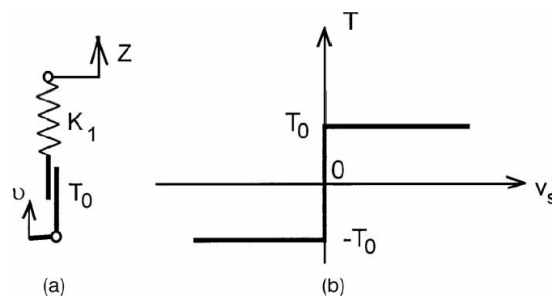
Figure 2.13: (a) Mechanical model. (b) Non-smooth Coulomb friction force (Piotrowski, 2010).
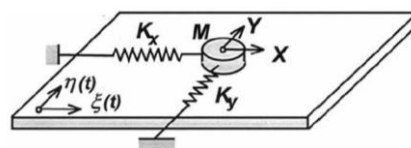
Figure 2.14: Two-degree-of-freedom mass-spring oscillator including the non-smooth Coulomb friction model and dither (Piotrowski, 2010).
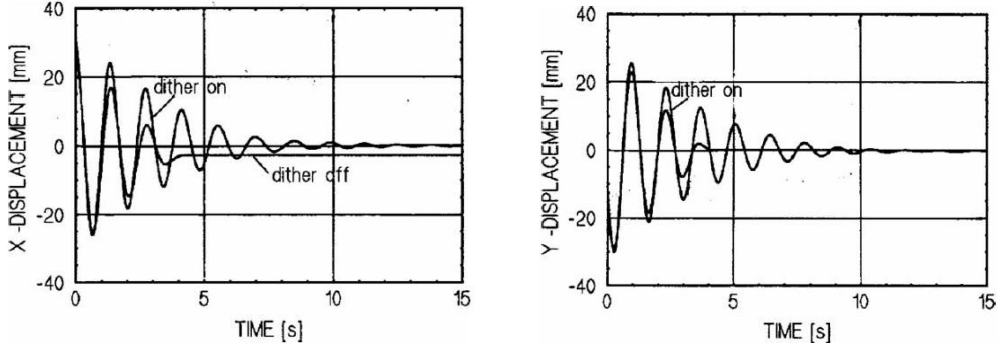
Figure 2.15: Displacement responses in the x and y directions with/without dither applied (Piotrowski, 2010).

The friction force vector **T** in the non-smooth rheological model as (Piotrowski, 2010) explains, is calculated using a "differential succession involving a contingent derivative of the non-smooth Coulomb force", see Equations (2.5) and (2.6). The function, $\Theta \in R^2$ is a set of permissible friction forces in two dimensional space, but the friction force vector as can be seen from Figure 2.16, is bound by the closed convex set Θ. Therefore, if $\phi(T) = 0$, the friction force is called the breakout force and the power of dissipation during the sliding phase of motion is calculated using Equation (2.7), where V_s^t is the sliding velocity vector.

The friction force during sliding is then assigned to the set, $T \in R^2$, which is when the power dissipation is at its maximum level, leading to the inequality shown in Equation (2.8), where $\widetilde{T} \in R^2$ is the so-called "variational" friction force. The non-smooth rheological model also takes anisotropic friction into account by allowing the friction forces in the x and y directions to be set independently, see Equation (2.9), which is another system property that is often neglected in rail vehicle MBS (Piotrowski, 2010).

$$\mathbf{T} \in R^2, \quad \mathbf{T} \in \Theta, \quad 0 \in \Theta \tag{2.5}$$

$$\Theta = \{T \in R^2, \; \phi(T) \leq 0\} \tag{2.6}$$
$$V_s^t . \mathbf{T} \geq 0 \tag{2.7}$$

$$V_s^t . \mathbf{T} \geq V_s^t . \widetilde{\mathbf{T}} \quad \forall \, \widetilde{\mathbf{T}} \in \Theta \tag{2.8}$$

$$\Theta = \left\{ \mathbf{T} \in R^2, \; \phi(T) = \left(\frac{T_x}{T_{0x}}\right)^2 + \left(\frac{T_y}{T_{0y}}\right)^2 - 1 \leq 0 \right\} \tag{2.9}$$
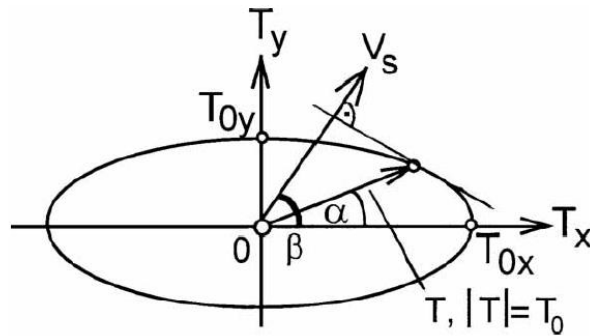
Figure 2.16: Smooth convex set with exemplary slip velocity and friction force (Piotrowski, 2010).

In the convex set shown above, β is the slip direction angle and α is the direction angle of the two-dimensional breakout force, $\mathbf{T_0}$. This parameter is calculated from the friction force components in

the x and y directions, T_{0x} and T_{0y}, using Equation (2.10) and the friction force direction angle is given in Equation (2.11).

For isotropic friction conditions $\alpha = \beta$, whereas for anisotropic friction, the direction angle is calculated from the principle of maximum power dissipation. The friction force in the rheological model is also described by the set of first order differential equations given in Equation (2.12), which makes it suitable to use in rail vehicle MBS. The dummy argument [u], is used to switch the sign of the friction force during the sliding phases of motion, see Equation (2.13). The slip direction angles are then calculated using Equations (2.14) and (2.15), where $\dot{\xi}$ and $\dot{\eta}$ are the dither profiles in the x and y directions respectively (Piotrowski, 2010).

$$\mathbf{T_0} = \frac{T_{0x}\,T_{0y}}{\sqrt{T_{0x}{}^2 \cos^2(\alpha) + T_{0y}{}^2 \sin^2(\alpha)}} \tag{2.10}$$

$$\tan(\alpha) = \frac{T_{0y}{}^2}{T_{0x}{}^2}\tan(\beta) \tag{2.11}$$

$$\dot{\mathbf{T}} = \begin{cases} k_1(\dot{v} - \dot{z}) & \text{if } |T| < T_0 \\ -[-k_1(\dot{v} - \dot{z})]^+ & \text{if } T = +T_0 \\ [k_1(\dot{v} - \dot{z})] & \text{if } T = -T_0 \end{cases} \tag{2.12}$$

$$[u]^+ = \begin{cases} u & \text{if } u \geq 0 \\ 0 & \text{if } u < 0 \end{cases} \tag{2.13}$$

$$\cos(\beta) = \frac{\dot{X} - \dot{\xi}}{D} \text{ and } \sin(\beta) = \frac{\dot{Y} - \dot{\eta}}{D} \tag{2.14}$$

$$D = \sqrt{\left(\dot{X} - \dot{\xi}\right)^2 + \left(\dot{Y} - \dot{\eta}\right)^2} \tag{2.15}$$

The non-smooth rheological friction model was then used in a two axle freight vehicle model which was validated against field and laboratory test data. During the on-track tests, the vertical accelerations of the Y25 axle boxes were measured while the vehicle was travelling at 36 m/s. These signals sampled at a frequency of 1 kHz and then filtered to remove the frequency content below 0.4 Hz. The filtered signals were then imported into the freight vehicle model simulation, which was also run on equivalent track at 36 m/s. The results from this analysis showed that the agreement between the measurements/simulations was good.

During the on-track tests however, the high sampling frequency of the dither measurements resulted in large volume data files that were difficult to handle efficiently in the MBS environment. (Piotrowski, 2012) then developed the non-smooth substitute model of dry friction to reduce these difficulties. This model comprises of a spring, friction element and viscous damper combination arranged in series. The displacement responses of substitute and basic model of non-smooth friction in the presence of dither are shown in Figure 2.17. From these results it is clear to see that agreement between the substitute/basic models is good. The main advantage of the substitute model however, is that the execution times are significantly faster due to the modelling the smoothing effects of dither with a liner viscous damper (Piotrowski, 2012).

The force across the damper in the substitute model is calculated using Equation (2.16), which is then rearranged to express the equation in terms of $\dot{z}_1$. This result is then substituted into Equation (2.17) to calculate the friction force. The direction angle of the friction force is calculated using Equation

(2.18), which corresponds to a one dimensional slip velocity when cos β = 0. When the slip velocity is acting in two-dimensions however, Equations (2.19) and (2.20) are used to calculate the direction angle of the friction force vector.

The breakout force $\mathbf{T_0}$ in the substitute model is calculated using Equation (2.10), whereas the viscous damping coefficients, C_x and C_y, are found by a parameter identification process which is explained in detail by (Piotrowski, 2012). Dry friction damping in the presence of ultrasonic vibrations and thermal agitations are also discussed in (Popov, 2010), (Montroll, 1956) and (Saaskilahti, Oksanen, Tulkki, & Volz, 2014). The following section discusses three-piece bogie wedge suspension models.
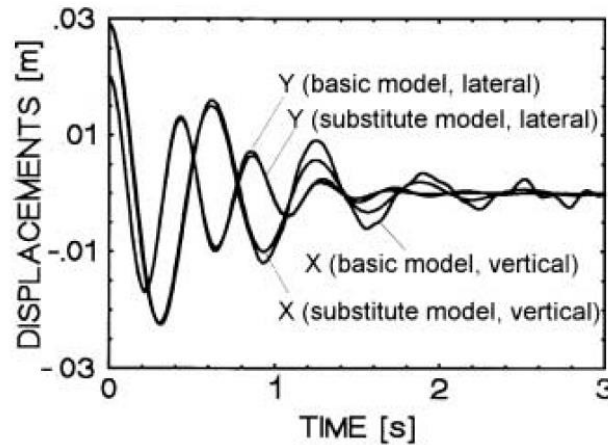
Figure 2.17: Comparison of the leading wheelset displacements in the x and y directions using the basic and substitute models of non-smooth dry friction with dither (Piotrowski, 2012).

$$C_s\,(\dot{z}_1 - \dot{z}) = T \tag{2.16}$$

$$\dot{T} = \begin{cases} k_1\left(\dot{\zeta} - \dot{z} - \frac{T}{C_s}\right) & \text{if } |T| < T_{0s} \\ -\left[-k_1(\dot{\zeta} - \dot{z} - \frac{T}{C_s})\right]^+ & \text{if } T = +T_{0s} \\ \left[-k_1(\dot{\zeta} - \dot{z} - \frac{T}{C_s})\right]^+ & \text{if } T = -T_{0s} \end{cases} \tag{2.17}$$

$$\alpha = \begin{cases} \frac{\pi}{2} & \text{if } \sin \beta = 1 \\ \frac{3\pi}{2} & \text{if } \sin \beta = -1 \end{cases} \tag{2.18}$$

$$\psi = \tan^{-1}\left(\frac{T_{0y}{}^2 \tan|\beta|}{T_{0x}{}^2}\right) \tag{2.19}$$

$$\alpha = \begin{cases} \psi & \text{if } \sin\beta > 0 \text{ and } \cos\beta > 0 \\ \pi - \psi & \text{if } \sin\beta > 0 \text{ and } \cos\beta < 0 \\ \pi + \psi & \text{if } \sin\beta < 0 \text{ and } \cos\beta < 0 \\ 2\pi - \psi & \text{if } \sin\beta < 0 \text{ and } \cos\beta > 0 \end{cases} \tag{2.20}$$

2.8. Wedge suspension models

The central suspension on the three-piece bogie provides the flexible connection between the side frames/bolster. The position of the springs relative to the axle boxes however, leads to a higher unsprung mass in comparison to the Y25 bogie. An in-depth review of the friction wedge modelling

methodologies that are used in ADAMS, MEDYNA, NUCARS, VAMPIRE, SIMPACK and GENSYS has been carried out by (Wu, Cole, Spiryagin, & Sun, 2014).

The basic free-body diagrams for different wedge suspensions and the forces acting on each component are shown in Figure 2.18. Picture (a) for example, shows the wedge suspension with no toe angles on the side frames/wedges and picture (b), shows a friction wedge with a toe-out configuration. The normal, tangential and inertia forces acting on the bolster contact surfaces are also shown in (c). The force element combination used to model the friction wedge in ADAMS is shown Figure 2.19 (a), which comprises of a friction element connected in series to spring and damper arranged in parallel. This force element is then connected to the 8-contact points on the friction wedge shown in Figure 2.19 (b).
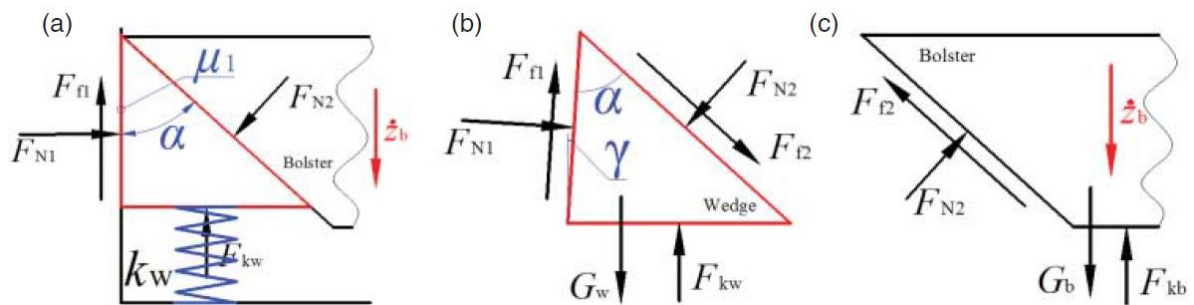
Figure 2.18: Free-body diagrams of the friction wedge suspension, where F_N, F_f and F_k are the normal, friction and spring forces, γ is the toe angle, α is the wedge angle and G represents the inertia forces of the wedge/bolster (Wu, Cole, Spiryagin, & Sun, 2014).
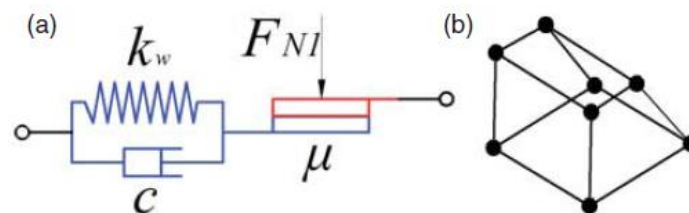
Figure 2.19: (a) Friction model used in Adams (b) Friction wedge modelled using 8-friction elements to analyse toe-in/out configurations (Wu, Cole, Spiryagin, & Sun, 2014).

The force element combination shown above was used by (Harder, 2000) to develop a wedge suspension model for the three-piece bogie in ADAMS-VIEW. The friction element however, used a simplified Heaviside step function to describe friction forces as well as to handle the velocity reversals during the sliding phases of motion, see Figure 2.20 (left). The ADAMS-VIEW wedge model was then validated against theoretical benchmarks before running it in a complete vehicle model of a three-piece bogie that had been developed in ADAMS-RAIL. The hysteresis responses of the wedge suspension for Coefficient of Friction (COF) values ranging from 0.2 – 0.5 are also shown to the right of Figure 2.20 and as can be seen, the vertical friction force between the side frame/bolster increases in proportion to the COF value.

The bogie model was then simulated in ADAMS-RAIL using the level 1 wheel/rail contact model, which is developed from Kalkers` simplified contact theory. Curving simulations were also carried out with the same vehicle model but with the level 3 contact model, which is based on Kalkers` complete non-linear theory. These simulations however, required 1000 – 1500 steps per second to converge to a solution (Harder, 2000). A detailed description of the different wheel/rail contact models is given in (Meymand, Keylin, & Ahmadian, 2016) and (Shackleton, 2009).

A bevelled friction wedge suspension model was also developed in the Universal Mechanism software package by (Ashtiani, 2017) to investigate the performance of different wedges geometries. This model had six Degrees-of-Freedom (DOF) and included 16-contact points on the wedge surfaces as well as the Stribeck friction force characteristics to describe the stick-slip response.
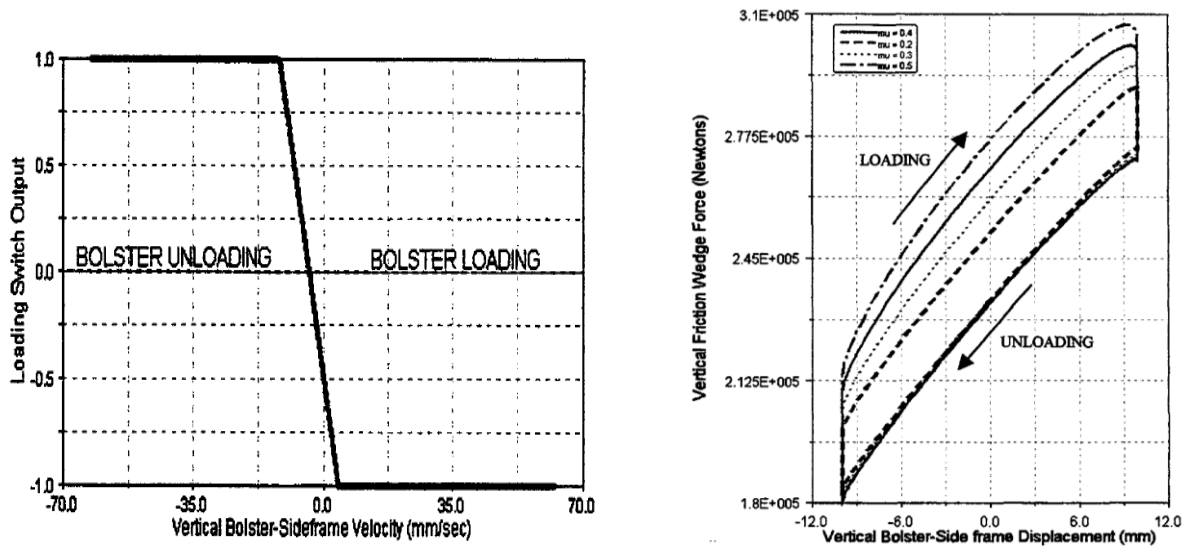
Figure 2.20: (Left) Loading switch function developed in Adams/view. (Right) Friction wedge hysteresis response for different coefficient of friction values (Harder, 2000).

The force element combination used in NUCARS to model the wedge suspension is shown in Figure 2.21. This model as can be seen, includes clearances in the normal and tangential directions, which are labelled as g_1 and g_2 respectively. The stiffness coefficients of the tare and laden springs in the normal direction are labelled as k_1 and k_2 and the viscous damping as C. In the tangential direction, the tare and laden stiffness parameters are labelled as k_3 and k_4 (Wu, Cole, Spiryagin, & Sun, 2014).

Earlier versions of the NUCARS wedge model however (Version 2.1), were less accurate as these did not take the inertial properties of the wedge into account. The review work of (Cusamano & Gardner, 2006) also highlighted another limitation, relating to the COF between the side-frame/wedges and wedges/bolster. In version 2.1, the COF values for each friction surface had to be set to the same value. After this critical review and further validation tests on the model using scaled laboratory test data, later editions of the NUCARS friction model were then improved to take these factors into account (Wu, Cole, Spiryagin, & Sun, 2014).
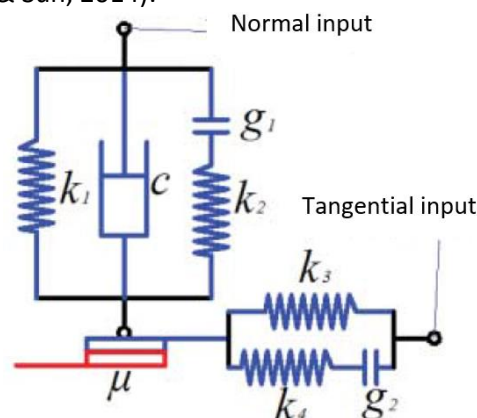
Figure 2.21: Complete wedge suspension friction model to describe the normal and tangential contact forces (Wu, Cole, Spiryagin, & Sun, 2014).

The two-dimensional friction model that was developed by (Xia, 2003), used the hyperbolic secant function as regularisation method to describe the friction forces, see Figure 2.22. This model was used to study the stick-slip motions of the mass when subjected to harmonic excitations in the x and y directions, which is a similar test case to the one studied by (Piotrowski, 2010).

The friction force vector $\mathbf{F}_f$ is calculated from the force components in the x and y directions, see Equation (2.21), where N is the normal force and μ is the COF. The COF parameter however, is multi-valued due to the difference between stick and kinetic COF values, μ_s and μ_k. The velocity dependent friction force vector is then given as $\mathbf{F}_f = -f(V).N$, where f(V) is the function used to switch the sign of the kinetic COF value, see Equation (2.22). The velocity of the mass is calculated from Equation (2.23)(Xia, 2003).
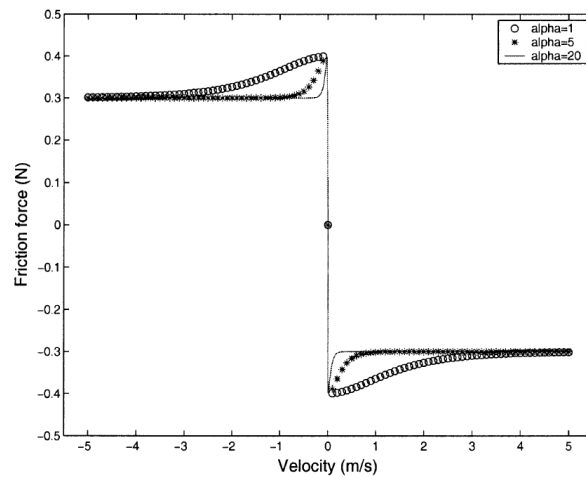
Figure 2.22: Friction characteristics of the hyperbolic secant function for different values of α (Xia, 2003).

$$\mathbf{F}_f = \sqrt{F_{fx}^2 + F_{fy}^2} \leq \mu N \tag{2.21}$$

$$f(V) = \begin{cases} \mu_k & \text{if } V > 0 \\ \mu_s \leq f(V) \leq \mu_s & \text{if } V = 0 \\ -\mu_k & \text{if } V < 0 \end{cases} \tag{2.22}$$

$$|V| = \sqrt{\dot{x}^2 + \dot{y}^2} \tag{2.23}$$

The velocity components in the x and y directions are then substituted into Equation (2.24) to calculate the slip angle, θ. Whereas the velocity dependent friction coefficient μ(v), is calculated using regularisation function given in Equation (2.25). The parameter α, is used to adjust the steepness of the curve that describes the transition from sticking to sliding, which is a continuous function of time.

The mass-spring oscillator was then subjected to harmonic excitations in the x and y directions to validate the friction model parameters. The displacement, velocity and friction force responses during these simulations are shown in Figure 2.23. The two-dimensional friction model was then integrated into a complete vehicle model to describe the frictional contacts in the central suspension of the three-piece bogie.

$$\theta = \begin{cases} \tan^{-1}(\frac{\dot{y}}{\dot{x}}) & (\dot{x} \geq 0,\ \dot{y} \neq 0) \\ \pi - \tan^{-1}(\frac{\dot{y}}{\dot{x}}) & (\dot{x} < 0,\ \dot{y} \geq 0) \\ \pi + \tan^{-1}(\frac{\dot{y}}{\dot{x}}) & (\dot{x} < 0,\ \dot{y} < 0) \end{cases} \tag{2.24}$$

$$\mu(v) = \mu_s.\text{sech}(\alpha|v|) + \mu_k(1 - \text{sech}(\alpha|v|))\tag{2.25}$$
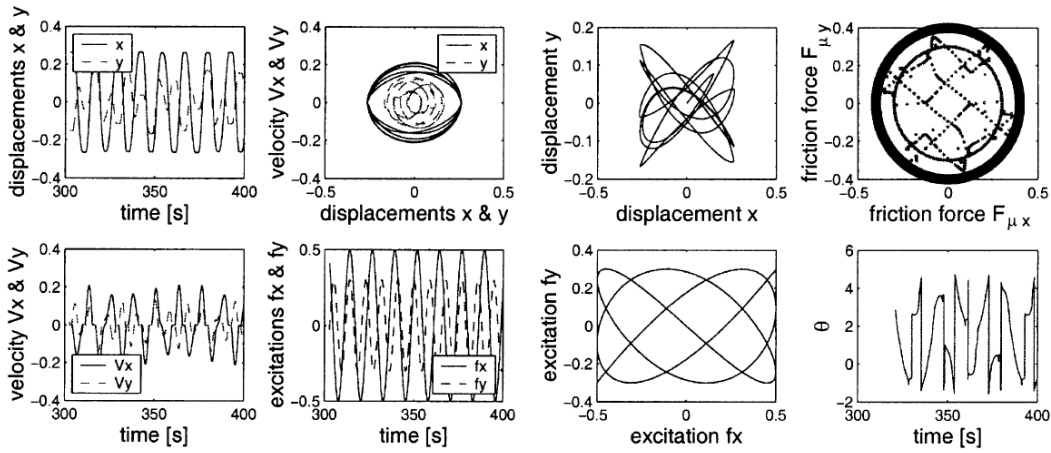
Figure 2.23: Responses of the 2-D system to harmonic excitations: μ_s = 0.4, μ_k= 0.3, $k_x = k_y = 1$, $c_x = c_y = 0$ (Xia, 2003).

The vehicle model that was developed by (True & Xia, 2004) had 19 rigid bodies in total including two three-piece bogies, four wheelsets, a wagon-body and the suspension components. The wheel/rail contact conditions in the normal direction were then modelled using Hertzian springs, whereas in the tangential direction, the Shen-Hendrick-Elkins nonlinear contact model was used to calculate the creep forces. A transient stability analysis was then carried out on the empty vehicle model to evaluate the linear and nonlinear critical speeds of the three-piece bogie.

The linear critical speed that was calculated from the simulations was shown to be in the region 28.5 m/s, whereas the nonlinear critical speed was 20.5 m/s. The dynamic response of the vehicle model running over track irregularities at 78 km/h was also analysed and then validated against on-track measurements. The agreement between the simulation/measurements was relatively good, although there were some noticeable discrepancies between the two sets of results. The authors attributed these to the worn condition of the test vehicle used in the on-track tests (True & Xia, 2004).

The critical hunting speed and curving performance parameters of the vehicle model were then analysed to identify the optimal wedge design parameters that resulted in the lowest derailment quotient, see Equation (2.26). The ratios of the lateral (Y) and vertical forces (Q) at the wheel/rail contacts have to be less than Nadal`s derailment criteria in order to comply with the GM/RT2141 Railway Group Standards. In this equation, γ is the contact angle in radians and μ is the wheel/rail COF (Ashtiani, 2017). The following section discusses the leaf spring suspension.

$$\frac{Y}{Q} < \frac{\tan(\gamma) - \mu}{1 + \mu.\tan(\gamma)}\tag{2.26}$$

2.9. Leaf spring suspension models

Leaf spring suspensions are used on two-axle freight wagons as well as bogies to connect the axle boxes to the wagon body or bogie frame, see Figure 2.24. This component has several steel leafs that

can be manufactured to various profiles and stiffness coefficients ranging from 5 – 15 MN/m. The leafs are then stacked on top of each other and clamped together by the buckle which rests on top of the axle box. The horn guides then allow the axle boxes to move in the longitudinal, lateral and vertical directions relative to the wagon body within the clearance limits (Iwnicki, Stichel, Orlova, & Hecht, 2015) and (Stichel & Jonsson, 2009).

The ends of the leaf springs are then connected to the wagon body or bogie frame via the two end bearings, links and pins. The main advantages of the leaf spring suspension are the low maintenance costs and that the stiffness and damping mechanisms are contained within a single component. The disadvantages however, are the unpredictable levels of damping due to the combination of rolling friction from the links and the sliding friction from the leafs, as well as wear and deterioration in service. The links also provide additional yaw stiffness to the vehicle and a longitudinal stiffness component due to the inclination angle of the links (Iwnicki, Stichel, Orlova, & Hecht, 2015) and (Boronenko & Orlova, 2006).

The mechanical model for a two layered leaf spring suspension with Coulomb damping is shown in Figure 2.25. This force element combination comprises of three linear springs connected in parallel, with two springs connected in series with friction elements. In the sticking condition when pre-sliding displacements are starting to take place for example, the stiffness of the leaf spring is the sum total of the spring elements, $K + k_{s1} + k_{s2}$. Whereas for the gross sliding state, the stiffness decreases to the value of K. The parameters of the springs and friction elements can then be tuned using laboratory/on-track test data, which was the method used in (Andersson, Stichel, & Jonsson, 2006).
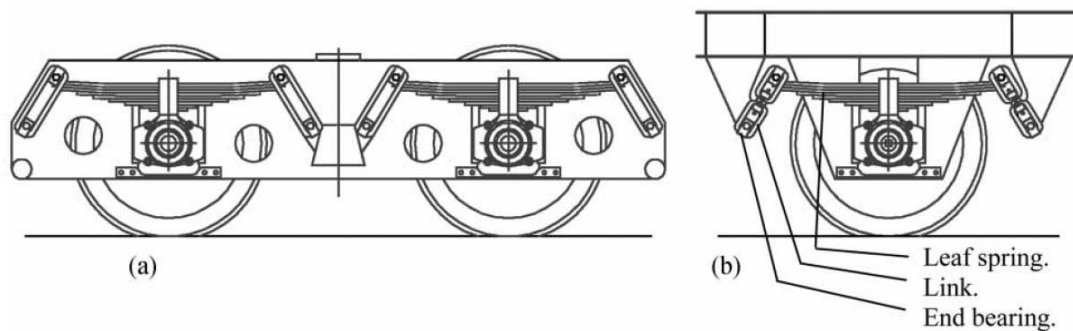
Figure 2.24: (Left) Deutsche Bahn bogie type 931 with double link leaf spring suspension. (Right) Two axle freight wagon with double link leaf spring suspension (Andersson, Stichel, & Jonsson, 2006).
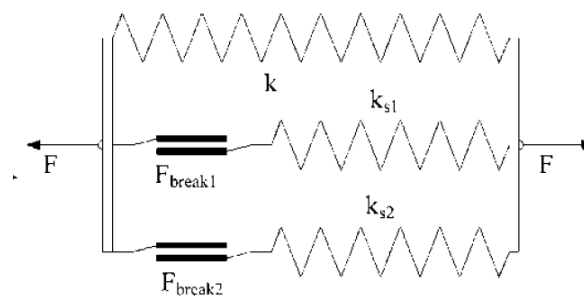
Figure 2.25: Mechanical model for a multi-layered double link leaf spring suspension (Andersson, Stichel, & Jonsson, 2006).

The responses of the leaf spring model for large and small displacements in the vertical direction are shown in Figure 2.26, where the hysteric behaviour is clear to see. It is also clear to see the changes in leaf stiffness for small displacements about the equilibrium position. The measurements that were

used to validate the leaf spring model however, show large amounts of variation in the responses of the wagons that were tested, see Figure 2.27. The reason for the wide range of results during these tests, was due to wear in the suspension components as well as contamination (Stichel & Jonsson, 2009).

Further research by (Stichel & Jonsson, 2009) also discusses an investigation that the Office for Research and Experiments (ORE) carried out on two axle freight vehicles. The findings from this work suggested that the levels of hysteresis in the leaf spring suspension can range from $\pm\,4-8\%$ of the vertical axle box load for new leaf springs. Whereas for reconditioned springs, the range was $\pm\,13-15\%$. These highly inconsistent characteristics however, make it more challenging to validate the leaf spring model within clearly defined confidence bounds (Stichel & Jonsson, 2009).
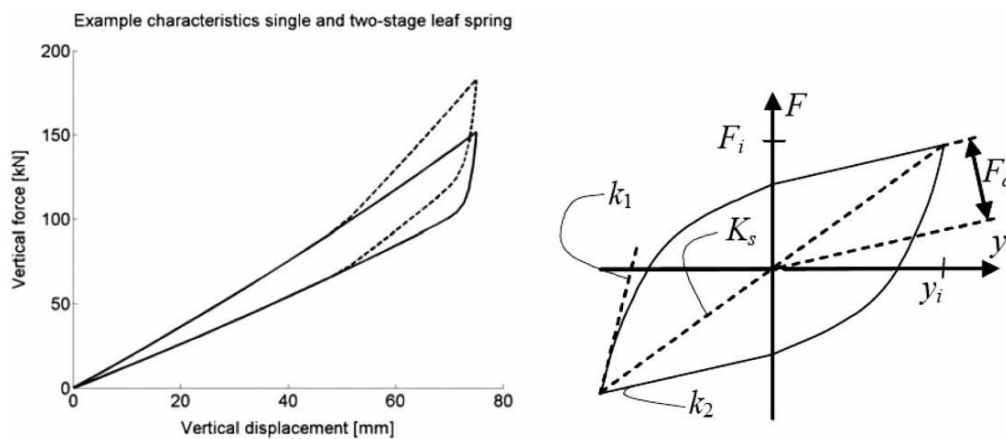
Figure 2.26: Force-displacement curves for a leaf spring model. (Left) Characteristics for large displacements in the vertical direction. (Right) Small displacements in the vertical direction (Bruni, Vinolas, Berg, Polach, & Stichel, 2011).
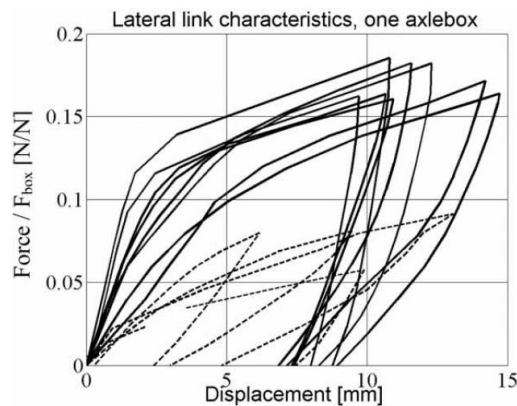
Figure 2.27: Stationary lateral force-displacement measurements on vehicles. The lateral force is normalised with the vertical axle box force (Andersson, Stichel, & Jonsson, 2006).

The work of (Jonsson & Stichel, 2009), aimed to establish if the two-axle freight wagon with leaf spring/double link suspension had a future in Sweden`s rail freight industry. To answer this question, the running performance of the two-axle freight wagon was analysed using on-track test measurements as well as dynamic simulations carried out in GENSYS. Measurements on two-axle freight wagons in the loaded state for example, suggested that on straight track, wagon body hunting motions start to develop at a frequency of $1-2.5$ Hz for vehicle speeds in the region of 70 km/h.

Whereas in the empty state at 100 km/h, wheelset hunting was also observed in the region of 4 – 6 Hz, which is caused by high wheel/rail conicities (Jonsson & Stichel, 2009).

The curving performance of three different freight vehicles with a 22.5 t axle load were also analysed and compared using GENSYS. The vehicle models included a two-axle freight wagon with leaf spring/double link suspension, a freight wagon with two bogies and leaf spring/double link suspension (Figure 2.24) and a wagon with Y25 bogies. The energy dissipation in the outer wheel/rail contact patch of the leading wheelset was then evaluated and used as the key performance metric. The energy dissipation or work done, is the product of the creep force and creepage. Results from the curving simulations, showed that the two-axle wagon could achieve radial steering on curves with radii as low as 300 m. Whereas Y25 bogie on the other hand, due to the longitudinally stiff suspension, could only achieved acceptable steering on curves with radii`s no less than 450 m. The bogie with leaf spring/double links however, demonstrated the best curving performances overall.

The track deterioration costs per ton-km for each vehicle were also evaluated using the component failure costs due to wear and Rolling Contact Fatigue (RCF) and the track settlement costs. These results were then normalised with the total costs for the Y25 bogie. This analysis suggested that on selected networks, a total saving of 30 – 40% in track deterioration costs could be achieved by opting to use vehicles with leaf spring/double link suspensions (Jonsson & Stichel, 2009).

Simulations were also carried out to investigate the influence of new, part-worn and worn suspension components on the limit cycling behaviours. Vehicle models with new components for example, started to hunt at speeds in the region of 110 km/h, whereas for vehicles with worn components, hunting developed in the region of 70 km/h which is in agreement with the field test measurements. To eliminate the low speed hunting modes associated with two-axle freight wagons, the recommendation was to use hydraulic yaw dampers and hydraulic lateral dampers on the axle boxes. With these design modifications included, simulation results suggested that speeds of 160 km/h could then be achieved by these vehicles when carrying light loads such as mail (Jonsson & Stichel, 2009).

The response of the leaf spring model with Coulomb damping was also compared against the response of a smooth leaf spring model using an equivalent dashpot damper in (Polach, Berg, & Iwnicki, Simualtion, 2006). The conclusions to this study were that the characteristics of the smooth model when subjected to harmonic excitations were in better agreement with the test measurements on rubber. However, it was also pointed out that the energy loss per cycle for frequencies above $\frac{4.k}{c}$, was too high and did not agree well with the measurements. The following section discusses elastomeric component models.

2.10.   Elastomeric component models

Elastomeric components such as rubber bushes for mounting suspension components, wear liners and rail pads for example, show complex frequency and displacement dependent behaviour where the dynamic stiffness generally increases with frequency. Linear models therefore, are not well suited to describing these components in Multibody Simulations (MBS). The generalised Zener model shown Figure 2.28 however, can be adapted and used to describe a wide range of elastomeric components to a good level of accuracy (Collina & Bruni, 2010).

In (Collina & Bruni, 2010), the methodologies applied to modelling elastomeric track components were reviewed. After this a series of laboratory tests were then carried out on a rail pad component under low and high harmonic forcing frequencies to quantify the equivalent stiffness and loss factor of the rail pad material and also, to generate benchmark test data for validating rail pad MBS models.

During the laboratory tests the pre-load on the rail pad was set to 12 kN and for the low frequency tests, different frequencies were investigated ranging between 5 − 100 Hertz (Hz) as well as three different displacement amplitudes, 0.07, 0.067 and 0.18 mm. The high frequency tests on the other hand, were carried out using frequencies ranging between 80 − 800 Hz.

The results from these tests showed that the equivalent stiffness parameters during the low and high frequency tests were not comparable, whereas the loss factors were. The loss factors for example, increased from zero to 0.25 between 0 − 300 Hz, then remained constant. Whereas the stiffness parameters as mentioned above, continued to increase with the forcing frequency (Collina & Bruni, 2010).

Further laboratory tests were then carried out on a 3.5 m section of track to measure the dynamic track response to an impact load of 8 kN. This load was applied using a half-sine waveform that was applied over a 2 milli-second time interval. An equivalent Zener/rheological MBS rail pad model was then developed and simulated under the same input parameters that were used in the laboratory tests. The frequency responses of the rheological model, as well as those of two simplified rail pad models that used a spring and viscous damper arranged in parallel, were then compared against the experimental results, see Figure 2.29.

From the frequency responses, it is clear to see that the amplitudes of the Zener model are in good agreement with the experimental results (Figure 2.29, left). It is also clear to see the first and third flexural modes of the rail without nodes in the region of 130 Hz and 400 Hz, as well as a second mode in the region of 155 Hz, which represents the rail with two nodes placed at distances of 1/4 and 3/4 the length of the rail section (Collina & Bruni, 2010).

The two simplified models, viscous model 130 Hz and viscous model 350 Hz (Figure 2.29, right), were tuned to the first and third resonant frequencies of the rail and as can be see, are both in good agreement with the respective modes. The viscous model tuned to 130 Hz however, is seen to overestimate the damping in the higher frequency range, whereas the model tuned to 350 Hz on the other hand, overestimates the damping in the lower frequency range. The simplified models therefore, are limited to specific frequency bands only, due to the break frequencies of the viscous dampers. This study concluded that the rail pad had a significant influence on the track response as well as the simulation results for the vehicle-track interaction (Collina & Bruni, 2010). The frequency dependent behaviour of elastomeric materials is also discussed in (Popov V. , 2010). The following section discusses secondary suspension component models.
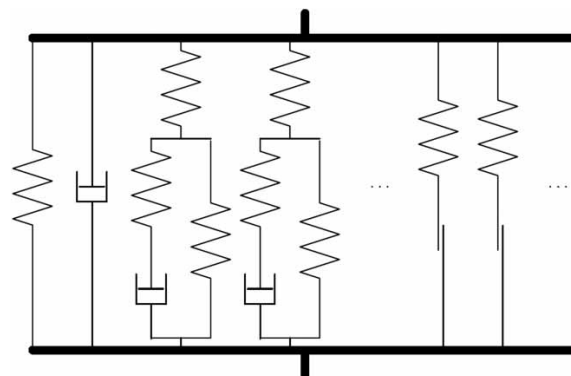
Figure 2.28: Generalised Zener model (Bruni, Vinolas, Berg, Polach, & Stichel, 2011).
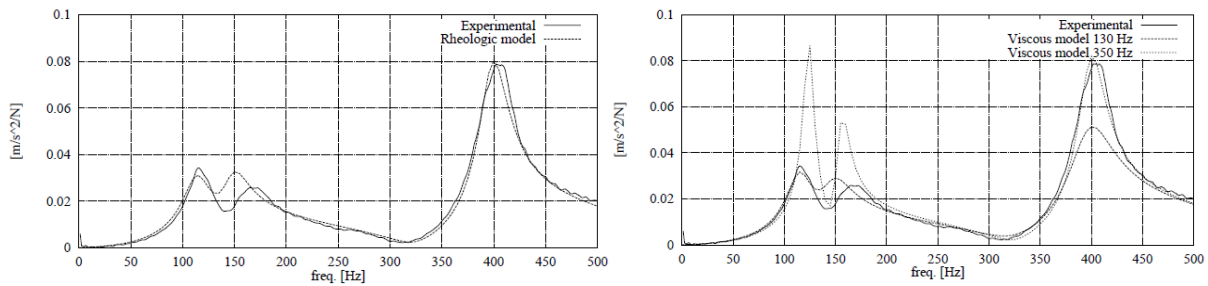
Figure 2.29: (Left) Zener rail pad model. (Right) Simplified rail pad model (Collina & Bruni, 2010).

2.11.   Secondary suspension models (Y25 bogie)

The secondary suspension components on the Y25 bogie support the wagon body load and provide the flexible connections between the bogies/wagon body. The spherical centre bowl/wear liner constrains translational motions between the bogie/wagon body but allows roll, pitch and yaw motions to take place and provides friction damping in these directions as well. The elastic side bearer's/wear liners, support around 31% of the wagon body tare load (reducing to 5% in the laden case) and provide friction damping to the yawing motions. These components also increase the roll stiffness of the wagon body and have clearances and bump-stops in the vertical direction to accommodate these movements as well as in the longitudinal direction (Evans & Rogers, 1998) and (Bosso, Gugliotta, & Soma, 2000).

In the research work of (Evans & Rogers, 1998), two versions of the Y25 bogie were developed using VAMPIRE which included a realistic model of a side bearer and a simplified model. These were then used to analyse and compare the effects of using different modelling methodologies on simulation results. The simplified model for example, did not take the $\pm$ 1 mm longitudinal clearances into account, whereas the realistic model did.

From the frequency responses of the lateral accelerations shown in Figure 2.30, it can be seen that without the clearances included, the agreement between the lateral ride measurements and simplified model response is not that good. Whereas the agreement between the measurements/realistic model is clearly better. The conclusions to this study were that freight vehicles with clearances and dry friction suspension components, required highly detailed Multibody Simulations (MBS) models to predict all of the nonlinear effects observed during on-track/laboratory tests (Evans & Rogers, 1998) and (Boronenko & Orlova, 2006).
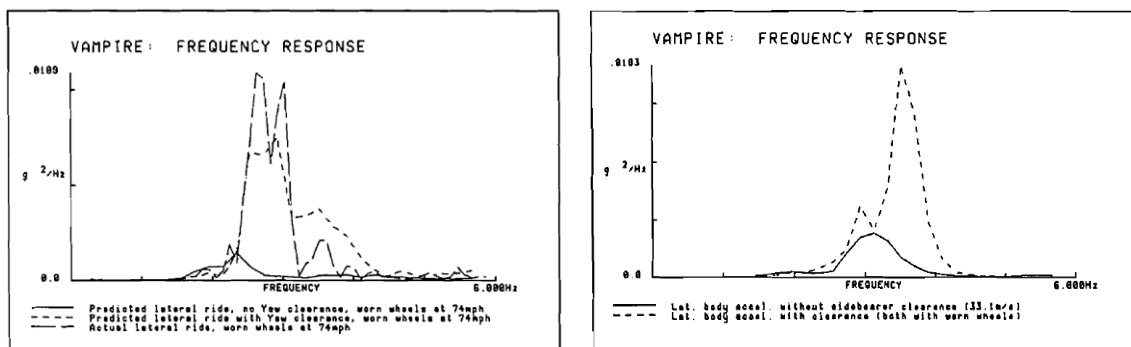
Figure 2.30: Side bearer with/without clearances. (Left) Tare lateral ride response. (Right) Part-laden lateral ride response (Evans & Rogers, 1998).

The sensitivities of friction damped freight vehicles to different track defects and suspension designs have also been discussed in several reports published by the Rail Accident Investigation Branch (RAIB).

In 2007 for example, the RAIB released a report detailing the root causes of a freight train derailment at Washwood Heath in September 2006. The Y25 bogie that was involved in this incident was part of a FFA container wagon, 9 foot 6 inches high and travelling at 14.9 mph (RAIB, 2007).

During this investigation, five random bogies were selected from the fleet, visually inspected and then subjected to a series of X-Factor tests to try and establish if the derailment had been caused by high rotational resistance. The design history of the fleet from 1999 onwards was also reviewed as part of this investigation, which indicated that there had been a design change in 2004 to the original side bearer wear plate arrangement shown in Figure 2.31 (Left). The wear plates on this design were inclined so that the bogie/wagon body could tilt more easily on curved sections of track (RAIB, 2007).
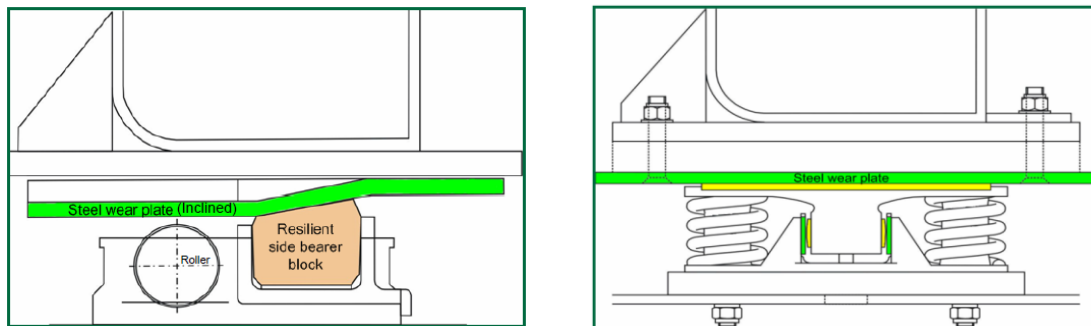
Figure 2.31: (Left) Original side-bearer design, (Right) UIC elastic side-bearer design (RAIB, 2007).

During 1999 – 2004 however, three more derailments occurred involving FFA wagons, which were all associated with track-twist faults causing excessive amounts of wheel unloading. The RAIB report pointed out that the levels of track-twist in the area of the derailments, were above the tolerances that should initiate track maintenance procedures to be carried out, as well as speed restrictions to be put in place. The track-twist tolerances specified in Network Rail`s maintenance standards to initiate corrective action for example, are shown to be 1 in 148 for unloaded vehicles and 1 in 108 for loaded ones. The identified faults should then be remedied within 14 days of discovery for the unloaded case, whereas for loaded case, the track-twist fault has to corrected within 36 hours (RAIB, 2007).

The inclined slide plates were then replaced with flat ones in 2004, but the side bearer assembly containing the roller/resilient block, was left in the original state. However, after the derailment in 2006, the side-bearer design was then re-analysed using quasi-static laboratory tests. The X-Factor measurements taken on the derailed bogie immediately after the accident in 2006, were shown to be 0.231 and 0.314 for the leading and trailing bogies respectively. These values however, exceed the 0.1 limit specified in the Railway Group Standard (RGS), GM/RT2141 (Issue 3). The measurements for the initial wheel unloading tests were also higher than the acceptable limit of 60%, measuring 79% (RAIB, 2007). The formula to calculate the X-factor value is given in Equation (2.27).

$$\text{X-Factor} = \frac{\text{Bogie/Body yaw torque}}{\text{Wheelbase x axle load}} = 0.1 \tag{2.27}$$

The X-Factor values and wheel unloading measurements on the randomly selected bogies were also dangerously high. The maximum/minimum X-factor values overall for example, were shown to be 0.459 and 0.327 and the wheel unloading measurements, 80 – 89%. The results from these tests clearly suggested that there was a general problem with the whole fleet. Further laboratory tests were then carried out to identify a suitable side bearer/slide plate design to make the bogie compliant with the RGS X-factor limit (RAIB, 2007).

The lowest X-Factor value that was measured during these tests was 0.057 with the original side bearers removed. Whereas when these components were included in the test, the lowest value was 0.231. After analysing the laboratory test data, the side bearers on the whole fleet were then changed to the elastic type shown to the right of Figure 2.31. The X-Factor values and wheel unloading test measurements with the elastic side bearers/flat slide plates fitted to the bogie were then shown to be in the region of 0.104 and 45% respectively.

The main conclusions from these investigations were that the side bearer design as well as the levels wear and damage to the resilient blocks/slide plates, were important causal factors in the high levels of bogie rotational resistance. These findings also agree with the suggestions made in (Tickell, Downing, & Jacobsen, 2004) and (Simson & Pearce, 2006), who were looking into the root causes of wheel squeal and wheel wear losses in freight vehicles. From these pieces of research in particular, it can be concluded that the correct understanding of the dry friction suspension components is essential to ensure acceptable performance is maintained throughout the vehicle`s life. The following section discusses secondary suspension models.

2.12.   Secondary suspension models (Three-piece bogie)

The three-piece bogie secondary suspension comprises of a flat circular centre plate and two side bearers. The side bearers on the three-piece bogie however, are dependent on the vehicle type and can be either Constant Contact Side Bearers (CCSB), elastically sprung, roller/resilient block type or rigid side bearers with clearances that only engage during curving. In (Ren, Shen, & Hu, 2007), a test-rig was designed to measure the warp and shear stiffness of the K1 and Z8A three-piece bogies, see Figure 2.32. The warp stiffness is defined by (Olshevskiy, Kim, & Yang, 2015) as, "the angular stiffness that inhibits angular deformation of the centre plate and side bearers".
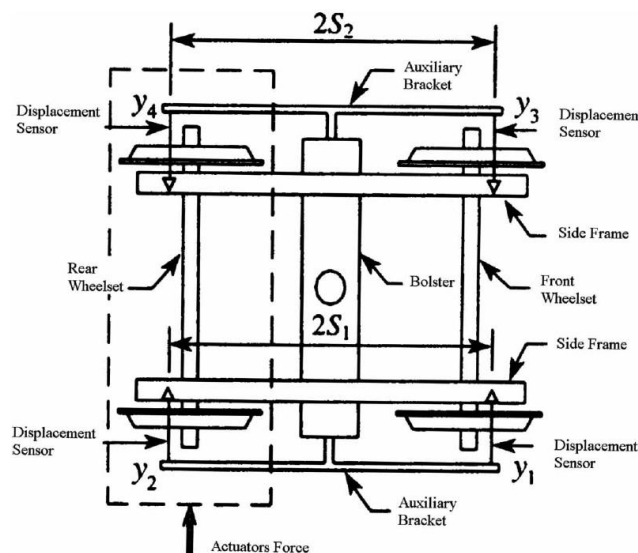
Figure 2.32: Test-rig used to measure the warp and shear stiffness of the three-piece bogie (Ren, Shen, & Hu, 2007).

The Z8A bogie is one of the most common freight bogies in China but is limited to a maximum running speed of 60 – 70 km/h in order to mitigate the derailment risks associated with low warp stiffness. (Ren, Shen, & Hu, 2007) for example, suggested that the warp stiffness of the Z8A bogie decreased significantly after 1-year in service which then caused wheelset instabilities to develop at low running speeds. It was also suggested that the warp stiffness parameter cannot be accurately measured until the bogie is fully assembled.

The warp angle θ of the bogie is calculated using Equation (2.28) and the friction moment T_{cp}, between bogie/wagon body, using Equation (2.29). This equation states that the bogie/wagon body friction moment is equal to the product of the actuator force F and half of the wheelbase length, L. The results from (2.28) and (2.29) are then substituted into Equation (2.30) to calculate the warp stiffness of the bogie, K_w.

$$\theta = \frac{1}{2}\left(\frac{y_2 - y_1}{2S_1} - \frac{y_4 - y_3}{2S_2}\right) \qquad (2.28)$$

$$T_{cp} = F.L \qquad (2.29)$$

$$K_w = \frac{T_{cp}}{\theta} \qquad (2.30)$$

The test rig illustrated above was also used by (Ren, Shen, & Hu, 2007) to evaluate the warp stiffness parameters of a Z8A bogie that had been in service for 2-years. The results from these tests showed that warp stiffness of this bogie under the tare load was in the region of 0.4 MN/rad and the critical speed, due to the relatively low warp stiffness, was less than 50 km/h. Under the laden loading conditions however, it was shown that the warp stiffness increased to 2 MN/rad. It was then suggested that a brand new Z8A bogie could achieve critical speeds in the region of 80 km/h (Ren, Shen, & Hu, 2007).

The warp stiffness parameters of the Z8A bogie were then compared against the K1 bogie, which is designed to run at service speeds in the region of 120 km/h. The improved running performance of the K1 bogie at high speeds is due to the high warp stiffness provided by the cross-bracing, the warp stiffness therefore, is in the region of 5.7 MN/rad. Figure 2.33 shows the torque responses of the Z8A and K1 bogies and Figure 2.34 shows the torque responses of Constant Contact Side Bearer (CCSB) under empty and loaded conditions.

These responses clearly show that the warp stiffness parameters and loading conditions have a significant influence on the frictional torque responses. The results from the field tests carried out by (Tickell, Downing, & Jacobsen, 2004), also showed in their frequency analysis, that noise emittance due to flanging wheels could be reduced by using elastic side bearers and in some cases, completely eliminated.
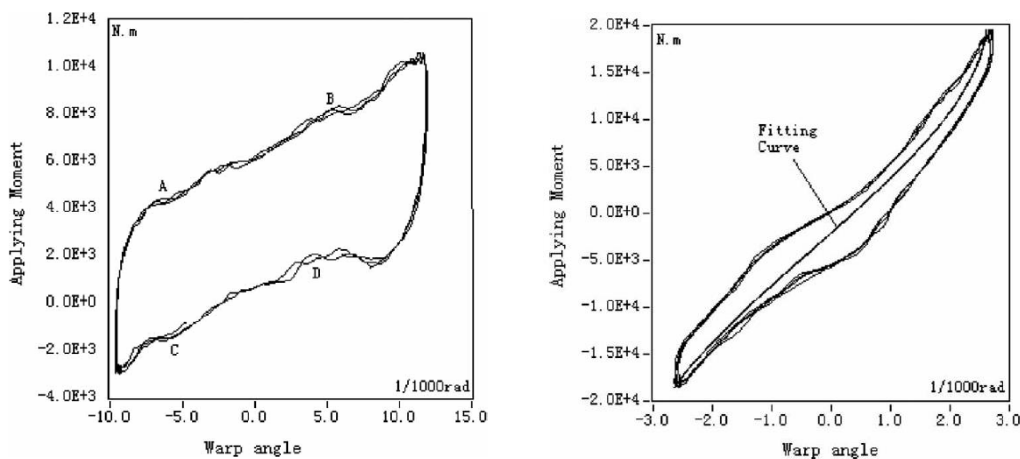
Figure 2.33: Warp stiffness with an empty gondola wagon. (Left) Z8A bogie. (Right) K1 Bogie (Ren, Shen, & Hu, 2007).
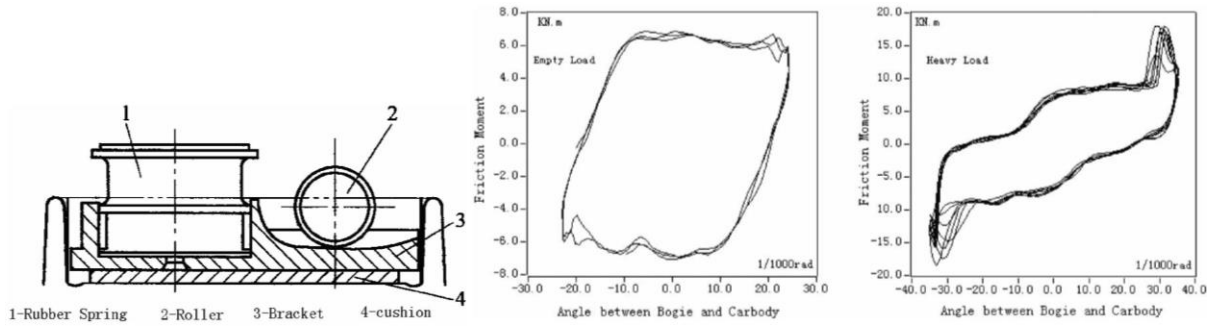
Figure 2.34: (Left) Constant contact side-bearer with a roller for the K1 bogie. (Right). Friction moment of the K1 bogie assembled with the side-bearers shown to the left (Ren, Shen, & Hu, 2007).

The research of (Fergusson , Frohling, & Klopper, 2008) focused on optimising the lateral/longitudinal primary suspension characteristics as well as the centre plate friction in the Scheffel MK-7 self-steering bogie to minimise wheel wear. This work reviewed on-track test data from a previous commissioning study carried out in Sweden using the same type of bogie, but carrying a 30-tonne (t) axle load. Track test data from Transnet`s own coal exporting line was also analysed, where the tare and laden loads are 17,500 and 65,500 kg respectively, see Figure 2.35 (Fergusson , Frohling, & Klopper, 2008).

Dynamic curving simulations were then carried out on a bogie model developed in ADAMS-RAIL using measured wheel/rail profiles. The basic model to described the centre plate friction in these simulations is shown in Figure 2.36, where the position of the friction element relative to the centre is shown to be two thirds the outer radius, R. The normal force is labelled as N and the centre plate Coefficient of Friction (COF) and frictional torque, as μ and T_{cp}. The centre plate torque is then calculated using Equation (2.31) (Fergusson , Frohling, & Klopper, 2008).

$$T_{cp} = \left(\frac{2}{3}\right).R.\mu.N \qquad (2.31)$$
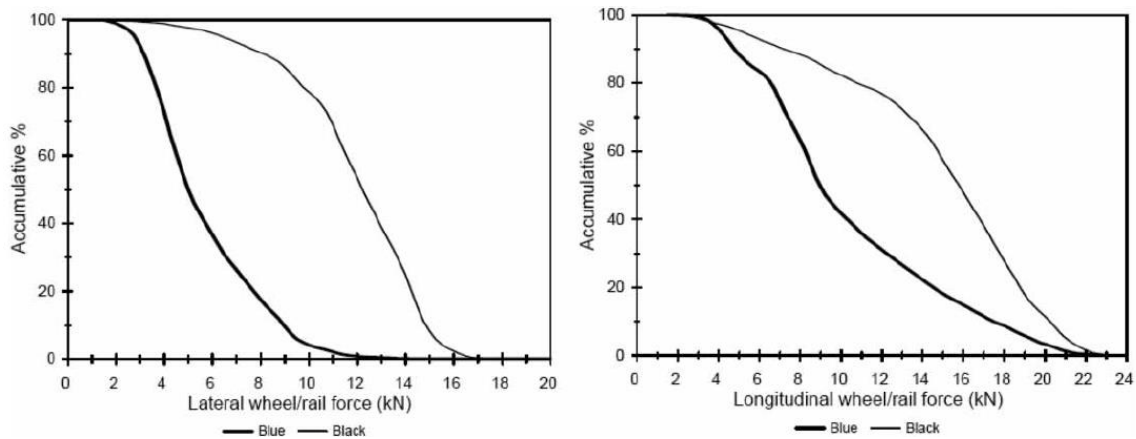
Figure 2.35: On-track test results for the wheel/rail forces in lateral and longitudinal directions using two different types of centre plate wear liner. Blue liner μ = 0.11, black liner μ = 0.49 (Fergusson , Frohling, & Klopper, 2008).
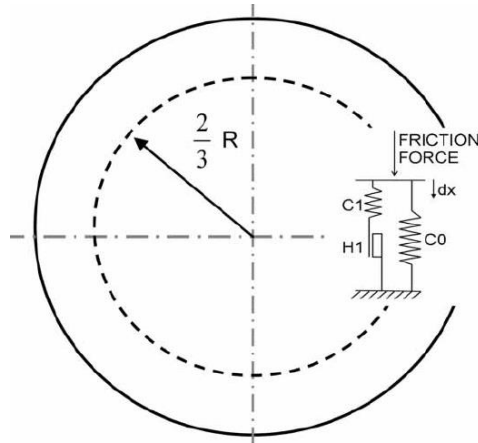
Figure 2.36: Centre plate model and the position of the friction element (Fergusson , Frohling, & Klopper, 2008).

In these simulations C_0 was set to zero and C_1 was set to 1 GN/m, thus making the connection to the friction element infinitely stiff. The empty and loaded vehicle model responses were then investigated whilst travelling at the balancing speed on smooth tracks with different curve radii, see Table 2.1. Several different combinations of lateral/longitudinal primary suspension parameters were then set-up in the vehicle model with the centre plate COF values set to 0, 0.11, 0.49 and fixed. The performance of each suspension configuration was then quantified using the wear number of the high rail/wheel contact on the leading wheelset, as well as the sum of the wheel wear numbers on the leading bogie (Fergusson , Frohling, & Klopper, 2008).

The curving simulation results of the modified vehicle models were then compared against the reference/standard self-steering bogie model. The conclusions from this study were that wheel wear could be reduced by 50% with the optimum lateral/longitudinal stiffness parameters, which were seen to be 50% lower than the reference model. Whereas the optimum COF value was suggested to be 0.11, see Figure 2.37.

It was also pointed out that care must be taken to ensure that any modifications to the suspension parameters do not have a negative impact on the vehicle stability. To check the stability of the vehicle model with the optimised stiffness and COF parameters, a simulation was then carried out on straight track that included gauge widening. The critical speed of the optimised vehicle was then evaluated and shown to be above Transnet`s minimum operating speed requirement, which is 80 km/h for an empty wagon and 140 km/h for a loaded one (Fergusson , Frohling, & Klopper, 2008).

Balancing speed [km/h]	Curve radius [m]	Track cant [mm]
37.86	300	40
24.43	500	10
34.55	1000	10

Table 2.1: Curving analysis model parameters (Fergusson , Frohling, & Klopper, 2008).
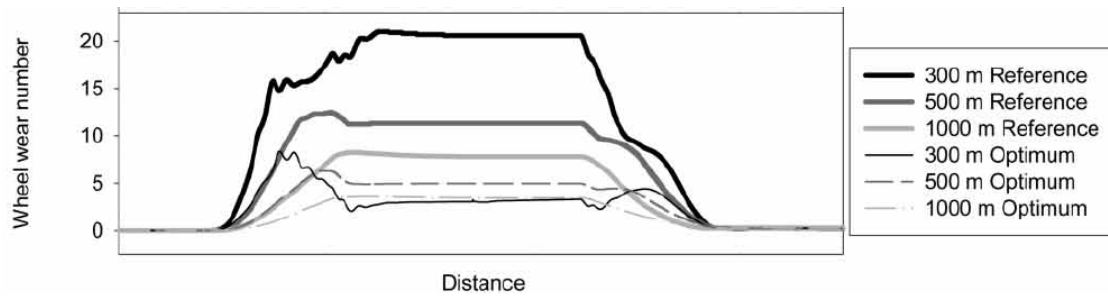
Figure 2.37: Curving analysis simulation results (Fergusson , Frohling, & Klopper, 2008).

Practical experience however, suggests that the secondary suspension components start to show signs of wear after 2-years in service. (Olshevskiya, Yang, & Kima, 2015) for example, carried out a comprehensive wear study on the Russian 18-100 three-piece bogie centre plate and wagon body pivot and confirmed this finding, see Figure 2.38. The first stage of this research involved collecting field measurement data on worn components during vehicle maintenance procedures.

The results from this analysis suggested that over a period of 12 – 15 years, the thickness of the wagon body pivot could wear by as much as 12 mm and the external diameter by 16mm. The worn shapes however, were elliptic rather circular. Whereas the internal diameter of the bogie centre bowl in the worst case scenario, was shown to have increased from 302 to 316 mm (Olshevskiya, Yang, & Kima, 2015).

Two models of the secondary suspension components were then developed which included a Finite Element Analysis (FEA) model, designed using Computer-Aided-Design (CAD). The CAD model was then discretised in NASTRAN and imported into the DSMFEM software package to calculate the contact pressures. The FEA model however, had approximately 64,000 Degrees of Freedom (DOF). The second model that was used in this work was a Multibody Simulations (MBS) model of the Russian 18-100 bogie, developed in UNIVERSAL MECHANISM (UM). This had 54 DOF and more than 80 points of contact in the friction surfaces (Olshevskiya, Yang, & Kima, 2015).

The wear in the centre plate was then calculated using Fleisher`s wear model, see Equation (2.32). In this equation, the wear U, is proportional to the contact pressure and the relative slip distance, p and s. The K term however, represents the proportionality coefficient which is specific to the materials forming the friction pair (Olshevskiya, Yang, & Kima, 2015).
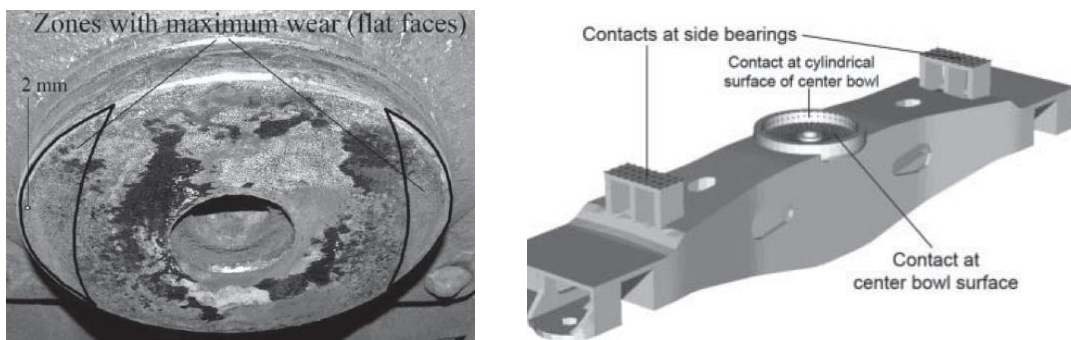
Figure 2.38: Wear analysis of a Russian 18-100 three-piece bogie centre plate. (Left) Worn wagon-body centre pivot. (Right) Finite Element model showing the contact points (Olshevskiy, Kim, & Yang, 2015).

$$U = K.p.s \qquad (2.32)$$

The contact pressures were then calculated using the FEA model with the COF set to 0.3, under the assumption that the pressures remain constant whilst the centre plate is rotating. In the DSMFEM software package however, there are two methods available to calculate the contact pressures, the relaxation method and force method which are explained in (Wriggers, 2006). The wear algorithm of (Olshevskiya, Yang, & Kima, 2015) used the force method as this is the fastest of the two, but less accurate due to neglecting the influence of friction in the redistribution of the contact pressures.

After comparing the two methods using FEA simulations, it was suggested that the effect of friction on the pressure distribution was small. Taking friction into account for example, caused a 6 − 8% increase in the contact pressures and a 5% reduction in the contact area. The force method was then validated against the analytical solutions given by the Hertz`s theory for spheres with different geometries under a range of loading conditions. The maximum error between the numerical/analytical solutions as can be seen from the results in Table 2.2, is 2.9% which is acceptable under the given modelling assumptions (Olshevskiya, Yang, & Kima, 2015).

Contacting bodies and load value	a (mm)	b (mm)	p_{max} (MPa), analytic/numerical	Error in p_{max} (%)
Sphere ($R = 20$ mm) and plane, $P = 10$ N	0.110	0.110	393/402	2.3
Sphere ($R_1 = 20$ mm) + sphere ($R_2 = 30$ mm), $P = 10$ N	0.108	0.108	410/419	2.2
Sphere ($R_1 = 20$ mm) + spherical recess ($R_2 = 30$ mm), $P = 4$ N	0.110	0.110	139/143	2.9
Sphere ($R_1 = 20$ mm) + cylinder ($R_2 = 50$ mm), $P = 5$ N	0.092	0.074	350/356	1.7
Sphere ($R_1 = 20$ mm) + cylindrical recess ($R_2 = 50$ mm), $P = 5$ N	0.113	0.080	265/272	2.6

Table 2.2: Validation results for the force method algorithm comparing the simulation/analytical solutions (Olshevskiy, Kim, & Yang, 2015).

The UM bogie model was then simulated on the curved section of track under varying speeds and loads to generate the loading combinations for the average vertical/lateral forces and roll and pitch torques shown in Table 2.3. These loads were then transferred to the FEA model to calculate the contact pressures and the amount of material removal as well as the wear rate of secondary suspension components as a function of the service mileage.

The computation speed of the FEA simulation was then increased by creating two sub-models which ran in parallel with the dynamic model. The first sub-model, was used to calculate the contact pressures acting on the centre plate and side bearers due to the vertical forces as well as the roll and pitch torques. Whereas the second FEA sub-model, used the lateral force from the UM model to calculate the contact pressures during rim contacts between the bolster/wagon body centre plate components. The results from both sub-models are then combined to calculate the wear rate for a given car mileage, see Figure 2.39 (Olshevskiya, Yang, & Kima, 2015).

The most important factors with regards to vehicle operating conditions on the Russian railways were then selected from the measured statistical data shown in Figure 2.40 and used as weighting factors in the FEA model. The assumptions that were applied to the wear model algorithm were as follows;

- The wear of the centre plate does not influence the dynamic behaviour of the vehicle model.
- Motions of the UM model in short sections of track include all real world motions.
- Wear is proportional to the work done by the friction forces.
- The material properties, surface roughness parameters and the wear coefficient K of the centre plate components remain constant throughout their useful service life.

Load	Value						
Vertical force, P_z, kN	0.10	98.07	225.55	343.23	441.30	588.40	725.69
Roll torque, M_y, kN m	0.00	19.61	49.03	78.45	117.68	166.71	–
Pitch torque, M_x, kN m	0.00	4.90	9.81	14.71	20.59	–	–
Lateral force, P_x, kN	0.10	0.98	1.96	3.92	5.88	7.85	10.79

Table 2.3: Loading values used in the simulations (Olshevskiya, Yang, & Kima, 2015).
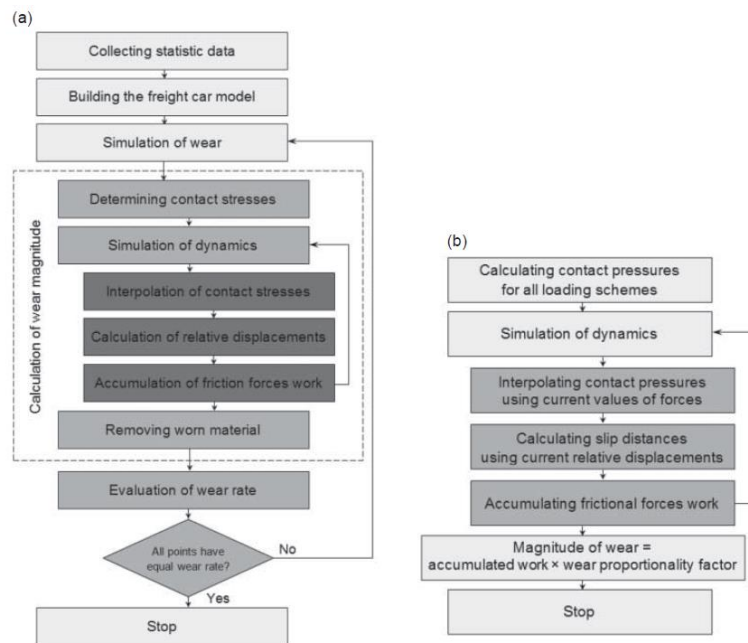
Figure 2.39: (a) General algorithm for the wear simulation. (b) Worn material removal calculation (Olshevskiy, Kim, & Yang, 2015).
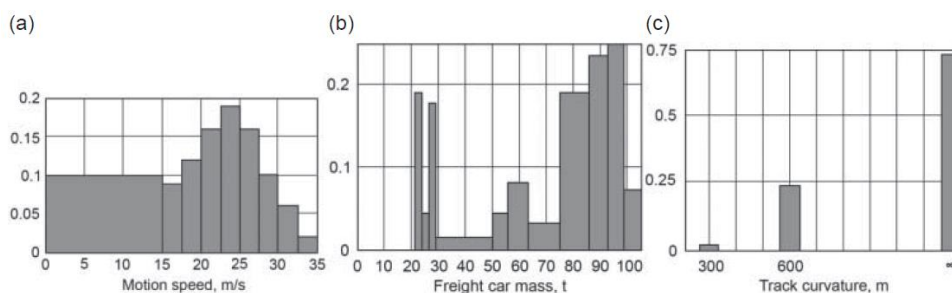
Figure 2.40: (a) Distributions of the motion speed. (b) Freight car mass. (b) Curved sections of track (Olshevskiya, Yang, & Kima, 2015).

To calculate the wear rate and wear value of the centre plate components, the nodal contact pressures in the FEA model are interpolated and the displacements at these nodes are then used to calculate the work done by the friction forces. A layer of material is then removed from the centre plate i.e. The positions of the contact nodes in the FEA model are updated when the applied forces on the vehicle model are high enough to initiate gross sliding. The results from the wear model predictions were then compared against the real wear measurements and shown to be in good agreement. The wear scars on the FEA model for example, were shown to be in same locations as those that were observed on the real components (Olshevskiya, Yang, & Kima, 2015).

The model also showed that the wear in the centre plate starts at the edges first and then works its way to the centre over time. For low mileages (Less than 2365 km), the wear rate at the edges of the centre plate was shown to be 35 times higher than wear rate in the centre. Whereas for the maximum mileage simulations (236000 km), the wear at the edge in comparison to the centre, was 1.6 times higher, which suggests that the surfaces have worn-in (Olshevskiya, Yang, & Kima, 2015).

The wear value that was calculated after the maximum mileage simulation was shown to be 2.36 mm, which is in close agreement with the measurement of 2.5 mm. The conclusions to this work were that for an annual mileage of 100,000 km, the average wear calculated by the wear simulation model was shown to be in the region of 1 mm, see Figure 2.41 (Olshevskiy, Kim, & Yang, 2015).
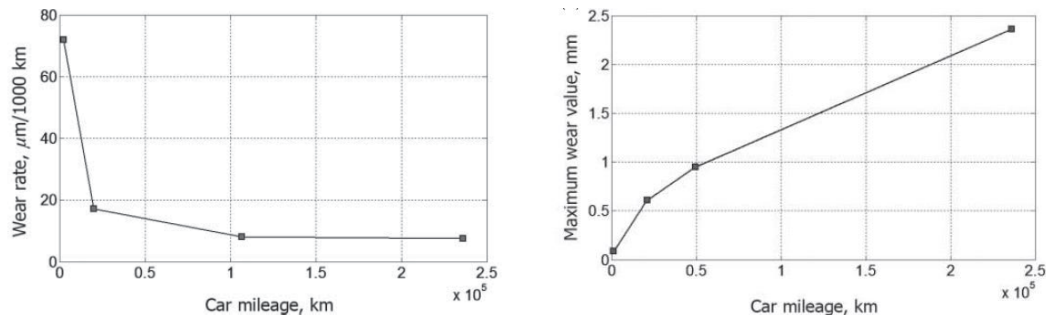
Figure 2.41: (Left) Value of the centre plate wear rate as a function of mileage. (Right) Maximum wear value in millimetres as a function of mileage (Olshevskiy, Kim, & Yang, 2015).

In (Wu & Robeda, 2004) there is a suggestion that the effects of centre plate lubrication are not fully understood by the rail freight industry. It was pointed out in this work that some freight operating companies lubricate the centre plate bearings, whereas others don`t as it is thought to reduce the critical speed of the bogie. As there were no standardise practices put in place for the industry to follow, the aim of this research was to address these gaps in knowledge.

During this research, on-track tests were used to analyse the curving performance of the three-piece bogie. The first set of track tests were carried out on a vehicle that had no lubrication between the bogie/wagon body centre plates i.e. Dry steel-on-steel contact (COF = 0.5). Whereas for the second set of tests, liquid lubrication was applied to the centre plate bearing surfaces to reduce the COF (COF = 0.1). For the dry condition test, it was clear to see from the measurements, that this configuration produced less relative displacements in reverse curves for the leading bogie. Whereas the lateral forces, which were measured when the vehicle reached the middle section of the curve, were seen to been approximately equal for the dry/lubricated centre plate conditions.

The Angles of Attack (AOA) of the leading/trailing wheelsets were also measured during the on-track tests. The AOA of the leading wheelset for the lubricated centre plate, was shown to be in the region of 9 mrad, whereas for the dry centre plate, the AOA was almost double at 17 mrad. The AOA of the trailing axles was also given and shown to range from 0 – 13 mrad. The post-test analysis of the measurements suggested that the creep forces in the leading axle wheel/rail contacts, become saturated when the AOA is above 5 mrad. Therefore, as the AOA continues to increase above this level, the change in lateral force is relatively small, whereas the lateral forces on the trailing axle, even though the AOA was lower, were higher (Wu & Robeda, 2004).

Dynamic simulations were then carried out on an equivalent MBS model of a 125 t coal hopper with three-piece bogies in the tare and laden loading condition using varying COF values. The pre-loads on the CCSB were set to 40% of the tare load and 6% of the laden load. The results from several simulations with different model parameters and side bearer configurations were then plotted on

comparison ratio chart. This chart showed that the bogie rotational resistance was 3 times higher in the tare condition. The highest rotational resistance for example, was shown to be for the vehicle model with the CCSB and the highest COF value which was 0.5 (Wu & Robeda, 2004).

The final conclusions from this study however, were that the centre plate friction was a secondary factor in relation to reducing wheel wear. The dominant factors were suggested to be the wheel/rail profiles (New/worn), as well as the levels of track lubrication. The following section discusses some of the testing procedures that are used in railway vehicle acceptance tests.

2.13.   Railway vehicle acceptance testing

Railway vehicle testing plays a key role in developing new technologies as well as validating the results produced by Multibody Simulations (MBS). As was mentioned in the introduction, the confidence levels in the modelling methodologies applied to passenger vehicle models are high. Whereas for freight vehicles with friction damped suspensions, the confidence levels are low due to the lack of test data and more significant modelling challenges (Iwnicki, Stichel, Orlova, & Hecht, 2015), (Allen, Perez, & Hatt, 2008) and (Berg & Evans, 2009).

Newly built and modified rail vehicles also have to demonstrate compliance to applicable standards. In the UK for example, vehicles have to comply with the Railway Group Standard GM/RT2141 (Issue 3), "Resistance of railway vehicles to derailment and roll-over", before they are allowed to operate on the rail network. This standard offers vehicle manufacturers three different methods of gaining acceptance which are dependent on the type of vehicle been tested.

Compliance method 1 is applicable to vehicles not having multi-bogie/axle configurations or novel suspensions/running gear. This method uses laboratory based wheel unloading tests ($\Delta Q/Q$) and bogie rotation tests as well as on-track ride tests. Compliance method 2 is the route for vehicles with multi-bogie/axle configurations, but without novel suspension/running gear. This method replaces the laboratory wheel unloading and bogie rotation tests with equivalent MBS tests using a vehicle model that has been validated against laboratory wheel unloading and bogie rotation test data. This model is then used to predict the Y/Q ratio as a time history (RSSB, 2009).

The most accurate method of assessing the derailment resistance of a rail vehicle on the other hand, is to measure the ratio of the lateral/vertical forces (Y/Q) at the wheel/rail interfaces during on-track tests. This is defined as compliance method 3 in the standard and is applicable to any type of vehicle. However, it is the only method available for vehicles with novel suspensions and running gear. In (Stow & Andersson, 2006), the importance of field testing is discussed in detail and the main reasons for carrying out these tasks are also given, which are as follows;

- Component characterisation
- Determination of parasitic/secondary effects
- Structural testing
- Validation testing
- Acceptance tests
- Reproducing track geometry
- Measuring wheel/rail profiles

Suspension components such as coil springs, bushings and dampers for example, are normally characterised using full scale/scale laboratory tests. These measurements are then used to tune the parameters of the MBS model. The parasitic effects of the Lenoir link on the Y25 bogie as well as the

warp stiffness of the three-piece bogie however, are more difficult to quantify without assembling the bogie/running gear first (Stow & Andersson, 2006).

Structural testing is carried out on rail vehicles to evaluate the strength of the car body/bogies frames as well as the crash worthiness. (Stow & Andersson, 2006) point out that all railway administrations around the world carry out vehicle acceptance tests which are specific to individual countries and operating companies. The acceptance testing procedures that are used in Australia (AS7509.2) and Europe (EN 14363) for example, are discussed in (Spiryagin, et al., 2012) and (Aizpun, Alonso, & Vinolas, 2015).

Wheel/rail profiles and track irregularities are also recorded during field tests as these parameters are critical to gauging studies, accident investigations and maintenance planning. Track defects such as gauge widening, track-twists and cyclic top have a significant influence on the vehicle behaviour which needs to be accounted for in MBS. A detailed discussion of the different testing methods and equipment used during full scale wheel unloading, sway and roller-rig tests can be found in (Jaschinski, Chollet, Iwnicki, Wickens, & Von Wurzen, 1999).

Scale testing is also widely used by the rail industry for research and validation purposes, as well as to characterise individual components such as rubber bushings, linkages, coil springs and hydraulic dampers (Karlsson & Persson, 2003). Several scale testing methodologies that are used by different research institutions around the world are discussed in (Allen, Scale Testing, 2006) and (Zhang, Dai, Shen, & Zeng, 2006).

The main benefit of using scale testing in comparison to full scale tests, are the lower development costs involved in designing and setting-up a test. Scale testing also allows problems such as wheel/rail wear to be studied under carefully controlled conditions. Whereas the limitation with field tests, are that the vehicle-track interactions are random, which makes it more challenging to accurately quantify the rates of wear and degradation (Drinkwater, Dwyer-Joyce, & Cawley, 1996) and (Dowson, 1997).

There are a number of limitations however to scale tests which are discussed in (Allen, Scale Testing, 2006). This author points out that a scientific based approach must be used in the scaling strategy so the effects of different scaling laws and errors associated with these can be easily understood. For example, whether/not the physical laws of similarity between the full scale system and scale model representation are valid. The following section discusses the recent developments in freight vehicle technologies.

2.14.   Recent developments in freight vehicle technologies

The freight bogies discussed so far in the literature review such as the Y25 bogie for example, was first developed in the late 1940`s, whereas the three-piece bogie on the other hand, was developed in the late 1800`s. The basic design of both bogies however, still remains the same after all this time, which owes testament to how good the original design concept is (Evans & Rogers, 1998) and (Stichel, Orlova, Hecht, & Iwnicki, 2015).

In recent decades changing industrial markets around the world has led to an increase in road congestion as well as high levels of air pollution in towns and cities. Part of the solution to address these growing concerns, is to shift more freight from road to rail. The potential increase in future demand for passenger and freight services however, is going to put more stress and strain on an already overstressed network. Building more network infrastructure for example, is the most challenging and costly engineering solution to implement. Whereas, increasing the axle loads and operating speeds of the vehicles is seen as a cheaper alternative, but at the expense of more

vehicle/track maintenance procedures as well as a revision of the relevant standards (Iwnicki, Stichel, Orlova, & Hecht, 2015).

To tackle some of the issues mentioned above with regards to the capacity constraints, (Shackleton, 2015) developed the Spectrum bogie, which was a novel concept idea of an optimised bogie. The bogie components were designed using a Computer-Aided-Design (CAD) and Multibody Simulations (MBS) were then used to identify the optimum suspension parameters. However, to reduce the development costs of the Spectrum bogie, suspension components that were familiar to freight vehicle maintenance depots, as well as certified by the UK rail industry were used in the final design, see Figure 2.42.
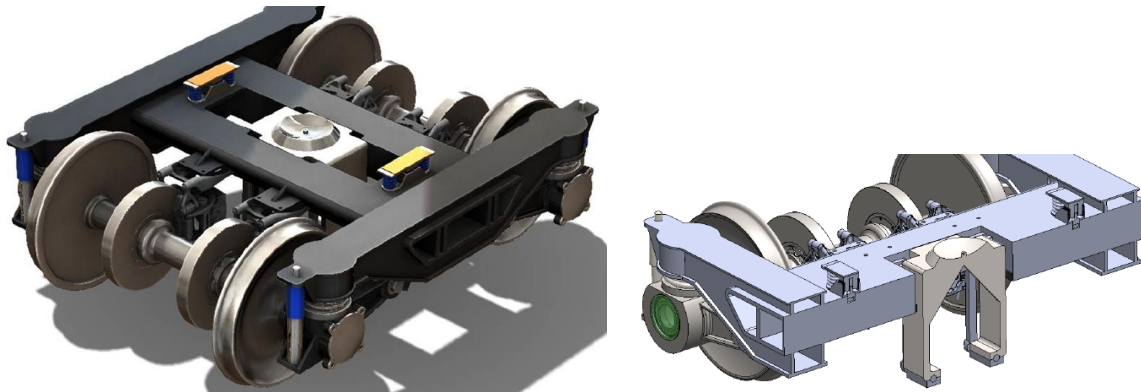
Figure 2.42: (Left) Spectrum bogie design. (Right) Spectrum bogie trailing arm suspension (Shackleton, 2015).

The main aim of the Spectrum project was to design a bogie that could run safely at 160 km/h as well as maintain good curving performance. A design review of existing freight vehicles was carried out to identify the ones with the best track performance qualities. These designs were then taken forward and further refined to meet the design requirements assigned to the Spectrum bogie. After many design iterations, a viscously damped trailing arm suspension shown to the right of Figure 2.42, was then selected for the final design as well as axle mounted brake discs (Shackleton, 2015).

To identify the optimum suspension parameters for the Spectrum bogie, MBS were carried out in VAMPIRE. The lateral responses for different wheel conicities and vehicle speeds, as a function of the secondary suspension lateral stiffness parameters are shown in Figure 2.43. From these results, it can be seen that the peak of the lateral instabilities occurs when the stiffness coefficient is in the region of 8 MN/m. After this analysis, it was then suggested that the ideal stiffness to maintain good running stability should be less than 0.2 MN/m (Shackleton, 2015).

Virtual vehicle acceptance tests were then carried following the GM/RT2141 Railway Group Standard as well as the EN 14363 standards. The Spectrum bogie demonstrated compliance with all the given safety requirements and was shown to be stable at running speeds up to 180 km/h. The cost benefits for freight operating companies using this type of bogie, if this concept is to be made available in the future, were also shown to be promising. The Variable Usage Charges (VUC) for the spectrum bogie in the tare and laden condition, were shown to be 6 and 18% lower than VUC currently applied to freight vehicles with friction damped suspensions (Shackleton, 2015).
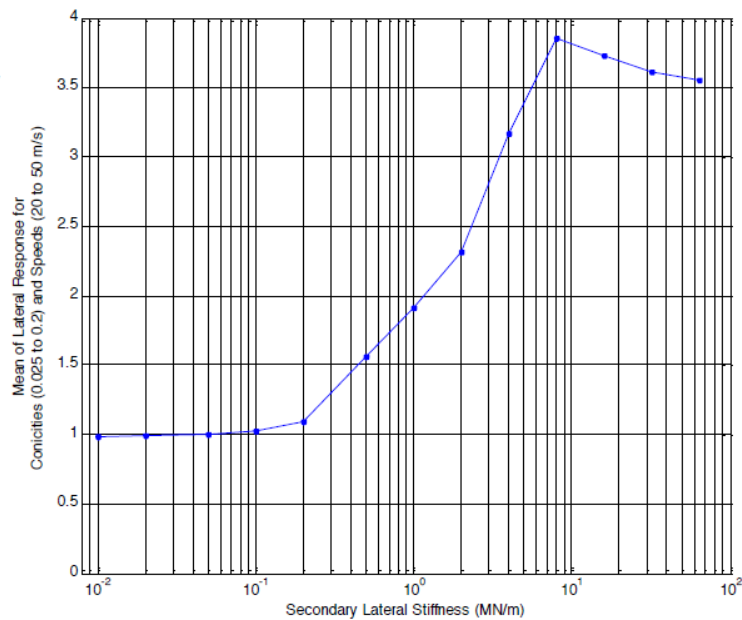
Figure 2.43: Dynamic stability analysis during the development stages of the spectrum bogie (Shackleton, 2015).

The Sustrail project was also carried out in the same year by (Benzin, Johnsson, Stichel, Orlova, & Iwnicki, 2015). The aims of this work were to design a high performance light weight bogie with low noise emitting properties. The performance requirements were to reduce the lateral track forces by 50% and total energy consumption by 20%. These improvements would then lead to a reduction in the total costs associated with vehicle and track maintenance issues (Benzin, Johnsson, Stichel, Orlova, & Iwnicki, 2015).

The first stage of the Sustrail project also involved an in-depth review of the proven rail technologies, different types of running gear and condition monitoring systems that are already used by the freight industry. This process identified the running gear components that could be used in Sustrail bogie to make the final design more commercially viable to freight operating companies in comparison to other alternatives, see Figure 2.44. This bogie is designed to run at 120 km/h under a 25 tonne (t) axle load, whereas the Y25 bogie on the other hand, is limited to a 20 t axle load at this speed (Adtranz, 2000). Higher operating speeds and axle loads however, can have a negative impact on the vehicle and track maintenance costs if the suspensions are not designed and tuned accordingly (Benzin, Jonsson, Stichel, Orlova, & Iwnicki, 2015).
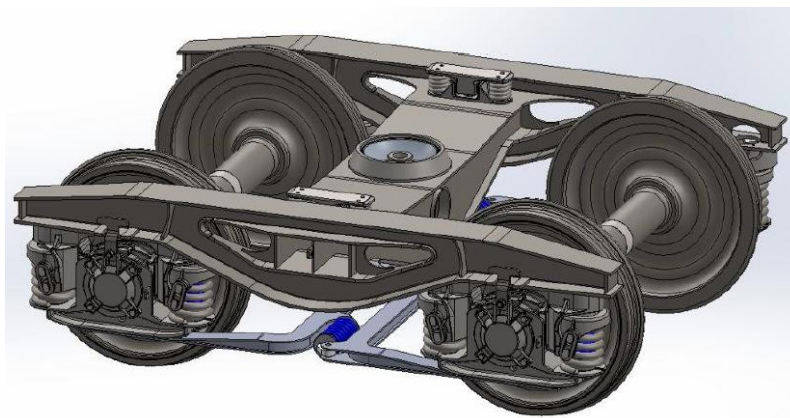
Figure 2.44: The Sustrail bogie (Benzin, Johnsson, Stichel, Orlova, & Iwnicki, 2015).

After short listing the running gear components that could be used in the Sustrail bogie design to make it out perform the Y25 bogie. Dynamic simulations were then carried out on different vehicle models using realistic wheel/rail profiles and a variety of software packages including VAMPIRE, SIMPACK, MEDYNA and GENSYS. Before starting the main analysis work however, the results from the different software packages were benchmarked using virtual performance tests and a vehicle model with standard Y25 bogies to ensure all the results were comparable.

Four different vehicle MBS models were then developed of the Y25 bogie to identify the optimum bogie design and suspension configuration. These included a standard vehicle model, one with double Lenoir links and another version with radial arms. The forth model had double Lenoir links as well as radial arms. The critical speed of each vehicle model was then determined by setting the initial velocity to 160 km/h, which then decreased to 40 km/h over a time period of 60 seconds. These simulations were carried out on straight sections of track with irregularities placed 40 m from the start (Benzin, Jonsson, Stichel, Orlova, & Iwnicki, 2015).

The speed at which the total lateral forces dropped below 2.5 kN, was then defined as the critical speed of the vehicle model. For the Sustrail bogie to achieve a stable running speed of 140 km/h under a 25 t axle load, the optimum stiffness parameters for the radial arm were shown to be in the region of 750 kN/m for the lateral direction. Whereas in the longitudinal, the stiffness parameters were left in their original state apart from the inclusion of the double Lenoir links (Benzin, Johnsson, Stichel, Orlova, & Iwnicki, 2015).

Simulations were also carried out to investigate the performance of the bogie with a secondary suspension ring placed around the periphery of the centre bowl, a design which is based on the LEILA bogie, see Figure 2.45 (Left). Each vehicle was then simulated in the tare, part-laden and laden loading conditions using a wide range of stiffness parameters for the centre bowl spring. From the amplitude responses shown to the right of Figure 2.45 however, it can be seen that the ratio of the lateral forces in the Sustrail bogie in the region of 2 Hz, are significantly higher than those seen in the standard Y25 bogie (Black line). The secondary suspension ring therefore, was not included in the final design (Benzin, Johnsson, Stichel, Orlova, & Iwnicki, 2015).

The radial steering arms and double Lenoir links however, were taken forward as these components led to improvements in the curving performance and running stability. An electronic braking system is also included in the final design which has led 3 dB reduction in braking noise. Wheelset acoustic condition monitoring systems have also been fitted to detect defects such as cracks. This information can then be used by freight operating companies to carry out pro-active vehicle maintenance as well as to prevent catastrophic failures of the wheelsets from occurring in service (Benzin, Johnsson, Stichel, Orlova, & Iwnicki, 2015). The following section draws some final conclusions on the literature review to identify the current gaps in knowledge relating to the experimental characterisation and modelling of freight vehicle secondary suspension components.
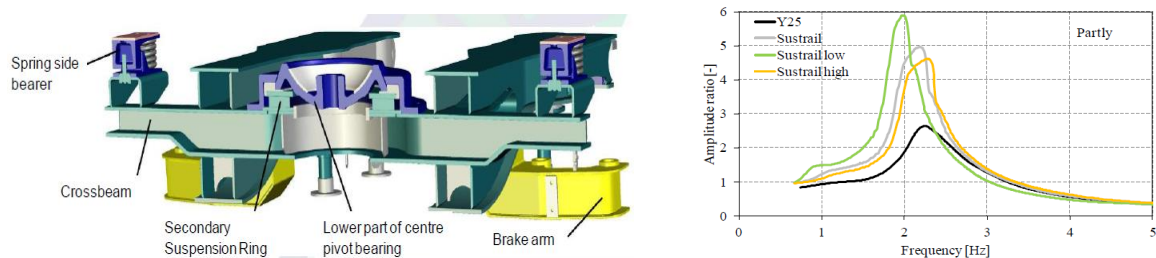
Figure 2.45: (Left) Sustrail bogie with the secondary suspension ring. (Right) Frequency response of the Sustrail bogie lateral forces (Benzin, Johnsson, Stichel, Orlova, & Iwnicki, 2015).

2.15.   Discussion and conclusions

The literature review has shown that there is a wide range of different testing and modelling methodologies available to analyse the dynamic performance of rail vehicle/infrastructure components. The physical testing of suspension components, whether it be on-track or laboratory tests, is a key ingredient to building more confidence in simulation results generated by highly nonlinear freight vehicle models, as these testing procedures also generate the benchmark test data that is required to validate Multibody Simulations (MBS) models.

From a MBS point of view, a significant amount of rail vehicle modelling experience and engineering judgement, is required in order to fully understand as well as justify the simplifying assumptions made by different software packages and how these influence the overall simulation results. A vehicle-track model that is too simple or contains incorrect modelling parameters for example, will produce misleading results. Whereas an overly complicated model will be computationally inefficient. Both of these points therefore, need to be taken into consideration at an early stage during the model building process.

The main conclusions to be drawn from the complete literature review are that the stiffness and damping parameters of the suspension components play a critical role in the running dynamics of the vehicle. The modelling methodologies applied to the secondary suspension components however, are often over simplified and tend to neglect the mechanical properties of the centre plate/side bearer wear liners. These components for example, are manufactured using either polymers or thermoset composite materials, but their parameters in the MBS environment, are generally lumped together with the steel properties of the bogie/wagon body suspension components.

The Coefficients of Friction (COF) values prescribed to the suspension components in MBS are more often than not, approximated using other works rather than specific measurement data from laboratory tests. The changes in friction characteristics of the secondary suspension components over time and how these influence the running dynamics of the vehicle are also not fully understood. This then leads to more uncertainties in the vehicle model.

This lack of understanding however, has led to a number of freight train derailments in the UK during the last two decades including those that occurred at Washwood Heath in September 2006 and March 2015. The Rail Accident Investigation Branch (RAIB) carried out extensive investigations into the root causes of these accidents, suggesting that high bogie rotational resistance was the causal factor in both cases. The first accident was caused by an inadequate side bearer design, whereas the second, was caused by a severely damaged centre pivot wear liner. This particular wear liner tore whilst in-service which led to significant levels of wear debris building-up in the pivot mechanism over time, as well as direct steel-on-steel contact between the bogie/wagon body suspension components.

From a practical/industrial perspective, this lack of understanding needs to be fully addressed in order to prevent similar incidents from occurring in the future. The inaccessibility of the secondary suspension components once the bogie/wagon body are coupled together however, makes visual inspections an almost impossible task, which makes it even more challenging for freight operating companies to define optimum maintenance schedules for their vehicle fleets.

This review clearly shows that there is an urgent industrial need to improve the confidence levels in secondary suspension testing and modelling methodologies so that freight vehicle performance and reliability can be improved. The remaining chapters of this thesis therefore, are devoted to the experimental characterisation of different industry standard wear liner materials, as well as the modelling of these components in MBS. The following chapter discusses the design of experiments.

3. Design of experiments

The laboratory tests discussed in this section were specifically designed to investigate the contact mechanics and friction characteristics of secondary suspension wear liner components, such as centre plate liner shown in Figure 3.1. This low friction component is fitted to the machined surface on the three-piece bogie bolster before connecting the wagon body/bogie to reduce the bogie rotational resistance as well as to prolong the useful service life of the secondary suspension components by preventing direct steel-on-steel contact. The wear liners also provide friction damping in the yawing and longitudinal/lateral directions and help to reduce the noise emittance of the vehicle (Tickell, Downing, & Jacobsen, 2004).

The findings from the laboratory test results will then be used to develop a more informative modelling methodology for dry friction suspension components, as well as a robust validation procedure. The main aim of this work from a modelling perspective is to build more confidence and certainty in the friction models used in freight vehicle Multibody Simulations (MBS), whereas from a practical point of view, this research is driven by the secondary suspension failure modes that lead to high bogie rotational resistance, see Appendix B. These figures show several suspension components in the new/used states with different failure modes ranging range from general wear and tear to catastrophic failures. From this analysis, it is clear to see that there is an industrial need to detect these failure modes at an early stage of their development in order to reduce vehicle and track maintenance costs.

The diameters of the wear liner product shown in Figure 3.1, range from $354 - 405$ m, see the specifications shown in Appendix C. However, once the bogie/wagon body are coupled together, the wear liners are completely inaccessible, which makes it impossible to carry out visual inspections in order to gauge the condition of these components in between planned maintenance schedules. Also, if no bogie condition monitoring systems are used on the network routes for example, then freight operating companies have to rely on the technical specifications published by the wear liner suppliers, as well as practical experience and knowledge to predict the optimum maintenance cycles for their fleets.

The main advantages of using scale model tests in comparison to full scale tests for this particular research work, are the low costs associated with designing and setting-up the laboratory experiments. The ability to carry out a large number of tests due to having easy access to the centre plate/wear liner components is another significant advantage to the testing methodology presented in this thesis. Whereas on the full size vehicle, a crane and several vehicle engineers would be required to remove the wagon body from the bogie, which would be more time consuming, expensive and potentially, more dangerous.

To better understand the friction characteristics of the centre plate/wear liner components and the changes that take place in these parameters over time, several scale model test cases were then investigated in the laboratory using three different industry standard wear liner components. Wear liner material A for example, is manufactured from a thermosetting composite material and used by freight operating companies throughout Europe, whereas materials B and C on the other hand, are manufactured from polymers with different levels of additives included mixes to give each liner its` own unique mechanical properties. The following section discusses the derivation of the scaling laws that were used to the design of the scale model centre plate components as well as the operating parameters for the laboratory tests (TENMAT Ltd, 2019) and (VESCONITE plastics, 2019).
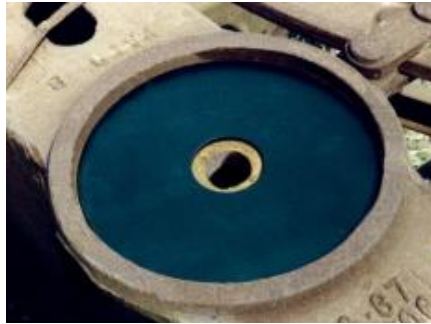
Figure 3.1: Three-piece bogie bolster Hollube wear liner. Outer diameter = 405 mm, inner diameter = 86 mm (Amsted Rail Company, 2014).

3.1. Centre plate scaling laws

This section discusses the 1:7 scaling laws that were derived to design the scale model centre plate/wear liner components as well as the operating conditions to investigate in the laboratory tests. The loading conditions for freight vehicles as was mentioned previously, are specific to individual countries and networks, but typically range from 5 – 30 t per-axle for the tare and laden operating states.

Before a vehicle is allowed to operate on the UK rail network however, newly built and modified vehicles with novel suspension systems, have to pass a series of vehicle acceptance performance tests, see the Railway Group Standard (RGS), GM/RT2141 (Issue 3). One of the tests that is used to evaluate the derailment resistance of a vehicle for example, is the X-Factor test. This test is normally carried out on a full size laboratory test-rig and is used to evaluate rotational resistance of the vehicle by measuring the bogie-to-wagon body yaw torque as the bogie is rotated relative to the static wagon body, see for example (Shi, Wu, Luo, & Guo, 2013) or (Simson & Brymer, 2008).

The yaw velocity parameters specified in the GM/RT2141 standards and GM/RC2641 guidelines, Recommendations for vehicle static testing, recommends using speeds ranging between 0.2 – 1 degree/s (°/s) for freight vehicles and between 3 – 4 °/s for high speed passenger vehicles. These are the peak yaw velocities that are likely to be seen by the vehicles when negotiating transitions into curves, as well as switches and crossings in service.

Due to the commercial sensitivity and the costs associated with accessing the test data generated from vehicle acceptance tests however, there is a lack of test data freely available for validating friction damped freight vehicle MBS models. The confidence levels in results generated by these highly nonlinear models therefore, are much lower in comparison to those generated by passenger vehicle models, which tend to be built using suspension elements with linear characteristics which are relatively easy to validate.

The main aim of the laboratory test cases presented in this thesis is to generate a wide range of benchmark data in order to systematically characterise different wear liner components as this data is not currently available. The critical system parameters that are required for developing optimised MBS models of these components, such as the Coefficient of Friction (COF) values, contact stiffnesses and evolution in these parameters over time, can then be calculated from the test data and used with more confidence in MBS.

Scale model tests were then used as part of this research work as no full-scale test-rigs were available when the project was being planned. The scaling parameters governing the geometry as well as the mechanical properties of the scale model centre plate/wear liner components then had to be carefully

considered in the initial design stages of the experiments to maintain similarity between the contact stresses acting on the full size/scale model components.

The contact stresses are deemed to be the most important parameters under investigation in this study as these are directly related to the wear rates of the wear liners, the contact stiffness and the COF`s. Also, to add more value to the benchmark results discussed in this thesis, wear liner products that are currently used throughout the rail freight industry were then characterised in the laboratory. The mechanical properties of the full size/scale model components therefore, are exactly the same so the scaling parameters for the normal stress φ_σ, shear stress φ_τ, strain φ_ε, Poisson`s ratio φ_ν and the COF φ_μ, are all equal to unity, see Equations (3.1) – (3.5).

$$\varphi_\sigma = \frac{\sigma_1}{\sigma_0} = 1 \tag{3.1}$$

$$\varphi_\tau = \frac{\tau_1}{\tau_0} = 1 \tag{3.2}$$

$$\varphi_\varepsilon = \frac{\varepsilon_1}{\varepsilon_0} = 1 \tag{3.3}$$

$$\varphi_\nu = \frac{\nu_1}{\nu_0} = 1 \tag{3.4}$$

$$\varphi_\mu = \frac{\mu_1}{\mu_0} = 1 \tag{3.5}$$

In these equations, the parameters with subscripts equal to one and zero, refer to the quantities in full size and scale model systems respectively, whereas the scaling factors, are the ratios of these two parameters. The scaling factors for the material density φ_ρ and Young`s Modulus φ_E are also equal to unity due to the material selection, see Equations (3.6) and (3.7).

$$\varphi_\rho = \frac{\rho_1}{\rho_0} = 1 \tag{3.6}$$

$$\varphi_E = \frac{E_1}{E_0} = 1 \tag{3.7}$$

The next set of parameters to consider are the geometric properties of the scale centre plate components. The external diameters of the full size Hollube wear liners range from 354 – 405 mm (Appendix C), whereas the internal diameter, which is a through hole for the king pin, is 86 mm. The contact stresses under the tare and laden axle loads, 5 – 30 t were then calculated using the maximum wear liner diameter of 405 mm to calculate the surface area of this component. The results from these calculations, which are discussed in the following section, show that the contact stresses under these loading conditions, minus the mass of the wheelsets/bogies, will range from 1.2 – 3.6 MPa.

The scaling parameters for the geometry of the scaled model components were then derived from the range of contact stresses discussed above, as well as the axial and torsional loading capacities of the universal testing machine available at the University of Huddersfield test facility. These parameters as can be seen from the specifications shown in Appendix D, are limited 10 kN and 100 Nm. To study the behaviour of the wear liner components under the equivalent scaled laden loading condition, the peak load of the testing machine was set to 9 kN. This limit therefore, would accommodate any increases in torque responses over time, as well as prevent the machine control from getting damaged and tripping if these events start to develop.

Length scaling factors φ_l ranging from 1:3, 1:4, 1:5, 1:6 and 1:7 were used in the design calculations to identify the scaling law that would enable the full range of contact stresses (1.2 – 3.6 MPa), to be investigated in the laboratory under peak loading condition of 9 kN. The process identified the 1:7 scaling law to be the most suitable under the given boundary conditions. The scaling factors for the radial length, surface area and volume, φ_l, φ_A, φ_V of the full size components therefore, are seen to

be 7, 49 and 343 times larger than 1:7 scale equivalents, see Equations (3.8), (3.9) and (3.10) respectively.

$$\varphi_l = \frac{l_1}{l_0} = 7 \qquad\qquad (3.8)$$

$$\varphi_A = \varphi_l{}^2 = 49 \qquad\qquad (3.9)$$

$$\varphi_V = \varphi_l{}^3 = 343 \qquad\qquad (3.10)$$

The scaling factors assigned to the stresses and surface area are then substituted into in Equations (3.11) to derive the scaling factor for the external forces φ_F. This analysis shows that in order to generate the equivalent contact stresses on the full size/scale model components, the forces acting on the full size components for example, will need to be 49 times higher than the loading conditions in the scale model laboratory tests. The contact stresses acting on the 1:7 scale centre plate components under the 9 kN loading condition therefore, are equivalent to stresses generated on the full size centre plate component under a load of 441 kN, which is in the correct the range of loads we are interested in studying.

The force and length scaling factors are then substituted into Equation (3.12) to derive the scaling factor for the externally applied moments φ_M, which is seen to be 343. The moments that are measured in the scale model laboratory tests under the given loading conditions therefore, will be 343 times smaller than the moments acting on the full size components.

$$\varphi_F = \frac{\sigma_1 A_1}{\sigma_0 A_0} = 49 \qquad\qquad (3.11)$$

$$\varphi_M = \frac{F_1 l_1}{F_0 l_2} = 343 \qquad\qquad (3.12)$$

The translational stiffness and damping scaling factors φ_k and φ_C for the wear liner materials as well as the torsional equivalents and $\varphi_{k\tau}$ and $\varphi_{C\tau}$, which are all equal to 7, are then derived by setting these parameters equal to the external forces and moments, divided by the length scaling parameter, see Equation (3.13) and (3.14) respectively.

$$\varphi_k = \varphi_c = \frac{\varphi_F}{\varphi_l} = 7 \qquad\qquad (3.13)$$

$$\varphi_{k\tau} = \varphi_{C\tau} = \frac{\varphi_M}{\varphi_l{}^2} = 7 \qquad\qquad (3.14)$$

The scaling factors for the mass φ_m and inertia φ_I of the full size components are derived using the scaling factors for the density, volume and length, see Equations (3.15) and (3.16). The mass and inertia of the full size components in comparison to the scale model equivalents, are 343 and 16807 times larger.

$$\varphi_m = \varphi_\rho\, \varphi_V = 343 \qquad\qquad (3.15)$$

$$\varphi_I = \varphi_m\, \varphi_l{}^2 = 16807 \qquad\qquad (3.16)$$

To maintain similarity between the dynamic forces and moments acting on the full size/scale model components during the laboratory tests, the scaling factors for time φ_t, circular frequency φ_ω and frequency φ_f are set equal to unity, see Equations (3.17) – (3.19).

$$\varphi_t = \frac{t_1}{t_0} = 1 \tag{3.17}$$

$$\varphi_\omega = \frac{\omega_1}{\omega_0} = 1 \tag{3.18}$$

$$\varphi_f = \frac{1}{\varphi_t} = 1 \tag{3.19}$$

The scaling factors for the acceleration φ_a and velocity φ_v of the full size centre plate are then derived using the time scaling factor and from Equations (3.20) and (3.21), it can be seen that these parameters are equal to 7. The rotational velocities in the scale model laboratory tests therefore, should range between 0.026 – 0.143 °/s in order to comply with the range of full scale equivalents given for the X-Factor tests, which are seen to be 0.2 – 1 °/s in the GM/RT2141 standards.

The rotational velocities that were used for the low/high speed test cases in the laboratory however, were set to 0.5 and 1 °/s to increase the number of case studies that could be carried out during this research. These parameters therefore, are outside of the GM/RT2141 recommendations when multiplied by the velocity scaling factor.

This scaling error suggests that the inertia forces as well as the wear rates of the 1:7 scale components for example, will be several times higher in the laboratory tests than the wear rates of the full size components. This parameter however, will not change the COF values for these materials and if it does have a significant influence, then this can be easily quantified by comparing the torque responses from the low/high speed test cases.

$$\varphi_v = \frac{\varphi_l}{\varphi_t} = 7 \tag{3.20}$$

$$\varphi_a = \frac{\varphi_l}{\varphi_t{}^2} = 7 \tag{3.21}$$

The derived scaling factors for the mass, stiffness and damping are then substituted into Newton`s second law of translational or angular motion, depending on the type of analysis, to check that dimensional correctness has been maintained between the full size/scale model systems (Allen, 2006). In these equations, m and I, are the mass and inertia of the system and c and k are material damping and stiffness coefficients. The external forces and moments are given as F and M and the translational acceleration, velocity and displacement, as $\ddot{x}$, $\dot{x}$ and x respectively. The angular equivalents of these variables are the $\ddot{\theta}$, $\dot{\theta}$ and θ terms, see Equations (3.22) – (3.25).

$$m\ddot{x} + c\dot{x} + k\mathbf{x} = \mathbf{F} \tag{3.22}$$

$$m\ddot{x}\left(\frac{\varphi_m\,\varphi_l}{\varphi_t{}^2}\right) + c\dot{x}\left(\frac{\varphi_c\,\varphi_l}{\varphi_t}\right) + k\mathbf{x}\,(\varphi_k\varphi_l) = \mathbf{F}\,(\varphi_F) \tag{3.23}$$

$$I\ddot{\theta} + C_T\dot{\theta} + K_T\boldsymbol{\theta} = \mathbf{M} \tag{3.24}$$

$$I\ddot{\theta}\left(\frac{\varphi_m\,\varphi_l{}^2}{\varphi_t{}^2}\right) + C_\tau\dot{\theta}\left(\frac{\varphi_{c\tau}\,\varphi_l{}^2}{\varphi_t}\right) + K_\tau\boldsymbol{\theta}\,(\varphi_{k\tau}\varphi_l{}^2) = \mathbf{M}\,(\varphi_M) \tag{3.25}$$

From the equations given above however, it can be seen that the internal and external forces and moments do not balance due to the scaling factors applied to inertia terms, $\left(\frac{\varphi_m\,\varphi_l}{\varphi_t{}^2}\right)$ and $\left(\frac{\varphi_m\,\varphi_l{}^2}{\varphi_t{}^2}\right)$, which give scaling factors of 2401 and 16807 respectively. Whereas the scaling factors for the external

forces and moments, are seen to be 49 and 343. Also, by setting the elastic forces equal to the gravitational forces, it can be seen that these forces do not balance either, see Equation (3.26).

However, by rearranging this expression, it can be seen in Equation (3.27), that both terms are equivalent to the square of the circular frequency of the system. Therefore, in order to maintain similarity between the external and gravitational forces, the gravity scaling factor φ_g, was reduced to 1:7 to balance the equations of motion, see Equation (3.28). A more comprehensive review of the different scaling methodologies used by several research institutions throughout Europe and China for example, can be found in (Allen, 2006). This completes the analysis of the scaling laws which are also listed in Appendix E. The following section discusses the scale model component designs and the laboratory testing parameters.

$$\varphi_k \varphi_l = \varphi_m \varphi_g \qquad (3.26)$$

$$\varphi_\omega{}^2 = \frac{\varphi_k}{\varphi_m} = \frac{\varphi_g}{\varphi_l} \qquad (3.27)$$

$$\varphi_g = \frac{1}{\varphi_l} = \frac{g_0}{g_1} = 1{:}7 \qquad (3.28)$$

3.2. Centre plate/wear liner component designs

This section discusses the 1:7 scale centre plate/wear liner component designs. Table 3.1 shows the geometric parameters of the full size/1:7 scale centre plates and from these, it can be seen that the outside radius of the scale model centre plate is 29 mm, which is seven times smaller than the full size equivalent, which is seen to 202.5 mm in Appendix C. Following the scaling laws derived in the previous section, the contact area of the scale model centre plate therefore, is 49 times smaller than the full size centre plate.

Component	Inner radius (mm)	Outer radius (mm)	Effective radius (mm)	Contact area (mm²)
Full size centre plate	43	202.5	135.1	123016
1:7 scale centre plate	6	29	19.3	2529

Table 3.1: Geometric parameters for the full size/scale model centre plate components.

The technical drawings for the dynamic and static centre plate designs are shown in Figures 3.2 and 3.3 respectively. These components were turned from a low carbon steel bar (C10), where the mechanical properties for the elastic moduli, shear moduli and Poisson`s ratio for example, are seen to be in the regions of 217 GPa, 81 GPa and 0.3 respectively. Whereas the thermal conductivity of this material at 20 °C, is seen to be relatively high in the engineering tables shown in (Higgins, 1993), ranging between 57.5 – 58.7 W/m.K.

The three wear liner materials on the other hand, are manufactured from two different types of polymer, as well as a thermosetting composite material. The elastic and shear moduli`s of these components as can be seen from the specifications shown in Appendix F, range between 2 – 2.5 GPa and 0.4 – 0.5 GPa respectively, which are significantly lower than the mechanical properties of the centre plates. The thermal conductivity of the wear liners is also considerably lower at 0.3 W/m.K, whereas the Poisson`s ratio for elastomeric materials, can range between 0.25 – 0.5 (Tottle, 1966) and (VESCONITE plastics, 2019).

The dynamic centre plate has a 10 mm blind-hole machined into the top-face which represents the feature for locating the king-pin, see Figure 3.2. The blind-hole machined into the back-face of this component, was for an ultrasound sensor to measure the local contact pressures in real-time. This sensor however, did not work as intended in the preliminary test cases, so it was not used in the experiments discussed in this thesis.

The static centre plate on the other hand, has two 10 mm blind-holes machined into the top-face for locating the ground dowel pins, see Figure 3.3. These pins protrude 3 mm above the top-face to locate the wear liners and prevent their rotation, which as can be seen from Figure 3.4, also have two blind-holes machined into the back-faces for locating the dowel pins. The complete test-rig with the centre plate/wear liner components assembled together, is shown in Figure 3.5. The following section discusses laboratory test parameters and the calculation methods that were used to obtain the COF values for the centre plate/wear liner components.
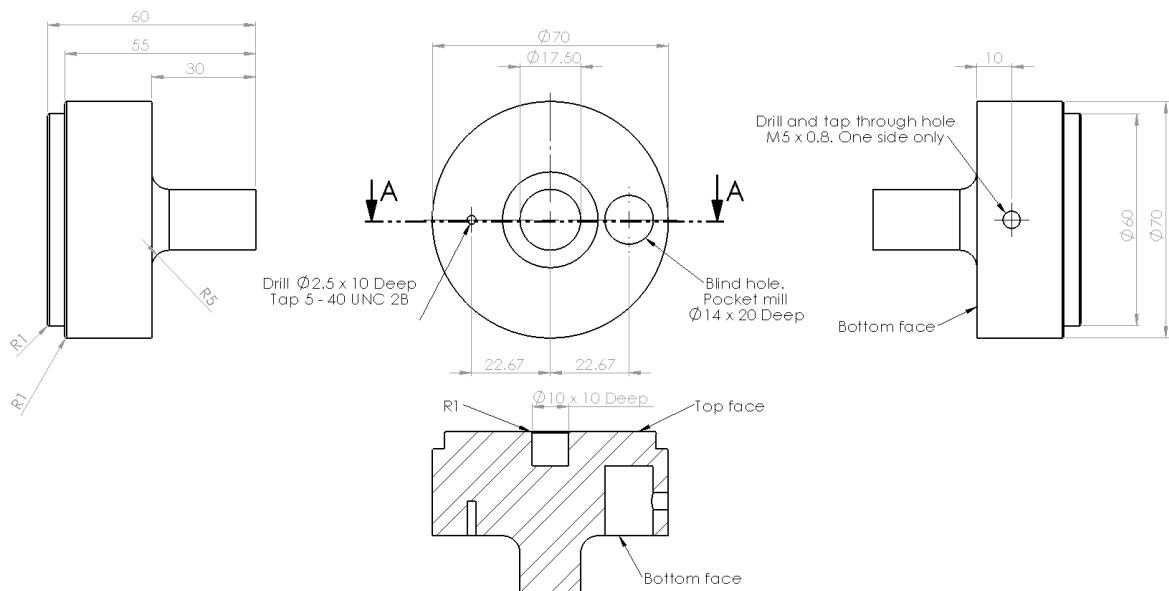
Figure 3.2: Dynamic centre plate design.
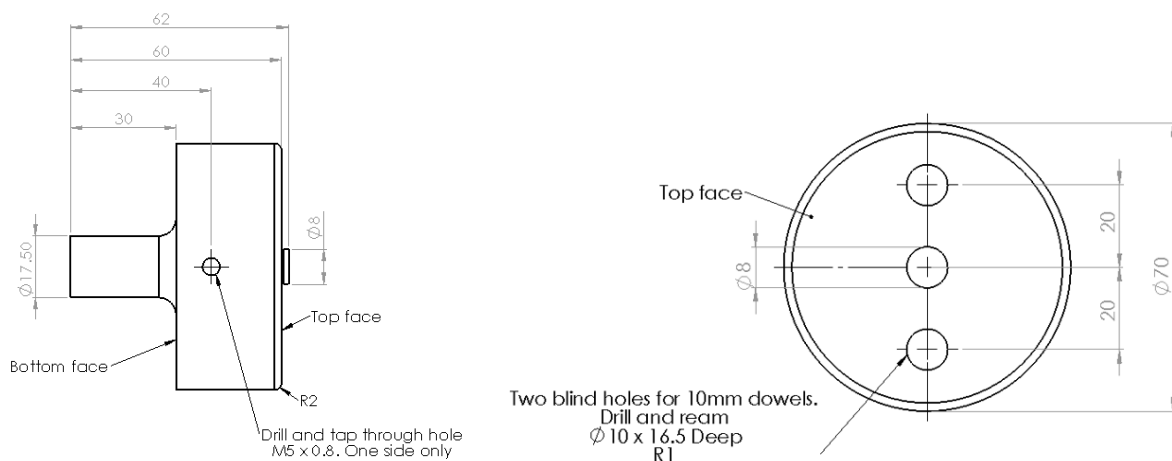
Figure 3.3: Static centre plate design.
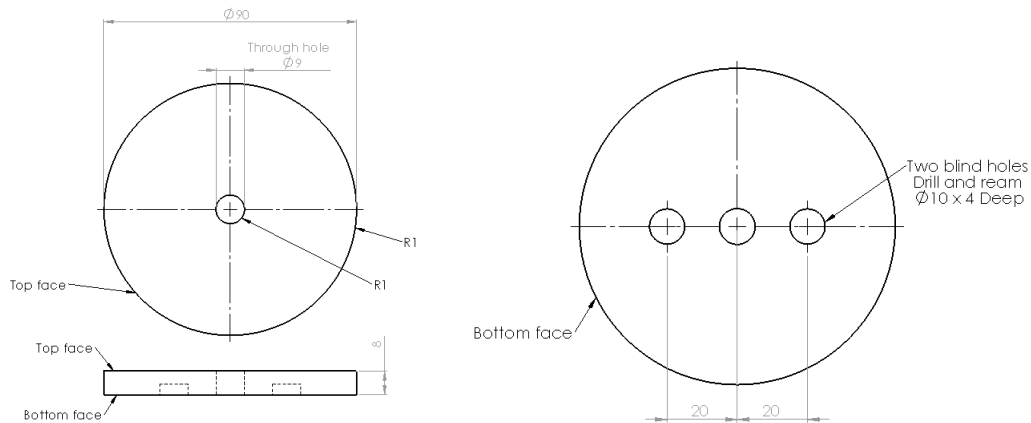
Figure 3.4: Wear liner design.
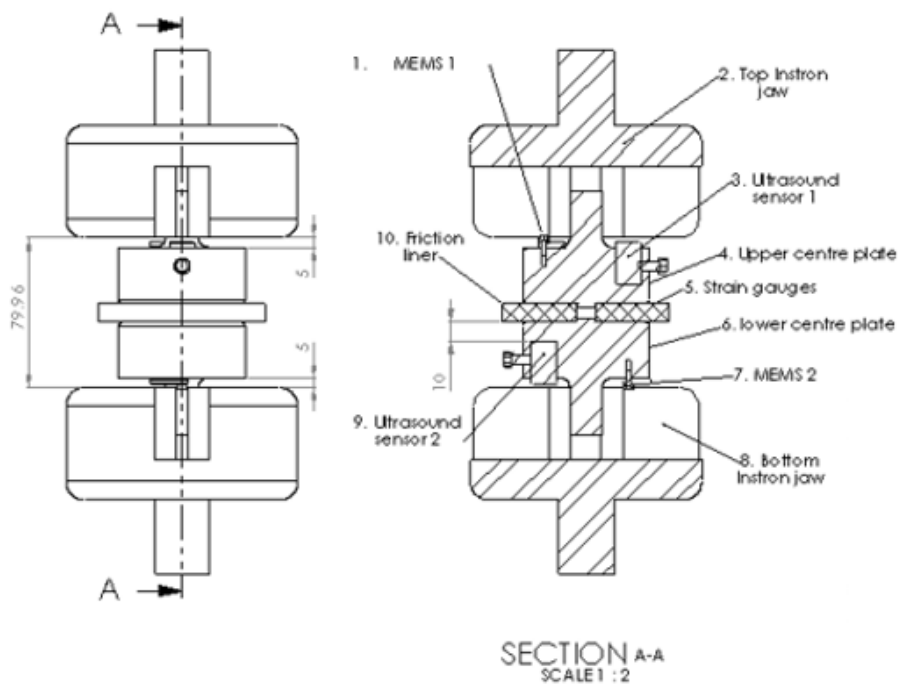
Figure 3.5: Scale model centre plate/wear liner test-rig.

3.3. Laboratory test parameters and the COF calculation method

The dynamic response of the 1:7 scale centre plate system was investigated under four different loading conditions, see Table 3.2. The new wear liner samples in each material group (A, B and C), were then subjected to two tests under each loading condition which were then carried out under the low and high sinusoidal forcing frequencies, 0.042 and 0.084 Hertz (Hz). These forcing frequencies generate rotational speeds that are equivalent to 0.5 and 1°/s respectively and are seen to be in agreement with the recommended speeds given in the Railway Group Standards (RGS), GM/RT2141 (Issue 3). Each cycle during the high and low speed test cases therefore, runs for either 11.9 or 23.8 seconds.

Running-in tests were then carried on the new wear liner samples at either the low/high forcing frequency. These tests then ran for 3000 cycles with the amplitude of motion and centre plate load set to $\pm$ 3 degrees and 0.5 kN. The contact pressures under this loading condition as can be seen from the results shown in Table 3.2, are similar to the range of pressures that act on the full size side bearer

components. The results from these test cases therefore, can be used to develop an optimised side bearer MBS model (Tickell, Downing, & Jacobsen, 2004).

The wear liner sample is then subjected to a 10800 cycle service test which is carried out at the same forcing frequency and amplitude of motion as the running-in test. Each wear sample therefore, is subjected to exactly the same number of cycles in order to quantify the wear rates of these components. The centre plate loading conditions however, are significantly higher in the service tests and seen to be either 3, 6 or 9 kN.

The contact pressures under these loading conditions as can be seen, range between 1.2 – 3.6 MPa (Table 3.2). To generate the equivalent range of pressures on the full size components for example, the centre plate loads would have to be 147, 294 and 441 kN respectively. In the discussions throughout this thesis, these loading conditions are called the tare, part-laden and laden for reference purposes.

Loading case	1:7 scale centre plate load (kN)	Full size centre plate load (kN)	Contact pressure (MPa)	Number of sinusoidal cycles	Amplitude of motion (± degrees)	Angular displacement per cycle (degrees)	0.042 Hertz forcing frequency test duration (hours)	0.084 Hertz forcing frequency test duration (hours)	Total angular displacement (degrees)
Running-in	0.5	24.5	0.2	3000	3	12	19.84	9.92	36000
Tare	3	147	1.2	10800	3	12	71.42	35.71	129600
Part-laden	6	294	2.4	10800	3	12	71.42	35.71	129600
Laden	9	441	3.6	10800	3	12	71.42	35.71	129600

Table 3.2: Operating parameters for the scale model laboratory tests.

The measured torque responses are then substituted into Equation (3.29) and then then rearranged to calculate the Coefficients of Friction (COF) for the wear liner samples. This equation shows that the resulting frictional torque τ_f, is equal to the integral of the product, $\mu.p.r.dr.d\theta$, which is the elemental torque generated by a surface element with an area equal to $dr.d\theta$. The local contact pressure acting on this area element and the radial distance to the axis of rotation are given as p and r respectively, whereas μ is the COF. The resultant frictional torque is then calculated by integrating this equation over the whole contact surface area. First with respect to the radial distance dr, and then with respect to the angular displacement $d\theta$ (Meriam & Kraige, 1998).

$$\tau_f = \int \mu.p.r.dr.d\theta \qquad (3.29)$$

In the analyses discussed in this section, it is assumed that the contact pressure p, is constant and uniformly distributed throughout the contact area. The normal force N_F acting on the entire contact surface therefore, is then found from the product of the constant pressure p and the total contact area, $\pi.R^2$, see Equation (3.30). Substituting this expression for the p term in (3.29), then gives the equation to calculate the total frictional moment τ_f for a constant normal force, see Equation (3.31).

$$\Pi.R^2.p = N_F \qquad (3.30)$$

$$\tau_f = \frac{\mu.N_F}{\pi.R^2} \int_0^{2\pi} \int_0^R r^2.dr.d\theta = \left(\frac{2}{3}\right).\mu.N_F.R \qquad (3.31)$$

The flat centre plate design however, has central hole for the king pin and hence, an inside radius R_i, as well as an outside radius R_o, which dictates the overall diameter. These parameters are then substituted for the radius term R in (3.31), thus resulting in the complete expression given in Equation

(3.32). The COF values are then calculated by substituting the measured torque responses, centre plate loads as well as the dimensions of the 1:7 scale centre plate component into (3.32). This formula is then rearranged to calculate the COF for the wear liner samples, see Equation (3.33).

$$\tau_f = \frac{2}{3}.\mu.N_F.\frac{R_o{}^3 - R_i{}^3}{R_o{}^2 - R_i{}^2} \tag{3.32}$$

$$\mu = \frac{\tau_f}{\left(\frac{2}{3}\right).R.N_F} \tag{3.33}$$

The time histories of the measured torque signals are then analysed in the frequency domain using a Fast Fourier Transform (FFT) as well as an inverse FFT coded in MATLAB using Equations (3.34) and (3.35) respectively. In these equations, $\hat{X}(f_k)$ and $X(t_j)$ are the Discrete Fourier Transforms (DFT) and Inverse Discrete Fourier Transforms (IDFT) in the frequency and time domains. N is the number of discretely sampled times in the time series, whereas j and k are arbitrary integers for indexing the calculation. The integer times for each sample and the spacing between these points, i.e. the time-step, are then given as t_j and Δt respectively, see Equation (3.36).

The discretised frequencies Δf in the DFT as can be seen from Equation (3.37), are equal to the sample rate f_s, divided by the number of sample points, N. The discretised frequency is then multiplied the by the arbitrary integer k to produce f_k, which is the frequency for indexing the computer algorithm, see Equation (3.38). f_k is then substituted into (3.34) and (3.35) to calculate the positive frequencies in the DFT`s and the IDFT`s.

The negative frequencies in this analysis, do not need to be considered as these are exactly the same as the positive ones. The maximum frequency of the original signal x(t) that can be accurately resolved in the DFT however, is limited to $\frac{f_s}{2}$, which the Nyquist frequency. The time period of the observation T, is then found by multiplying the time-step by the number of sample times, see Equation (3.39) (Gough, Richards, & Williams, 1983).

The main purpose of the spectral analysis on the measured torque signals is to characterise the frequency responses of the centre plate/wear liner components, as well as the changes in these parameters over time. The vibration frequencies associated with the fluid and structural borne noises due to the hydraulic transmission on the universal testing machine, which is currently in the un-damped state, were also characterised as part of this analysis. The following chapter discusses dynamic simulations and validation testing as well as the centre plate system modelling methodology.

$$\hat{X}(f_k) = \sum_{j=0}^{N-1} X(t_j).e^{-i.2\pi.f_k.t_j} \qquad k = 0,1,2\ldots,N\text{-}1 \tag{3.34}$$

$$X(t_j) = \sum_{j=0}^{N-1} \hat{X}(f_k).e^{-i.2\pi.f_k.t_j} \qquad j = 0,1,2\ldots,N\text{-}1 \tag{3.35}$$

$$t_j = j.\Delta t \tag{3.36}$$

$$\Delta f = 1/(N.\Delta t) = f_s/N \tag{3.37}$$

$$f_k = k.\Delta f \tag{3.38}$$

$$T = N.\Delta t \tag{3.39}$$

4. Dynamic simulations and validation testing

Multibody Simulations (MBS) play an important role in railway vehicle design, product development, virtual prototype testing, acceptance testing and accident investigations. The main advantages of using MBS to study the dynamic behaviour of railway vehicles in comparison to the traditional design analysis methods include, the ease of making design changes to the suspension system configuration and to the parameters of the vehicle/infrastructure models. Also, from an accident investigation point of view, MBS models can be simulated under running conditions that are not permissible in the real-world environment, which mitigates the safety risks involved with on-track testing (Bruni, Vinolas, Berg, Polach, & Stichel, 2011).

It is widely accepted amongst research institutions that there are many benefits associated with using MBS to analyse vehicle dynamics problems. However, it should also be pointed out that in the context of freight vehicles with dry friction suspension components for example, the confidence levels in current friction modelling methodologies applied to developing these highly non-linear vehicle models, are not as high as they could/should be. The reasons for the low confidence levels associated with simulation results generated by highly non-linear freight vehicle models however, can be attributed to several factors which are mainly focused around the lack of extensive field/laboratory test data.

The lack of field/laboratory test data for freight vehicles in particular, has then led to less scientific knowledge and understanding been available to industry experts as well as researchers/academics, in relation to how the centre plate/wear liner components actually perform in the real-world/railway environment. The majority of the freight vehicle MBS models discussed in the literature review for example, are considered to be validated when all of the requirements relating to the vehicle acceptance tests documented in the RGS, GM/RT2141, have been met. These requirements however, are based on the limited amount of field test data, so are not as robust or comprehensive as they could be.

The wide range of commercial MBS software packages available to use also introduces a number of significant modelling challenges, as well as uncertainties into the modelling methodologies applied to freight vehicles. These software packages for example, apply their own unique simplifying assumptions and modelling parameters to the various force elements available in the MBS libraries in order to reduce the simulation solutions times.

These assumptions however, can be difficult to justify in some cases, as the test data that was used to develop the force elements in the first place, such as the friction models or wheel/rail contact models for example, tends not to be included in the user`s manuals. This has then led to over-simplified friction models been implemented in freight vehicle MBS models, so the confidence levels in these simulation results are relatively low in comparison to the confidence in the results generated by passenger vehicle models, which tend to have linear suspension characteristics due to the hydraulic damping (Allen, Hatt, & Perez, 2007) and (Berg & Evans, 2009).

Therefore, to better understand the simplifying assumptions and to improve the confidence levels in the techniques applied to modelling friction damped suspension components in MBS, several simulation cases were investigated as part of this research work. These simulations were specifically designed to analyse the dynamic response of a one dimensional mass-spring-damper system to various excitations including un-damped/damped free vibrations, constant velocity and acceleration excitations. The system response was also analysed using sinusoidal forcing functions as well as dither excitations. The following sections discuss the development of the centre plate friction model that was used to carry out these simulations.

4.1. Centre plate/wear liner modelling methodology

The main components in the secondary suspensions considered here are the bogie frame, the centre bowl/plate depending on the type of vehicle, the two side bearers and the replaceable wear liners fitted to these components. The wagon body as can be seen from the various diagrams shown in the literature review and Appendix A, is supported by two bogies as well as the secondary suspension components and slide plates which are fastened to the underside of the wagon body.

For the simulation test cases discussed throughout this section, the centre plate components have been isolated from the complete vehicle system and simplified to the mechanical system shown in Figure 4.1. The dynamic centre plate model as can be seen, comprises of the bogie and wagon body inertia`s which are labelled as I_1 and I_2 respectively. These components are then coupled together via the friction element N_F and the viscous damper $C_{\tau 1}$, which are arranged in series. In the following simulation test cases, the bogie moves as rigid body and provides the inputs to the friction element/damper.

The wagon body on the other hand, provides the response and is modelled as an elastic body due to the flexibility provided by the wear liner components. The mechanical properties of the centre plate/wear liner components are then described in the MBS model using a torsional spring and damper force element combination arranged in parallel, which are shown as $k_{\tau 2}$ and $C_{\tau 2}$ in Figure 4.1. The free-body diagram for the centre plate system is shown in Figure 4.2 and from this, it can be seen that the arrangement of this dynamic model, is similar to the X-factor test set-up, where the bogie for example, rotates relative to the stationary wagon body.

The MATLAB/SIMULINK environment was then selected to model and analyse the dynamic behaviour of the centre plate system due to the advanced capabilities of the SIMSCAPE friction model, see Figure 4.3. This model is based on the LuGre friction model shown to the right of Figure 4.3, which as can be seen, eliminates the discontinuities associated with the Coulomb friction model in the region of zero velocity. The linear elastic region of the SIMSCAPE friction model as can be seen, is bounded by a user-defined velocity threshold parameter w_{th}, which has to be greater than zero. The SIMSCAPE friction model therefore, exhibits creepage under initial displacement conditions, as zero velocity is not defined in the model parameters.

The LuGre model force element combination also enables the friction surfaces to exhibit pre-sliding displacements during the breakout events as well as the Stribeck effect, a phenomenon which describes the material behaviour during the transition events, where the torque response is seen to decrease exponentially from breakout torque to the Coulomb torque limit. These model parameters are labelled as T_{brk}, T_C and T_S respectively in Figure 4.3. The nonlinear transition region however, is bounded by the ω_{th} and ω_{min} velocity parameters, where ω_{min} defines the velocity at which the frictional torque reaches its minimum value during the transition regime and is calculated from the following function, $\omega_{min} = \frac{4}{C_v}$, where C_v represents the transition coefficient (Canudas de Wit, Olsson, Astrom, & Lischinsky, 1995) and (The MathWorks, Inc, 2015).

If the relative velocity across the friction element is greater than ω_{min}, the gross-sliding regime then comes into play where the viscous damping in the friction element T_v, is summed together with the Coulomb torque T_C, which produces a friction characteristic that increases in proportion to the relative velocity. The viscous damping parameters however, can be set to zero if required. Appendix G contains a full description of the MATLAB/SIMSCAPE friction model parameters. The following section discusses the equations of motion for the centre plate system and the SIMSCAPE friction model.
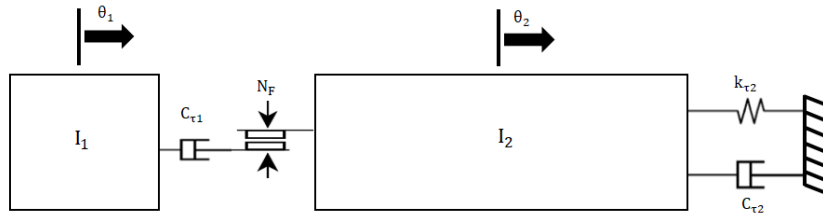
Figure 4.1: One dimensional model of the bogie/wagon body secondary suspension elements.
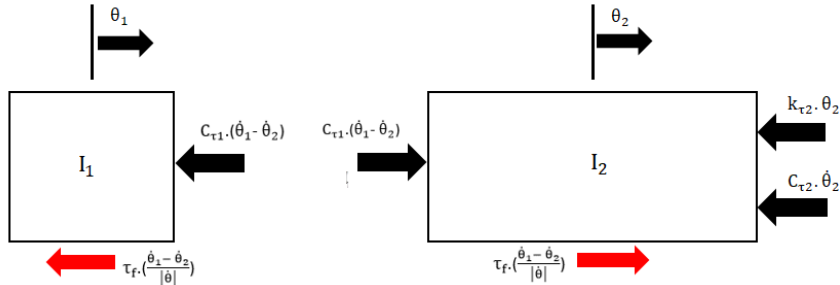
Figure 4.2: Free body diagram for the Bogie/wagon-body centre-pivot system.
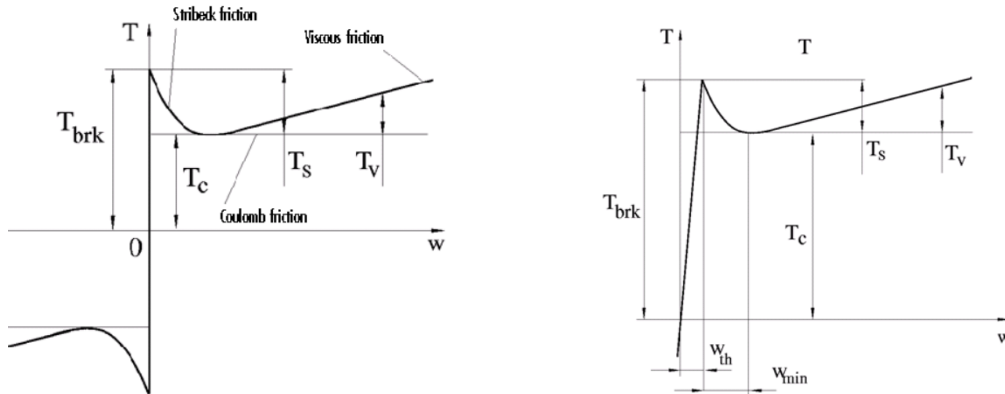
Figure 4.3: (Left) Discontinuous friction model. (Right) MATLAB/SIMSCAPE friction model (The MathWorks, Inc, 2015).

4.2. Centre plate equations of motion

The equations of motion for the bogie/wagon body centre plate system are discussed in this section. These equations were derived from Newton`s second law of motion given in Equation (4.1). Newton`s law for translational motion states that the vector sum of the externally applied forces **F** acting on a given body, is proportional to the mass m, and the time rate of change of the linear momentum of that body $\frac{d\mathbf{v}}{dt}$, or alternatively the acceleration of the body, $\ddot{\mathbf{x}}$ (Meriam & Kraige, 2012).

The expression to calculate the moment **M** of a force about an axis perpendicular to the line of action and that does not intersect this line, is then derived using the vector cross-product method shown in Equation (4.2). In this equation, **r** is the position vector that runs from the moment reference axis, to any given point on the line of action. The magnitude of the moment M on the other hand, is calculated using the dot product method shown in Equation (4.3). In this equation F is the magnitude of the force vector, α is the angle between the force and position vectors and d is the length of the moment arm (Greenwood, 1988).

$$\mathbf{F} = m\,\frac{d\mathbf{v}}{dt} = m\ddot{\mathbf{x}} \qquad (4.1)$$

$$\mathbf{M} = \mathbf{r}\ x\ m\ddot{\mathbf{x}}. = \mathbf{r}\ x\ \mathbf{F} \qquad (4.2)$$

$$M = Fr.\sin(\alpha) = F.d \qquad (4.3)$$

For a system of multiple bodies, the general form of Newton`s Laws for translation and rotation are arranged into a set of first order equations and solved simultaneously using the matrix notation given in Equations (4.4) and (4.5) respectively. In these equations, $\mathbf{F}_f$ and $\boldsymbol{\tau}_f$ are the frictional force and torque vectors and [M], [C] and [K] and [I], [C$_\tau$] and [K$_\tau$], are the matrices for the system masses/inertias, damping and stiffness properties. The $\ddot{\mathbf{x}}$, $\dot{\mathbf{x}}$, x and $\ddot{\theta}$, $\dot{\theta}$, θ terms, are the variables representing the translational/angular accelerations, velocities and displacements of the system. The translational and rotational equations of motion for the wagon body mass and inertia are given in Equations (4.6) and (4.7). In these equations, the v and ω terms represent the relative velocities between the input and the response (Meriam & Kraige, 2012).

$$\mathbf{F} = [M].\ddot{\mathbf{x}} + [C].\dot{\mathbf{x}} + [K].\mathbf{x} + \mathbf{F}_f.\left(\frac{\mathbf{v}}{|\mathbf{v}|}\right) \qquad (4.4)$$

$$\mathbf{M} = [I].\ddot{\boldsymbol{\theta}} + [C_\tau].\dot{\boldsymbol{\theta}} + [K_\tau].\boldsymbol{\theta} + \boldsymbol{\tau}_f.\left(\frac{\omega}{|\omega|}\right) \qquad (4.5)$$

$$m_2.\ddot{\mathbf{x}}_2 = C_1.\dot{\mathbf{x}}_1 - (C_1 + C_2).\dot{\mathbf{x}}_2 - k_2.\mathbf{x}_2 + \mathbf{F}_f.\left(\frac{\mathbf{v}}{|\mathbf{v}|}\right) + \mathbf{F} \qquad (4.6)$$

$$I_2.\ddot{\boldsymbol{\theta}}_2 = C_{\tau 1}.\dot{\boldsymbol{\theta}}_1 - (C_{\tau 1} + C_{\tau 2}).\dot{\boldsymbol{\theta}}_2 - K_{\tau 2}.\boldsymbol{\theta}_2 + \boldsymbol{\tau}_f.\left(\frac{\omega}{|\omega|}\right) + \mathbf{M} \qquad (4.7)$$

The translational friction force $\mathbf{F}_f$ in the LuGre model as can be seen from Equation (4.8), takes into account the contact stiffness and average deflection of the surface asperities, which are represented by the σ_0 term and the position vector, $\mathbf{z}$. The viscous damping effect of asperities is also included in the LuGre friction model and is labelled as σ_1, whereas the viscous damping for the whole system is represented by σ_2 in this equation.

The state variable for the surface asperities on the other hand $\dot{\mathbf{z}}$, is calculated from the formula given in Equation (4.9). This function as can be seen, calculates the difference between rigid body velocities and the ratio of the spring force, which represents the stiffness of the surface asperities in this model, to the friction force.

The Stribeck effect function $g(\dot{\mathbf{x}})$ is also included in the LuGre friction model and is calculated using Equation (4.10). This phenomenon however, has a destabilising influence on the system dynamics due to the difference between the Coulomb and stiction friction forces, F_c and F_s. When the friction surfaces have broken out of the stiction region in this model for example, the friction force decreases from F_s to F_c, in an exponential manner. The Stribeck function as can be seen, is dependent on the shape factor and the Stribeck velocity, j and v_s, which can be found from experimental tests. For an in-depth discussion on the capabilities of the LuGre friction model, see either (Canudas de Wit, Olsson, Astrom, & Lischinsky, 1995) or (Liu, Li, Zhang, Hu, & Zhang, 2015).

$$\mathbf{F}_f = \sigma_0.\mathbf{z} + \sigma_1.\dot{\mathbf{z}} + \sigma_2.\dot{\mathbf{x}} \qquad (4.8)$$

$$\dot{\mathbf{z}} = \dot{\mathbf{x}} - \sigma_0.\left(\frac{\dot{\mathbf{x}}}{g(\dot{\mathbf{x}})}\right).\mathbf{z} \qquad (4.9)$$

$$g(\dot{\mathbf{x}}) = F_c + (F_s - F_c).\exp^{-\left(\left|\frac{\dot{\mathbf{x}}}{v_s}\right|\right)^j} \qquad (4.10)$$

The descriptions given above are also applicable to the SIMSCAPE friction model describing the rotational dynamics of the centre plate. The frictional torque at the velocity threshold limit $T_{brk\_\omega_{th}}$ is calculated first of all in the numerical routine using Equation (4.11). The first term on the right-hand side of this equation is the viscous damping component in the friction element and the second and third terms, are the Coulomb friction and Stribeck effect.

The angular velocity across the friction element ω, is then calculated from the absolute relative velocities of the bogie/wagon body, $|\dot{\theta}_1|$ and $|\dot{\theta}_2|$, see Equation (4.12). The result from this calculation is then used by the friction model algorithm to determine if the element is in the sticking state, transitioning state or gross-sliding state.

$$T_{brk\_\omega_{th}} = C_{\tau 1}.\omega_{th} + T_c + (T_{brk} - T_c).\exp^{(-c_v.\omega_{th})} \qquad (4.11)$$

$$\omega = |\dot{\theta}_1| - |\dot{\theta}_2| \qquad (4.12)$$

The conditional statements given in Equation (4.13) are then used to calculate the frictional torque responses for the different regimes mentioned above. The linear function contained within the **IF** statement for example, calculates the frictional torque τ_f when the relative velocity across the friction element is less than or equal to the threshold limit, ω_{th}. This state indicates that the system is sticking. If the relative velocity across the friction element is greater than ω_{th} on the other hand, then system is either transitioning from the sticking to gross-sliding state, or alternatively, just gross-sliding. The frictional torque responses for positive and negative relative velocities are then calculated using the non-linear equations contained within the **ELSE IF** and **ELSE** statements.

The rate at which the transition from sticking to gross-sliding takes place in the friction model however, can be tuned to match experimental results if required via the transition coefficient parameter, C_v. The following section discusses the MATLAB/SIMULINK centre plate model and the friction model parameter settings.

$$\textbf{IF } |\omega| <= \omega_{th} \qquad (4.13)$$

$$\tau_f = \frac{\omega.T_{brk\_\omega_{th}}}{\omega_{th}}$$

ELSE IF $\omega > \omega_{th}$
$$\tau_f = C_{\tau 1}.\omega + T_C + (T_{brk} - T_c). \exp^{(-c_v.\omega)}$$

ELSE
$$\tau_f = C_{\tau 1}.\omega + T_C - (T_{brk} - T_c). \exp^{(-c_v.|\omega|)}$$

4.3. Dynamic centre plate model

This section discusses the development of the bogie/wagon body centre plate friction model. The basic framework of this dynamic Multibody Simulations (MBS) model, is freely available from the MATLAB examples and can be downloaded to the workspace by typing, `Mechanical Rotational System with stick-slip motion' into the command window (The MathWorks, Inc, 2015).

This dynamic model runs in SIMULINK and as can be seen from the top-level layout shown in Figure 4.4, uses pre-defined SIMULINK as well as SIMSCAPE function blocks to describe the force characteristics of the centre plate components. The rigid body motions of the bogie are then modelled using the drive signal block shown in the lower left-hand corner of Figure 4.4. This function block supplies an ideal velocity source to the centre plate system and also generates the driving torque to the left-hand side of the SIMSCAPE rotational friction element, see the sub-model diagram shown in Figure 4.5. Several SIMULINK/SIMSCAPE signal converters are then used in the complete model to connect the elements of the different platforms together.

The inertia of the wagon body as can be seen in Figure 4.4, is then connected to the right-hand side of the friction element and also suspended to ground by the torsional spring and damper arranged parallel. The motions of the bogie and wagon body are then measured relative to the fixed reference frames. The torque responses and kinematic motions of the centre plate system are then sent to the sensors block. This block as can be seen, contains a sub-system that uses these variables to calculate the net torque, velocity as well as the angle of the centre plate during each step of the simulation, see Figure 4.6. The simulation results can then be either viewed in real-time via the scope in SIMULINK or exported to the MATLAB workspace for post-processing.

The parameters of the SIMSCAPE friction element as can be seen in Figure 4.7, includes the breakout and Coulomb torque, the velocity threshold parameter, the viscous friction coefficient and the transition coefficient. The velocity threshold parameter for the simulations discussed in this thesis however, was set to 1×10^{-6} m/s instead of the default value which is 1×10^{-4} m/s. This step was taken to prevent unrealistic amounts of creepage in the friction models. Also, for the simulation cases discussed in the following sections, it is assumed that the normal force N_F, is constant and concentrated at a single point. The following section discusses the simulation test cases.
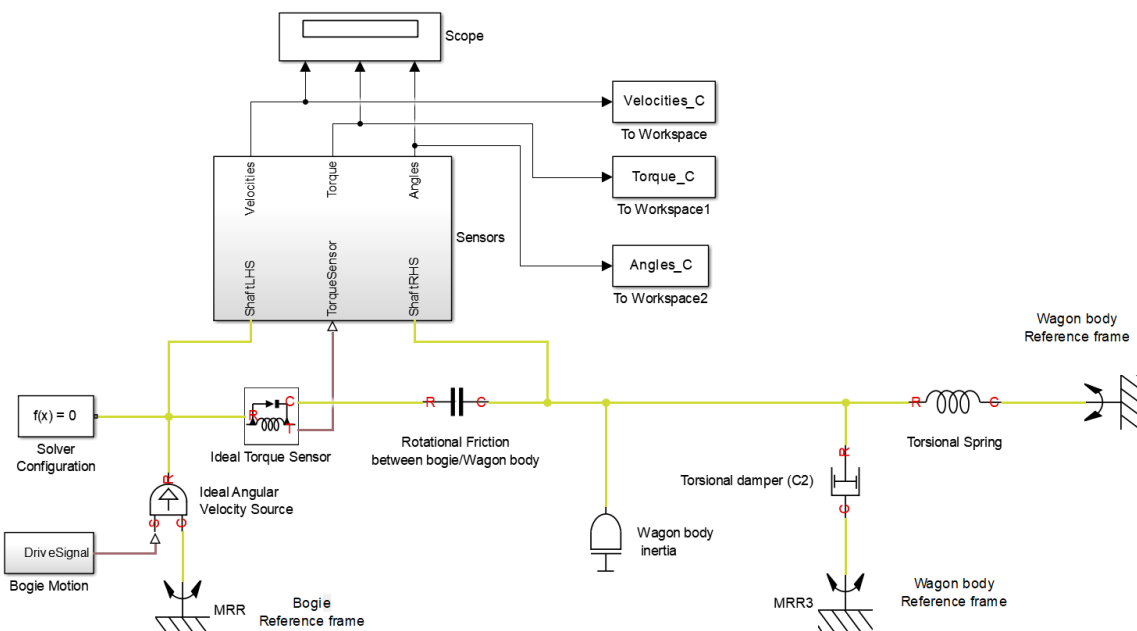
Figure 4.4: SIMULINK/SIMSCAPE dynamic friction model.
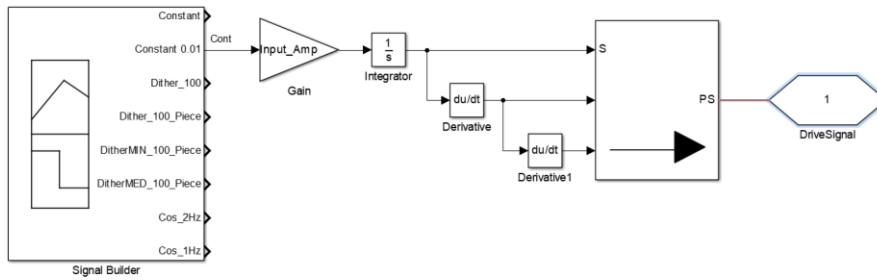
Figure 4.5: SIMULINK Drive signal block using the first and second derivatives.
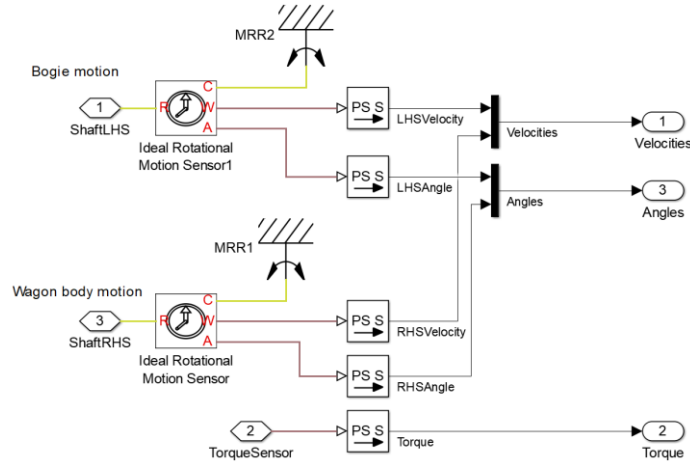
Figure 4.6: Torque and motion sensors sub-system block.
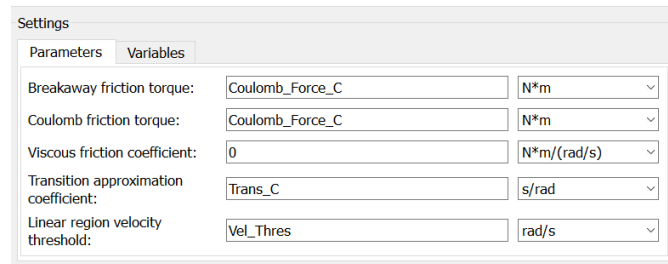
Figure 4.7: SIMSCAPE rotational friction element model parameters.

4.4. Simulation test cases and model parameters

Multibody Simulations (MBS) involving contact mechanics and dry friction damping increases the modelling challenges with regards to validation. Therefore, to better understand these challenges as well as the velocity threshold limits and how these influence the stiction and transition regimes in the SIMULINK/SIMSCAPE friction model, six simulation cases have been developed in order to verify the model responses and gain confidence in the simulation results, see Table 4.1.

Test case	Simulation description
1	Free vibration: Un-damped mass-spring oscillator
2	Free vibration: Damped mass-spring oscillator
3	Constant velocity excitation
4	Constant accelertion excitation
5	Dither excitations
6	Harmonic excitations

Table 4.1: Dynamic simulation test cases.

Five simulations involving translational motions in one dimension were carried out as part of this work, as well as harmonic motion simulations to study the rotational dynamics of the SIMSCAPE friction model. The system parameters that are relatively straight forward to verify from these simulation test cases, are the kinematic motions and natural frequencies of the mass, as well as the responses of the force/torque elements.

The performance of several solvers available in MATLAB/SIMULINK were also been benchmarked in this study as these have a significant impact on the accuracy and solution times of the simulations. The test cases discussed in this thesis also coincides with some of the works published by other authors to provide another level of verification, see for example, (Piotrowski, 2012), (Opala, 2018) and (Liu, Li, Zhang, Hu, & Zhang, 2016).

To better understand the differences between dry and mixed friction damping conditions, three different friction models have been developed to investigate the translational and rotational test cases, see Tables 4.2 and 4.3. From these tables, it can be seen that the mass, inertia, transition coefficient, velocity threshold and contact stiffness parameters are exactly the same in each model. Whereas the Coefficients of Friction (COF) and viscous damping coefficients, are different.

Model description	Mass (kg)	Transition coefficient (s/m)	Velocity threshold (mm/s)	Viscous damping (N.s/m)	Stiffness (N/m)	μ_c	μ_{ss}	Breakout force (N)	Coulomb force (N)
Coulomb	1	10	0.001	0	500	0.2	0.2	1.962	1.962
Stick-slip	1	10	0.001	0	500	0.2	0.3	2.943	1.962
Coulomb-viscous	1	10	0.001	2.2	500	0.2	0.2	1.962	1.962

Table 4.2: Translational friction model parameters.

Model description	Inertia (kg.m²)	Bogie displacement amplitude (mrad)	Transition coefficient (s/rad)	Velocity threshold (mrad/s)	Viscous damping (N.m.s/rad)	Torsional stiffness (N.m/rad)	μ_c	μ_{ss}	Breakout torque (N.m)	Coulomb torque (N.m)
Coulomb	1	104.5	10	0.001	0	500	0.2	0.2	1.962	1.962
Stick-slip	1	104.5	10	0.001	0	500	0.2	0.3	2.943	1.962
Coulomb-viscous	1	104.5	10	0.001	2.2	500	0.2	0.2	1.962	1.962

Table 4.3: Rotational friction model parameters.

The Coulomb and Stick-slip models for example, were developed to investigate the centre plate response under a constant friction, as well as a stick-slip friction force characteristic. These effects can be easily modelled in the SIMSCAPE friction model by setting the stick-slip/breakout and Coulomb COF parameters, μ_{ss} and μ_c, to different values.

The COF parameters in the Coulomb model as can be seen in the tables below, were both set to 0.2, whereas in the Stick-slip model, the COF values were set to 0.3 for the stick-slip/breakout parameter, and to 0.2 for the dynamic/gross-slipping COF parameter (Figure 4.7). The viscous damping coefficient in these two models however, were set to zero to represent dry friction surfaces.

The Coulomb-viscous model on the other hand, was developed to study the influence of lubrication on the friction surfaces. The stick-slip and Coulomb COF parameters in this model as can be seen, were both set to 0.2, whereas the viscous damping coefficient was set to 2.2 Ns/m. This value was derived from Equation (4.14) and is seen to be equivalent to 5% of the critical damping ratio for the given system parameters.

The viscous damping coefficient of $C_{\tau 2}$ on the other hand, which is the damper that connects the wagon body to the ground/reference frame (Figure 4.4), was set to zero for the simulations discussed

in this section. This simplification allows us to focus on the friction model parameters and the influence these have on the dynamic response of the system. The following section discusses the free vibration simulation test case.

$$C_{(5\%)} = 0.05.(2.\sqrt{k.m})$$ (4.14)

4.5. Un-damped free vibration simulation

The equation of motion for a one dimensional single degree of freedom un-damped mass-spring system is given in Equation (4.15). The constant coefficients representing the mass and elasticity of the system are labelled as m and k respectively, whereas the **x** and **ẍ** terms are the displacement and acceleration vectors. Also, as there are no external forces acting on a free vibrating system, the force vector **F** as can be seen, is equal to zero.

$$m.\ddot{x} + k.x = 0$$ (4.15)

Several system parameters can now be analysed and validated using this simple model. These include the kinematics of the system mass and the magnitudes of the internal forces. The natural frequency of the system and time period of the un-damped oscillations can also be checked using Equations (4.16) and (4.17). From these equations and the parameters given in Tables 4.2 and 4.3, the un-damped natural frequency of the system ω_n and time period T, are shown to be 3.56 Hertz (Hz) and 0.281 seconds. The damped natural frequency of the Coulomb-viscous model on the other hand, is calculated using Equation (4.18) and is seen to be slightly lower at 3.54 Hz (Greenwood, 1988).

$$\omega_n = \sqrt{\frac{k}{m}}$$ (4.16)

$$T = \frac{2.\pi}{\sqrt{\frac{k}{m}}}$$ (4.17)

$$\omega_d = \sqrt{\frac{k}{m} - \frac{c^2}{4.m^2}}$$ (4.18)

The total mechanical energy of the mass-spring system, E, is then calculated using Equation (4.19), which comprises of the kinetic and potential energies of the system, which are labelled as T and V respectively in Equations (4.20) and (4.21). The kinetic energy as can be seen, is calculated as a function of the system velocity v, whereas the potential energy, is shown to be a function of the position, as well as the gravitational body force g and the changes in altitude h of the centre of mass with respect to a fixed datum point (Greenwood, 1988) and (Meriam & Kraige, 2012).

$$E = T + V$$ (4.19)

$$T = \frac{1}{2}.m.v^2$$ (4.20)

$$V = \frac{1}{2}.k.x^2 + m.g.h$$ (4.21)

In the following simulation cases however, it is assumed that the equilibrium position of the concentrated point mass, lies in the datum plane, meaning that the gravitational component in (4.21), can be set to zero. By considering the conservation of energy and applying these principles to the un-damped mass-spring system, the accuracy of the different solvers available in SIMULINK can be quantified and compared. The results from these simulations are discussed in the following sections.

4.5.1. Un-damped free vibration results and discussion

This section discusses the un-damped free vibration responses. For this analysis, the wagon body mass was given an initial displacement of 0.1 m and then released at the start of the simulation. The breakout and Coulomb friction forces however, had to be set to 1 x 10^{-10} N, as the SIMSCAPE friction model only allows non-zero values. The friction model parameters, system mass, stiffness and damping properties for this model are shown in Table 4.4.

Parameter	Value
Mass (kg)	1
Gravity (m/s²)	9.81
Initial displacement (m)	0.1
Stiffness (N/m)	500
Viscous damping (N.s/m)	0
Stiction force (N)	1 x 10^{-10}
Coulomb force (N)	1 x 10^{-10}
Transition coefficient (s/m)	10
Velocity threshold (m/s)	1 x 10^{-6}

Table 4.4: Un-damped free-vibration simulation model parameters.

The kinetic, potential and mechanical energies of the wagon body mass during this simulation are shown by the green, red and blue lines respectively in Figure 4.8, whereas the total friction energy is shown by the black line. This colour scheme applies to all of the energy results presented in this thesis. These system parameters were calculated to validate the accuracy of the numerical model as well as the time-step size. The first simulation for example, was carried using the Ode 23t implicit solver with the time-step set to 1 x 10^{-4} seconds (Figure 4.8).

From these responses shown in this figure, it is clear to see that the solution does not agree with the conservation of energy. The mechanical energy of the wagon body as can be seen (Red line), does not remain constant throughout the 5 second simulation. The initial value of 2.5 Joules (J) for example, is correct, whereas the final solution of 2.38 J, is incorrect. This error however, is due to the large time-step and after several more simulations using different step-sizes, the correct solution was found by setting this parameter to 1 x 10^{-6} seconds. The mechanical energy of the system as can be seen in Figure 4.9, is now constant, which suggests that the model and solver are working correctly.

The displacement and velocity responses also need to be checked before moving onto the following simulation cases, see Figures 4.10 and 4.11 respectively. From these responses it can be seen that the initial displacement and peak the velocities of the model are correct. The spring force and natural frequency of the system are also seen to be correct at 50 N and 3.56 Hz, see Figure 4.12.

The final set of results to verify are the time histories of the friction forces and hysteresis responses, see Figures 4.13 and 4.14. The friction forces and displacements as can be seen, are shown to be 1 x 10^{-10} N and 0.1 m, which is in agreement with the user defined model parameters. This analysis has now identified the most efficient and reliable solvers to use in the remaining simulation cases. The solver performance results during the free vibration simulations are discussed in the following section.
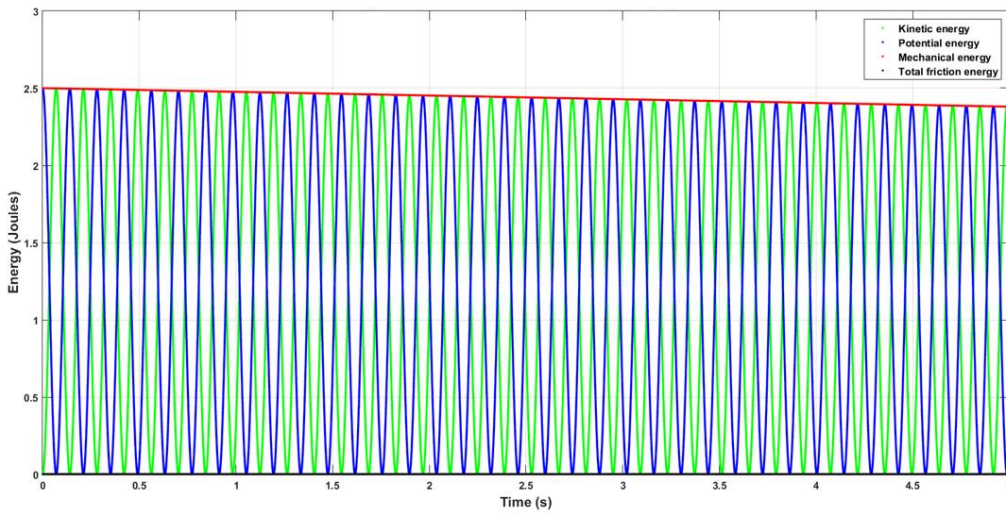
Figure 4.8: Energy responses using the Ode 23t solver and a time-step size equal to 1×10^{-4} seconds.
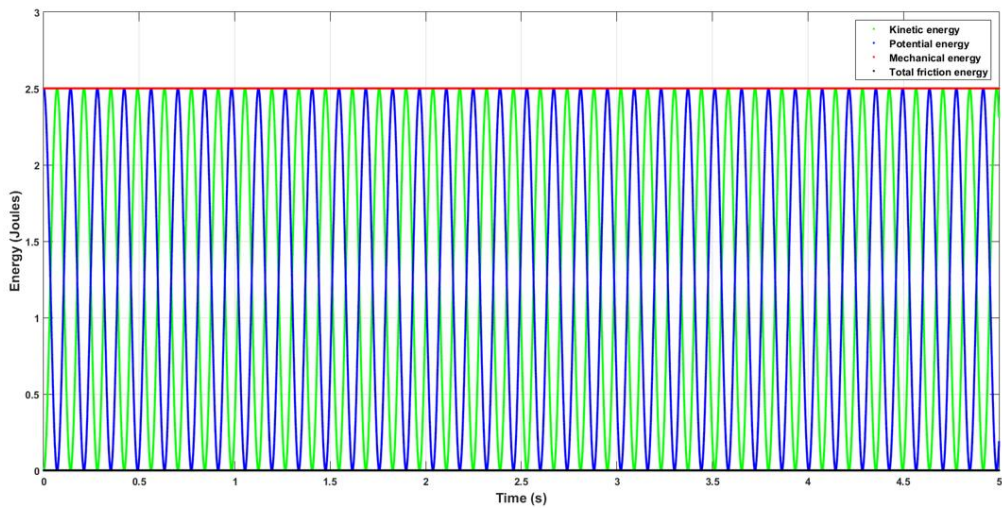
Figure 4.9: Energy responses using the Ode 23t solver and a time-step size equal to 1×10^{-6} seconds.
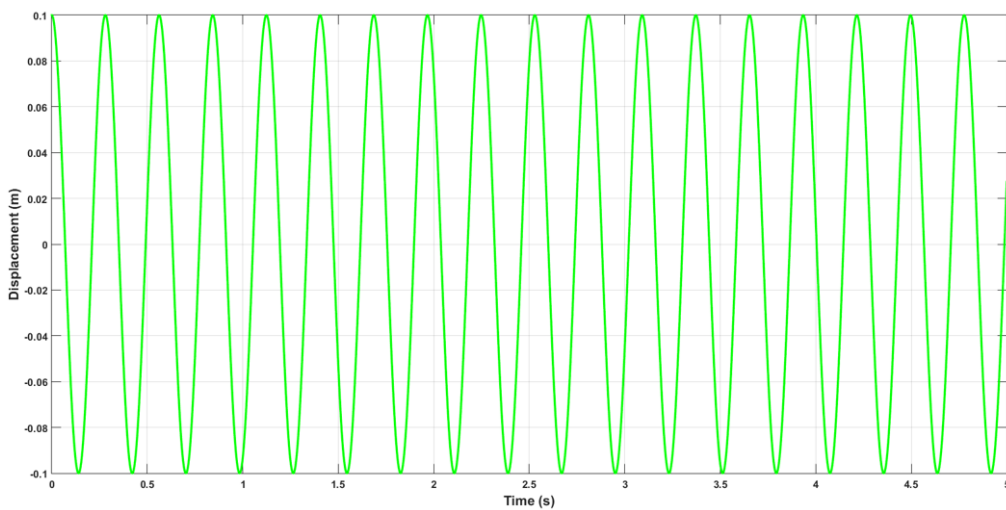
Figure 4.10: Displacement response using the Ode 23t solver.
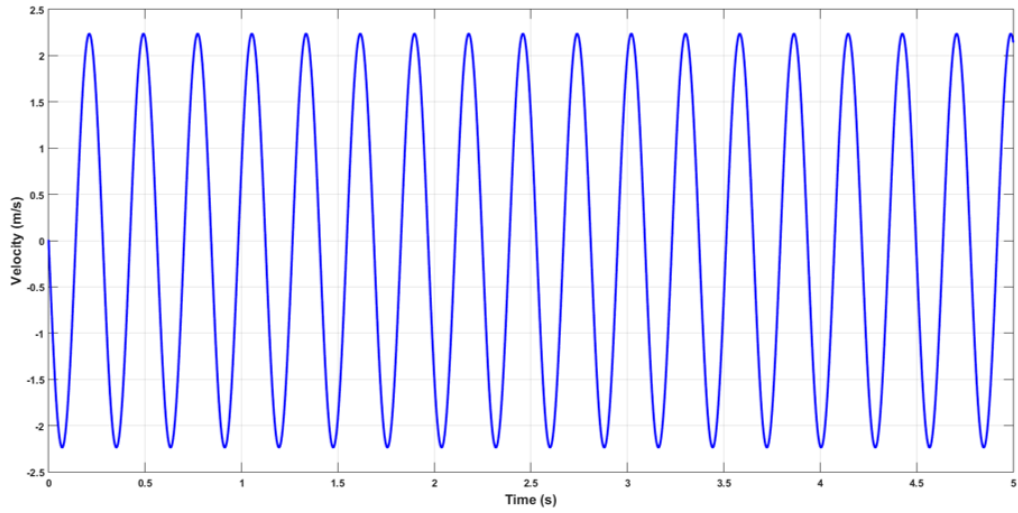
Figure 4.11: Velocity response using the Ode 23t solver.
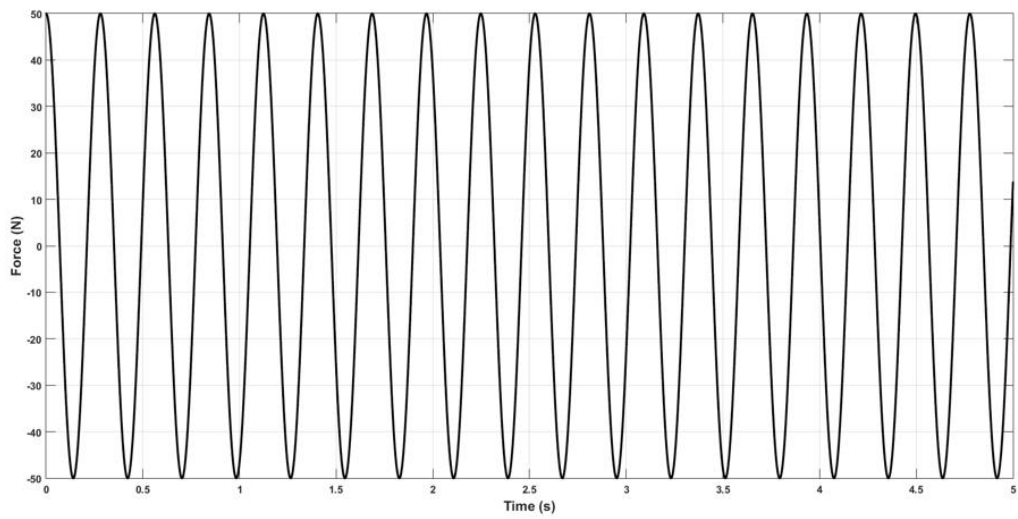
Figure 4.12: Spring force as a function of time.
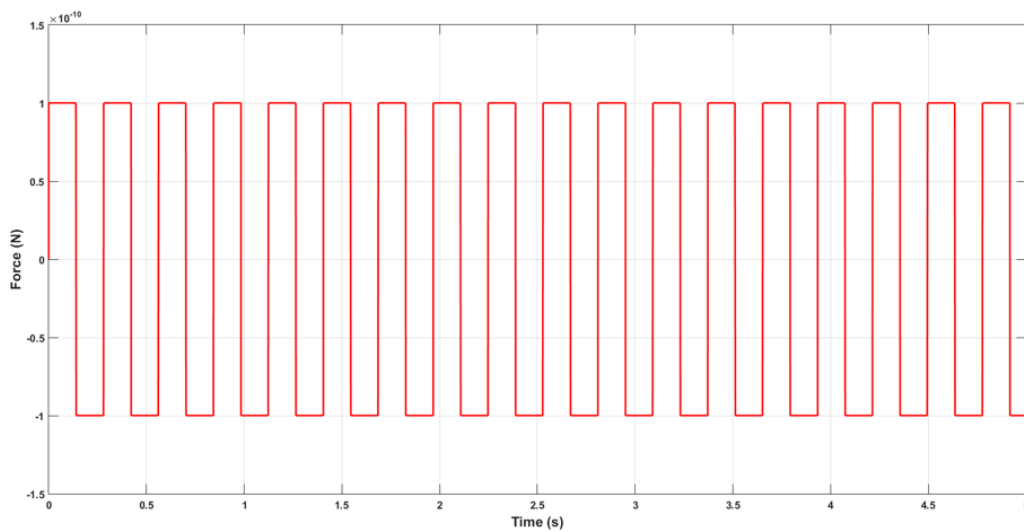
Figure 4.13: Friction force as a function of time.
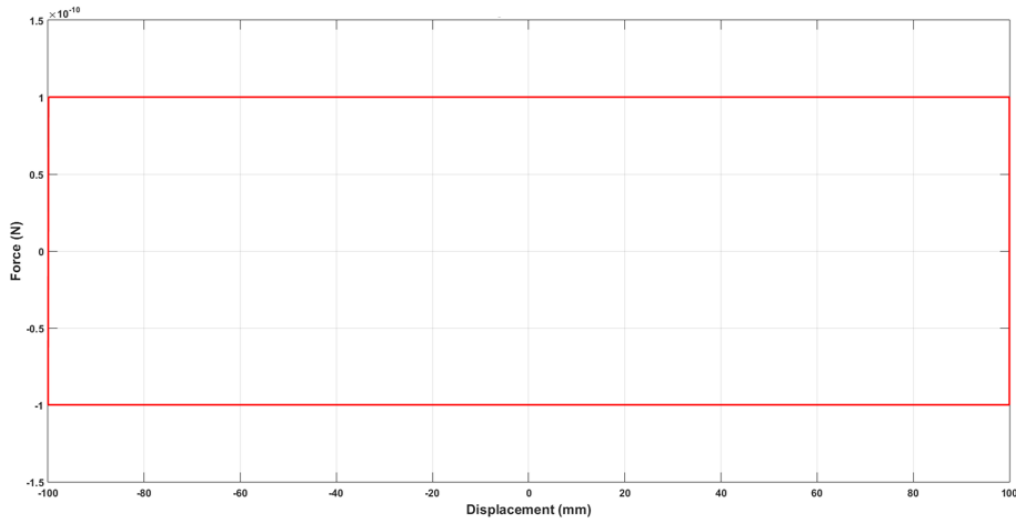
Figure 4.14: Hysteresis during the un-damped free vibration simulation.

4.6. Solver performance results

The performance and accuracy of the different SIMULINK solvers were analysed and compared using the responses from the free vibration simulations. For this analysis, the centre plate model was simulated with different solvers as well as time-step sizes, then the times taken for the simulations to converge to the correct solution of 2.5 J were then recorded, see Table 4.5. From these results, it can be seen that the fastest time overall for the 5 second simulation to converge to the correct solution, was 12.5 seconds using the Ode 23tb solver. Whereas the slowest time, was 98 seconds with the Ode 23t solver.

The simulations using the Ode 1, Ode 2 Ode 4, Ode 14x and Ode 15s solvers however, either did not converge to the correct solution no matter what time-step was used, or produced a warning during the simulations due to the system equations of motion, containing dynamic as well as algebraic equations. The advice from SIMULINK was to use an implicit solver in the model as these require fewer input derivatives for the input signal generator. The solvers that are highlighted in green on the other hand, are suitable to use in the remaining simulations. The following section discusses the results from the damped vibration simulations.

Numerical solver	Solver type	Dynamic Model	Time-step size (s)	Initial displacement (m)	Initial energy (Joules)	Final energy (Joules)	Simulation time (s)	Real time (s)	Is this solver reliable?
Ode 1	Explicit (Fixed step)	Undamped	0.001	0.1	2.5	2.501	5	4	No
Ode 15s	Explicit (Variable step)	Undamped	0.001	0.1	2.5	2.444	5	19.5	No
Ode 15s	Explicit (Variable step)	Undamped	0.0001	0.1	2.5	2.447	5	20.5	No
Ode 15s	Explicit (Variable step)	Undamped	0.00001	0.1	2.5	2.488	5	26.5	No
Ode 15s	Explicit (Variable step)	Undamped	0.000001	0.1	2.5	2.496	5	116	No
Ode 23t	Implicit (Variable step)	Undamped	0.0001	0.1	2.5	2.38	5	9.5	No
Ode 23t	Implicit (Variable step)	Undamped	0.00001	0.1	2.5	2.495	5	18	No
Ode 23t	Implicit (Variable step)	Undamped	0.000001	0.1	2.5	2.5	5	98	Yes
Ode 23tb	Explicit (Variable step)	Undamped	0.001	0.1	2.5	2.5	5	12.5	Yes
Ode 23tb	Explicit (Variable step)	Undamped	0.0001	0.1	2.5	2.5	5	15	Yes
Ode 45	Explicit (Variable step)	Undamped	0.001	0.1	2.5	2.5	5	13	Yes
Ode 45	Explicit (Variable step)	Undamped	0.0001	0.1	2.5	2.5	5	13.5	Yes
Ode 14x	Implicit (Fixed step)	Undamped	0.001	0.1	2.5	2.501	5	5	Warnings
Ode 14x	Implicit (Fixed step)	Undamped	0.0001	0.1	2.5	2.5	5	5.5	Warnings
Ode 4	Explicit (Fixed step)	Undamped	0.0001	0.1	2.5	2.5	5	6	Warnings
Ode 4	Explicit (Fixed step)	Undamped	0.00001	0.1	2.5	2.5	5	27	Warnings
Ode 2	Explicit (Fixed step)	Undamped	0.00001	0.1	2.5	2.5	5	19.5	Warnings
Ode 1	Explicit (Fixed step)	Undamped	0.0001	0.1	2.5	2.5	5	4.5	Warnings
Ode 1	Explicit (Fixed step)	Undamped	0.00001	0.1	2.5	2.5	5	19.5	Warnings

Table 4.5: Summary of the un-damped mass-spring oscillator free vibration simulation results.

4.7. Damped free vibration simulation

The modelling parameters for the damped free vibration simulations have been selected to reflect those used in the simulation work of (Opala M. , 2018), see Table 4.6. The results from these simulations will enable comparisons to be made between the different friction models and provide another level of validation to the MATLAB/SIMULINK centre plate model.

The friction force in the Coulomb model as can be seen, was set to 1.962 N, whereas the breakout and Coulomb friction forces in the Stick-slip model, were set to 2.943 and 1.962 N respectively. These forces were calculated by setting the COF values in Equation (2.2), Section 2.7, to 0.2 and 0.3 and the normal force, to 9.81 N.

The Coulomb-viscous model on the other hand, has a viscous damping, as well as a constant Coulomb friction force. The viscous damping coefficient was set to 2.2 Ns/m, so the equation of motion used in the previous analysis, does not apply to this model. The modified expression for the mass-spring-damper system (Coulomb-viscous model), is given in Equation (4.22) which now includes the friction and viscous damping forces, $\mathbf{F_f}$ and $c.\dot{\mathbf{x}}$.

Parameter	Value
Mass (kg)	1
Gravity (m/s²)	9.81
Initial displacement (m)	0.1
Stiffness (N/m)	500
Viscous damping (N.s/m)	2.2
Stiction force (N)	2.943
Coulomb force (N)	1.962
Transition coefficient (s/m)	10
Velocity threshold (m/s)	1×10^{-6}

Table 4.6: Damped free vibration simulation model parameters.

$$m.\ddot{\mathbf{x}} + c.\dot{\mathbf{x}} + k.\mathbf{x} = \mathbf{F_f} \qquad (4.22)$$

4.7.1. Displacement responses

This section discusses the displacement responses of the wagon body mass during the damped free vibration simulations using the Coulomb, Stick-slip and Coulomb-viscous friction models. The displacement responses are shown in Figure 4.15 by the green, red and blue lines respectively and from these, it can be seen that the oscillatory behaviour of the Coulomb-viscous model for example, takes approximately 0.985 seconds to settle to a steady state which is seen to be in the region of -0.24 mm. Whereas the Stick-slip and Coulomb friction models on the other hand, are seen to settle in the regions of 2.02 and 4.15 mm respectively, but take around 1.687 and 1.826 seconds respectively to reach this state.

The displacement responses from the free vibration simulations carried out by (Opala M. , 2018) are shown in Figure 4.16. In this work, the dynamic response of a Y-Series spherical centre bowl model was studied using several different friction models. These included the LuGre and the Karnopp models, a Coulomb model as well as a smooth/regularised Coulomb model. The non-smooth substitute friction model developed by (Piotrowski, 2012) was also analysed in this work. After comparing the displacement responses shown in Figure 4.15 and 4.16, it is clear to see that the agreements between the displacement amplitudes, final settling times and positions for example, are good.
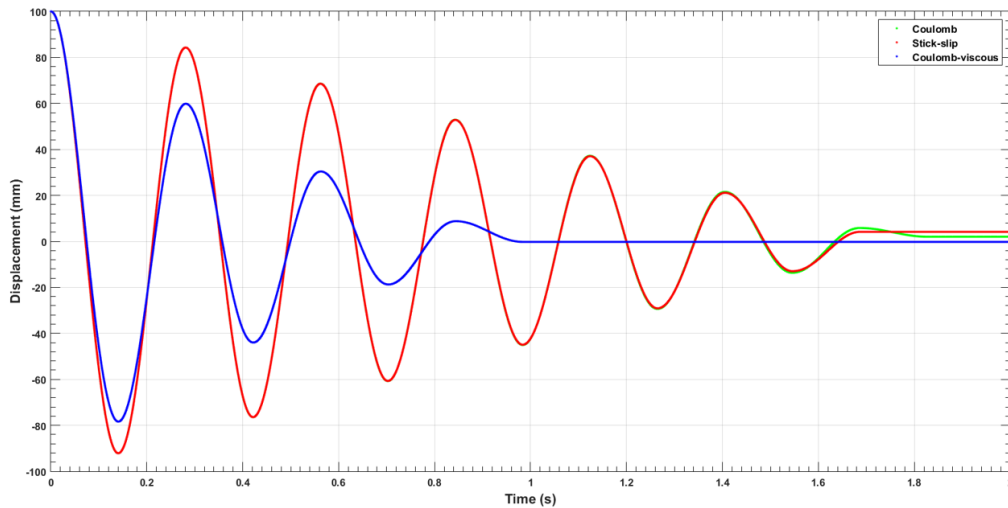
Figure 4.15: Displacement responses of the wagon body mass.
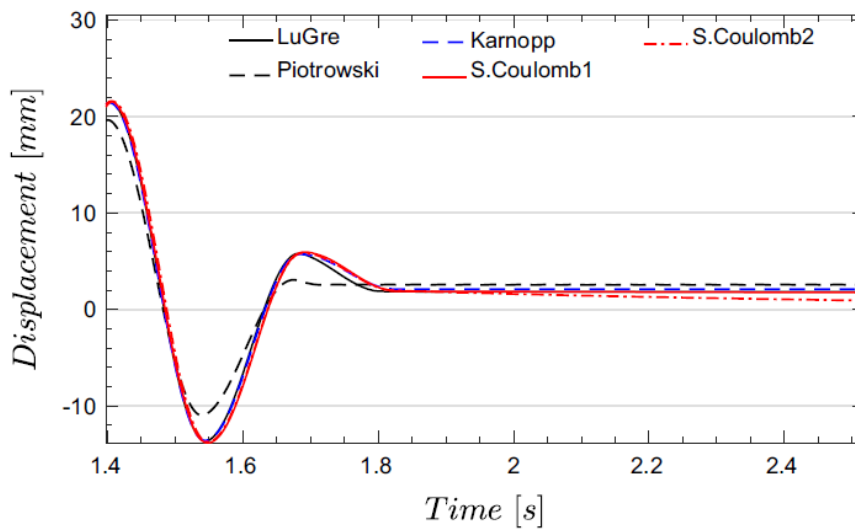
Figure 4.16: Displacement responses from the simulations carried out by (Opala, 2018).

4.7.2. Friction force responses

The time histories of the friction force responses are shown in Figure 4.17 and from these, the differences in the damping characteristics of each model are clear to see. During the first 0.6 seconds of the simulation for example, the friction forces in the Coulomb-viscous model are seen to be 2-3 times higher than those generated by the dry friction models. The friction force in the Coulomb model as expected, remains constant at 1.962 N after the breakout events, whereas the force in the Stick-slip model, is seen to increase to 2.943 N during these events and then decrease to 1.962 N during the gross-sliding events, see the hysteresis responses shown in Figure 4.18.

The kinematic motions and friction forces of the Coulomb, Stick-slip and Coulomb-viscous models during the damped free vibration simulations are summarised in Table 4.7. From these results it can be seen that the real-time taken for the 5 second simulation to reach a valid solution with the Ode 23tb solver, was between 14 − 15.5 seconds. This is a significant improvement in comparison to the Ode 23t solver for example, which took 98 seconds to converge during the un-damped simulation case. The energy responses of the friction models are discussed in the following section.
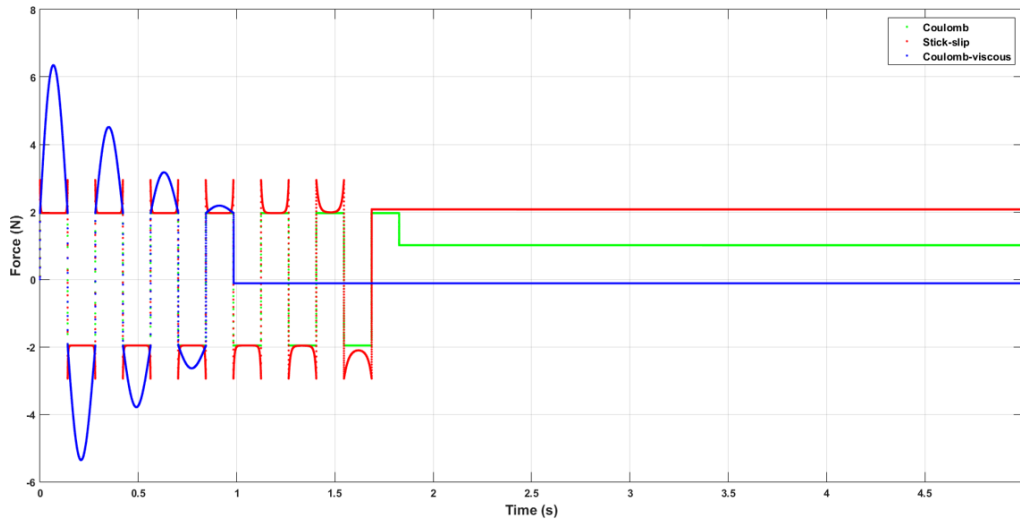
Figure 4.17: Friction forces as a function of time.
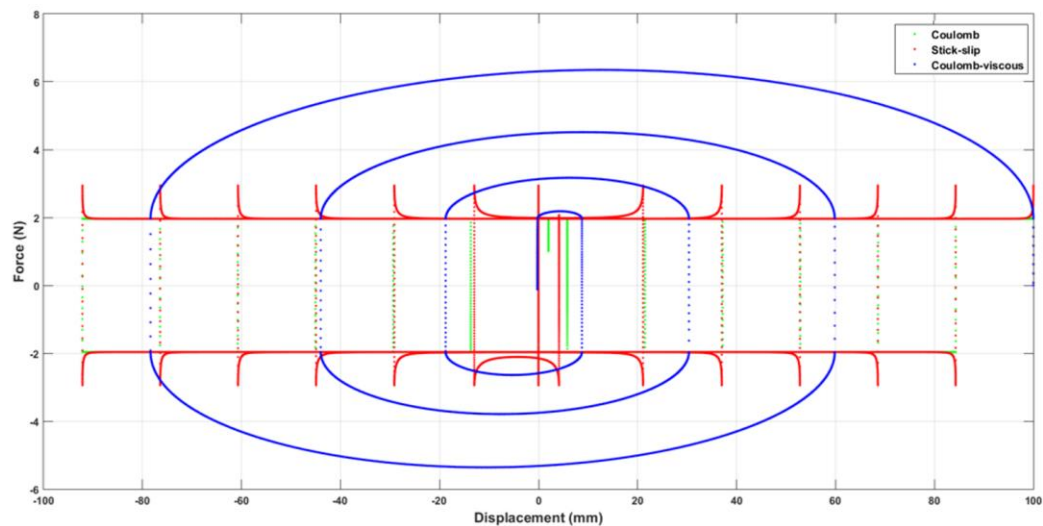
Figure 4.18: Hysteresis during the damped free vibration simulations.

Friction model	Breakout position (mm)	Maximum displacement (mm)	Displacement after 1 cycle (mm)	Non-zero residual displacement (mm)	Settling time (s)	Maximum velocity (mm/s)	Maximum spring force (N)	Spring force after 1 cycle (N)	Maximum friction force (N)	Sliding friction force (N)	Final friction force (N)	Simulation time (s)	Real-time (s)
Coulomb	3.9	0.1	84.3	2.02	1.827	-2148.3	50	42.15	1.962	1.962	1.012	5	14
Stick-slip	5.88	0.1	84.28	4.15	1.687	-2148.2	50	42.14	2.943	1.962	2.073	5	13.5
Coulomb-viscous	3.9	0.1	59.86	-0.237	0.985	-1993.2	50	29.93	6.347	1.962	-0.118	5	15.5

Table 4.7: Summary of the wagon body displacements, velocities and forces.

4.7.3. Energy responses

The energy responses of the Coulomb, stick-slip and Coulomb-viscous friction models are shown in Figures 4.19, 4.20 and 4.21 respectively. In these figures, the kinetic, potential and mechanical energies of the friction models are shown by the green, blue and red lines respectively, whereas the total friction energies, are shown by the black lines.

By comparing the total friction energy curves of the Coulomb and Stick-slip friction models in Figures 4.19 and 4.20 for example, it can be seen that the characteristics and gradients of these responses are

very similar. Whereas the gradients of the Coulomb-viscous model energy curves on the other hand, are significantly steeper due to the viscous damping force which is proportional to the system velocity.

The energy responses are summarised in Table 4.8 and from these results, it can be seen that the kinetic energies of the dry friction models are around 16% higher than the kinetic energy in the Coulomb-viscous model. The constant velocity simulation cases are discussed in the following section.
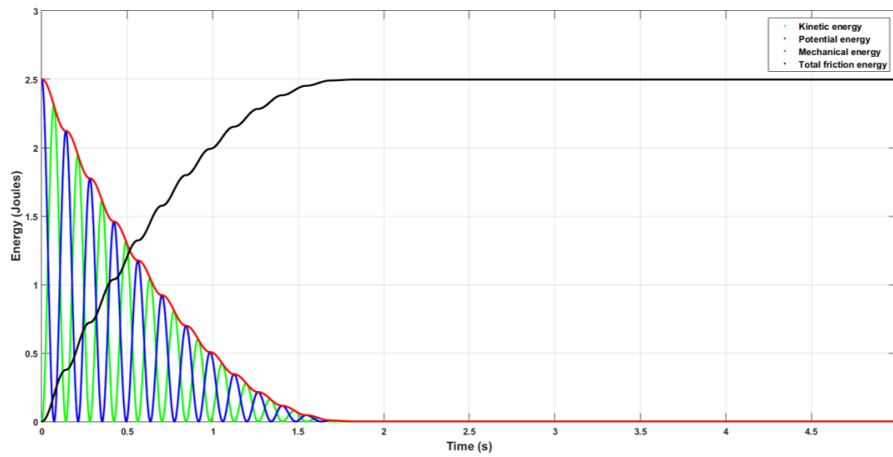
Figure 4.19: Energy responses using the Coulomb friction model.
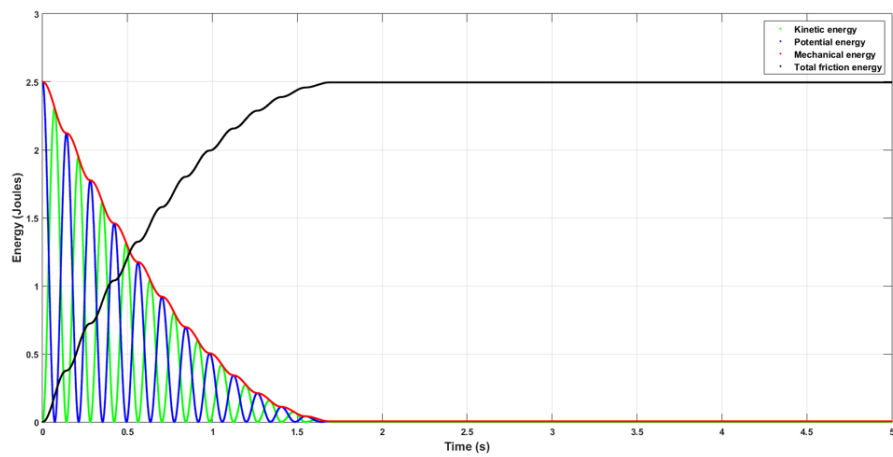
Figure 4.20: Energy responses using the Stick-slip friction model.
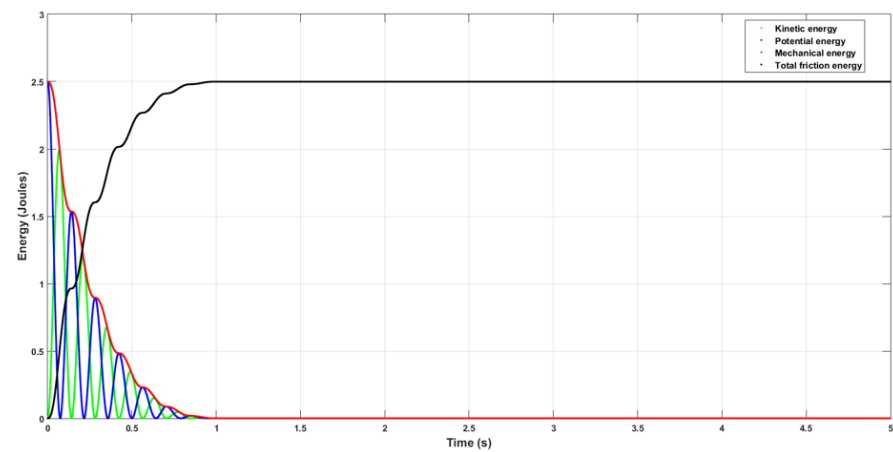
Figure 4.21: Energy responses using the Coulomb-viscous friction model.

Friction model	Maximum kinetic energy (Joules)	Maximum potential energy (Joules)	Maximum mechanical energy (Joules)	Total friction energy (Joules)	Simulation time (s)	Real time (s)
Coulomb	2.308	2.5	2.5	2.495	5	14
Stick-slip	2.307	2.5	2.5	2.498	5	13.5
Coulomb-viscous	1.986	2.5	2.5	2.499	5	15.5

Table 4.8: Summary of damped free vibration system energies.

4.8. Constant velocity input simulation

The model parameters for the constant velocity input simulations are shown in Table 4.9. For this simulation case, the bogie moves in the positive direction at a constant velocity of 0.01 m/s. The signal builder block however, had to be reconfigured to the arrangement shown in Figure 4.22, as only the first derivative of the input signal was required for these simulations.

Parameter	Value
Mass (kg)	1
Gravity (m/s^2)	9.81
Initial displacement (m)	0
Input velocity (m/s)	0.01
Stiffness (N/m)	500
Viscous damping (N.s/m)	2.2
Stiction force (N)	2.943
Coulomb force (N)	1.962
Transition coefficient (s/m)	10
Velocity threshold (m/s)	1×10^{-6}

Table 4.9: Model parameters for the constant velocity input simulations.
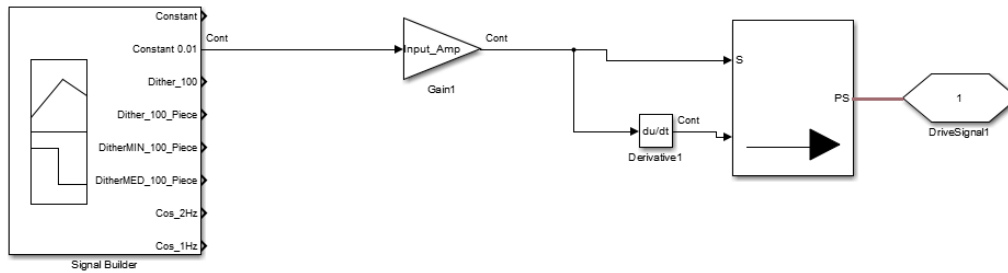
Figure 4.22: Signal builder block configuration for the constant velocity input simulations.

The displacement and velocity responses of the bogie/input during these simulations, s_b and v_b, are calculated using Equations (4.23) and (4.24) respectively. The u_b and a_b terms in these equations, represent the initial velocity and acceleration and t, is the time interval (Meriam & Kraige, 2012).

$$s_b = u_b.t + \frac{1}{2}.a_b.t^2 \quad \text{or} \quad s_b = ((u_b + v_b)/2).t \qquad (4.23)$$

$$v_b = u_b + a_b.t \qquad (4.24)$$

The breakout positions of the Coulomb and Stick-slip friction models, x_C and x_{ss}, are calculated by dividing the peak friction forces, F_C and F_{ss}, by the system stiffness K, see Equation (4.25) and (4.26) respectively. The dynamic displacements about the breakout positions due to the wagon body inertia on the other hand, are calculated using Equations (4.27) and (4.28).

The time it takes for the friction models to breakout of the stiction regions at the start of the simulation can also be evaluated from the breakout position and the relative velocity, see Equation (4.29). The equation of motion to describe the system with a constant velocity input is then given in Equation (4.30), which now includes the excitation force, **F**. The displacement and velocity responses are discussed in the following section.

$$x_{C \text{ (breakout)}} = \frac{F_c}{K} \tag{4.25}$$

$$x_{ss \text{ (breakout)}} = \frac{F_{ss}}{K} \tag{4.26}$$

$$x_{C \text{ (dynamic)}} = \frac{(F_c + m_2.\ddot{x}_2)}{K} \tag{4.27}$$

$$x_{ss \text{ (dynamic)}} = \frac{(F_{ss} + m_2.\ddot{x}_2)}{K} \tag{4.28}$$

$$t_{\text{(breakout)}} = \frac{x_c}{v} \text{ or } \frac{x_{ss}}{v} \tag{4.29}$$

$$m.\ddot{\textbf{x}} + c.\dot{\textbf{x}} + k.\textbf{x} = \textbf{F}_f + \textbf{F} \tag{4.30}$$

4.8.1. Displacement and velocity responses

The displacement responses of the wagon body mass using the Coulomb, Stick-slip and Coulomb-viscous friction models are shown in Figure 4.23 by the green, red and blue lines respectively. From these, it can be seen that the breakout points of the Coulomb and Coulomb-viscous models are in the regions of 3.92 mm which are in exact agreement with the pre-calculated values shown in Table 4.7, Section 4.7.2. The maximum and minimum dynamic displacements about the breakout points however, are seen to be in the regions of 4.37 and 3.48 mm, which is equivalent to a vibration amplitude of $\pm$ 0.45 mm.

The breakout point in the Stick-slip model is seen to be in the region of 5.88 mm which is also in agreement with the pre-calculated values. The maximum and minimum dynamic displacements relative to the breakout points however, are seen to be in the regions of 6.3 and 4.625 mm respectively. The overshoot in this response is 0.45 mm, whereas the undershoot is nearly three times larger at –1.25 mm.

The velocity responses of the wagon body mass are shown in Figure 4.24 and from these, the time it takes for the friction models to break out of sticking regimes at the start of the simulations can be evaluated. The Coulomb and Coulomb-viscous models for example (Green and blue lines), take around 0.392 seconds to breakout, whereas for the Stick-slip friction model on the other hand (Red line), takes 0.588 seconds due to the higher breakout force.

The velocity response of the Coulomb-viscous model eventually decays towards zero after the breakout event, whereas the response of the Coulomb friction model is seen to oscillate about equilibrium point with an amplitude of $\pm$ 9.95 mm/s. The response of the Stick-slip model is also oscillatory, but is seen to have a significant bias towards higher negative velocities. The minimum value for example, is in the region of -18.55 mm/s, which is almost double in comparison to the sliding velocities in the Coulomb and Coulomb-viscous models.

The state space trajectories of the wagon body mass are shown in Figure 4.25 and from these, it is clear to see that the friction characteristics of the Stick-slip model are not symmetrical about the breakout point, whereas in the Coulomb model, they are. The responses of the constant velocity

simulations that were carried out by (Opala M. , 2018) are also shown in Figure 4.26. From these results, it can be seen that the velocities and displacements of the LuGre, Piotrowski, Karnopp and the two versions of the Coulomb dry friction models for example, are in good agreement with the MATLAB/SIMULINK Coulomb friction model responses.

The peak velocities of the Stick-slip model however (Figures 4.24 and 4.25), are slightly higher in comparison to the velocities in the LuGre model shown in Figure 4.26. The absolute value of the peak velocity using the Stick-slip model is in the region of 28.55 mm/s, whereas the peak in the LuGre model, is 22 mm/s. The breakout positions of the Stick-slip and LuGre friction models are also different.

The differences between the Stick-slip and LuGre friction model responses, are possibly due to different parameters being used for the transition coefficients as well as different solvers. (Opala M. , 2018) for example, used the Ode 45 solver, whereas in this work, the Stick-slip friction model was simulated using the Ode 23tb solver. The performance of these two solvers were then compared using the Coulomb dry friction model and as can be seen, the Ode 23tb solver took 8 seconds to reach a solution, whereas the Ode 45 solver, took 22 seconds, see Table 4.10. The following section discusses the friction force responses during these simulations.
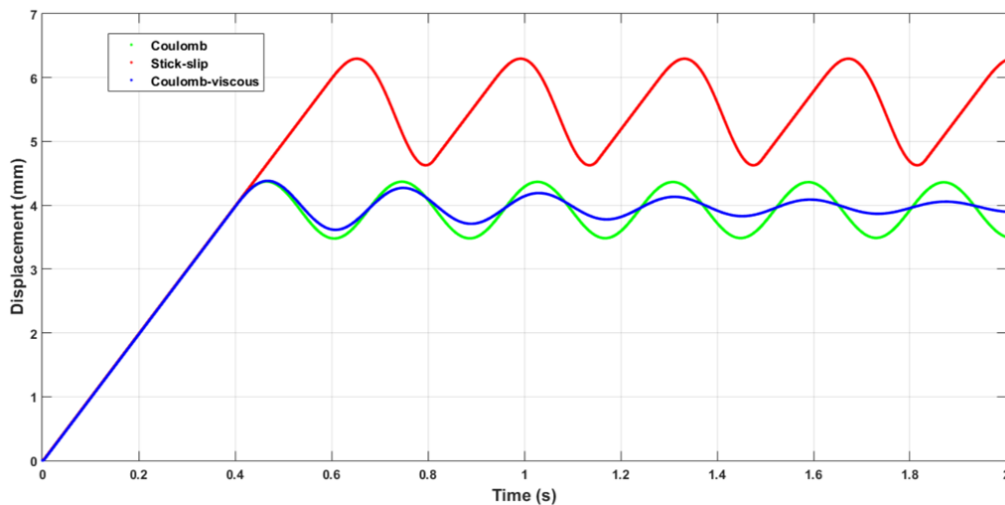
Figure 4.23: Wagon body displacement responses.
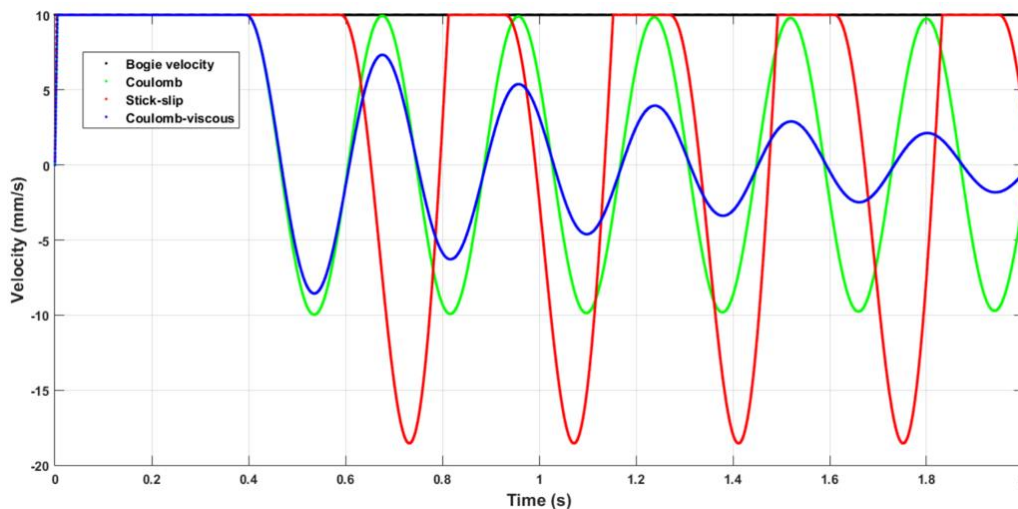
Figure 4.24: Wagon body velocity responses.

93
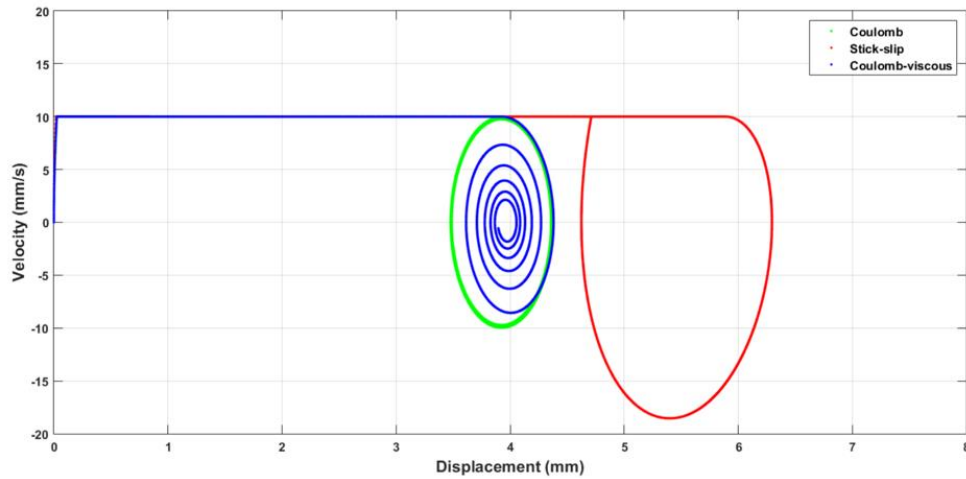
Figure 4.25: Wagon body state space trajectories (MATLAB/SIMULINK models).
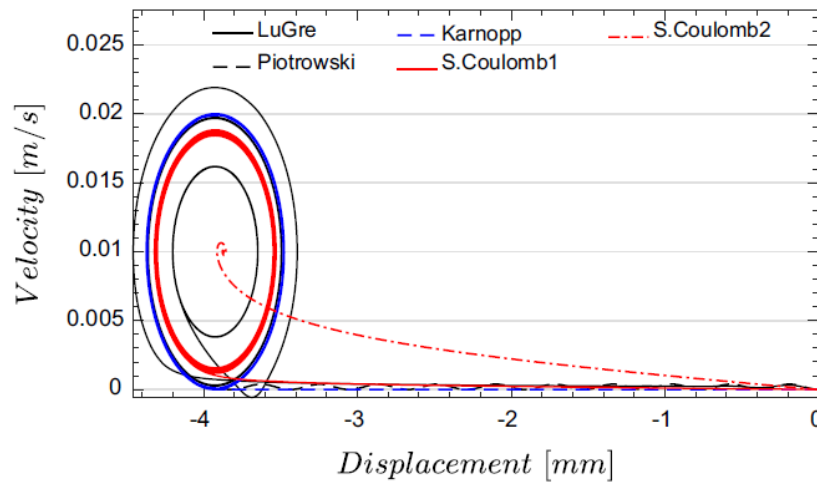
Figure 4.26: State space trajectories published by (Opala M. , 2018).

Numerical solver	Solver type	Dynamic Model	Time-step size (s)	Constant velocity (mm/s)	Maximum displacement (mm)	Minimum displacement (mm)	Breakout point (mm)	Maximum friction force (N)	Minimum friction force (N)	Total friction energy (Joules)	Simulation time (s)	Real time (s)
Ode 45	Explicit (Variable step)	Coulomb	0.0001	10	4.37	3.47	3.92	1.962	1.962	0.035	2	23
Ode 23t	Implicit (Variable step)	Coulomb	0.000001	10	4.37	3.47	3.92	1.962	1.962	0.035	2	42
Ode 23tb	Explicit (Variable step)	Coulomb	0.0001	10	4.37	3.47	3.92	1.962	1.962	0.035	2	8

Table 4.10: Solver performance during the constant velocity input simulations.

4.8.2. Friction force responses

The friction force responses as a function of time are shown in Figure 4.27 and from these, it can be seen that the maximum forces in the Coulomb, Stick-slip and Coulomb-viscous models are 1.962, 2 and 2.943 N respectively. The constant input velocity of 10 mm/s however, gives rise to large inertia forces at the start of the simulations and when these are damped out, the masses then start to move at the same rate as the input velocity. The friction force is then seen to increase in proportion to the mass displacement.

During the transition from the sticking to slipping in the Stick-slip model (Red line), the friction force starts to decrease from the peak value of 2.943 towards 2.7 N, but then increases again due to friction surfaces sticking. This analysis clearly shows that the Stick-slip model does not fully transition into the

gross-sliding regime because if it had, then the friction force would have decreased to 1.962 N. The spring in the Stick-slip model however, tends to unload/relax just before the subsequent sticking events start to develop, behaviour which is clear to see by the periodic vertical lines.

From the hysteresis responses shown in Figure 4.28, it can be seen that the Coulomb and Stick-slip friction models approach stable limit cycles about the breakout points, which are seen to be in the region of 3.92 and 5.88 mm respectively. Whereas the limit cycling behaviour of the Coulomb-viscous model on the other hand, is attenuated due to the viscous damping.

The kinematic motions and friction forces during these simulations are summarised in Table 4.11 and from these results, it can be seen that the real-time taken for the 2 second simulation to reach a solution using the Ode 23tb solver, was between 8 – 9 seconds. The following section discusses the energy responses.
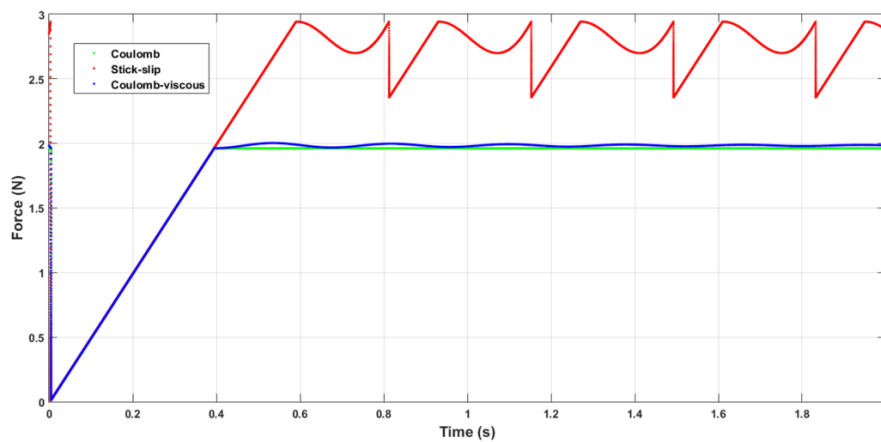
Figure 4.27: Friction forces as a function of time.
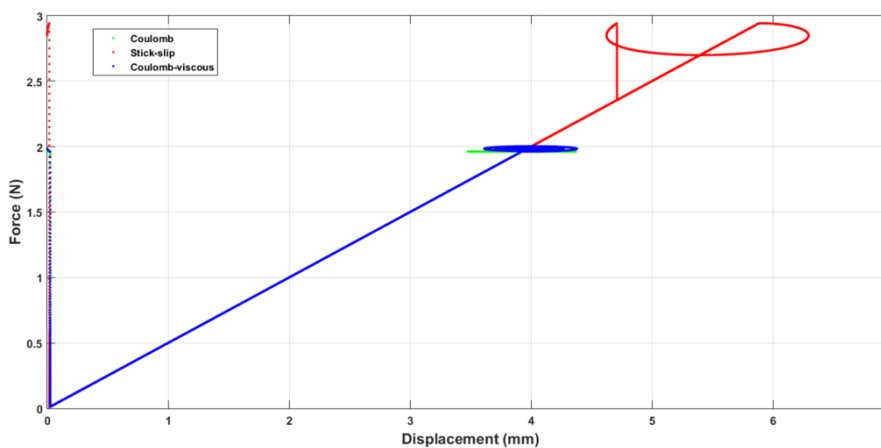
Figure 4.28: Hysteresis responses.

Friction model	Breakout position (mm)	Maximum displacement (mm)	Minimum displacement after the breakout (mm)	Maximum velocity (mm/s)	Minimum velocity (mm/s)	Maximum spring force (N)	Minimum spring force after the breakout (N)	Maximum friction force (N)	Mininmum friction force during the transition (N)	Sliding friction force (N)	Simulation time (s)	Real time (s)
Coulomb	3.9	4.37	3.48	10	-9.974	2.185	1.739	1.962	1.962	1.962	2	8
Stick-slip	5.88	6.3	4.625	10	-18.55	3.148	2.313	2.943	2.35	2.7	2	9
Coulomb-viscous	3.9	4.38	3.614	10	-8.57	2.19	1.807	2	1.968	1.968	2	8

Table 4.11: Summary of the constant velocity input simulation results using the Ode 23tb solver.

4.8.3. Energy responses

The frictional energies of the Coulomb, Coulomb-viscous and Stick-slip models during the constant velocity input simulations are summarised in Table 4.12. The total friction energy of the Stick-slip model as can be seen, is the highest overall at 47.7 x 10^{-3} J, whereas the Coulomb and Coulomb viscous models are seen to be almost equal at 35.4 and 35.8 x 10^{-3} J. The following section discusses the results from the constant acceleration input simulations.

Friction model	Maximum kinetic energy (Joules)	Maximum potential energy (Joules)	Maximum mechanical energy (Joules)	Total friction energy (Joules)	Simulation time (s)	Real time (s)
Coulomb	0.00005	0.00478	0.00478	0.0354	2	8
Stick-slip	0.000172	0.00991	0.00991	0.0477	2	9
Coulomb-viscous	0.00005	0.0048	0.0048	0.0358	2	8

Table 4.12: Summary of the friction model energies.

4.9. Constant acceleration simulation

The simulations discussed in this section have been developed to investigate the response of the wagon body mass to a constant acceleration input. This scenario could develop for example, when the vehicle is accelerating on curve entry/exit transitions. For the following simulations, the SIMSCAPE friction model parameters were set-up using the values shown in Table 4.13. The bogie was then modelled as a rigid body and given a constant acceleration of 0.01 m/s² during the 2 second simulation.

The displacement and velocity of the bogie during these simulations were also calculated using Equations (4.26) and (4.27) in Section 4.8. The responses from the constant acceleration simulations can then be compared and contrasted against the responses produced during the constant velocity simulations. The following section discusses the displacement and velocity responses of the Coulomb, Stick-slip and Coulomb-viscous friction models.

Parameter	Value
Mass (kg)	1
Gravity (m/s²)	9.81
Initial displacement (m)	0
Input velocity (m/s)	0
Input acceleration (m/s²)	0.01
Stiffness (N/m)	500
Viscous damping (N.s/m)	2.2
Stiction force (N)	2.943
Coulomb force (N)	1.962
Transition coefficient (s/m)	10
Velocity threshold (m/s)	1 x 10^{-6}

Table 4.13: Model parameters for the constant acceleration input simulations.

4.9.1. Displacement and velocity responses

The displacement responses of the wagon body mass using the Coulomb, Stick-slip and Coulomb-viscous friction models are shown in Figure 4.29 by the green, blue and red lines respectively. The displacement of the bogie/input is also shown by the black line. From these responses it can be seen the maximum displacements of the Coulomb and Coulomb-viscous models are in the region of 4.32 – 4.33 mm, which are approximately equal to the constant velocity responses.

The maximum displacements in the Stick-slip model on the other hand, are seen to be in the region of 6.59 mm, which is an increase of 0.29 mm in comparison to the peak displacements that were

observed during the constant velocity simulations. After the breakout events have occurred, the wagon body is then seen to slip in the negative direction relative to the bogie, where the displacements of the wagon body mass using the Coulomb, Coulomb-viscous and the Stick-slip friction models, are then seen to reach 3.57, 3.66 and 3.83 mm respectively.

The velocity responses are shown in Figure 4.30 and from these, it can be seen that the initial sticking regimes in the Coulomb and Coulomb-viscous for example (Green and blue lines), take place between 0 − 0.885 seconds. As the simulation time approaches 0.885 seconds however, the velocity of the bogie/wagon body mass is seen to be in the region of 8.847 mm/s, which causes these two models to transition straight into the gross-sliding regimes. The velocity response of the Coulomb model as can be seen, then continues to oscillate about the breakout position, whereas the oscillations in the Coulomb viscous model, decay towards zero due to the viscous damping effect which is similar to the behaviours that were observed during the constant velocity input simulations.

The Stick-slip model on the other hand (Red lines), starts to breakout when the simulation time is in the region of 1.083 seconds, or alternatively, when the absolute velocity of the wagon body approaches 10.83 mm/s, see Figure 4.30. The wagon body then starts to slip in-phase with the motion of the bogie until the wagon body velocity crosses the zero point, where the bogie/wagon body are then seen to start to slipping out-of-phase. The velocity responses of the Stick-slip model during the sliding phases of motions are then seen to increase over time due to the differences between the breakout and Coulomb friction forces, as well as the additional inertia forces due to the acceleration. The peak sliding velocity under these simulation conditions as can be seen, reaches −30.65 mm/s, whereas in the constant velocity input simulations, the peak was slightly lower at −28.55 mm/s.

From the state space trajectories shown in Figure 4.31, it can be seen that the responses of the Coulomb and Coulomb-viscous models are the same as they were in the constant velocity input simulations. The response of the Stick-slip model on the other hand, is clearly more unstable. In the constant velocity input simulation for example, the Stick-slip friction model approached a stable limit cycle around the breakout point, whereas in this simulation, the amplitudes of the limit cycles are increasing over time and are also biased towards higher negative velocities. The following section discusses the friction force responses.
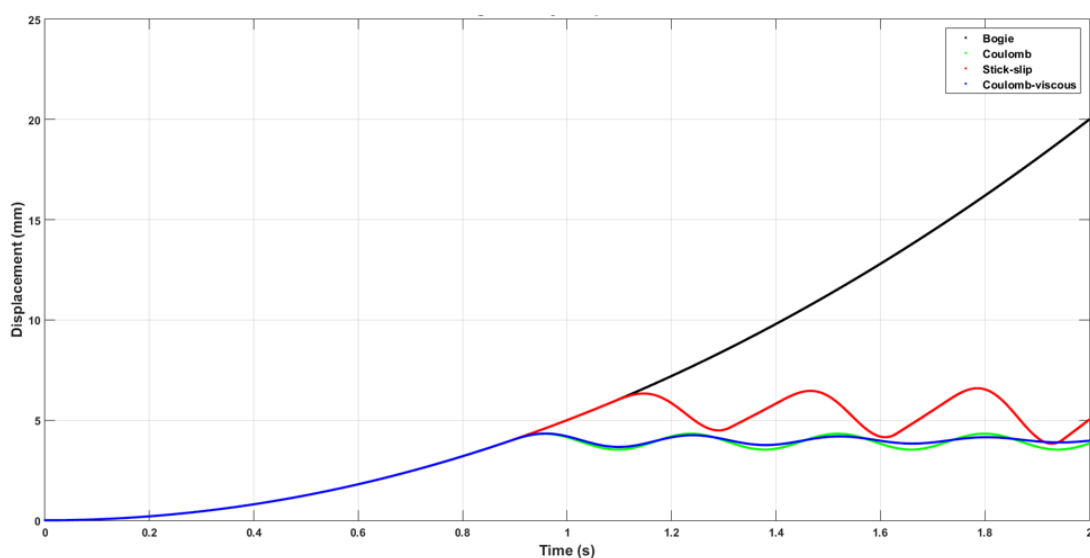
Figure 4.29: Wagon body displacement responses.
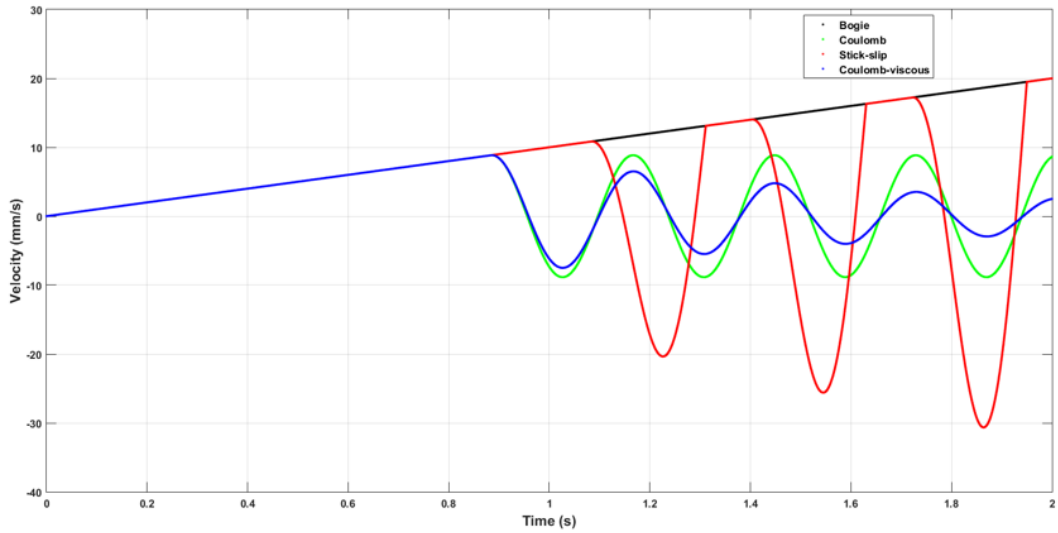
Figure 4.30: Wagon body velocity responses.
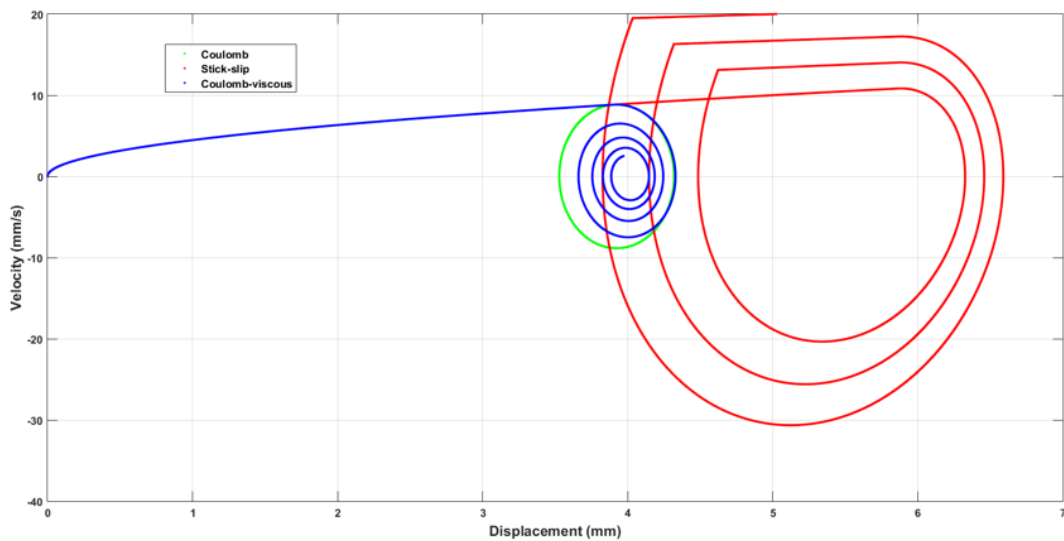
Figure 4.31: Wagon body state space trajectories.

4.9.2. Friction force responses

The friction force responses as a function of time and as a function of the wagon body displacement are shown in Figure 4.32 and 4.33. From these responses, it can be seen that the peak friction force of 2.943 N in the Stick-slip model remains constant over time (Red lines), whereas the minimum force during the slipping/transition phases of motion, starts off in the region of 2.4 N, but by the end of the simulation run, is seen to be in the region of 2.03 N. The friction forces in the Coulomb and Coulomb-viscous on the other hand, remain constant over time.

The performance of the Ode 45 and Ode 23t solvers were also compared during these simulations. The Ode 45 solver as can be seen from the results shown in Table 4.14, took 83.5 seconds of real-time to converge to a valid solution, whereas the Ode 23t solver, took 43 seconds. This solver was then selected to carry out the remaining constant acceleration simulations. The results for kinematic motions and friction forces using this solver are summarised in Table 4.15. The following section discusses the energy responses.
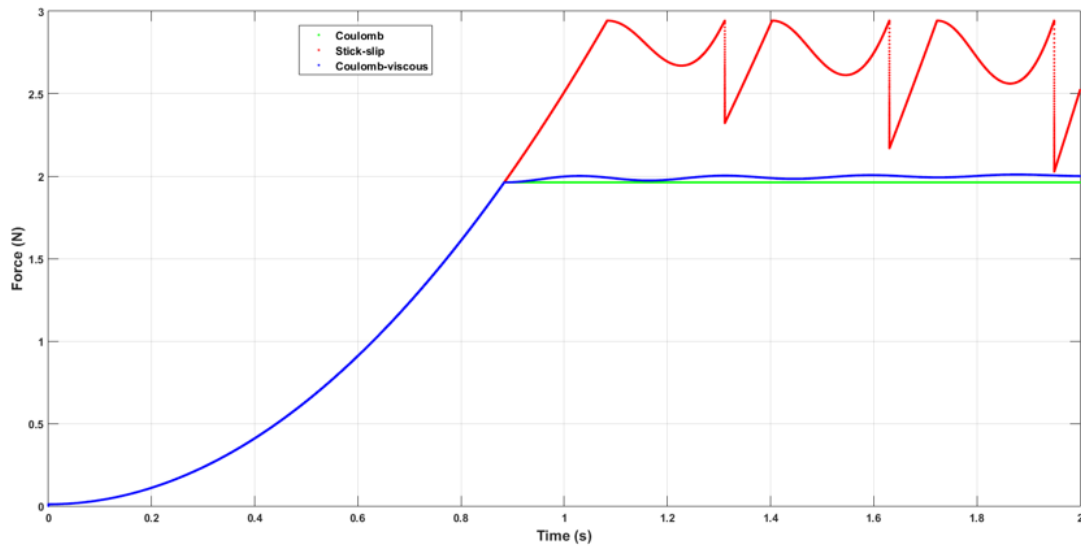
Figure 4.32: Friction forces as a function of time.
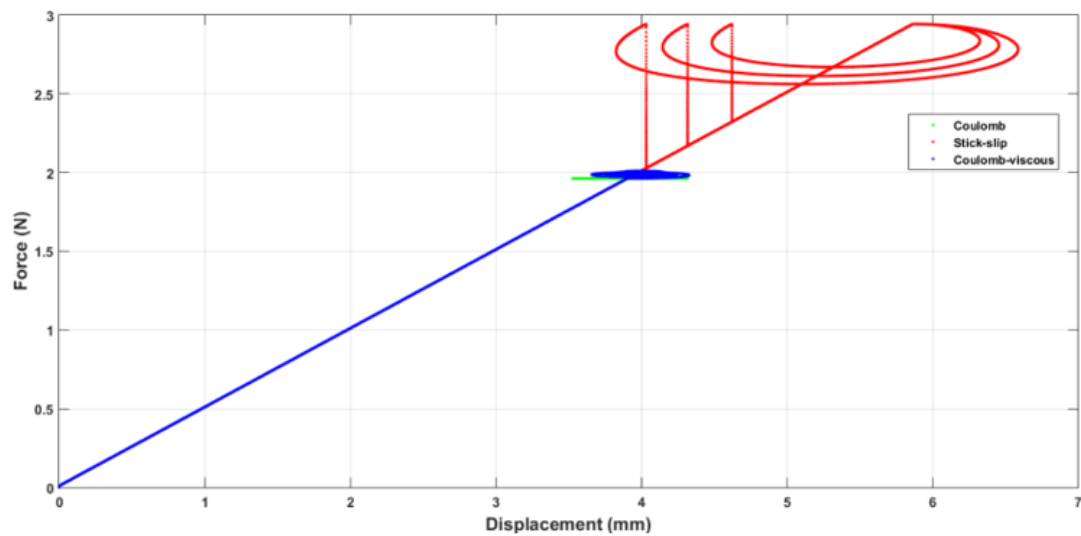
Figure 4.33: Hysteresis responses.

Numerical solver	Solver type	Dynamic Model	Time-step size (s)	Constant acceleration (mm/s²)	Maximum displacement (mm)	Minimum displacement (mm)	Breakout point (mm)	Maximum velocity (mm/s)	Minimum velocity (mm/s)	Maximum friction force (N)	Minimum friction force (N)	Total friction energy (Joules)	Simulation time (s)	Real time (s)
Ode 23t	Implicit(Variable step)	Coulomb	0.000001	10	4.32	3.53	3.92	8.85	-8.85	1.962	1.962	0.035	2	41
Ode 23t	Implicit(Variable step)	Stick-slip	0.000001	10	6.6	3.83	5.21	20	-30.7	2.943	2.03	0.047	2	41
Ode 23t	Implicit(Variable step)	Coulomb-viscous	0.000001	10	4.33	3.66	4.00	8.85	-7.5	2	1.962	0.036	2	42
Ode 45	Explicit(Variable step)	Stick-slip	0.0001	10	6.6	3.83	5.21	20	-30.7	2.943	2.03	0.047	2	83.5

Table 4.14: Solver performance during the constant acceleration input simulations.

Friction model	Breakout position (mm)	Maximum displacement (mm)	Minimum displacement after the breakout (mm)	Maximum velocity (mm/s)	Minimum velocity (mm/s)	Maximum spring force (N)	Minimum spring force after the breakout (N)	Maximum friction force (N)	Minimum friction force during the transition (N)	Sliding friction force (N)	Simulation time (s)	Real time (s)
Coulomb	3.9	4.32	3.565	8.847	-8.847	2.16	1.764	1.962	1.962	1.962	2	43.5
Stick-slip	5.88	6.59	3.828	20	-30.65	3.295	2.245	2.943	2.028	2.56	2	42.5
Coulomb-viscous	3.9	4.33	3.66	8.847	-7.497	2.165	1.83	2.01	1.968	1.968	2	43

Table 4.15: Summary of the constant acceleration simulation results using the Ode 23t solver.

4.9.3. Energy responses

The energy responses of the friction models during the constant acceleration input simulations are summarised in Table 4.16. From these results, it can be seen that the maximum potential and mechanical energies of the Coulomb and Coulomb-viscous model for example, are equal at 4.67 x 10^{-3} J. The total friction energies of these models are also similar, ranging between $35.4 - 36$ x 10^{-3}J.

The maximum potential and mechanical energies of the Stick-slip model on the other hand, are more than double and seen to be in the region of 10.9 x 10^{-3} J. The kinetic energy however, is 4.7 x 10^{-3} J, which is 120 times higher than the kinetic energies in the Coulomb and Coulomb-viscous models. The total friction energy of the Stick-slip model is also the highest overall at 46.7 x 10^{-3} J. From the energy responses, it can be concluded that the increase in kinetic energy of the Stick-slip model, is due to the difference between the breakout and Coulomb friction forces. The following section discusses the dither simulations.

Friction model	Maximum kinetic energy (Joules)	Maximum potential energy (Joules)	Maximum mechanical energy (Joules)	Total friction energy (Joules)	Simulation time (s)	Real time (s)
Coulomb	0.000039	0.00467	0.00467	0.0354	2	43.5
Stick-slip	0.0047	0.0109	0.0109	0.0467	2	42.5
Coulomb-viscous	0.000039	0.00469	0.00469	0.036	2	43

Table 4.16: Summary of system energies during the constant acceleration simulations.

4.10. Dither excitation simulations

This section discusses the responses of the centre plate system under the influence of translational dither excitations in one dimension. Dither in the context of railway freight vehicle dynamics for example, can arise from a number of sources which include structural borne noise due to the wheel/rail surface roughness in rolling contact, as well as air borne noises from passing trains. (Piotrowski, 2012) also suggests that dither has a smoothing influence on the dynamic behaviour of dry friction suspension components.

To better understand as well as quantify the impact this phenomenon has on the friction characteristics of the centre plate system, the MATALAB/SIMULINK friction model was subjected to the dither excitation cases shown in Table 4.17. These simulations were then carried out using the Coulomb friction model parameters to simplify the analysis, see Table 4.2 in Section 4.4.

Simulation case	Dither frequency (Hz)	Dither amplitude (mm)	Dither velocity (mm/s)
1	106.8	0	0
2	106.8	0.001	0.671
3	106.8	0.01	6.71
4	106.8	0.1	67.1
5	106.8	1	671
6	106.8	10	6710

Table 4.17: Dither excitation simulation test cases.

The first stage of this analysis involved a benchmarking simulation to quantify the response of the friction model with no dither applied to the input. Whereas for test cases $2 - 6$, sinusoidal dither was applied to the model in the same plane and direction as the friction force. The frequency of the dither in these simulations was set to 106.8 Hertz (Hz), which is thirty times higher than the natural frequency

of the mass-spring system, see Equation (4.31). The amplitude of the dither in each case however, was increased by a factor of 10.

The displacement and velocity of the bogie are then calculated using the harmonic functions given in Equations (4.32) and (4.33) respectively. The equation of motion for the wagon body mass is then derived by substituting these variables into Newton`s second law of motion given in Equation (4.6), Section 4.2. The translational friction model equations are also shown in Equation (4.34) for reference purposes. The following section discusses the system response without dither applied to the input.

$$\omega_{dither} = 30.\sqrt{\frac{k}{m}} \tag{4.31}$$

$$\mathbf{x}_B = A.\sin(\omega_{dither}.t) \tag{4.32}$$

$$\dot{\mathbf{x}}_B = A.\omega_{dither}.\cos(\omega_{dither}.t) \tag{4.33}$$

IF $|v| < v_{th}$ $\tag{4.34}$

$$F_f = v.\frac{(C.v_{th} + (F_c + (F_{brk} - F_c).\exp^{(-C_v.v_{th})}))}{v_{th}}$$

ELSE IF $|v| >= v_{th}$

$$F_f = (F_c + (F_{brk} - F_c).\exp^{(-C_v.|v|)}) + C.v$$

4.10.1. System response without dither

This section discusses the system responses with no dither applied to the bogie/wagon body centre plate model. For these simulations, the wagon body mass is given an initial displacement of 3.9 mm and then released. Under these conditions however, the mass should remain stationary/locked-in, due to the spring and friction forces balancing at the breakout point, which is also 3.9 mm for the Coulomb model. This situation for example, could develop on the entries/exits of curves/transitions, during loading/unloading, accelerating/braking. It could also occur after maintenance rebuilds if the vehicle is not correctly assembled.

The displacement response of the wagon body is shown in Figure 4.34 and from this, it can be seen that the initial position of the wagon body is correct at 3.9 mm. However, during this 5 second simulation run, the wagon body mass is seen to creep by 5 µm, when in reality and under the given initial conditions, it should be stationary. This effect as was mentioned previously, is due to the velocity threshold limit, which is used in the SIMSCAPE friction element to eliminate the numerical problems associated with the discontinuous Coulomb friction force model in the region of zero velocity, see Figure 4.3 in Section 4.1.

The levels of creepage in the SIMSCAPE friction model however, can be increased/decreased by adjusting the velocity threshold parameter. The default value is 100 µm/s, which would have resulted in 500 µm of creepage during the 5 second simulation run. Whereas for the simulations discussed throughout this thesis, the velocity threshold parameter was set to, 1 µm/s, see Figure 4.35. This optimised setting however, led to higher computational costs per simulation, but given the short length of the simulation run, was seen to be a good compromise in terms of the improved accuracy.

Although the creepage is not a realistic material behaviour under the given initial simulation conditions, the amount of creepage in each simulation run is exactly the same. This means that the creepage can then be subtracted off the final settling positions of the wagon body mass if required,

but for the following analyses, this procedure is not necessary, as it is the dynamic response of the SIMSCAPE friction model that is the main focus of these simulations.

The friction force and system energies are shown in Figures 4.36 and 4.37 and from these responses, it can be seen that the friction force remains constant at 1.962 N. The total friction energy during this simulation however, is negligible. This concludes the analysis of the friction model response without dither applied. The following sections discuss the system responses with sinusoidal dither applied to the input of the dynamic model.
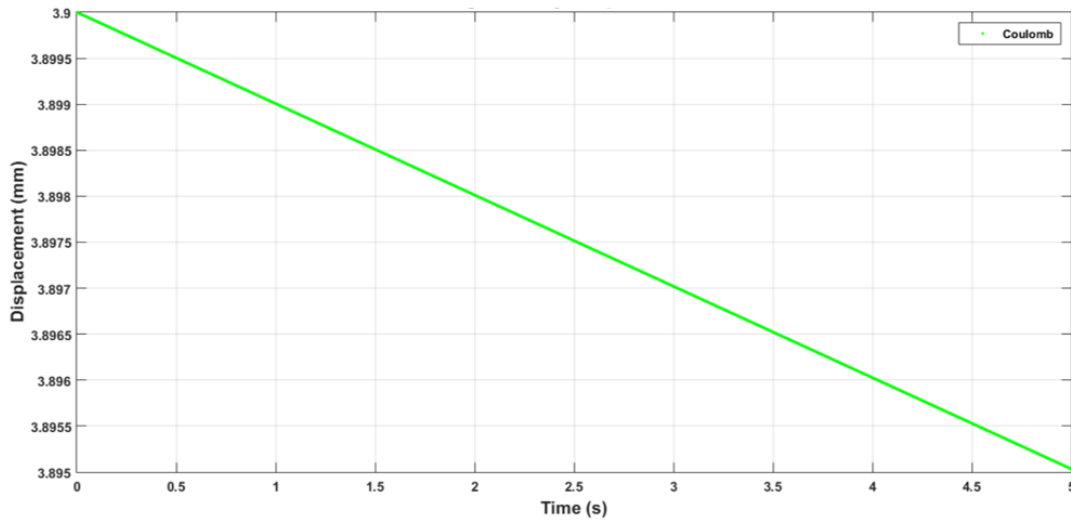
Figure 4.34: Wagon body displacement response without dither.
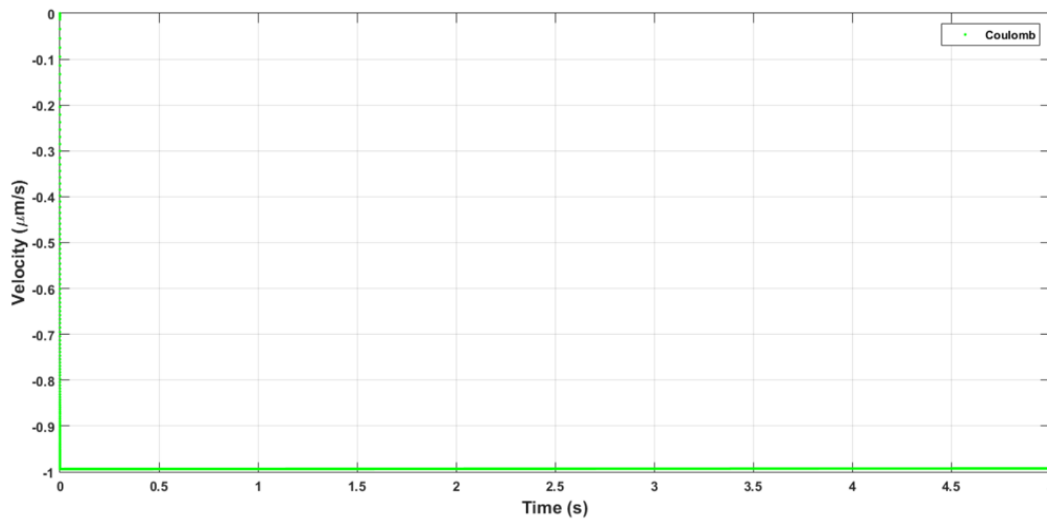
Figure 4.35: Wagon body velocity response without dither.
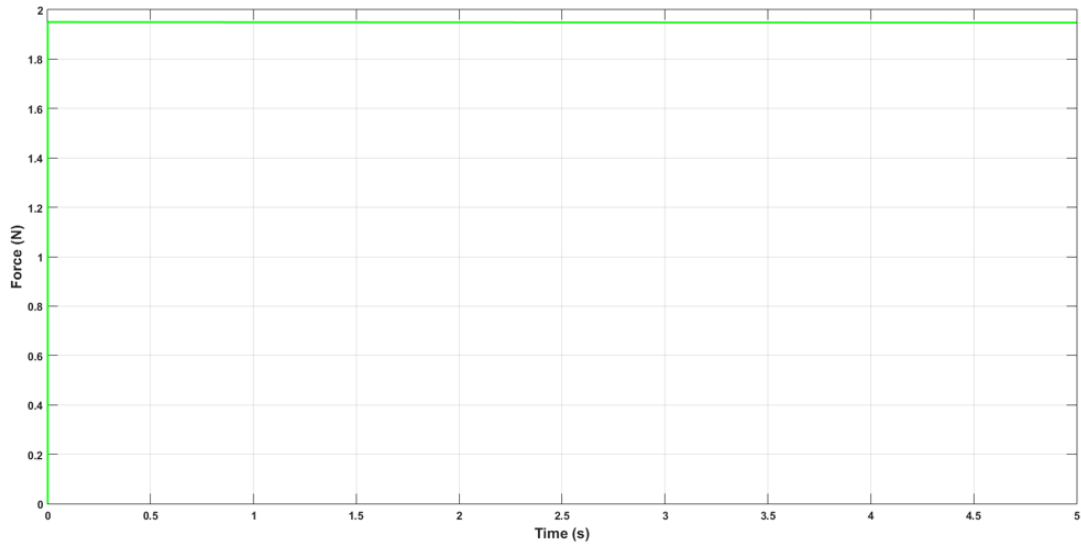
Figure 4.36: Friction force response without dither.
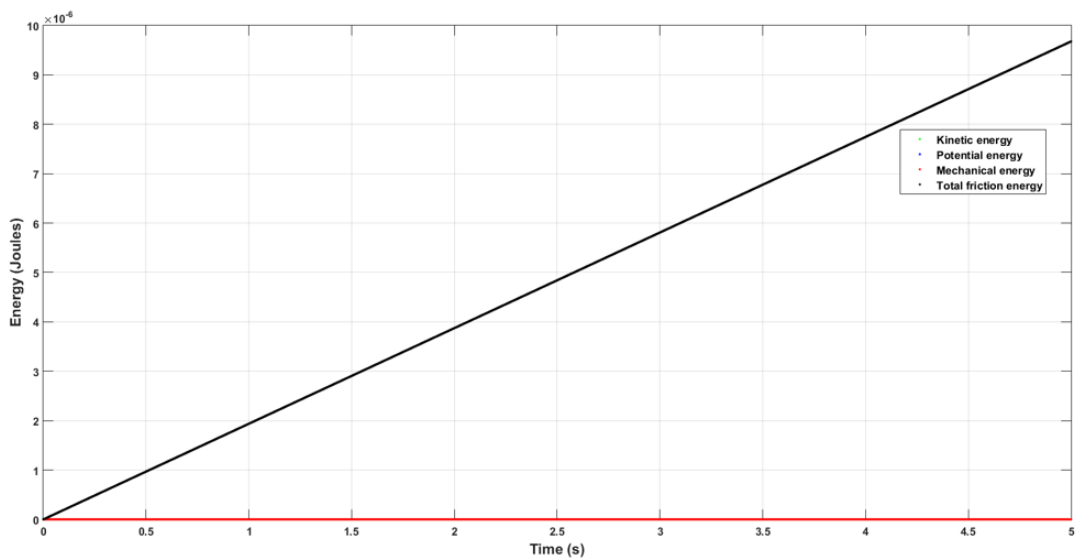
Figure 4.37: Coulomb friction model energies without dither.

4.10.2. Displacement and velocity responses with dither

This section discusses the displacement and velocity responses of the Coulomb friction model with sinusoidal dither applied to the input. The displacement responses of the wagon body are shown in Figure 4.38 where the black line shows the response without dither and the green, blue and red lines, show the responses for the 0.001, 0.01 and 0.1 mm dither amplitudes respectively. The cyan and magenta lines, are the responses for the 1 and 10 mm amplitudes. The dither excitations as can be seen, are applied to the system between $1 - 3.12$ seconds.

The wagon body mass is seen to be stationary when no dither is applied to the system, but when the amplitude of the dither is increased to 0.001 and 0.01 mm (Green and blue lines), the mass starts to slip. The final settling positions of the Coulomb model under these dither amplitudes are seen to be – 3.831 and –0.496 mm respectively, which also includes the 5 µm of creepage due to the influence of the velocity threshold parameter. The final settling positions for the 0.1, 1 and 10 mm dither amplitudes, are seen to be –3.895, –4.44 and –7.035 mm respectively.

From the displacement responses, it can also be seen that when the dither amplitude is equal to or less than 0.1 mm for example, the envelopes of the of the green, blue and red lines, appear to decay exponentially over time, which suggests that the system is behaving as if it were viscously damped. Whereas for the 1 and 10 mm dither amplitudes on the other hand (Cyan and magenta lines), the wagon body masses are seen to break out of the stiction regions and transition into gross-sliding. This state however, gives rise to the constant Coulomb friction force which then causes the displacement responses to decrease over time in straight line envelopes.

The velocity responses are shown in Figure 4.39 and from these, it can be seen that when the dither amplitude is set to 0.001, 0.01 and 0.1 mm for example, the peak velocities of the Coulomb model reach −0.672, −6.711 and −52.88 mm/s respectively. When the dither amplitude is increased to 1 and 10 mm however, the peak velocities of the wagon body mass are seen to be in the region of −86.15 and −91.2 mm/s. From this analysis, it is clear to see that the velocity responses in the 0.001, 0.01 and 0.1 mm dither cases, increase by a factor of 9 − 10 relative to each other. Whereas the response in the 10 mm dither case, only increases by a factor 1.05 relative to response of the 1 mm case.

This analysis clearly shows that when the dither amplitude is an order of magnitude less than the displacement of the dominant forcing function, which in these simulations is the constant friction force preventing the spring from relaxing, the dither is seen to introduce a viscously damped response into the system dynamics. Whereas when the amplitude of the dither is equal to or greater than the magnitude of the forcing function displacement, the dither then becomes the dominant forcing function, rather than the dither.
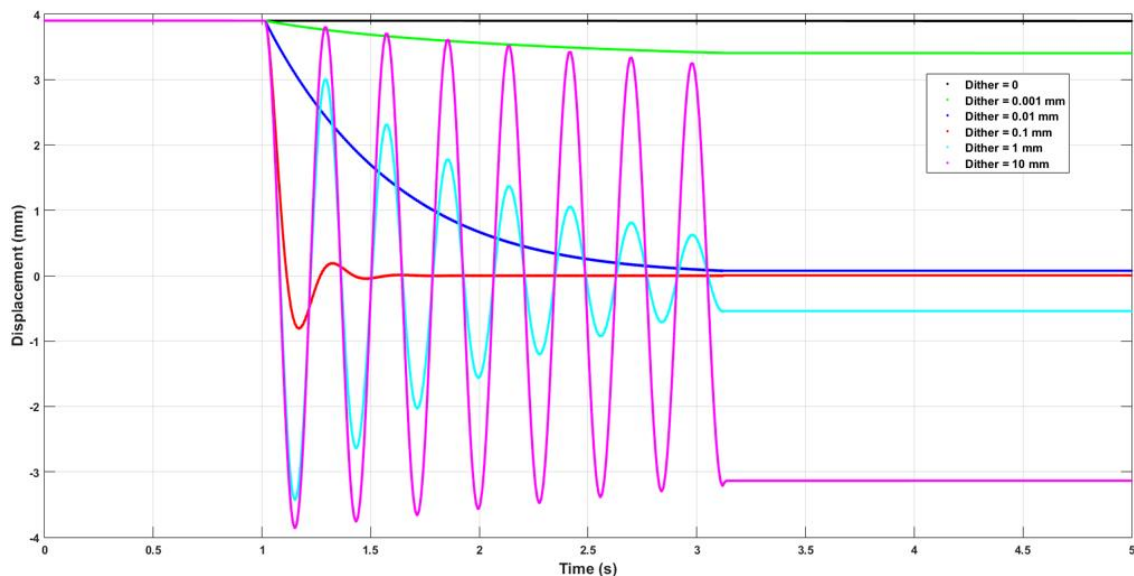
Figure 4.38: Wagon body displacement responses during the dither simulations.
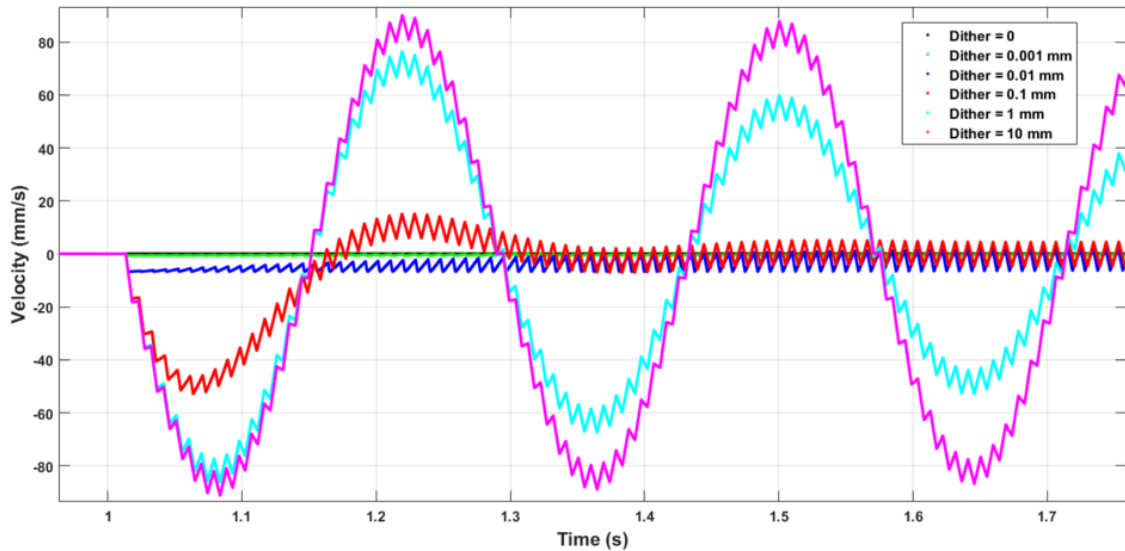
Figure 4.39: Close-up of the wagon body velocity responses.

The state space trajectories of the wagon body mass during the 0.001 and 0.01 mm dither simulations are shown in Figure 4.40 by the green and blue lines. The system response without dither applied is also shown in the top-plot of this figure for comparison purposes (Black line). From these responses, it is clear to see the stick-slip behaviour developing as the dither amplitude is increased from 0.001 to 0.01 mm. The wagon body mass for example, slides at total distance of 0.4 and 3.9 mm respectively under these conditions, minus the 5 µm of creepage.

When the amplitude of the dither is set to 0.1, 1 and 10 mm however, it can be seen that the sliding behaviour becomes more dominant in the responses, see Figure 4.41. Also, when the amplitude of the dither is less than 0.1 mm for example, the system oscillates at the same frequency as the dither, which is 106.8 Hz. Whereas when the amplitude is greater than 0.1 mm on the other hand, the response oscillates at 3.56 Hz, which is the natural frequency of this system. This analysis clearly shows that dither has a significant influence on the dynamic response of the centre plate model. The following section discusses the friction force responses.
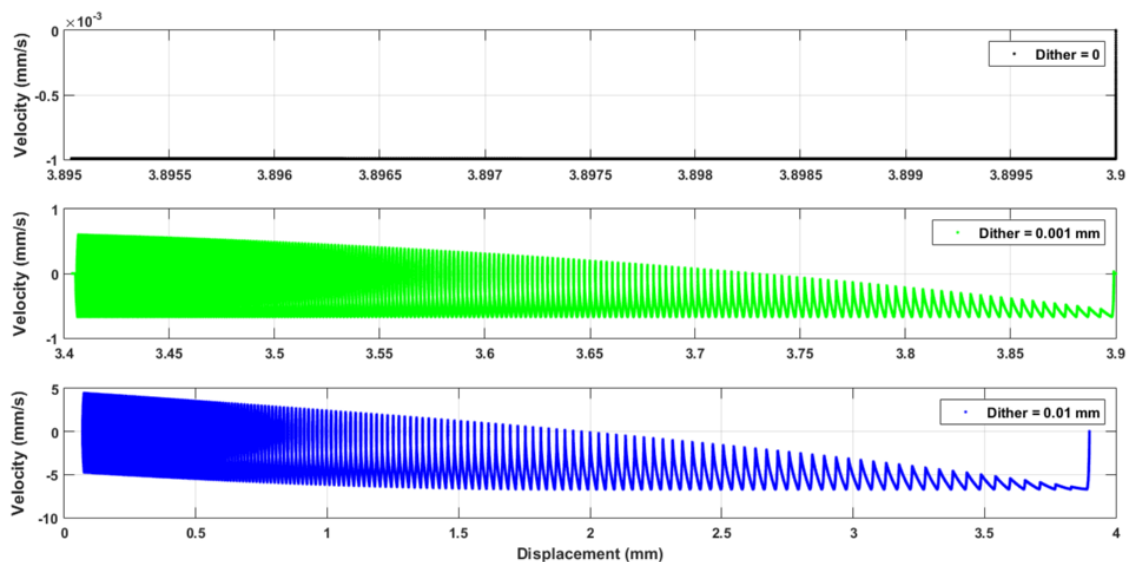
Figure 4.40: Wagon body state space trajectories during the 0, 0.001 and 0.01 mm dither simulations.

105
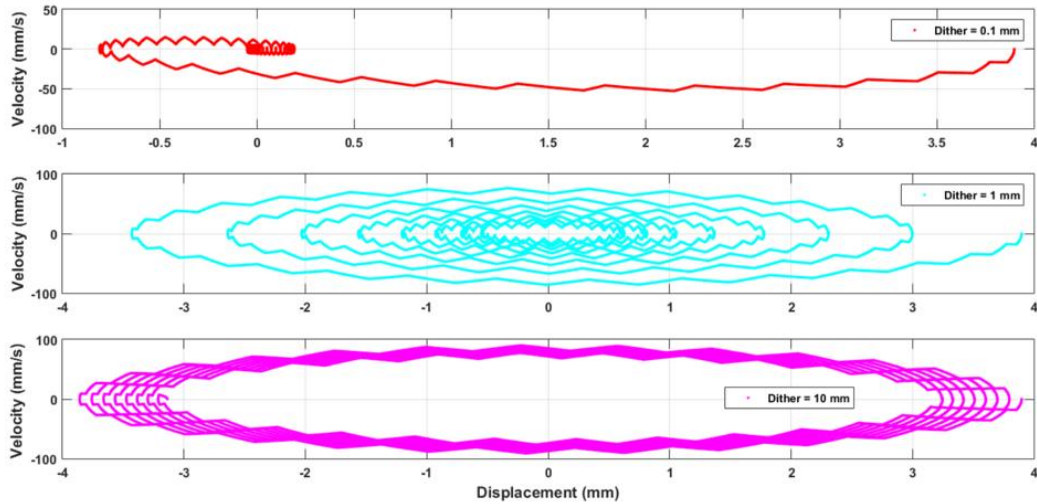
Figure 4.41: Wagon body state space trajectories during the 0.1, 1 and 10 mm dither simulations.

4.10.3. Friction force responses

The time histories of friction forces during the 0, 0.001 and 0.01 mm dither simulations are shown in Figure 4.42 and Figure 4.43 shows the responses during the 0.1, 1 and 10 mm simulations. From these it is clear to see the stick-slip behaviour occuring at the same frequency as the dither as well as the Non-Zero Residual Displacements (NZRD) at the end of the simulation run.

From the hysteresis responses shown in Figures 4.44 and 4.45, it can be seen that when the dither amplitude is 0.001 mm for example (Green line), the NZRD is seen to be in the region of 3.41 mm which suggests that the mass has slipped a total distance of 0.5 mm. Whereas when the amplitude is 0.01 mm (Blue line), the total sliding distance and NZRD, are seen to be 3.8 and 0.1 mm. This analysis strongly suggests that the either the dither amplitude or frequency for example, could potentially be tuned in order to dicate the final settling positions of the sliding surfaces.

The displacement, velocity and force responses during the dither simulations are summarised in Table 4.18 and from these results, it can be seen that the 5 second simulation took between 18.5 – 20.5 seconds of real time to reach a solution. The following section discusses the energy responses of the Coulomb friction model with dither.
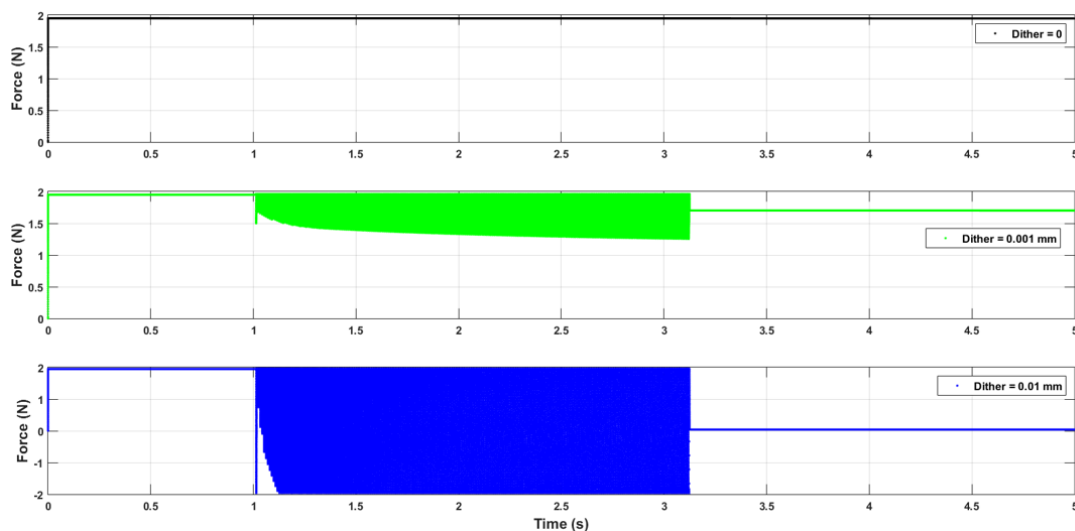
Figure 4.42: Friction forces as a function of time during the 0, 0.001 and 0.01 mm dither simulations.
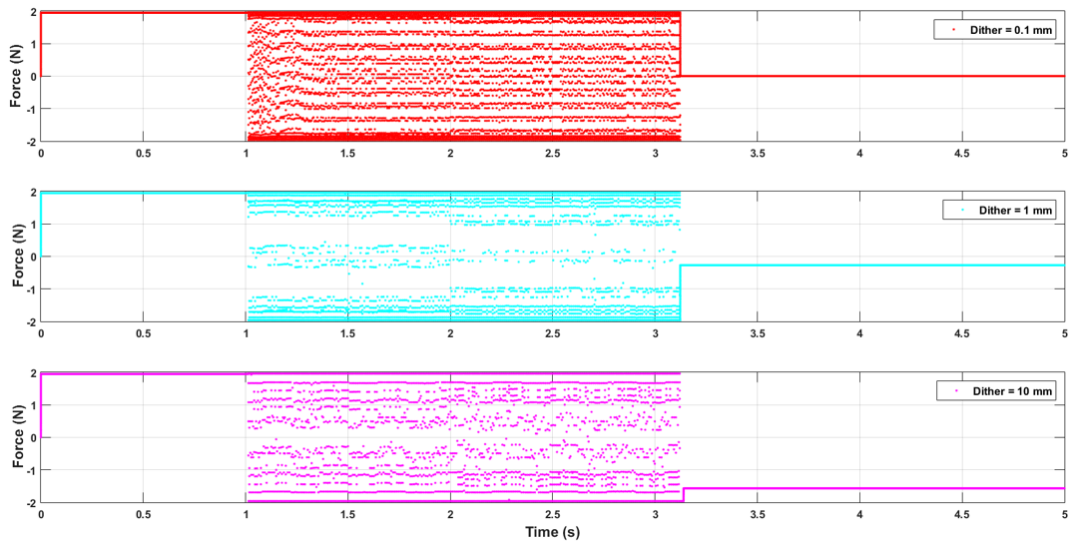
Figure 4.43: Friction forces as a function of time during the 0.1, 1 and 10 mm dither simulations.
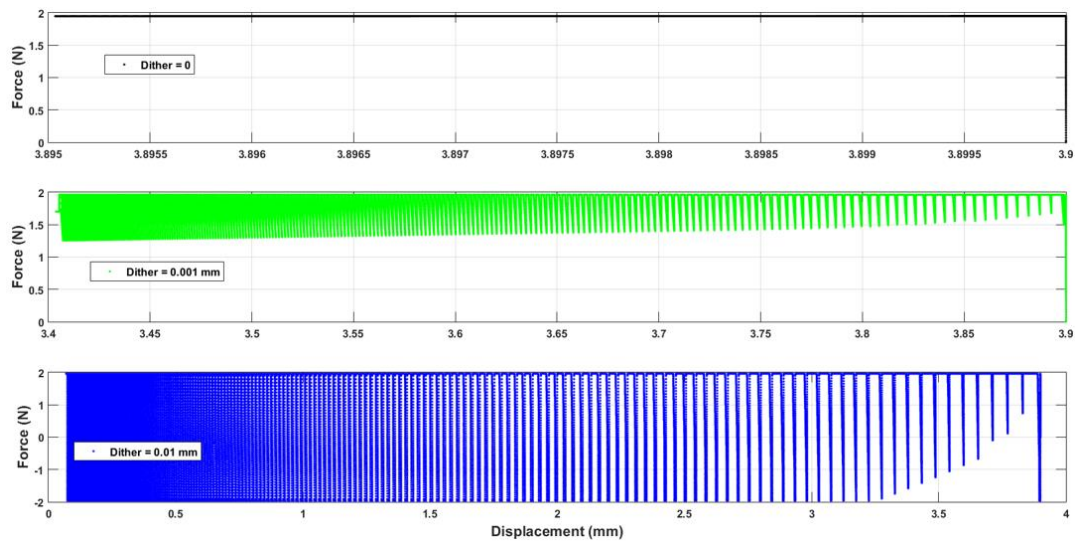
Figure 4.44: Hysteresis responses during the 0, 0.001 and 0.01 mm dither simulations.
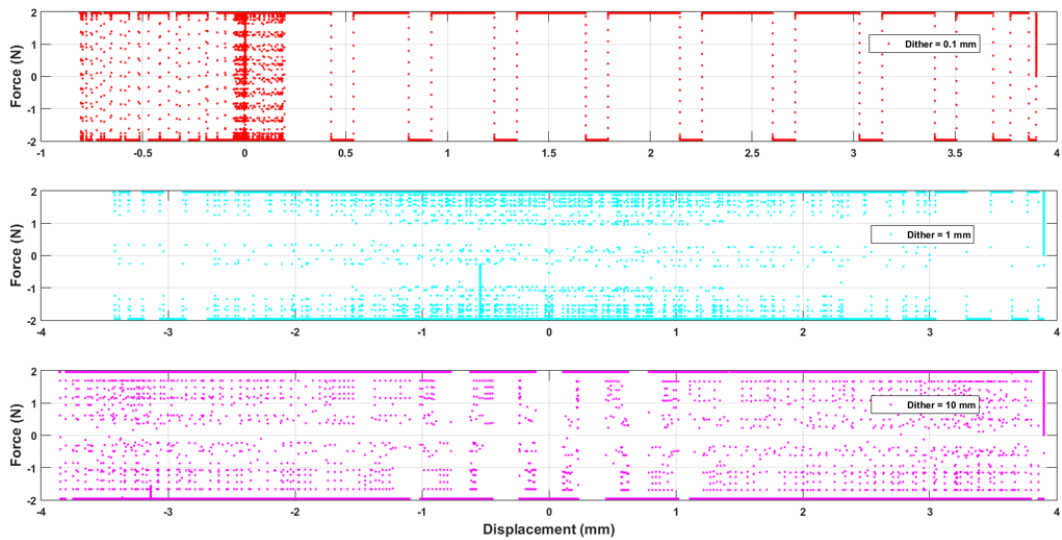
Figure 4.45: Hysteresis responses during the 0.1, 1 and 10 mm dither simulations.

Simulation case	Dither amplitude (mm)	Initial position (mm)	Settling position (mm)	Maximum velocity (mm/s)	Minimum velocity (mm/s)	Maximum spring force (N)	Final spring force (N)	Initial friction force (N)	Final friction force (N)	Simulation time (s)	Real time (s)
1	0	3.9	3.895	0	-0.001	1.95	1.948	1.962	1.948	5	18.5
2	0.001	3.9	3.404	0.6015	-0.672	1.95	1.702	1.962	1.702	5	19
3	0.01	3.9	0.069	4.45	-6.71	1.95	0.035	1.962	0.035	5	20
4	0.1	3.9	0.005	15.18	-52.9	1.95	0.003	1.962	0.0026	5	19
5	1	3.9	-0.54	76.4	-86.15	1.95	-0.27	1.962	-0.27	5	19.5
6	10	3.9	-3.135	90.1	-91.2	1.95	-1.57	1.962	-1.57	5	20.5

Table 4.18: Summary of the wagon body displacements, velocities and forces during the dither simulations.

4.10.4. Energy responses

The energy responses of the wagon body mass with no dither applied to the system are shown in Figure 4.46. The kinetic, potential and mechanical energies are shown by the green, blue and red lines respectively, whereas the total friction energy is shown by the black line. From these responses, it can be seen that the mechanical energy of the system remains constant throughout the simulation due to the wagon body mass sticking after being released.

The energy responses during the 0.001 mm dither simulation are shown in Figure 4.47 and from these, it can be seen that the wagon body mass is starting to slip. This amplitude however, is not large enough to dissipate all of the initial potential energy from the spring, whereas when the amplitude of the dither is 0.01 mm, the mechanical energy of the system (Red lines), decreases towards zero, see Figure 4.48. This analysis clearly shows that the mechanical and frictional energies of the centre plate model are proportional to the amplitude of the dither.
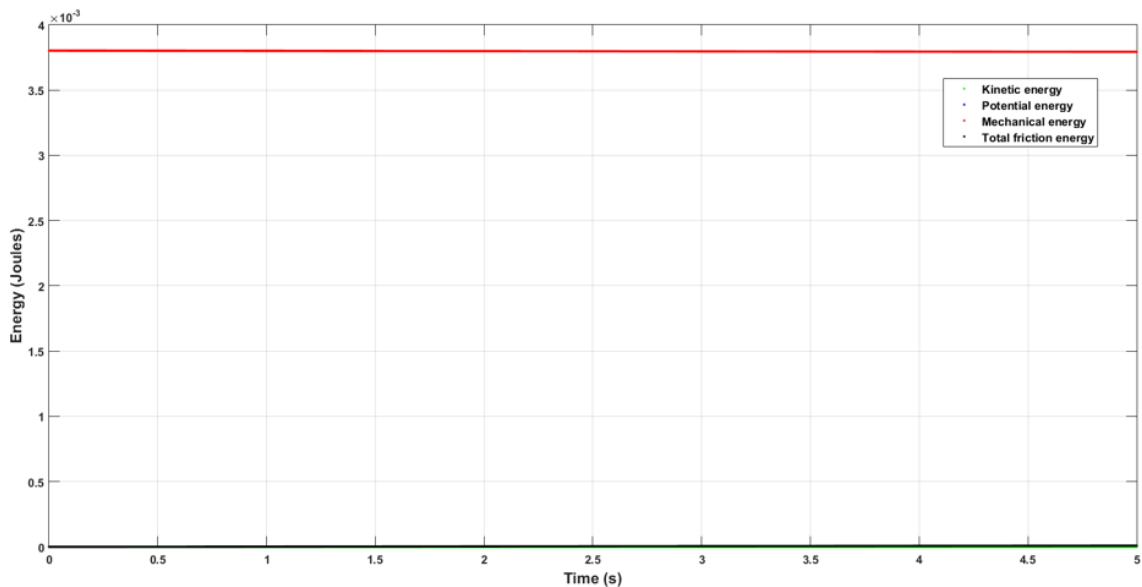
Figure 4.46: Energy response without dither.
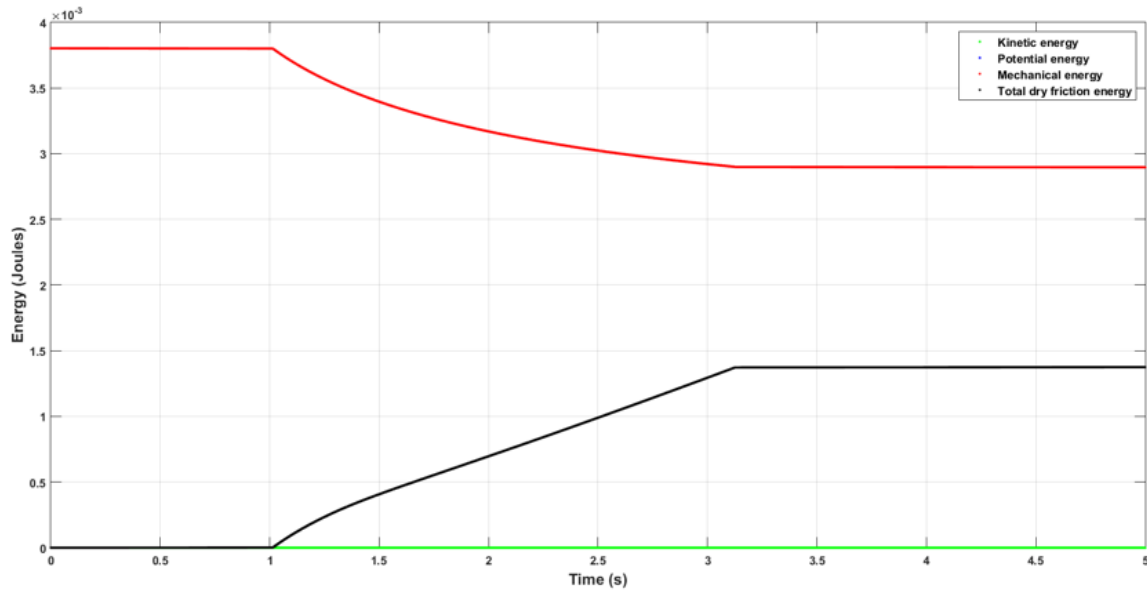
Figure 4.47: Energy response during the 0.001 mm dither simulation.
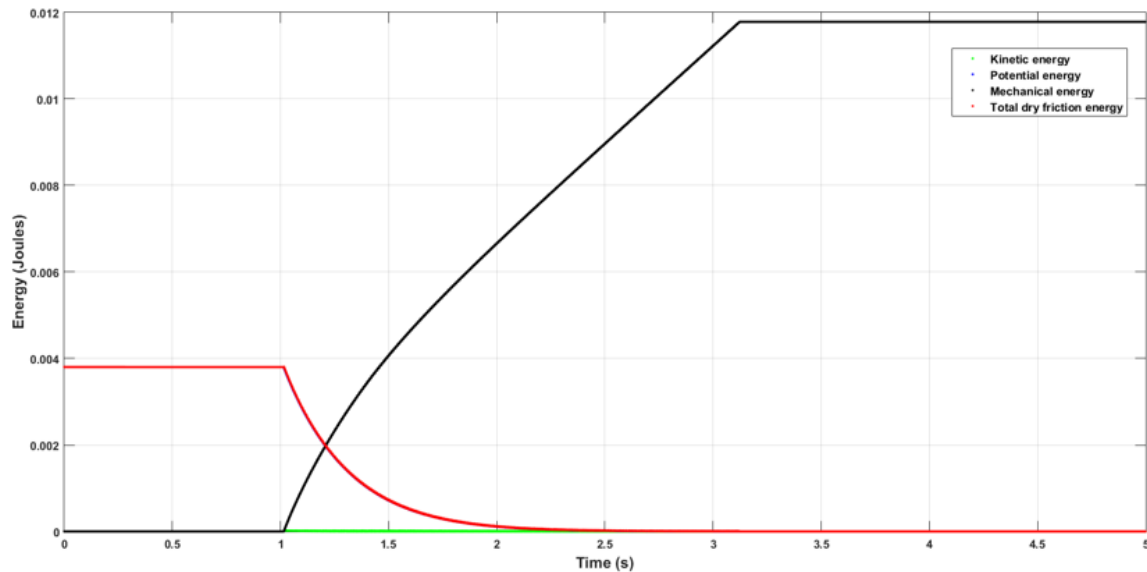
Figure 4.48: Energy response during the 0.01 mm dither simulation.

The energy responses during the 0.1 mm dither simulation are shown in Figure 4.49 and from these, it is clear to see the changes in the mechanical energy characteristics in comparison to the 0.001 and 0.01 mm responses (Red lines). When the dither amplitude is set to 0.1 mm for example, there is a steep rise in the frictional energy curve between 1 second and 1.2 seconds, see Figure 4.50 (Black line). Whereas when all of the initial mechanical energy has been dissipated from the system between 1.3 – 1.4 seconds, just after the kink in the friction energy curve (Black line), the gradient starts to decrease and then level off when the dither is removed.

The total frictional energy at the end of this simulation run as can be seen, is 19.5 x 10^{-3} J, whereas after the 0.001 and 0.01 mm dither simulations, the total frictional energies were seen to be 1.38 x 10^{-3} and 11.8 x 10^{-3} J respectively. This analysis also shows that the frictional energy responses are proportional to the amplitude of the dither.

Figure 4.51 shows the energy responses during the 1 mm dither simulation and from these, it can be seen that the spring is now starting to oscillate at the natural frequency of the system due to the initiation of the gross-sliding regime. The parabolic profile of the friction energy curve however, suggests that the system is still heavily damped by the dry friction. Whereas when the amplitude of the dither is increased to 10 mm, see Figure 4.52 as well as the close-up of this response shown in Figure 4.53, the frictional energy curve appears to have a linear profile due to the increase in the mechanical energy of the system.

From the summary of the energy results shown in Table 4.19, it can be seen that the total frictional energies of the 1 and 10 mm dither cases, are 0.1 and 0.21 J respectively. These energies however, are 5 and 10 times higher than the frictional energy that was measured during the 0.1 mm dither simulation. The following section discusses the harmonic motion simulation responses.
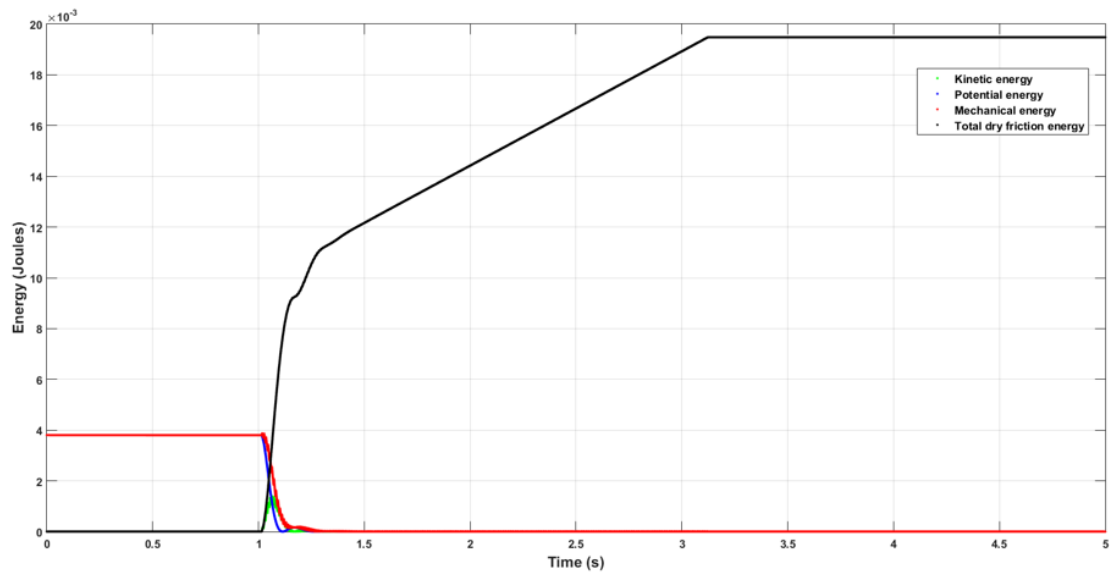
Figure 4.49: Energy response during the 0.1 mm dither simulation.
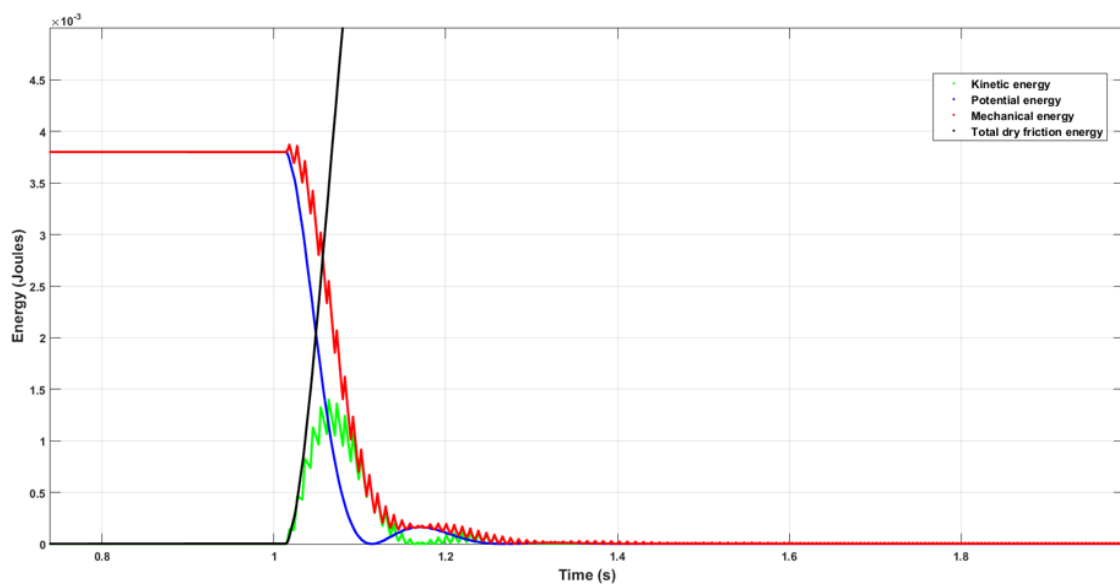
Figure 4.50: Close-up of the kinetic and mechanical energy responses during the 0.1 mm dither simulation.
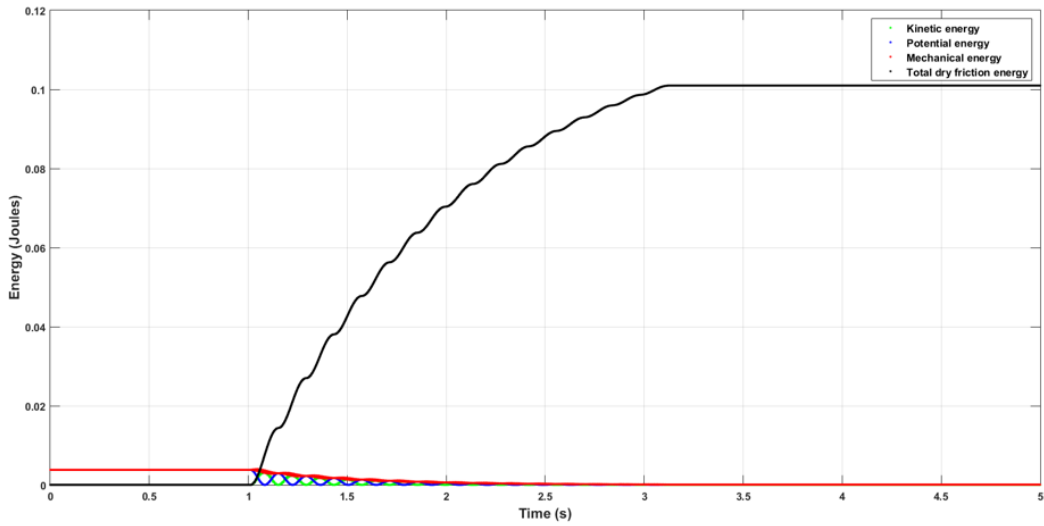
Figure 4.51: Energy response during the 1 mm dither simulation.
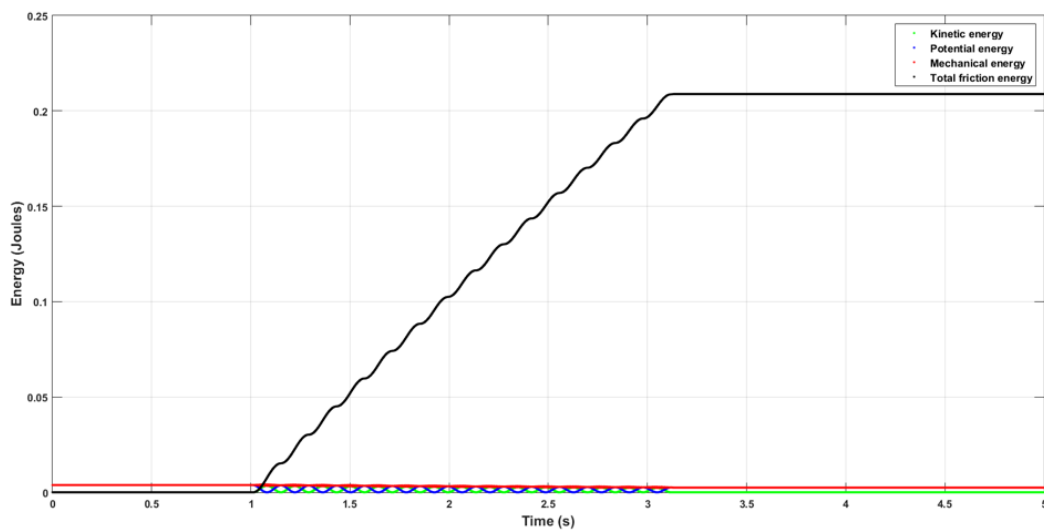
Figure 4.52: Energy response during the 10 mm dither simulation.
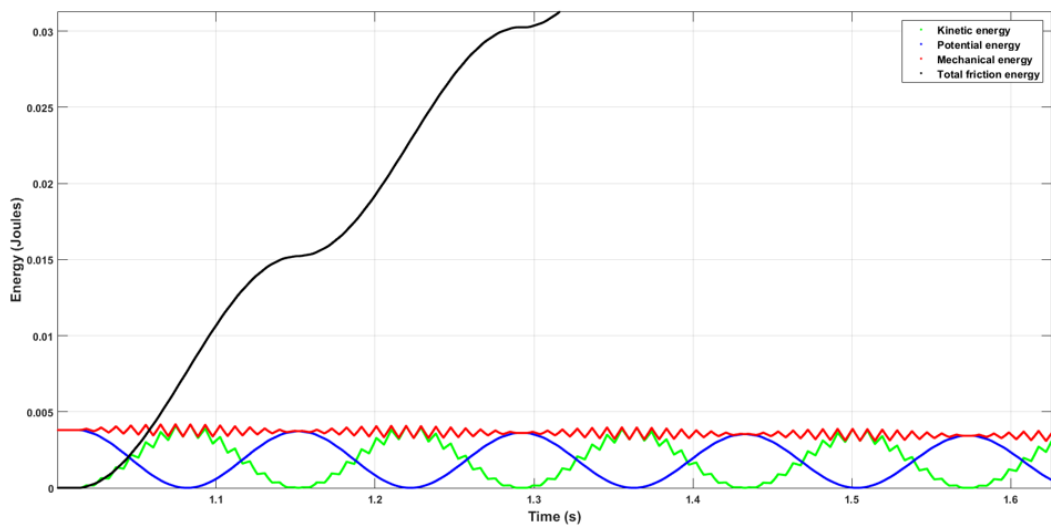
Figure 4.53: Close-up of the kinetic and mechanical energy responses during the 10 mm dither simulation.

Simulation case	Dither amplitude (mm)	Maximum kinetic energy (Joules)	Maximum potential energy (Joules)	Maximum mechanical energy (Joules)	Total friction energy (Joules)	Simulation time (s)	Real time (s)
1	0	0	3.80E-03	3.80E-03	9.70E-06	5	18.5
2	0.001	2.26E-07	3.80E-03	3.80E-03	1.38E-03	5	19
3	0.01	2.25E-05	3.80E-03	3.80E-03	1.18E-02	5	20
4	0.1	1.40E-03	3.80E-03	3.80E-03	1.95E-02	5	19
5	1	3.70E-03	3.80E-03	4.00E-03	1.00E-01	5	19.5
6	10	4.20E-03	3.80E-03	4.20E-03	2.10E-01	5	20.5

Table 4.19: Summary of the energy responses during the dither simulations.

4.11.   Harmonic motion simulations

The harmonic motion simulations have been designed to replicate the X-Factor testing procedure used during railway vehicle acceptance tests. This vehicle performance test is explained in the Railway Group Standards GM/RT 2141, GM/RC2641 as well as the European equivalent, EN 14363. Newly built as well as modified vehicles for example, have to undergo this test in order to demonstrate that the rotational resistance is below the X-Factor limit, which is calculated using Equation (2.27) in Section 2.11.

The curving performance and running behaviour of the bogie on straight sections as was discussed in the literature review, is highly dependent on the rotational resistance. This system parameter therefore, needs to be monitored and controlled throughout the life-cycle of the vehicle in order to reduce the derailment risks and maintenance costs associated with high bogie rotational resistance (Wickens, 2006).

In the following simulations the bogie rotates with simple harmonic motion to a maximum angle of six degrees or alternatively, 104.5 mrad. Two simulations were then carried out with the forcing frequency set at 0.5 Hertz (Hz) and 1 Hz so that comparisons could then be made between the two sets of results. The Equation of motion for the bogie/wagon body centre plate system is given in Equation (4.7), Section 4.2, whereas the equation to describe the velocity of the bogie/input, $\dot{\theta}_B$, is given in Equation (4.35).

The equations to describe the displacement θ_{WB}, velocity and acceleration of the wagon body are also shown in Equations (4.36), (4.37) and (4.38) respectively. The Coulomb, Stick-slip and Coulomb-viscous friction model parameters for these simulations are shown in Table 4.3 in Section 4.4. The following section discusses the displacement and velocity responses during the 0.5 Hz forcing frequency simulations.

$$\dot{\theta}_B = A.\omega.\cos(\omega.t + \phi) \tag{4.35}$$

$$\theta_{WB} = B.\sin(\omega_n.t + \phi) \tag{4.36}$$

$$\dot{\theta}_{WB} = B.\omega_n.\cos(\omega_n.t + \phi) \tag{4.37}$$

$$\ddot{\theta}_{WB} = -B.\omega_n^2.\sin(\omega_n.t + \phi) \tag{4.38}$$

4.11.1. Angular displacement and velocity responses (0.5 Hz)

The angular displacement responses of the wagon body mass using the Coulomb, Stick-slip and Coulomb-viscous models are shown in Figure 4.54 by the green, red and blue lines respectively. The displacement of the bogie is also shown by the black line, but this response had to be multiplied by a factor of 1:10, to view it alongside the displacement responses of the wagon body. From these responses it can be seen that the peak of the dynamic displacements in the Coulomb model about the breakout points for example, are 6.89 mrad when the velocity of the input is positive and −7.52 mrad when the input velocity is negative.

The dynamic displacements of the Coulomb-viscous and Stick-slip models about the breakout points however, are slightly higher, ranging between 7.53 and −7.89 mrad and 11.45 and −11.57 mrad respectively. It can also be seen that the displacement responses in the Coulomb and Coulomb-viscous models, either remain constant, or decay slightly during the gross-sliding events, whereas in the Stick-slip model, they are seen to increase over time.

The angular velocity responses are shown in Figure 4.55 and from these it can be seen that when the bogie/input velocity is positive, the peak velocities in the Coulomb model approach $\pm$ 66.4 milli-radian/second (mrad/s). Whereas when the bogie velocity is negative, the sliding velocities increase to $\pm$ 80 mrad/s. The velocity responses of the Stick-slip model when the bogie velocity is positive and negative however, are significantly higher, ranging between 140 and −163 mrad/s, and between −141 to 166.1 mrad/s respectively. The peak velocities in the Coulomb-viscous model on the other hand, are much closer together, ranging between 77.4 and −85.4 mrad/s. The peak velocity of the bogie as can be seen (Black lines), was the highest overall at $\pm$ 164.2 mrad/s.

From the state space trajectories shown in Figure 4.56 and the responses of the Stick-slip model for example (Red lines), it is clear to see the influence of the velocity feedback phenomenon due to the momentum of the wagon body mass during the gross-sliding events (Altpeter, 1999). These periodic events as can be seen, are the straight line sections of the state space trajectories and always occur during the third slip cycle. At this point in time however, the velocity of the bogie is seen to be decreasing away from the peak values (Decelerating), whereas the wagon body on the other hand, is seen to be increasing towards the peak values (Accelerating).

The velocities of the bogie/wagon body are then seen to approach the same value of $\pm$ 140 mrad/s, which causes the friction surfaces to stick together. However, when the system starts to slip again after this event, the torque in the spring of the Stick-slip model, is significantly higher than it was during the initial breakout event, which is seen to take place between 0 − 0.25 seconds. The friction surface on the wagon body then starts to slip past the equilibrium position as can be seen by the displacement responses (Figure 4.54), which then leads to a rapid reduction in the frictional torque due to the spring unloading, see the torque responses shown in the following section.

It can also be seen from the state space trajectories, that the characteristics of the limit cycles in the Stick-slip model for example, are similar to those that were observed in the constant acceleration simulations (Section 4.9). The instabilities of the Stick-slip friction model during the 0.5 Hz forcing frequency simulation however, are significantly worse due to the higher sliding velocities. For an in-depth discussion on velocity feedback phenomenon as well as the instabilities this behaviour introduces into positioning control systems, see (Altpeter, 1999). The following section discusses the frictional torque responses.
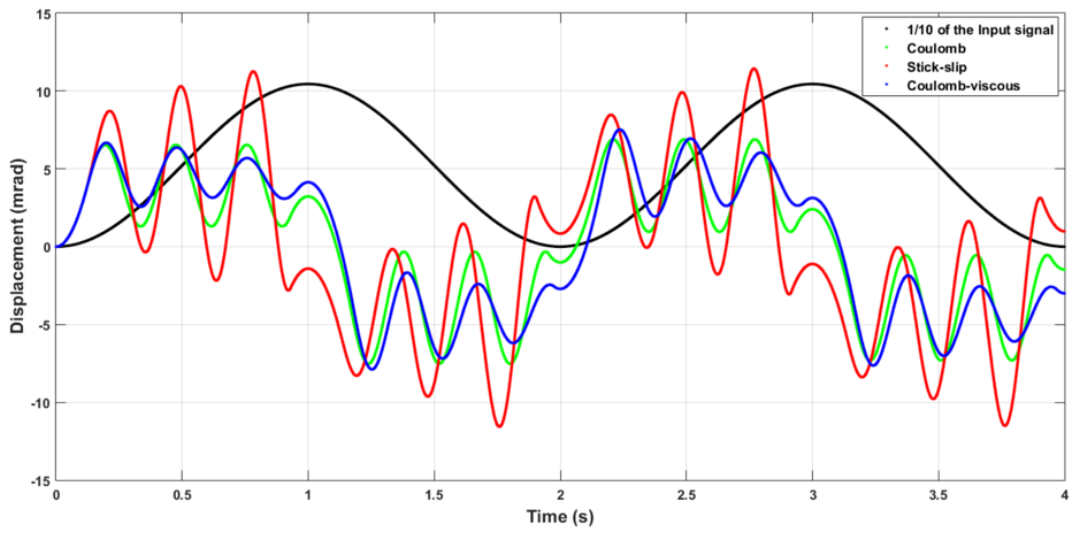
Figure 4.54: Wagon body angular displacement responses.
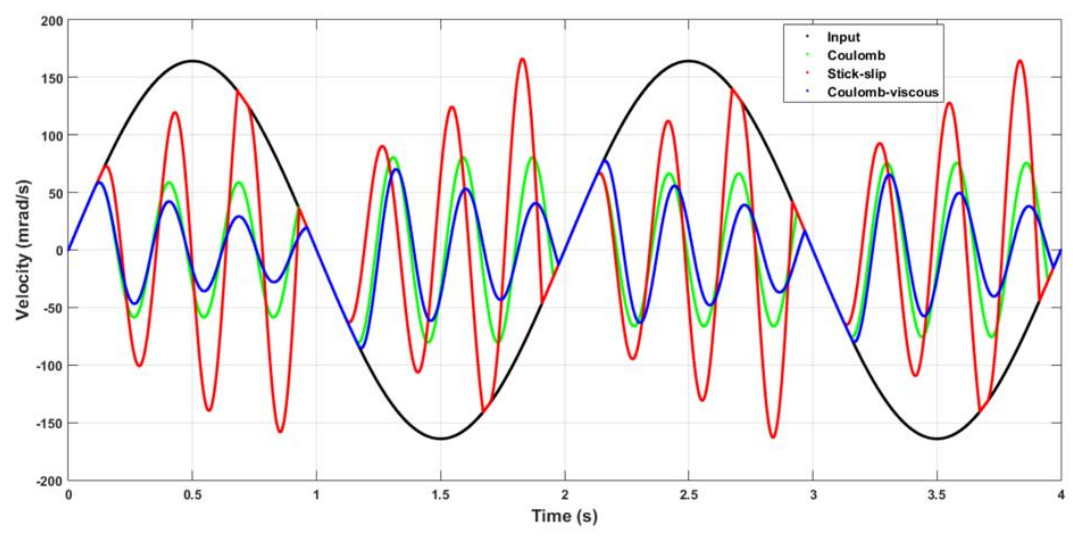
Figure 4.55: Wagon body angular velocity responses.
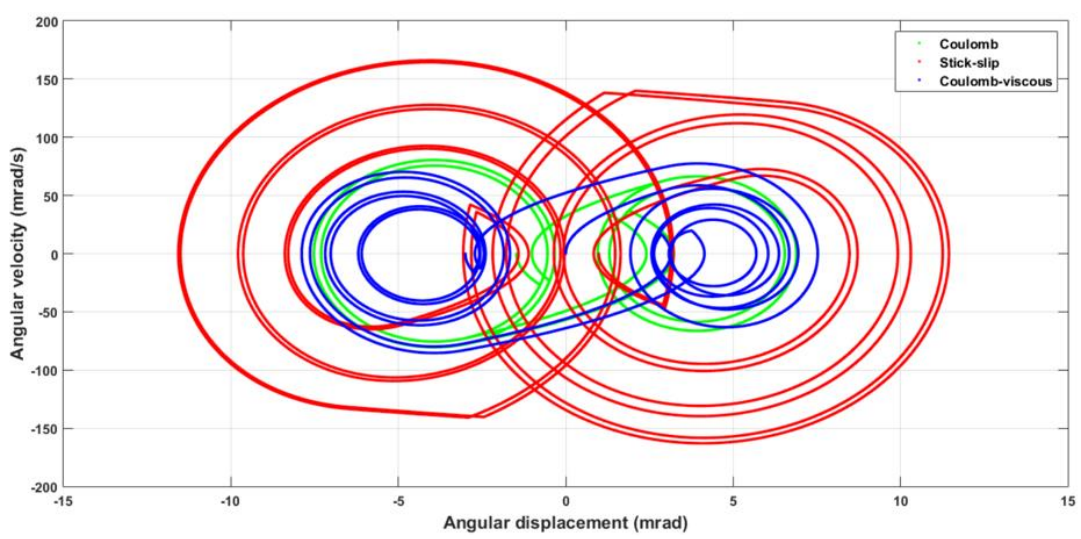
Figure 4.56: Wagon body state space trajectories.

114

4.11.2. Frictional torque responses (0.5 Hz)

The frictional torque responses of the Coulomb, Stick-slip and Coulomb viscous models as a function of time, are shown in Figure 4.57 by the green, red and blue lines respectively. From these responses, the differences in friction force characteristics of each model during the sticking, transition and gross-sliding regimes are clear to see, as well as the inertia forces at the start of the simulations, which cause the frictional torque responses to rise almost instantaneously from 0 to 0.5 Nm.

The bogie/wagon body masses then start to move at the same velocity due to sticking, which causes the frictional torque to increase over time up to the limits of the breakout torque. The Coulomb friction model (Green line), then transitions straight into the gross-sliding regime where the torque response is seen to remain constant at $\pm$ 1.962 Nm. The torque in the Coulomb-viscous model on the other hand (Blue line), continues to increase towards $\pm$ 2.417 Nm because the viscous damping torque is proportional to the relative velocity.

The torque response in the Stick-slip model as can be seen (Figure 4.57), reaches a peak value of $\pm$ 2.943 Nm during the initial breakout event. The frictional torque then starts to decrease over time towards the Coulomb torque level which is 1.962 Nm. The Stick-slip model however, does not fully transition into the gross-sliding regime because the relative velocities between the bogie/wagon body mass are obviously too low. It can also be seen that there are several periodic jumps, where the frictional torque decreases rapidly from the peak values of $\pm$ 2.943, to $\pm$ 0.3 and $\pm$ 1 Nm. This behaviour is related to the velocity feedback phenomenon discussed in the previous section (Altpeter, 1999).

From the hysteresis responses shown in Figure 4.58, it can be seen that the rapid decreases in the torque responses of the Stick-slip model always take place between 79 – 86 mrad and 21 – 26 mrad. This behaviour is also seen to occur, although to a lesser extent, in all three friction models at extremities of the hysteresis responses, see the vertical lines in the close-up shown to the right of Figure 4.58. These events are then seen to take place when the input velocity is either decreasing, or changing direction and under these conditions, a finite proportion of the recoverable elastic energy that was stored in the torsional spring during the breakout events, is then returned back to the system.

The breakout angles were also quantified from the hysteresis responses and for the Coulomb model, these are seen to range between $\pm$ 2.95 – 4 mrad, whereas for Coulomb-viscous and Stick-slip models, the breakout angles ranged between $\pm$ 2.95 – 5.7 mrad and $\pm$ 4.1 – 4.95 mrad respectively. These values as can be seen are in line with the pre-calculated breakout angles shown in Table 4.20. The kinematic motions, torque responses and simulation run times are also shown and from these results, it can be seen that the 4 second simulation, took 16 seconds of real time to reach a solution when the time step was set to 1×10^{-5} seconds. The following section discusses the frictional energy responses.
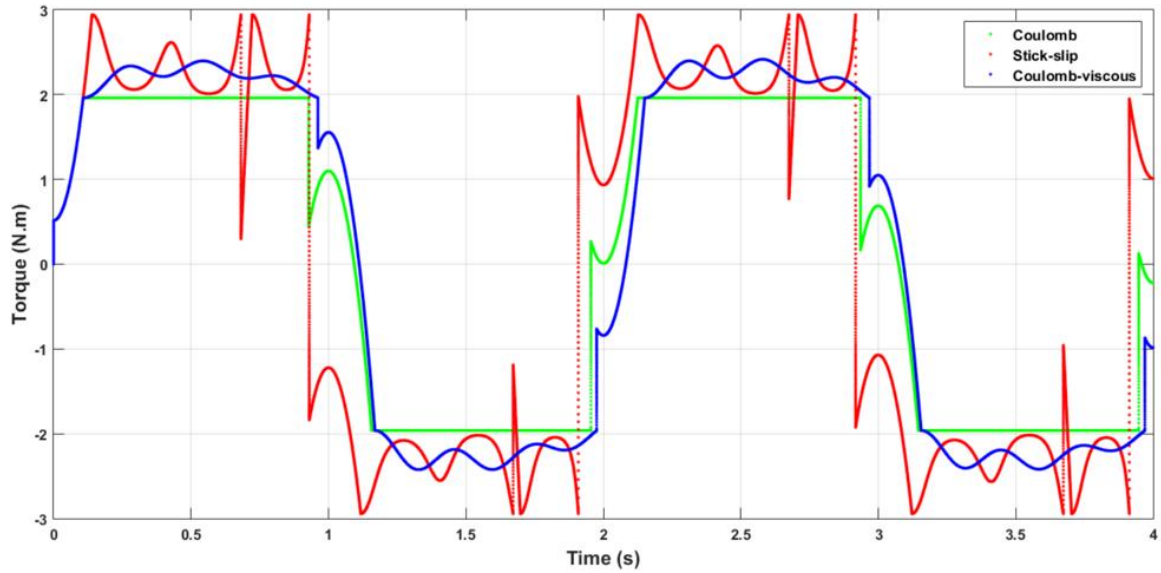
Figure 4.57: Torque responses as a function of time.
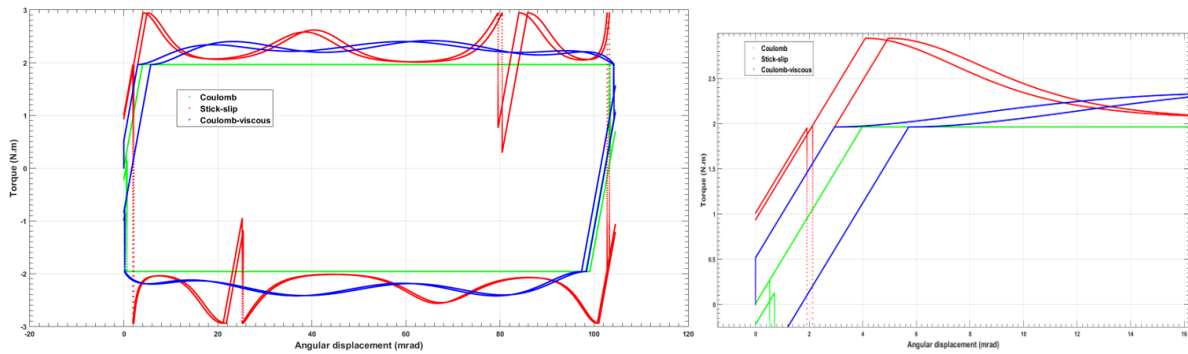
Figure 4.58: (Left) Hysteresis responses. (Right) Close-up of the breakout regions.

Friction model	Forcing frequency (Hertz)	Breakout angle (mrad)	Maximum angular displacement (mrad)	Minimum angular displacement (mrad)	Maximum angular velocity (mrad/s)	Minimum angular velocity (mrad/s)	Maximum spring torque (N.m)	Minimum spring torque (N.m)	Breakout torque (N.m)	Minimum torque during the transition (N.m)	Sliding torque (N.m)	Simulation time (s)	Real time (s)
Coulomb	0.5	3.9	6.893	-7.521	±80	±66.4	3.446	-3.761	1.962	0.17	1.962	4	16
Stick-slip	0.5	5.88	11.45	-11.57	166.1	-141	5.723	-5.785	2.943	-1.924	2.02	4	16
Coulomb-viscous	0.5	3.9	7.528	-7.886	77.46	-85.39	3.764	-3.943	1.962	0.92	2.417	4	16

Table 4.20: Summary of kinematic motions and torque responses during the 0.5 Hz simulations (Ode 23t solver).

4.11.3. Energy responses (0.5 Hz)

The energy responses of the Coulomb friction model during the 0.5 Hz harmonic forcing frequency simulations are shown Figure 4.59. The kinetic, potential and mechanical energies of the system are shown by the green, blue and red lines respectively and the total frictional energy, which has been calculated as a function of the bogie displacement, is shown by the black line. The maximum potential and mechanical energies are seen to be the same at 14.1 x 10^{-3} J, whereas the kinetic energy is significantly lower and shown to be 3.23 x 10^{-3} J. The total friction energy of this model is also the lowest overall at 0.795 J.

The maximum potential and mechanical energies of the Coulomb-viscous friction model as can be seen from the responses shown in Figure 4.60, are 15.6 x 10^{-3} J. The kinetic energy of this model is seen to be 3.65 x 10^{-3} J, whereas the total friction energy is 0.912 J, which is similar to the frictional energy of the Stick-slip model.

The energy responses of the Stick-slip friction model are shown in Figure 4.61 and from these, it can be seen that the maximum potential and mechanical energies are 33.5 x 10^{-3} J. The kinetic energy is 13.8 x 10^{-3} J and the total frictional energy is the highest overall at 0.935 J, which is a 17.5% increase in comparison to the total energy of the Coulomb model. From this analysis, it is clear to see that the potential/mechanical energies of the Stick-slip friction model for example, are twice as high as they are in the Coulomb/Coulomb-viscous models, which then gives rise to the velocity feedback phenomenon (Altpeter, 1999).

From the close-up of the Stick-slip model responses shown to the right of Figure 4.61, it is also clear to see in the regions of $0.65 - 0.7$ and $0.9 - 0.95$ seconds for example, the velocity feedback influencing the energy responses. The summary of the energy responses shown in Table 4.21, can now be compared against results for the 1 Hz forcing frequency simulations, which are discussed in the following section.

Friction model	Forcing frequency (Hertz)	Maximum kinetic energy (Joules)	Maximum potential energy (Joules)	Maximum mechanical energy (Joules)	Total friction energy (Joules)	Simulation time (s)	Real time (s)
Coulomb	0.5	0.00323	0.0141	0.0141	0.795	4	16
Stick-slip	0.5	0.0138	0.0335	0.0335	0.935	4	16
Coulomb-viscous	0.5	0.00365	0.0156	0.0156	0.912	4	16

Table 4.21: Summary of the energy responses during the 0.5 Hz simulations.
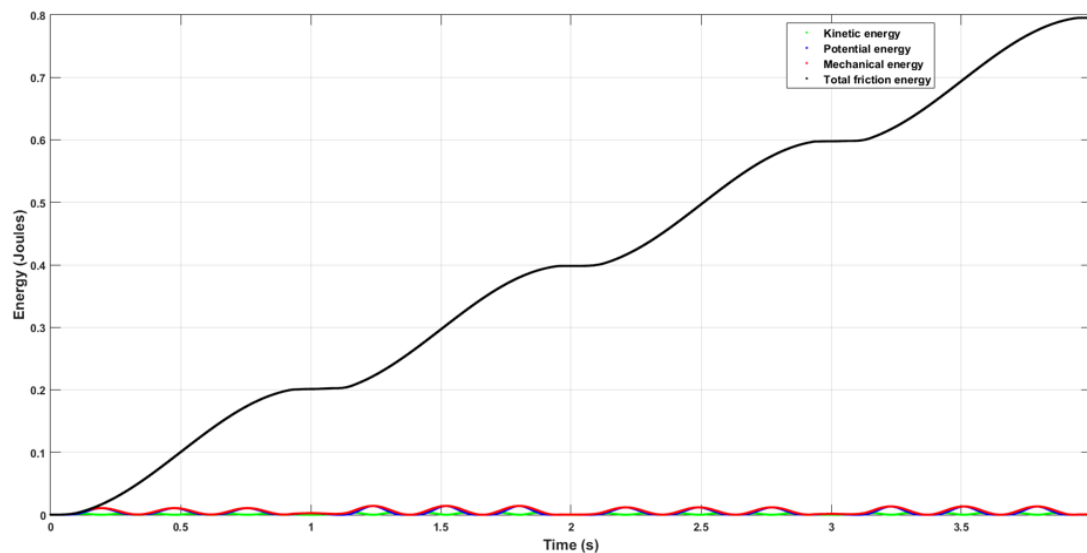
Figure 4.59: Energy responses of the Coulomb friction model.
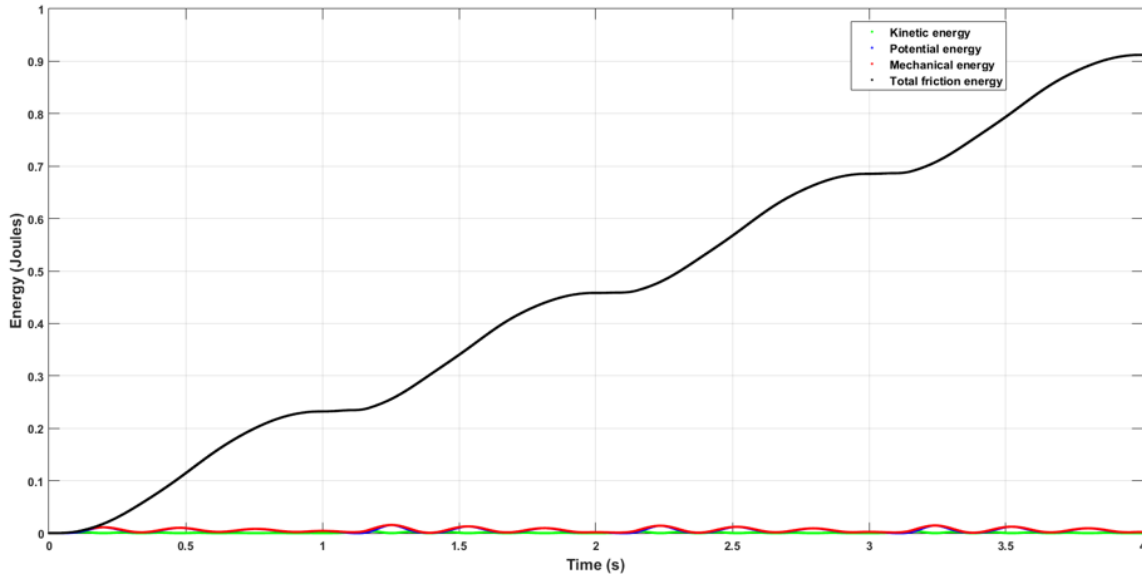
Figure 4.60: Energy responses of the Coulomb-viscous friction model.
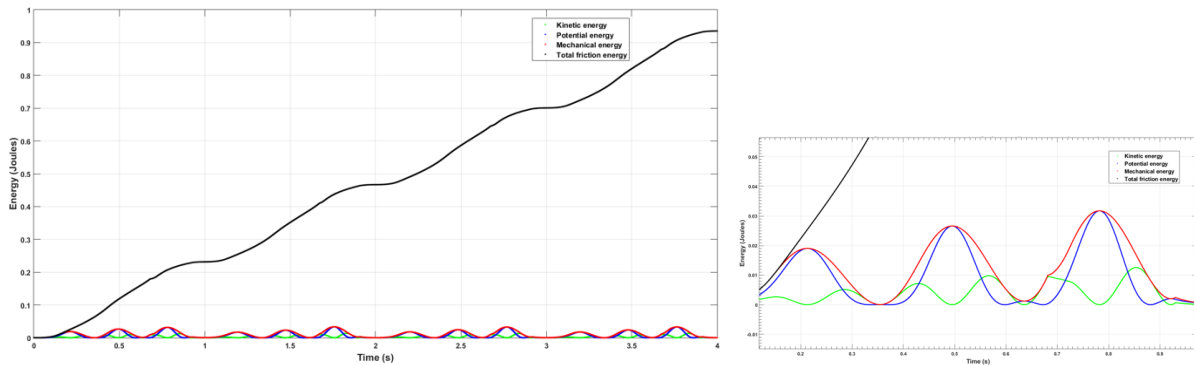
Figure 4.61: (Left) Energy responses of the Stick-slip friction model. (Right) Close-up of the Stick-slip friction model energies.

4.11.4. Angular displacement and velocity responses (1 Hz)

This section discusses the displacement and velocity responses from the 1 Hz sinusoidal forcing frequency simulations. The green, blue and red lines in Figure 4.62, show the angular displacement responses of the Coulomb, Coulomb-viscous and Stick-slip friction models respectively. The displacement of the bogie/input is also shown by the black line which has been scaled by a factor of 1:10 to view it alongside the responses of the friction models.

From these responses, it can be seen that the maximum dynamic displacements of the Coulomb model for example, are seen to range from 9.026 to –9.462 mrad. The maximum displacements in the Coulomb-viscous on the other hand, are seen to be equal in both directions at $\pm$ 10.78 mrad, whereas in the Stick-slip model, the dynamic displacements are seen to be the highest overall, ranging from 11.27 to –11.09 mrad.

The angular velocity responses are shown in Figure 4.63 and from these, it is clear to see the changes in system behaviour due to a doubling in forcing frequency from 0.5 to 1 Hz (Black line). Increasing the forcing frequency by this amount as can be seen, has eliminated the intermittent sticking cycle in the Stick-slip model (Red lines), as well as reduced the frequency of wagon body oscillations during the gross-sliding events, from 3.56 Hz, which is the natural frequency of the system, to 1.78 Hz. From the

velocity responses, it can also be seen that the peak velocity of the bogie has doubled from $\pm$ 164.2 to $\pm$ 328.3 mrad/s, which suggests that both models are set-up correctly.

The state space trajectories of the friction models are shown in Figure 4.64 and from these it is clear to see the differences, as well as the smoothness in the responses of the Stick-slip model (Red line) in comparison to the 0.5 Hz responses. The plataeu`s for example, have been completely eliminated from the responses shown below due to the higher input velocities. The peak sliding velocities of the Stick-slip model during this simulation however, range between 153 and –158 mrad/s, whereas during the 0.5 Hz simulations, the peak and minimum velocities in the Stick-slip model were seen to be 166 and –141 mrad/s respectively (Table 4.20). The full range of the velocity responses under both forcing frequencies however, are seen to be in close agreement at 311 and 307 mrad/s.

The velocity responses of the Coulomb model (Green line), are seen to be the lowest overall at $\pm$ 123.8 mrad/s, as well as equal in both directions. The velocity responses of the Coulomb-viscous model are also equal in both directions but slightly higher at $\pm$ 143 mrad/s (Blue lines). The velocities in these two friction models as can be seen, have also doubled in comparison to those that were observed during the 0.5 Hz simulations. The following section discusses the frictional torque responses.
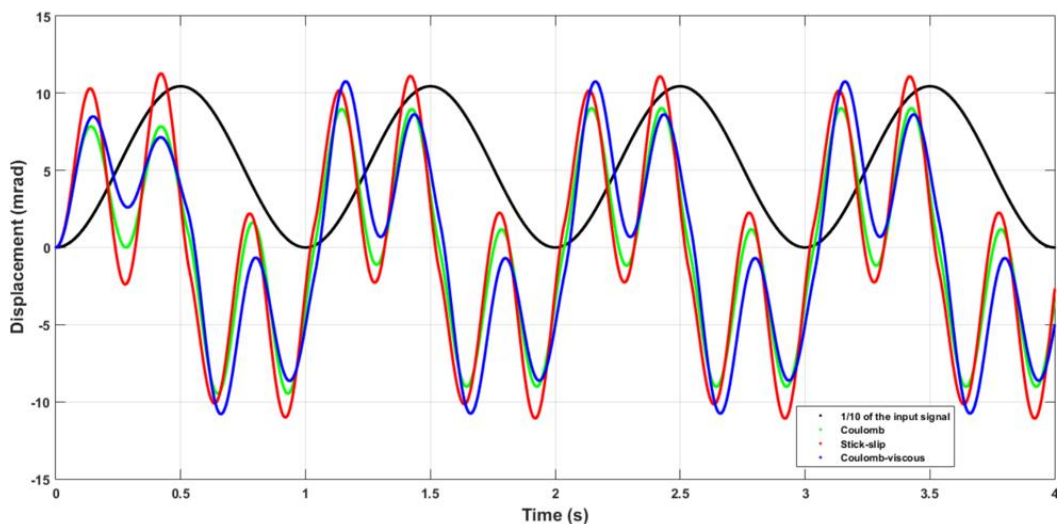
Figure 4.62: Wagon body angular displacement responses.
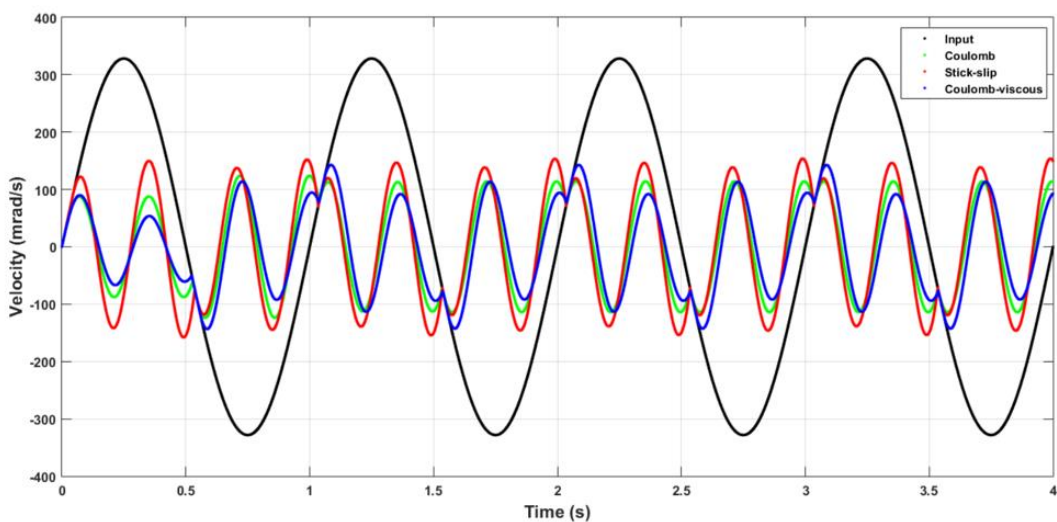
Figure 4.63: Wagon body angular velocity responses.

119
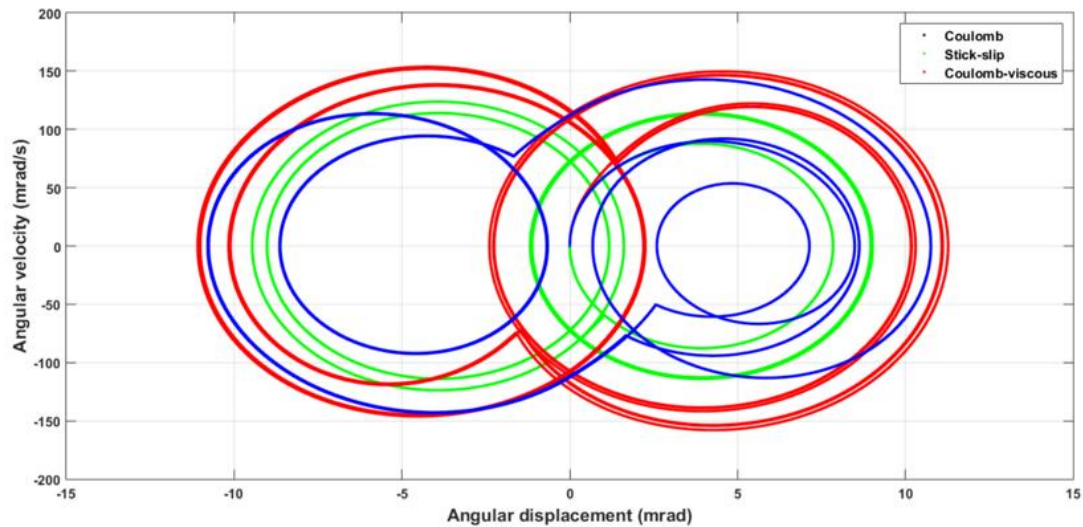
Figure 4.64: Wagon body state space trajectories.

4.11.5. Frictional torque responses (1 Hz)

The time histories of the frictional torque responses for the Coulomb, Coulomb-viscous and Stick-slip models are shown in Figure 4.65 by the green, blue and red lines respectively. The torque in the Coulomb model as can be seen, remains constant at 1.962 Nm once the system has broken out of the stiction region. The torque in the Coulomb-viscous model however, continues to increase towards $\pm$ 2.948 Nm.

The torque response in the Stick-slip model as can be seen, increases to the breakout limit of 2.943 Nm during the initial breakout event. The torque is then seen to decrease to 1.962 Nm during the transition into the gross-sliding regime, which is the Coulomb torque limit. From the close-up shown to the right of Figure 4.65, it can be seen that the Stick-slip model transitions into the gross-sliding regimes when the bogie velocity is approaching the region of $\pm$ 328.3 mrad/s. Whereas in the previous simulations (0.5 Hz), the system remained in the transition state during these phases of motion.

The hysteresis responses are shown in Figure 4.66 and from these it can be seen that the breakout angles of the Coulomb, Coulomb-viscous and Stick-slip models, range between $0 - 1.5$, $0 - 3.2$ and $1.7 - 1.9$ mrad respectively. These breakout angles are much closer together in comparison to the ones that were measured during the 0.5 Hz simulations, but are significantly less than the pre-calculated breakout angles shown in Table 4.22.

From the close-up shown to the right of Figure 4.66 it can be seen that the initial breakout angles of the friction models about the zero points for example, shift to the right by approximately $1 - 1.6$ mrad after the first loading cycle. This behaviour is caused by the elastic pre-sliding displacements in the breakout regions which pre-load the torsional spring, as well as the non-recoverable elastic energy that is dissipated during the transition and gross-sliding phases of motion, which prevents the mass from returning to the equilibrium position.

Also, in the region of 0 mrad for example, it can be seen that the torque response in the Stick-slip model (Red line), starts to increase when the bogie/input velocity is approaching zero. This behaviour suggests that the wagon body friction surface, which represents the surface asperity/bristle in the LuGre friction model, has suffered permanent deformation, as this surface is trying to slip back to the new equilibrium position which is now located in the region of $1 - 1.6$ mrad.

This analysis clearly shows that the higher forcing frequency input has a noticeable smoothing effect on the torque responses of the friction models. The results for the kinematic motions, torque responses and run times during these simulations are also shown in Table 4.22 and from these, it can be seen that the 4 second simulation for example, took 15 seconds of real time to reach a solution. The following section discusses the energy responses.

Friction model	Forcing frequency (Hertz)	Breakout angle (mrad)	Maximum displacement (mrad)	Minimum displacement (mrad)	Maximum velocity (mrad/s)	Minimum velocity (mrad/s)	Maximum spring torque (N.m)	Minimum spring torque (N.m)	Breakout torque (N.m)	Minimum torque during the transition (N.m)	Sliding torque (N.m)	Simulation time (s)	Real time (s)
Coulomb	1	3.9	9.026	-9.462	123.8	-123.8	4.513	-4.731	1.962	1.962	1.962	4	15
Stick-slip	1	5.88	11.27	-11.09	153.7	-158	5.637	-5.543	2.943	1.962	1.962	4	15
Coulomb-viscous	1	3.9	10.76	-10.79	142.8	-143.4	5.382	-5.395	1.962	2.928	2.928	4	15

Table 4.22: Summary of kinematic motions and frictional torque responses during the 1 Hz simulations.
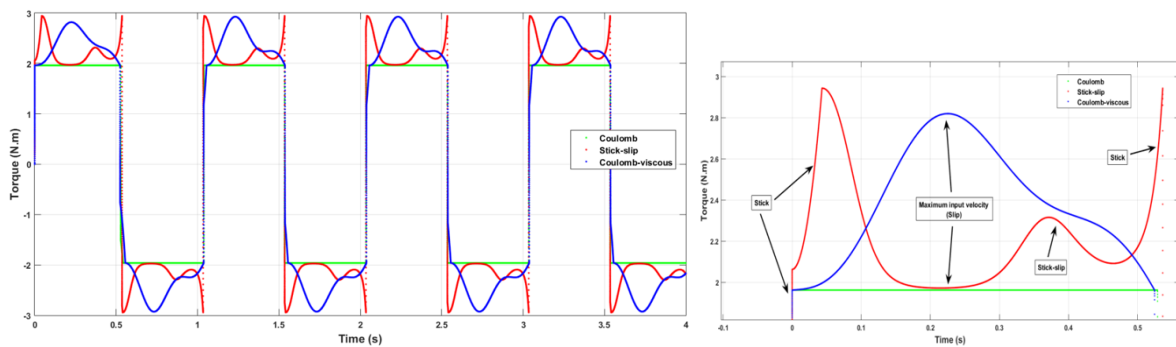
Figure 4.65: (Left) Frictional torque responses as a function of time. (Right) Close-up of the transition from sticking to gross-sliding.
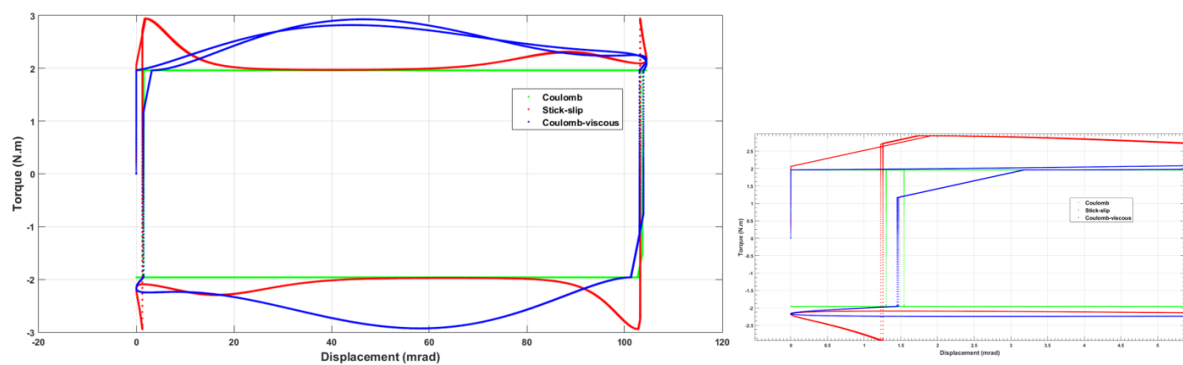
Figure 4.66: (Left) Hysteresis responses. (Right) Close-up of the sticking/breakout regions.

4.11.6. Energy responses (1 Hz)

The summary of the energy responses for the friction models are shown in Table 4.23 and from these it can be seen that the potential and mechanical energies of the Coulomb model are in the region of 22.4×10^{-3} J. The kinetic energy is significantly lower at 7.67×10^{-3} J, whereas the total frictional energy as expected, has doubled in comparison to the 0.5 Hz responses and is now shown to be in the region 1.64 J. The peak of the potential/mechanical energies of the Stick-slip model during the 1 Hz simulations however, are slightly lower at 31.8×10^{-3} J, in comparison the 0.5 Hz simulations, where the peak values were seen to be in the region of 33.5×10^{-3} J (Table 4.20). The total frictional energy relative to the 0.5 Hz energy responses on the other hand, has increased by a factor of 1.9, to 1.785 J.

The potential and mechanical energies of the Coulomb-viscous model are seen to be in the region of 29.1×10^{-3} J and the kinetic energy, 10.3×10^{-3} J. The total frictional energy of this model however, is seen to be the highest overall at 2.097 J. Whereas in the previous simulations (0.5 Hz), the total friction energy of the Stick-slip model was shown to be the highest overall at 0.935 J. This analysis shows that the viscous damping effect becomes more dominant as the forcing frequency increases, whereas the stick-slip behaviour on the other hand, becomes less dominant. This completes the analysis of the harmonic motion simulations. The following section draws some final conclusions on the simulation results discussed in this chapter.

Friction model	Forcing frequency (Hertz)	Maximum kinetic energy (Joules)	Maximum potential energy (Joules)	Maximum mechanical energy (Joules)	Total friction energy (Joules)	Simulation time (s)	Real time (s)
Coulomb	1	0.00767	0.0224	0.0224	1.64	4	15
Stick-slip	1	0.01248	0.0318	0.0318	1.785	4	15
Coulomb-viscous	1	0.0103	0.0291	0.0291	2.097	4	15

Table 4.23: Summary of the energy responses during the 1 Hz simulations.

4.12.   Discussion and conclusions

The dynamic simulation results are discussed and concluded in this section. The free vibration tests on the un-damped mass-spring system identified a number of benefits as well as limitations in relation to the accuracy and efficiency of the MATLAB/SIMULINK implicit/explicit solvers. Quantifying the mechanical energy of the un-damped system over the 5 second simulation also provided a quick and simple benchmarking method to verify the responses of the model and the performance of the various solvers.

The friction force parameters in the SIMSCAPE friction model had to be set values greater than zero in these simulations, which could be seen as a limitation in some cases. However, having a mechanical system with no friction at all, is also an unrealistic expectation/assumption in the real world environment. Setting this parameter set to 1×10^{-10} N in the SIMSCAPE friction model therefore, was seen to be a good compromise in the un-damped simulation test case.

The Ode 23tb explicit solver was then shown to be the most efficient in the free-vibration simulations, taking only 12.5 seconds to converge to the correct solution. The Ode 23t solver however, took 98 seconds, which is approximately 8-times longer to reach the same solution. The most reliable solvers to use in the simulation cases discussed in this thesis were then identified and shown to be the Ode 23t and Ode 23tb implicit solvers, as well as the Ode 45 explicit solver.

The damped free vibration simulations were then carried out on the Coulomb, Coulomb-viscous and Stick-slip models to better understand the influence of stick-slip behaviour and lubrication on the centre plate friction surfaces. The responses of these models were then shown to be in good agreement with the simulation results published by (Opala, 2018). The pre-calculated breakout angles and dynamic displacements of the different friction models about these points, were then validated using the displacement responses of the wagon body masses.

From the damped free vibration simulation responses, it was clear to see the differences in the settling times of the masses, as well as the Non-Zero Residual Displacements (NZRD) at the end of the simulations. The Coulomb-viscous model for example, took 0.985 seconds to settle in the region of – 0.237mm, which was quickest settling time and lowest NZRD overall. Whereas the settling times of

the Coulomb and Stick-slip friction models were almost double, taking approximately 1.827 seconds and 1.687 seconds respectively to settle to the steady state solution.

The NZRD of the Coulomb and Stick-slip models were significantly larger in comparison to the Coulomb-viscous model and shown to be in the region of 2.02 and 4.15 mm respectively. These NZRD, especially in the context of freight vehicles with friction damped suspension components however, would lead to significant tracking issues on both curved/straight sections of track, as well as higher levels of vehicle/track maintenance.

During the damped free vibration simulations, the peak velocities of the Coulomb-viscous model were seen to be the lowest overall. Between 0 – 0.3 seconds for example, the velocities of the dry friction models were shown to be in the region of –2148 mm/s, whereas in the Coulomb-viscous model, the peak velocity was –1993 mm/s. The damping forces in the Coulomb-viscous model during the first oscillation cycle however, were seen to be 2 – 3 times higher. The lighter damping forces in the dry friction models therefore, obviously resulted in larger dynamic displacements during the gross-sliding phases of motion. This analysis clearly shows that the viscous damper is more effective at dissipating the mechanical energy from the system under the given initial conditions.

The responses from constant velocity input simulations were then shown to be in good agreement with the simulation results of (Opala, 2018), apart from some minor differences which were as follows; The free end of the spring in MATLAB/SIMULINK centre plate model, is fixed to the inertial reference frame which has zero velocity. Whereas in the simulation models of (Opala, 2018), the free end of the spring is moving at the same velocity as the input signal.

During the constant velocity input simulations it was also clear to see the stable limit cycling behaviour developing in the state space responses of the Coulomb and Sick-slip models during the gross-sliding events. The Stribeck effect was also clear to see in the Stick-slip model responses during the transition phases of motion. This model however, never fully transitioned into gross-sliding due to the low relative velocities between the friction surfaces. These conditions then led to the build-up of residual elastic potential energy in the spring, which was later released during the stick-slip cycles, thus causing a rapid decrease in the friction force responses due to the velocity feedback phenomenon and the inertia of the system (Altpeter, 1999). The friction model responses were then quantified using principles of work and energy and this analysis showed that the peak kinetic energy of the Stick-slip friction model was 3.5 times higher than the energies in the Coulomb and Coulomb-viscous models.

The constant acceleration simulations were carried to better understand how the inertia forces influence the dynamic response as well as the friction characteristics of the centre plate system. During these simulations the Stick-slip model revealed several interesting behaviours, including unstable hunting/limit cycling behaviour, as well as stick-slip oscillations. The displacement responses of the Stick-slip model were also seen to increase over time and by the end of the simulation, the maximum dynamic displacement had increased from 6.33 to 6.59 mm. Whereas during the out-of-phase gross-sliding events, the displacement responses started off in the region of 4.63 mm, but by the end of the simulation, were seen to be in the region of 3.83 mm.

This unstable limit cycling behaviour as well as the non-symmetric friction characteristics of the Stick-slip friction model however, could lead to uneven wheel/track wear, lower critical speed limits, bogie/wagon body hunting on straight track and instabilities through curves, transitions and crossings etc. The combined effect of these unfavourable running conditions, if these were to develop in service, would be the increased risk of a derailment under normal operating conditions and higher levels of vehicle/track maintenance (Zimmermann, Zeidis, Pivovarov, & Abaza, 2006).

From the constant acceleration simulation results, it was also shown that the viscous damping force in the Coulomb-viscous model, minimised the limit cycling behaviour during the gross-sliding events. These results therefore, strongly suggest that some form of lubrication could be used in the suspension components to improve the stability of the centre plate system. The noise emitted from the vehicle could also be reduced by using a wear liner material that has similar characteristics to the Coulomb-viscous model (Simson & Brymer, 2008), (Frohiling, Fergusson, & Klopper, 2009).

The MATLAB/SIMULINK centre plate model was also analysed under the influence of dither excitations. The frequency of the dither in these simulations was 106.8 Hz, which is thirty times higher than the natural frequency of the system. The first simulation case involved running the dynamic model with no dither in order to quantify the quasi-static behaviour of the system.

These responses however, showed that when the centre plate model is in the static state and with the friction force locked-in at the maximum limit, the SIMSCAPE friction model demonstrates creepage due to the velocity threshold parameter. The creepage was then minimised by setting the velocity threshold parameter to 1 μm/s, so over a 5 second simulation run, the total amount of creepage due to the behaviour of the model rather than the physical behaviour of the system, would be 5 μm. This value could then be subtracted off the final settling position of the wagon body mass if required.

During the simulations where the amplitude of the dither was set to 0.001, 0.01 and 0.1 mm, it was clear to see stick-slip behaviour developing in the responses, but no gross-sliding. Whereas the 1 and 10 mm amplitudes on the other hand, did initiate gross-sliding. These results suggested that when the amplitude of the dither is the same order of magnitude as the displacement of the forcing function, the dither behaves more like a forcing function rather than dither.

One important point to make with regards to the responses during the low amplitude simulations however (0.001, 0.01 and 0.1 mm), is that the friction damping in the SIMSCAPE friction model during the breakout/sticking events, is proportional to the velocity. This attribute therefore, is probably the main reason why these responses, due to the relative velocities between the friction surfaces been below the user-defined threshold parameter, look like they are viscously damped. Therefore, it is difficult to conclude with absolute confidence if dry friction dampers behave like viscous dampers in the presence of dither due to the limitations of the SIMSCAPE friction model. However, it can be concluded with confidence, that dither does have a noticeable influence on the system dynamics as well as the stick-slip behaviour of dry friction dampers that should be taken into account in MBS (Piotrowski, 2012).

This analysis also suggests that the accuracy of freight vehicle models in particular, could potentially be improved by including dither in railway vehicle dynamic simulations. Track access charges for freight vehicles with novel suspension systems for example, are significantly higher than the charges that are applied to passenger vehicles. Therefore, if dither is not being properly accounted for in MBS, then the calculations for evaluating these charges, may not be representative of the actual running conditions. This could then be damaging the potential market growth of the UK rail freight industry by making it more expensive, as well as less attractive to alternative modes of freight transportation, such as road and air for example (Piotrowski, 2012), (Shackleton, 2015) and (Benzin, Jonsson, Stichel, Orlova, & Iwnicki, 2015).

Two harmonic motion simulations were also carried out on the MATLAB/SIMULINK centre plate model at 0.5 and 1 Hz, as these types of excitations were going to be investigated in the laboratory tests. The responses of the Stick-slip friction model during the 0.5 Hz simulation however, were highly unstable in comparison to the 1 Hz responses. During the 0.5 Hz simulation, it was clear to see the system

response oscillating at 3.56 Hz during the gross-sliding events, which is the natural frequency of the centre plate model. Whereas when the forcing frequency was increased to 1 Hz, the frequency response decreased to 1.78 Hz, which appeared to prevent the intermittent stick-slip behaviour.

From the time histories of the frictional torque responses during the 0.5 Hz simulations, it was also clear to see the responses of the Stick-slip model, jumping from the breakout limit of 2.943 Nm, down to 0.5 – 1 Nm. This behaviour however, only started to develop when the bogie/input velocity was decreasing, whereas when it was increasing, the responses were noticeably smoother. This was also shown to be the case in the 1 Hz simulation responses, where there wasn`t any jumps at all due to the forcing velocity being twice as high.

The torque responses of the Stick-slip model during the 1 Hz simulations were also seen to fully transition into the gross-sliding regimes, whereas when the forcing frequency was 0.5 Hz, the responses remained in either the stick or transition state which then led to excess potential energy building-up in the system, as well as the unstable limit cycling behaviour.

The final conclusions to make with regards to the simulation results discussed in this chapter are related to the uncertainties in the modelling parameters. First of all, it is not clear what engineering material the stiffness coefficients of 500 N/m or 500 Nm/rad apply to, as these values were selected from other research work (Opala M. , 2017). Secondly, the values that were used for the breakout and Coulomb COF parameters, μ_{ss} and μ_c, were set to 0.3 and 0.2 for the simulations discussed in this section. These parameters however, are also difficult to justify without any application specific field/laboratory test data.

To build more confidence and certainty in the MATLAB/SIMULINK centre plate model parameters and responses, several benchmarking laboratory tests were carried out using scaled model centre plate/wear liner components to obtain realistic stiffness and COF parameters to use in rail vehicle MBS. The following chapter discusses the laboratory testing methodology and some of the results from these investigations.

5. Laboratory testing methodology

This chapter discusses the laboratory tests that were carried out using the 1:7 scale centre plate components. The main focus of this research work was to characterise and benchmark the dynamic performance of three different rail industry standard wear liner materials. Several test cases were analysed as part of this work in order to better understand the nonlinearities and the failure modes that are associated with dry friction secondary suspension components.

The impact of these failures modes on the vehicle and track life-cycle costs however, are not currently fully understood, especially when these components start to wear out over time. Therefore, obtaining reliable measurement data in order to derive accurate modelling parameters for these components is vital to the rail industry, as this process will generate new knowledge and understanding with regards to how different wear liner materials actually perform in the railway environment. This information and data can then be used by vehicle dynamics engineers to improve the confidence levels in freight vehicle testing and modelling methodologies.

The laboratory test cases that are discussed in this thesis have been designed to replicate the X-Factor test which is used by the UK rail industry during vehicle acceptance procedures, see the Railway Group standard GM/RT2141 (Issue 3). The X-Factor test is one of several key performance tests that are carried out on newly built/modified freight vehicles to evaluate the rotational resistance between the bogie/wagon body. If any of the compliance requirements defined in the in the GM/RT2141 standards are not met however, then the vehicle will not be accepted into service until the further testing and analysis has been carried out to rectify the problems causing the initial failure modes.

Once a vehicle has been accepted into service, the axle loads for freight vehicles operating on the UK network are then seen to be specific to individual routes which are then classified by Network Rail, using Route Availability (RA) values ranging from $1-10$. The typical axle loads of a 4-axle freight vehicle in the tare condition for example, is around 5 t per axle, whereas for the laden condition, the maximum axle load on a route that has a RA value of 10, is 25.4 t per axle, see (Network Rail, 2018). The 5:1 loading ratio is the main reason why nested tare/laden coil springs are used in the primary/central suspensions of the Y25 and three-piece bogies (Boronenko & Orlova, 2006).

Investigating axle loads ranging from $5 - 25.4$ t in the laboratory however, requires dedicated equipment/test-rig which was not available during the initial planning stages of this research. The alternative testing method given the small budget as well as the time constraints imposed on this research project, was to use scale model tests and the INSTRON universal testing machine available at the University of Huddersfield`s, Institute of Railway Research (IRR).

The axial and torsional loading capabilities of the INSTRON however, are limited to 10 kN and 100 Nm (Appendix D). Therefore, in order to investigate the dynamic performance of the wear liners under the range of loads discussed above, a suitable scaling strategy had to be derived from first principles to maintain similarity between the contact stresses acting on the full size/scale model components. A geometric scaling factor of 1:7 was then applied to design dimensions of the scale model components, so an axial load of 9 kN in the scale model tests under the given scaling laws, is now equivalent to 441 kN in the full size system, which is in correct range of centre plate loads we are interested in analysing.

The flow chart of the various stages involved in the scale model laboratory tests is shown in Figure 5.1 and from this, it can be seen that the first stage of testing process involves recording pre-test surface roughness measurements on the centre plate/wear liner samples as well as recording the mass properties of the wear liner samples. The pre-test surface roughness and mass property results were

then used to monitor the changes in these parameters over time by comparing these to the post-test results.

The new wear liner samples are then subjected to a 3000 cycle running-in test at either the low or high forcing frequency (0.042 Hz or 0.084 Hz), before carrying out the service tests. These tests then ran for 10800 cycles at the same forcing frequency as the running-in tests. The centre plate loads in the service tests however, were increased from 0.5 kN, to either 3, 6 or 9 kN, which under the 1:7 scaling laws derived in Section 3, are equivalent to 24.5, 147, 294 and 441 kN respectively in the full size system. A steel-on-steel test was also carried out on the 1:7 scale centre plate components to quantify the friction characteristics of the system with no wear liner included.

In the context of a full size vehicle for example, the load cases investigated in the scale model laboratory tests, are similar to the range of loads supported by the side bearers and centre plate components during the tare, part-laden and laden operating conditions. The results from these tests were then used to evaluate and compare the performance requirements of the different wear liner materials under operating conditions that are relevant to the rail industry.

Post-test surface roughness and mass property measurements were then recorded on the centre plate/wear components to quantify the changes in these parameters over time. After completing this analysis, the centre plate components were then sent to the machining department for re-turning. The test data was then checked for obvious errors prior to calculating the Coefficients of Friction (COF), contact stiffnesses, natural frequencies and X-Factor values for the centre plate/wear liner samples. The calculated material parameters were then used to optimise as well as validate the performance of the MATLAB/SIMULINK centre plate model. The following section discusses the laboratory testing equipment.
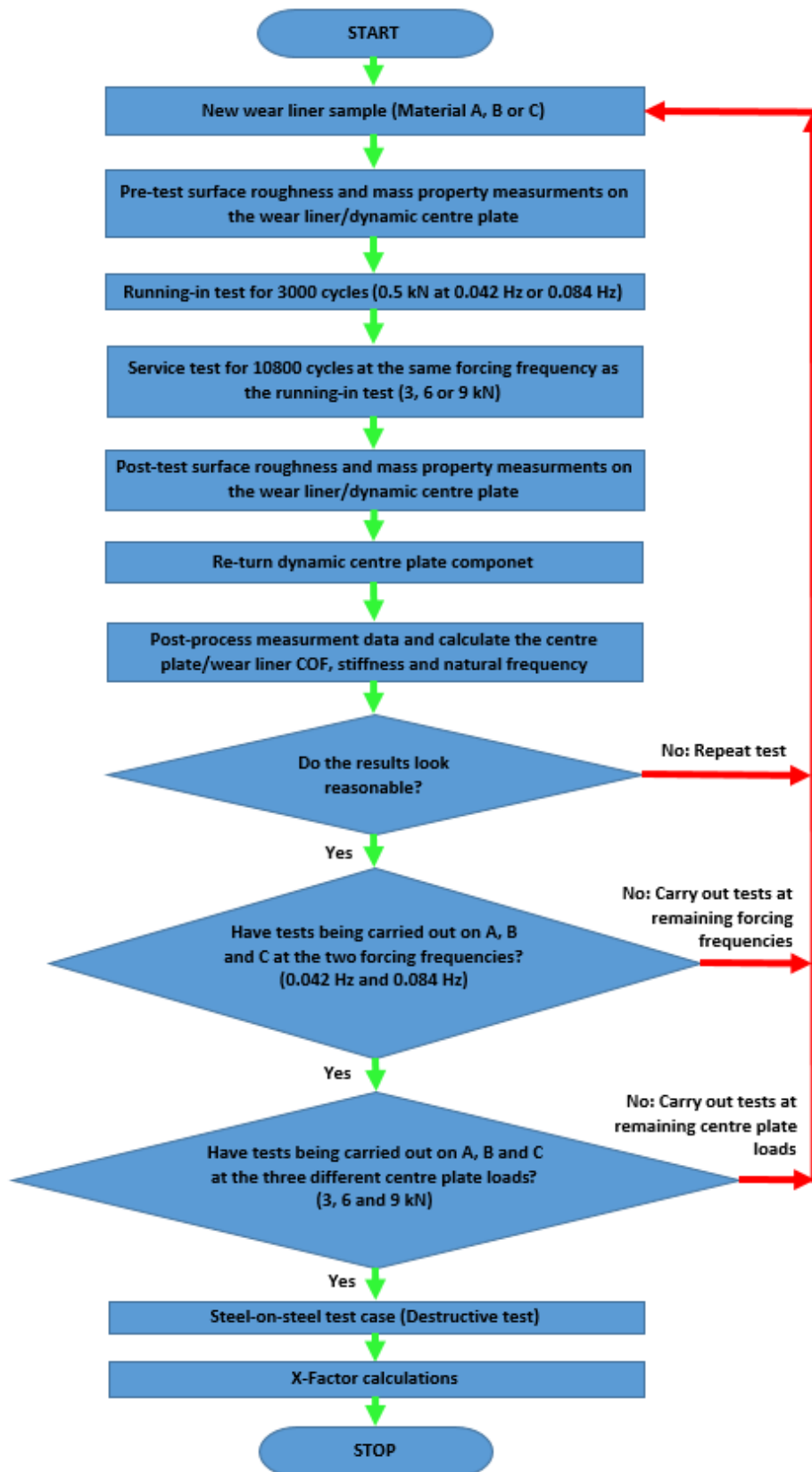
Figure 5.1: Laboratory testing flow chart.

5.1. Laboratory testing equipment

This section discusses the laboratory testing equipment that was used to carry out the testing procedures. A wide range of benchmark tests were carried out on the three different wear liner materials shown in Figure 5.2 to quantify their unique friction characteristics, as well as to better understand their maintenance requirements.

Figure 5.3 shows the dynamic centre plate component clamped in the jaws of the hydraulic actuator and the static centre plate with the wear liner is omitted for clarity, so the reader can observe the two ground dowel pins which prevent the liners from rotating during the testing process. The pins also ensure that the positions of the samples relative to the static centre plate, are exactly the same in each test case. The spigot in the centre of the static centre plate is a turned feature representing the king pin.

Two blind-holes were then machined into the back-face of the 1:7 scale wear liner samples to a depth that provided 1 mm of clearance between the heads of the dowel pins and the bottoms of the holes, see Figure 5.4. A through hole was also machined in the centre of the wear liner samples to locate the king pin, which is a standard feature on the full size components. The actual wear liners on the Y25 and three-piece bogies however, are press-fitted into the centre bowl/centre plate components, whereas the side bearer wear liners on the other hand, are riveted to the slide plates.

The dynamic centre plate, as can be seen from the test-rig with the wear liner included shown in Figure 5.5, also has a hole feature for the king pin. The dynamic loads and motions of this component were programmed into the machine control using a waveform generator. The axial and rotational motions of the dynamic centre plate are then measured via the displacement transducers located in the crosshead and hydraulic actuator. The load and torque is measured via a Bi-axial Dynacell located in the stationary holding device which has an accuracy of $\pm$ 0.5% of the measured load or alternatively, $\pm$ 0.005% of the load cell capacity (INSTRON, 2019).

The data acquisition rate during the scale model laboratory tests was set to 1 kHz for the low and high forcing frequency test cases. The raw data signals were then post-processed using a 4-pole Butterworth filter. The cut-off frequency was set to 200 Hz for the frequency responses discussed in this thesis, which rolls-off at 6 dB per octave, per pole (INSTRON, 2019). The high sampling rate as well as the length of test duration however, generated extremely large volume data files for each test case which had to be split into smaller, more manageable, files for post-processing. The following section discusses the surface roughness measurement methodology that was used during this research work to inspect and evaluate the surface roughness parameters of the centre plates/wear liner components.

Figure 5.2: Post-test wear liner samples: (Left) Material A, (Middle) Material B, (Right) Material C.
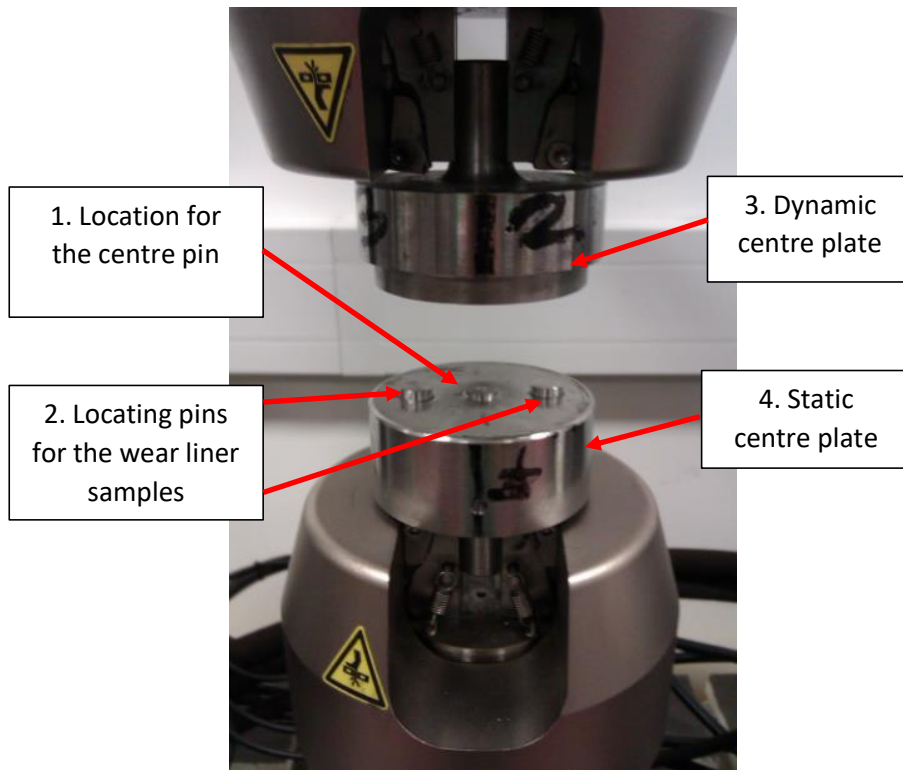
Figure 5.3: Instron torsional/axial fatigue testing machine.
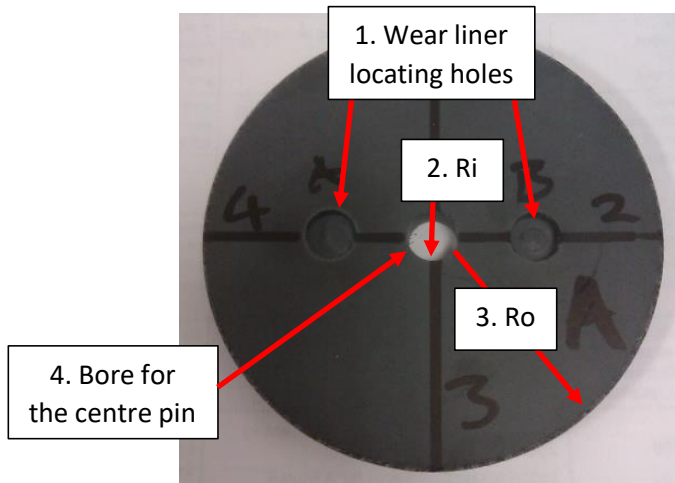
Figure 5.4: Locating holes on the back-face of the wear liner samples.
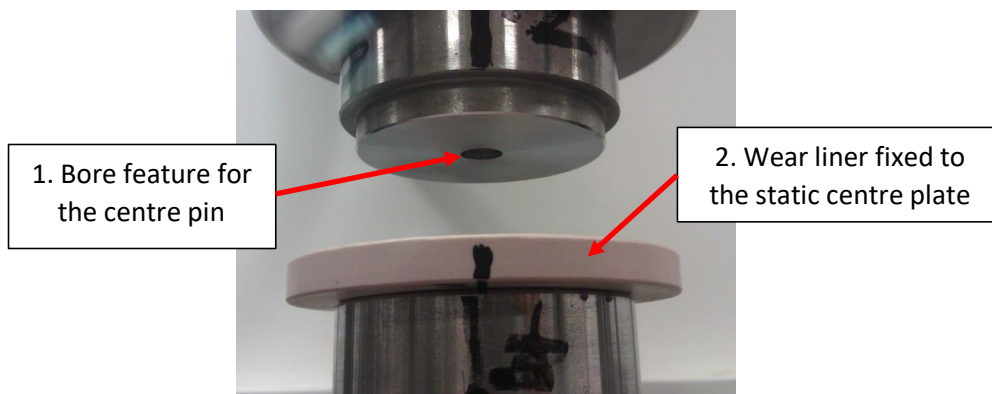
Figure 5.5: Scale model centre plate/wear liner components.

5.2. Surface roughness measurement methodology.

The pre/post-test surface roughness measurements for the centre plates and wear liner samples are discussed in this section. Figure 5.6 shows a schematic diagram of the measurement methodology that was used to analyse and quantify the surface roughness characteristics of the centre plate/wear liner components. This measurement data can then be used to better understand how the surface roughness parameters influence the friction characteristics and wear rates of the different wear liner materials.

The single numbers around the perimeter of the circle (1, 2, 3, 4), show the radial lines where the measurements are recorded, whereas the numbers labelled 1.1, 1.2 and 1.3, show the boundaries of the three measurement areas, which each have a radial length of approximately 7.5 mm. Whereas the travel, evaluation length and sample lengths of the stylus, are 4.8, 4 and 0.8 mm respectively (Figure 5.6). The short/long wavelength cut-off values as well as the radius of the stylus probe used throughout the pre/post-test roughness measurements, were configured to the EN ISO 4288 standards given in (British Standards Institute, 2002).

Nine surface roughness parameters were measured in total during the pre/post-test analyses of the centre plate/wear liner components which are discussed in detail in Appendix H. The four parameters that are analysed in the following sections include the arithmetical mean-surface roughness values (Ra), the maximum peak-valley depth (Rt) and the root-mean-square of the roughness and waviness slope profiles, ($R_{\Delta q}$) and ($W_{\Delta q}$). The raw measurement data is then post-processed and filtered by the software packages supplied with the measuring equipment using a Gaussian filter. The analysis software also separates the filtered data into the form, roughness and waviness profiles, see Figure 5.7 (Taylor Hobson , 2011).

Parameter	Value
Stylus travel (mm)	4.8
Sample points	9600
Evaluation length (mm)	4
Sample length (mm)	0.8
Vertical range (µm)	65.5
Vertical resolution (nm/pt)	1
Stylus radius (µm)	5
Stylus force (mg)	5
Scan speed (µm/s)	320
Scan duration (s)	15
Lower Cut-off Ls (µm)	2.5
Upper Cut-off Lc (mm)	0.8
Bandwidth (ISO)	300:1
Height discrimination (%)	10
Spacing discrimination (%)	1
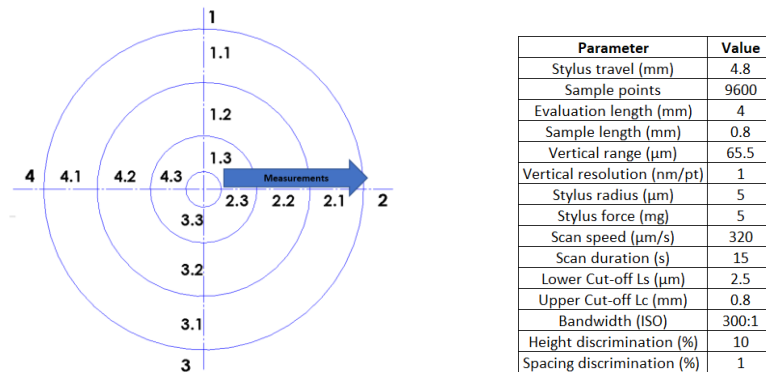
Figure 5.6: (Left) Centre plate/wear liner surface roughness measurement methodology. (Right) Surface roughness measurement settings for the Taylor-Hobson PGI, Bruker-Dektak and Alicona measuring equipment.
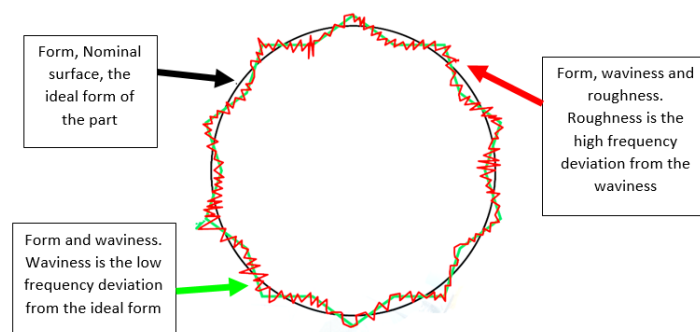
Figure 5.7: Schematic diagram of the form, waviness and roughness profiles (Zaworka, 2012).

Twelve separate measurements were then recorded on the centre plate/wear liner components in the pre/post-test analyses (3-areas, 4-radial lines). The mean value of these twelve measurements was then used to quantify the changes in the nine roughness parameters that were measured on each component, see Appendix H.

A list of test cases that were studied during this research is shown Table 5.1 and from this, it can be seen that seven tests were carried out on materials A and B, whereas only three tests were carried out on material C at the higher forcing frequency due to the time constraints. Also, to reduce the down time of the universal testing machine during these seventeen test cases, two dynamic centre plates were manufactured for the laboratory tests. The contact surfaces on these components were then re-machined after completing the service tests on a CNC lathe using the same tooling and speeds/feeds (180 m/min, 0.2 mm/rev).

The pre-test surface roughness measurements were also carried out for quality control purposes to ensure that the centre plate/wear liner components were being manufactured to similar specifications before starting the laboratory tests. The pre-test measurements also provide the benchmarks for the post-test measurements, as well as assurances to other researchers and component suppliers, that all of the test results discussed in this thesis have obtained under consistent test conditions.

The two measurement machines that were used to quantify the roughness characteristics of the centre plates/wear liner components are shown in Figure 5.8. During this work, two different surface profilers had to be used because the 1:7 scale centre plate components were too large to fit into the working envelope of the Bruker Dektak-XT, shown to the left of Figure 5.8. This profiler however, was used to measure the wear liner samples, whereas the centre plates were measured on the Taylor-Hobson Form Talysurf Phase Grating Interferometer (PGI) shown to the right of Figure 5.8 as this machine has a larger working envelope. The following section discusses the surface roughness measurement results for the centre plate components.

Test case	Centre plate	Wear liner sample	Material	Forcing frequency (Hz)	Running-in test load (kN)	Service test load (kN)	Total number of running cycles
1	1	A	A	0.042	0.5	3	13800
2	2	B	A	0.042	0.5	6	13800
3	1	C	A	0.042	0.5	9	13800
4	2	D	A	0.042	0.5	6	13800
5	1	E	A	0.084	0.5	3	13800
6	2	F	A	0.084	0.5	6	13800
7	1	G	A	0.084	0.5	9	13800
8	1	AA	B	0.042	0.5	3	13800
9	1	II	B	0.042	0.5	6	13800
10	2	JJ	B	0.042	0.5	9	13800
11	1	KK	B	0.042	0.5	9	13800
12	2	BB	B	0.084	0.5	3	13800
13	1	GG	B	0.084	0.5	6	13800
14	2	HH	B	0.084	0.5	9	13800
15	1	A	C	0.084	0.5	3	13800
16	2	B	C	0.084	0.5	6	13800
17	1	C	C	0.084	0.5	9	13800

Table 5.1: Summary of the scale model test cases.
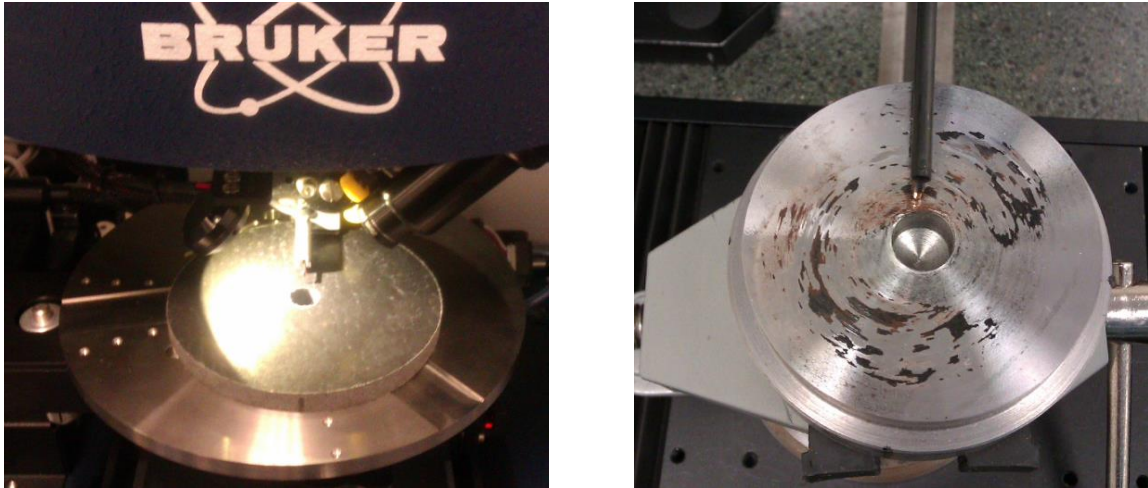
Figure 5.8: Tactile stylus surface profilers. (Left) Bruker Dektak-XT. (Right) Taylor & Hobson PGI.

5.2.1. Centre plate surface roughness measurements

The pre/post-test surface roughness measurement results for the two 1:7 scale dynamic centre plate components are discussed in this section. Appendix I also shows a full breakdown of the surface measurement results for the centre plate components.

The pre/post-test mean surface roughness (Ra) and maximum peak-valley depth (Rt) measurement results for the two centre plates are shown by the box and whisker plots in Figure 5.9. The interquartile ranges with the black boarders, whiskers and vertical hatching lines, show the results for the pre-test measurements. Whereas the boxes with the red borders and diagonal hatching lines, show the post-test results. The Ra and Rt measurements are then shown by the green and blue colours respectively. The pre/post-test Ra and Rt values for Centre plates 1 and 2 as can be seen, are similar, ranging between $1 - 2.3$ μm and $5.7 - 16$ μm respectively.

The pre/post-test slope measurements, $R_{\Delta q}$ and $W_{\Delta q}$, are shown in Figure 5.10 by the green and box and whisker plots respectively. From these results as well as those shown in Appendix I, it can be seen that the $R_{\Delta q}$ values for Centre plates 1 and 2 range from -0.122 to 0.016 degrees. The pre/post-test $W_{\Delta q}$ values on the other hand (Blue boxes), are signifcantly higher than the $R_{\Delta q}$ values, ranging between $0.49 - 1.26$ degrees. From this analysis it is clear to see that all of $W_{\Delta q}$ slope values are positive, as well as $4 - 10$ times higher than the $R_{\Delta q}$ values. This analyses also shows that the contact surfaces on the centre plates are not perfectly flat which could play an significant role in the repeatability of the laboratory tests.

The waviness profiles in the case of the turning process however, are generated from a number of sources that are difficult to control in comparison to the roughness profiles. These include wear on the leadscrews and slideways of the lathe which can lead to the development of tool chatter during the cutting process, as well as work-piece deflections and structual vibrations. Residual stresses in the work-piece material can also have an influence the waviness profiles (Taylor Hobson , 2011).

Surface roughness measurements were also taken on a new, unused, full size Y25 centre pivot component, see Appendix J. These measurements were then used to verify the surface roughness quality of the 1:7 scale centre plate components and as can be seen, the mean Ra value for the eight measurements on the Y25 centre pivot is 2.745 μm, whereas for Centre plates 1 and 2, the pre-test Ra value was seen to be slightly lower at 1.757 μm (Appendix I).

The main conclusions to be drawn from this analysis are that both of the 1:7 scale centre plate components are very similar in terms of surface roughness quality and after 13800 cycles of testing, the pre/post-test roughness values appear to remain within stable and measurable boundaries that have now been quantified.

The roughness values that were measured on the 1:7 scale centre plate components, are also seen to be in agreement with the achievable surface finishes given in Appendix K, which are seen to range between 0.8 – 3.2 µm for the turning process. This analyses therefore, suggests that the roughness measurements on the 1:7 scale centre plates/Y25 centre pivot components are in good agreement. The following section discusses the surface roughness measurement results for the wear liner components.
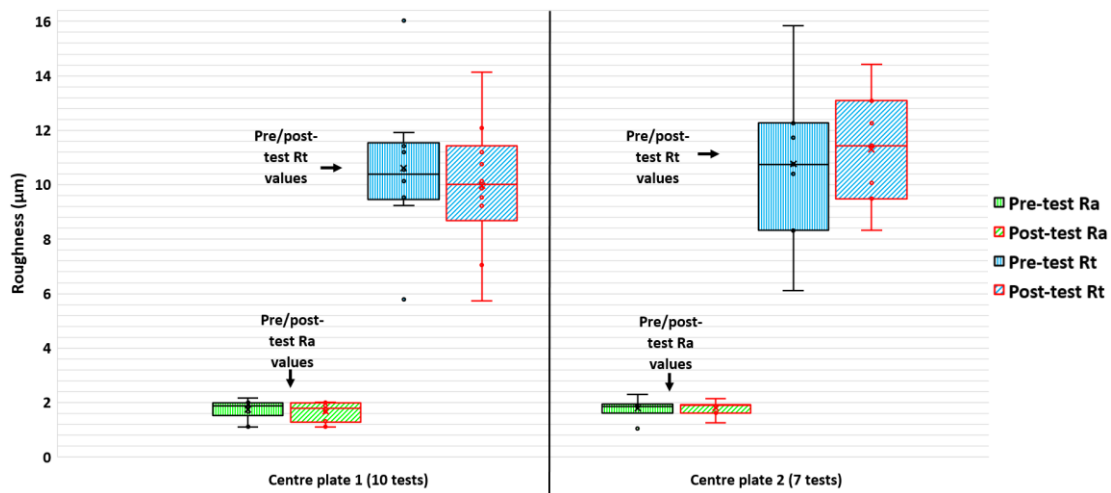
Figure 5.9: Centre plate pre/post-test mean surface roughness (Ra) and maximum peak-valley depth measurements (Rt).
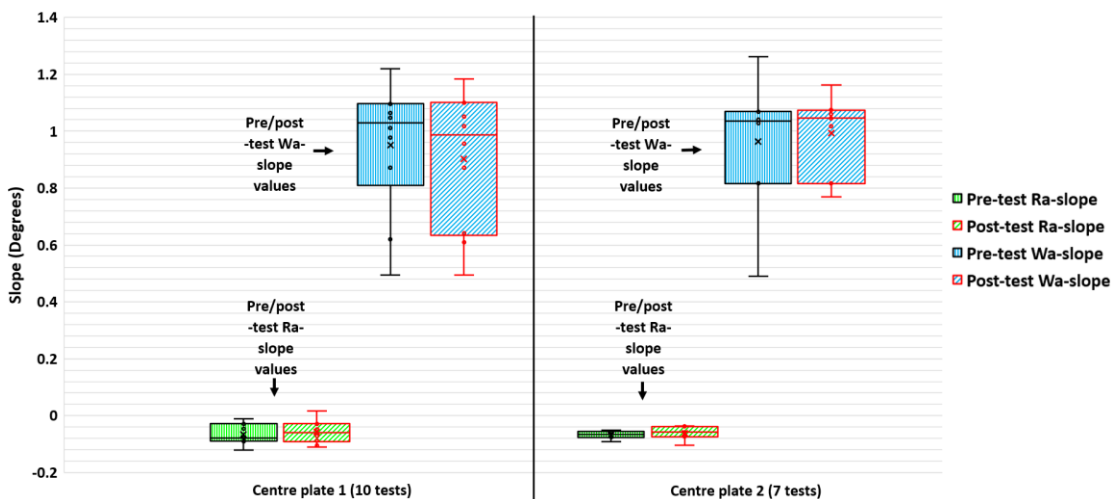
Figure 5.10: Centre plate pre/post-test Ra-slope and Wa-slope measurements.

5.2.2. Wear liner surface roughness measurements

This section discusses the surface roughness measurement results for the three different wear liner components, which are called materials A, B and C in the following results. The contact surfaces on these components are in the, `as delivered state`, and as they would be when installed on a bogie.

The pre/post-test mean surface roughness (Ra) values and maximum peak-valley depth (Rt) measurement results are shown by the box and whisker plots in Figure 5.11. The interquartile ranges with the black boarders and vertical hatching lines show the pre-test measurements and the boxes with the red borders and diagonal hatching lines, show the post-test measurements. The Ra and Rt measurements are then shown by the green and blue colours respectively. Appendix L shows a full breakdown of the surface measurement results for these components.

From these results, it can be seen that the pre/post-test Ra values for the eight test cases that were carried out using material A for example, range between 0.325 – 5.344 µm and 0.425 – 4.587 µm respectively. Whereas the Ra values for the six pre/post-test measurements on material B are seen to be significantly lower, ranging between 1.871 – 2.395 µm and 1.25 – 2.095 µm. The pre/post-test Ra values that were measured on material C however, are seen to be the lowest overall as well as the most consistent, ranging between 1.467 – 1.517 µm and between 1.231 – 1.297 µm respectively.

The pre/post-test Rt measurements on material A also show the largest amounts of variation, ranging between 3.755 – 69.137 µm and 3.551 – 85.042 µm respectively. The post-test Rt value of 85.042 µm however, appears to be an outlier and could potentially be a false reading due to debris on the stylus probe. The pre/post-test Rt measurements on material B, range between 18.086 – 21.915 µm and from 10.884 – 17.977 µm, whereas for material C, the pre/post-test Rt values range between 12.4 – 13.033 µm and 9.921 – 12.005 µm respectively. This analysis clearly shows that the Ra and Rt values for material C, are the lowest overall, as well as the most consistent.

The pre/post-test $R_{\Delta q}$ and $W_{\Delta q}$ slope measurements are shown in Figure 5.12 by the green and blue boxes respectively. From these, it is clear to see the large changes between the pre/post-test measurements on material A, especially in comparison to the slopes that were measured on materials B and C. The pre and post-test $R_{\Delta q}$ slope measurements on material A for example, range from –0.004 to 0.088 degrees and from –0.047 to 0.121 degrees (Green boxes). Whereas for materials B and C, the pre and post-test $R_{\Delta q}$ slope measurements are seen to range from –0.022 to 0.012 degrees and from –0.018 to 0.011 degrees. The range of pre/post $R_{\Delta q}$ values that were measured on materials A, B and C however, are similar to the range of values that were measured on the centre plates, which can be seen by comparing the results shown Figures 5.10 and 5.12.

The pre/post-test $W_{\Delta q}$ slope measurements on the wear liner samples however, are significantly lower in comparison to the values that were measured on the centre plates. From the results shown in Figure 5.12 for example, it can be seen that the pre/post-test $W_{\Delta q}$ values for material A, range from –0.09 to 0.017 degrees and from -0.109 to 0.047 degrees respectively (Blue boxes). The pre/post-test $W_{\Delta q}$ slope measurements for materials B and C, are seen to be the lowest overall, ranging from –0.008 to 0.039 degrees and from –0.007 to 0.019 degrees.

The wide range of roughness values that have been measured throughout this analysis are mainly due to the different manufacturing methods that are used to make the wear liners. Material A for example, is manufactured from a thermoset composite material consisting of a porous fabric matrix which is then formed and bonded together in a casting mould under high pressures/temperatures, see Figure 5.13. The surface lay of this wear liner therefore, is referred to as "particulate" lay in the engineering drawings standards, as this surface texture is clearly more random, as well as more porous in comparison to the concentric lay of turned surfaces of the centre plate, see Figure 5.14 (Taylor Hobson , 2011).

Materials B and C on the other hand, are manufactured from polymers with different levels of additives included in the polymer mixes to give each product its own unique properties. The finished

bar/plate is then sawn to size and milled to the required thickness which leaves a radial surface lay on the finished components. This manufacturing method as can be seen by comparing all of the surface measurement results on the centre plates/wear liner components, appears to be the most consistent one overall. The following section discusses the pre/post-test mass property results for the wear liner components (VESCONITE plastics, 2019).
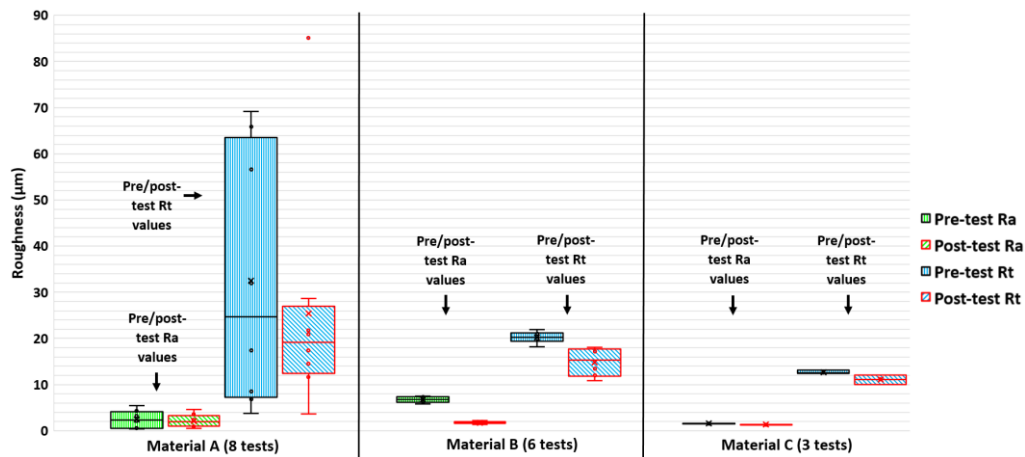
Figure 5.11: Wear liner pre/post-test mean surface roughness and maximum peak-valley depth measurements.
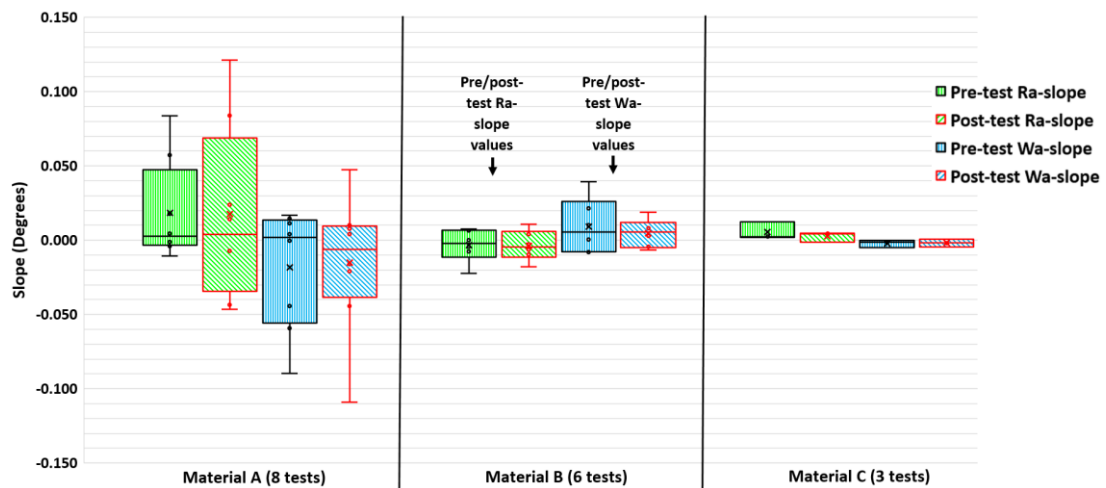
Figure 5.12: Wear liner pre/post-test Ra-slope and Wa-slope surface roughness measurements.
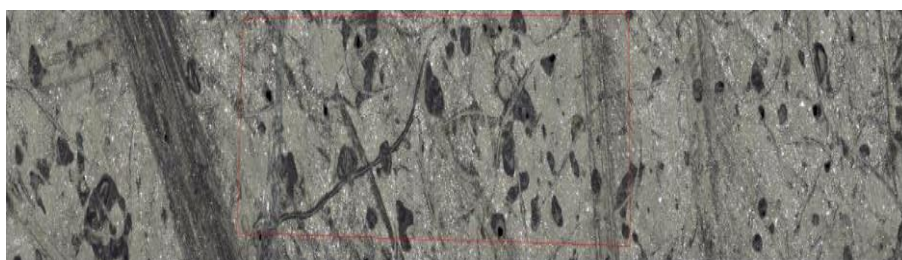
Figure 5.13: Pre-test surface image of material A using the Alicona 3D optical microscope.
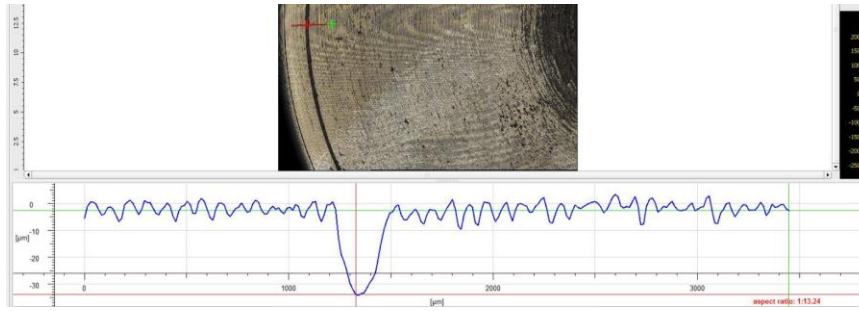
Figure 5.14: Benchmark surface roughness measurement of a turning mark on the 1:7 scale centre plate.

5.2.3. Wear liner mass property results

This section discusses the pre/post-test mass properties results for the wear liner samples. These parameters were measured to determine if there is a relationship between the running conditions and the levels wear/degradation observed in these components after each test case. The resolution of the weighing scales that were used for this analysis, was 0.1 mg within a temperature range of 5 – 40°C. The relative humidity, ambient temperatures and dew points during all of the laboratory test cases discussed in this thesis were also monitored as part of this analyses.

The laboratory tests for example, were carried out between the months of June 2016 to January 2017 and were running for 2 – 3 days at a time, all through the day/night. The temperatures inside the laboratory over this eight-month period were then seen to range between 10 – 26°C, whereas the relative humidity`s and dew points, ranged between 20 – 40% and 2 – 13% respectively.

The post-test mass property results for the wear liner samples were then normalised by dividing these values with the pre-test measurements, see Figure 5.15. A full breakdown of these results as well as the loading conditions and statistical analysis is also shown in Appendix M. The green, blue and red solid bars in this figure, show the post-test results for materials A, B and C after the high speed test cases (0.084 Hz). Whereas the green, blue and red bars with hatching lines, show the post-test results for low speed test cases (0.042 Hz).

From these results it can be seen that the maximum reduction in mass after the four tests that were carried out on material A at the 0.042 Hz for example, was after test case 3 and is shown to be 0.179% in Appendix M. Whereas for the 0.084 Hz test cases, the maximum reduction in mass for this material was after test case 7, which is seen to be almost double at 0.352%. Both of these test cases were carried out under the 9 kN centre plate load which suggests that the wear rate of material A for example, increases in proportion to the increases in the rotational speed as well as the centre plate loading conditions.

This suggestion is also supported by the post-test mass property results for test cases 1 and 5. These cases were running under the 3 kN loading conditions and as can be seen, have the lowest levels of mass reduction overall after 13800 cycles of testing. The wear liner sample that was used in test case 5 however, appears to have gained the most mass overall out of the 16 test cases, but this liner was contaminated with hydraulic oil. The wear behaviour of this particular sample therefore, cannot be compared against the others.

The maximum reduction in mass for the test cases that were carried out on material B and running at 0.042 Hz for example, was 0.06% after test case 9. This value is almost 3 times lower than the maximum reduction in mass that was measured on material A at this rotational speed. Whereas for the 0.084 Hz test cases on material B, the maximum reduction in mass was 0.048% after test case 13.

These tests as can be seen from the results shown in Appendix M, were both running under the 6 kN centre plate load. The peak reduction in mass for material B after the high forcing frequency test cases therefore, is 7.3 times lower than the mass loss that was measured in material A. The data from test case 10 is not available due to a post-processing error.

The post-test mass measurements for material C on the other hand (Test cases 15 – 17), are all seen to be slightly higher than the pre-test measurements which suggests that this material has the lowest wear rate overall. The maximum increase in mass for example, was seen to be after test case 16 which was also running under the 6 kN load, same as material B.

From the summary of these results shown in Appendix M, it can also be seen that the densities of the wear liner materials are all different. The densities of materials A and C for example, are seen to be closely matched at 1.68 and 1.64 kg/cm³ respectively, whereas the density of material B, is 38 – 41% lower at 1.19 kg/cm³. The Standard Deviations (SD) of these measurements for the complete data set however, are all less than 1% which suggests the bulk mechanical properties of the samples and the manufacturing methods are consistent. These measurements are also seen to be in reasonable agreement with the manufacturers specifications shown in Appendix F.

The SD of the pre-test Ra and Rt surface roughness values for the centre plates and wear liner samples on the other hand, see Appendix I and Appendix L respectively, range between 20.6 – 93.8%. Whereas the SD of the pre-test Ra-slope and Wa-slope measurements, cover an even wider range, ranging between 23.8 – 308.3%.

From the analysis of the surface roughness measurements and mass property results, it is suggested that the surface roughness characteristics of the suspension components are the main source of the nonlinearities in the centre plate system. The differences in these parameters is also one of the contributing factors in the non-repeatability of laboratory tests involving contact and dry friction and why these experiments tend to produce a wide range of results under the same operating conditions, see Figure 2.27 in Section 2.9 for example, or the test results presented in this thesis (Jonsson, 2004).

The final conclusions to make based on the analysis of the pre/post-test mass property results, are that material A would require more maintenance over hauls during the life-cycle of the vehicle in comparison materials B and C. The surface roughness and mass property measurement data could also be used to develop optimised Finite Element Analysis (FEA), as well as Multibody Simulations (MBS) wear models for secondary suspension components. The following section discusses the running-in test cases.
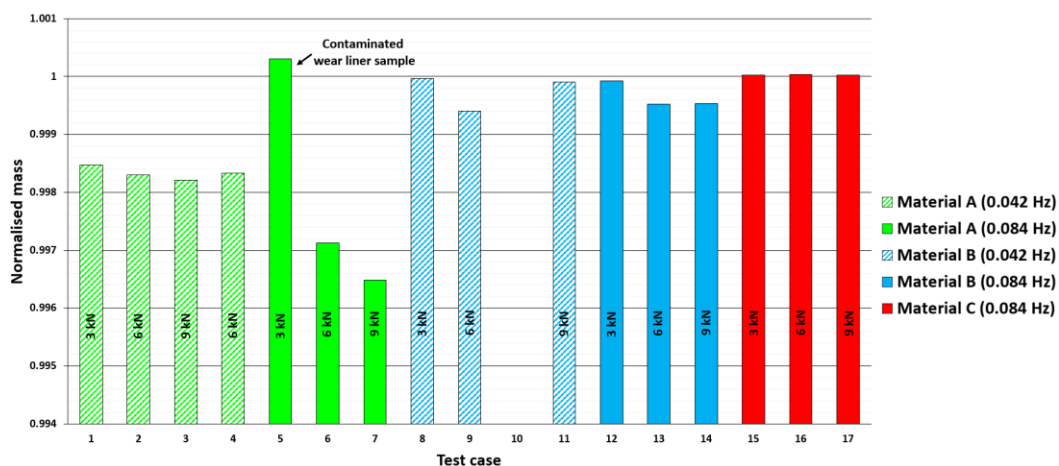
Figure 5.15: Normalised post-test mass property results for materials A, B and C.

5.3. Running-in test case description

This section discusses the running-in test cases that were carried out on the centre plate/wear liner components. These tests ran for 3000 cycles with the harmonic forcing frequency set to either 0.042 or 0.084 Hertz (Hz) and the amplitude of motion to $\pm$ 3 degrees. The running-in tests were carried out on the new components to wear-in the contact surfaces of the centre plates/wear liner samples, as well as to benchmark the friction characteristics of the new wear liner surfaces and the changes in these parameters over time. These tests were also carried out to investigate the wear liner responses under contact stresses similar to those supported by the side bearers on a freight bogie.

Seventeen running-in test cases were carried out as part of this work, seven on material A, seven on material B and three on material C. These tests then ran for approximately 10 and 20 hours during the low and high forcing frequency test cases. The results from these test cases were then compared to better understand how the angular velocity of the centre plate influences the friction characteristics and wear rates of the different wear liner materials.

The running-in test results were then post-processed using a global as well as local analysis method. The global analysis method for example, recorded the peak torque responses every cycle of the test case for the Clockwise/Counter-clockwise rotations. These data files were then used to generate a trend of the increases/decreases in the torque responses over time. This measurement method therefore, only generates small volume data files during the running-in/service test cases.

The local analysis method on the other hand, samples every cycle at a rate of 1 kHz, which produces extremely large volume data files. These files however, are required to plot the hysteresis responses of centre plate/wear liner components and the changes in vibration signatures over time. The stick and slip Coefficient of Friction (COF) values are also calculated from the local analysis results as well as the torsional stiffness properties of the individual test samples.

The system parameters that were calculated from the running-in test cases were then used to develop an optimised Multibody Simulations (MBS) component model of a Constant Contact Side Bearer (CCSB). The following section discusses the global analysis results for material A.

5.3.1. Global analysis results for material A

This section discusses the global analysis results for the seven running-in test cases that were carried using material A. The responses for the tests that were running at 0.042 Hz are shown in Figure 5.16 by the sold lines, whereas the dashed lines show the responses for the 0.084 Hz test cases. Appendix N also shows a summary of the running-in results.

The torque responses that were measured on material A during the running-in test cases range between 0.496 – 1.95 Nm. It can also be seen that there is a rapid increase in all of the torque responses during the first 2-hours of testing, whereas between 2 – 20 hours, the torque responses appear to be stabilising apart from test case 5 (Yellow lines). The torque curve of this test case as can be seen, is clearly out of character in comparison to the other samples that were tested under the 0.5 kN centre plate load, as this response continues to increase between 2 – 10 hours. The initial torque in test case 5 is also significantly higher than the other samples at 1 Nm and by the end of the 10-hour test, is seen to be the highest overall at 1.95 Nm. This analysis strongly suggested that there was an issue with either the centre plate component or the wear liner sample that was used in test case 5.

The percentage increase in the torque response of test case 5 however, is seen to be 88.8% in Appendix N which is in line with the mean percentage increase for the complete data set (7 test cases). The mean percentage increase in the torque measurements on material A for example, is seen to be

71.9% with a Standard Deviation (SD) of 41.6%. This analysis therefore, suggests that the responses of this particular sample are not out of character.

This test case however due to the high torque response, was repeated using a new wear liner sample/re-turned centre plate component, see test case 6 in Figure 5.16 (Blue dashed lines). Using new components as can be seen, appears to have resolved the issue with the divergent torque response of test case 5, as the responses of test case 6, are now seen to be in the same region as the five other test cases (1, 2, 3, 4, 7). Test case 5 it should be pointed out, was still subjected to the 10800 cycle service test to see if the torque responses continued to rise when the centre plate load was increased to 3 kN. The results from this test case are discussed in Section 5.4.

The measured torque responses were then substituted into Equation (3.33) in Section 3.3, to calculate the COF values for the wear liner samples. These test cases due to the sinusoidal forcing function, include motions in the Clockwise (CW +), as well as Counter-Clockwise (CCW −) directions, so produces two COF values. The absolute COF values are then plotted against each other to quantify the differences between the magnitudes of the torque responses in CW/CCW directions, see Figure 5.17.
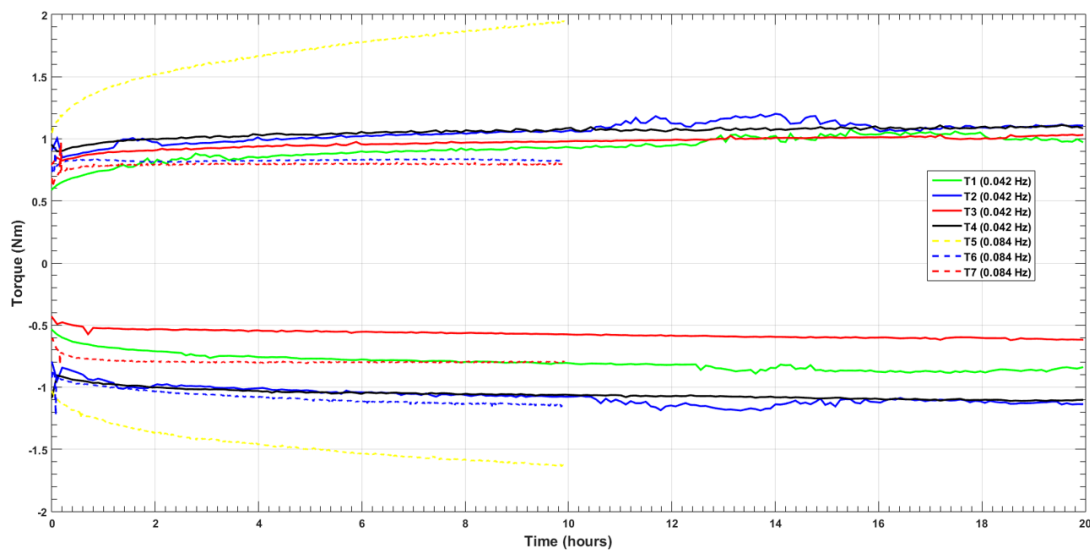
Figure 5.16: Torque responses for material A during the running-in tests.
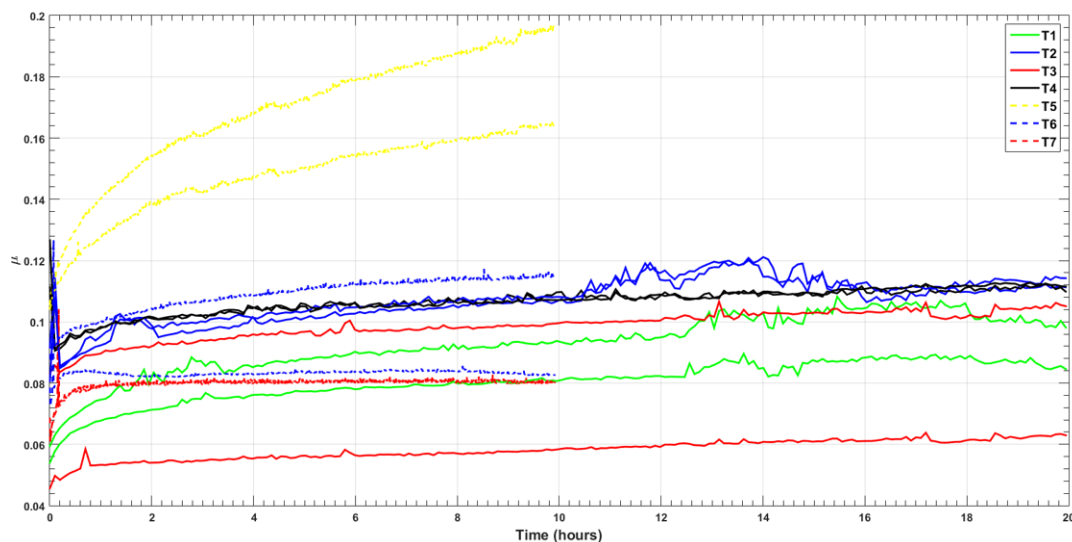
Figure 5.17: Clockwise/counter-clockwise COF responses for material A.

The mean COF value for the complete data set as can be seen from the results shown in Appendix N, is 0.098 with a SD of 25.6%. The minimum and maximum COF values that were calculated for this material under the 0.5 kN loading condition are seen to be 0.05 and 0.195, whereas the peak COF values that were calculated after test case 5 are seen to be the highest overall at 0.195 for the CW direction and 0.165 for the CCW direction, which is a difference of 18%. The differences in the COF values for the CW and CCW directions during test case 3 however (Red lines), are seen to be 0.104 and 0.064 respectively, which is the largest difference overall at 62%. In (Zimmermann, Zeidis, Pivovarov, & Abaza, 2006) for example, this phenomenon is called, "non-symmetric dry friction".

The differences between the COF values for the CW/CCW directions as well as the increases in these values over time can be attributed to several factors. These include changes to the geometrical parameters of the centre plate/wear liner components, such as the flatness of the contact surfaces, as well as the roughness and waviness profiles. These surface features, especially on the steel centre plates for example, can start to work harden over time due to plastic deformations and the tensile/compressive stresses introduced by the cyclic loading conditions.

Work hardening processes cause the mechanical properties of the materials forming the contacts to change over time. The initial yield strength σ_{Y0} of the surface roughness features for example, can increase under repeated loading conditions which then leads to a reduction in the ductility, hence more brittle fracture mechanisms and therefore, more wear debris. If isotropic hardening regimes start to develop, then the yield stress σ_Y under tension/compression as can be seen in Figure 5.18, increases in parallel. Whereas for kinematic hardening regimes on the other hand, the yield stress under tension/compression is seen to be different due to the non-symmetric friction characteristic or alternatively, the so-called "Bauschinger effect" as it is referred to in solid mechanics text books (Bertram & Gluge, 2013) and (Tottle, 1966).
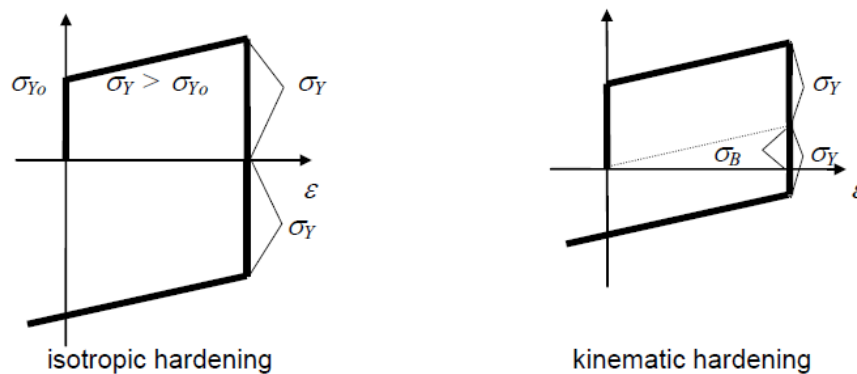
Figure 5.18: Isotropic and kinematic hardening regimes (Bertram & Gluge, 2013).

The Bauschinger effect is a phenomenon that takes place in all real materials under cyclic loading conditions due to the varying orientation of the grains forming the crystal lattice (Tottle, 1966). When materials are plastically deformed under cyclic loads for example, dislocations within the micro-structures start to glide along various slip planes as well as build-up along grain boundaries that are not favourably orientated to allow easy slippage. These dislocations then introduce a back stress σ_B into the crystal lattice that opposes the direction of the applied stresses which are then released during load reversals or removals. For the kinematic hardening example shown to the right of Figure 5.18, the yield stress under tension is seen to be higher than under compression (Bertram & Gluge, 2013) and (Tottle, 1966).

Another interesting feature to point out in the COF responses for material A, are the intervals of unstable behaviour developing in test cases 1 and 2, which is clear to see between 1.5 – 4 hours as

well as 10 – 16 hours (Green and blue solid lines). These instabilities however, appear to have been caused by either wear debris building-up in the contact interfaces or alternatively, material softening mechanisms, as the COF values are seen to decrease after these events. Whereas if work hardening was taking place, the COF values would continue to increase (Tottle, 1966).

The main conclusions that can be drawn from the global analysis results for material A, are that the responses of test case 5 are completely different to the other samples that were tested under the running-in loading condition. This sample therefore, requires further analysis at the end of the service test to establish the root causes of the diverging torque/COF responses. The global analysis method has also proved to be extremely efficient at identifying abnormal torque responses, as well as specific regions of the torque curves to further investigate using the local analysis methods. The following section discusses the global analysis results for material B.

5.3.2. Global analysis results for material B

The global analysis results for material B during the running-in test cases are discussed in this section. From the responses shown in Figure 5.19 as well as the summary of results shown in Appendix N, it can be seen that the torque responses for this material range between 0.897 – 3.2 Nm. This range however, is double in comparison to the range of torque responses that were measured on material A. The mean percentage increase in the torque responses for material B however (7 test cases), was 98.1% which is 26% higher than material A.

The COF values that were calculated from the torque responses as can be seen in Figure 5.20, range between 0.09 – 0.32. The mean value for the complete data set however is 0.157, which is 60% higher than the mean COF value that was calculated for material A. From the COF responses, it is also clear to see instabilities developing in the last four hours of test cases 11 and 14 (Black solid lines and red dashed lines), as well as the non-symmetrical COF characteristics, especially in test cases 9, 10, 11, 13 and 14. The maximum differences between the COF values in the CW/CCW directions for example, are seen to range between 6 – 50%, whereas for material A, the maximum difference was in the region of 62%.

The non-symmetrical friction characteristics observed during the running-in tests using wear liner materials A and B and in the context of a full size vehicle however, could potentially lead to uneven wheel wear, bogie crabbing/warping, as well as tracking issues and hunting instabilities on tangent track. The curving performance of the vehicle could also be adversely affected by the differences between the COF values for the CW/CCW directions (Tickell, Downing, & Jacobsen, 2004). The following section discusses the global analysis results for material C.
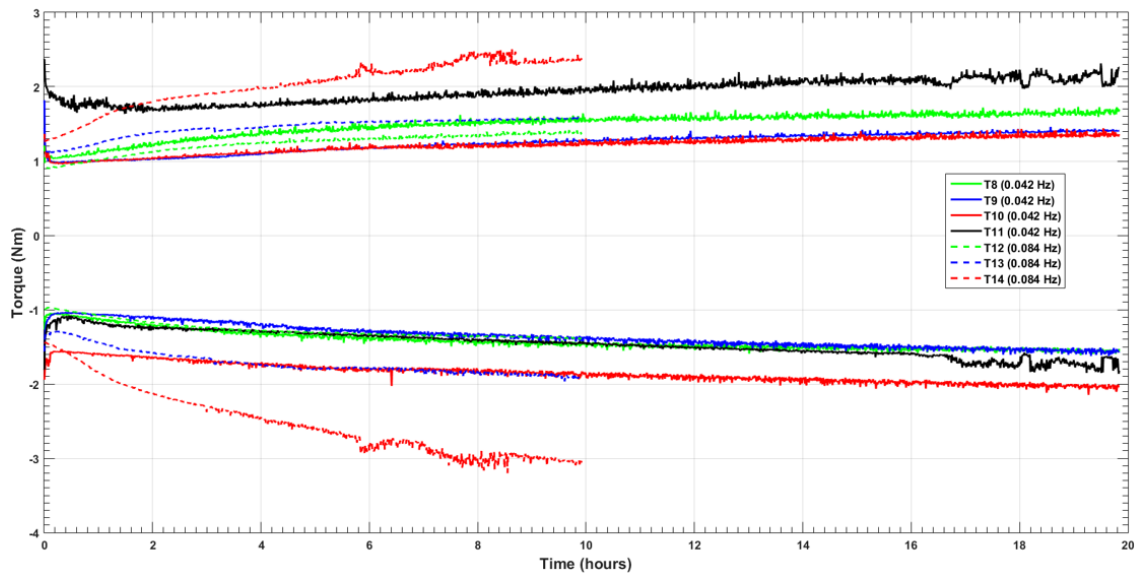
Figure 5.19: Torque responses for material B during the running-in tests.
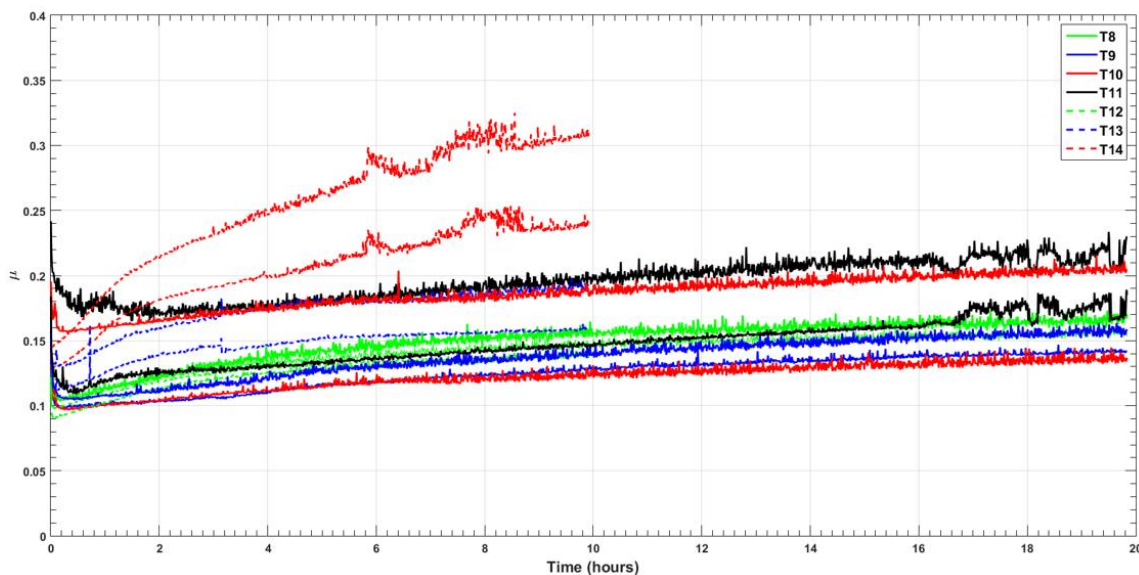
Figure 5.20: Clockwise/counter-clockwise COF responses for material B.

5.3.3. Global analysis results for material C

The torque responses for the three running-in tests that were carried out on material C at the 0.084 Hz forcing frequency are shown in Figure 5.21. From these responses as well as the summary of results shown in Appendix N, it can be seen that the torque ranges between 1.16 – 2.83 Nm, which is similar to the range of values that were measured on material B. The peak torque response on material C however, is 13% lower in comparison to material B. Material A therefore, has the lowest torque responses overall under the 0.5 kN loading conditions.

The COF responses for material C as can be seen in Figure 5.22, range between 0.116 – 0.283 and the mean COF value for the complete data set (3 test cases), is seen to be 0.199, see Appendix N. This COF value however, is more than double the mean value that was calculated for material A which is seen to be 0.098. Whereas it is only 27% higher than the mean COF value for material B, which is seen to be 0.157 under the 0.5 kN loading conditions. The non-symmetric friction characteristics of material

C however, are slightly higher but more consistent than those that were observed on material A and are seen to range between 50 – 65% in Figure 5.22.

The mean percentage increase in the torque responses for material C on the other hand, is seen to be the lowest overall at 39.1%, which is around 2 – 3 times lower than the mean values that were calculated for materials A and B. The general friction characteristics of this material also appear to be smoother in comparison to those that were observed during test cases 2 and 14 for example, using materials A and B. This completes the analyses of the global running-in test results. The following sections discusses the local analysis results for material A during the first and last 25 cycles of the running-in tests.
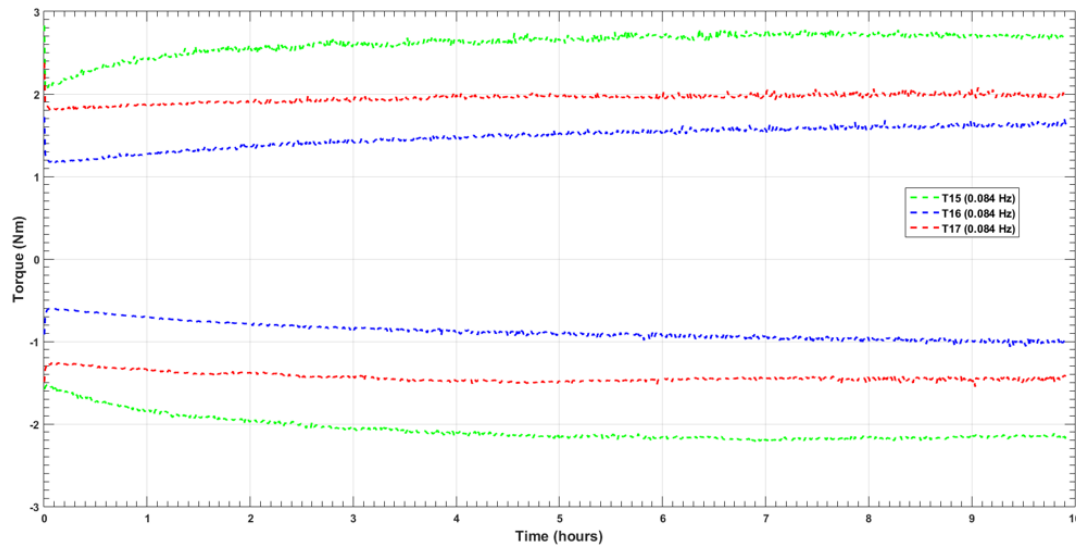
Figure 5.21: Torque responses for material C during the running-in tests.
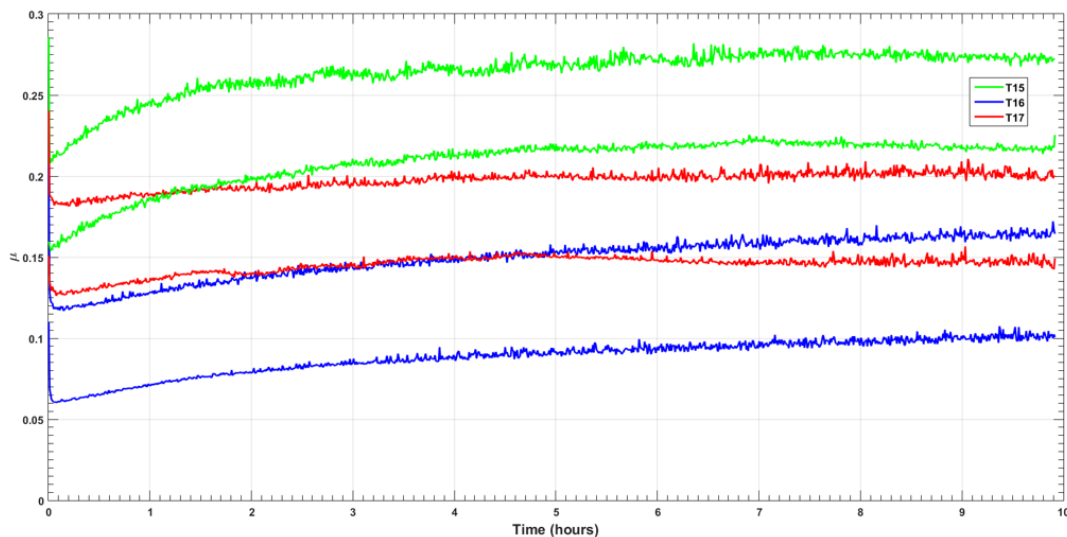
Figure 5.22: Clockwise/counter-clockwise COF responses for material C.

5.3.4. Local analysis results for material A

The section discusses local analysis results for material A during the first and last 25 cycles of the running-in test cases. The local analysis method was used to obtain the static and dynamic COF values, as well as the torsional coefficients and breakout angles for each wear liner sample. The vibration signatures of the centre plate/wear liner components were also mapped to the hysteresis responses

144

as part of this analyses. The full summary of the local analysis results for the running-in test cases are shown in Appendix O.

The hysteresis responses during the first 25 cycles of the 0.042 and 0.084 Hz test cases are shown in Figures 5.23 and 5.24 respectively. The variations in the torque responses for each test case were quantified over the 25 cycles using the data analytics in MATLAB. The standard deviation of these measurements (y std), as can be seen in Figure 5.23 for example, gives the lower limits of the frictional torque in the CW/CCW directions, whereas the maximum/minimum values (y min and y max), give the upper limits of the responses. From these responses it can be seen that the torque ranges between 0.54 – 1.24 Nm during the first 25 cycles. The non-symmetric friction characteristics of test cases 3 and 6 are also clear in these responses (Red, yellow and black lines).

The torsional stiffness parameters and breakout angles of the wear liner samples in the stiction/pre-sliding displacement regions were then quantified using the data points shown in Figure 5.25. From the summary of results shown in Appendix O, it can be seen that the torsional stiffnesses and breakout angles for material A under the 0.5 kN centre plate load, range between from 1418 – 4301 Nm/rad and 0.22 – 0.82 degrees. From this analysis, it can also be seen that the samples with the highest stiffness coefficients have the smallest breakout angles. The torque required to initiate gross sliding in these samples therefore, tends to be higher in comparison to the softer samples that are exhibiting viscoelastic characteristics in the breakout regions, see for example, test cases 1, 3 and 5.

In the region of –52 mrad and when the torque response is greater than zero for example, the centre plate velocity is increasing from zero towards the maximum which leads to the development of the pre-sliding displacements/breakout events. During these events however, elastic energy is stored in the surface asperities on the centre plate/wear liner components, which is then released back to the system in the region of 52 mrad. The pre-sliding displacements/breakout events then start to develop in this region as the torque response switches from positive to negative.

The vertical lines in the regions of $\pm$ 52 mrad are a clear indication that the centre plate/wear liner material behaviour is highly elastic in some cases, see test cases 2, 4, 6 and 7. Whereas in others, such as test cases 1, 3 and 5 for example, the responses are vertical to some extent, but mostly curved in these regions which suggests the material behaviour is viscoelastic. During the gross-sliding events the torque responses are then seen to remain fairly constant (Bertram & Gluge, 2013).
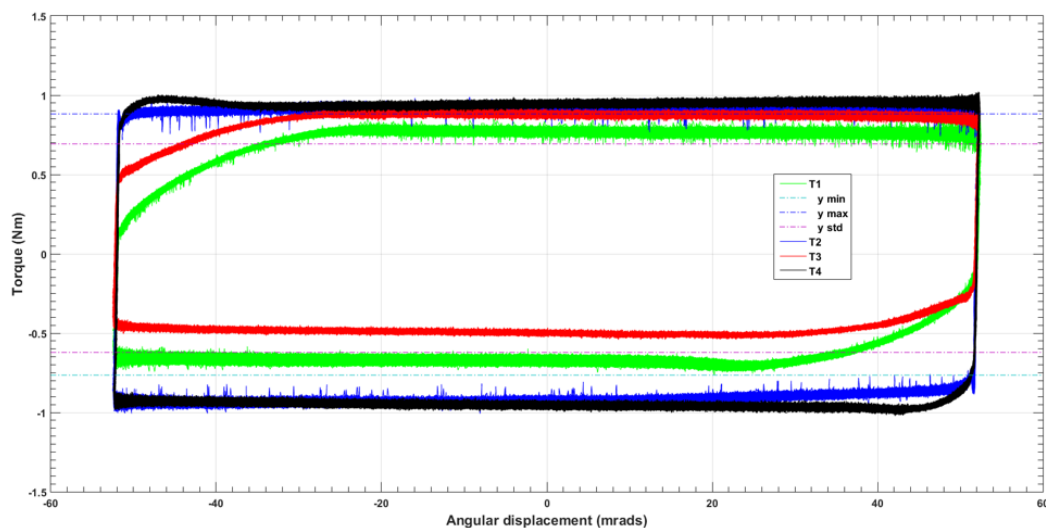
Figure 5.23: Hysteresis during the first 25 cycles of the 0.042 Hz test cases.
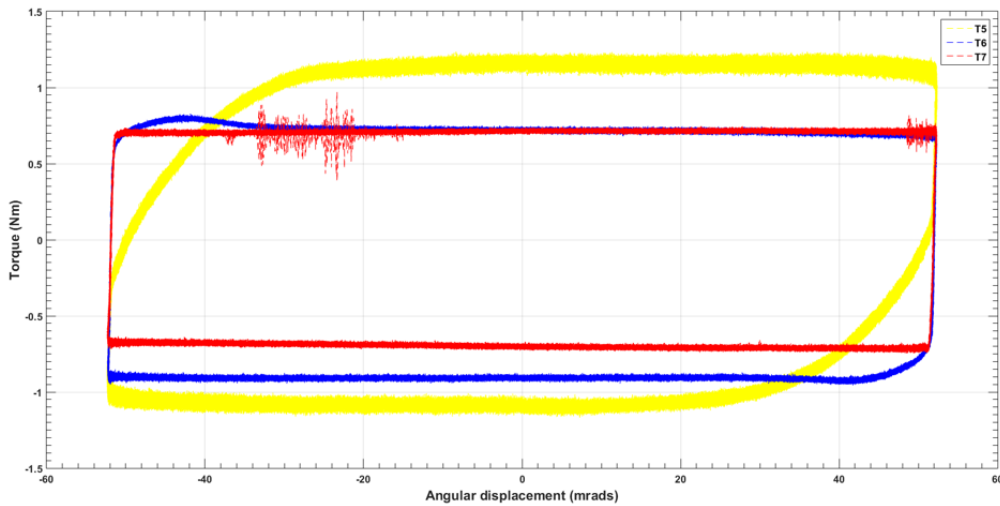
Figure 5.24: Hysteresis during the first 25 cycles of the 0.084 Hz test cases.
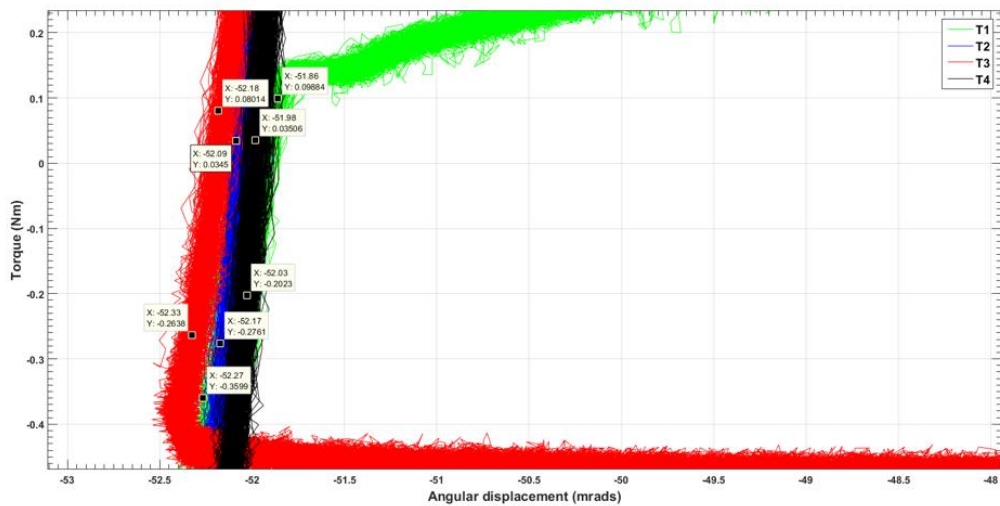
Figure 5.25: Close-up of the sticking/breakout regions during the first 25 cycles.

The hysteresis responses during the last 25 cycles of the 0.042 and 0.084 Hz running-in test cases are shown in Figures 5.26 and 5.27 respectively. From these, it can be seen that the majority of the torque responses appear to be stabilising between $\pm$ 0.5 and $\pm$ 1 Nm, apart from test case 5 (Yellow lines). The peak torque in the CW direction as can be seen, has increased by 56% from 1.24 to 1.94 Nm, whereas in the CCW direction, it has increased from –1.17 to –1.64 Nm. The torque responses in test cases 1 and 3 are also seen to be higher in the CW directions (Green and red lines), whereas for test case 6 (Blue lines), the torque response is higher in the CCW direction. This analysis shows the differences between the torque responses in the CW/CCW directions for these particular test cases, range between 25 – 62%.

From looking at the summary of results shown in Appendix O, it can be seen by comparing the torque responses during the first and last 25 cycles of the running-in tests for example, that the range has increased from 28.6 to 35.9 Nm, which is a 25% increase in torque over time. Whereas by comparing the torque responses during cycles 1475 – 1500 and the last 25 cycles, it can be seen that the range has increased from 34.5 to 35.9 Nm, which is a 4 % increase. This analysis suggests that 3000 sinusoidal cycles on the Instron testing machine under a 0.5 kN axial load, is sufficient to stabilise the torque responses of the centre plate/wear liner components.

146

The main conclusions to draw from this analysis are that the centre plate/wear liner samples with the viscoelastic responses would lead to a reduction in the wheel/rail forces on tight curves, see for example, test cases 1, 3 and 5. The running stability of the vehicle on tangent track however, could also be adversely affected by the non-symmetric friction characteristics observed in these samples, such as a reduction in the critical speed of the vehicle as well as accelerated levels of uneven wheel/rail wear. The following section discusses the local analysis results for material B (Fergusson, Frohling, & Klopper, 2008) and (Meymand, Keylin, & Ahmadian, 2016).
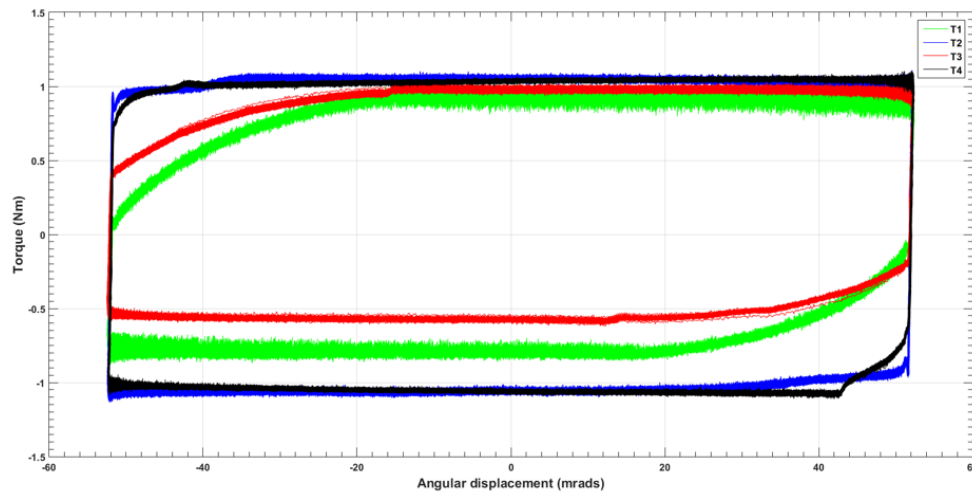
Figure 5.26: Hysteresis during the last 25 cycles of the 0.042 Hz test cases.
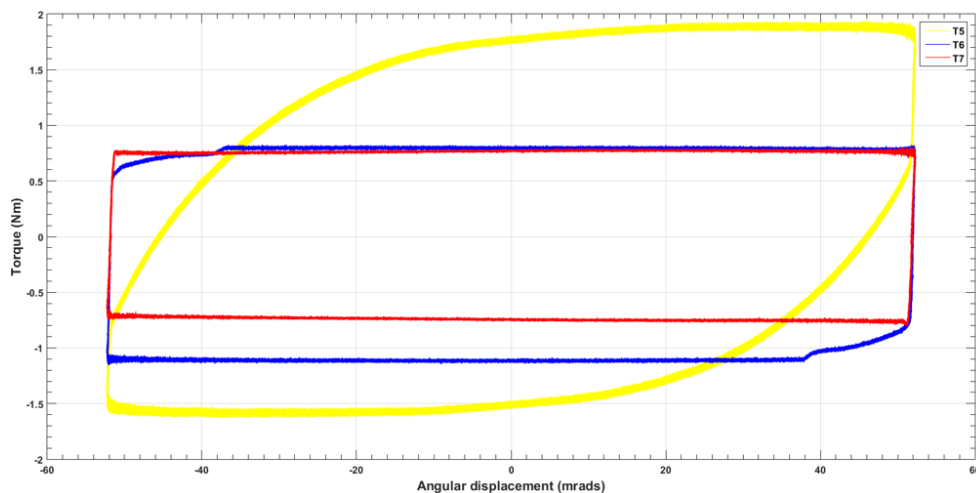
Figure 5.27: Hysteresis during the last 25 cycles of the 0.084 Hz test cases.

5.3.5. Local analysis results for material B

The local analysis results for material B during the first and last 25 cycles of the running-in tests are discussed in this section. The hysteresis responses during the first 25 cycles of the 0.042 and 0.084 Hz test cases are shown in Figures 5.28 and 5.29 respectively and from these, as well as the summary of results shown in Appendix O, it can be seen that torque responses for this wear liner material range between 0.94 – 1.9 Nm.

The torque characteristics in test cases 10, 11, 13 and 14 as can be seen, are also non-symmetrical. During test case 10 in Figure 5.28 for example (Red lines), the torque responses are seen to be 50% higher in the CCW direction (-), whereas in test case 11 (Black lines), the torque is 50% higher in the

CW direction. Stick-slip behaviour is also developing in test cases 11 and 14, but the transition from sticking to slipping in test case 14 in Figure 5.29 (Red lines), appears to be much smoother in comparison to test case 11. The only difference between these two responses however, are that test case 11 was running at 0.042 Hz, whereas test case 14 was running at 0.084 Hz. Test case 11 also appears to have additional noise components in the torque responses during the gross-sliding events which are not present in any of the other responses.

The torsional stiffness coefficients, breakout angles and natural frequencies of the centre plate/wear liner samples were then calculated from the torque responses during the first 25 cycles of the running-in test, see Appendix O. From these results, it can be seen that these parameters range between 2353 – 4572 Nm/rad, 0.26 – 0.57 degrees and between 52.7 – 73.5 Hz respectively.

The noise components observed in the torque responses of test case 11 were then further analysed using a Direct Fast Fourier Transform (DFFT) function in MATLAB, see Section 5.3.7. This process was also carried out to identify the frequency components associated with the fluid/structural borne vibrations due to the testing machine, as well as those corresponding to the changes in the friction characteristics of the centre plate/wear liner components.

From the responses of test cases 8, 10, 12, 13 and 14 shown in Figures 5.28 and 5.29, it can also be seen that material B has viscoelastic characteristics in the pre-sliding displacement/breakout regions, which is similar to the behaviour that was observed in test cases 1, 3 and 5 using material A (Figures 5.23 and 5.24). The main difference between the responses of material B in comparison to material A however, is the stick-slip behaviour developing in test cases 11 and 14 in the regions of $\pm$ 52 mrad, which is where the centre plate velocity is approaching zero.

The torque responses in the regions of 0 mrad on the other hand, are lower in comparison to the responses in the regions $\pm$ 52 mrad. In the regions of 0 mrad, the centre plate velocity approaches its maximum values in the positive/negative directions which initiates gross-sliding between the contact surfaces. During the gross-sliding events the material behaviour is elastic/plastic rather than elastic which is seen to be the case in the breakout/break-in regions ($\pm$ 52 mrad). These different material behaviours therefore, lead to changes in the torque responses of the contact surfaces (Tottle, 1966).
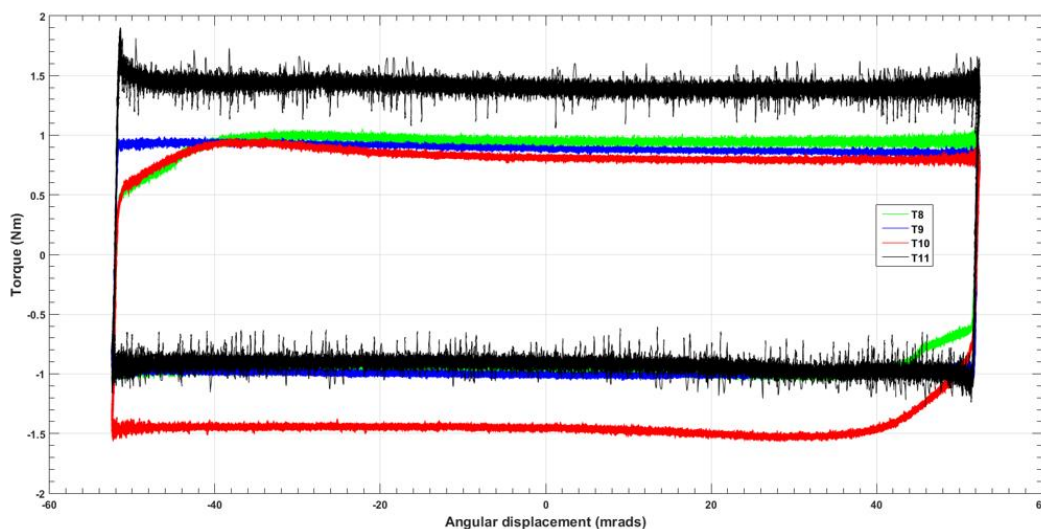
Figure 5.28: Hysteresis during the first 25 cycles of the 0.042 Hz test cases.
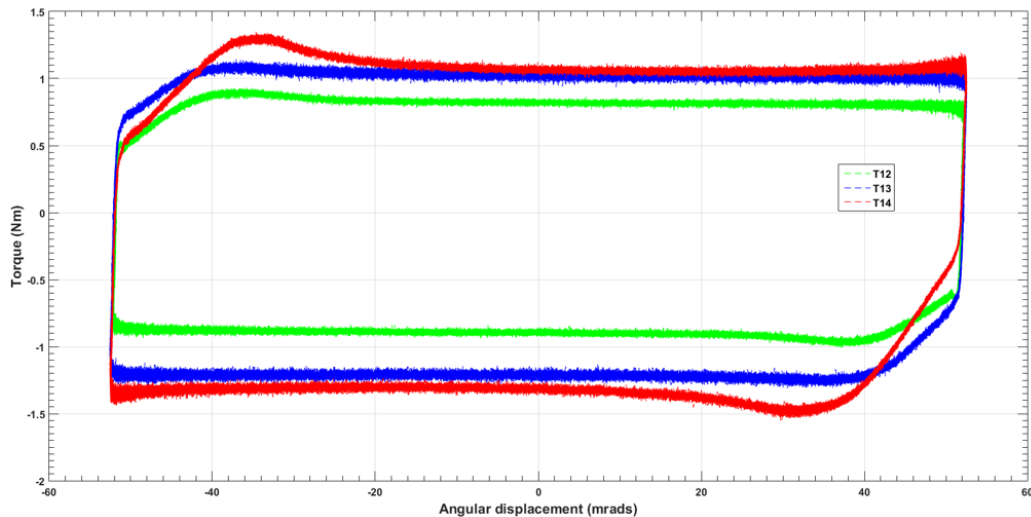
Figure 5.29: Hysteresis during the first 25 cycles of the 0.084 Hz test cases.

The hysteresis responses during the last 25 cycles of the 0.042 and 0.084 Hz running-in tests are shown in Figures 5.30 and 5.31 respectively. From the torque responses shown in Figure 5.30, it can be seen that the noise components in test case 11 have become more noticeable over time (Black lines). The peak torque in this test case has also increased by 19% relative to the first 25 cycles, from 1.9 to 2.26 Nm. The peak torque in test case 9 however has increased by 70% (Blue lines), but now appears to be stabilising in the region of 1.72 Nm, see Appendix O. This conclusion can be drawn by comparing the peak torque responses for the complete data sets during the last 25 cycles and those from cycles 1475 – 1500, where the increase between the peak torque responses is seen to be less than 2%.

From the responses of the 0.042 Hz test cases shown in Figure 5.30 it can also be seen that test cases 10 and 11 appear to be the worst samples overall in terms of non-symmetric friction characteristics (Black and red lines). The peak torque responses in test case 10 for the CW and CCW directions for example, are seen to be 1.41 and –2.11 Nm respectively. Whereas for test case 11, these parameters are seen to be 2.26 and –1.86 Nm. The differences between the torque responses in the CW/CCW directions for this material therefore, range between 22 – 50% under the 0.5 kN loading conditions and are seen to be slightly lower than the differences that were measured on material A.

Significant differences in the torque responses for the CW/CCW directions in the 0.084 Hz test cases can also be seen in Figure 5.31. The maximum torque in CCW direction during test cases 13 and 14 for example (Blue and red lines), are seen to be –1.95 and –3.1 Nm in Appendix O. Whereas in the CW direction, the torque responses for these test cases are seen to be 1.62 and 2.38 Nm respectively. The differences in the CW/CCW torque responses for the 0.084 Hz test cases therefore, are slightly lower in comparison to the 0.042 Hz test cases and are seen to range between 20 – 30%.

The viscoelastic response of test case 14 is also seen to be more dominant during the last 25 cycles of the running-in test, see Figure 5.31 (Red lines). During the first 25 cycles for example, this sample was seen to be transitioning from viscoelastic to plastic behaviour in the regions of $\pm$ 30 – 36 mrad. Whereas in the last 25 cycles, this event is seen to be taking place in the region of $\pm$ 10 – 16 mrad. The sticking behaviour at the end of the sliding phases of motion, in the regions of $\pm$ 46 – 52 mrad, is also becoming more noticeable in these responses. The following section discusses the local analysis results for material C.

149
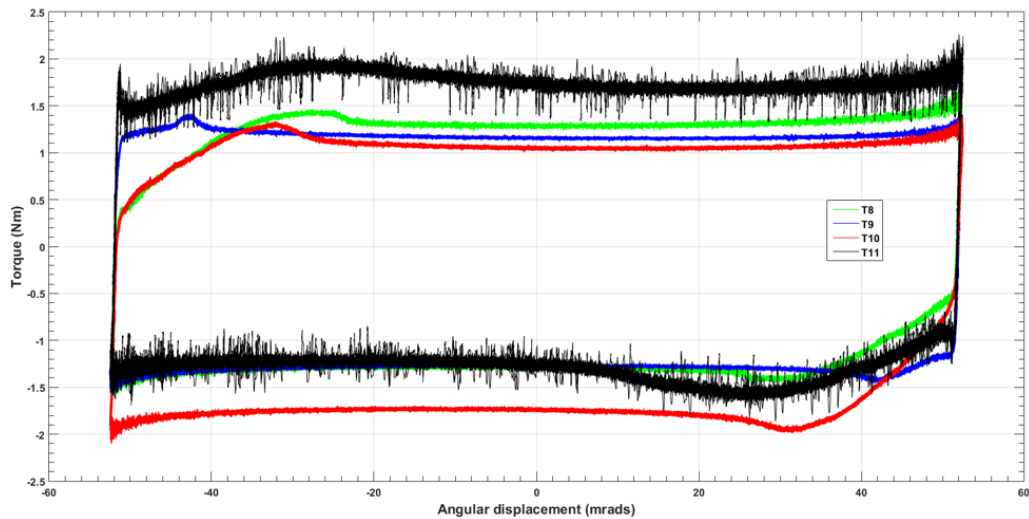
Figure 5.30: Hysteresis during the last 25 cycles of the 0.042 Hz test cases.
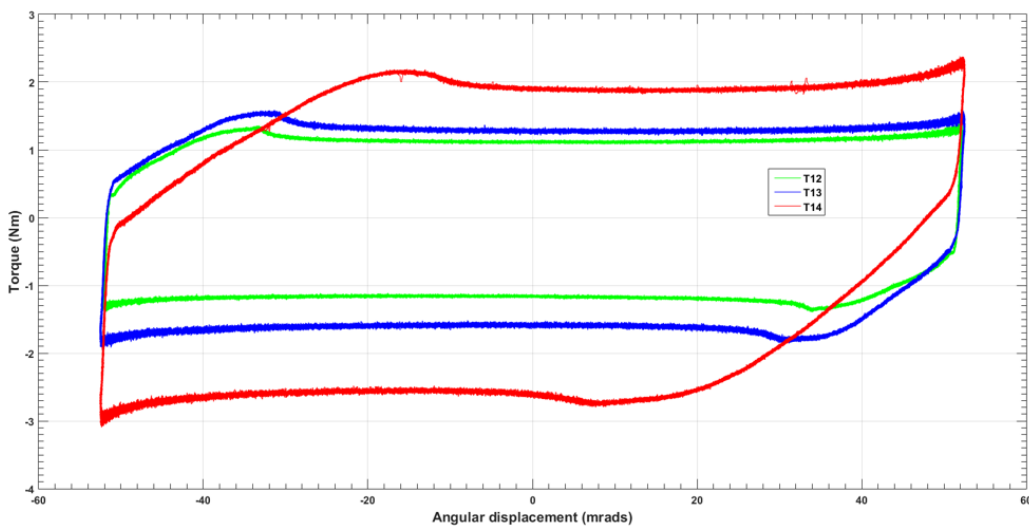
Figure 5.31: Hysteresis during the last 25 cycles of the 0.084 Hz test cases.

5.3.6. Local analysis results for material C

The local analysis results for material C during the first and last 25 cycles of the running-in tests are discussed in this section. Due to the time constraints on this work however, only three tests were carried out on material C at the 0.084 Hz forcing frequency. Figure 5.32 shows the hysteresis responses during the first 25 cycles and from these, as well as the summary of results shown in Appendix O, it can be seen that the torque responses for this material are the highest overall, ranging between 0.63 − 2.24 Nm. Whereas the torque responses for material A under the 0.5 kN loading condition, were seen to be between 0.54 − 1.24 Nm which is the lowest range overall.

From the responses shown in Figure 5.32, it can also be seen that the torque characteristics of test 16 (Blue lines), are noticeably different in comparison to the responses of test cases test 15 and 17. In the vicinity of ± 52 mrad for example, the friction surfaces in test cases 15 and 17, breakout out the stiction regions and transition straight into the gross-sliding regimes. Whereas in test case 16 on the other hand, the torque responses continue to increase in a viscoelastic manner after the breakout events before the transition into the gross-sliding regimes is seen to occur in the region of ± 28 mrad.

150

The differences between the torque responses in the CW/CCW directions on these three samples are similar to those that were observed on materials A and B. The peak torque in the CW direction during test case 15 for example (Green lines), is seen to be in the region of 2.24 Nm (Appendix O), whereas in the CCW direction, the torque response is –1.7 Nm, which is a difference of 32%. During the gross-sliding regimes on the other hand, the torque responses in the CW and CCW directions are seen to be in the regions of 1.8 and –1.1 Nm respectively, which is a difference of 65%. This analysis clearly shows that the non-symmetric friction characteristics are a common feature in the centre plate/wear liner materials under the 0.5 kN loading conditions (Zimmermann, Zeidis, Pivovarov, & Abaza, 2006).

The hysteresis responses during the last 25 cycles are shown in Figure 5.33 and from these, it can be seen that torque responses now range between 1.04 – 2.73 Nm. The peak value of the complete data set therefore (3 test cases), has increased by 120% relative to the first 25 cycles, see Appendix O. These values are similar to the range of torque responses that were measured on material B which were seen to be the highest overall during the last 25 cycles of the running-in test cases, ranging between 1.4 – 3.1 Nm. Whereas the lowest range of torque responses was measured on material A and seen to be in the region of 0.62 – 1.94 Nm.

From the global analysis results shown in Appendix N, it can also be seen that the percentage increases in the torque responses during test case 15, 16 and 17 for example, are the most consistent overall, ranging between 32.3 – 47.9%. Whereas the percentage increases for material B, were seen to range between 57.8 – 154% which is the highest range overall. The lowest percentage increase on the other hand, was seen to be 23.5%, which was measured during test 4 using material A, whereas the maximum increase for this material was seen to be 108.4%. It can also be seen from these results, that the mean percentage increase for the complete data set (17 test cases), is 76.9% with a SD of 46.5%.

This analysis strongly suggests that material C is the most stable material under the running-in loading conditions because the hardening mechanisms in this material for example, are not as dominant as they are in materials A and B. The following section discusses the spectral analyses results for the centre plate/wear liner components during the running-in test cases.
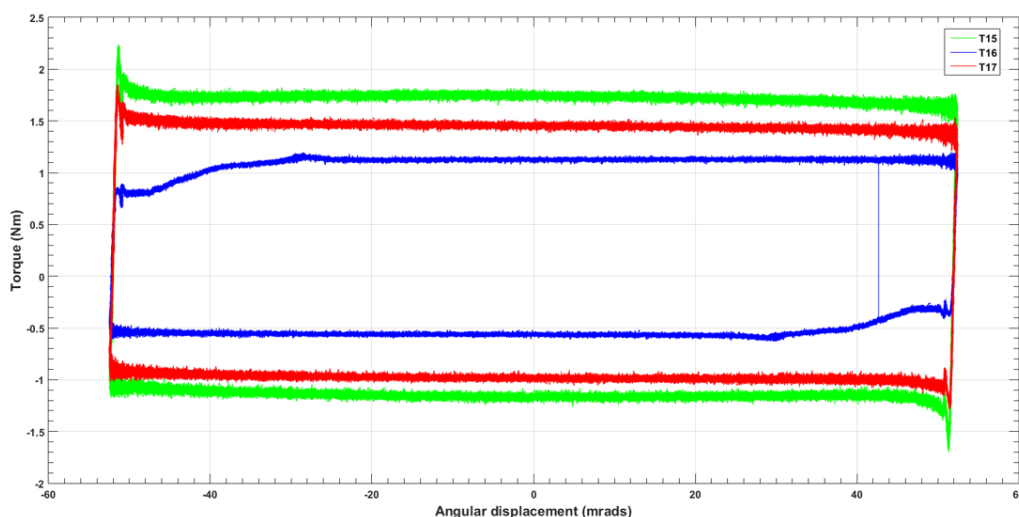
Figure 5.32: Hysteresis during the first 25 cycles of the 0.084 Hertz test cases.
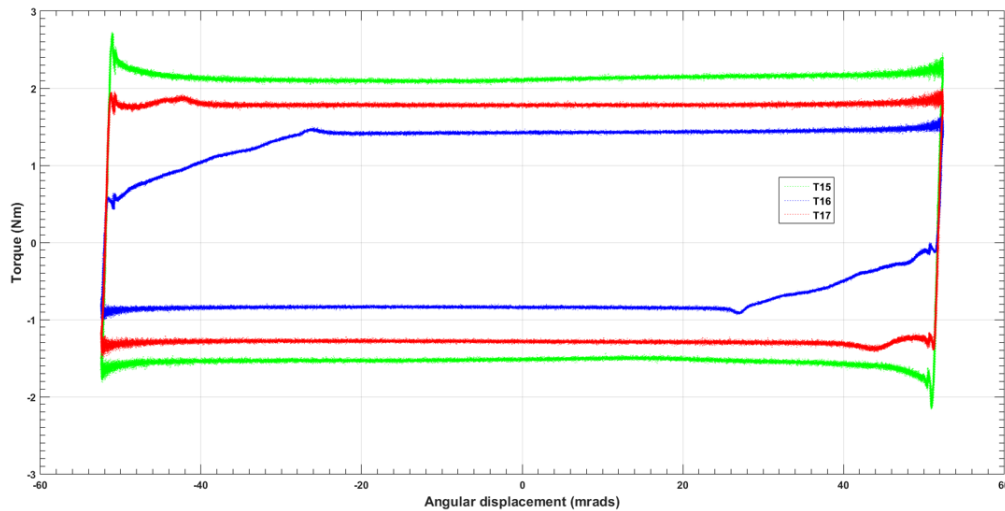
Figure 5.33: Hysteresis during the last 25 cycles of the 0.084 Hertz test cases.

5.3.7. Spectral analysis responses during the running-in test cases

This section discusses the spectral analysis responses of the centre plate/wear liner components during the running-in test cases. The main purpose of this analyses is to separate the fluid/structural borne vibrations introduced into the measured signals by the Instron testing machine, from the actual vibrations caused by the changes in the friction characteristics of the centre plate/wear liner components. This task was carried out in MATLAB using Equation (3.34) – (3.39) in Section 3.3.

During the post-test analysis of the hysteresis responses it was clear to see the additional noise components contained within the sampled measurements. The dynamic actuator on the testing machine for example, is powered by a 4-pole induction motor which drives a positive displacement, swash-plate type pump. The hydraulic fluid is then pumped to the actuator via nine cylindrical pistons, but as the hydraulic circuit on the machine is not equipped with a pulsation damper, these signals are also detected by the load cell along with the responses of the centre plate/wear liner components.

The frequency of the fluid pulsations and machine frame vibrations however, can be calculated from the specifications given in Table 5.2 and are shown to be in the region of 223.5 and 151 Hz respectively. Whereas the natural frequencies of the centre plate/wear liner components under the 0.5 kN loading condition, which were calculated from the local analysis results shown in Appendix O, should be in the region of 40.9 – 73.5 Hz, see Table 5.3. The following section discusses the spectral analysis results for material A.

Parameter	Value
Flow rate (L/min)	26
Max working pressure (bar)	210
Voltage (V)	400
Motor power (kW)	11
Motor speed (Rpm)	1490
Power supply frequency (Hz)	50
Empty weight of power unit (kg)	480
Maximum operating torque (N.m)	100
Maximum dynamic axial load (kN)	10
Machine frame mass (kg)	287
Machine frame axial stiffness (MN/m)	260

Table 5.2: Specifications for the Instron testing machine (INSTRON, 2019).

Component	Natural Frequency (Hz)	1:7 scale model mean torsional stiffness (Nm/rad)	1:7 scale model mean breakout angles (mrad)	Full scale mean torsional stiffness (kNm/rad)	Full scale breakout angles (mrad)	Standard deviation of the torsional stiffness (%)	Min μ	Max μ	Mean μ	Standard deviation of μ (%)	Percentage increase in μ over time (%)
Centre plate/Wear liner	40.9 - 75.4	3149 - 3215	0.41 - 0.52	22 - 22.5	2.87 - 3.64	30.1	0.05	0.32	0.14	36.3	23.5 - 154
Fluid pulsations	223.5	-	-	-	-	-	-	-	-	-	-
Machine frame	151	-	-	-	-	-	-	-	-	-	-

Table 5.3: Calculated torsional vibration modes for the machine frame, fluid pulsations and 1:7 scale centre plate/wear liner components.

5.3.7.1. Spectral analysis results for material A

The Power Spectral Densities (PSD) of the torque signals that were measured on material A during the running-in test cases are discussed in this section. The frequency responses during the first and last 25 cycles of the running-in tests are shown in Figures 5.34 and 5.35 respectively. From these responses it is clear to see the signature of the fluid pulsations in the region of 223 Hz which is seen to be in good agreement with the pre-calculated value in Table 5.3.

This analysis clearly shows that the hydraulic transmission is having a measurable influence on the torque responses. However, it is also reasonable to assume that these effects are exactly the same throughout all of the test cases that have been studied. This constant signal in the frequency domain therefore, can be used to our advantage, as a reference marker for example, to identify as well as verify, the frequencies that appear in the system responses due to changes taking place in the friction characteristics of the centre plate/wear liner components.

The signatures in the regions of 266 – 300 Hz for example (Figure 5.34), appear to coincide with the higher harmonics of 0.042 Hz and 0.084 Hz forcing frequencies, as well as the 2nd harmonic of the machine frame and the 5/6th harmonics of the centre plates/wear liner components. This analysis is based on the mean values and standard deviations of the natural frequencies that were calculated for the complete data set (17 tests). These frequencies as can be seen from the local analysis results shown in Appendix O, range between 60 – 61 Hz and 11.9 – 16% respectively.

Test case 5 as can be seen in Figure 5.34, is the only sample with a frequency response in the region of 162.5 Hz (Yellow lines). This signature appears coincide with the 3/4th harmonics of the fundamental frequencies that were calculated for this test case, which are seen to range between 40.9 – 52.8 Hz (Appendix O). The higher harmonics of the 0.084 Hz forcing frequency could also be contributing to this signature. The band-width of this frequency response is also seen to be 3 – 4 times wider than the band-widths of the multiple signals observed in the regions of 266 – 320 Hz.

The COF values that were calculated during test case 5 were also seen to be the highest overall and from the hysteresis responses, it was clear to see the highly viscoelastic behaviour of this material sample in the breakout as well as gross-sliding regions. This type of behaviour however, was not present to the same extent in the other test cases, which strongly suggested that there was a problem with either the centre plate or wear liner component that was used in test case 5.

The PSD of material A during the last 25 cycles of the running-in test cases are shown in Figure 5.35. From these responses it is clear to see that the vibration characteristics of test case 5 (Yellow lines), are changing over time. The frequency band and power amplitude in the region of 162.5 Hz for example, is narrowing as well as reducing in height.

The multiple signals that were observed in the region of 266 – 300 Hz during the first 25 cycles, have also shifted to the right in Figure 5.35 and are now seen to be oscillating in the region of 360 – 430 Hz. These signatures however, appear to coincide with the 6/7th harmonics of material A. The mean values of the natural frequencies under the 0.5 kN loading condition as can be seen from the results shown in Appendix O for example, range between 55.5 – 60.3 Hz. The following section discusses the spectral analysis results for material B.
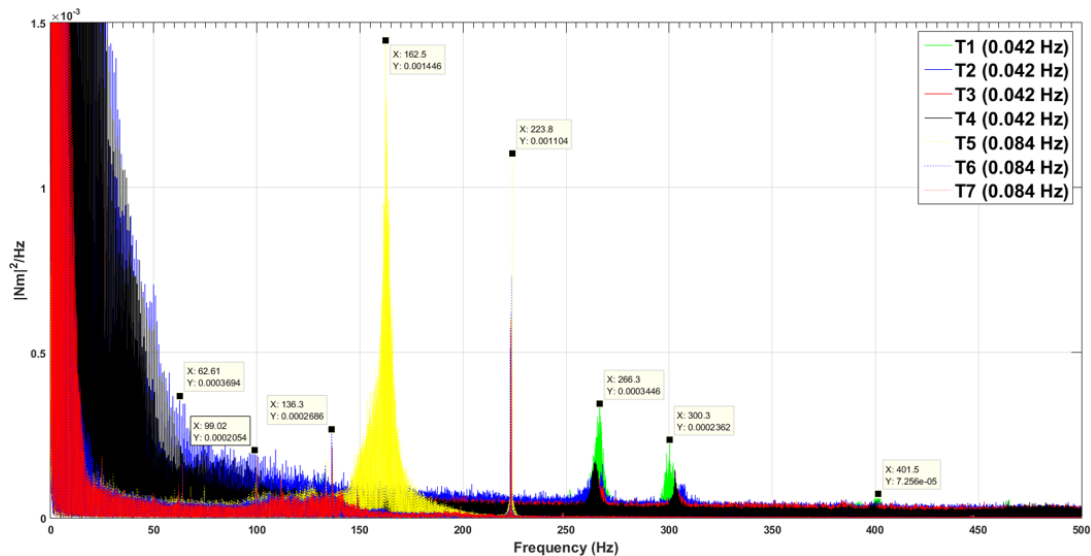
Figure 5.34: PSD of the torque signals during the first 25 cycles of the running-in tests.
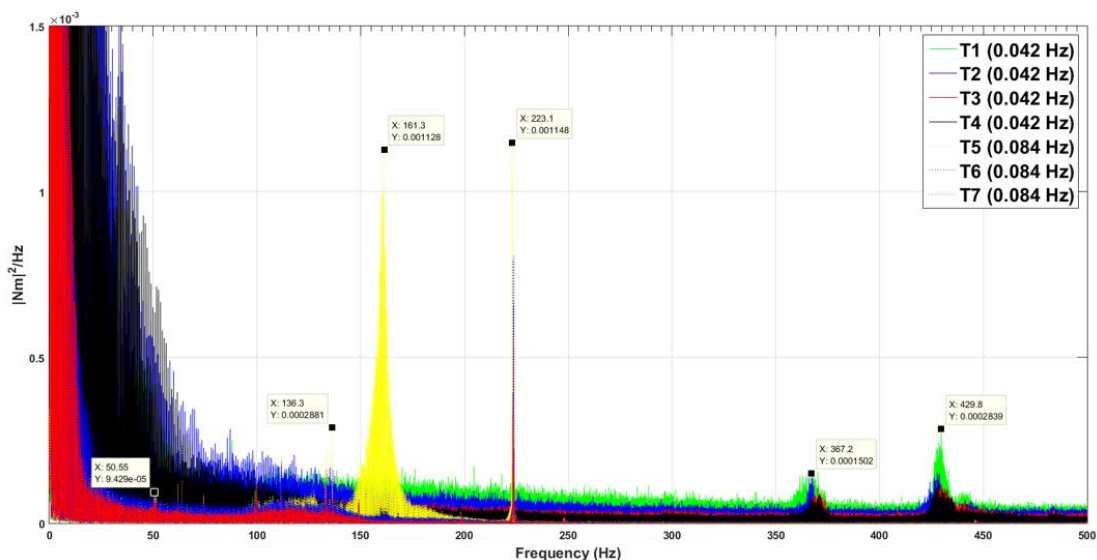
Figure 5.35: PSD of the torque signals during the last 25 cycles of the running-in tests.

5.3.7.2.   Spectral analysis results for material B

The Power Spectral Densities (PSD) of the torque signals that were measured on material B during the running-in test cases are discussed in this section. Figure 5.36 shows the PSD during the first 25 cycles and Figure 5.37, shows the responses during the last 25 cycles. The first major difference to point out in these responses in comparison to the responses of material A, are the increases in power amplitudes due to the fluid pulsations in the region of 223 Hz.

The power amplitudes that were measured on material A in this frequency range for example (223 Hz), were in the region of 7.5 x 10^{-3} |Nm|²/Hz, whereas in all the test cases studied using material B, the amplitudes are off the scale on the y-axis, which has a limit of 1.5 x 10^{-3} |Nm|²/Hz. The scales of the axes in all of the PSD results discussed in this section however, are exactly the same in order to emphasise the subtle changes that are taking place in the vibration signatures of the centre plate/wear liner components throughout the running-in tests.

From the summary of local analysis results shown in Appendix O, it can be seen that the mean torsional stiffness coefficients for material B under the 0.5 kN loading condition (7 test cases), range between 3142 – 3373 Nm/rad. Whereas for material A (7 test cases), these parameters were seen to be slightly lower, ranging between 2696 – 3162 Nm/rad. The mean values of the peak torque responses for materials A and B however, were seen to be 1.22 and 2.09 Nm respectively, which shows that peak torque responses in material A are 65% lower. The differences in the mechanical properties of the wear liner materials therefore, appears to be having a measurable influence on the power amplitudes observed in the region of 223 Hz.

The frequency responses in Figure 5.36, also show that the signatures that were occurring in material A above 223 Hz for example, have been completely attenuated in the responses of material B. However, after a closer inspection, it can be seen that there are still some underlying vibration components in the region of 440 Hz, which is very close to the range of frequencies that were observed in material A during the last 25 cycles of the running-in test (See Figure 5.35 in Section 5.3.7.1).

It can also be seen from the responses shown in Figure 5.36 that test case 13 for example, has a distinct signature developing in the region of 133.7 Hz (Blue dashed lines). Whereas during the last 25 cycles as can be seen in Figure 5.37, this signature is still present but not as dominant. Material A was also seen to have a frequency response in this region which suggests that these signatures are related to the changes in the friction surfaces of the centre plate/wear liner components and the forcing frequencies, rather than the fluid/structural borne vibrations of the Instron machine.

These signatures as can be seen from the results shown in Appendix O, appear to be in the same region as the 2nd harmonic of the centre plate/wear liner components. This analysis is based on the mean values for the natural frequencies that were calculated for the complete data set (17 test cases). These parameters as can be seen, range between 60.3 – 61.1 Hz with a standard deviation of 14%

The frequency components in the regions of 223 and 446 Hz therefore, are associated with the 1st/2nd harmonics of the hydraulic fluid pulsations. Whereas the 1/2nd harmonics of the Instron machine frame vibrations on the other hand, should be located in the regions of 151 and 302 Hz. From this analysis it can be concluded that the signatures below 151 Hz correspond to changes in friction characteristics of the centre plate/wear liner components over time, as well as the higher harmonics of the centre plate forcing frequencies. The following section discusses the spectral analysis results for material C.
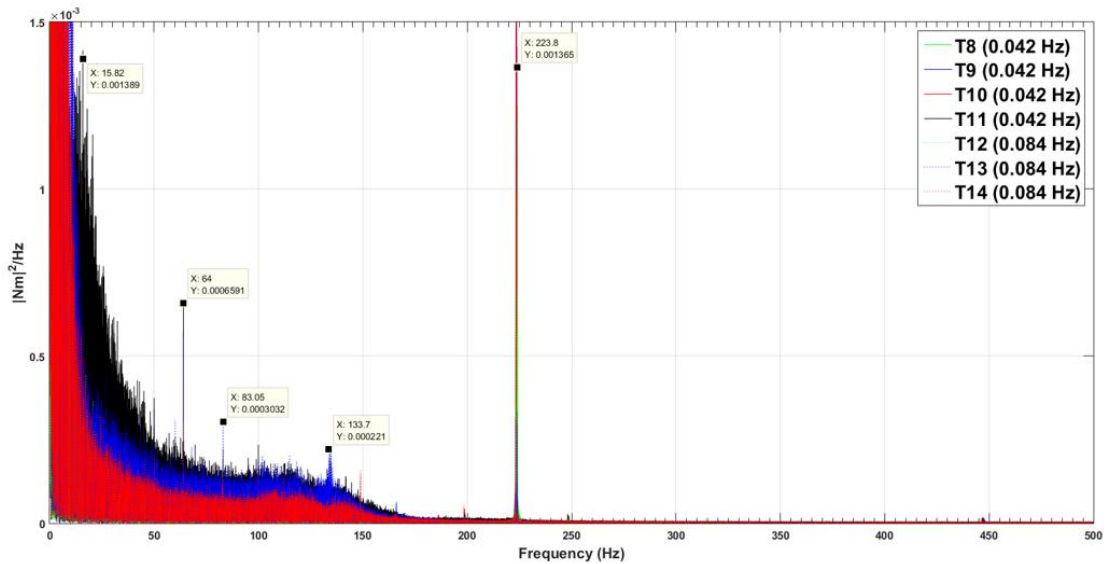
Figure 5.36: PSD of the torque signals during the first 25 cycles of the running-in tests.
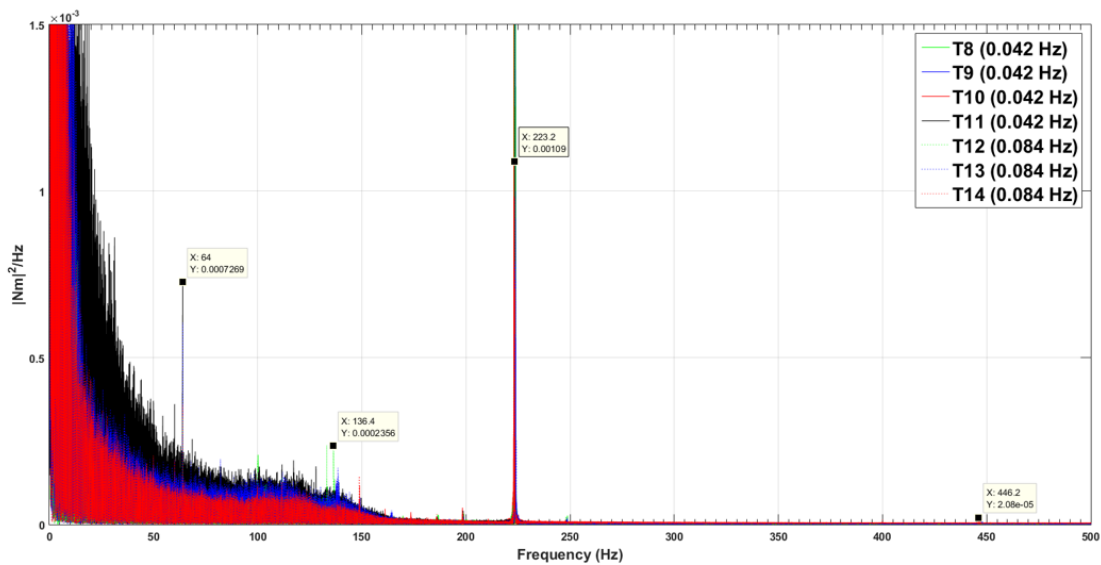
Figure 5.37: PSD of the torque signals during the last 25 cycles of the running-in tests.

5.3.7.3.   Spectral analysis results for material C

The Power Spectral Densities (PSD) of the torque signals that were measured on material C are discussed in this section. Figure 5.38 shows the PSD during the first 25 cycles of testing and as can be seen, the power amplitudes in the region of 64 and 223 Hz for example, are significantly lower than the amplitudes that were observed on material B. The signatures above 223 Hz on the other hand, are similar to those that were seen in the responses of material B.

The PSD during the last 25 cycles of the running-in tests are shown in Figure 5.39 and from these, it can be seen that the power amplitudes in the regions of 64 and 223 Hz, have decreased by around 50% in comparison to the amplitudes during the first 25 cycles. It can also be seen from looking at the local analysis results for material C in Appendix O, that the mean natural frequencies for the complete data set under the 0.5 kN centre plate loading condition (3 tests), range from 61.8 – 65.5 Hz with a standard deviation of 13%. The signatures in the region of 111 Hz therefore, appear to be in agreement with the 2nd harmonic of the fundamental frequencies for the centre plate/wear liner components.

156

The narrow spikes in the regions of 64 and 223 Hz however, are referred to as `line spectrums' in (Gough, Richards, & Williams, 1983), as these signatures are infinitely narrow as well as high, which corresponds to long duration signals, such as the harmonics of the forcing frequencies. Whereas the broader spectrums in the regions of 133, 163, 266 and 300 Hz on the other hand, correspond to short duration signals, such as the breakout events and stick-slip behaviour. This completes the analysis of the running-in test results. The following section discusses the significant findings and conclusions from the 17 running-in test cases.
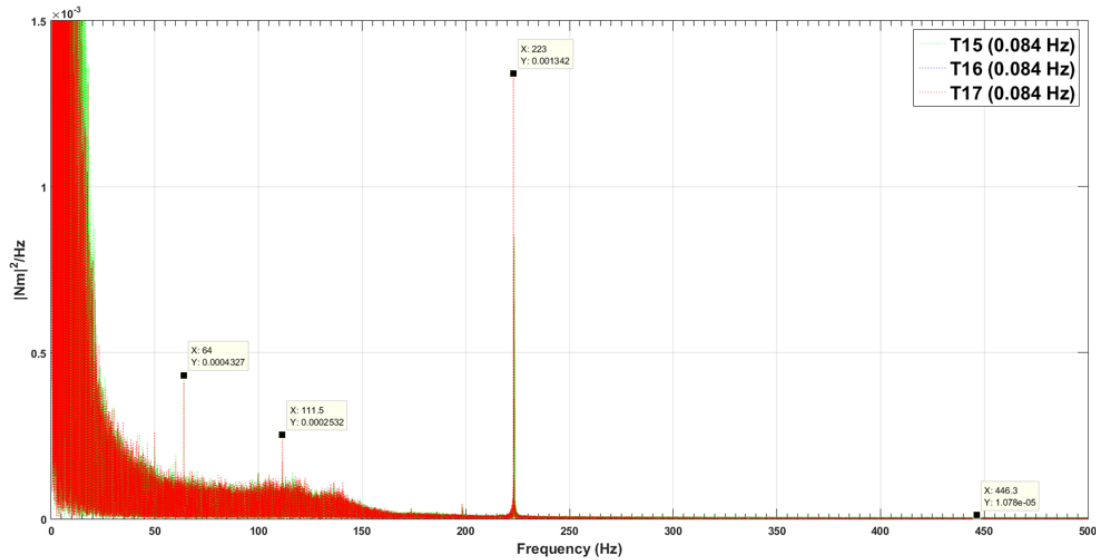
Figure 5.38: PSD of the torque signals during the first 25 cycles of the running-in tests.
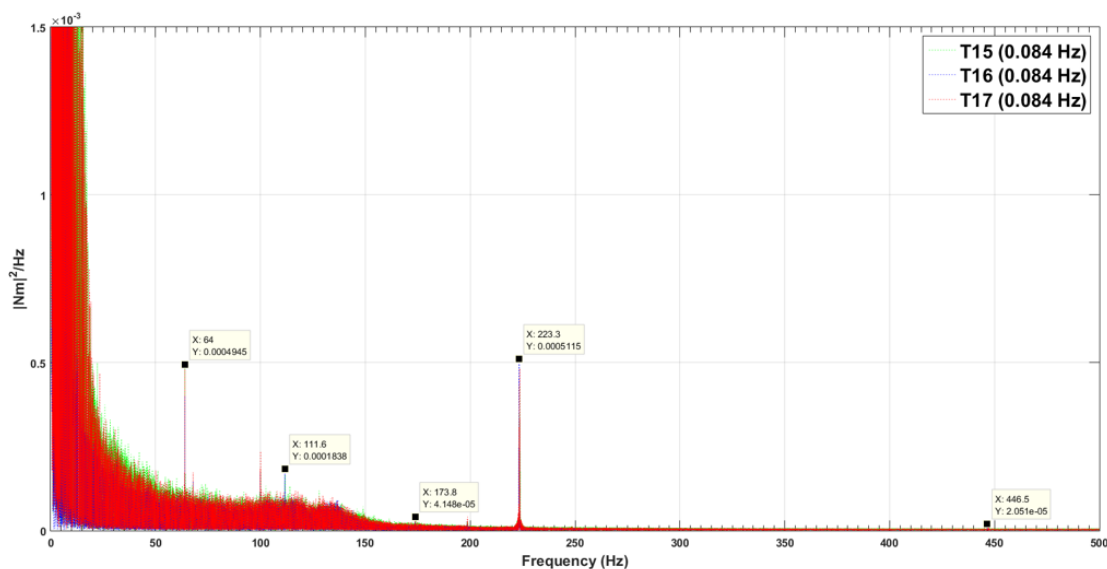
Figure 5.39: PSD of the torque signals during the last 25 cycles of the running-in tests.

5.3.8. Discussion and conclusions

The running-in tests have provided a unique insight into the friction characteristics of the three different wear liner materials under the 0.5 kN centre plate loading condition. This benchmark test data and the parameters that were calculated from the responses of the 17 test cases such as the torsional stiffness coefficients, COF values, frequency responses and the changes in these parameters

over time for example, can now be used to develop an optimised Multibody Simulations (MBS) model of a Constant Contact Side Bearer (CCSB) component.

The global analysis methods provided a quick overview of the increases in the peak torque responses/peak COF values for each material sample over time. Whereas local analysis method on the other hand, generated the larger data files in order to produce the hysteresis responses and from these, the torsional stiffnesses and stick/slip COF parameters could then be quantified. These files were also used to analyse the non-symmetric torque characteristics in the Clockwise/Counter-clockwise (CW/CCW), as well as the spectral components of the measured signals.

The torque responses that were measured for the complete data set during the first and last 25 cycles of the running-in tests, ranged between 0.54 – 2.24 Nm and 0.62 – 0.31 Nm respectively. The mean percentage increase in the torque responses over time and the Standard Deviation (SD) for the complete data set however, were 76.9 and 46.5%, see Appendix N. From the global analysis results, it could also be seen that the hardening rates of material B under the 0.5 kN loading conditions were the highest overall at 98.1%, whereas for materials A and C, these parameters were shown to be 71.9 and 39.1%.

The COF values that were calculated for material A under the 0.5 kN centre plate loading conditions were shown to be the lowest overall, ranging between 0.05 – 0.195 (Appendix O). The COF values for materials B and C were the highest overall but in close agreement, ranging between 0.09 – 0.32 and 0.116 – 0.283 respectively. The mean COF values for materials A, B and C were shown to be 0.098, 0.157 and 0.199 respectively, whereas the SD ranged between 30 – 41.5%.

The centre plate forcing frequency as was shown in the laboratory test results, had a negligible influence on the magnitude of the torque responses. The SD of the pre-test Ra-slope and Wa-slope measurements on the centre plate components on the other hand (Appendix I), were shown to range between 23.8 – 41.2%, which suggested that these parameters had a relatively strong influence on the variations observed in the COF values for wear liner samples of the same material.

The non-symmetric friction characteristics of the centre plate/wear liner samples were also analysed and quantified during various stages of the running-in tests using the local analysis methods. From the hysteresis responses it was clear to see the differences between the torque responses in the CW/CCW directions, which were shown to differ by as much as 20 - 65% in several of the test cases (See test cases 3, 5, 11, 14 and 15 in Sections 5.3.4 – 5.3.6). Further research into the causes of the non-symmetric friction characteristics then led to the discovery of the Bauschinger effect, as well as isotropic/kinematic hardening regimes (Bertram & Gluge, 2013) and (Tottle, 1966).

The hardening regimes that develop in elastic materials due to cold-working for example, can either be isotropic, which is when the yield strength of the contact interface increases by the same amounts in the CW/CCW directions. Whereas for kinematic hardening regimes, which was shown to be a common feature throughout the running-in test cases, the yield strength in the CW/CCW directions increases by different amounts due to the influence of the Bauschinger effect, which is an intrinsic material behaviour, see for example, (Tottle, 1966) or (Bertram & Gluge, 2013). Wear and lubrication/contamination between the friction surfaces, were also shown to have a significant influence on the hardening regimes that were developing in the centre plate/wear liner samples over time.

The torsional stiffness coefficients that were calculated for materials B and C were also seen to be in close agreement under the 0.5 kN loading conditions, ranging between 2300 – 4309 and 2353 – 4572 Nm/rad respectively. The stiffness coefficients for material A on the other hand, were shown be the

least consistent overall, ranging between 1418 – 4819 Nm/rad. These parameters also had a significant influence on the range of breakout angles that were calculated, which shown to range between 0.2 – 1.14 and 0.26 – 0.88 mrad for materials A and B, and between 0.4 – 0.69 mrad for material C.

Test cases 1 and 5 on material A also had the lowest torsional stiffness coefficients overall during the first 25 cycles of the running-in test cases, ranging between 1418 – 1513 Nm/rad (Appendix O). Whereas the mean stiffness coefficient and SD for the complete data set (17 test cases), were shown to be 3149 Nm/rad and 30.1%. This analyses clearly suggested that there was an issue with either the centre plate/wear liner samples that were used in test cases 1 and 5 which required further investigations to better understand the root causes of these relatively low values.

By comparing the local analysis results and the hysteresis responses of the complete data set (17 test cases), it was then clear to see that the majority of the test cases to some extent, responded in a viscoelastic manner in the breakout regions. The viscoelastic responses of test case 5 however, were shown to be completely out of character in comparison to the other test cases, which clearly suggested that there was a problem with the wear liner sample that was used in this test (See Figure 5.27 in Section 5.3.4).

However, after completing the service test and removing this wear liner from the testing machine, it was then discovered that the sample had become saturated in hydraulic oil prior to starting the running-in test as a result of an operator error. This oil was then absorbed into the back face of the wear liner sample, which obviously led to the significant change in the stiffness/COF characteristics of this particular sample. The stiffness characteristics of test case 1 were also shown to be highly viscoelastic in the breakout regions of the hysteresis responses, but not to the same extent due to the fact that this wear liner sample was not contaminated/lubricated (Figure 5.26).

The spectral components of the measured torque signals were also analysed in MATLAB using Discrete Fast Fourier Transforms (DFFT) to better understand the significant differences that were been observed in the hysteresis responses. The natural frequencies that were calculated from the torsional stiffness and inertia parameters for example, were seen to range between 40.9 – 75.4 Hz for material A, and between 52.1 – 73.5 Hz materials B and C.

The constant frequency components in the region of 224 Hz due to the power unit on the Instron testing machine however, were clear to see in all of the samples that were tested. These signatures were then used as obvious reference markers to validate the frequency components that were occurring in the centre plate/wear liner responses, due to the changes that were developing in the friction characteristics of the system over time. From this analyses it was then shown that the frequency responses in the region of 163 Hz during test case 5 for example (Material A), were clearly unique in comparison to the other samples that were tested. This signature therefore, was probably related to the viscous damping force that was introduced as a result of the hydraulic oil contamination.

From the mass property results for the complete data set (16 test cases, Appendix M), it was also shown that the maximum SD of the pre/post-test measurements were all less than 1%, which suggested that the mechanical properties of the wear liner samples were consistent. Whereas the SD of the pre-test surface roughness measurements on the centre plate/wear liner components, were shown to range between 20.6 – 41.5% and 1.2 – 308.3% respectively (Appendices I and L). From this analyses it can also be concluded that the geometric parameters of the friction surfaces such as the flatness and surface roughness properties for example, are the most influential factors in the wide range of nonlinearities that were observed in the running-in test torque responses.

However, it should also be pointed out, that this conclusion only applies to the test cases that were carried out using dry/uncontaminated wear liners. Whereas for the contaminated sample that was used in test case 5, the highly nonlinear behaviour was also exacerbated by the hydraulic oil contamination which then led to a noticeable change in the mechanical properties of the material, as well as a strong viscous damping effect.

These conclusions can be drawn based on the following reasoning;

Each test case was carried out under a constant centre plate load of 0.5 kN, running at either the 0.042 or 0.084 Hz forcing frequency. The magnitudes of the torque responses under both forcing frequencies however, were very similar which clearly suggests that the dry friction characteristics of the wear liner materials are not dependent on the angular velocity of the centre plate i.e. the relationship between these two system parameters is relatively weak, unless contamination is present. The dependency of the torque responses on the surface roughness characteristics on the other hand, is relatively strong in comparison and this is why we are observing a wide range of responses under the exact same testing conditions.

The running-in test data presented in this section can now be used to develop an optimised MBS friction model of a CCSB component that is capable of describing the unique friction characteristics of materials A, B and C. This benchmark data can also be used by the rail freight industry to optimise vehicle maintenance schedules, as well as by research institutions to validate the existing friction models that are currently being used in freight vehicle MBS. The following section discusses the service test cases.

5.4. Service test case description

This section discusses the service tests that were carried out on each wear liner sample after the running-in tests. The service tests ran at the same forcing frequency as the running-in test, but for 10800 cycles instead of 3000 cycles. The main purpose of these test cases, was to benchmark the performance of materials A, B and C in the laboratory under centre plate loads of 3, 6 and 9 kN. The contact stresses generated under these loads are equivalent to those that would be generated on the full size centre plate component under loads of 147, 294 and 441 kN respectively.

The service test cases that were studied throughout this research work are shown in Table 5.1 (Section 5.2). The measurement data for test case 10 however (Material B), was over written during the data acquisition process, due to another operator error. The service test results are presented in the same format as the running-in test results, discussing the global analysis results first, as these are used to obtain the peak torque responses over time as well as the Coefficients of Friction (COF) values.

The service test torque responses are then analysed from the local perspective, as this method is used to calculate the torsional stiffnesses and the breakout angles for the centre plate/wear liner samples as well as the frictional energies. The frequency responses of each test case are then analysed in detail during the first and last 25 cycles of the 10800 cycle service test. The system parameters obtained from these test results will then be used to develop an optimised Multibody Simulation (MBS) centre plate component model. The global analysis results for the 3 kN service test cases are discussed in the following section.

5.4.1. Global analysis results for the 3 kN service test cases

The global torque responses for materials A, B and C under the 3 kN centre plate loading conditions are shown in Figure 5.40. The green and yellow lines show the responses of material A and the blue and red lines, show the responses of materials B and C respectively. The torque responses of test cases 5 during the first 3 - 5 hours of the service test as can be seen (Yellow lines), are in the region of ± 11

Nm, which is similar to the levels of torque that were measured during test cases 8 and 12 using material B (Blue lines). The torque responses during test case 1 on the other hand (Material A), are seen to be the lowest overall at $\pm$ 5.25 Nm (Green lines). The torque responses for material C in test case 15 during the 3 – 5 hours of testing however (Red lines), are seen to be the highest overall at $\pm$ 18 Nm.

In Figure 5.40, it can also be seen that after 5 hours of testing for example, the torque responses in material C for example, start to decrease and after 15 hours of running, start to converge with the torque responses of test cases 5, 8 and 12 on materials A and B. The responses in material C are then seen to decrease even further over the next 10 hours of the test, until they eventually converge with the torque curves in test case 1 on material A (Green lines).

From the summary of the global analysis results shown in Appendix P, it can be seen that the frictional energies per cycle during test case 1 on material A were the lowest overall at 1.1 Joules (J) per cycle. Whereas the energies for materials B and C were seen to be the highest overall, ranging between 3.27 – 3.66 J per cycle. The percentage increases in the torque responses were also calculated and are seen to range between 78.9 – 105.9%, whereas the mean value for the complete data set (5 test cases), is seen to be 90.4% with a Standard Deviation (SD) of 11.6%. During the running-in test cases however, the mean percentage increase for the complete data set (17 test cases), was seen to be slightly lower at 76.9%, whereas the SD was significantly higher at 46.5% (Appendix N).

The final point to make is that the minimum torque value of 0.496 Nm that was measured during the running-in test cases under the 0.5 kN loading conditions for example, is 10 times lower than the minimum value that was measured under the 3 kN loading condition which was seen to be 5.25 Nm. The maximum value of 17.5 Nm on the other hand, is only 5 – 6 times higher than the maximum value that was measured during the running-in tests which is closer agreement with the expected behaviour. The centre plate load in the 3 kN cases for example, is six-times higher than the loading conditions that were used in the running-in test cases. The torque responses therefore, should also increase by a factor of six if the friction surfaces are perfectly smooth as well as flat. The following section discusses the global analysis results for the 6 kN service test cases.
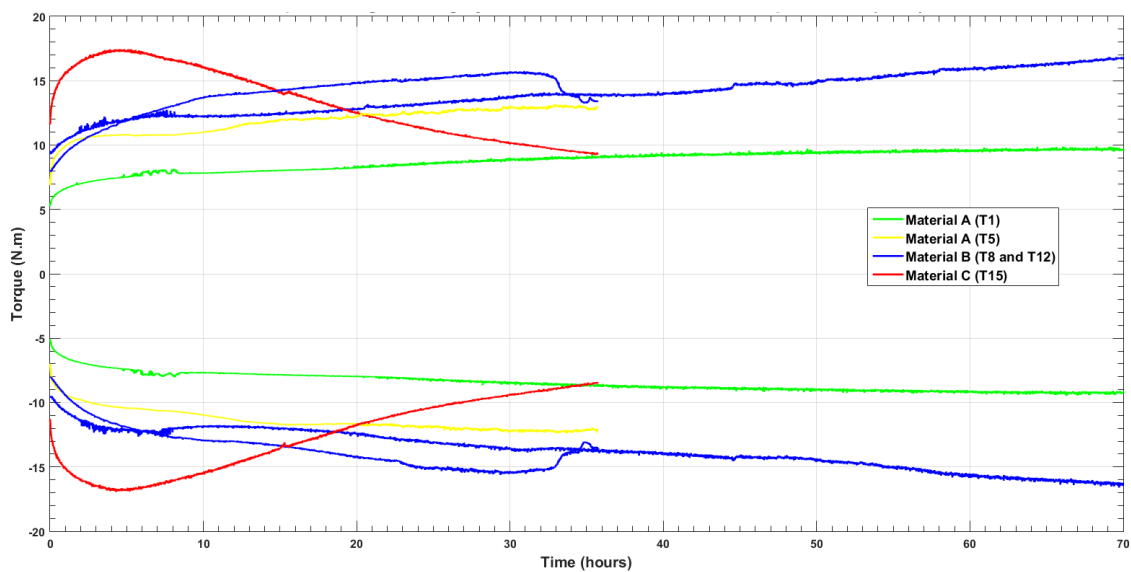
Figure 5.40: Global torque responses during the 3 kN service test cases.

5.4.2. Global analysis results for the 6 kN service test cases

The torque responses that were measured on the materials A, B and C under the 6 kN centre plate loading conditions are discussed in this section. The green and black lines in Figure 5.41 show the responses of material A and the blue and red lines, show the responses of materials B and C respectively. Three tests were carried out on material A due to repeating test case 2 which was running at the 0.042 Hz forcing frequency (Green lines).

The torque responses in test case 2 as can be seen, started to diverge from the nominal range of $\pm$ 15 Nm for this material after 30 hours of testing and by the end of the 72 hour service test, the responses were seen to be in the region of $\pm$ 44.8 Nm, which is similar to the torque responses during test case 9 on material B (Blue lines). After making this observation, it was then decided to repeat test case 2 with new centre plate/wear liner components in order to check the validity of this result, see test case 4 (Black lines). From these responses, it can be seen that this sample maintained a nominal, as well as a constant level of torque throughout the service test.

The wear liner sample that was used in test case 2 however (Material A), looked perfectly normal in comparison to the one used in test case 4 after a visual inspection, as well as in the post-test analysis results of the mass properties and surface roughness characteristics. This analysis therefore, was not conclusive in establishing the root causes of the instabilities that were seen to be developing in the torque responses of test case 2. The torque responses of the two test cases that were carried out using material B as can be seen, were also amongst the highest overall (Blue lines). The maximum torque during test cases 9 and 13 for example, are shown to be in the region of $\pm$ 40.4 Nm and $\pm$ 47.4 Nm respectively.

The torque responses of material C during test case 16 are seen to reach a maximum level of $\pm$ 25.2 Nm, after 12 – 13 hours of testing (Red lines). The torque is then seen to decrease gradually over the following 22 – 23 hours at a rate of 0.36 Nm per hour. Under the 3 kN centre plate load however, the maximum torque in material C was seen to reach $\pm$ 17 Nm then after 5 hours testing, the rate of decrease in torque response was shown to be in the region of 0.23 Nm per hour, which is 35% lower than the rate of decrease that was observed in the 6 kN loading case. The gradients of the slopes in Figures 5.40 and 5.41 look different due to the scaling used on the y-axes. In Figure 5.40 for example, the increments on the y-axis are every 1 Nm, whereas in Figure 5.41 below, they are every 4 Nm due to the increases in magnitudes of the torque responses.

From the summary of the results shown in Appendix P, it can be seen that the minimum and maximum frictional energies per cycle have increased by a factor of 2 – 3 relative to the 3 kN responses and are now seen to be in the region of 2.43 and 9.93 Joules per cycle respectively, see test cases 4 and 13 on materials A and B in Figure 5.41. The final point to consider are the percentage increases in torque responses under the 6 kN loading condition, which are seen to range between 13.8 – 251.8%. The mean percentage increase for the complete data set (6 test cases), is also significantly higher in comparison to the responses under the 3 kN loading conditions and is now seen to be in the region of 115% with a Standard Deviation (SD) of 81.2%.

Under the 0.5 and 3 kN centre plate loading conditions, the mean percentage increase in the torque responses were seen to be in the region of 76.9 and 90.4% respectively, whereas the SD were seen to be 45.6 and 11.6% This analysis strongly suggests that the friction characteristics of the centre plate/wear liner components are more sensitive to changes in the loading conditions than they are to changes in the angular velocity. This conclusion is based on the fact that the only parameter that has changed since the previous analysis, is the centre plate load. The following section discusses the global analysis results for the 9 kN service test cases.
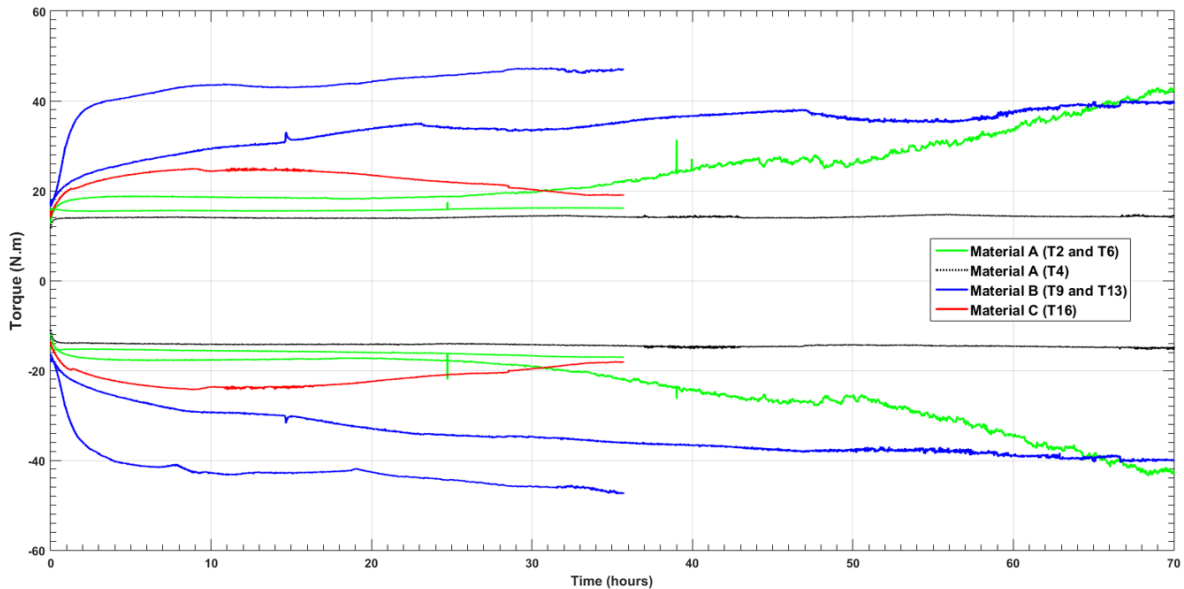
Figure 5.41: Global torque responses during the 6 kN service test cases.

5.4.3. Global analysis results for the 9 kN service test cases

The torque responses of the centre plate/wear liner components under the 9 kN centre plate loading conditions are discussed in this section. The torque responses of materials A, B and C are shown in Figure 5.42 by the green, blue and red lines respectively. From these it can be seen that the torque in the two tests that were carried out on material A for example, start off in the region of $\pm$ 17.5 Nm and by the end of 36/72 hour service tests, are seen to be in the region of $\pm$ 28.5 Nm which is a 62% increase in these torque responses.

The torque responses during test cases 11 and 14 on material B however, are seen to be the highest overall under the 9 kN loading condition, ranging between $\pm$ 26 − 28 Nm at the start of the test and by the end of the test, are seen to be in the region of $\pm$ 93.4 − 96.2 Nm, which is an overall increase of 270%, see the summary of results shown in Appendix P.

The torque responses of material C on the other hand, appear to be the most consistent overall and following the same pattern of behaviours throughout all of the service test cases. The torque responses as can be seen, reach the maximum value of $\pm$ 41.6 Nm after 5 hours of running, which is same time that the responses under the 3 kN loading condition reached the peak value of $\pm$ 17.5 Nm, before the responses started to decrease again. The rate of decrease under the 9 kN load however, is seen to be in the region of 0.4 Nm per hour, which is the highest rate out of decrease overall. It should also be pointed out, that material C is the only wear liner that exhibits the decreasing torque characteristics. Whereas the torque responses of materials A and B on the other hand, either remain at a constant level after the initial 3 − 5 hours of running, or increase as the number of cycles increases.

From the summary of results shown in appendix P, it can also be seen that the mean torque value for the complete data set under this loading condition (5 test cases), is $\pm$ 39.6 Nm with a Standard Deviation (SD) of 49.8%. Whereas under the 3 and 6 kN centre plate loads, the mean torque responses were seen to be in the region of $\pm$ 11.1 Nm and $\pm$ 23.2 Nm respectively, whereas the SD were 11.6 and 46.5%. This analysis also suggests that the torque response is directly proportional to the centre plate load.

The mean value analysis method however, can be misleading, as these results suggest that the relationship between the centre plate load and torque response for example, is linear. Whereas the

163

peak torque values that were measured during the 3, 6 and 9 kN service test cases, were seen to be in the regions of $\pm$ 17.5, $\pm$ 47.4 and $\pm$ 96.2 Nm respectively. This analysis on the other hand, suggests that the relationship between the torque responses and the centre plate load, is nonlinear.

The minimum frictional energy under the 9 kN centre plate loading condition is seen to 3.66 Joules (J) per cycle in Appendix P, whereas the maximum is 20.14 J per cycle, which is double in comparison to the maximum frictional energy that was calculated for the 6 kN loading condition. The percentage increases in the torque responses however, are seen to range between 31.8 – 270%, which is similar to the range of increases that were observed under the 6 kN loading conditions (13.8 – 251.8%).

The range of global torque responses that were measured under the 0.5, 3, 6 and 9 kN loading conditions are summarised in Table 5.4. The equivalent full scale loads and torques are also shown and from these results, it can be seen by looking at the mean percentage increases as well as the SD for example, that the torque responses become more nonlinear as the centre plate load increases. This completes the discussion on the global analysis torque responses. The following section discusses the Coefficient of Friction results that were calculated from the global torque measurements on materials A, B and C during the service tests.
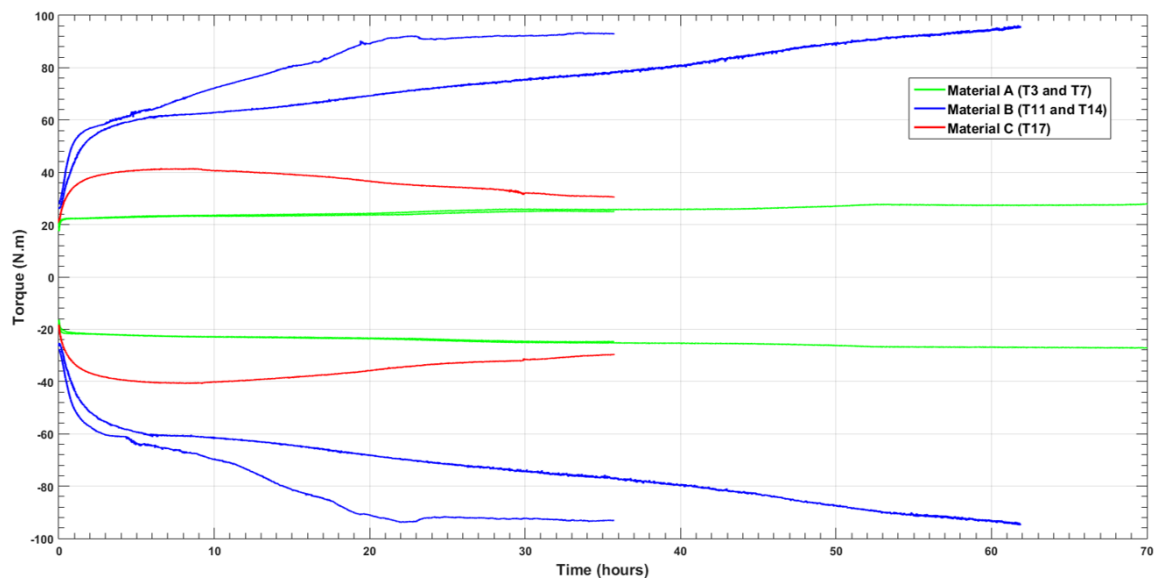
Figure 5.42: Global torque responses during the 9 kN service test cases.

1:7 scale centre plate load (kN)	1:7 scale centre plate inertia (kg.m²)	Min torque (Nm)	Max torque (Nm)	Mean torque (Nm)	Full scale centre plate load (kN)	Full scale centre plate inertia (kg.m²)	Full scale min torque (Nm)	Full scale max torque (Nm)	Full scale mean torque (Nm)	Min μ	Max μ	Mean μ	Min % increase	Max % increase	Mean % increase	Standard deviation of the percentage increase (%)
0.5	0.02145	0.50	3.20	1.85	24.5	360.5	172	1098	635	0.05	0.32	0.19	23.5	154.0	78.6	48.3
3	0.13	5.25	17.50	11.38	147	2184.9	1801	6003	3902	0.09	0.28	0.19	78.9	105.9	90.4	11.6
6	0.26	11.60	47.43	29.52	294	4369.8	3979	16268	10124	0.09	0.39	0.24	13.8	251.8	115.0	81.2
9	0.39	17.50	96.20	56.85	441	6554.7	6003	32997	19500	0.10	0.54	0.32	31.8	270.0	141.1	74.7
Maximum	0.39	17.50	96.20	56.85	441.0	6554.7	6003	32997	19500	0.10	0.54	0.32	78.9	270.0	141.1	81.2
Minimum	0.02	0.50	3.20	1.85	24.5	360.5	172	1098	635	0.05	0.28	0.19	13.8	105.9	78.6	11.6
Range	0.37	17.00	93.00	55.00	416.5	6194.2	5831	31899	18865	0.05	0.26	0.14	65.1	164.1	62.5	69.6
Mean	0.20	8.71	41.08	24.90	226.6	3367.5	2988	14091	8540	0.08	0.38	0.23	37.0	195.4	106.3	54.0
Standard deviation	0.16	7.42	41.11	24.20	180.5	2683.5	2544	14100	8299	0.02	0.11	0.06	28.9	78.5	27.7	31.6
Standard deviation (%)	79.7	85.1	100.1	97.2	79.6	79.7	85.1	100.1	97.2	26.9	29.9	27.5	78.1	40.2	26.1	58.6

Table 5.4: Summary of the global analysis results for the running-in and service tests.

5.4.4. Global analysis COF results for materials A, B and C

This section discusses the Coefficients of Friction (COF) values that were calculated from the service test torque measurements. The COF responses for the test cases that were carried on material A under 3 kN centre plate load are shown in Figure 5.43 by the green and yellow lines, whereas the blue and black lines, show the COF responses for the 6 kN loading cases and the responses during the 9 kN loading cases, are shown by the red lines. The black solid/dashed lines in these figures are the solutions to the power series friction models that were developed to model and quantify the differences in COF responses.

The black solid line for example, show the mean COF value for the material group as a function of time and the dashed lines, show the upper/lower confidence limits of the models. After a considerable amount of trial/error with different curve fitting procedures, the closet fit to the measured data points on materials A and B, was shown to be the power series function given in Equation (5.1). The constant coefficients, a, b and c, are then obtained from the curve fitting processes, see Table 5.5. The C_f terms in this equation are then used as a correction factor to adjust the boundaries of the power series models to find the best fit. The correction factor for the lower limit of Model 1 which was used to describe the COF responses of material A for example, was set to 0.63, whereas the upper limit was set to 1.57.

$$\mu(t) = (a.t^b + c).C_f \tag{5.1}$$

From the COF responses shown in Figure 5.43 however, it can be seen that there are still some differences between the torque responses in the CW/CCW directions under the 3, 6 and 9 kN centre plate loads. These differences however, are in the region of $5 - 10\%$, which are relatively small in comparison to the non-symmetric friction characteristics that were observed during the running-in test cases, which were seen to range between $20 - 62\%$.

The COF values that were calculated for material A under the 3, 6 and 9 kN centre plate loads as can be seen from the summary of results shown in Table 5.5 and Appendix Q, range between $0.09 - 0.36$. During the running-in tests however, the COF values were seen to be slightly lower, ranging between $0.05 - 0.195$, see Appendix O.

This analysis suggests that the COF values on material A for example, are dynamic and increase in proportion to the loading conditions as well as the number of running cycles. It can also be seen from this analysis that the power series models, despite the wide range of COF values, are in good agreement with the upper/lower boundaries of the COF responses for material A.
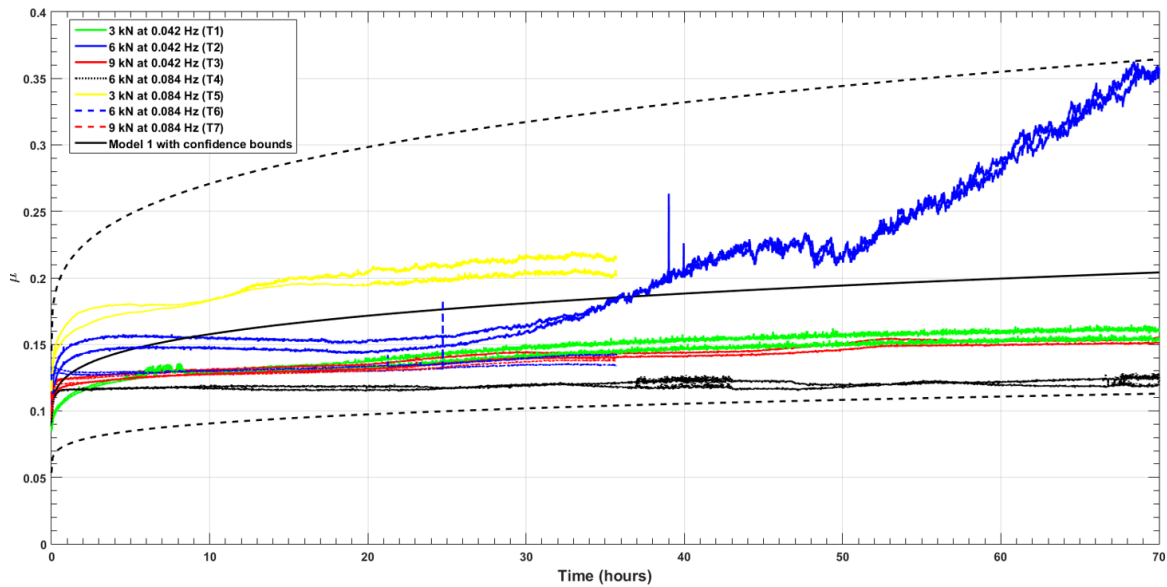
Figure 5.43: COF responses for material A during the 3, 6 and 9 kN service tests (Model 1).

Wear liner material	Friction model	Model coefficients			Correction factor (Cf)	Range of measured COF values
		a	b	c		
A	Model 1 (Mean)	0.0376	0.2642	0.0886	1	0.09 - 0.36
	Upper bound	0.0414	0.2861	0.0924	1.57	
	Lower bound	0.0338	0.2423	0.0848	0.63	
B	Model 2 (Mean)	0.1706	0.2646	0.0884	1	0.1 - 0.54
	Upper bound	0.1788	0.2727	0.0974	1.02	
	Lower bound	0.1623	0.2564	0.0794	1	
C	Model 1 (Mean)	0.0376	0.2642	0.0886	1.4	0.11 - 0.27
	Upper bound	0.0414	0.2861	0.0924	1.94	
	Lower bound	0.0338	0.2423	0.0848	0.82	

Table 5.5: Power series friction models parameters and the range COF values for each wear liner material.

The COF responses that were calculated for material B under the 3, 6 and 9 kN centre plate loading conditions are shown in Figure 5.44 by the green, blue and red lines respectively. The power series model that was used for this analyses as can be seen (Black lines, Model 2), was developed using the torque measurements from test case 14. This test case is seen to be the worst overall in terms of the peak torque responses as well as the rate of increase in these parameters.

From the responses shown in Figure 5.44, it is clear to see that Model 2 is in good agreement with the measured data points. It can also be seen that the lower limit of this model could provide a reasonable solution for test cases 11 and 13 with some adjustment via the correction factors. Also, from looking at the COF values for test cases 11, 13 and 14 for example, it is clear to see that this Model 2 is capable of describing the rapid increases in COF values during the first 3 – 4 hours of these tests, which appears to be a common characteristic in this wear liner material.

The COF responses that were calculated for material B after the service tests however, were seen to cover the widest range overall out of the three different wear liner materials that were tested, ranging between 0.1 – 0.54, see Table 5.5 above, or Appendix Q. The non-symmetric friction characteristics in this material under the service test loading conditions on the other hand, are all seen to be below 5%.

This analysis also strongly suggests that the non-symmetric friction characteristics of the centre plate/wear components for example, are influenced not only by the Bauschinger effect, kinematic

hardening, and geometric differences in the contact surfaces, but also by the centre plate loading conditions. What is also interesting to see, is the softening behaviour developing during the latter stages of test case 12 after 32 hours of testing (Green lines), which was running under the 3 kN loading condition and at 0.084 Hz (Tottle, 1966) and (Bertram & Gluge, 2013).
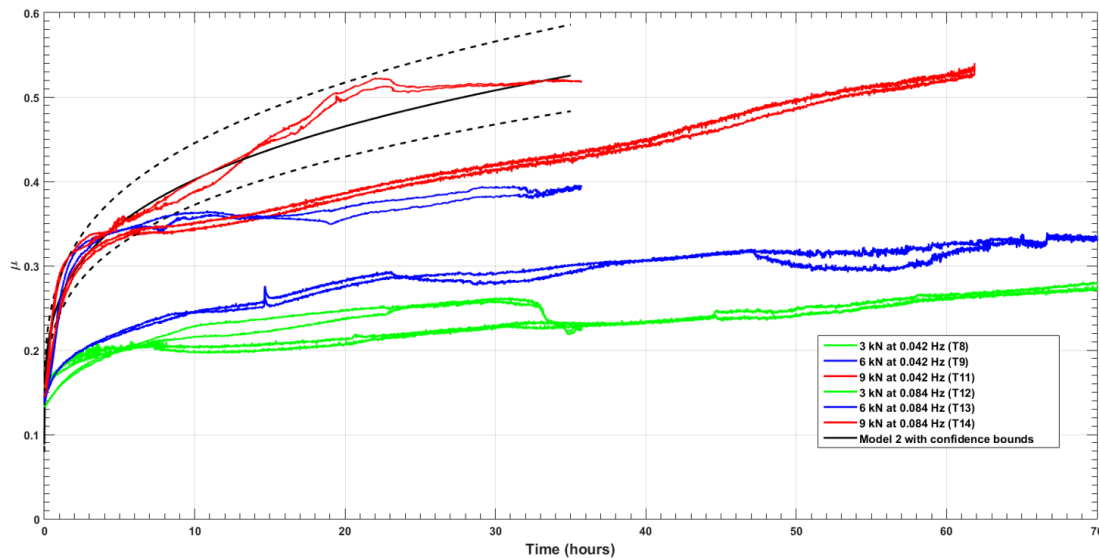
Figure 5.44: COF responses for material B during the 3, 6 and 9 kN service tests (Model 2).

The COF responses that were calculated for material C after the 3, 6 and 9 kN service tests are shown in Figure 5.45 by the green, blue and red lines respectively. From these responses, it can be seen that the non-symmetric friction characteristics in material C, are now less than 5% in all three test cases, whereas under the 0.5 kN loading conditions these parameters were seen to range between $50 - 65\%$. From the analysis of the running-in/service test COF responses, it is clear to see that the loading conditions have a significant influence on the non-symmetric friction characteristics of the centre plate/wear liner components.

The power series model that was fitted to the measurement data of material A (Model 1), was also used to quantify the COF responses of material C. The upper/lower limits and the mean values of the model however, had to be adjusted to 1.94, 0.82 and 1.4 respectively, whereas on material A, the upper/lower limits and mean values were shown to be 1.57, 0.63 and 1 respectively, see Table 5.5. From these results, it can be seen that COF values for material C, range between $0.11 - 0.27$.

This analysis method clearly shows that material A has the most stable band of COF values out of three materials during the first 15 hours of the service tests. Whereas after $15 - 20$ hours, the COF responses in material C are then seen to decrease significantly and converge to the same region of COF values, at the same point in time. This finding seems pretty remarkable, considering all of the highly nonlinear phenomenon associated with dry friction and tribology in general, see for example (Moore, 1975) or (Popov V. , 2010). The final COF values in material C as can be seen, all range between $0.14 - 0.17$, whereas the upper limit of the model on the other hand, predicts a COF value of 0.39, which is far too high for this particular material.

From the responses shown in Figure 5.45 it can be seen that the upper limit of the power series model for example, is in good agreement with the measurements of test case 15 during the first 5 hours of testing. Whereas the mean line of the power series model over the same period, is seen to be in better agreement with test cases 16 and 17 (Blue and red lines). However, between $25 - 35$ hours, it can also be seen that the lower limit of the power series model is seen to be in better agreement with the

measurements. The majority of COF values that were calculated for material A on the other hand, remained within the limits of the lower boundary and the mean line of the power series model throughout the service tests, apart from test case 2 and test case 5, which was the contaminated wear liner sample.

The final points to make on the COF responses of material C, are that this material is the only one to exhibit the decreasing friction characteristics out of the three that were tested. This material also appears to be the most consistent overall as the COF values after 20 hours of testing under the 3, 6 and 9 kN centre plate loads as can be seen, are seen to almost the same, whereas for materials A and B on the other hand, the COF values were seen to cover a much wider range at the end of the service tests. The COF responses discussed in this section will now be used to develop an optimised Multibody Simulations (MBS) secondary suspension evolutionary friction model. The following section discusses the methods that were used to develop the evolutionary friction models.
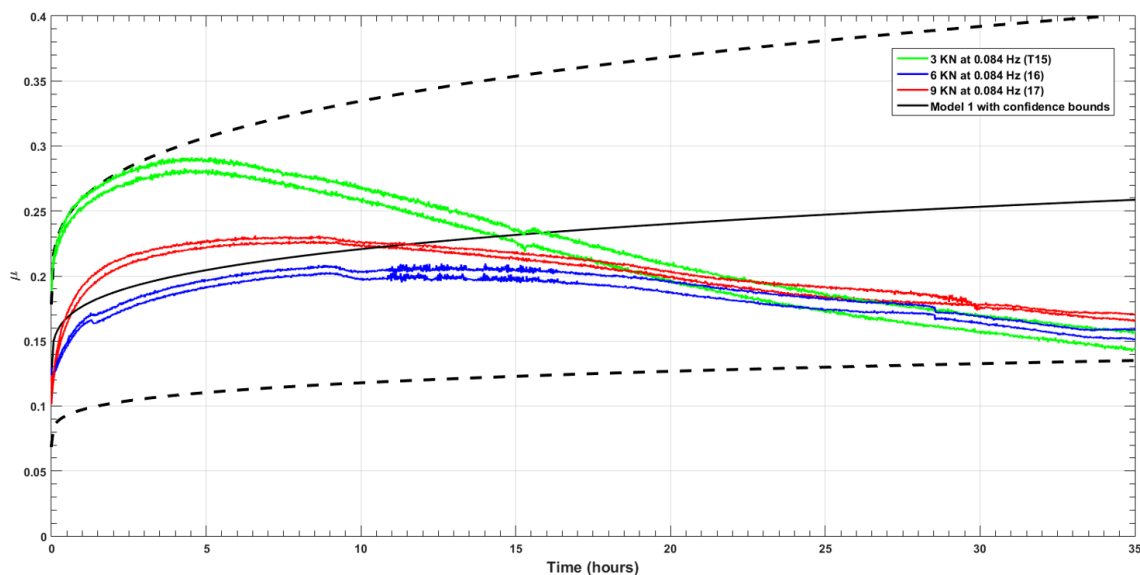
Figure 5.45: COF responses for material C during the 3, 6 and 9 kN service tests (Model 1).

5.4.5. Global evolutionary friction models

This section discusses the global evolutionary friction models that were developed from the torque measurements on materials A, B and C during the service tests. The post-test analysis of the service test results showed that the COF values that were calculated for material A for example, ranged between $0.09 - 0.36$. Whereas for materials B and C, the COF values are seen to range between $0.13 - 0.54$ and $0.11 - 0.27$ respectively in Appendix Q.

The COF values that were calculated for material A during the running-in test cases on the hand, were seen to range between $0.05 - 0.195$ which suggests that the peak COF value under the service test loading conditions has increased by 85% (3, 6 and 9 kN). The COF values for material B during the running-in test cases however, were the seen highest overall, ranging between $0.09 - 0.32$. The peak value under the service test loading cases therefore, has increased by 69%. Whereas for material C, the COF values were seen to range between $0.116 - 0.283$ after the running-in tests, which is approximately the same as the range of COF values that were calculated after the service tests.

This analysis strongly suggests that material C is the most consistent material out of the three that were tested during this research work. It also suggests that each wear liner material requires a `tailored made` evolutionary friction model to describe the changes in friction characteristics as a

function of time. Therefore, based on the knowledge and experience gained from our observations and analyses of the running-in/service test case responses in the laboratory, the power series models discussed in the previous section have now been optimised to meet this requirement.

From the complete data set of COF results shown in Appendix Q (16 test cases), five evolutionary friction models were then developed to describe the changes in friction characteristics of the three wear liner materials as a function of time, see Figure 5.46. These power series models were also developed using Equation (5.1) and the constant coefficients and correction factors shown in Table 5.6.

Model	Material	Test case	Predicted range of COF values	a	b	c	SSE	R-Square	Adjusted R-Square	RMSE	Correction factor (Cf)
1	B	11	0.055 - 0.117	0.025	0.559	0.236	1.193	0.963	0.963	0.013	0.65
2	B	11	0.1 - 0.235	0.026	0.569	0.239	1.193	0.963	0.963	0.013	1.15
3	B	9	0.095 - 0.4	0.097	0.222	0.078	0.106	0.991	0.991	0.004	1.22
4	B	14	0.09 - 0.535	0.171	0.265	0.088	0.630	0.972	0.972	0.013	1.02
5	B	8	0.24 - 0.54	0.038	0.264	0.886	0.009	0.945	0.944	0.003	1.03

Table 5.6: Summary of the evolutionary friction model parameters.
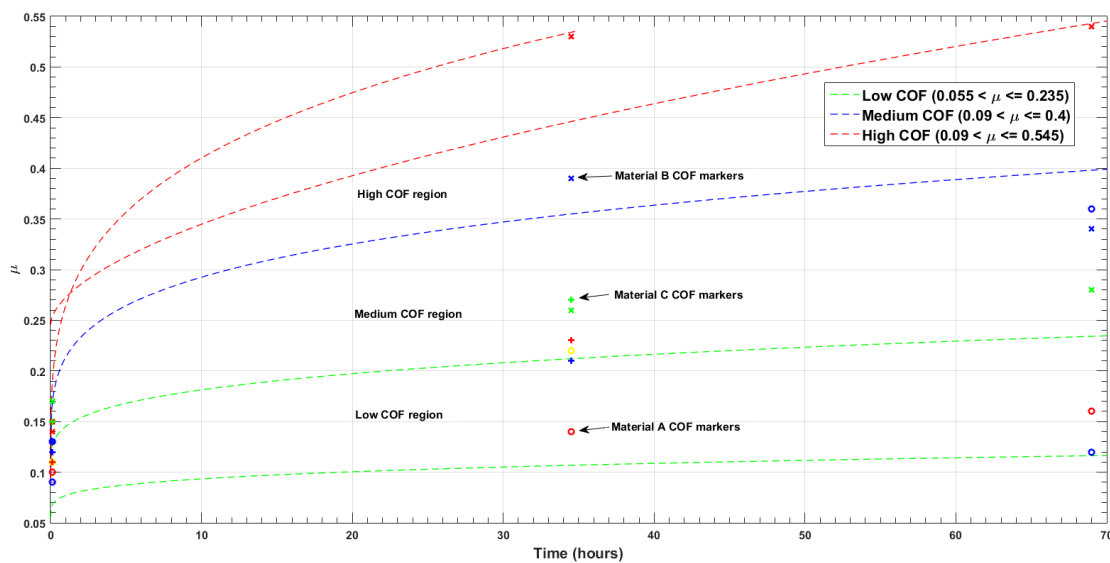
Figure 5.46: Evolutionary friction models plotted against the service test COF values.

The solid green lines for example, show the two power series models that were used to describe the low COF region, which includes COF values ranging from $0.055 - 0.235$. The green, blue and red circles in this figure, show the COF values for material A under the 3, 6 and 9 kN centre plate loads respectively. Whereas the yellow circle, shows the COF value for test case 5, which was the contaminated wear liner sample. This model as can be seen, is in good agreement with the majority of the test cases for material A. Test case 2 however (Blue circle), which was running under the 6 kN centre plate loading condition and at 0.042 Hz, is seen to be in the medium COF because the peak COF value during this test case was seen to be in the region of 0.36, which is above the upper limit of low COF region.

Figure 5.47 shows a close-up of the calculated COF values plotted against the evolutionary friction model predictions. The COF values for material C during the 3, 6 and 9 kN loading cases are shown in this figure by the green, blue and red plus signs respectively, whereas the crosses show the COF values for material B. From this, it can be seen that the majority of the initial COF values for materials A, B and C during the service test cases for example, start off in the low-medium COF regions. Test case 8

on material B however, did not fit this trend as the initial COF value was seen to be in the region of 0.17 (Green cross).

The power series models describing the medium and high COF regions were then developed to accommodate COF values ranging from 0.095 – 0.4 and from 0.09 – 0.545 (Blue and red lines). From the results shown in Figure 5.47, it can be seen that all of the initial COF values for materials A, B and C, now fall within one of three COF regions. The model and error estimation parameters for the low, medium and high COF power series models are also shown in Table 5.7 with the material and test cases that were used to develop the individual evolutionary friction models. This analysis suggests that the power series friction models provide a good representation of the evolutionary friction characteristics of the three different wear liner materials.

The evolutionary friction models can now be used in Multibody Simulations (MBS) to update the frictional torque and COF parameters for example, either manually or automatically during the numerical routine. These models as can be seen, are capable of describing the steep rises in the COF values observed during the initial stages of the running-in/service test cases, as well as the gradual increases in COF values over time. The following section discusses the local analysis results for materials A, B and C during the service tests.
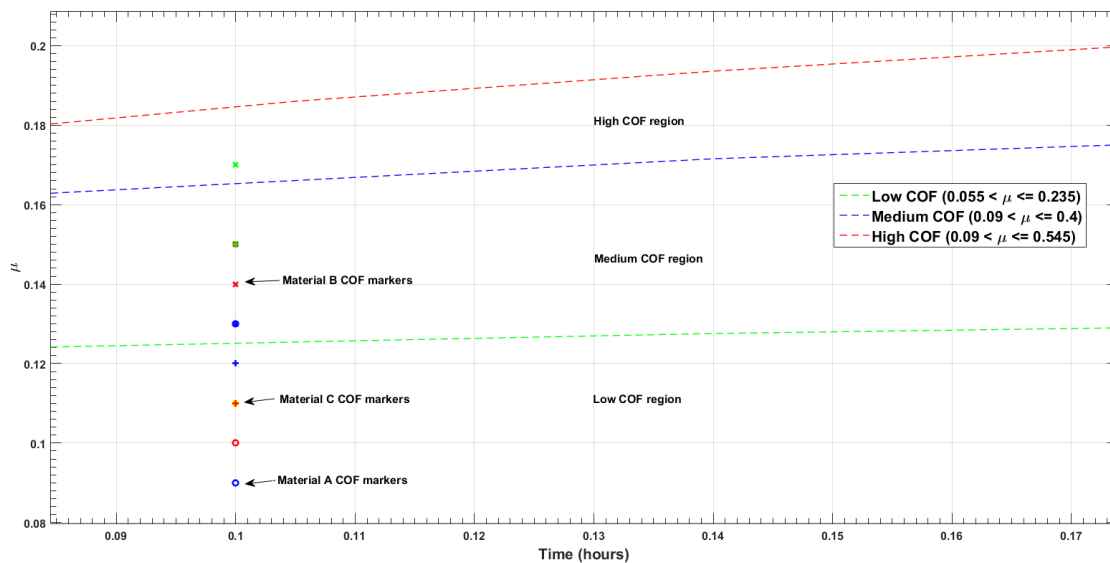
Figure 5.47: Close-up of the initial COF values during the service tests.

5.4.6. Local analysis results for the service test cases

The local analysis results for materials A, B and C during the service test cases are discussed in this section. From the hysteresis responses for example, the breakout/stick and slip Coefficient of Friction values for each wear liner sample are calculated, as well as the torsional stiffness parameters and breakout angles using the data points shown in Figure 5.47. These data points as can be seen, contain the angular displacement/torque values which are then substituted into Equation (5.2) to calculate the torsional stiffness, where $d\theta$, dM and K_τ, represent the differential angular displacement, friction moment and torsional stiffness.

The amplitudes of the breakout and slip frictional torques are also measured from the hysteresis responses and then substituted into Equation (5.3) to calculate the shear stresses in the centre plate/wear liner components. In this equation, R is the effective radius of the centre plate and A is surface area of the contact interface. Dividing the shear stresses by the breakout angles, then gives

the shear moduli of each material sample. The natural frequencies under the 3, 6 and 9 kN loading conditions were also calculated from the stiffness and system inertial parameters.

The results for materials A, B and C during the service tests are discussed in this section using the same format that was used in post-test analyses of the running-in test results. The service tests however, ran for 10800 cycles and for either 36 or 72 hours, depending on the forcing frequency that was used in the test. The responses of each test case in this study therefore, are measured during the first/last 25 cycles of the service tests and between cycles 5375 – 5400, which is the halfway point of the service test. The local analysis results for material A are discussed in the following section.
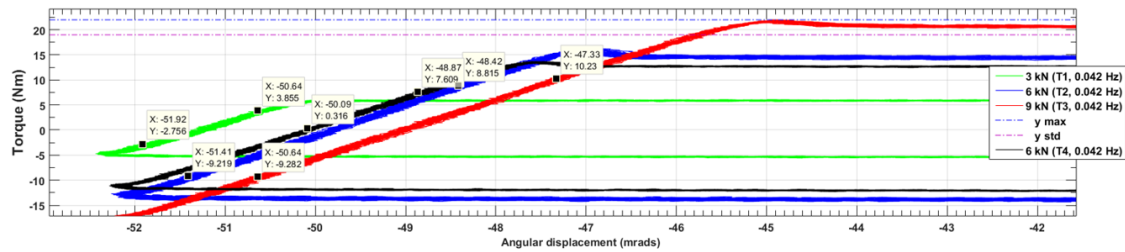
Figure 5.48: Data points to calculate the torsional stiffness and breakout angles for the wear liner samples.

$$d\theta_{breakout} = \frac{dM}{K_\tau} \qquad (5.2)$$

$$\tau = \frac{3.M}{2.R.A} \qquad (5.3)$$

5.4.6.1. Local analysis results for material A

The hysteresis responses of material A during the first 25 cycles of the service tests are shown in Figure 5.49. The top and bottom parts of these figure shows the responses of the 0.042 and 0.084 Hz test cases respectively. The green, blue and red lines, show the responses for the 3, 6 and 9 kN loading cases, whereas the black and yellow lines, show the responses of test cases 4 and 5, which were running under the 6 and 3 kN centre plate loads. Test case 4 however, is a repeat of test case 2, whereas test case 5, is the response of the contaminated sample which appears to be performing better under the 3 kN centre plate load.

The stick torque responses during the first 25 cycles of the service tests as can be seen from the summary of results shown in Appendix R for example, range between 6.2 – 22.3 Nm/rad, whereas the slip torque responses are slightly lower, ranging between 5.4 – 19 Nm/rad. This analysis suggests that the stick torque is 17% higher than the slip torque. The torsional stiffness under the service test loading conditions has also increased and now seen to be in the region of 5188 – 6226 Nm/rad, whereas during the running-in tests, the torsional stiffness was seen to range between 1418 – 4819 Nm/rad. This analysis suggests that there has been a 29% increase in the peak torsional stiffness as a result of increasing the centre plate load from 0.5 to 9 kN, see test case 7 in Figure 5.49 (Red lines).

The range of natural frequencies for material A during the service tests however, has decreased to 19.7 – 34.4 Hz due to the increases in centre plate loading conditions. During the running-in tests for example, the natural frequencies for this material were seen to range between 40.9 – 75.4 Hz. The shear stresses were also calculated as part of the local analyses and as can be seen from the results shown in Appendix R, the stresses during stick/breakout and slip events, are seen to range between 120.5 – 435.8 kN/m² and 106.7 – 372.2 kN/m² respectively. The shear moduli`s of the material samples

during the breakout and slip events were then calculated and are seen to range between 20.3 – 101.6 MN/m² and 14.2 – 89.9 MN/m² respectively.

The normal stresses under the 3, 6 and 9 kN centre plate loading conditions as can be seen in Appendix R, range between 1135.5 – 3406.4 kN/m², which are seen in good agreement with the pre-calculated values given in Table 3.2, Section 3.3. The COF values during the first 25 cycles of the service tests on material A were also calculated and shown to be in the range of 0.09 – 0.16. The last set of system variables to be quantified, are the frictional energies per cycle, which are seen to range between 1.13 – 4.63 Joules (J) per cycle. The energy parameters of the individual test samples will now be used to validate the dynamic response of the Multibody Simulations (MBS) centre plate friction model.
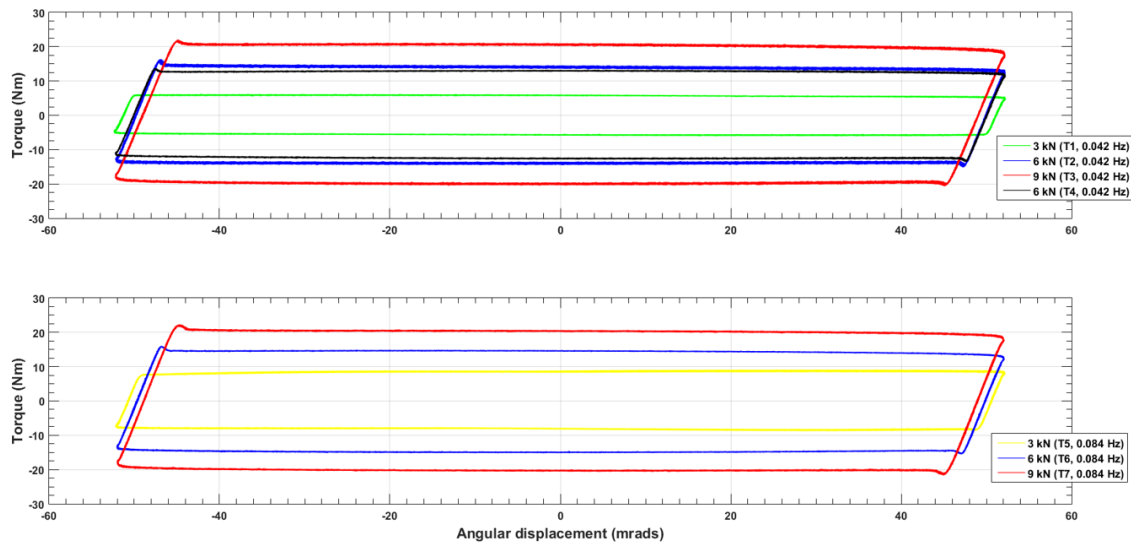
Figure 5.49: Hysteresis during the first 25 cycles.

The hysteresis responses during cycles 5375 – 5400 of the 0.042 and 0.084 Hz service tests are shown in Figure 5.50. From these responses, it can be seen that the peak torque during test case 2 for example (Blue lines, top plot), has increased from 16.3 to 29.4 Nm and is now seen to be the highest overall during this stage of the service test. This test case however, was running under the 6 kN centre plate load, whereas test case 3 on the other hand (red lines), was running under the 9 kN centre plate load, so you would expect this torque response to be the highest overall, but it isn`t for some unknown reason and is seen to be slightly lower at 25.9 Nm.

During the first 25 cycles as can be seen in the top plot of Figure 5.49 on the other hand, the torque responses in test case 3 were the highest overall at 22 Nm, which they should be as this test was running under the 9 kN loading condition. Test case 2 therefore, was repeated due to this peculiar result, see test case 4 and as can be seen (Black lines), this response now appears to be in line with the expected behaviour i.e. The torque responses of the 6 kN loading cases for example, should lie in between the responses of the 3 and 9 kN cases.

The responses of the 0.084 Hz test cases, which are shown in the bottom plot of Figure 5.50, appear to be more stable in comparison to the responses of the 0.042 Hz test cases. From the summary of results shown in Appendix R, it can be seen that the mean torsional stiffness for the complete data set (7 tests), has increased by 13.5 %, from 5188 Nm/rad during the first 25 cycles, to 5883 Nm/rad during cycles 5375 – 5400. Whereas the mean values of the stick and slip shear stresses and COF values on the other hand, have increased by another 23%.
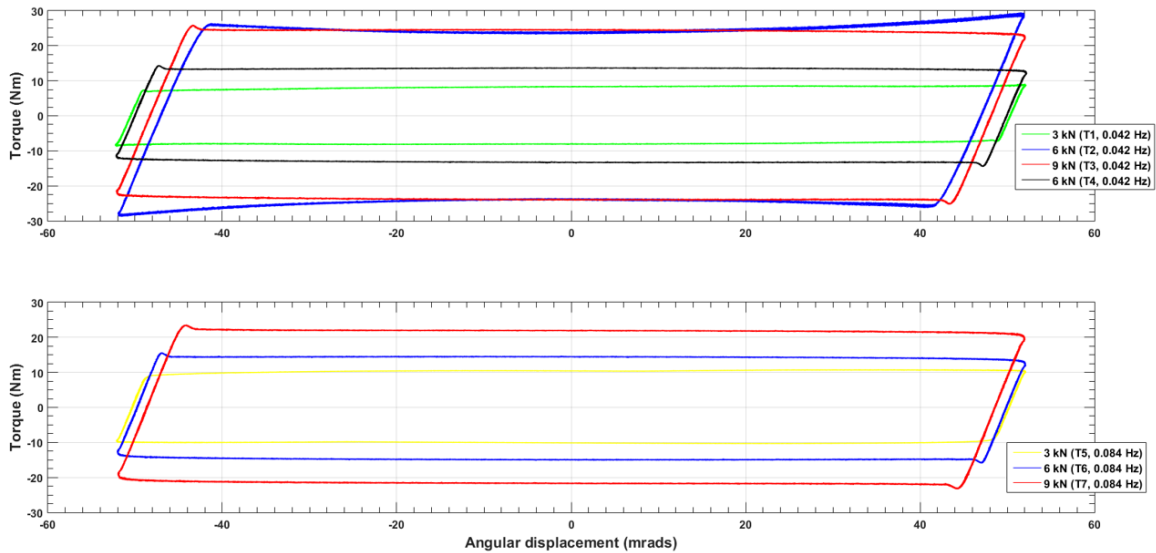
Figure 5.50: Hysteresis during cycles 5375 – 5400.

The hysteresis responses during the last 25 cycles of the service tests are shown in Figure 5.51 and from these, it can be seen that there have been some significant changes as well as increases in the torque responses/characteristics of test case 2 (Blue lines). The peak torque for example, is now seen to be in the region of 44.6 Nm, which is a 52% increase relative to the peak torque that was measured during cycles 5375 – 5400. A step has also started to develop in the breakout regions of test case 2, hence there are two breakout events in this response, see the close-up of the second one shown in Figure 5.52.

The breakout angles of the sample that was used in test case 2 are also the largest overall, ranging from 3.73 to 7.71 mrad during the various stages of the service tests, see Appendix R. Whereas the mean values for the complete data set, are seen to ranges between 2.52 – 3.6 mrad. The increases in the torque responses during test case 2 were also seen to be the highest overall at 251.8%. This analysis also suggested that there was an underlying issue with the centre plate/wear liner components that were used in test case 2 and this is why the test was repeated.

From the responses of the 0.084 Hz test cases shown in the bottom plot of Figure 5.51 (test cases 5, 6 and 7), it can be seen that the peak torque for example, has increased by another 1 – 7% relative to the previous analyses, which suggests the that the surfaces are now worn-in. This suggestion is also supported by the summary of results shown in Appendix R, where the mean torsional stiffness for the complete data set during the last 25 cycles of the service test for example, is seen to be in the region of 5897 Nm/rad. Whereas during cycles 5375 – 5400, the stiffness was 5883 Nm/rad.

However, although the responses of the centre plates/material A now appear to be finally stabilising after 10800 cycles of testing, it can be seen that the Standard Deviations (SD) of the torque responses during the last 25 cycles for example, range between 55.8 – 57.6% (Appendix R). This suggests that the responses are becoming more widely dispersed about the mean values as the number of cycles increases. The SD prior to this analysis, were closer to the mean values and seen to be in the region of 40%. The following section discusses the local analysis results for material B.
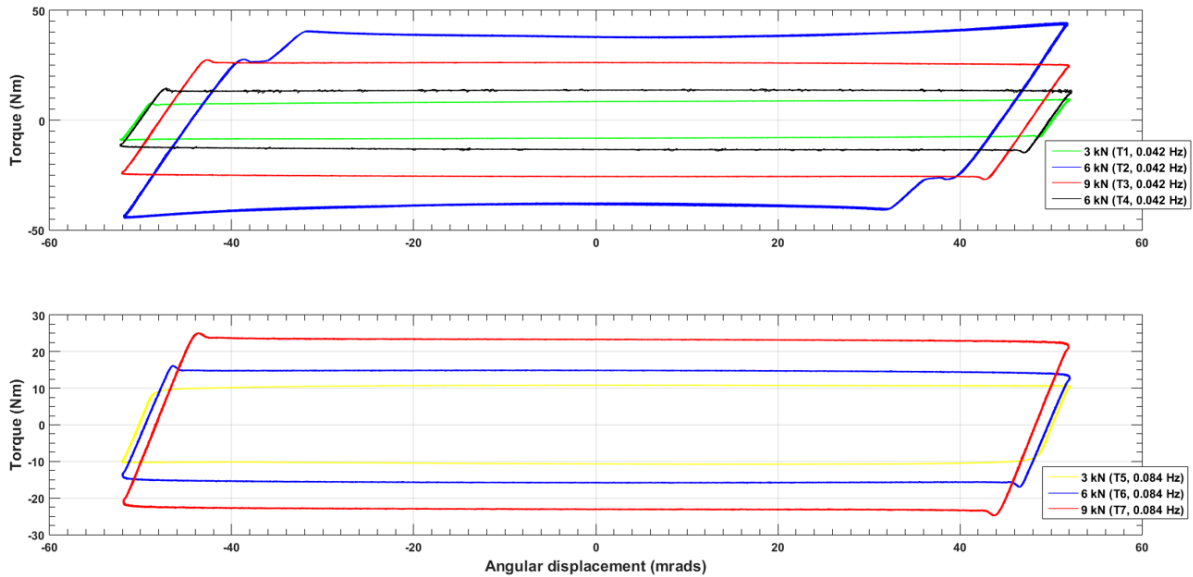
Figure 5.51: Hysteresis during the last 25 cycles.
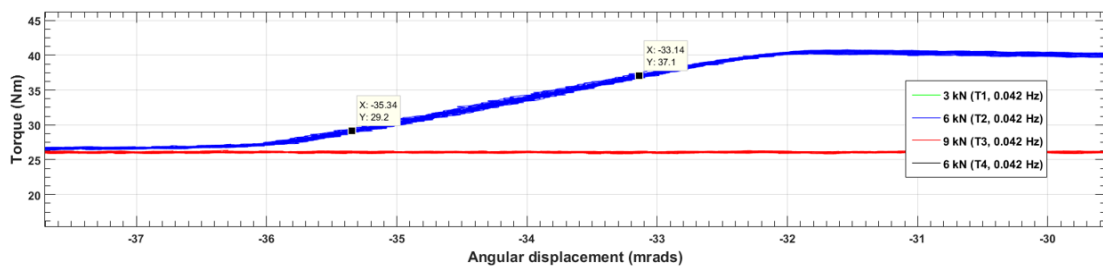
Figure 5.52: Close-up of the second breakout event during test case 2.

5.4.6.2. Local analysis results for material B

This section discusses the hysteresis responses of material B during the service test cases. Figure 5.53 shows a close-up of the breakout events taking place in this material and Figure 5.54 shows the hysteresis responses during the first 25 cycles of the 3, 6 and 9 kN centre plate loading cases, which are shown by the green, blue and red lines respectively. The test cases that were running at the 0.042 and 0.084 Hz forcing frequencies are then shown in the top and bottom plots respectively. From these responses, it is clear to see the differences in torque responses during the sticking/breakout events and the gross-sliding regimes under all three loading conditions.

The stick torque during the first 25 cycles for example, is seen to range between 8.5 – 36 Nm, whereas the slip torque, is 67% lower, ranging between 5.5 – 21.6 Nm, see Appendix R. The stick torque for material A however, was only 17% higher than the slip torque. The mean torsional stiffness of material B for the complete data (6 tests), is seen to be 5638 Nm/rad, whereas for material A, the mean stiffness during the first 25 cycles was seen to be slightly lower at 5897 Nm/rad. The range of natural frequencies for material B under the service test loading conditions therefore, are similar to material A, ranging between 18 Hz – 32 Hz.

From the close-up of the torque responses it can be seen that the transition events during test case 11 for example (Red lines in Figure 5.53), take place over a distance of 2.47 mrad. The final breakout events then take place in the regions of $\pm$ 41 mrad. This is the region where a finite amount of elastic energy that was stored in the centre plate/wear liner components during the pre-sliding displacement events, is returned back to the system just before the system is seen to fully transition into the gross-

sliding regimes. The stick torque during the 3 kN loading cases for example (Green lines), is seen to be 55% higher than the slip torque. Whereas during the 6 and 9kN loading cases, the stick responses are seen to be 50 and 66% higher than the slip responses.

The stick and slip shear stresses for material B during the first 25 cycles of the service tests are also significantly higher than the stresses in material A and are seen to range between $166.1 - 705.2$ kN/m² and $108.3 - 422.1$ kN/m² respectively, see Appendix R. The mean value for the stick shear moduli for the complete data set using material B however (6 tests), is slightly lower at 110.4 MN/m², whereas the mean value for material A was 115.4 MN/m². The slip shear modulus for material B is seen to be 69.6 MN/m², which is also lower than the slip shear moduli that was calculated for material A during the first 25 cycles of the service tests (99.8 MN/m²).

The COF values for material B during this stage of the service tests as can be seen in Appendix R, range between $0.1 - 0.21$. The minimum values in this range therefore, are in close agreement with the minimum COF values for material A. Whereas the peak COF value of 0.21 on the other hand, is significantly higher than the peak value that was calculated for material A, which was seen to be 0.16. The frictional energy responses for material B also cover a much wider range in comparison to the energies of material A, ranging between $1.76 - 7.49$ J per cycle.
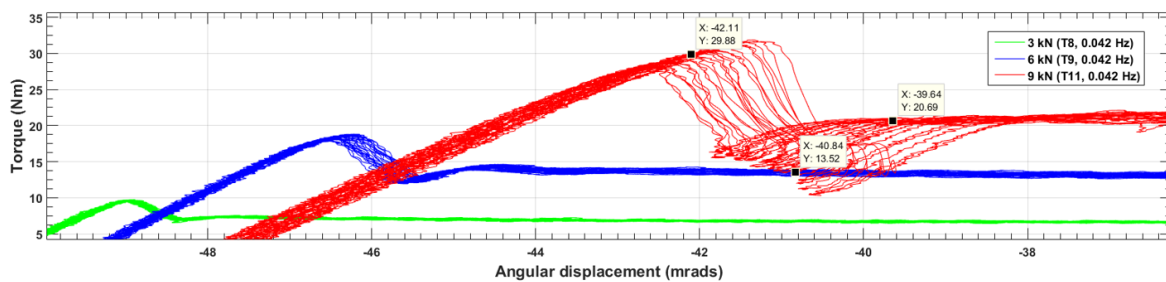
Figure 5.53: Close-up of the stick-slip response during test case 11.
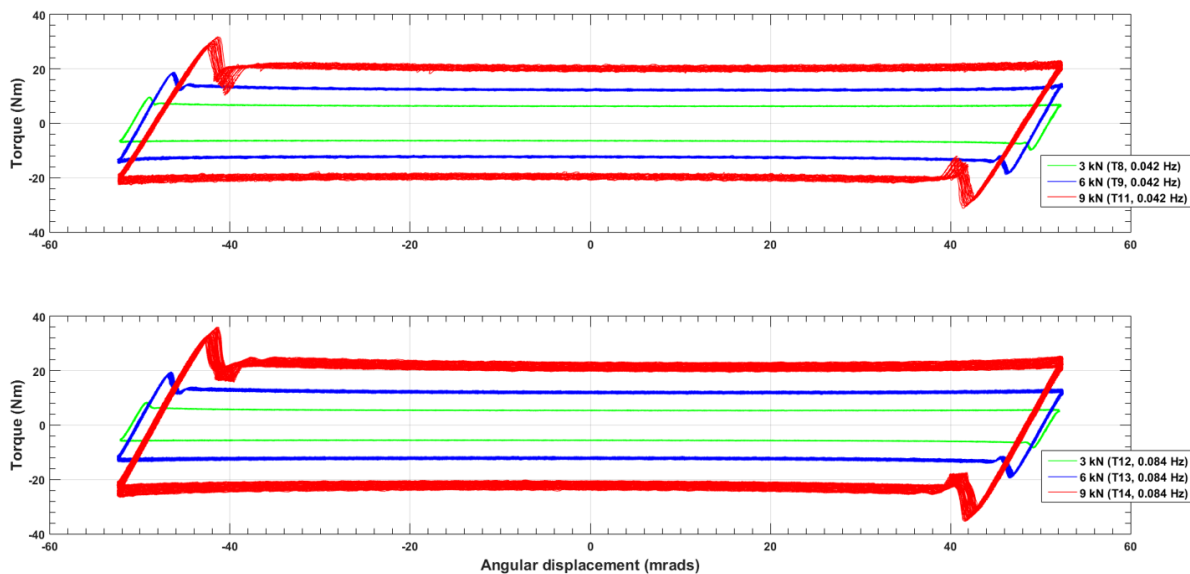
Figure: 5.54: Hysteresis during the first 25 cycles.

The responses of material B during cycles $5375 - 5400$ of the service tests are shown in Figure 5.55 and from these, it can be seen that there have been a number of significant developments in the friction characteristics of these test cases. Test case 11 which was running under the 9 kN centre plate load and at the 0.042 Hz forcing frequency for example (Red lines in the top plot), is now seen to be

exhibiting intermittent stick-slip behaviour during the Clockwise (CW+) as well as Counter-Clockwise (CCW-) rotations. Half of the response is seen to be sliding, whilst the other half is seen to be sticking and slipping.

From the close-up of the stiction/breakout region shown in Figure 5.56, it can be seen that the material stiffness during test case 11 for example (Red lines), decreases from 5650 Nm/rad to 3357 Nm/rad during the transition events. These characteristics can also be observed in the torque responses of test case 9 which was running under the 6 kN centre plate load (Blue lines). The stick torque in test case 9 however, has increased by 89% relative to the first 25 cycles, whereas in test case 11, this parameter increased by another 132%. The 3 kN test case on the other hand (Green lines), saw the lowest increase in torque overall at 40%.

It can also be seen from the close-up shown in Figure 5.56, that the wavelength of the stick-slip cycles in test case 9 for example, is in the region of 3 – 4 mrad, whereas the total sliding distances between the breakout regions is approximately 78 mrad. The frequency of the stick-slip cycles therefore, ranges between 19.5 – 26 Hz, which is seen to be in close agreement with the natural frequencies of the centre plate/wear liner components under the 6 and 9 kN loading conditions, see Appendix R.

The responses of the 0.084 Hz forcing frequency test cases, which are shown in the bottom plots of these figures, also appear to be smoother in comparison to the responses of the 0.042 Hz tests, with the exception of test case 14 (Red lines). The torque response during this test case as can be seen, is constant whilst the centre plate is rotating in the CW direction, whereas in the CCW direction, stick-slip behaviour appears to be dominating the responses.

This response therefore, appears to be another form of a non-symmetric friction characteristic, as the magnitudes of the torque responses in the CW/CCW directions are seen to be the same, whereas the friction characteristics in these directions, are completely different. This analysis therefore, also suggests that the friction characteristics are also strongly dependent on the sliding direction as well as the centre plate loading condition (Zimmermann, Zeidis, Pivovarov, & Abaza, 2006).

The stick torque in test cases 13 and 14 has also more than doubled in comparison to the torque that was measured during the first 25 cycles (Blue and red lines). The peak torque responses in these two test cases for example, are now shown to be in the region of $\pm$ 43.7 and $\pm$ 86.7 Nm respectively, see the summary of results shown in Appendix R. During the first 25 cycles, the stick values were seen to be in the region of $\pm$ 19.6 and $\pm$ 36 Nm. These mean values for the stick and slip shear stresses for the complete data set have also more than doubled since the previous analysis and are now seen to be in the region of 876.2 and 691.7 kN/m² respectively which is also seen to be the case for the energy responses.

From the summary of results shown in Appendix R, it can also be seen that the peak COF value at this stage of the service tests is 0.5 (Test case 14, red lines), whereas the minimum COF value is seen to be 0.2 (Test case 8, green lines). The SD of the mean COF value has also increased from 10.6 to 29.9%, which suggests that the responses are becoming more nonlinear as the number of cycles increases.
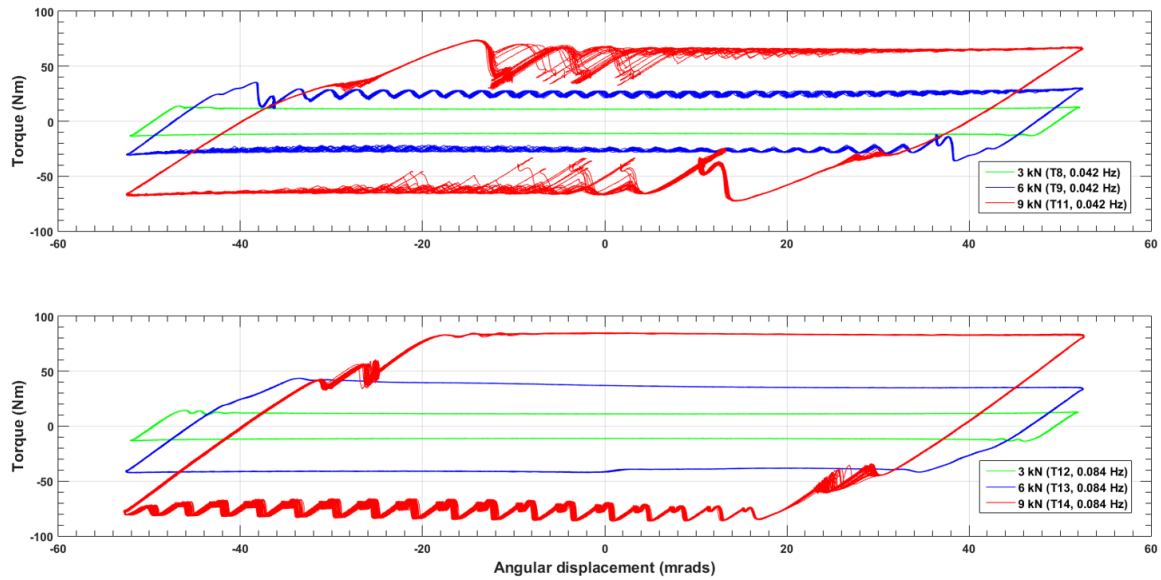
Figure 5.55: Hysteresis during cycles 5375 – 5400.
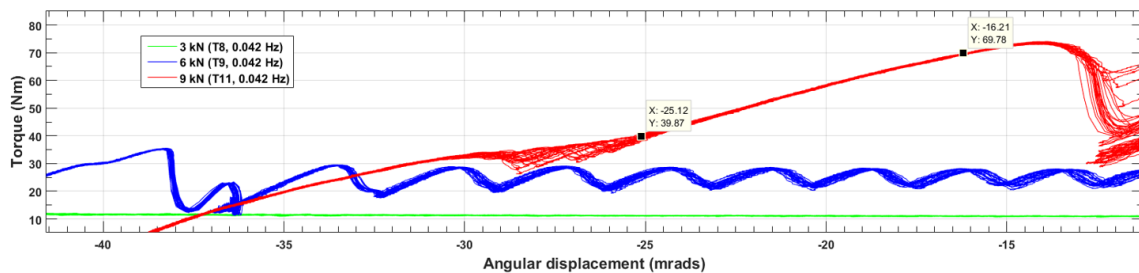
Figure 5.56: Close-up of stick-slip responses in test case 9 and the breakout events in test case 11.

The hysteresis responses during the last 25 cycles are shown in Figure 5.57 and as can be seen, test case 9 which was running under the 6 kN centre plate load and at the 0.042 Hz forcing frequency (Blue lines, top plot), has now transitioned into fully developed stick-slip behaviour. The torque response during the sticking events has also increased relative to the previous analysis from $\pm$ 35.6 to $\pm$ 40.1 Nm. Whereas the torque during the slipping events, has increased from 25.5 to 25.6 Nm, which shows that the slip torque responses in test case 9, are 36% lower than the stick responses. The stick and slip torque responses in test case 11 have also increased from 74 to 91.4 Nm and from 56.5 to 71.7 Nm respectively relative to the previous analyses. The slip torque in this sample therefore, is 23% lower than the stick torque.

The torque responses of test case 14 as can be seen in the bottom plot of Figure 5.57 (Red lines), have also transitioned into full stick-slip behaviour instead of gross-sliding, which is then seen to taper-off slightly in the regions of $\pm$ 52 mrads. Between –52 and 0 mrad of the hysteresis curve and when the torque responses are positive for example, the angular velocity of the centre plate is increasing from zero towards the maximum (Accelerating). Whereas between 0 and 52 mrad on the other hand, the velocity is seen to be decreasing from the maximum towards zero (Decelerating).

This analysis suggests that the amplitudes of the stick and slip torque responses are also dependent on the rate of change of the rotational velocity which is directly related to the inertial properties of the centre plate system. This suggestion is also supported by the responses of the 6 kN test case (Blue lines), which are also seen to decay slightly in the regions where the centre plate velocity is approaching zero. In the responses of test cases 9 and 14 (Figure 5.57), it can also be seen that there

are at least 19 – 20 stick-slip cycles during the two gross-sliding events. The number of stick-slip cycles however, appears to coincide with the natural frequencies of material B under the 6 and 9 kN loading conditions.

From the summary of results shown in Appendix R for example, it can be seen that these parameters range between 19.9 – 24.1 Hz. The mean torsional stiffness and breakout angle parameters for the complete data set on the other hand (6 tests), appear to have stabilised in the regions of 5697 Nm/rad and 8.94 mrad respectively. The mean torsional stiffness for material A after completing the service tests for example, was also seen to be in the same region at 5897 Nm/rad, whereas the breakout angle was seen to be significantly lower at 3.6 mrad.

This analysis clearly shows that as the contact surface areas of the centre plate/wear liner components become more conformal over time due to wear for example, the shear stresses in the materials then start to rise which causes COF values to increase. These processes also develop in response to the cyclic running conditions in the scale model laboratory tests where the contact surfaces are exposed to work-hardening via cold working processes (Tottle, 1966). The peak COF value of material B during the first 25 cycles of the service tests for example, was seen to be 0.21, whereas during the last 25 cycles, this value is seen to in the region of 0.54, which is a 257% increase.

The increases in the SD of the torque measurements on material B throughout the various stages of the service tests also shows that the responses become more nonlinear as the number of cycles increases. This analysis therefore, strongly suggests that the mechanical properties of the centre plate/wear liner components also have the strong influence on the stick-slip responses, as well as the centre plate velocity and loading conditions. The following section discusses the local analysis results for material C.
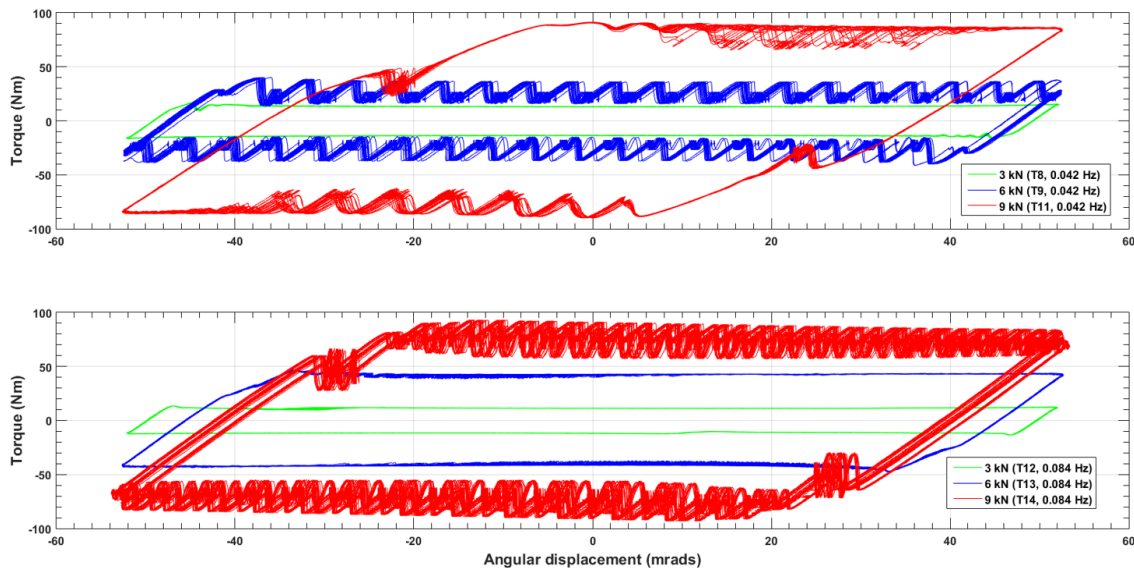
Figure 5.57: Hysteresis during the last 25 cycles.

5.4.6.3. Local analysis results for material C

The hysteresis responses of material C during the service test cases are discussed in this section. The responses during the first 25 cycles of the 3, 6 and 9 kN loading cases are shown in Figure 5.58, by the green, blue and red lines respectively. From these responses as well as the summary of results shown in Appendix R, it is clear to see the stick-slip behaviour developing in all three test cases, where the

slip torque responses in test cases 15, 16 and 17 for example, is seen 30 – 35% lower than the stick torque.

The stick and slip torque responses during the 3 kN loading case for example, are seen to be in the region of 14.3 and 9.7 Nm (Green lines), whereas during the 6 kN loading case, the stick torque is seen to be 17 Nm and the slip torque, 11.8 Nm. From the close-up of the stick-slip behaviour in test case 17 which was running under the 9 kN centre plate load, it can be seen that the stick and slip torque responses are in the region of 30.7 and 19.7 Nm respectively, see Figure 5.59. The differentials between the stick and slip torque responses in this particular wear liner material therefore (30 – 35%), are fairly constant irrespective of the loading condition. The differences between the stick and slip torque responses in materials A and B however, were seen to be slightly lower at 18 and 23% respectively, see Appendix R.

From the summary of results shown in Appendix R, it can be seen that material C has the lowest stick and slip shear moduli`s out of three materials that were tested. The stick shear modulus of this material is in the region of 95.7 N/m², whereas slip modulus is 64.2 N/m². The mean torsional stiffness and natural frequency parameters for the complete data set (3 test cases), are seen to range between at 4888 – 5039 Nm/rad and 23.6 – 24 Hz, whereas for materials A and B, the mean torsional stiffnesses were seen to be significantly higher at 5906 and 5638 Nm/rad respectively.
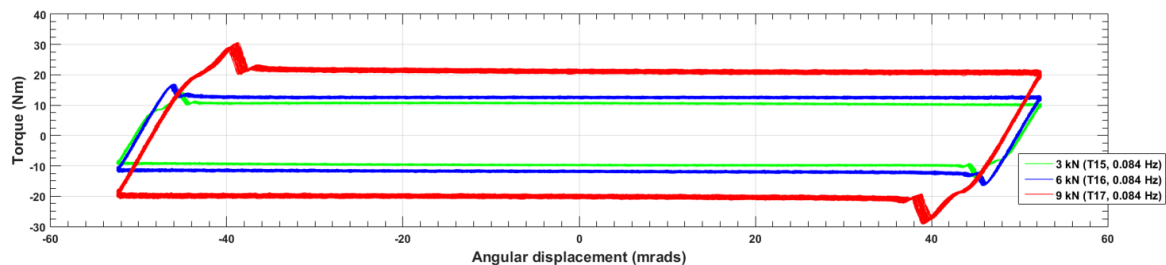
Figure 5.58: Hysteresis responses during the first 25 cycles.
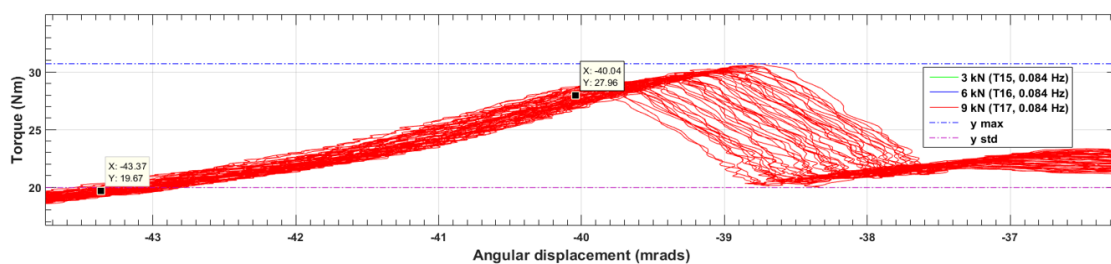
Figure 5.59: Close-up of the stick-slip behaviour during test case 17.

Figure 5.60 shows the hysteresis responses during cycles 5375 – 5400 and from these it can be seen that the peak torque in test case 16 for example, has increased from 17 to 24.1 Nm (Blue lines), which is the largest increase overall at 42%. Whereas the peak torque in test case 17 has increased by another 24% relative to the previous analysis, from 30.7 to 38.1 Nm. The peak torque in test case 15 on the other hand (Green lines), has decreased from 14.3 to 13.4 Nm. Under the 9 kN centre plate loading condition however (Test case 17, red lines), it is clear to see stick-slip behaviour developing in the regions $\pm$ 52 mrad, which are the regions where the system is transitioning from the breakout events, to the gross sliding regimes.

The mean stick and slip COF values for material C at this stage of the service tests as can be seen from the summary of results shown in Appendix R, are shown to be 0.19 and 0.13, which are similar to the

values that were calculated for Material A. The SD of the COF values for material C however, are seen to be the lowest overall at 5.2 – 5.5%, whereas for materials A and B, the SD of the COF values are significantly higher, ranging between 25.7 – 27.5% and between 29 – 31.2% respectively.

This analysis suggests that the torque responses of material C are the most consistent overall. However, due to the limited number of tests that were carried out on this material due to the time constraints (3 test cases), it is difficult to conclude with absolute certainty, if material C would also be the most consistent under the 0.042 Hz forcing frequencies without further testing.

The hysteresis responses during the last 25 cycles of the service tests are shown in Figure 5.61 and from these, it can be seen that the torque responses appear to be smoother in comparison to the previous analysis. The stick torque responses in the 3, 6 and 9 kN loading cases for example, have also decreased from 13.4, 24.1 and 38.1 Nm, to 9.5, 19.2 and 30.8 Nm respectively which are 20% lower, as well as similar to the torque responses that were measured during the first 25 cycles.

The mean COF values for material C are also the lowest overall at this stage of the service tests, ranging between 0.14 – 0.17 (Appendices R). The mean COF values that were calculated for material A were slightly higher at 0.16 – 0.19, whereas the mean COF values for material B were almost double and seen to range between 0.3 – 0.39. The following section discusses the spectral analysis responses during the three stages of the service tests that have been analysed throughout this section.
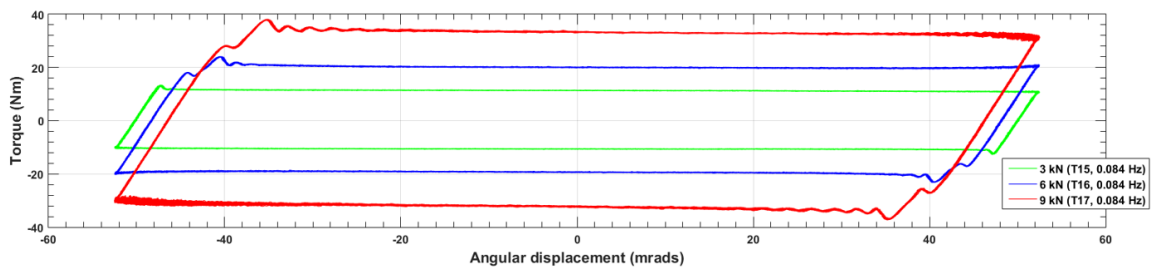
Figure 5.60: Hysteresis responses during cycles 5375 – 5400.
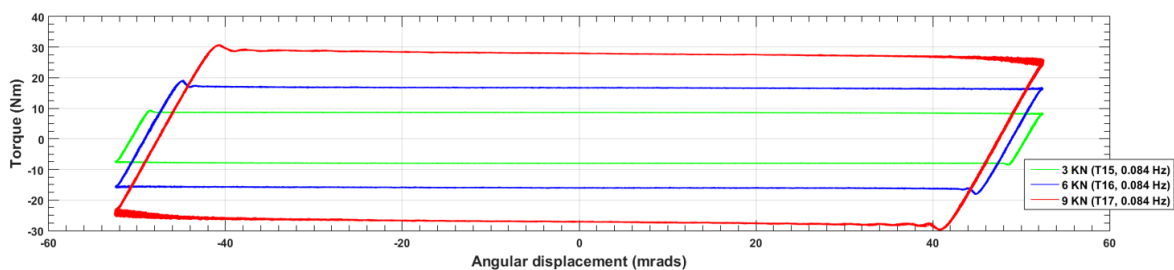
Figure 5.61: Hysteresis during the last 25 cycles.

5.4.7. Spectral analysis responses during the service test cases

This section discusses the Power Spectral Densities (PSD) of materials A, B and C during the service tests. Table 5.7 shows the range of torsional natural frequencies that were calculated from the stiffness and inertial properties of the centre plate/wear liner components and as can be seen, are expected to be in the region of 18 – 34.2 Hertz (Hz). The frequency of the fluid pulsations and Instron machine frame vibrations on the other hand, are seen to be 223.5 and 151 Hz respectively.

Test cases 5, 13 and 17 as can be seen, were carried out using materials A, B and C and under the 3, 6 and 9 kN loading conditions respectively. The torsional stiffness parameters that were used for this analyses and the full scale equivalents as well as the percentage increases in the COF values are also

shown in Table 5.7. The range of standard deviations for the stiffness and mean COF parameters that were calculated for each material are also shown in this table, which were obtained from the summary of results in Appendix R. The spectral analysis results for materials A are discussed in the following section.

Component	Natural frequency (Hz)	Test case	1:7 scale model load (kN)	1:7 scale model inertia (kg.m²)	1:7 scale model torsional stiffness (Nm/rad)	1:7 scale model breakout angle (mrad)	Standard deviation of the stiffness (%)	Full scale load (kN)	Full scale inertia (kg.m²)	Full scale torsional stiffness (kNm/rad)	Full scale breakout angle (mrad)	Stick μ	Slip μ	Mean μ	Standard deviation of μ (%)	Percentage increase in μ over time (%)
Centre plate/Wear liner (Lower)	18	17	9	0.39	4916	6.25	3.4	147	2184.9	34.4	43.8	0.18	0.11	0.145	4.2 - 27.1	106.6
Centre plate/Wear liner (Mean)	24	13	6	0.26	5872	3.33	5.3	294	4369.8	41.1	23.3	0.17	0.10	0.135	10.6 - 31.3	188
Centre plate/Wear liner (Upper)	34.2	5	3	0.13	5940	1.53	5.7	441	6554.7	41.6	10.7	0.16	0.14	0.150	12.5 - 43.3	88.4
Fluid pulsations	223.5	-	-	-	-	-	-	-	-	-	-	-	-	-	-	-
Machine frame	151	-	-	-	-	-	-	-	-	-	-	-	-	-	-	-

Table 5.7: Torsional vibration modes during the service tests.

5.4.7.1.   Spectral analysis results for material A

The PSD of material A during the three different stages of the service tests are discussed in this section. The top part of Figure 5.62 shows the responses during the first 25 cycles of the tests that were running at the 0.042 Hz and the bottom part, shows the responses of the tests that were running at 0.084 Hz. The first feature to point out in these figures are the limits on the y-axes, which are seen to be 3-times larger than the limits that were used for the analysis of the running-in test torque signals. This analysis strongly suggests that the power amplitudes of the frequency components are proportional to the torque responses.

The power amplitudes during the 9 kN loading cases for example (Red lines), are seen to be the largest overall during the first 25 cycles, with the exception of test case 6 which was running under the 6 kN centre plate load and at the 0.084 Hz forcing frequency (Blue lines) Whereas the power amplitudes of the 3 kN loading cases are much smaller in comparison and due to this factor, are not clearly visible in the PSD`s (Green lines).

The signatures of the fluid pulsations are also clear to see in the region of 223 Hz, as well as the broad band of frequencies in the region of 163 Hz (Yellow lines). This is the frequency response of test case 5 using the wear liner sample that was accidently contaminated with hydraulic oil prior to starting the running-in test. The power amplitudes of this signature however, are decreasing as the number of cycles increases which is clear to see by comparing the responses during the first 25 cycles and between cycles 5375 – 5400 shown in Figure 5.63. The frequency responses of the 6 and 9 kN loading cases that were running at 0.084 Hz are also seen to be broadening out in the region of 18 – 24 Hz. These signatures as can be seen from the results shown in Table 5.7 and Appendix R, appear to coincide with natural frequencies of the centre plate/wear liner components.

The PSD of material A during the last 25 cycles of the service tests are shown in Figure 5.64 and from these responses, it can be seen that the power amplitudes in the region of 163 Hz during test case 5, have decreased by another 25% relative to the amplitudes that were observed during cycles 5375 – 5400. Whereas the amplitudes of test case 2 which was running under the 6 kN loading condition and at the 0.042 Hz forcing frequency (Blue lines, top plot), are now seen to be the highest overall.

Test case 2 was then repeated using a new centre plate/wear liner sample and after this re-test, the frequency response is now seen to be in line with the expected behaviour, see test case 4 in the top plot of Figure 5.64 (Black lines). The power amplitudes in this test case as can be seen, are now slightly lower than the amplitudes of test case 3 (red lines), which was running under the 9 kN centre plate loading condition. The following section discusses the frequency responses of material B throughout the different stages of the service tests.
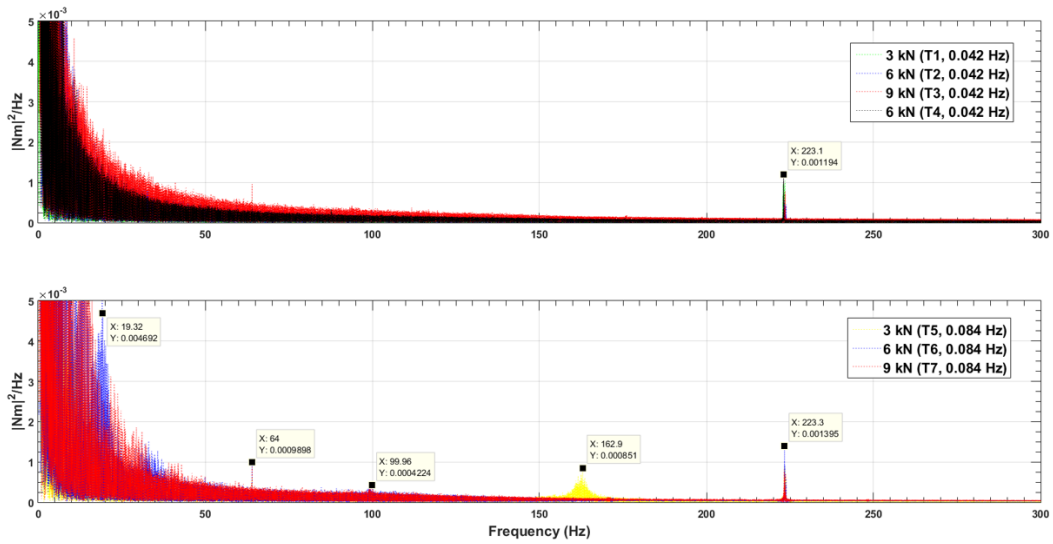
Figure 5.62: PSD during the first 25 cycles.
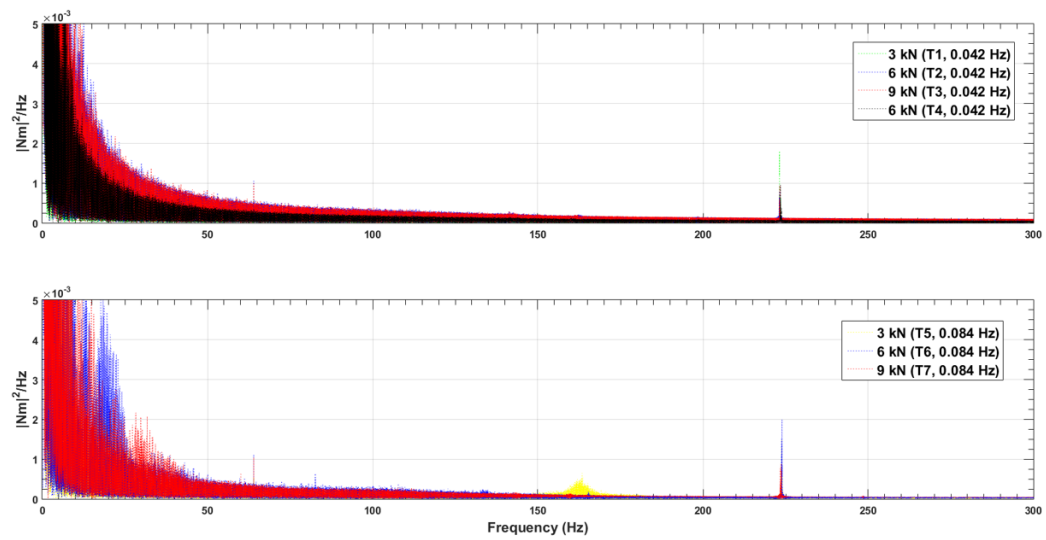
Figure 5.63: PSD during cycles 5375 − 5400.
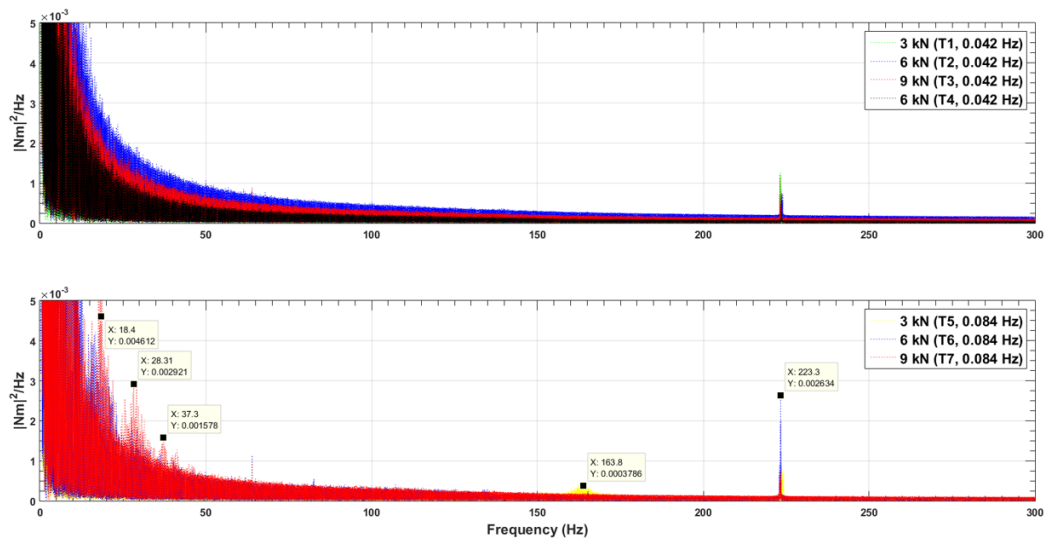
Figure 5.64: PSD during the last 25 cycles.

5.4.7.2.   Spectral analysis results for material B

The PSD of material B during the service tests are discussed in this section. Figure 5.65 shows the responses during the first 25 cycles and as can be seen, the power amplitudes of the 9 kN load cases are the largest overall (Red lines). From looking at the responses of test case 14 which was running under the 9 kN centre plate load and at 0.084 Hz, it is also clear to see a band of signatures starting to develop in the region of 61 Hz.

The PSD during cycles 5375 – 5400 are shown in Figure 5.66 and from these it can be seen that the responses of test cases 9 and 11 for example (Blue and red lines), which were running under the 6 and 9 kN centre plate loads and at 0.042 Hz, are starting to oscillate in the region of 75 – 150 Hz. The power amplitudes of these responses however, are significantly lower in comparison to test case 14, which was running under the 9 kN centre plate load and at the 0.084 Hz forcing frequency, see the bottom plot in Figure 5.66. The y-axis in this plot as can be seen, has increased by a factor of two relative to the power responses during the first 25 cycles, from 0.005 to 0.01 $|Nm|^2/Hz$. This analysis clearly shows that the changes in the stick-slip responses of the centre plate/wear liner components can be detected to a good degree of accuracy using spectral analysis techniques.

The frequency responses during the last 25 cycles of the service tests are shown in Figure 5.67 and from these, it can be seen that the limits of the y-axes in 0.042 and 0.084 Hz test cases have increased by a factor of four. The power amplitudes of test case 9 in the region of 100 – 150 Hz for example (Blue lines, 6 kN), are now seen to be higher than the responses of test case 11 (Red lines, 9 kN). The limits of the y-axes in the top and bottom plots of Figure 5.67 for example, are now seen to be 0.02 and 0.04 $|Nm|^2/Hz$ due to the increases in power responses as a result of the stick-slip behaviour.

The peak torque responses in test case 9 however, which was running under the 6 kN centre plate load and as can be seen from the hysteresis responses shown in Section 5.4.6.2, as well as the summary of results shown in Appendix R, are significantly lower. The peak torque during test case 9 is seen to be 40.1 Nm, whereas in test case 11 this parameter is seen to be in the region of 93.3 Nm. From the hysteresis responses, it can also be seen that the stick-slip response during the last 25 cycles of test case 11, is not fully developed, so the power response is lower than test case 9.

This analysis strongly suggests that the power amplitudes of the signatures developing in the region of 100 – 150 Hz as the number of cycles increases, are highly dependent on the stick-slip response of the centre plate/wear liner components rather than the magnitude of the torque. When there is no stick-slip behaviour for example, the power amplitudes of the frequency responses are seen to increase in proportion to the torque across the full range of frequencies below the 200 Hz cut-off. Whereas when there is fully developed stick-slip behaviour present in the hysteresis responses, the power amplitudes are seen to be 3 – 4 times higher. The following section discusses the spectral analysis results for material C.
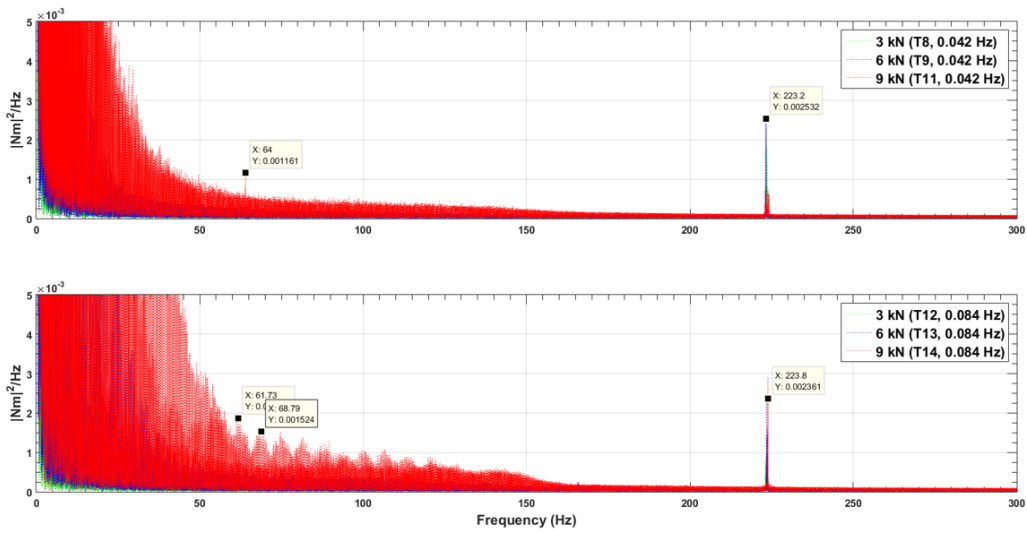
Figure 5.65: PSD during the first 25 cycles.
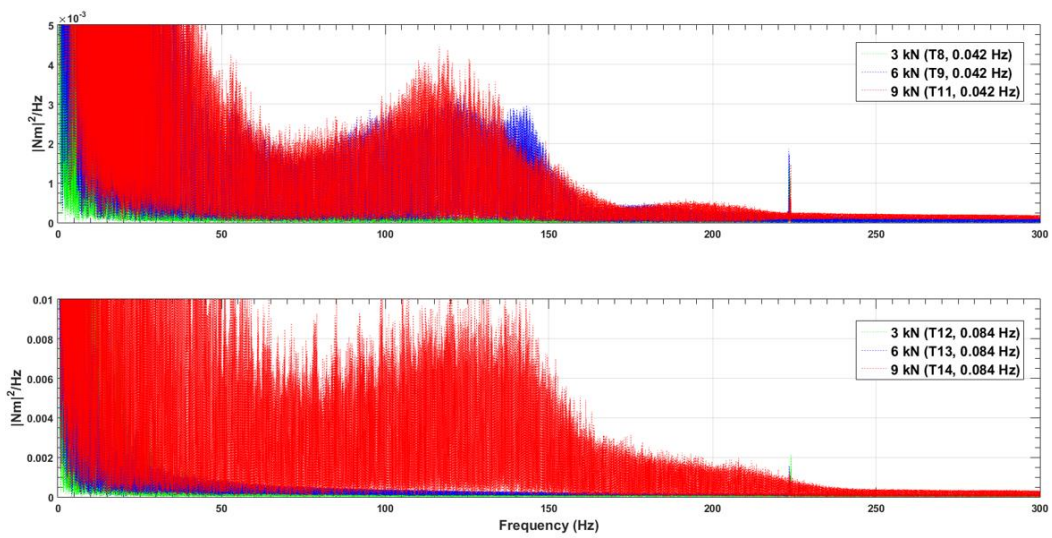
Figure 5.66: PSD during cycles 5375 − 5400.
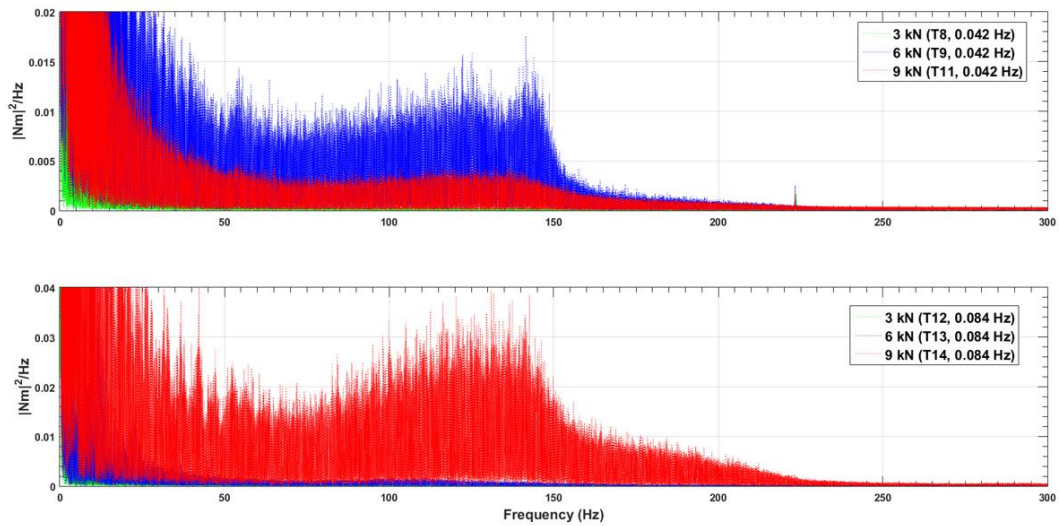
Figure 5.67: PSD during the last 25 cycles.

5.4.7.3. Spectral analysis results for material C

The PSD for material C are discussed in this section. Figures 5.68, 5.69 and 5.70 show the frequency responses during the first 25 cycles, between cycles 5375 – 5400 and during the last 25 cycles of the service tests. From these responses it can be seen that the frequency components and power amplitudes of materials A and C, appear to be very similar. From the hysteresis responses of these two materials for example, it was shown that the stick-slip response only occurred in the breakout regions, whereas for material B, the stick-slip response was also observed during the sliding phases of motion.

The frequency responses of material C suggest that the increases in power amplitudes in the region of 20 – 40 Hz for example, are related to the natural frequencies of the centre plate/wear liner components and develop in response to the initial breakout events. Whereas the signatures that were seen to be developing in the region of 100 – 150 Hz on material B which are clearly not present in these responses, are introduced when the stick-slip oscillations start to develop during the sliding phases of motion. The responses during the last 25 cycles also support this idea, as there are no broad-band signatures present above 100 Hz, see Figure 5.70.

The overall conclusions to be drawn from the spectral analysis results are that the stick-slip responses are closely related to the mechanical properties of the centre plate/wear liner components. However, to better understand the developments in the frequency responses that have been taking place throughout the various stages of the service tests and to conclude the scale model laboratory tests and dynamic analyses of the centre plate system. The following section discusses the steel-on-steel test case that was carried out as the final part of this research work in order to identify the frequency signatures associated with steel-on-steel contact conditions.
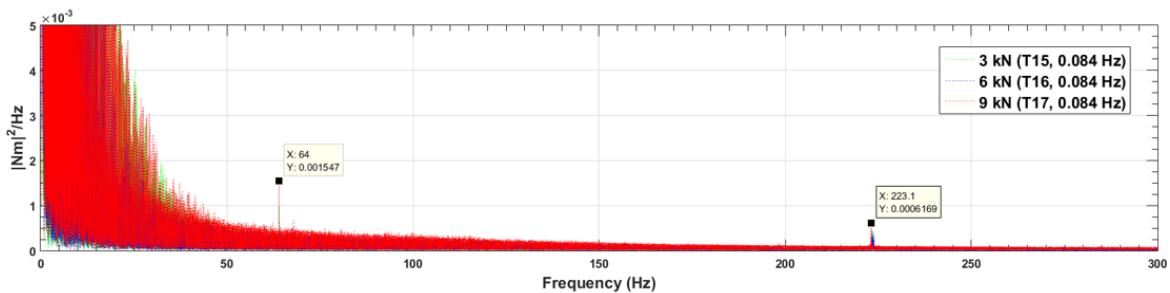
Figure 5.68: PSD during the first 25 cycles.
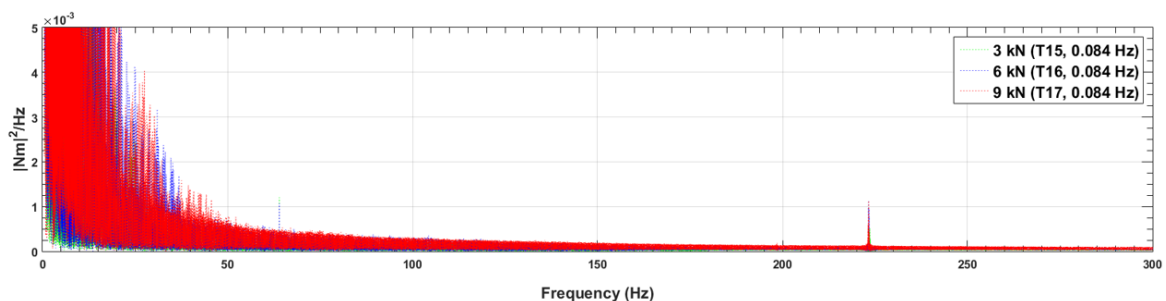
Figure 5.69: PSD during cycles 5375 - 5400.
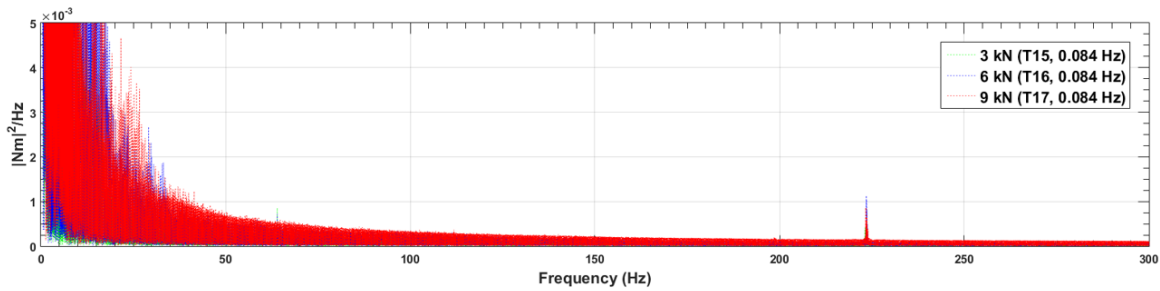
Figure 5.70: PSD during the last 25 cycles.

5.4.8. Steel-on-steel test case description

This section discusses the results from the steel-on-steel test case which was carried out to quantify the torsional stiffness parameters and COF values for the 1:7 scale centre plate components. This test case was also used to analyse the dynamic behaviour of the centre plate system under the most unfavourable running conditions in order to better understand how the steel-on-steel contact conditions influence the hardening mechanisms of the centre plate components, as well as the hysteresis and frequency responses under different loading regimes. These results were then compared and contrasted against those with the wear liner samples included in the test (Sections 5.3 – 5.4.7.3).

The sinusoidal forcing frequency and amplitude of motion during this test case was also set to 0.084 Hz and $\pm$ 3 degrees to match the parameters that were used in the running-in/service test cases. The main differences between the steel-on-steel and running-in/service test cases however, are that the steel-on-steel test case is designed to investigate the response of the centre plate system under start-stop conditions, such as those which occur for example, when freight is being loaded/unloaded on to the train at the depot.

These start-stop running conditions were replicated in the laboratory using a five hour testing program which was split-up into five different phases, see Table 5.8. The first phase as can be seen, ran for 30 minutes and was carried out with the centre plate load set to 0.5 kN, whereas second phase, ran for a further 90 minutes and was carried out with the load ramped-up to 3 kN. The centre plate was then held stationary during the third phase of the test for 1 hour and with the load held constant at 3 kN. The sinusoidal forcing frequency was then resumed after the 1 hour stopping period at 0.084 Hz during phase four, which as can be seen, also ran for 90 minutes under the 3 kN centre plate loading condition. The load was then ramped back down to 0.5 kN for the last 30 minutes of the start-stop test case.

The post-test images of the static/dynamic centre plates after the start-stop testing program are shown in Figure 5.71. Pictures A and B show the post-test images of the static centre plate and the wear debris/particles adhering to the contact surfaces of the dynamic centre plate. Pictures C and D also show the wear scars and pitting marks in the contact surfaces of the centre plate components after removing the wear debris. These images clearly show the mechanisms that lead to the transformation of steel material on to the surfaces wear liner components. When the wear liner components were included in the experiments for example, it could be seen that these particles embedded themselves in the surfaces of the liners, see the post-test images of these components shown in Figure 5.2, Section 5.1.

From the post-test images shown in Figure 5.71, it can also be seen that the severe damage mechanisms such as the burnishing, pitting marks and wear scars on the contact surfaces of the centre

plates for example, appear to be concentrated in two very distinct localised areas, as the turning marks are still clearly visible in the regions where no contact has taken place at all. The initial assumption in relation to the contact pressures being uniformly distributed throughout the contact area therefore, is clearly incorrect. The torque responses and COF values during the steel-on-steel test case are discussed in the following section.

Test phase	Centre plate load (kN)	Centre plate radius (m)	Mass moment of Inertia (kg.m²)	Equivalent mass (kg)	Forcing frequency (Hz)	Amplitude of motion (± degrees)	Number of running cycles	Run time (minutes)
1	0.5	0.029	0.02	51.0	0.084	3	150	0 - 30
2	3	0.029	0.13	305.8	0.084	3	450	30 - 120
3	3	0.029	0.13	305.8	0	0	0	120 - 180
4	3	0.029	0.13	305.8	0.084	3	450	180 - 270
5	0.5	0.029	0.02	51.0	0.084	3	150	270 - 300

Table 5.8: Testing procedure for the steel-on-steel test case.

Figure 5.71: (Picture A) Static centre plate. (Picture B) Dynamic centre plate. (Picture C) Dynamic centre plate after the post-test analysis. (Picture D) Static centre plate after the post-test analysis.

5.4.8.1.   Global analysis results

The peak torque responses during the steel-on-steel test case are shown in Figure 5.72 and from these it can be seen that the initial torque during phase one of the test starts off in the region of ± 3 Nm. These responses are then seen to increase continually towards a final value of ± 13 Nm over the 30 minute test cycle.

The centre plate load is then ramped-up to 3 kN during phase two which runs for a further 90 minutes. The torque response during this event as can be seen, jumps up to $\pm$ 42 Nm and remains in this region for the first 15 minutes of phase two. The response then diverges towards $\pm$ 62 Nm and settles in this region for around 10 minutes before it starts to decrease again. This decrease as can be seen, continues to develop over the next 15 minutes until the torque responses reach the region of $\pm$ 48 Nm. However, after 70 minutes of continuous running, it is clear to see the spikes where the torque responses jump back up to $\pm$ 62 Nm, almost instantaneously which clearly suggests that the friction characteristics of the centre plate system are unstable.

The torque then starts to decrease again towards $\pm$ 48 Nm, before the jump up to $\pm$ 70 Nm occurs, which is seen to be the highest level of torque throughout the steel-on-steel test case. The response then decreases from the peak over the next 20 minutes of running towards $\pm$ 50 Nm and after reaching this level, starts to oscillate between $\pm$ 50 and $\pm$ 60 Nm before the centre plate motion ceases.

The centre plate motion was then stopped for 1 hour with the load held constant at 3 kN during the third phase of the test where the torque is seen to decrease from $\pm$ 50 to $\pm$ 45.5 Nm. This time dependent behaviour however, strongly suggests that the contact surfaces of the centre plates are creeping due to the residual stresses in the material micro-structures for example, relaxing over time (Tottle, 1966) and (Ashby & Jones, 1980).

However, after setting the centre plate in motion again during phase four, it can be seen that the torque responses start to gradually build-up towards $\pm$ 50 Nm again during the first 5 minutes of running. The torque then suddenly jumps back up to $\pm$ 62 Nm and then during the next 10 minutes of running, is seen to oscillate between $\pm$ 50 and $\pm$ 62 Nm, which is similar to the oscillatory behaviour that was starting to develop during latter stages of phase two, just before the centre plate motion was stopped. This pattern of behaviour as can be seen, continues to develop over the remaining 1 hour and 15 minutes of phase four, but with the torque gradually decreasing towards the region $\pm$ 40 Nm as the number of cycles increases.

The centre plate load was then ramped back down to 0.5 kN during phase five which is clear to see by the rapid decreases in the torque responses from $\pm$ 40 to $\pm$ 10 Nm (Figure 5.72). The responses during this final phase however, appear to be more stable in comparison to the first phase, where the responses continued to increase from an initial value of $\pm$ 3 Nm, to a final value of $\pm$ 13 Nm. The main differences between the torque responses observed during the steel-on-steel test case and those with the wear liner included for example, are the sudden jumps/spikes in the global analysis torque curves, which were not present to the same extent in the centre plate/wear liner torque responses.

These rapid changes in the torque responses therefore, strongly suggest that the friction surfaces have suffered some form of catastrophic damage due to fatigue failure, thus, leading to the burnishing, pitting marks and wear scars on the centre plate components. Whereas the gradual increases/decreases in the torque responses over time, which was seen to be the case in the centre plate/wear test cases, suggests that contact surfaces are been subjected to gradual wear, as well as hardening and softening mechanisms as the number of running cycles increases (Tottle, 1966).
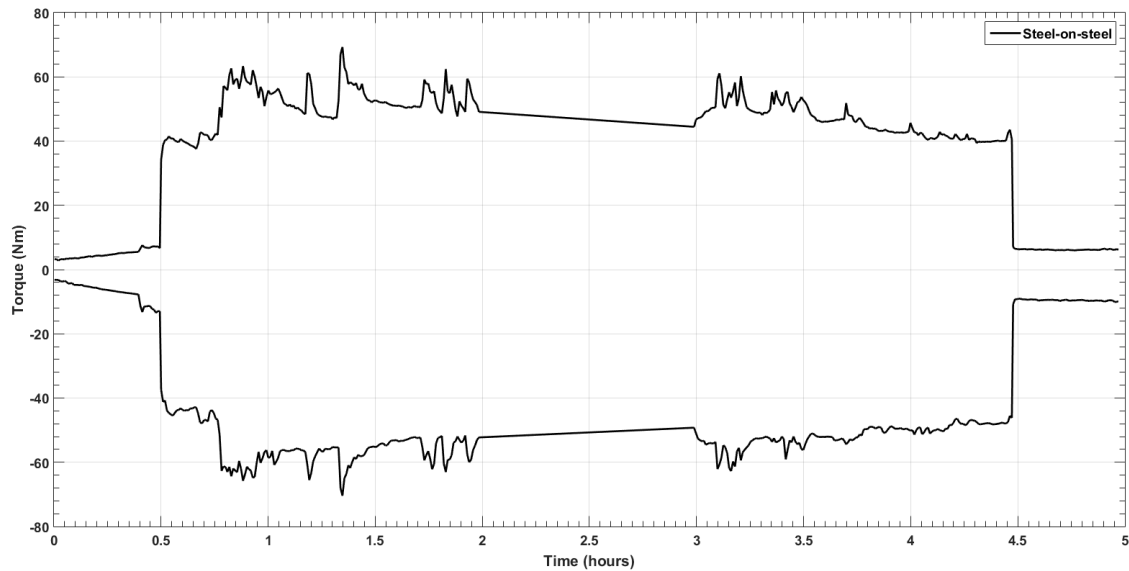
Figure 5.72: Peak torque responses during the steel-on-steel test case (0.084 Hz).

The COF values that were calculated from the steel-on-steel responses are shown in Figure 5.73. From these responses the non-symmetric friction characteristics throughout the different phases of the test are much easier to see. The solid and dashed lines show the COF values for Clockwise (CW+) and Counter-Clockwise (CCW-) directions and from these, it can be seen that the peak value during the first phase of the test reaches 0.78 in the CW direction, whereas in the CCW direction, the COF is seen to be 90% higher at 1.48 which is the worst non-symmetric friction characteristic that has been observed overall throughout the research work discussed in this thesis.

During the initial stages of phase two however, it can be seen that the COF values in both directions decrease significantly and appear to settle in the region of 0.65 – 0.75 when the centre plate load ramps up to 3 kN, which is surprising. This response suggests that the contact surfaces are becoming more conformal under the heavier loading condition as the non-symmetric friction characteristics are much less pronounced in comparison to those that were observed during the first phase of the test run, which was also seen to be the case during the service tests with the wear liner included. The COF values in the CW/CCW directions are then seen to start oscillating between 0.8 – 1.1 after 20 minutes of running in phase two and remain in this region until the centre plate motion ceases.

The straight line sections in Figure 5.73 show that the centre plate is stationary during phase three, however, it can also be seen that the COF values in the CW/CCW directions for example, decrease by 0.05 over this interval which suggests that the friction surfaces are creeping/relaxing under the constant 3 kN loading condition.

The centre plate was then set in motion again under the 3 kN load during phase four of the test, which as can be seen, caused the COF values to start increasing towards the region of 0.8 – 0.9, before jumping up to 1 after the first 5 minutes of running, which is similar to the COF values as well as the behaviours that were observed during the latter stages of phase two. The COF values are then seen to remain in the region of 0.8 – 0.95 until the total run time approaches 3.5 hours, where they then start to decrease again towards the region of 0.65 – 0.75 during the last hour of phase four.

During phase five, the centre plate load was ramped back down to 0.5 kN, see Figure 5.73. This action as can be seen, caused the COF values in the CCW direction to jump-up from 0.8 to 1.1, whereas in the CW direction, the COF values appeared to be more stable and remained in the region of 0.6 – 0.7 throughout this phase of the test. The differences between the CW/CCW COF values therefore, are in

189

the region of 57%. The COF values in the CCW direction however, then started to decrease towards 0.95 and remained in this region until the end of the start-stop test which is 36% higher than the COF values in the CW direction.

From this analysis it can be concluded that the geometries and surface textures of the contact interfaces on the centre plate components have a very strong influence on the torque responses/COF values. Under the lightest loading conditions where the contacts are just starting to form for example (0.5 kN), the non-symmetric friction characteristics during the steel-on-steel test case, as well as the test cases with the wear liners included, were seen to be significantly worse in comparison to the responses were the centre plate load was either 3, 6 or 9 kN.

Also, during the 3, 6 and 9 kN loading cases for example, the contacts between the surface asperities on the centre plates form over a larger surface area in the CW/CCW directions which clearly produces a more symmetric friction characteristic. This analysis also suggests that the COF values of the friction surfaces are highly dynamic rather than constant. The following section discusses the local analysis results during the different phases of the steel-on-steel test case (Popov V. L., 2010).
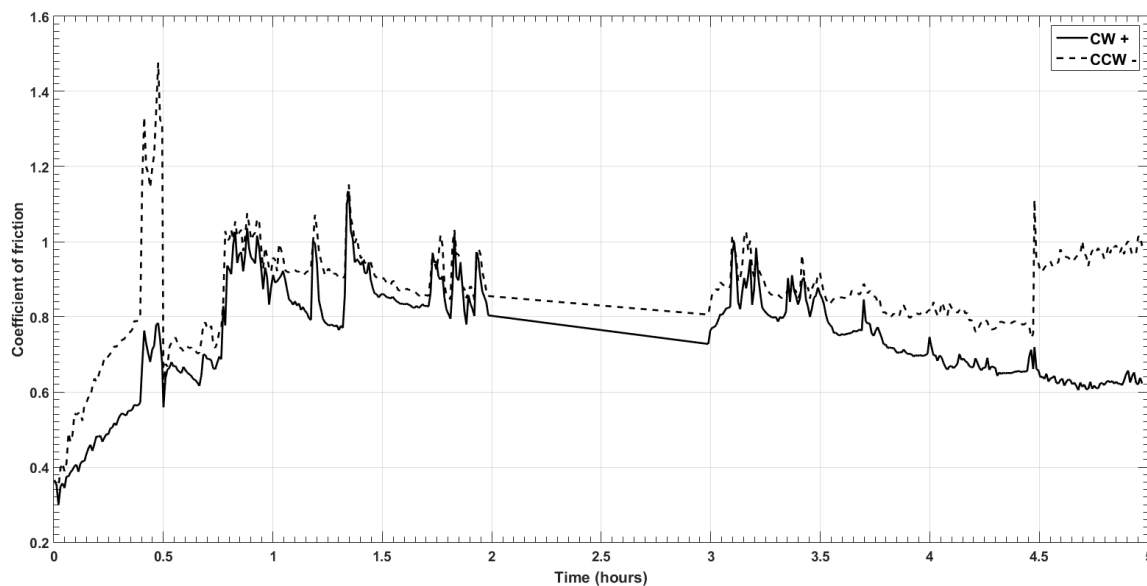
Figure 5.73: Peak COF values during the steel-on-steel test case (0.084 Hz).

5.4.8.2.   Local analysis results

This section discusses the hysteresis responses during the different phases of the steel-on-steel test case. Figure 5.74 shows the responses during the first 50 cycles of phase one and from these it can be seen that the torque characteristics are highly non-symmetrical. The responses in the CW directions for example, are seen to be sticking as well as slipping during the gross-sliding phases of motion, whereas in the CCW directions (-), the responses appear to be a lot smoother once the system is sliding. The stick/breakout torque responses in the CW direction as can be seen, range between $2 - 5$ Nm, whereas the slip toque during the gross-sliding events, is seen to be approximately $1 - 2.5$ Nm lower than the sticking torque which is a difference of 50% between the stick and slip torque responses.

The torque responses are also seen to increase in proportion to the number of running cycles, which suggests that the contact surfaces of the steel centre plates are hardening over time. Hunting behaviour is also seen to be taking place when the centre plate starts breaking out in the CCW

directions, see the regions to the right of Figure 5.74. Whereas in the CW direction on the other hand, the torque responses appear to follow the same trajectories (Bertram & Gluge, 2013).

The torsional stiffness coefficients for the centre plate components were then calculated from the hysteresis responses. These parameters however, were more challenging to quantify in comparison to the stiffness parameters for the centre plate/wear liner components due to the highly nonlinear behaviour. The torsional stiffness of the steel centre plates under the 0.5 kN loading condition for example (Figure 5.74), comprises of at least three stiffness parameters, K1, K2 and K3, which represent three different kinds of material behaviours.

The first stiffness parameter for example, K1, represents the elasticity of the steel material during the breakout events and is calculated using the almost straight vertical lines. Whereas the K2 and K3 parameters on the other hand, are the torsional stiffness coefficients where the system is seen to transition from elastic to elastic-plastic material behaviour and where the material hardness starts to change during the gross-sliding events. The torsional stiffness coefficients during the first 50 cycles of phase one (k1, K2 and K3), were then calculated from the data points shown in Figure 5.74 and are seen to be 4174, 113 and 104 Nm/rad respectively in Table 5.9 at the end of this section.

During phase two however, all three stiffness parameters were seen to increase slightly to 5737, 5135 and 143 Nm/rad respectively under the 3 kN load. From the hysteresis responses during the first 50 cycles of phase two shown in Figure 5.75, it can be seen that the peak torque starts off in the region of $\pm$ 45 Nm, whereas under the previous loading condition of 0.5 kN, the initial torque was seen to be 15 times lower at $\pm$ 3 Nm. The torque characteristics under the 3 kN loading condition however, are clearly more symmetrical, as well as more stable in comparison the responses shown in Figure 5.74.

The significant increases in the torque responses and the K1/K2 stiffness parameters, also suggests that the contact interfaces are more conformal under the 3 kN loading condition, as well as highly elastic in the breakout regions rather than elastic-plastic which was seen to be the case in Figure 5.74. Whereas the increase in the K3 stiffness parameter on the other hand, albeit relatively small, suggests that the contact interfaces are hardening at a slightly different rate under the 3 kN loading.

The torque responses under the 3 kN loading condition as can be seen, initially breakout in the regions of $\pm$ 40 mrad when the torque reaches approximately 22 and $-$15 Nm in the CW and CCW directions respectively. The torque is then seen to decrease in both directions by at least 5 $-$ 15 Nm when the system transitions into the gross-sliding regimes. During gross-sliding however, it can be seen that the torque responses continue to rise towards the same values that were observed during the initial breakout events (22 Nm and $-$15 Nm). When the torque reaches this level, it can be seen that the system starts to stick again when the angular displacement of the centre plate is in the region of $\pm$ 20 mrad.

This second sticking event however, causes the torque responses to step-up from 22 to 34 Nm and from $-$15 to $-$38 Nm, when the centre plate is rotating in the CW and CCW directions respectively. The torque responses are then seen to breakout again and smoothly transition into the second gross-sliding regimes where the torque continues to increase towards the peak value of 42 Nm in the CW direction, whereas in the CCW direction, the peak value is seen to be $-$45 Nm.
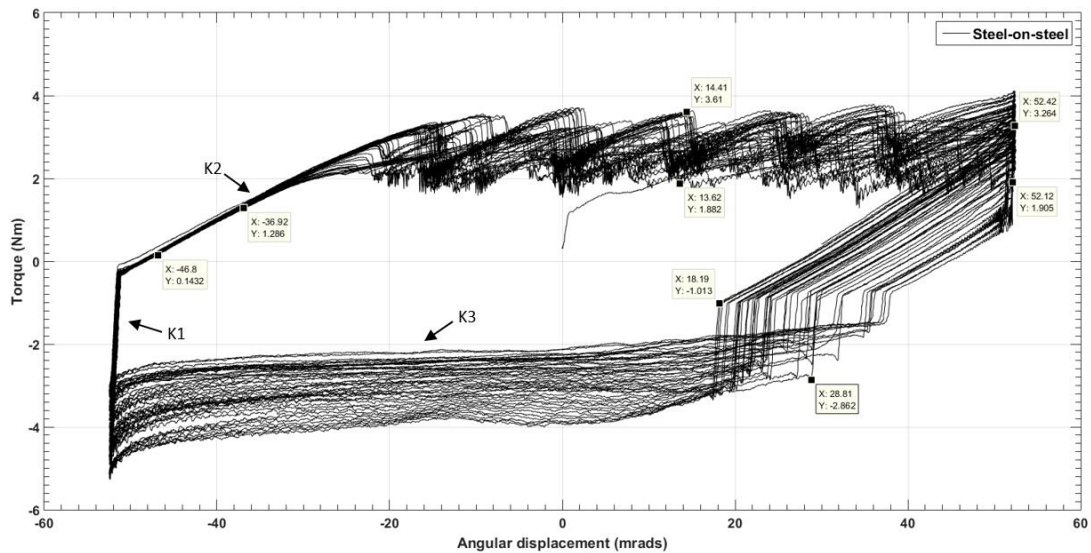
Figure 5.74: Hysteresis during the first 50 cycles of phase one.
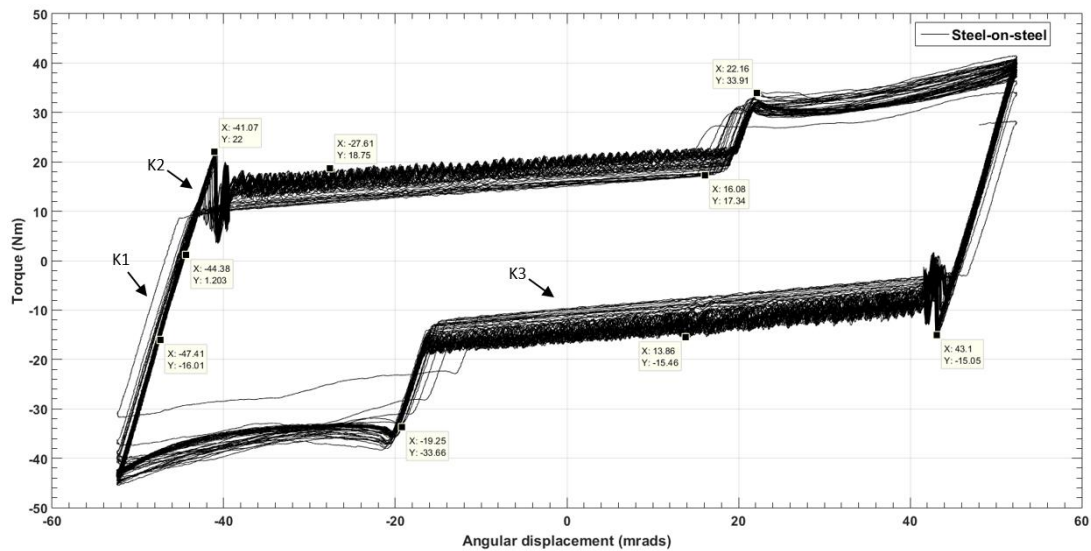
Figure 5.75: Hysteresis during the first 50 cycles of phase two.

The hysteresis responses during the last 25 cycles of phase four and the first 25 cycles of phase five are shown in Figure 5.76. From these responses, it is clear to see that the characteristics of the hysteresis curves under the 0.5 and 3 kN loading conditions are very similar. The peak torque responses under the 0.5 and 3 kN loading as can be seen, are in the region of −10 and −48 Nm in the CCW directions, whereas in the CW direction, the torque responses are slightly lower, but remain fairly constant throughout the gross-sliding regimes at 40 − 43 Nm and 6 − 6.5 Nm respectively. The stick-slip behaviour has also been attenuated in the responses shown below.

During the last 50 cycles of phase five however, it can be seen that torque responses have reverted back to their highly non-symmetric characteristics, see Figure 5.77. In the CW direction for example, the torque responses during the gross-sliding regimes are seen to be in the region of 6 Nm and remain fairly constant. Whereas in the CCW direction, the responses are seen to have two break events, the first one occurring in the region of ± 52 mrad and the second, in the region of 0 mrad.

From the summary of results shown in Table 5.9, it can be seen that the K1 torsional stiffness parameter for example, ranges between 4174 − 4963 Nm/rad under the 0.5 kN centre plate load and

between 5535 – 5737 Nm/rad under the 3 kN load. Whereas the K2 parameters under these loading conditions, are seen to be in the region of 113 – 146 Nm/rad and 5135 Nm/rad. The K3 stiffness parameters on the other hand, are much closer together, ranging between 55 – 164 Nm/rad throughout the different phases of the steel-on-steel test.

The torsional stiffness coefficients when the wear liner samples were included in the experiments, were seen to be in close agreement with the steel-on-steel parameters, ranging between 1418 – 4819 Nm/rad under the 0.5 kN loading conditions and between 4709 – 5940 Nm/rad during the 3 kN loading cases, see Appendices O and R respectively. However, due to the changes in stiffness during the breakout and gross-sliding events in the steel-on-steel test case, the natural frequencies of the centre plate components are seen to cover a much broader range, especially in the lower part of the spectrum (5.3 – 79.3 Hz).

The COF values during the steel-on-steel test case however (Table 5.9), are seen to range between 0.3 – 1.6, whereas when the wear liner components were included in the centre plate system, the COF values under the same loading conditions were seen to be 5 – 6 times lower, ranging between 0.05 – 0.32, see Appendices O, Q and R. The overall mean COF value for the five different phases of the steel-on-steel test case is also seen to be significantly higher at 0.9, whereas the mean COF values under the 0.5 and 3 kN loading conditions with the wear liners included, were seen to be in the regions of 0.11 and 0.18 respectively, with a Standard Deviation (SD) of 36.2 and 21.8%. The SD of the mean COF value for the steel-on-steel test case on the other hand, is 2 – 3 times lower at 10.5%, which suggests that the variation in the steel-on-steel COF values for example, are fairly consistent under both loading conditions.

The percentage increases in the torque responses during the steel-on-steel test case however, are seen to be in same regions as the increases that were measured during the centre plate/wear liner test cases, see Appendix I. During phase one of the steel-on-steel test case for example, the torque response was seen to increase by 333.3%, whereas during phases 2, 4 and 5, the increases were seen to be much lower, ranging between 55 – 86.7%. The torque responses during phase three however, were seen to decrease by 16.9% over the 1 hour stopping period.

This analyses clearly shows that the loading conditions as well as the mechanical properties and geometrical features on the centre plate components, such as the surface roughness and flatness for example, have a very strong influence on the variations observed in friction characteristics and dynamic responses of the centre plate system during the scale model tests. The following section discusses the spectral analysis results for the steel-on-steel test case.
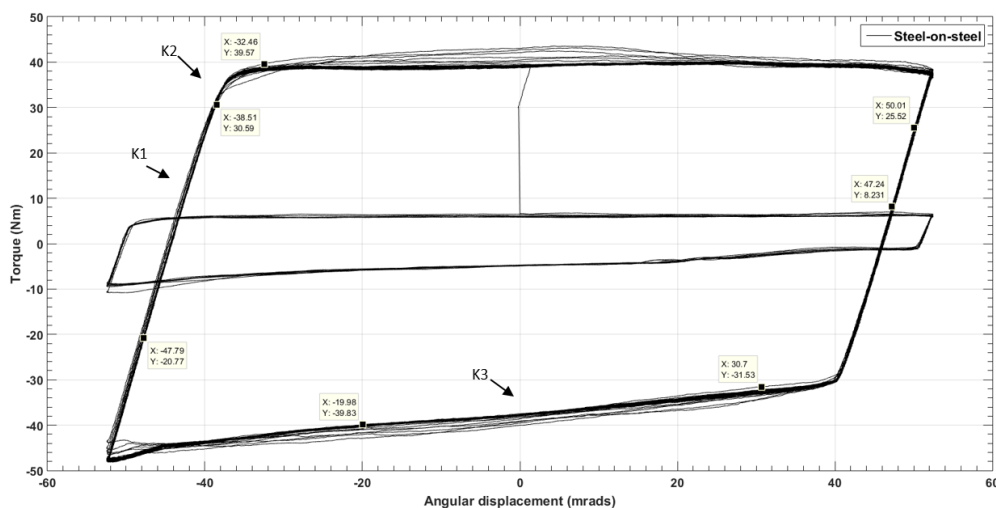
Figure 5.76: Hysteresis during the last 25 cycles of phase four and the first 25 cycles of phase five.
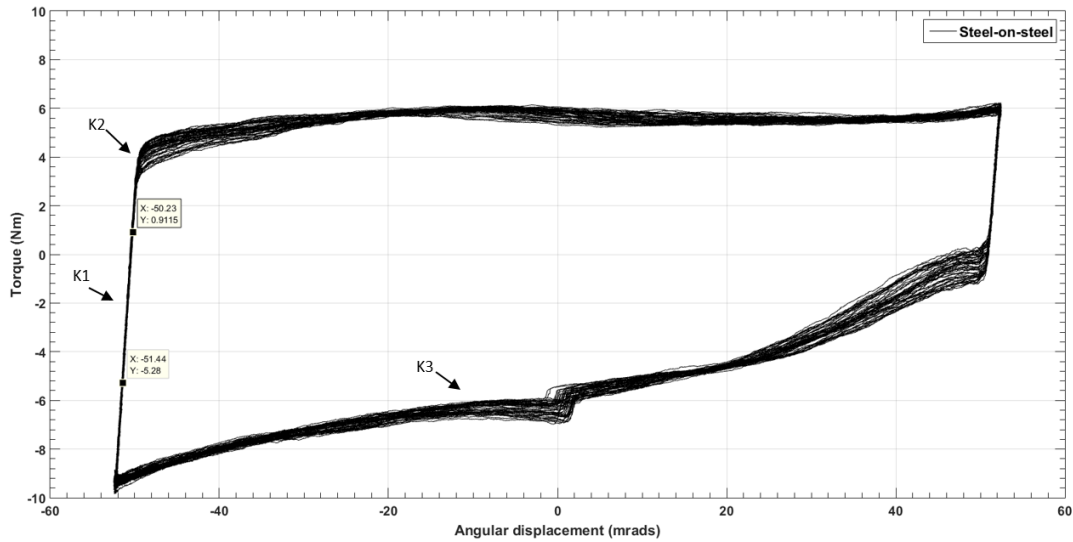
Figure 5.77: Hysteresis responses during the last 50 cycles of phase five.

Test phase	Centre plate load (kN)	Centre plate radius (m)	Mass moment of Inertia (kg.m²)	Equivalent mass (kg)	Time (minutes)	Forcing frequency (Hz)	Max torque (Nm)	Min torque (Nm)	Torsional stiffness K1 (Nm/rad)	Torsional stiffness K2 (Nm/rad)	Torsional stiffness K3 (Nm/rad)	Breakout angle using K1 (mrad)	Torsional natural frequency using K1 (Hertz)	Torsional natural frequency using K3 (Hertz)	Min μ	Max μ	Mean μ	Percentage increase/ decrease (%)
1	0.5	0.029	0.02	51.0	0 - 30	0.084	13.0	3.0	4174	113	104	3.11	70.2	11.1	0.30	1.48	0.89	333.3
2	3	0.029	0.13	305.8	30 - 120	0.084	70.0	37.5	5737	5135	143	12.20	33.6	5.3	0.55	1.55	1.05	86.7
3	3	0.029	0.13	305.8	120 - 180	0	52.0	44.5	5737	5135	143	9.06	33.6	5.3	0.73	0.86	0.79	16.9
4	3	0.029	0.13	305.8	180 - 270	0.084	62.0	40.0	5535	5135	164	11.20	32.8	5.6	0.73	1.12	0.93	55.0
5	0.5	0.029	0.02	51.0	270 - 300	0.084	10.0	6.0	4963	146	55	2.02	79.3	8.3	0.60	1.12	0.86	66.7
Maximum							70.0	44.5	5737	5135	164	12.2	79.3	11.1	0.7	1.6	1.1	333.3
Minimum							10.0	3.0	4174	113	55	2.0	32.8	5.3	0.3	0.9	0.8	16.9
Range							60.0	41.5	1563	5022	109	10.2	46.4	5.8	0.4	0.7	0.3	316.5
Mean							41.4	26.2	5229	3133	122	7.5	49.9	7.1	0.6	1.2	0.9	111.7
Standard deviation							28.0	20.0	669	2742	43	4.7	22.9	2.6	0.2	0.3	0.1	126.5
Standard deviation (%)							67.8	76.3	12.8	87.5	35.5	62.2	45.9	35.8	30.3	23.4	10.5	113.2

Table 5.9: Summary of the start-stop test results for the steel-on-steel test case.

5.4.8.3. Spectral analysis results

The Power Spectral Densities (PSD) during the four dynamic phases of the steel-on-steel test case are discussed in this section. Figure 5.78 shows the frequency responses during the first 50 cycles of phase one and from these, it can be seen that there is a broad range of signatures in the sampled torque signals. The signatures in the region of 224 Hertz (Hz) due to the fluid pulsations are also present in these responses, which suggests the spectral analysis methodology is accurate and reliable.

The signatures in the region of 190 – 210 Hz however, appear to be specific to the steel-on-steel test case, as these were not present in any of the frequency responses with the wear liners included, see Sections 5.3.7 and 5.4.7. The frequency components in the regions of 134, 62 and 40 Hz on the other hand, do appear to be signatures that are common to all of the frequency responses that have been discussed throughout this thesis. The power responses in the steel-on-steel test case however, are slightly higher as well as more clearly defined which suggests that the wear liner components attenuate the power responses of the centre plate system.

During the first 50 cycles of phase two shown in Figure 5.79, it can be seen that there has been a significant increase in the power amplitudes due to the centre plate load ramping-up to 3 kN. The scale on the y-axis for example, has increased by a factor of six relative to the scale that was used to analyse the spectral components under the 0.5 kN loading condition (Figure 5.78). The four distinctive signatures in the regions of 40, 62 and 134 Hz, have also merged into a broad-band signal under the 3 kN loading condition, but the peaks in these regions are still clear to see.

The characteristics of the signatures in the region of 150 Hz however (Figure 5.79), appear to be exactly the same as those that were present in the region of 140 Hz during the first 50 cycles of phase one. This finding strongly suggests that it is the same phenomenon causing this band of frequencies to develop in the responses. Also, from the list of natural frequencies shown in Table 5.9, it can be seen that the measured signatures for example, are in close agreement with the 2nd/5th harmonics of the centre plate components. These calculations are based on the K1 stiffness parameters, as well as the inertial properties of the centre plate system under the 0.5 and 3 kN loading conditions.

The broad-band signals in the region of 100 – 150 Hz were also present in the centre plate/wear liner responses using material B during the latter stages of the 6 and 9 kN service tests, see Figures 5.65 – 5.67 in Section 5.4.7.2. This analyses therefore, suggests that it is the material transfer from the steel centre plate to the wear liner components for example, causing the stick-slip behaviour to develop in the centre plate system.

This suggestion is also supported by the wear rates of materials B and C as can be seen in Section or 5.2.3 or Appendix M, which are relatively low in comparison to the wear rates of material A. This finding also suggests that the wear rates of the centre plate components in the test cases using materials B and C for example, are higher which is also contributing to the amounts of steel material that is transferred to the surfaces of the wear liner components, see Figure 5.2 in Section 5.1.

The wear characteristics of material A on the other hand, suggest that steel material is still been transferred between the centre plate/wear liner friction surfaces, but is also worn away as the number of running cycles increases. The normalised post-test mass property results for material A in the majority of test cases therefore, are seen to be 6 – 7 times lower than post-test mass property results for materials B and C.
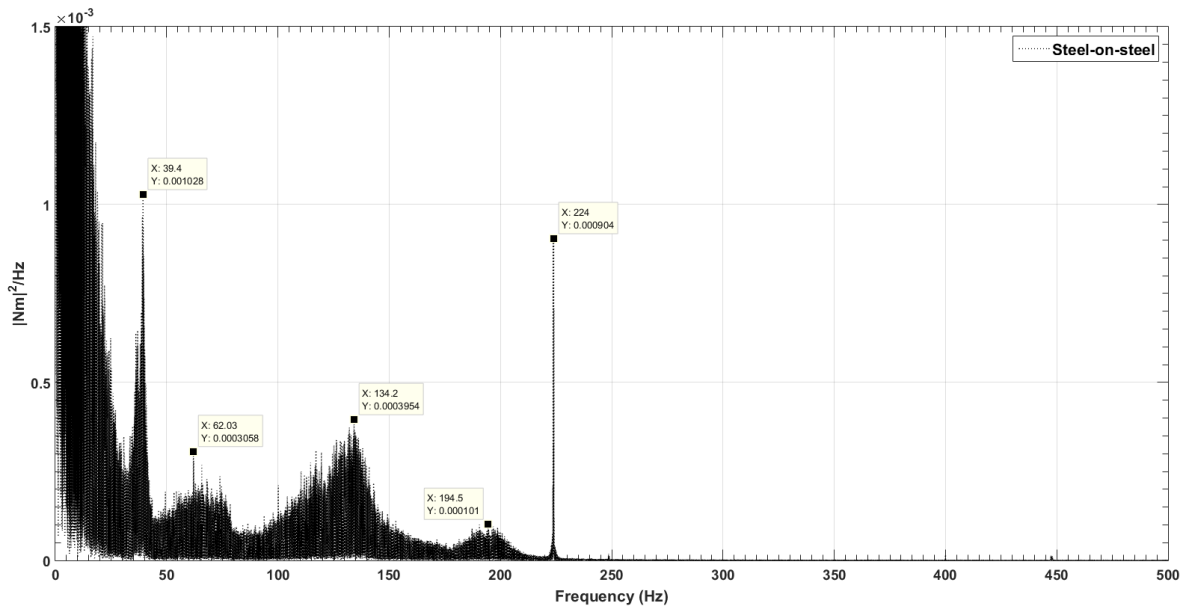
Figure 5.78: PSD during the first 50 cycles of phase one.
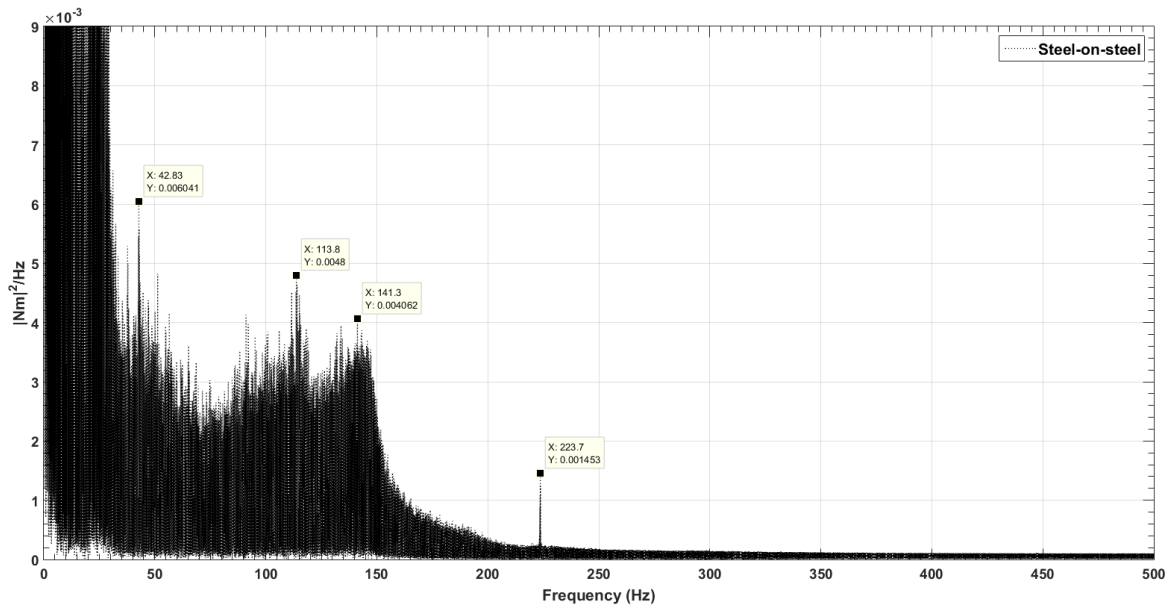
Figure 5.79: PSD during the first 50 cycles of phase two.

The PSD during the last and first 25 cycles of phases four and five are shown in Figure 5.80 and from these, it can be seen that the scale on the y-axis has decreased by a factor of two in comparison to the scale that was used in Figure 5.79. The peak torque responses during phases two and four for example (3 kN), were seen to range between 62 – 70 Nm (Table 5.9) and during phases one and five (0.5 kN), the peak torque responses were seen to range between 10 – 13 Nm, which is in line with the expected behaviour as these torque responses are 5 – 6 times lower.

The main differences between the hysteresis responses during phases one/two and those that were generated during phases four/five however, are the transients during the breakout events and the stick-slip behaviour developing during the gross-sliding regimes, see Figures 5.74 – 5.77 in the previous section. This analysis suggests that the frequency components in the regions of 40 – 65 Hz and 100 – 150 Hz for example, are related to the stick-slip behaviour and natural frequencies of the centre plate system.

The PSD during the last 50 cycles of phase five are shown in Figure 5.81 and from these it can be seen that the frequency responses are much smoother in comparison to the responses during the first 50 cycles of phase one. The frequency components in the region of 134 – 136 Hz are still present in the responses shown in Figure 5.81, but the power amplitudes as can be seen, are at least 50% lower. This analysis also suggests that the unique signatures of the stick-slip response for example, start to develop in the region of 130 – 150 Hz. This range of frequencies as can be seen from the summary of results shown in Table 5.10, are in the same region as the 2nd harmonic of the centre plate system, which are seen to range between 70.2 and 79.3 Hz under the 0.5 kN loading conditions.

Under the 3 kN loading conditions the fundamental frequencies of the centre plate system are seen to range between 32.8 and 33.6 Hz (Table 5.9). This analysis therefore, also suggests that the stick-slip behaviour starts to excite the 4th harmonic of the system under this loading condition. This completes the analyses of the steel-on-steel test case and the laboratory test results. The following section discusses the X-Factor test results that were calculated from the running-in/service test torque responses.
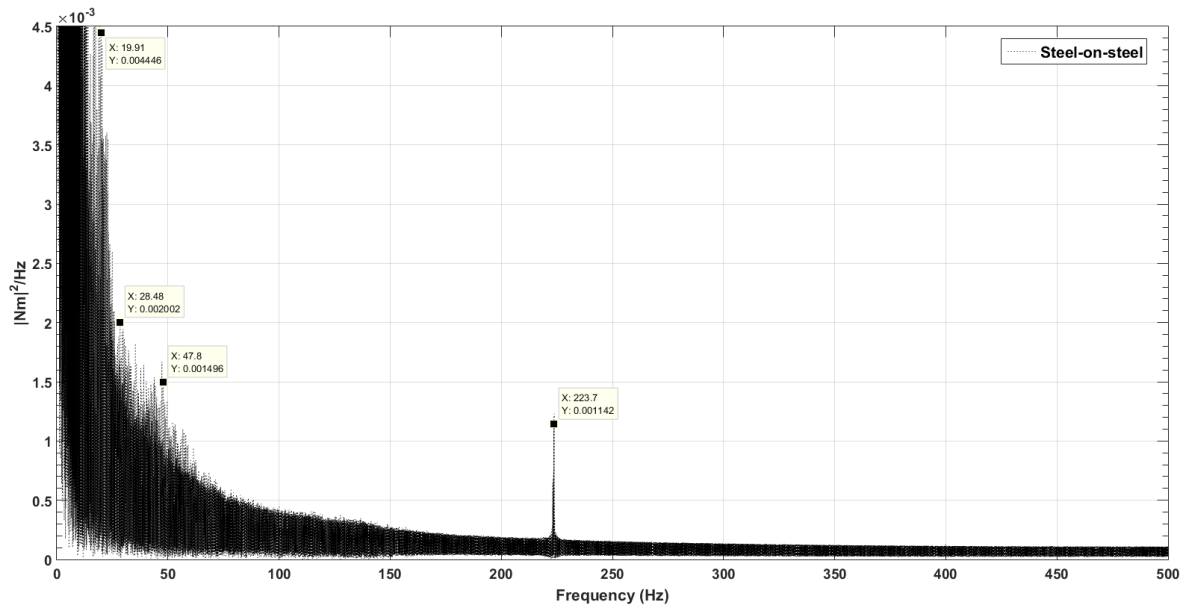
Figure 5.80: PSD during last 25 cycles of phase four and the first 25 cycles of phase five.
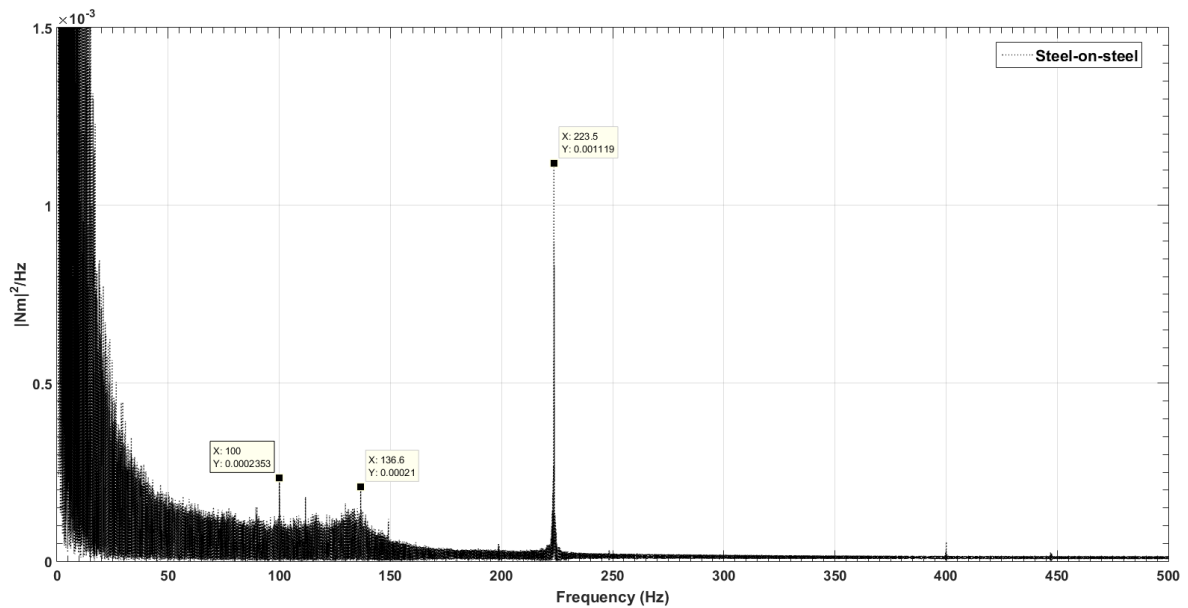
Figure 5.81: PSD during the last 50 cycles of phase five.

5.4.9. X-Factor test case description

The X-Factor results that were calculated from the running-in/service test torque responses are discussed in this section. Railway vehicles in the UK for example, have to demonstrate compliance with the Railway Group Standards (RGS), GM/RT2141 (Issue 3), `Resistance of Railway Vehicles to Derailment and roll-over', before they are allowed to operate on the rail network. The X-Factor test as was explained previously in Sections 2.13 and 3.1, is one of several key performance tests that is carried out on newly built/modified passenger/freight vehicles during vehicle acceptance procedures to evaluate the rotational resistance of the vehicle.

Vehicle manufacturers` can demonstrate that a newly built/modified vehicle is compliant with the GM/RT2141 standards following the methods shown in Figure 5.82, which as can be seen, are dependent on the classification of vehicle being tested. Vehicles that do not have multi-bogie/axle

configurations, novel suspension systems or running gear, such as a passenger vehicle for example, can demonstrate compliance using any of the three testing methods, which includes quasi-static laboratory testing, on-track ride tests as well as virtual testing using computer simulations and validated vehicle models, see Figure 5.83.

	Method 1	Method 2	Method 3
Vehicles having neither novel suspension or running gear nor a multi-bogie / axle configuration	X	X	X
Vehicles having a multi-bogie / axle configuration but not having a novel suspension or running gear		X	X
Vehicles having a novel suspension or running gear			X

Figure 5.82: Methods of acceptance for different vehicle types (RSSB, 2009).

	Appendix A	Appendix B	Appendix C	Appendix D	Appendix E
	Static or quasi-static measurement of wheel unloading on twisted track	Measurement of bogie rotational resistance	Computer simulations designed to examine whether the vehicle has an acceptable resistance to flange climbing derailment at low speed	On-track ride tests	On-track dynamic measurement of Y/Q ratio and analysis of the results
Method 1	X	X		X	
Method 2			X	X	
Method 3					X

Figure 5.83: Simulations and laboratory/on-track tests applicable to the different methods of acceptance (RSSB, 2009).

The route to demonstrate compliance for vehicles with novel suspension systems and running gear on the other hand, such as a freight vehicle with friction damping for example, is method 3. This method as can be seen, includes on-track testing and dynamic measurements of the derailment quotient, $\frac{Y}{Q}$, using load sensing wheelsets or in-direct measurements of the forces/displacements in the suspension springs, as well as measuring the accelerations of the bogie frame/wagon body. The derailment acceptance limit is then found by equating the $\frac{Y}{Q}$ ratio to Nadal`s limit, which is given in Equation (2.26), Section 2.8 (RSSB, 2009).

The rotational resistance of vehicles with novel suspensions as can be seen in (Simson & Brymer, 2008) or (Aizpun, Alonso, & Vinolas, 2015) for example, is then measured using dedicated equipment and laboratory tests. The measurement results from these tests are then substituted into Equation (2.27) in Section 2.11 to calculate the X-Factor value for the vehicle. If the rotational resistance of the vehicle then exceeds the X-Factor threshold limit, which for vehicles carrying axle loads above 8 tonnes for example, is seen to be 0.1 in the GM/RT2141 standards. The vehicle will not be accepted into service until the problem has been rectified due to the increased risk of a flange climbing derailment (RSSB, 2009).

The rotational resistance between the bogie/wagon body obviously has a significant influence on the vehicle performance, such as the ability to negotiate curves, switches and crossings safely and efficiently without causing damage to either the wheel/rail or any other vehicle component. The rotational resistance also plays an important role in maintaining vehicle stability at high speeds on straight sections of track. This parameter therefore, needs to be carefully controlled and monitored throughout the life-cycle of the vehicle to ensure the vehicle performance is maintained within the acceptable limits defined in the GM/RT2141 standards. The following section discusses the calculation method that was used to obtain the X-Factor results for the centre plate/wear liner components.

5.4.9.1.   X-Factor calculation method

The centre plate loading conditions that were used in the scale model laboratory tests were scaled to the full size equivalents following the 1:7 scaling laws that were derived in Section 3. The scaling factor for the 1:7 scale centre plate load for example, is 49, so the 3, 6 and 9 kN loading conditions are seen to be equivalent 24.5, 147, 294 and 441 kN respectively in the full size system.

The GM/RT2141 standard states that the X-Factor test should be carried out using rotational speeds ranging between $0.2 - 1$ ^{o}/s, which is representative of the range curve entry/exit speeds likely to be seen by a freight vehicle while operating under normal service conditions. The two forcing frequencies that were used to carry out the laboratory test cases discussed in this thesis (0.042 Hz and 0.084 Hz), are equivalent to rotational speeds of 0.5 and 1 ^{o}/s respectively, so are in line with the GM/RT2141 standards. From the hysteresis responses that were measured during the 0.042 and 0.084 Hz running-in/service test cases however, it was shown that the torque responses of the centre plate/wear liners for example, were independent of the rotational velocity.

The power amplitudes of the frequency responses on the other hand, were seen to be dependent on the rotational velocity, so as was mentioned in Section 3, will be seven times higher than they actually should be in the scale model torque responses. The wear rates and torsional inertia of the centre plate/wear liner components will also be several times higher in the scale model tests. This is due to the scaling applied to the rotational velocity parameter, which should have ranged between $0.029 - 0.143$ ^{o}/s in the scale model laboratory tests in order to maintain similarity between the full size/1:7 scale velocity responses under the given X-Factor test specifications.

However, from the mass property results shown in Figure 5.15 (Section 5.2.3), it can be seen that the wear parameters for materials B and C for example, appear to be independent of the rotational velocity. The modelling parameters and responses presented in this thesis therefore, can still be used with confidence in order to gain a better understanding of how different wear liner materials perform under a wide range of running conditions.

The effects of increasing the torsional inertia of the centre plate system in the scale model tests as a result of using rotational speeds ranging between $0.5 - 1$ ^{o}/s, which would scale-up to $3.5 - 7$ ^{o}/s in the full size system, are more difficult to quantify without having the on-track/laboratory test data to fully justify this scaling error. In the GM/RC2641 document however, the representative rotational speeds of a passenger vehicle for example, are suggested to be in the region of $3 - 4$ ^{o}/s, which is more in line with the speeds used in the scale model tests and also shows that the scale model test results are still relevant to the rail industry, even though the scaling factor for the rotational velocity, in the context of freight vehicles for example, is in error (RSSB, 2007).

The torque responses that were measured during the running-in/service test cases were then scaled-up to the full size equivalents using a scaling factor of 343. The results from the 0.5 kN running-in test cases for example, were used to develop the loading conditions for a Constant Contact Side Bearer

(CCSB) component model, whereas the centre plate models on the other hand, were developed from the service test results.

The COF values for the CCSB component models as can be seen from the results shown in Table 5.10, range between 0.05 – 0.32, whereas the COF values for the centre plate system are 69 – 80% higher and range between 0.09 – 0.54. This increase is due to the heavier loading conditions as well as the increased number of running cycles during the service test cases. The highest COF value that was calculated for each wear liner material after the running-in test cases was then used in the CCSB X-Factor calculations, which for materials A, B and C, are seen to be 0.2, 0.32 and 0.28 respectively in Appendix N.

The COF values for the CCSB components in the following X-Factor calculations however, remain constant in order to simplify the analyses, whereas the COF values for the centre plate/wear liner components on the other hand, are dynamic values, meaning that these parameters can increase/decrease as a function of the number of running cycles.

The names given to the three X-Factor test loading conditions it should be pointed out (Table 5.10), were used for reference purposes only and are not meant to be exact representations of the real-world tare, part-laden and laden axle loads, as these are specific to individual countries and network operators. The laden axle load of 269.5 kN however, is close to the real-world loading condition and this is the reason why the other two loading cases were referenced as the tare and part-laden axle loads. The following section discusses the X-Factor results for tare loading conditions.

Parameter	Unit
Bogie mass (kg)	2000
Wheelset mass (kg)	1500
Wagon-body tare mass (kg)	39949
Wagon-body part-laden mass (kg)	69918
Wagon-body laden mass (kg)	99888
Bogie wheelbase (m)	1.8
Side bearer position (m)	0.85
Side bear coefficient of friction	0.05 - 0.32
Centre plate coefficient of friction	0.09 - 0.54
Distance between centre plates (m)	6.77
Minimum curve radius (m)	65
Load supported by each side bearer (kN)	24.5
Tare axle load (kN)	122.5
Part-laden axle load (kN)	196
Laden axle load (kN)	269.5

Table 5.10: X-Factor calculation parameters.

5.4.9.2. Tare X-Factor test results

The X-Factor responses for materials A, B and C during the 3 kN/tare loading cases are shown in Figure 5.84. The green and yellow lines show the responses of test cases 1 and 5 using material A, whereas the blue and red lines, show the responses of test cases 8, 12 and 15 using materials B and C. The X-Factor limit of 0.1 is also shown by dashed black line. From the responses shown in Figure 5.84 and the summary of results shown in Appendix S, it can be seen that the X-Factor values for the complete data set for example (5 test cases), range between 0.044 – 0.085. The minimum and maximum values under this loading condition were calculated for materials A and B (Green lines and blue lines). From the results shown in Appendix S, it can also be seen that the mean percentage increase in the X-Factor values throughout the tare service tests is in the region of 16.8%.
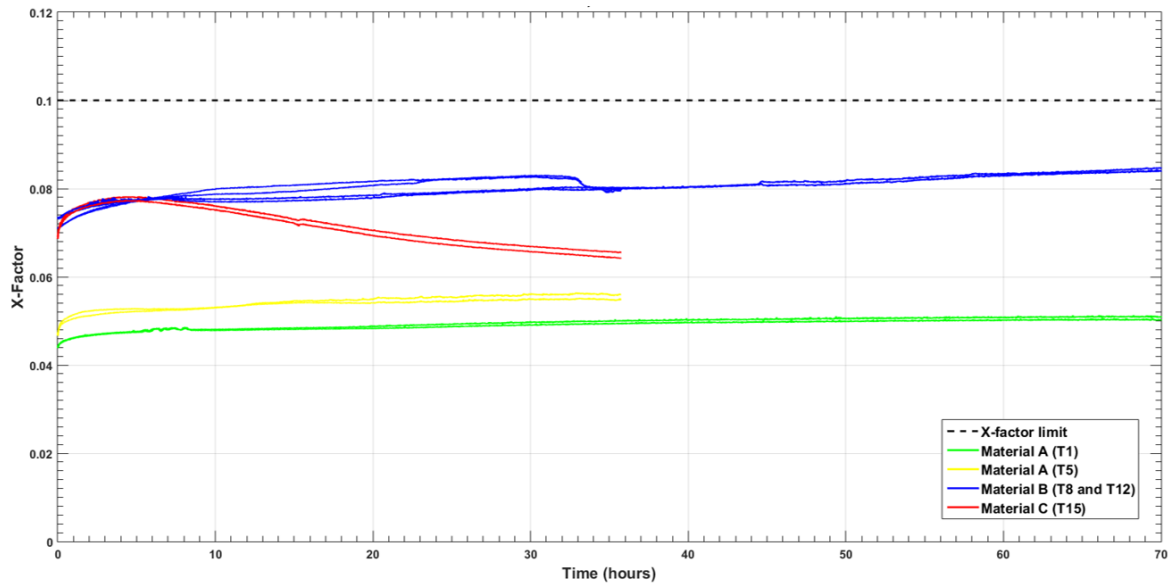
Figure 5.84: X-Factor values during the tare loading cases.

The normal distributions of the minimum/maximum X-Factors values are shown in Figure 5.85 and from these, it can be seen that the mean of the minimum values for example, which was obtained during the first 25 cycles of the service tests, is 0.061 (Green lines). Whereas the Standard Deviation (SD) and Standard Error of the Mean (SEM), are seen to be 0.014 and 0.0063 respectively. The expected mean value of the data set including three SEM therefore (99.7% Confidence Interval (CI)), could vary between 0.042 – 0.08, which is compliant with the 0.1 X-Factor limit. The upper boundary of the minimum distribution curve as can be seen (+3 SD), is in the region of 0.103 which is above the X-Factor limit, but with 3 SEM included in the estimation, this region extends to 0.122 which is not acceptable.

However, during the bogie rotational resistance tests that were carried out by (RAIB, 2007) after the Washwood Heath derailment incident in September 2006, the X-Factor value that was measured on the tested vehicle with the original CCSB`s was suggested to be 0.119. When these components were replaced with UIC sprung side bearers, the X-Factor values were seen to range between 0.102 and 0.113, see page 15 of this report (RAIB, 2007). This analysis suggests that the X-Factor results that have been calculated from the 1:7 scale model laboratory test results, are in exact agreement with the results obtained from full size vehicle tests which obviously increases the confidence levels in the 1:7 scale testing methodology.

The probability of an X-Factor failure occurring due to faulty centre plate/wear liner components can then be estimated using the SD of the complete data set, as well as the normal distribution table given in (Stroud, 1995). From this table it can be shown that there is a 0.4% chance of a new centre plate/wear liner component for example, causing a vehicle to fail the X-Factor test, see the minimum distribution curve shown in Figure 5.85 (99.7% CI).

Therefore, by considering a new train with 20 wagons/40 bogies and assuming that there is one centre plate and two side bearers on each bogie for example (3 wear liners per bogie), then the results from the statistical analyses suggest that all of the centre plate/wear liner components in the new condition should enable the vehicle to pass the X-Factor test (99.7% CI).

The maximum X-Factor values on the other hand, were calculated during the last 25 cycles of the service tests and from this distribution (Red line), it can be seen that the mean value, SD and SEM for

the data set have increased to 0.071, 0.016 and 0.0072 respectively. The mean value with 3 SEM included in the estimation therefore, could be in the region of 0.049 – 0.093, but would also be classed as acceptable. Whereas the upper boundary of this distribution is 0.12, but with the 3 SEM included, extends to 0.14 and is clearly above the 0.1 X-Factor limit.

The probability of an X-Factor failure occurring under the tare loading conditions during the life-cycle of the centre plate/wear liner components therefore, increases to 3 – 4% (99.7% CI), which amounts to 3 – 5 centre plate/wear liner components out of 120 for example, causing the X-Factor values to increase to the region of 0.1 – 0.14 which obviously increases the risk of a derailment. Also, from the summary of results (Appendix S), it can be seen that the SD of the minimum/maximum X-Factor values after 13800 cycles of testing including the running-in test cycles, are in close agreement, ranging between 22.2 – 23.3%. This analyses suggests that the variations in the centre plate system parameters as the number cycles increases for example, are consistent.
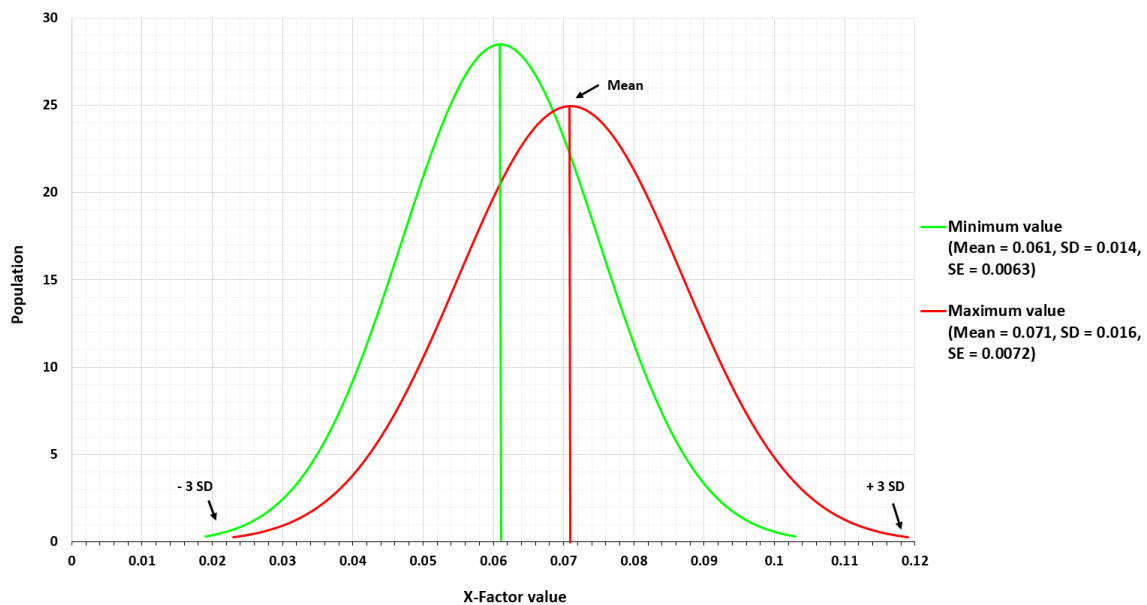
Figure 5.85: Normal distribution of the X-Factor values during the tare loading cases.

The X-Factor values for each material sample were then analysed in a probability density plot and then a histogram to quantify the distribution of the sampled data points throughout the 10800 cycle service tests. The data sets from the 0.042 and 0.084 Hz test cases were separated into 40 equally spaced bins, but after fitting the normal and Weibull distribution curves to the sampled data points, it was clear to see that these two distributions were not in good agreement with the highly nonlinear observations, see Figures 5.86 – 5.88. In these figures, the X-Factor values during the 0.042 and 0.084 Hz forcing frequency test cases are shown by the green and red bars and the black lines show the Kernel Density Estimations (KDE). These fits as can be seen, take the nonlinearities of the distributions into account, whereas the normal and Weibull distribution curves didn`t.

The distributions of the X-Factor values for material A are shown in Figure 5.86 and from these, it can be seen that the values range between 0.045 – 0.06. This range of values are just below the mean X-Factor value of 0.061 for the complete data set as can be seen by looking at the normal distributions shown in Figure 5.85 above (5 test cases). The characteristics of the 0.042 and 0.084 Hz distributions are also very similar, but the 0.084 Hz distributions appear to have shifted to the right by a factor of 0.0042. The histogram bars are also 50% less dense in the 0.084 Hz test cases which suggests that the rate of change in the COF/X-Factor values is higher.

The X-Factor values for materials B and C are seen to be 44 - 50% higher in Figures 5.87 and 5.88 respectively, ranging between $0.065 - 0.09$. The mean X-Factor values for material B are also seen to be the highest overall at 0.0813 and 0.0792 under the tare loading conditions. From the normal distributions shown in Figure 5.85, it can be seen that this range is located above the mean of the maximum X-Factor values. This analysis suggests that the chances of a vehicle failing the X-Factor test during the life-cycle of the centre plate/wear components using material B for example, is $3 - 4\%$, whereas the potential failure rate for material A under these loading conditions is 0.4% (99.7% CI).

The distributions of X-Factor values for materials A and B however, both suggest that the rates of change in the initial values that were calculated at the start of the service tests, are quite high as the histogram bars in the regions of $0.045 - 0.05$ and $0.07 - 0.075$ for example, are less densely populated in comparison to bars above the mean values. This is also where the gradients of the KDE curves start to increase due to the X-Factor values settling in the regions above the mean values.

The distributions of material C on the other hand (Figure 5.88), are clearly unique and suggest that this material does not behave in the same way as materials A and B under the tare loading condition. The torque responses in materials A and B for example, were seen to increase in proportion to the number of running cycles, whereas the responses in material C (Figure 5.84, Red lines), were seen to increase in proportion to the number of running cycles during the first $3 - 4$ hours of the service test. Or alternatively, the first $907 - 1210$ cycles of this test towards the peak values of 0.078, but then started to decrease again back towards the initial values.

The X-Factor values for material C therefore, are seen to be evenly distributed about the mean value, so the likelihood of an X-Factor failure occurring using this particular wear liner material would actually start to decrease after achieving the critical number of continuous running cycles ($907 - 1210$). However, this unique material behaviour may not be repeatable under the start-stop test conditions that were discussed in Section 5.4.8, if for example, these behaviours are related to the temperature changes in the centre plate/wear liner components. The start-stop test is actually closer to reality in the context of freight vehicle operating conditions, so would allow the suspension components to cool down over time which could also cause the X-Factor/COF values to start increasing once the system is set in motion again, but requires further research to establish if this would be the case. The following section discusses the X-Factor results for the part-laden loading cases.
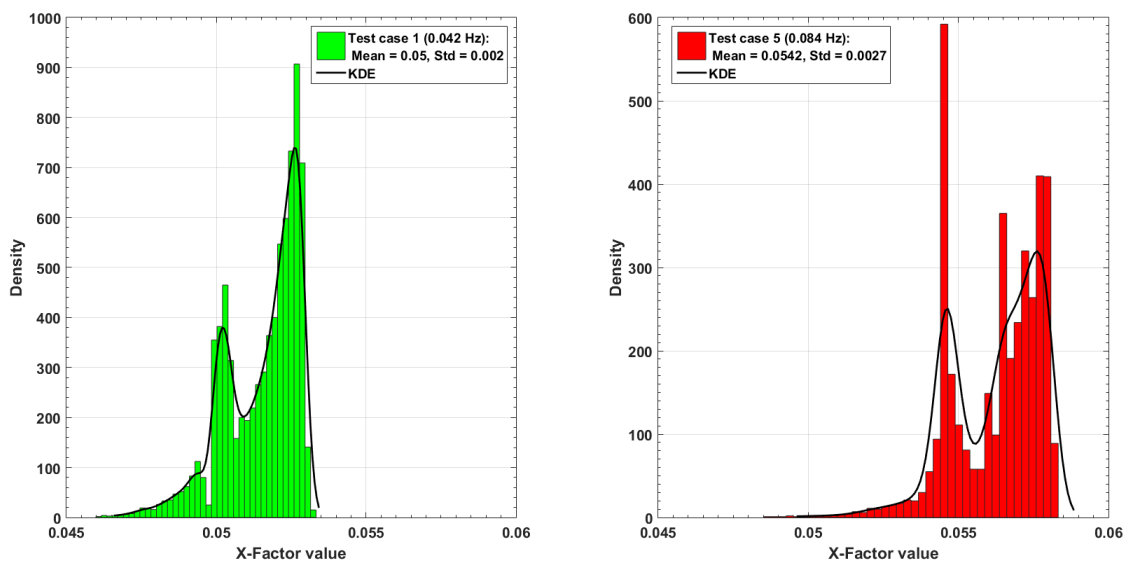
Figure 5.86: Distribution of the X-Factor values for material A.
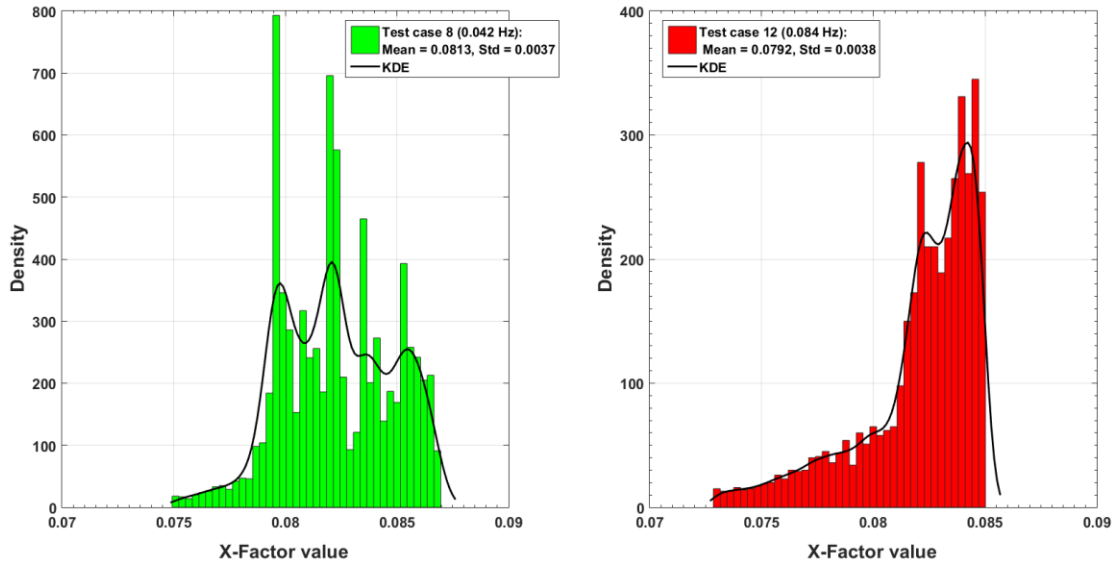
Figure 5.87: Distribution of the X-Factor values for material B.
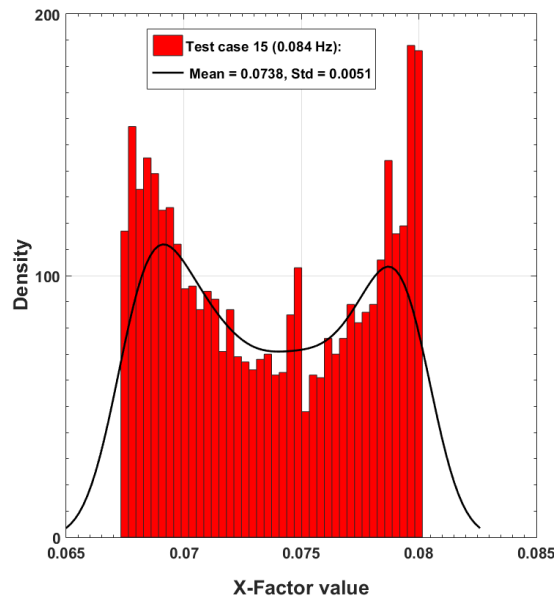
Figure 5.88: Distribution of the X-Factor values for material C.

5.4.9.3. Part-laden X-Factor test results

The X-Factor responses under the part-laden loading conditions are shown in Figure 5.89 and from these, it can be seen that the range of values have decreased slightly to $0.033 – 0.083$. The maximum value under this loading condition was calculated during test case 13 using material B (Blue lines), whereas the minimum value was calculated during test case 4 using material A (Black lines). The mean percentage increase in the X-Factor values however, has increased from 16.8 to 39.2%. The SD of this parameter under the part-laden loading condition is also seen to be significantly higher at 87.8%, whereas for the tare loading cases, this parameter was seen to be 22.2% which is four times lower, see Appendix S.
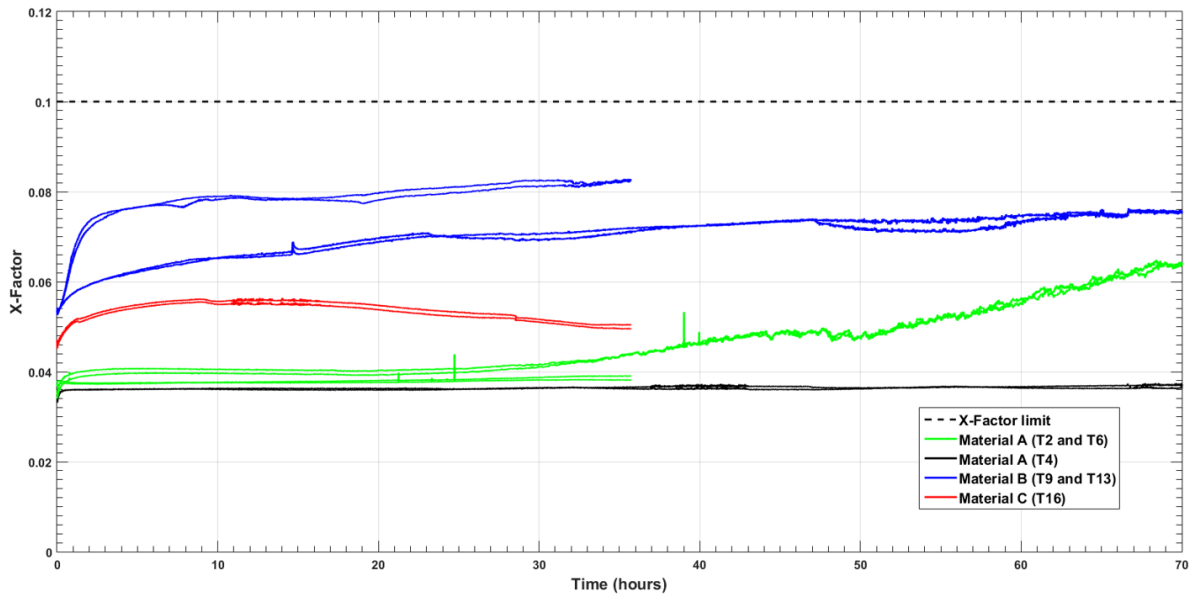
Figure 5.89: X-Factor values during the part-laden loading cases.

The normal distribution curve of the minimum X-Factor values is shown in Figure 5.90 and from this (Green lines), it can be seen that the mean values, SD and SEM relative to the tare loading conditions for example, have decreased to 0.043, 0.009 and 0.0037 respectively. The expected mean value for the complete data set including the 3 SEM therefore (6 test cases, 99.7% CI), could vary between 0.032 – 0.054, which is 32.5 % lower than the range of mean values that were calculated during the tare loading conditions. The upper boundary of this model with the 3 SD and 3 SEM included in the estimation, is seen to be 0.093 which is also compliant with the 0.1 X-Factor limit. This analyses suggests that all of the new centre plate/wear liner components under the part-laden loading conditions for example, will pass the X-Factor test (99.7% CI).

The mean, SD and SEM of the maximum X-Factor values have also decreased relative to the tare loading cases and are now seen to be 0.06, 0.019 and 0.0078 respectively (Red line). The expected mean value for the complete data set including the 3 SEM therefore (99.7% CI), could be in the region 0.037 – 0.083, which is 11% lower than the range of maximum values that were calculated during the tare loading conditions. The upper boundary of the maximum distribution curve however, is seen to be in the region 0.117, which is already above the X-Factor limit, but with the 3 SEM included in the estimation, extends to 0.14, which as can be seen, is the same region as the upper boundary of the tare distribution after 13800 cycles of testing, see Figure 5.85.

From the normal distribution table in (Stroud, 1995), it can be shown that there is a 1 – 2% chance of a potential X-Factor failure occurring under the part-loading conditions during the life-cycle of the centre plate/wear liner components. This analysis suggests that approximately 1 – 3 centre plate/wear liners components out of 120 in the context of the example discussed in the previous section, could be causing the X-Factor values to increase to the region of 0.1 – 0.14. The SD relative to the tare conditions have also increased by 10% and are now seen to range between 22 – 32.7% (Appendix S).
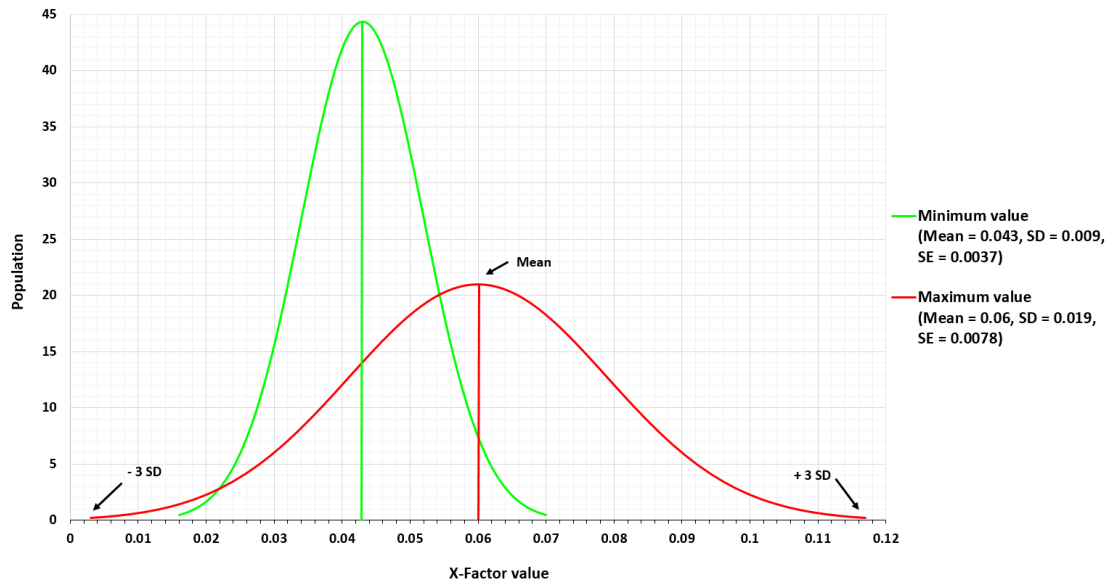
Figure 5.90: Normal distribution of the X-Factor values during the part-laden loading cases.

The distributions of the X-Factor values for material A during the 0.042 and 0.084 Hz test cases are shown in Figure 5.91. From these results it can be seen that the values during test case 2 for example, range between 0.035 – 0.07 which is the widest range overall for this material, but still within the range of minimum X-Factor values as can be seen from the normal distribution shown in Figure 5.90 (Green line). Whereas the range of X-Factor values during test case 4, which is a re-run of test case 2 using new centre plate/wear liner samples, are significantly lower as well as more consistent and seen to range between 0.0365 – 0.038.

The X-Factor values during the 0.084 Hz test are also lower than those that were calculated for test case 2 and are seen to range between 0.0385 – 0.0395. This analyses suggests that there was a problem with either the centre plate or wear liner samples that were used in test case 2. The mean value of the 0.084 Hz test case as can be seen (Test case 6), is also slightly higher than the mean value of 0.042 Hz test case (Test case 4), which is similar to the tare loading conditions (Figure 5.86).

From the distributions shown in Figure 5.92, it can be seen that the X-Factor values for material B during the service tests, range between 0.05 – 0.085. The mean values during the 0.042 and 0.084 Hz test cases however, are the highest overall at 0.0664 and 0.0695 respectively. The characteristics of the distributed X-Factor values on the other hand, are similar to those that were observed during the tare loading cases (Figure 5.87), where the density of the bins below the mean X-Factor values for example, are seen to be the least densely populated due to the X-Factor values changing rapidly during the first 2 – 3 hours of the service tests, see Figure 5.89.

It can also be seen from the normal distributions shown in Figure 5.90, that the X-Factor values for material B are located above the mean of the maximum distribution for the complete data set (6 test cases, redline), but with a significant bias towards the higher values in this range. The probability of a vehicle failing the X-Factor test during the life-cycle of the centre plate/wear liner components therefore, is 1 – 2%, whereas during the tare loading conditions the probability was in the region of 3 – 4% (99.7% CI).

The distributions of the X-Factor values for material C are shown in Figure 5.93 and from these it can be seen that the mean value of 0.0529, as well as the range of values are similar to test case 2 using material A. The sparsely populated bins in the region of 0.045 – 0.05, also shows that the lowest X-Factor values overall for example, form the smallest part of the data set, which suggests that the higher X-Factor values are closer to reality once the centre plate system has been subjected to the

206

initial running-in period. From the time histories shown in Figure 5.89 it can be seen that under the part-laden loading conditions, this period is suggested to be in the region of 2 – 3 hours for the majority of wear liner samples that were characterised, or alternatively, between 302 – 454 and 604 – 908 cycles for the 0.042 and 0.084 Hz test cases respectively.

The X-Factor values for materials A and C as can be seen from the normal distributions shown in Figure 5.90 (Green line), are also more closely aligned with the mean of the minimum X-Factor values (0.043). The chances of a vehicle failing the X-Factor test during the life-cycle of the centre plate/wear liner components using these materials and under normal running/wear conditions therefore, is 0.3% (99.7% CI). The following section discusses the distributions of the X-Factor values during the laden loading cases.
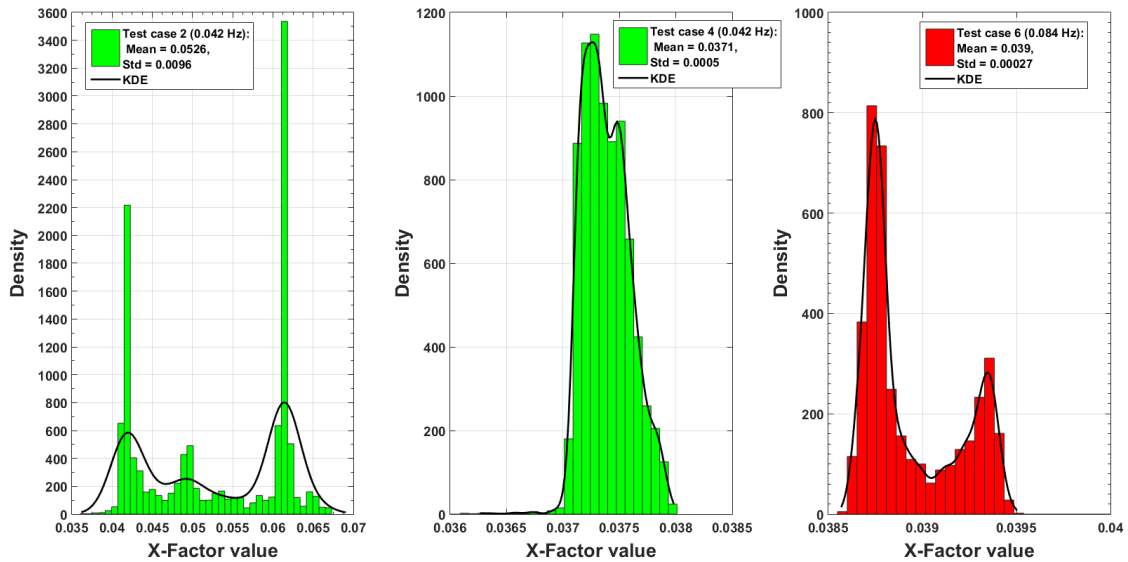
Figure 5.91: Distribution of the X-Factor values for material A.
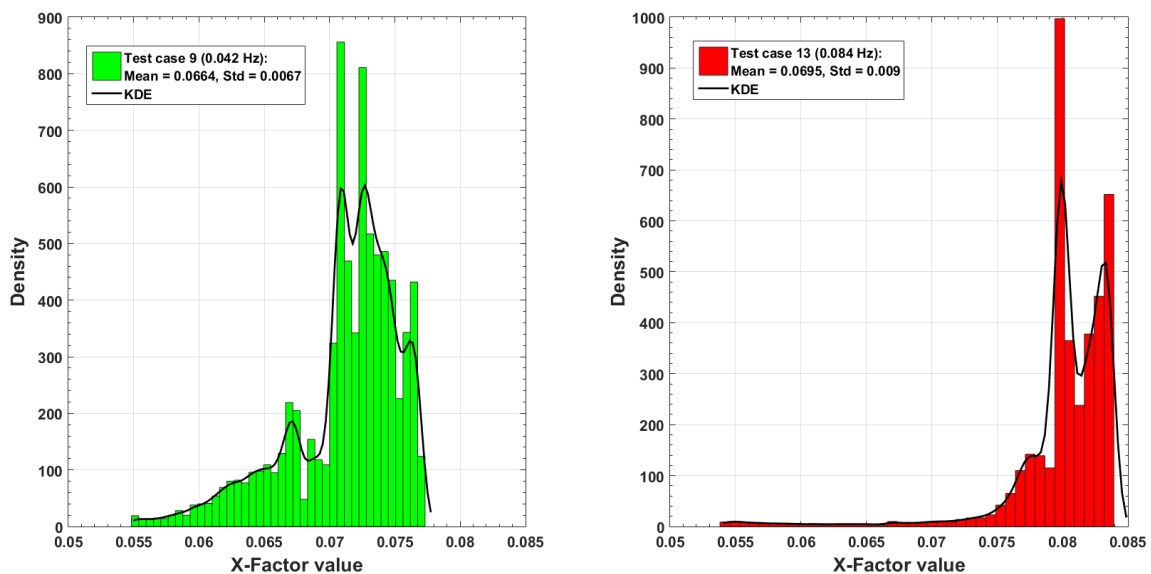
Figure 5.92: Distribution of the X-Factor values for material B.
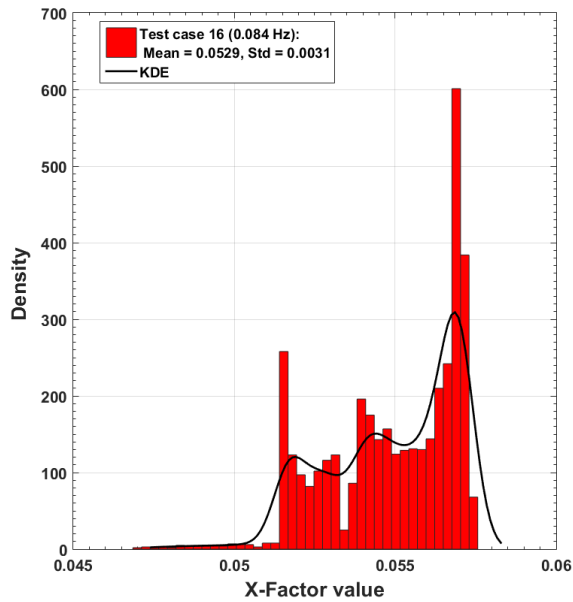
Figure 5.93: Distribution of the X-Factor values for material C.

5.4.9.4. Laden X-Factor test results

The time histories of the X-Factor responses during the laden loading cases are shown in Figure 5.94 and from these as well as the summary of results shown in Appendix S, it can be seen that the X-Factor values now range between 0.029 – 0.095 which is the highest range overall. The maximum values during test cases 11 and 14 on material B as can be seen (Blue lines), are extremely close to the 0.1 limit.

The minimum X-Factor value of 0.029 during test case 7 using material A however (Green lines), is seen to be the lowest value overall, whereas the minimum values during the tare and part-laden loading cases were seen to be slightly higher at 0.044 and 0.033 respectively. It can also be seen that the mean percentage increase in the X-Factor values for the complete data set (5 tests, Appendix S), has increased from 39.2 to 58.8% relative to the part-laden responses, whereas the SD is seen to be lower at 77.5%, which shows that these increases are more consistent.
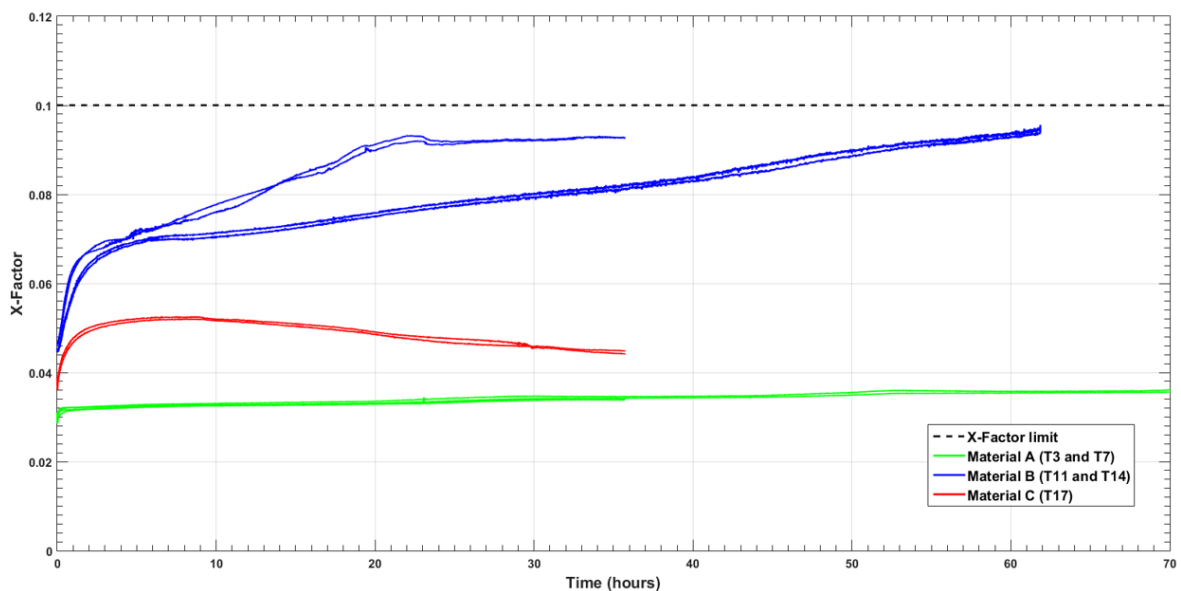
Figure 5.94: X-Factor values during the laden loading cases.

The normal distribution curve of the minimum X-Factor values in Figure 5.95 on the other hand, shows that the mean, SD and SEM of this data set are the lowest overall at 0.037, 0.008 and 0.0036 respectively. The expected mean value with the 3 SEM included therefore, could be in the region 0.026 – 0.048 (99.7% CI), which is slightly narrower than the distribution that was observed under the part-laden loading conditions. The upper limit of this model is also within the X-Factor limit, even with the 3 SEM included in the estimation. From this analyses we can be fairly confident that all the new centre plate/wear liner components out of 120 for example, will pass the X-Factor test under the laden loading conditions (99.7% CI).

The mean value, SD and SEM of the maximum X-Factor values on the other hand (Red line), have increased relative to the part-laden loading conditions and are now seen to be 0.062, 0.03 and 0.0134 respectively. The expected mean value with 3 SEM included in the estimation therefore, could be in the region of 0.022 – 0.102, which is on the X-Factor limit, but would be accepted under the current GM/RT2141 standards.

The upper boundary of this model is seen to be in the region of 0.152 and from the normal distribution table, it can be shown that the probability of an X-Factor failure is already in the region 11 – 12%. This analyses suggests that 13 – 14 centre plate/wear liner components could be in breach of the X-Factor limit after 13800 cycles of testing. This analysis is based on the findings from the scale model running-in/service test results and in the case of the example discussed previously, suggests that 13 – 14 centre plate/wear liner components out of 120, could potentially fail the X-Factor test.

However, with the 3 SEM included in the estimation, the upper boundary of the X-Factor values extends to 0.192. The probability of an X-Factor failure occurring during the life-cycle of the centre plate/wear liner components therefore, increases to 58%, which suggests that 69 – 70 samples out of 120 could be in breach of the 0.1 X-Factor limit. From the summary of results in Appendix S, it can also be seen that the SD under the laden loading condition for example, now range between 20.9 – 48.2%, which are 26 and 16% higher than the variations that were observed under the tare and part-laden loading conditions.
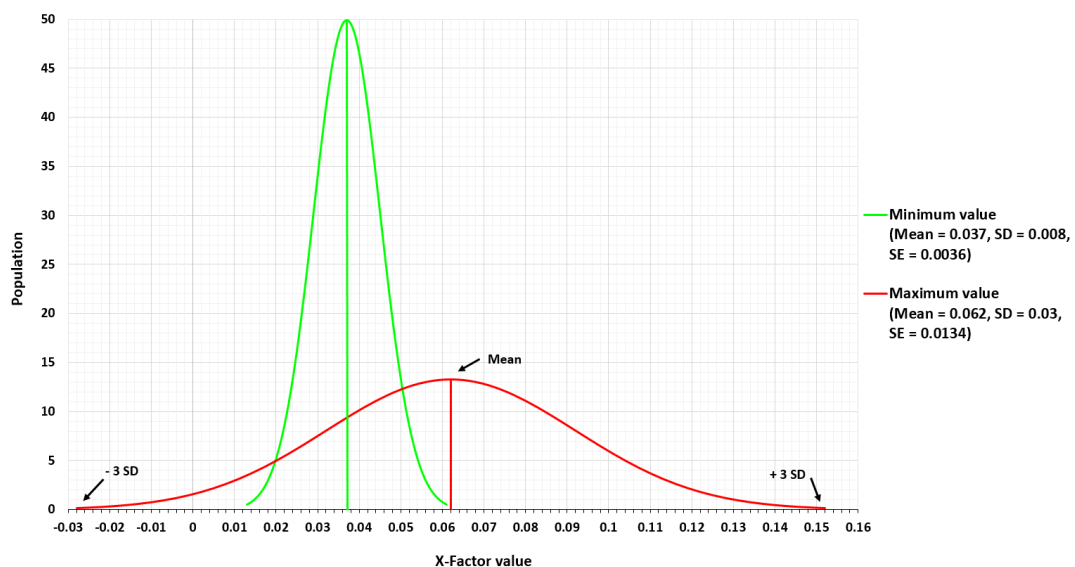
Figure 5.95: Normal distribution of the X-Factor values during the laden loading cases.

The distributions of the X-Factor values for material A during the laden loading cases are shown in Figure 5.96. From these results it can be seen that X-Factor values in both data sets for example (0.042/0.084 Hz), are tightly dispersed around the mean values of 0.0348 and 0.0335 which are also

seen to be the lowest values overall out of the three materials that were studied. Material A also appears to be the most consistent overall under all three loading conditions when the centre plate/wear liner samples are operating within in the nominal X-Factor range for this material, which is seen to be within the normal distributions of minimum values for the complete data set, which also includes the values of materials B and C, see Figures 5.85, 5.90 and 5.95.

Figure 5.97 shows the distributions of the X-Factor values for material B during the 0.042/0.084 Hz laden loading cases and from these, it can be seen the X-Factor values range between 0.045 – 0.095. The mean values for this material however, are in the region of 0.072 – 0.073 which are seen to be the highest values overall. The distributions of material B as can be seen, also appear to be very similar under all three loading conditions, with the low density bins concentrated below the mean values for example, as well as a relatively wide dispersion of results about these parameters which increases in proportion to the centre plate loading conditions.

The range of X-Factor values for material B are also seen to be consistently above the mean of the maximum values for the complete data sets, see Figures 5.85, 5.90 and 5.95. Under the laden conditions for example (Figure 5.95), this distribution with the 3 SD and 3 SEM included in the estimation, suggests that potential X-Factor failure rate using this wear liner material will increase to 58% during the life cycle of the centre plate/wear liner components, whereas for materials A and C on the other hand, the failure rate still remains at 0.3% (99.7% CI).

The overall conclusions that can be drawn from these analyses are that the X-Factor values for material A are the lowest overall as well as the most consistent, ranging between 0.029 – 0.067. Whereas the highest values overall were calculated for material B and are seen to range between 0.045 – 0.095. The X-Factor values for material C however, were slightly lower and seen to range between 0.036 – 0.078, which is in between the values for materials A and B, see Appendix S.

It can also be suggested from the X-Factor results that the centre plate loading conditions as well as the number of running cycles and surface roughness parameters of the centre plate/wear liner components for example, have the strongest influence on the variations observed in the X-Factor/COF results and therefore, the maintenance requirement of these components. The pre-test surface roughness measurements on the centre plate components shown in Appendix I also support these conclusions, where the SD of the Ra-slope parameter for example, is seen to be 41.2% which is in close agreement with the SD of the maximum X-Factor values that were produced during the laden loading cases (48.2%).

However, from the mass property results shown in Appendix M, it can be seen that these parameters are all different for materials A, B and C, which strongly suggests that the maintenance requirements of the secondary suspension components, are specific to the service conditions, as well as the type of wear liner material that is been used by the freight operating company. The wear rate of material A for example, is seen to be 6 – 7 times higher than the wear rates of materials B and C in Appendix M.

This wear liner therefore, would require more maintenance overalls during the life cycle of the vehicle which obviously lead to an increase in the operating costs. Contamination such as the hydraulic oil for example (Test case 5), also had a significant influence on the friction characteristics of material A, which could potentially make it more challenging to devise the optimum maintenance schedules for these wear liners as they are operating in harsh environments on a daily basis. The following section draws some final conclusions on the significant findings from different test cases that have been analysed and quantified during this research work.
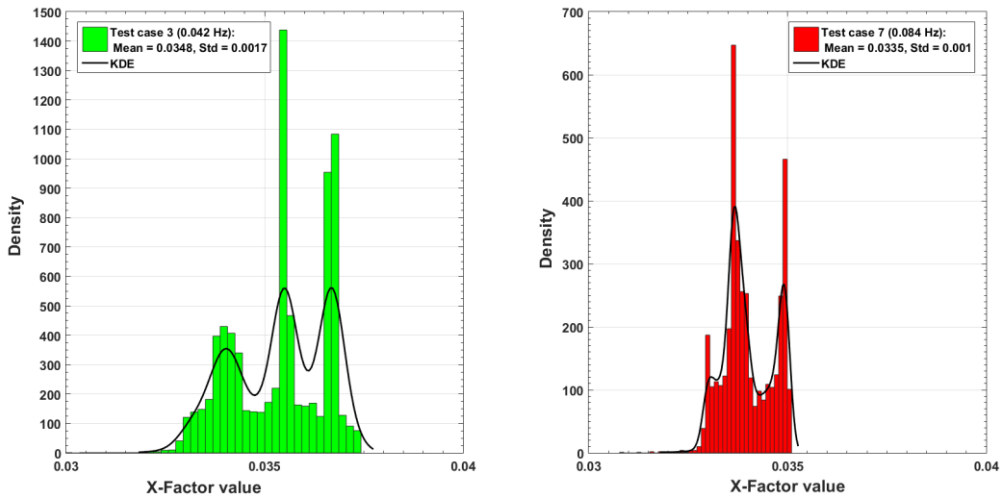
Figure 5.96: Distribution of the X-Factor values for material A.
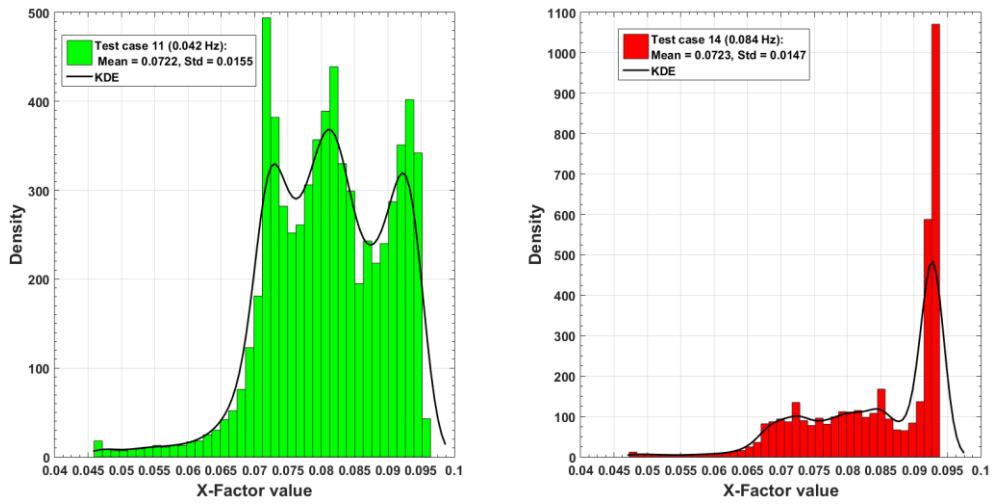
Figure 5.97: Distribution of the X-Factor values for material B.
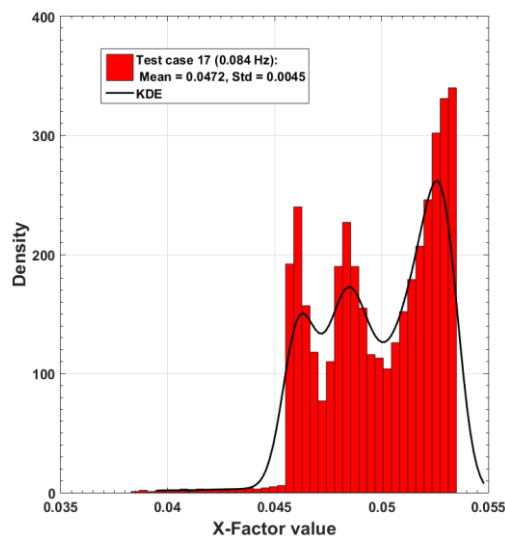
Figure 5.98: Distribution of the X-Factor values for material C.

5.5. Discussion and conclusions

The scale model laboratory tests have generated a wide range of new and novel benchmark test data for three different wear liner components that wasn`t available prior to carrying out this research work. The local/global analysis test data can now be used in conjunction with the results shown in Table 5.4 (Section 5.4.3), by vehicle engineers and researchers for example, to better understand the maintenance and modelling requirements of the secondary suspension components.

This test data will enable researchers to make an informed choice on the most suitable friction models to use in freight vehicle Multibody Simulations (MBS) and also aid in validation of these models. It could be used also inspire the future direction of freight vehicle on-track/laboratory testing and virtual vehicle testing using MBS. The pre/post-test surface roughness measurement data for the centre plate/wear liner components can also be used by the centre plate/wear liner component suppliers, as well as material scientists to develop accurate Finite Element Analysis (FEA) models of these suspension components.

The Standard Deviations (SD) of the nine pre-test surface roughness parameters that were measured on the centre plates components, were seen to range between $20.6 - 41.2\%$, whereas for the wear liners, these parameters were significantly higher and seen to range between $1.2 - 308.3\%$, see Appendices I and L respectively. The highest SD of 41.2 and 308.3% however, were always associated with the measurements describing the slopes of the roughness and waviness profiles. From this analysis, it can be suggested that slope parameters have the strongest influence on the variations observed in torque responses of the centre plates/wear liner components during the laboratory tests, especially at the local level (Taylor Hobson , 2011).

The seven other surfaces roughness parameters that were measured in the pre/post-test analyses on the other hand, appear to be closely related to the levels of material transfer between the centre plate/wear liners, as well as the wear rates and hardening regimes developing in these components. This suggestion is made based on the changes taking place in the pre/post-test measurements of these parameters, which are relatively small in comparison to changes that were taking place in the slopes, see Appendices I and L.

From the post-test images of the wear liners shown in Figure 5.2 (Section 5.1), it can also be seen that material transfer is common to all of the samples that were tested. Ploughing marks for example, are clearly visible in these samples which are obviously caused by the turning marks on the harder surface of the steel centre plates. This analysis also shows that the effective surface areas of the contact interfaces, are actually larger than the design geometry of the centre plate/wear liner components because the surfaces are wavy and rough, as opposed to flat and smooth.

The centre plates were turned on a CNC lathe after each test case, so have a circular surface lay, which is the pattern we are seeing in the post-test images. An increase in the effective surface area however, would then lead to an increase in the breakout torque, as well as higher levels of damping during the gross-sliding events because the yield stresses in the materials forming the contacts for example, are inversely proportional to the area supporting the load (Moore, 1975).

This analysis strongly suggests that the manufacturing procedures and the effective areas that these processes generate on the friction surfaces of engineering components, should be taken into account in analytical calculations in order to achieve a better prediction of the frictional force/torque responses. Engineering surfaces as mentioned above, are very rarely flat or perfectly smooth and it is these factors that need to be seriously considered, as these simplifying assumptions are partly

responsible for the uncertainties associated with freight vehicle testing and friction modelling methodologies that were discussed in the literature review, see for example (Jonsson, 2004).

The running-in tests were then carried out on each new centre plate/wear liner sample for 3000 cycles under the 0.5 kN loading condition. The torque responses during the test cases using materials A, B and C for example, were seen to range between 0.54 − 1.94, 0.94 − 3.1 and 0.63 − 2.73 Nm respectively, see the local analysis results shown in Appendix O. The COF values for material A were also seen to be the lowest overall during the running-in test cases, ranging between 0.05 − 0.19, whereas for materials B and C, the COF values were seen to range between 0.09 − 0.32 and 0.06 − 0.27 respectively, which are 42 − 68% higher.

The non-symmetric friction characteristics of the centre plate/wear liner components were also seen to be extremely severe under the running-in loading conditions (0.5 kN), ranging between 20 − 65% in several of the test cases. This parameter was also shown to be highly dependent on the centre plate loading conditions, as the non-symmetric characteristics during the 3, 6 and 9 kN loading cases for example, were all seen to be less than 10%. This phenomenon however, is not mentioned at all in the literature review relating to freight vehicle secondary suspension systems. Whereas in solid mechanics text books on the other hand, this phenomenon is well understood and is called the "Bauschinger effect" (Bertram & Gluge, 2013) and (Tottle, 1966).

The percentage increases in the torque responses for materials A, B and C during the running-in tests were seen to range between 23.5 − 108.4, 57.8 − 154 and 32.3 − 47.9% respectively. From the torque responses of these test cases, it was also clear to see kinematic as well as isotropic hardening regimes developing in the centre plate/wear liner components as the number of cycles increased over time. Kinematic hardening however, is not ideal in the context of railway freight vehicle dynamics as this condition could have a negative impact on the vehicle running stability at high speeds and could also be contributing towards accelerated rates of uneven wheel/rail wear as well as excessive noise emissions in curves (Tickell, Downing, & Jacobsen, 2004).

The Power Spectral Densities (PSD) of running-in test torque signals were then further analysed using the Discrete Fast Fourier Transforms (DFFT) to better understand the changes that were seen to be taking place in the hysteresis responses over time. The dominant frequencies from the hydraulic power pack on the Instron machine as expected, were clear to see in all of the responses in the region of 223 − 224 Hz, see the pre-calculated value given in Table 5.3 (Section 5.3.7). These constant frequency components were then used as a reference signal in order to quantify the changes in the frequency responses that were taking place in the region of 100 − 150 Hz due to the sliding contact. These signatures however, were more difficult to clearly distinguish/identify especially when there was no contamination in between the friction surfaces or stick-slip behaviour present in the torque responses.

The unique signatures developing in the region of 163 Hz during test case 5 on material A however (Contaminated sample), were clear to see in the frequency responses. The power amplitudes of the frequency components were also seen to be proportional to the changes in the torque responses and the centre plate velocity, which is in agreement with the research findings in (Shahidi, Maraini, Hopkins, & Seidel, 2014).

The hysteresis responses on the other hand, were less sensitive to changes in this system parameter. Also, when stick-slip behaviour started to occur in the responses during the service tests and steel-on-steel test case for example, it was clear to see a broad-band of distinct signatures developing in the region of 100 − 150 Hz that were not present in the running-in test torque signals. This analyses clearly

suggests that the number of running cycles, as well as the centre plate loading conditions and the mechanical properties of the centre plate/wear liner components for example, have a significant influence of the stick-slip response of the centre plate system.

The results from the running-in test spectral analysis responses therefore, strongly suggest that different secondary suspension operating conditions, as well as developing failure modes for example, can be mapped-out to a good degree of accuracy using scale model laboratory tests which has obvious cost and safety benefits in comparison to full scale laboratory/on-track testing. These results could then be used to optimise bogie condition monitoring equipment in order to better to detect poor bogie performance at the earliest possible stage of its development, therefore, reducing the life-cycle costs that are associated with vehicle/track maintenance (Shahidi, Maraini, Hopkins, & Seidel, 2014).

The service tests were then carried out at the same forcing frequency as the running-in tests, but ran for 10800 cycles. During the 3 kN loading cases, the peak torque responses of materials A, B and C, were seen to range between 5.2 – 13, 8 – 17 and 8.5 – 17.5 Nm respectively. The increases in the torque responses during these tests were seen to range between 78.9 – 105.9%, whereas the increases during the running-in test cases, were seen to be slightly higher and cover a wider range, 23.5 – 154% (Table 5.4, Section 5.4.3). The most significant increases in the torque responses during the running-in/service tests however, occurred during the first 2 – 5 hours testing and were then seen to start levelling off during the remaining part of the service tests in materials A and B, whereas the torque responses in material C on the other hand, started to decrease after the completing the first 3 – 5 hours of the service test.

The torque responses under the 6 kN loading condition were seen to range between 11.6 – 44.8 and 16.5 – 47.4 Nm for materials A and B. Whereas the responses for material C were seen to range 14.2 – 25.2 Nm, which is the lowest range overall under the 6 kN loading conditions. The percentage increases in the torque responses however, were shown to range between 13.8 – 251.8%, which is significantly higher than increases that were observed under 3 kN loading conditions.

During the 9 kN loading cases, the torque responses in materials A and C were seen to range between 17.5 – 28.5 and 20.1 – 41.6 Nm respectively. The torque responses for material B however, were seen to be the highest overall, ranging between 26 – 96.2 Nm. The percentage increases in these parameters for the complete data set (5 test cases), were also seen to be the highest overall, ranging between 31.8 – 270%.

This analysis clearly suggests that the torque responses of the centre plate/wear liner components are highly dependent on the loading conditions. During the 0.5 and 3 kN centre plate loading cases for example, all three materials responded in a viscoelastic manner with no stick-slip behaviour present in the torque responses. Whereas during the 6 and 9kN loading cases, stick-slip behaviour was starting to develop, especially in the responses of materials B and C.

The torque responses in material C however, then started to decrease again after 3 – 5 hours of testing, which is a characteristic that is unique to this wear liner material and behaviour that repeatedly takes place under the 3, 6 and 9 kN centre plate loading conditions. During the 0.5 kN loading cases on the other hand, the torque responses in material C were seen to increase in proportion to the number of running cycles.

The COF values during the 3, 6 and 9 kN loading cases were also calculated (Appendix Q), which are seen to range between 0.09 – 0.36 and 0.1 – 0.27 respectively for materials A and C. Whereas for material B, the COF values under these loading conditions were seen to range between 0.1 – 0.54 which is the highest range overall. From this analysis it is clear to see that the COF values for materials

A and B for example, increase in response to an increase in the centre plate load. The COF values for material C on the other hand, were seen to remain within a fairly consistent range regardless of the loading conditions.

The global evolutionary friction models were then developed after the service test cases to describe the increases in the COF parameters of the centre plate wear liner sample as a function number of running cycles, which was then converted to a time history plot. These responses were then classified into the low, medium and high COF regimes, which included values ranging from 0.055 – 0.23, 0.09 – 0.4 and 0.09 – 0.545 respectively, see Figure 5.46 in Section 5.4.5. After carrying out this analyses, it could be seen that materials A and C tended to occupy the low and medium COF regimes by the end of the 10800 cycle service tests. Three out of the six test cases that were studied in the laboratory using material B on the other hand, were seen to migrate from the medium to high COF regions by the end of the service tests.

The final test case that was carried out on the scale model components before calculating the X-Factor values, was the steel-on-steel test case, see Section 5.4.8. The peak COF values under these test conditions however, were seen to be 2 – 3 times than the COF values that were observed during the test cases with the wear liners included. The steel-on-steel COF values for example, were seen to range between 0.3 – 1.5 and 0.6 – 1.1 during phases one and five, which were both running under the 0.5 kN loading conditions. Whereas during phases two and four, which were running at the same forcing frequency as phases one/five but under the 3 kN loading conditions, were seen to range between 0.55 – 1.55 and 0.73 – 1.1 (Table 5.9).

The non-symmetric torque characteristics of the steel-on-steel test cases were also more pronounced during the 0.5 kN loading conditions (Figures 5.74 and 5.77), which was also seen to be the case during the running-in tests with the wear liner components included. Severe hunting behaviour however, was observed during the steel-on-steel test case, which was then prevented from becoming too excessive and damaging the Instron machine, by the spigot/bore features that were machined into the static/dynamic centre plate components.

This analysis also suggested that the surface roughness parameters and geometrical irregularities on the centre plate components had the strongest influence on the variations observed in the COF values. This suggestion was also supported by comparing the hysteresis responses of material B against those that were generated during the steel-on-steel test case (See Figures 5.55 and 5.57 in Section 5.4.6.2 and Figure 5.74 in Section 5.4.8). The non-symmetric characteristics in these responses during the gross-sliding events as can be seen, are very similar, smooth in one direction, whilst exhibiting stick-slip behaviour in the other.

The spectral analysis results for the steel-on-steel test case also suggested that the peaks in power amplitudes during the service tests with the wear liners included, were due to material transfer taking place between the steel centre plates/polymer wear liners. The distinct signatures that were observed during the steel-on-steel test case in the region of 100 – 150 Hz for example (Figures 5.78 and 5.79), were also present in the centre plate/wear liner responses (Figures 5.66 and 5.67). This analysis also suggests that material transfer between the centre plate/wear liner components, has a significant influence on the frequency responses as well as the hardening regimes developing in the centre plate system.

The X-Factor values for the centre plate/wear liner samples under the given loading conditions were then calculated from the laboratory test data in order to identify the worst running conditions in terms of critically high X-Factors values. During the 3, 6 and 9 kN loading conditions for example, the X-Factor

values were seen to range between 0.044 – 0.085, 0.033 – 0.083 and 0.029 – 0.095 respectively (Appendix S). The SD of the minimum values under all three loading conditions however, were seen to be closely matched, ranging between 20.9 – 23.3%, which suggested that the range of minimum values are fairly constant regardless of the centre plate loading conditions. Whereas the SD of the maximum X-Factor values were significantly higher, ranging between 22.2 – 48.2%. These parameters were also seen to increase in proportion to the loading conditions.

The mean percentage increase in the X-Factor values for the 3, 6 and 9 kN loading conditions were also calculated and seen to be 16.8, 39.2 and 58.8% respectively, whereas the SD of these parameters were in the regions of 22.2, 87.8 and 77.5%. This analysis clearly shows that the 6 and 9 kN loading condition for example, are the most unstable overall. However, it should also be pointed out, that the peak values were only observed during the later stages of the service tests and as can be seen in Figures 5.84 – 5.86 (Section 5.4.9.2), all three materials under the full range of loading conditions that have been studied, would have been compliant with 0.1 X-Factor limit, see the GM/RT2141 standards (Issue 3).

The normal distributions during the latter stages of the service tests with the Standard Error of the Mean (SEM) parameters included in the estimations however, suggested that the probability of a vehicle failing the X-Factor test during the life-cycle of the centre plate/wear liner components under the tare loading conditions was in the region of 1 – 2%. Whereas for a brand new set of components on the other hand, the probability of a failure was seen to be highly unlikely at 0.4%. Under the part-laden loading conditions, the probability of a X-Factor failure was seen to increase to 11 – 12% during the latter stages of the service tests. Whereas for the laden loading conditions, the probability of a failure occurring after 13800 cycles of testing, was seen to be in the region of 58%. The mean percentage increase in the torque responses as a function of the number of running cycles was also seen to be the highest overall at 141% during the 9 kN/laden loading cases (Appendix P).

From the analyses of the percentage increases in the torque/COF parameters it can be concluded, that majority of the responses that were measured on the new centre plate/wear liner components for example, tend to increase by a factor of 2 – 3 over the course of 3000 and 10800 cycle running-in/service tests. Therefore, it is strongly suggested that the percentage increases and the SD and SEM associated with these parameters be taken into account in X-Factor tests carried out on new vehicles, as well as in MBS modelling this vehicle performance test. This factor in particular, is bound to have a significant impact on the derailment resistance of the vehicle if left unchecked over the life-cycle of the vehicle.

For vehicle fleets where condition monitoring equipment/data is not available, it is also recommended that random vehicles for example, re-take the X-Factor test multiple times in between scheduled maintenance cycles. The measurements from these tests can then be cross-referenced with the laboratory test data given in Appendices O and R, in order to better estimate the current condition of the centre plate/wear liner components without having to remove the wagon body first. The SD corresponding to each loading condition and the number of running cycles, could then be used to predict the condition of the whole fleet from a single X-Factor measurement.

The limitations to the X-Factor testing methodology presented in this thesis however, are the missing components of the vehicle, such as the wheelsets, axle boxes, bearings, brake linkages and bogie frame, as well as the secondary suspension components. These components contribute to the parasitic stiffness as well as the friction damping of the centre plate system, so the results presented in this thesis could potentially be on the conservative side in comparison to some of the results produced from X-Factor tests carried out on full size vehicles, see for example (RAIB, 2007), where the

X-Factor values in a number of cases were seen to range between 0.327 – 0.459, see page 20 of this report.

During these investigations however, several X-Factor tests were carried out on random vehicles with/without the Constant Contact Side Bearers (CCSB) fitted to the bogie assembly and after these tests, the X-Factor values for the new centre plate/wear liner components for example, were seen to be in the region of 0.057 – 0.058 which is in very close agreement with mean X-Factor values presented in this thesis. Whereas when the CCSB were fitted to the bogie, the X-Factor values were seen to range between 0.23 – 0.314 (RAIB, 2007).

The CCSB were then replaced with UIC sprung side bearers which then led to a significant reduction in the X-Factor values of the tested vehicles to 0.102 – 0.113. These values are also seen to be in good agreement with the normal distribution curves of the X-Factor values shown in Section 5.4.9.2. The average wheel unloading also reduced to 45% with the UIC side bearer design, whereas beforehand, the nominal value for the tested vehicles was 89%, which is above the 60% limit (RAIB, 2007). This investigation in particular, highlighted some fundamental issues relating to the lack of understanding towards the design and testing requirements, as well as the sensitivities of the secondary suspension system whilst negotiating switches and crossing (Prosser, 2014).

The final conclusions to draw from the laboratory benchmark test results, are that the friction and wear characteristics of the centre plate system are highly dependent on the surface roughness parameters and mechanical properties of the centre plate/wear liner components, as well as the normal contact pressure and the number of running cycles. The frequency responses on the other hand, are more sensitive to changes in the angular velocity of the centre plate, as well as detecting the stick-slip behaviour in the early stages of it development. The following chapter discusses the optimised centre plate/wear liner friction models that have been developed from the benchmark test data in order to describe the unique friction characteristics of the three different wear liner materials.

6. Secondary suspension component friction models

This section discusses the modelling methodologies that were used to develop the optimised friction models for the 1:7 scale secondary suspension system. The procedures that were used to validate the simulation results are also discussed. The torque responses that were measured on materials A, B and C during test cases 2, 14 and 17 for example (Service tests), were then used to develop three optimised friction models for the centre plate/wear liner components using the dynamic model shown in Figure 4.4 (Section 4.3). The modelling parameters for centre plate/wear liner friction models are shown in Table 6.1.

Material	Test case	Centre plate load (kN)	Inertia (kg.m²)	Simulation time (s)	Real time (s)	Transition coefficient (s/rad)	Torsional Stiffness (Nm/rad)	Breakout torque (Nm/rad)	Breakout angle (mrad)	Coulomb torque (Nm/rad)	Torque correction factor	Viscous damping C1 (Nms/rad)	Viscous damping C2 (Nms/rad)	Stick μ	Slip μ	Mean μ
A	2	6	0.26	30	102	10	5787	44.6	7.71	37.6	1	0	200	0.38	0.32	0.35
B	14	9	0.39	30	102	15	6027	93.3	15.48	85	1.1	0	0	0.54	0.4	0.47
C	17	9	0.39	30	102	1.1	5063	38.1	7.53	30.1	0.96	0	10	0.22	0.17	0.2

Table 6.1: Parameters for the centre plate/wear liner friction models (0.042 Hz simulations).

This table shows the test case number and centre plate load for each material, the simulation run time as well as the real time taken to reach a solution. The Coefficient of Friction (COF) values are also shown, as well as the torsional stiffnesses and damping coefficients for each wear liner material. The stiffness coefficients that were used to represent the mechanical properties of materials B and C as can be seen, are the highest and lowest overall at 6027 and 5063 Nm/rad respectively, whereas the stiffness of material A, is seen to be in between these values at 5787 Nm/rad. The torque correction factors in the model parameters were then used to calibrate the peak torque responses of the dynamic models in order to bring them into line with the measurement results for test cases 2, 14 and 17 which are shown in Appendix R.

The amplitude of the angular displacement and forcing frequency of the centre plate during these simulations was also set to $\pm$ 3 degrees per cycle and 0.042 Hz to match the parameter settings that were used in the laboratory test cases. These simulations were then carried out using the Ode 23t solver with the time step set to 1×10^{-5} seconds, whereas the velocity threshold parameter in the friction model was set to 1×10^{-3} mrad/s. The simulation results were then quantified and validated using the peak torque responses as well as the mean frictional energies per cycle from these 3 test cases as the key metric to evaluate the matching errors between the simulation/measurement results.

The centre plate friction model as can be seen from Figure 6.1, is comprised of two key components. The global evolutionary friction models for example, are used in Multibody Simulations (MBS) to describe the increases in COF values as a function of the number of running cycles or time, see Section 5.4.5. Whereas the local models on the other hand, are used to describe the hysteresis responses as well as the Power Spectral Densities (PSD) of the centre plate/wear liner components, see Sections 5.4.6 – 5.4.7. The following section discusses the angular displacement and velocity responses of the optimised centre plate/wear liner friction models.
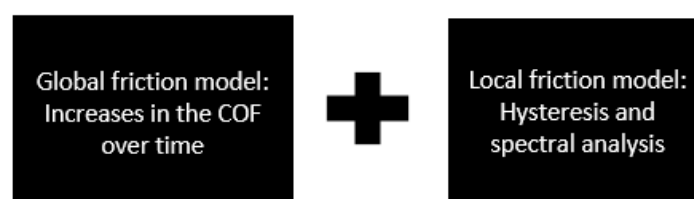
Figure 6.1: Global/local friction model combination for the secondary suspension components.

6.1. Angular displacement and velocity responses

This section discusses the simulation results generated by the three optimised friction models. The angular displacement responses of materials A, B and C during the 0.042 Hz sinusoidal forcing frequency simulations are shown in Figure 6.2 by the green, blue and red lines respectively. The bogie/input response is also shown by the black line, but this has had to be scaled by a factor of 1:10 to view it in the same figure as the wear liner responses. The peak displacements of materials A and C during this simulation are seen to be similar, while that for material B is significantly higher.

The velocity responses are shown in Figure 6.3 and from these, it is clear to see the oscillatory behaviour developing in material B after the breakout events (Blue lines). The response of material A on the other hand (Green lines), appears to be stable throughout the transition from the breakout event to the gross-sliding regime. This stable response is due to the high viscous damping which was set to 200 Nms/rad in this model. Whereas the responses of material C (Red lines), are seen to oscillate after the breakout events and throughout the transitions into the gross-sliding regimes. These transients however, are then damped out of the responses when the gross-sliding regimes become fully developed, which takes place, 3 – 4 seconds after the breakout events.

The viscous damping coefficient that was used in the friction model to describe material C (10 Nms/rad), has therefore led to a significant improvement in the stability of the wear liner material during the gross-sliding regimes in comparison to material B, where the viscous damping was set to zero. The peak velocities of material C for example, are seen to be in the region of $\pm$ 9.5 mrad/s (Red lines), whereas for material B, the peak velocities were in the region of $\pm$ 167.7 mrad/s.

From the state space trajectories shown in Figure 6.4 for example, it is clear to see the locations of the breakout points of each friction model, as well as the differences between the oscillatory behaviours observed in materials B and C (Blue and red lines). The velocity responses of material A on the other hand (Green lines), are seen to tend towards zero during the gross-sliding regimes.

By comparing the pre-calculated breakout angles of materials B and C in Table 6.1 against the maximum angular displacements that were observed during the dynamic simulations, it can be seen that there are some differences between the calculations/simulation results. These differences however, are due to the influence of the rotational inertias of the dynamic centre plate/wear liner friction models, parameters that are not taken into account in the pre-calculated values. These results are summarised at the end of the following section, after discussing the frictional torque responses.
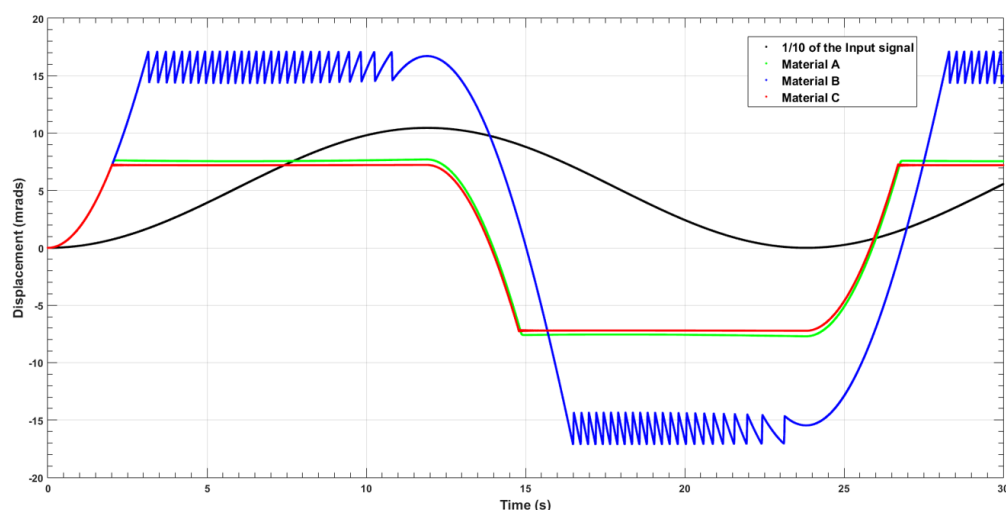
Figure 6.2: Angular displacement responses.
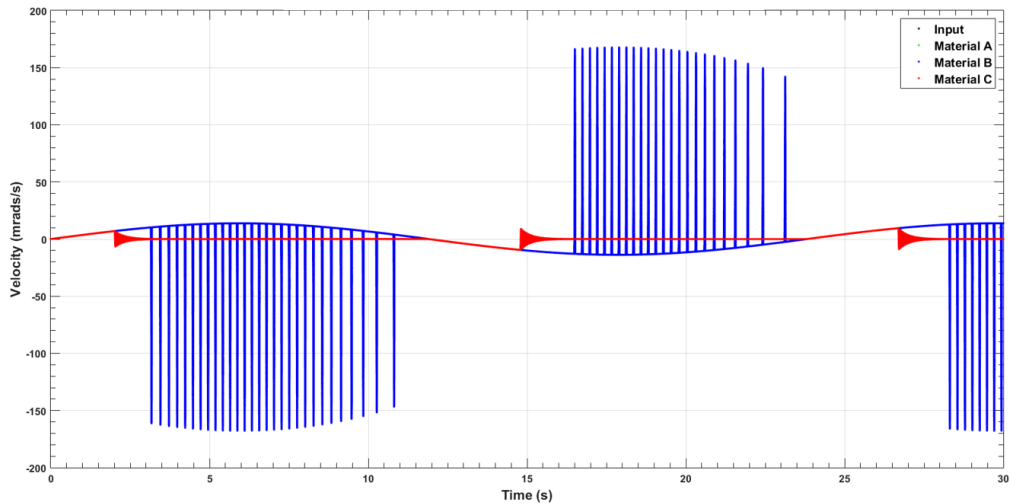
Figure 6.3: Angular velocity responses.
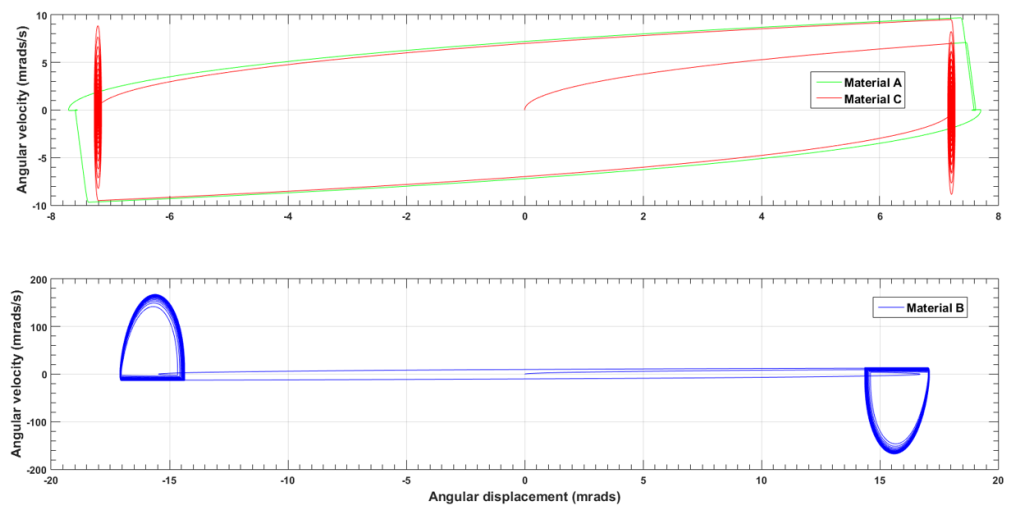
Figure 6.4: State space trajectories of the centre plate/wear liner friction models.

6.2. Frictional torque responses

This section discusses the frictional torque responses of the centre plate/wear liner friction models. The responses of materials A, B and C are shown in Figure 6.5 by the green, blue and red lines respectively. During the first 3 seconds of the simulations for example, it can be seen that friction models start off in the stick state which causes the frictional torque to increase in proportion to the velocity of the input signal. The breakout events in materials A and C are seen to occur when the torque responses are in the regions of $\pm$ 44.6 and $\pm$ 38.1 Nm, whereas material B breaks out when the torque response is in the region of $\pm$ 103.1 Nm.

The stick-slip responses of the friction model describing test case 14 as can be seen from the hysteresis responses shown in Figure 6.6 (Blue lines), are in good agreement with the measurements shown in Figure 5.57 (Section 5.4.6.2). The responses of the models describing test cases 2 and 17 using materials A and C (Green and red lines), are also seen to be in good agreement with the measurements, see the hysteresis responses shown in Sections 5.4.6.1 and 5.4.6.3 respectively. The subtle differences in the stiffness characteristics of each material are also evident in the simulation responses.

A summary of the results discussed in this, as well as the previous section, is shown in Table 6.2. The following section discusses the energy responses and the procedures that were used to validate the responses of the centre plate/wear liner friction models.
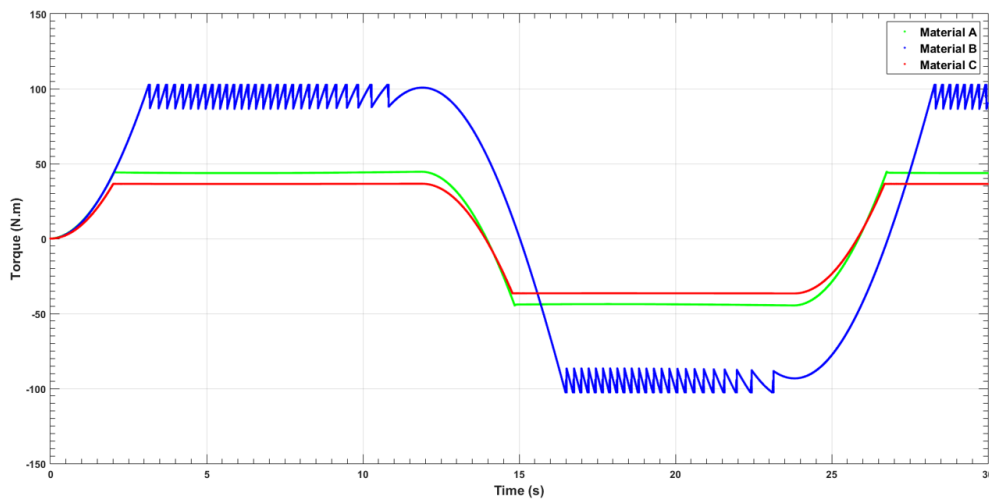
Figure 6.5: Frictional torque responses as a function time.
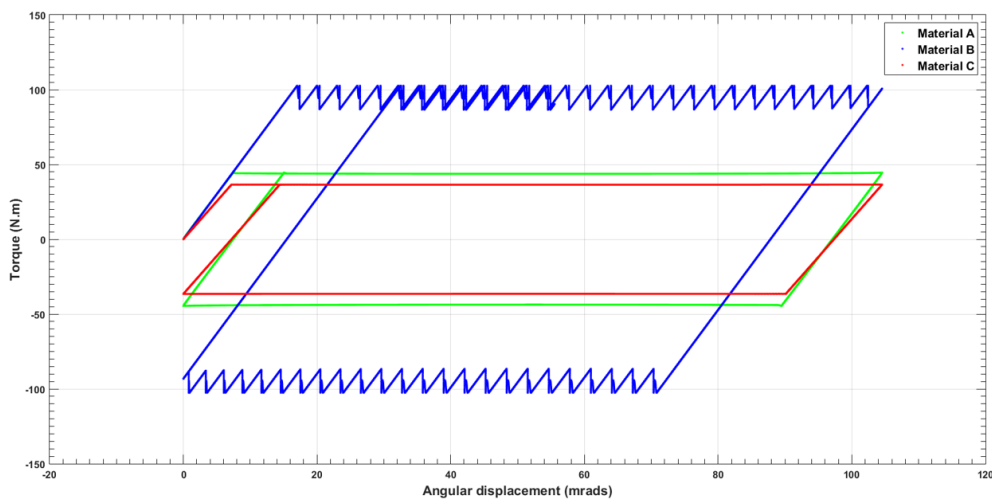
Figure 6.6: Hysteresis responses.

Material	Centre plate load (kN)	Inertia (kg.m²)	Test case	Maximum displacement (mrad)	Minimum displacement during slip (mrad)	Mean displacement during slip (mrad)	Maximum velocity (mrad/s)	Centre plate maximum velocity (mrad/s)	Stick torque (N.m)	Sliding torque (N.m)	Mean torque (N.m)	Torsional stiffness (Nm/rad)	Breakout angle (mrad)	Torsional natural frequency (Hertz)
A	6	0.26	2	7.71	7.55	7.63	9.7	13.8	44.6	43.7	44.2	5787	7.71	23.9
B	9	0.39	14	17.10	14.36	15.73	167.7	13.8	102.6	85.3	93.9	6027	17.02	19.9
C	9	0.39	17	7.27	7.20	7.24	9.5	13.8	36.6	36.5	36.5	5063	7.22	18.2
Maximum				17.10	14.36	15.73	167.7	13.8	102.6	85.3	93.9	6027	17.02	23.9
Minimum				7.27	7.20	7.24	9.5	13.8	36.6	36.5	36.5	5063	7.22	18.2
Mean				10.69	9.70	10.20	62.3	13.8	61.3	55.1	58.2	5626	10.65	20.7
Range				9.83	7.16	8.49	158.2	0.0	66.0	48.8	57.4	964	9.80	5.7
Standard deviation				5.55	4.04	4.79	91.3	0.0	36.0	26.3	31.2	502	5.52	2.9
Standard deviation (%)				51.9	41.6	47.0	146.5	0.0	58.8	47.8	53.6	8.9	51.9	14.2

Table 6.2: Summary of the centre plate/wear liner kinematic motions and frictional torque responses.

221

6.3. Frictional energy responses and the model validation procedure

The energy responses of the centre plate/wear liner friction models during the 0.042 Hz forcing frequency simulations. The procedures that were used to validate the model responses are also discussed. From the summary of results shown in Table 6.3, it can be seen that the peak torque responses of the simulation models describing the responses of test cases 2, 14 and 17 are seen to be 44.6, 102.6 and 36.6 Nm respectively. Whereas the measured torque responses of these test cases, which are shown in Appendix R, are seen to be 44.6, 93.3, 38.1 Nm.

The absolute matching errors for the friction/simulation models were then calculated using Equation 6.1 and are shown to be 0, 9.3 and 1.5 Nm for test cases 2, 14 and 17 respectively. The absolute errors of the simulation models must not exceed 15%, which is the specification given in the GM/RC2641 standards, `Recommendations for vehicle static testing', The centre plate/wear liner friction models therefore, are considered to be validated in terms of the absolute matching errors.

The percentage matching errors of the friction models were also calculated using Equation 6.2. The frictional energy/cycle was then used as the key parameter to quantify these errors (See GM/RC2641). From the results shown in Table 6.3, it can be seen that frictional energy/cycle of the models describing materials A and C during these simulations, were 8.56 and 7.14 Joules (J) respectively. Whereas the frictional energy/cycle of the model describing material B, was twice as high at 17 J.

The measurement results for the frictional energy/cycle during test cases 2, 14 and 17 however, are seen to be 8.55, 7.09 and 16.9 J respectively, see Table 6.3 or Appendix R. From this analysis it can be seen that the percentage matching error of test case 2 is the lowest overall at 0.2%, whereas the errors in the models describing materials B and C, are the highest at 0.6 and 0.7% respectively. These errors however, are still below the 7% limit defined in the GM/RC2641 standards, so are also considered to be valid under the given specifications.

From the analyses of the simulation results for the centre plate/wear liner models, it can be clearly seen that the majority of the friction phenomena that was been observed during the scale model laboratory tests, such as the stick-slip and viscoelastic behaviour for example, are now being modelled to a good degree of accuracy in the validated centre plate/wear liner friction models. The following section discusses the spectral analysis results for the centre plate/wear liner friction models.

$$\text{Absolute matching error} = |\text{Simulation} - \text{measured}| \qquad (6.1)$$

$$\text{Percentage matching error} = \frac{|\text{Simulation} - \text{measured}|}{0.5 \text{ x } |\text{Simulation} + \text{measured}|} \text{ x } 100 \qquad (6.2)$$

Material	Centre plate load (kN)	Inertia (kg.m²)	Test case	Maximum kinetic energy (Joules)	Maximum potential energy (Joules)	Maximum mechanical energy (Joules)	Total friction energy (Joules)	SIMULATION: Peak torque (Nm)	SIMULATION: Mean friction energy per cycle (Joules)	MEASUREMENT: Peak torque (Nm)	MEASUREMENT: Mean friction energy per cycle (Joules)	Absolute matching error (Nm)	Percentage matching error between simulation/ measurements
A	6	0.29	2	0.00001	0.172	0.172	10.79	44.6	8.56	44.6	8.55	0	0.2
B	9	0.39	14	0.00548	0.881	0.881	21.42	102.6	17.00	93.3	16.90	9.3	0.6
C	9	0.39	17	0.00001	0.134	0.134	9.00	36.6	7.14	38.1	7.09	1.5	0.7
Maximum				0.00548	0.881	0.881	21.42	102.6	17.00	93.3	16.90	9.3	0.7
Minimum				0.00001	0.134	0.134	9.00	36.6	7.14	38.1	7.09	0.0	0.2
Mean				0.00184	0.396	0.396	13.74	61.3	10.90	58.7	10.85	3.6	0.5
Standard deviation				0.00316	0.421	0.421	6.71	36.0	5.33	30.2	5.30	5.0	0.3
Standard deviation (%)				172.1	106.4	106.4	48.9	58.8	48.9	51.4	48.8	138.7	51.4

Table 6.3: Summary of the centre plate/wear liner energy responses and matching errors (0.042 Hz).

6.4. Spectral analysis responses

The Power Spectral Densities (PSD) of the centre plate/wear liner friction models during the 0.042 Hertz (Hz) forcing frequency simulations are discussed in this section. The responses of materials A, B and C are shown in Figure 6.7 by the green, blue and red lines respectively. From these it is clear to see that the power amplitudes of the simulation models are also dependent on the magnitudes of the torque responses, which was also seen to be the case in the scale model laboratory tests. The power amplitudes of material B for example (Blue lines), are more than double in comparison to the amplitudes of materials A and C.

Simulations were also carried out on the centre plate/wear liner friction models at the 0.084 Hz forcing frequency for comparison purposes, see Figure 6.8. From these responses, it can be seen that the changes in the power amplitudes of the friction models, are proportional to the changes in the centre plate forcing frequency, which also agrees with the findings from the laboratory test results. The power amplitudes of material B in the region of 50 Hz for example, are nearly double in 0.084 Hz forcing frequency simulations, which you can clearly see by comparing the responses shown in Figure 6.7 and 6.8. The power amplitudes of materials A and C however, are significantly lower due to the relatively low torque responses during the 6 and 9 kN loading cases.

Also, by comparing the power amplitudes of the centre plate/wear liner friction model frequency responses against those that were measured during the service test cases, as well as the steel-on-steel test case for example, see Sections 5.4.7 and 5.4.8.3. It can be seen that the magnitudes of the power amplitudes in the models/measured responses, are in the similar regions, $1.5 - 9 \times 10^{-3}$ |Nm|²/Hz, which shows that the agreement between the responses is relatively good.
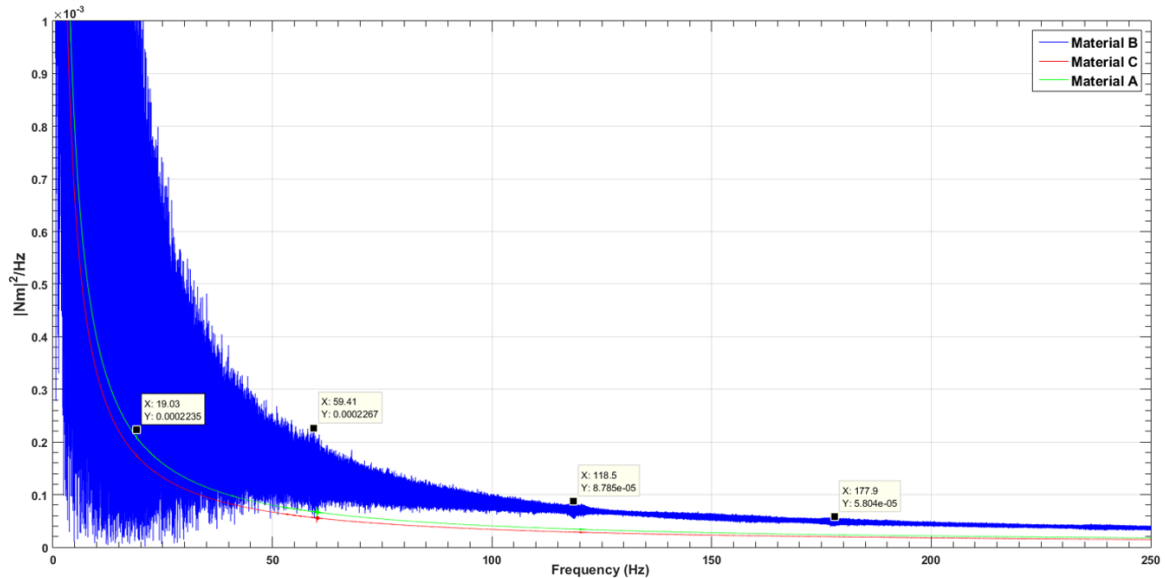
Figure 6.7: PSD during the 0.042 Hz forcing frequency simulations.
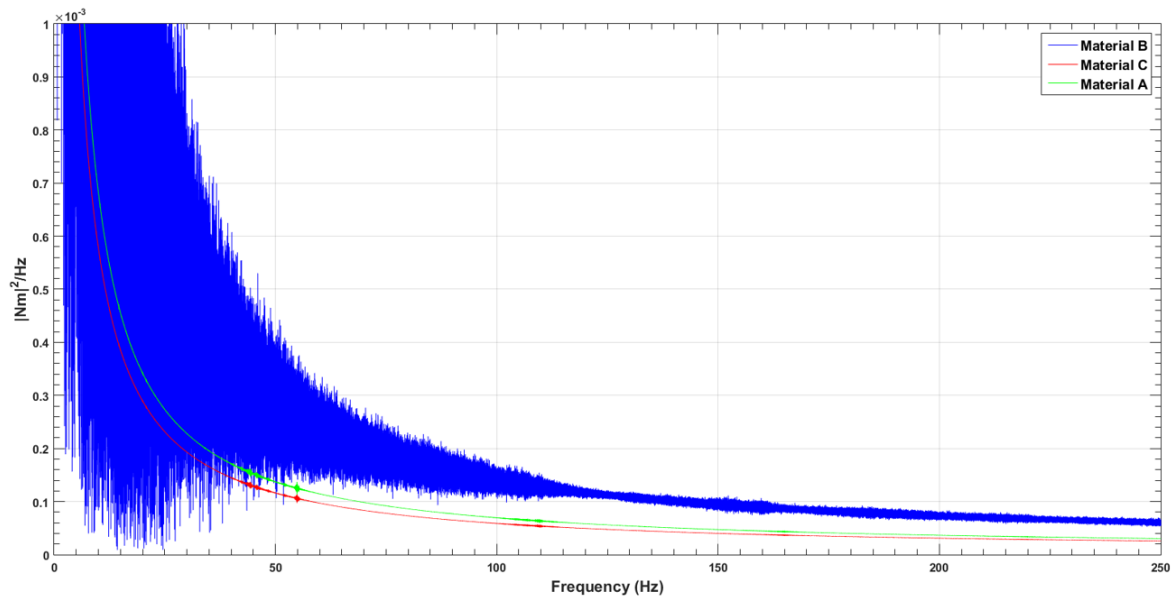
Figure 6.8: PSD during the 0.084 Hz forcing frequency simulations.

The reasons for the differences between the measurement/simulation results, are possibly due to the influence of the fluid pulsations from the hydraulic power unit on the Instron testing machine, as well as the structural vibrations from this machine, components that have not been included in the MATLAB/SIMULINK friction models.

During the service test cases that were carried out using material A for example, frequency components were developing in the regions of $18-37$ Hz when no stick-slip behaviour was present in the hysteresis responses, see Figure 5.64 in Section 5.4.7.1. However, when the torque responses of the wear liner sample that was contaminated with hydraulic oil were analysed in the frequency domain (Test case 5), it was clear to see that this particular sample had a distinct, as well as unique signature developing in the region of 163 Hz, see Figures 5.34 and 5.35 in Section 5.3.7.1 or Figures $5.62-5.64$ in Section 5.4.7.1.

The hysteresis responses during test cases 9, 11 and 14 using material B on the other hand, were seen to be relatively smooth during the first half of the service tests, whereas during the last half, stick-slip behaviour was seen to be fully developed in the responses, see Figures $5.53-5.57$ in Section 5.4.6.2. These developments were also clear to see in the spectral analysis responses, as these three test cases, were the only ones out of the 17 samples that were tested, that had a broad-band of distinct signatures developing in the regions of $100-150$ Hz, see Figures 5.66 and 5.67 in Section 5.4.7.2.

The final conclusions to make with regards to the spectral analyses of the simulation responses are in relation to the frequency components developing in the regions of 19, $40-60$, $100-120$ and 177 Hz (Figure 6.7). The natural frequencies of the friction models under the 6 and 9 kN loading conditions for example (Table 6.2 in Section 6.2), are seen to range between $18.2-23.9$ Hz, which suggests that different friction characteristics excite specific harmonics of the centre plate/wear liner components, which can obviously be detected as well as monitored, by carrying out Fast Fourier Transforms (FFT) on the measured torque responses. The following section discusses the development of the optimised MATLAB/SIMULINK Constant Contact Side Bearer (CCSB) friction models.

6.5. Constant Contact Side Bearer/wear liner friction models

The development of the optimised 1:7 scale Constant Contact Side Bearer (CCSB)/wear liner friction models are discussed in this section. These models were configured in exactly the same way as the

centre plate/wear liner models, see Figures 4.4 – 4.7 in Section 4.3, but using the modelling parameters shown in Table 6.4. These simulations were also carried out using the Ode 23t solver with the time step and velocity threshold parameter of the friction model, set to 1 x 10^{-5} seconds and 1 x 10^{-3} mrad/s respectively. The torque correction factors for materials A and B however, were set to 0.1 and 0.75 respectively, due to the high viscous damping forces which appeared to be more dominant under the 0.5 kN centre plate loading conditions.

Material	Test case	Centre plate load (kN)	Inertia (kg.m²)	Simulation time (s)	Real time (s)	Transition coefficient (s/rad)	Torsional Stiffness (Nm/rad)	Breakout torque (Nm/rad)	Breakout angle (mrad)	Coulomb torque (Nm/rad)	Torque correction factor	Viscous damping C1 (Nms/rad)	Viscous damping C2 (Nms/rad)	Stick μ	Slip μ	Mean μ
A	5	0.5	0.0215	15	72	10	1227	1.94	1.58	1.64	0.1	58	0	0.19	0.16	0.175
B	11	0.5	0.0215	15	72	50	4176	2.26	0.54	1.86	0.75	10	20	0.23	0.19	0.21
C	15	0.5	0.0215	15	72	50	3676	2.73	0.74	2.17	1	0	20	0.27	0.22	0.245

Table 6.4: Parameters for the CCSB/wear liner friction models (0.084 Hz simulations).

From these parameters it can be seen that the model representing test case 5 using material A for example, which was the carried out on the contaminated wear liner sample, was developed using the lowest stiffness coefficient overall, combined with the highest viscous damping coefficient for the C1 parameter, which are seen to be 1227 Nm/rad and 58 Nms/rad respectively.

The stiffness coefficient for the model that was used to describe the responses of material B however, is seen to be the highest overall at 4176 Nm/rad. The viscous damping coefficients for the C1 and C2 parameters in this model were set to 10 and 20 Nms/rad respectively under the 0.5 kN loading condition (Table 6.4), whereas for the models describing materials A and C, the C2 parameters were set to zero and 20 Nms/rad.

The CCSB/wear liner component models were then simulated using the local analysis friction models to describe the torque responses of the system as a function of time/sliding displacement. The global analysis friction models can also be used with these models to describe the evolutionary friction characteristics of the system during the simulation runs if required.

The amplitude of the angular displacements during the CCSB/wear liner simulations were set to ± 3 degrees per cycle to match the centre plate/wear liner simulations. Whereas the forcing frequency during the CCSB/wear liner simulations were set to 0.084 Hz rather than 0.042 Hz in order to investigate the model behaviour under the higher forcing frequency. The same validation procedure however, using the mean energy per cycle as the key metric to quantify the matching errors, can still be applied to validating the CCSB/wear liner responses, as this parameter is the same in each test case regardless of the forcing frequency. The following section discusses the angular displacement and velocity responses of the CCSB/wear liner friction models.

6.6. Angular displacement and velocity responses

The angular displacements and velocity responses of the CCSB/wear liner friction models are discussed in this section. The displacements of materials A, B and C during these simulations are shown in Figure 6.9 by the green, blue and red lines respectively and the black line shows the displacement response of the bogie/input signal, which has been scaled by a factor of 1:100. The peak displacements of material A during this simulation as can be seen, are in the region of 1.456 mrad, whereas the displacements of materials B and C on the other hand, are seen to be in the regions of 0.418 and 0.741 mrad respectively, which are 2 – 3 times smaller in comparison to the displacements in material A.

The angular velocity responses are shown Figure 6.10 and from these, it can be seen that the response of the input signal for example, has been scaled by a factor of 1:4 due to the peak velocity reaching

27.59 mrad/s (Black lines). The peak velocities of the wear liners on the other hand, are seen to be significantly lower, ranging between $3.1 - 7.1$ mrad/s. Whereas the responses of material C (Red lines), appear to be quite unique due to the oscillatory behaviour throughout the transition regimes, which occurs after the breakout events and also, when the velocity response of the input signal is decreasing towards zero.
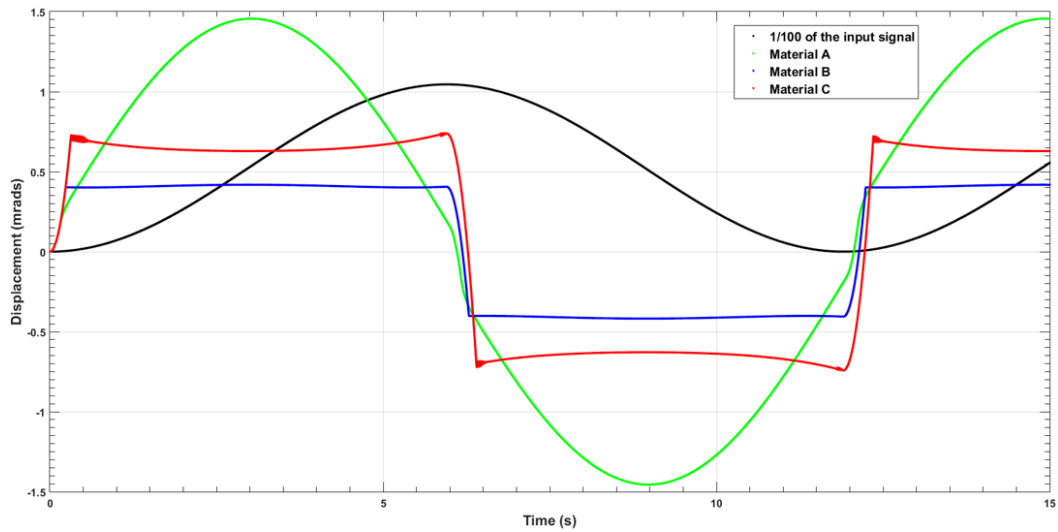
Figure 6.9: Angular displacement responses.
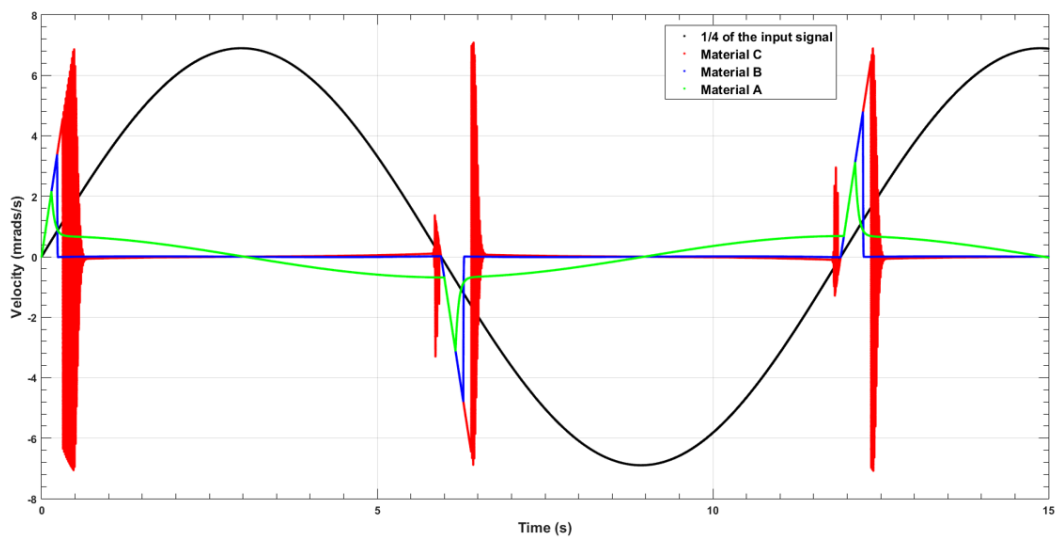
Figure 6.10: Angular velocity responses.

The development of this complex behaviour is clearer to see in the state space trajectories shown in Figure 6.11, as well as the close-ups of the right and left-hand envelopes shown in Figures 6.12 and 6.13 respectively. From these responses, it can be seen that there are two limit cycles in the trajectories of material C (Red lines). The ones occurring during the breakout events for example, oscillate with the largest amplitudes and for the longest periods of time. During these events, it can also be seen in Figures 6.12 and 6.13, that a small proportion of the elastic potential energy that was stored in the torsional spring during the breakout events, is suddenly released. This release of energy however, then causes the displacement responses in the right-hand envelope of the state space, to decrease rapidly, from 0.69 to 0.63 mrad. Whereas in the left-hand envelope, these events cause the displacement responses to increase, from –0.69 to –0.63 mrad.

After the excess potential is dissipated from the CCSB/wear liner system by the dry friction during the gross-sliding regimes however, the liner then starts to stick again, which then causes the displacement responses in the right/left-hand envelopes of the state-space, to start increasing back towards the regions of ± 0.74 mrad, where the second limit cycles then start to develop. These smaller amplitude limit cycles however, develop when the velocity of the bogie/input signal is decreasing, rather than increasing, which is seen to be the case during the breakout events.

The friction model describing material C as can be seen, also behaves differently in the right and left-hand envelopes, which is due to the differences between the breakout/Coulomb torque parameters, as well as the inertia of the system and the relatively low viscous damping coefficient that was used in this model (20 Nms/rad). The effective damping in the model describing material B on the other hand (Blue lines), was set to 30 Nms/rad and is 50% higher, hence no oscillatory behaviour. Whereas the torsional stiffness of the model describing the responses of material B was 4176 Nm/rad (Table 6.4), which is only 14% higher than the parameter that was used to model material C.

From the analysis, it can be concluded that the dynamic responses of the CCSB/wear liner friction models are extremely sensitive to relatively small changes in the torsional stiffnesses, COF values and viscous damping parameters of the system. The following section discusses the frictional torque responses.
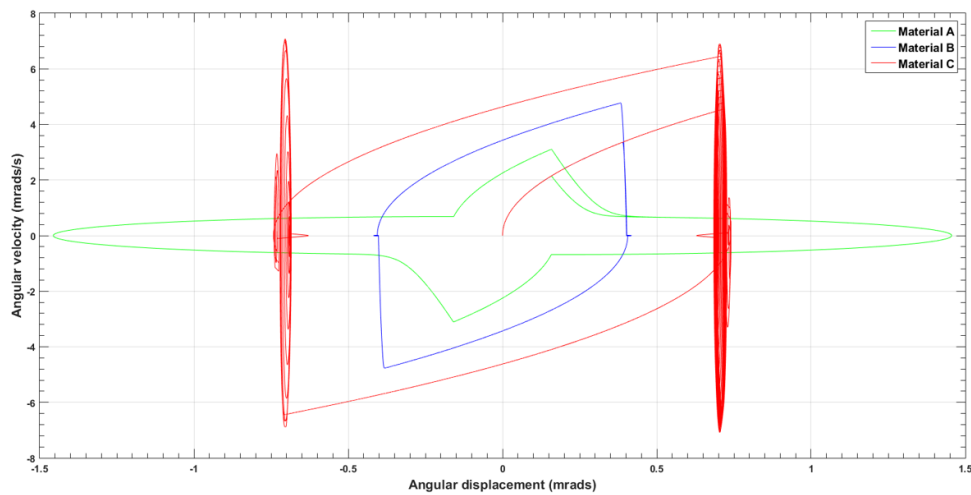
Figure 6.11: State space trajectories.
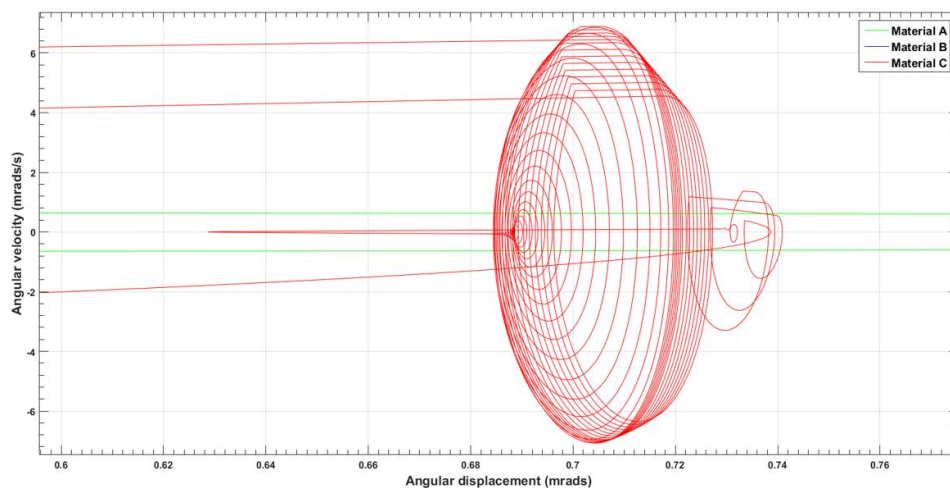
Figure 6.12: Close-up of the breakout points in the right-hand envelope of the state space.
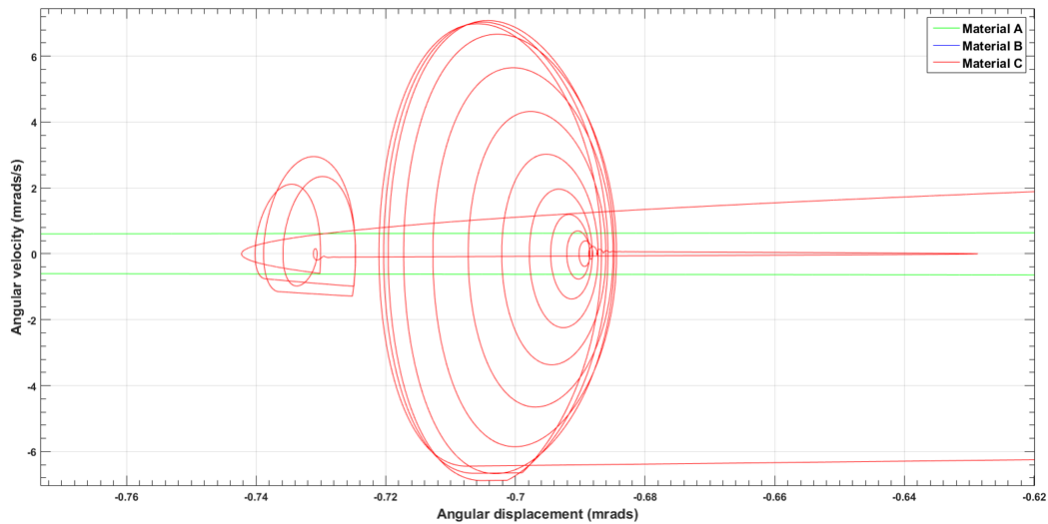
Figure 6.13: Close-up of the breakout points in the left-hand envelope of the state space.

6.7. Frictional torque responses

The time histories of the CCSB/wear liner frictional torque responses are discussed in this section. The responses of the models describing materials A, B and C are shown Figure 6.14 by the green, blue and red lines respectively. From these it is clear to see the differences in the friction characteristics of each model during the breakout events as well as the gross-sliding regimes.

The breakout events in material A for example, are seen to take place when the torque responses are in the region of $\pm$ 0.25 Nm, but due to the high viscous damping coefficient in this model, the force continues to rise in proportion to the excitation velocity until they reach the peak values of $\pm$ 1.79 Nm. The breakout events in the friction models describing materials B and C, take place when the torque responses approach the regions of $\pm$ 1.75 and $\pm$ 2.72 Nm respectively. During the transitions from the breakout events to the gross-sliding regimes, it can be seen that the torque responses in material B remain fairly constant at $\pm$ 1.75 Nm (Blue lines), whereas the responses of material C (Red lines), are seen to oscillate throughout the transitions, but then decrease towards $\pm$ 2.31 Nm during the gross-sliding regimes.

From the hysteresis responses shown in Figure 6.15, it can be seen that the model describing material A for example (Green lines), generates the lowest levels of damping in the regions of 0 – 40 mrad and 64 – 104 mrad in comparison to the models describing materials B and C (Blue and red lines). Whereas in the region of 40 – 64 mrad, it can be seen that the torque responses in material A are slightly higher than material B. This behaviour therefore, is clearly related to the viscous force as well as the changes in the velocity responses of the bogie/input signals due to the sinusoidal forcing frequency.

By comparing the simulation hysteresis responses against the actual responses for test cases 5, 11 and 15 on materials A, B and C shown in Figures 5.27, 5.28 and 5.33 respectively in Sections 5.3.4 – 5.3.6. It can be seen that the magnitudes as well as the general characteristics of the torque responses for example, are in good agreement. From this analyses it is also clear to see that we have successfully managed to replicate the majority of the friction phenomenon in the optimised CCSB/wear liner friction models, that was been observed in the laboratory during the running-in test cases.

The summary of the results discussed in this and the previous section is shown in Table 6.5. From these it can be seen that the Standard Deviations (SD) of the mean torque response for the complete data set (3 test cases), is 42.8%, whereas for the measurements shown in Appendix O, the SD of the

17 test cases during the 3000 cycle running-in tests, are seen to range between 28.6 – 35.9%, which also suggests that the simulation/measurement results are in close agreement. The following section discusses the energy responses of the optimised CCSB/wear liner friction models.
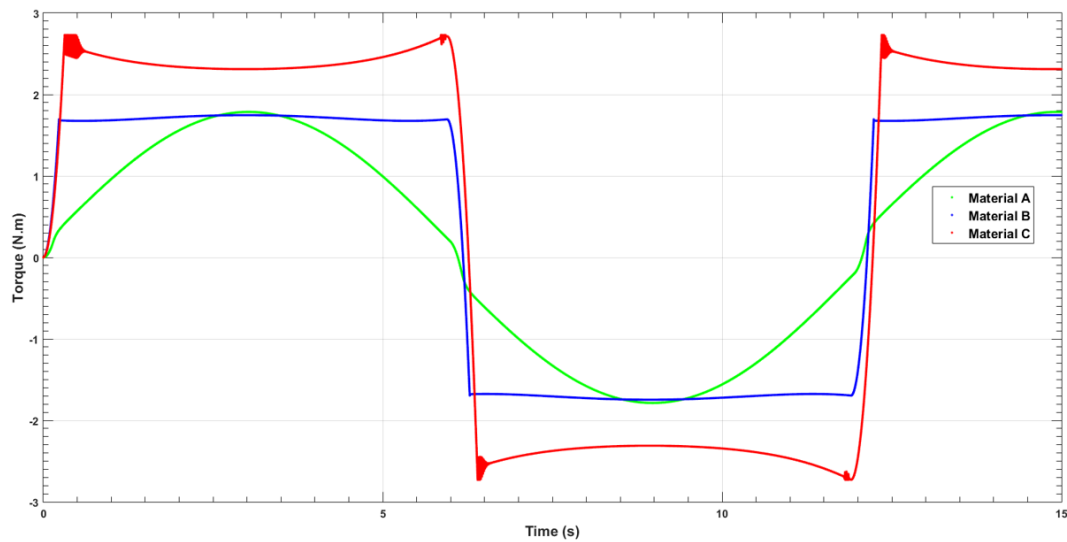
Figure 6.14: Frictional torque responses as a function of time.
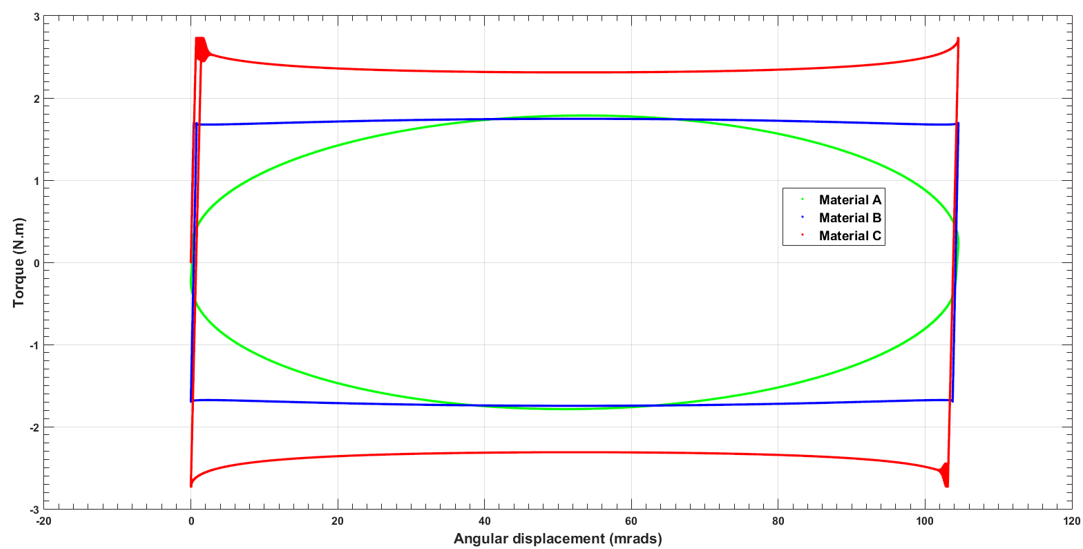
Figure 6.15: Hysteresis responses.

Material	Centre plate load (kN)	Inertia (kg.m²)	Test case	Maximum displacement (mrad)	Minimum displacement during slip (mrad)	Mean displacement during slip (mrad)	Maximum velocity (mrad/s)	Stick torque (N.m)	Sliding torque (N.m)	Mean torque (N.m)	Torsional stiffness (Nm/rad)	Breakout angle (mrad)	Torsional natural frequency (Hertz)
A	0.5	0.022	5	1.456	0.200	0.828	3.1	1.79	0.25	1.02	1227	1.46	38.1
B	0.5	0.022	11	0.418	0.415	0.417	4.8	1.75	1.68	1.72	4176	0.42	70.2
C	0.5	0.022	15	0.741	0.630	0.685	7.1	2.72	2.31	2.52	3676	0.74	65.9
Maximum				1.456	0.630	0.828	7.1	2.72	2.31	2.52	4176	1.46	70.2
Minimum				0.418	0.200	0.417	3.1	1.75	0.25	1.02	1227	0.42	38.1
Mean				0.872	0.415	0.643	5.0	2.09	1.41	1.75	3026	0.87	58.1
Range				1.038	0.430	0.411	4.0	0.97	2.06	1.50	2949	1.04	32.1
Standard deviation				0.531	0.215	0.209	2.0	0.55	1.06	0.75	1578	0.53	17.4
Standard deviation (%)				60.9	51.8	32.5	40.0	26.4	74.7	42.8	52.1	60.9	30.0

Table 6.5: Summary of the CCSB/wear liner kinematic motions and frictional torque responses.

6.8. Frictional energy responses and the model validation procedure

The frictional energy responses of the CCSB/wear liner friction models are discussed. The processes that was used to validate the friction model responses are also discussed. From the summary of results shown in Table 6.6, it can be seen that the matching errors between the simulation/measurement results are relatively good for materials B and C, whereas for material A, the agreement is not as good.

The absolute matching errors between the peak torque responses of the simulations/measurements results for example, range between $0.03 - 0.15$ Nm, which are all seen to below the 15% limit specified in the GM/RC2641 standards. Whereas the percentage matching errors for materials A and B on the other hand, are 11.5 and 8.6%, which are clearly above the 7% matching limit. The percentage errors in these two models can be can be brought into closer agreement with the measurements by tuning the Torque Correction Factors (TCF) for the friction models, see Table 64.

Increasing the TCF of the model describing material A for example, which is currently set to 0.1, will increase the frictional energy/cycle and hence, reduce the percentage matching error of this model. Whereas for the model describing material B on the other hand, decreasing the TCF will bring the energy response of this model into line with the measurements and the limits defined in the GM/RC2641 standards.

This exercise however, is left up to the reader as the percentage error of the friction model describing material C for example, is 2.8%. This analysis therefore, clearly shows that the friction modelling methodologies and validation procedures that have been developed throughout this research work, are accurate, as well as capable of describing the inherent friction characteristics of different wear liner materials. The following section discusses spectral analysis responses of the CCSB/wear liner friction models.

Material	Centre plate load (kN)	Inertia (kg.m²)	Test case	Maximum kinetic energy (Joules)	Maximum potential energy (Joules)	Maximum mechanical energy (Joules)	Total friction energy (Joules)	SIMULATION: Peak torque (Nm)	SIMULATION: Mean friction energy per cycle (Joules)	MEASUREMENT: Peak torque (Nm)	MEASUREMENT: Mean friction energy per cycle (Joules)	Absolute matching error (Nm)	Percentage matching error between simulation/ measurements
A	0.5	0.0215	5	-	0.0013	0.0013	0.382	1.79	0.30	1.72	0.34	0.07	11.5
B	0.5	0.0215	11	-	0.0004	0.0004	0.453	1.75	0.36	1.90	0.33	0.15	8.6
C	0.5	0.0215	15	-	0.0010	0.0010	0.622	2.72	0.49	2.69	0.51	0.03	2.8
Maximum				-	0.0013	0.0013	0.622	2.72	0.49	2.69	0.51	0.15	11.5
Minimum				-	0.0004	0.0004	0.382	1.75	0.30	1.72	0.33	0.03	2.8
Mean				-	0.0009	0.0009	0.486	2.09	0.39	2.10	0.39	0.08	7.6
Standard deviation				-	0.0005	0.0005	0.123	0.55	0.10	0.52	0.10	0.06	4.4
Standard deviation (%)				-	53.7	53.7	25.4	26.4	25.4	24.5	25.5	75.1	57.8

Table 6.6: Summary of the CCSB/wear liner energy responses and matching errors (0.084 Hz).

6.9. Spectral analysis responses

The Power Spectral Densities (PSD) of the 1:7 scale CCSB/wear liner friction models are discussed in this section. The PSD of the models describing materials A, B and C are shown in Figure 6.16 by the green, blue and red lines respectively. These simulations were running under the 0.5 kN centre plate loading condition and at the 0.084 Hz forcing frequency. From these responses, it is clear to see that the power amplitudes of the CCSB/wear liner models are also proportional to the magnitude of the torque responses. This was also seen to be the case in the spectral analysis responses of the centre plate/wear liner friction models, as well as in the responses of the running-in/service test cases.

The power amplitudes of materials A and B in the region of 50 Hz are also very similar due to the fact that the peak torque responses in these simulations were in the same regions, $1.75 - 1.79$ Nm (Table 6.6). Whereas the peak torque responses in material C on the other hand, is 2.72 Nm which is 63% higher, hence the reason why the power amplitudes of this model in the region of 50 Hz in comparison to materials A and B for example, are around 63% higher.

From the responses shown in Figure 6.16 (Red lines), it can also be seen that there are two distinct signatures developing in the region of 44 – 52 Hz. These peaks in power as can be seen from the local analysis results shown in Appendix O, appear to coincide with the natural frequencies of the centre plate/wear liner system under the 0.5 kN loading condition. The mean natural frequency and Standard Deviation (SD) of this parameter during the 17 running-in test cases for example, are seen to be the region of 60 Hz and 12 – 16% respectively. The signatures developing in the regions of 107 – 208 Hz therefore, are potentially related to the higher harmonics of the CCSB/wear liner friction models.

This was also seen to be the case during the latter stages of the service tests using material B, where some of the centre plate/wear liner samples were seen to be exhibiting stick-slip behaviour during the gross-sliding regimes. This behaviour as the number of cycles increased throughout the service tests for example, was then clear to see developing in the region of 100 – 150 Hz in the PSD of these particular samples, see the frequency responses of test cases 9, 11 and 14 shown in Figures 5.65 – 5.67, Section 5.4.7.2.

However, after comparing the frequency responses of the running-in test results shown in Section 5.3.7, against the PSD of the CCSB/wear liner friction models presented in this section (Figures 6.7, 6.8 and 6.16). It can be seen that the agreement between the amplitudes and the general characteristics of the frequency components in the regions of 0 – 50 Hz and 100 – 150 Hz is not good. The power amplitudes during the running-in test cases for example, were seen to be in the region of 1.5 |Nm|²/Hz, whereas in the CCSB/wear liner friction models, the amplitudes are two orders of magnitude lower.

The spectral analysis results from every cycle of the steel-on-steel test case were then further analysed to determine if any of these frequency responses were in closer agreement with the ones shown in Figure 6.16. From this analysis it could then be seen that the general characteristics of the PSD during phase one and cycles 50 – 100 of the steel-on-steel test case for example, which were not discussed in Section 5.4.8, were in closer agreement with the frequency responses of the CCSB/wear liner friction models, see Figure 6.17. Although the power amplitudes of the steel-on-steel test case responses, which was running under the 0.5 kN loading condition and at 0.084 Hz during this phase of the test, are still two orders of magnitude larger, the general characteristics of the steel-on-steel frequency responses are seen to be in better agreement with the CCSB/wear liner, as well as the centre plate/wear liner friction model responses.

The differences between the measured/simulation frequency responses however, are possibly due to the influence of the structural/fluid borne vibrations generated by the Instron testing machine, effects that have not been taken into account in the optimised friction models. The surface roughness parameters of the 1:7 scale centre plate/wear liner components have also not been included in the dynamic model. These effects however, were suggested to have the most significant influence on the variations in the friction characteristics that were been observed during the laboratory test cases. The following section discusses the complete secondary suspension friction modelling methodology.
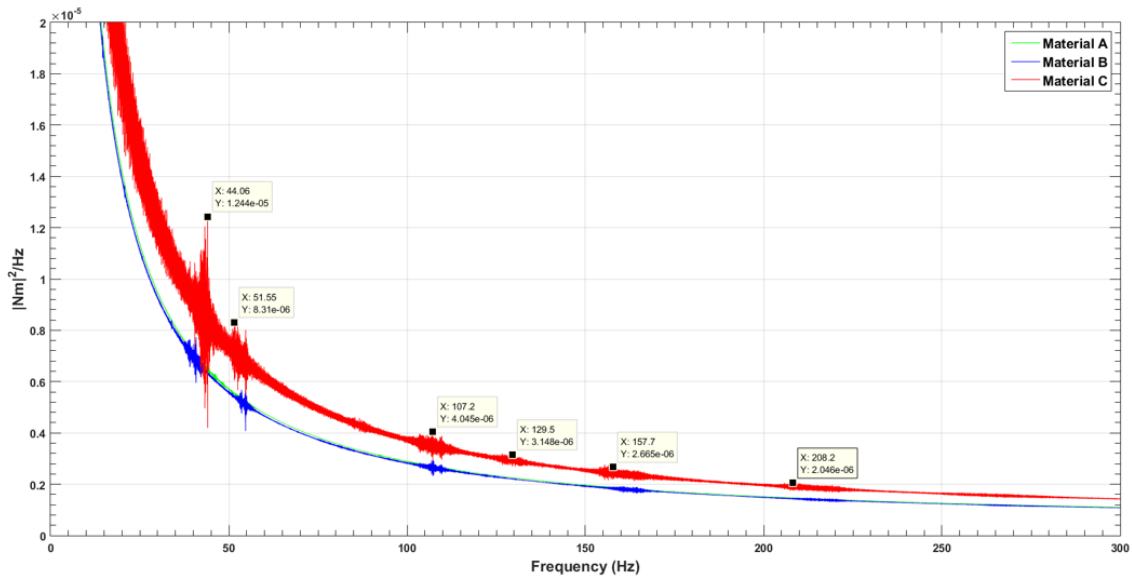
Figure 6.16: PSD during the 0.084 Hz forcing frequency simulations.
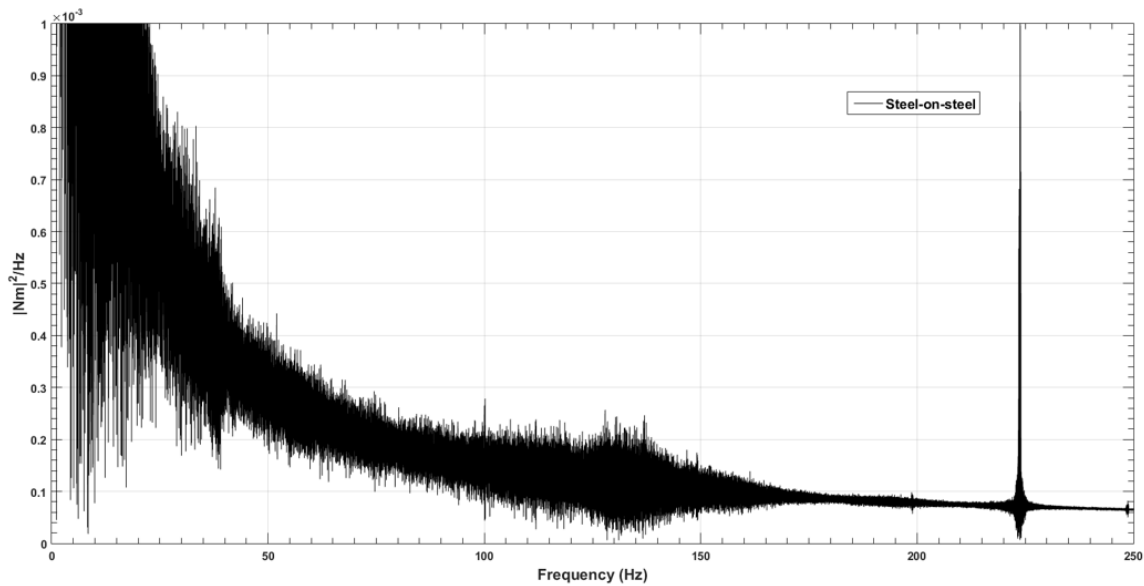
Figure 6.17: PSD during phase 1 of the steel-on-steel test case (Cycles 50 – 100).

6.10.   Complete secondary suspension friction modelling methodology

The complete secondary suspension friction modelling methodology and the 1:7 scale component models that has been developed from the laboratory test results presented in this thesis are is discussed in this section. The complete friction model architecture as can be seen in Figure 6.18, is called the, "Stick-slip 2120 friction model", to represent the names of the wear liner materials that were characterised in the laboratory test cases, as well as the capabilities of the MATLAB/SIMSCAPE friction model.
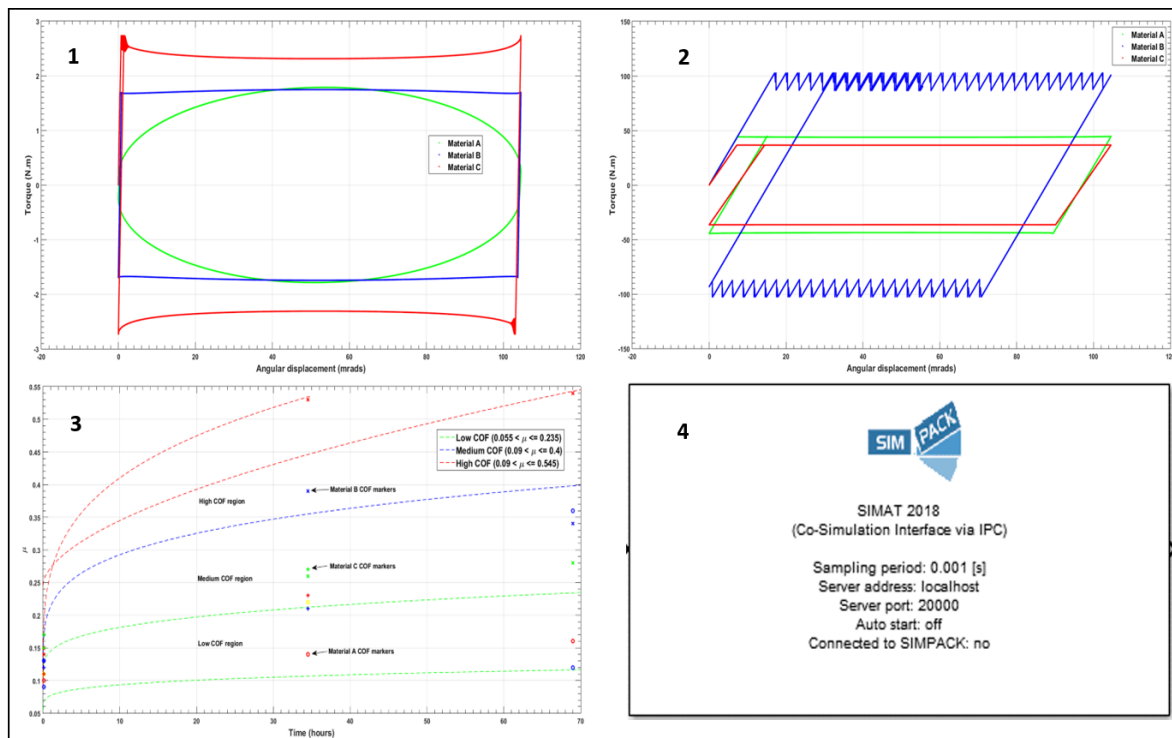
Figure 6.18: The key components of the optimised Stick-slip 2120 secondary suspension friction model.

The complete secondary suspension model as can be seen, comprises of four fundamental components. These are the two optimised local CCSB/wear liner and centre plate/wear liner friction models that were developed to describe the hysteresis responses and spectral components of the centre plate/wear liner materials. The third element is global evolutionary friction model that was developed to describe the increases in the wear liner Coefficient of Friction (COF) values as a function of the number of loading cycles or time. The fourth component of the Stick-slip 2120 friction model, is the SIMAT function block, which is used to connect the MATLAB/SIMULINK secondary suspension models via the co-simulation ports, to a complete Multibody Simulations (MBS) vehicle model developed in SIMPACK.

The optimised friction modelling methodologies that have been developed from this research work however, have two main advantages in comparison to the current friction modelling approaches discussed in the literature review (Chapter 2). The first is associated with the Stick-slip 2120 friction model parameters, which have been validated using wear liner materials and loading/running conditions that are specific to the rail industry. The second advantage is associated with the wide range of laboratory test data that is now available, which will help vehicle engineers/researchers to make informative comparisons between the different friction modelling approaches that are currently been used in railway vehicle MBS. The test data can also be used to verify the responses of the friction models discussed in the literature review, which will then increase the confidence levels in the predictions generated by these models.

The laboratory test data and optimised secondary suspension component models also have commercial value. The laboratory test data for example, could be used by component designers as well as material scientists to develop new products. Whereas the optimised component models could be used in MBS to help vehicle/track engineers to better the performance and maintenance requirements of different dry friction suspension components and how the rates of wear/degradation

in these components over time for example, then influences the levels of damaged suffered by vehicle/track in between planned maintenance cycles.

The proposed architecture of the Stick-slip 2120 friction modelling methodology shown in Figure 6.18, is feasible, but the implementation of this into a complete freight vehicle model developed in SIMPACK however, must be the subject of further work which is discussed in Section 8. The following section discusses the significant findings and conclusions from this research, as well as the main system parameters to consider when modelling dynamical contact with dry friction in railway vehicle MBS.

7. Discussion

The highly nonlinear suspension characteristics of friction damped freight vehicles increases the testing and modelling challenges in vehicle acceptance procedures and Multibody Simulations (MBS). To better understand these challenges as well as the differences between on-track/laboratory test results and those produced by representative vehicle models in MBS, the literature associated with freight vehicle testing and modelling was reviewed.

The research discussed in the literature review clearly suggest that there is no generalised friction testing and modelling methodology currently available due to the complexities and nonlinearities associated with dynamical contact problems. Friction models that are implemented in railway freight vehicle MBS therefore need to be validated using the measurement data from comparative experimental laboratory/on-track tests. This is a necessary requirement as the dry friction characteristics of engineering materials in contact are application specific and highly dependent on the normal load, as well as the number of running cycles and the operating/environmental conditions.

The changes in the secondary suspension system parameters during the life-cycle of the vehicle are not currently fully understood from a testing and modelling perspective due to the lack of laboratory/on-track test data. From the analysis of the benefits/limitations associated with the friction testing and modelling methodologies that are used by the rail industry during vehicle acceptance procedures, accident investigations and gauging studies for example. Scope was identified to develop a new secondary suspension friction modelling methodology, optimised to include the mechanical properties of a range of different wear liner components, as well as the effects of stick-slip behaviour and wear over time.

The new secondary suspension model, named the Stick-slip 2120 friction model, was developed based on the formulation of the LuGre friction model which includes the Stribeck effect (Canudas de Wit, Olsson, Astrom, & Lischinsky, 1995). The centre plate and Constant Contact Side Bearer (CCSB) component models were developed in MATLAB/SIMULINK, as this platform has a co-simulation functionality that is compatible with the SIMPACK software package. The co-simulation function can then be integrated into the centre plate and CCSB component models within the complete vehicle model.

Results from the component models were seen to compare favourably with the works of other authors during the damped free-vibration and dither simulations (Opala M. , 2018) and (Piotrowski, 2012). The damped free-vibration simulations however, were extremely limited in their application due to the fact that the modelling parameters did not relate back to the physical parameters of the actual vehicle. This academic exercise was demonstrating the differences between the Karnopp, LuGre, Piotrowski and Coulomb friction models, but without demonstrating the differences between these models and the test data in (Opala M. , 2018), which would have been more beneficial from a practical/application point of view, as the limitations of these models are well understood from a MBS point of view.

A scale test-rig was designed to generate validation data for freight vehicle MBS friction models and the optimised friction modelling methodology presented in this thesis. Proposals were sent out to two wear liner component suppliers to obtain products that are currently used on freight vehicles throughout Europe and Africa, which obviously adds more value to the research work and results. The experimental work in the laboratory utilised 1:7 scale centre plate/wear liner components to characterise the dynamic characteristics of three different wear liner materials under representative real world loading and running conditions. These tests were carried out following the X-Factor testing methodology defined in the GM/RT2141 Railway Group Standards (Issue 3).

The experimental work achieved its aim of providing a wide range of validation test data that certainly raises more questions than it answers, especially in the context of railway freight vehicle dynamics, which are not currently discussed or quantified in the literature, or even considered at all in freight vehicle MBS models. From the experimental test cases however, it was clear to see that each wear liner material had its own unique friction characteristics and that these were dynamic properties of the centre plate system, rather than static ones, which is the oversimplified assumption that is currently used in railway freight vehicle dynamic simulations.

From the analysis of the pre/post surface roughness and mass property measurements on the centre plate/wear liner components, it was shown that the Standard Deviations (SD) of the surface roughness measurements on the centre plate components, were closely related to the variations that were observed in the torque responses throughout the running-in/service test cases. These variations therefore, should be taken into account in vehicle acceptance procedures, as well as in freight vehicle MBS in order to improve the fidelity of these analysis methods.

7.1. Running-in test results

For contact cases where the loading conditions on the secondary suspension components are in the region of 24.5 kN, which is the full scale equivalent of the 0.5 kN centre plate loading condition, and where the friction surfaces of the centre plate/wear liner components are in the new state for example. The minimum torque responses, which were calculated for materials A, B and C at the start of the running-in tests for example (New components), can be expected to rise by at least 100 – 120, 40 – 125 and 64 – 77% respectively after 3000 cycles of testing (Appendix N).

The magnitudes and ranges of the torque responses for materials A, B and C however, are all different and were shown to be in the regions 0.5 – 1.95, 0.9 – 3.2 and 1.16 – 2.83 Nm respectively. This analysis suggests that material C is the liner material with the most consistent wear out of the three that were tested under the running-in loading conditions.

The Coefficient of Friction (COF) values for the wear liner components were also shown to be unique to materials A, B and C, ranging between 0.05 – 0.195, 0.09 – 0.32 and 0.12 – 0.28 and as can be seen, materials A and B produced the lowest and highest ranges of values overall. This wide range of system parameters however, will obviously have a significant impact on the dynamic performance of the vehicle, as well as the vehicle/track maintenance costs if for example, a freight operating company decided to change the wear liner product during the life-cycle of the vehicle (RAIB, 2016).

The percentage increases in the torque responses as a function of the number of running cycles should also be considered from a vehicle maintenance, as well as a friction modelling requirements perspective. The torque responses of the new friction surfaces are relatively low in comparison to the magnitude of the responses after 3000 cycles of testing. The torque responses of materials A, B and C during the running-in test cases for example, were seen to increase by 23.5 – 108.4, 57.8 – 154 and 32.3 – 47.9% respectively.

From this analyses it is clear to see that the increases in the torque responses in proportion to the number of running cycles are common to all of the wear liner samples that were tested. These factors therefore, should be taken into account in freight vehicle X-Factor test calculations to achieve a better estimation of the range of X-Factor values that are likely to be distributed throughout the whole fleet, as opposed to using one single measurement, which is the current method used to demonstrate compliance with the GM/RT2141 standards.

These factors should also be taken into account in freight vehicle MBS, as the variations and changes in the suspension system parameters over time for example, will definitely have an influence on the

vehicle performance. However, these changes can be easily analysed and quantified in the MBS environment using a validated vehicle model. The results from this model could then be applied in the field and used by freight operating companies to carry out pro-active, rather than reactive maintenance procedures, based on the findings generated by the MBS models, as well as the data from track-side condition monitoring equipment, such as Wheel Impact Load Detectors (WILD) for example.

A data driven MBS model for example, would be a more cost-effective monitoring system in comparison to having to install condition monitoring equipment on every single vehicle. It would also be a more accurate system in comparison to employing empirical knowledge as well as engineering judgement to predict the optimum maintenance schedules for freight vehicle suspension components (Shahidi, Maraini, Hopkins, & Seidel, 2014).

The non-symmetric friction characteristics of the centre plate/wear liners due to the Bauschinger effect, contamination and the surface roughness properties of suspension components should also be taken into account in friction tests and freight vehicle MBS models. These parameters were shown to range between 20 – 65% in the majority of the running-in test cases, with only 3 out of the 17 centre plate/wear liner samples, producing symmetrical friction characteristics. From the analyses of the pre/post-test surface measurement results on the centre plate components for example (Appendix I), the Standard Deviations (SD) of the Ra-slope and Wa-slope parameters were shown to range between 21.9 – 54%, which are in the same range as the SD of the percentage increases, as well as the non-symmetric characteristics of the torque responses in percentage terms.

This finding strongly suggests that these system parameters are closely related. Therefore, by systematically measuring the roughness parameters of the friction surfaces prior to carrying out friction tests in the laboratory, a better estimation of the expected variations between the torque responses of the same materials can then be obtained. These measurements also help in understanding the wear/degradation rates of the different wear liner materials and also, how these system parameters then respond to the varying loading conditions as well as the number of running cycles.

The significant discrepancies between the COF results generated in this research work and the manufacturers specifications should also be considered. From this analyses it could be argued that the friction models that are currently been used in MBS to describe the secondary suspension components, are not truly representative of the centre plate/side bearer systems over a wide range of operating conditions, which obviously leads to more uncertainties in the modelling methodologies (Berg & Evans, 2009).

However, to enhance the capabilities of existing friction models such as the Coulomb model for example, it is recommended that the global evolutionary friction models developed in this research work (Section 5.4.5) be used in combination with this model in freight vehicle MBS. This can be achieved in two ways; the first is to implement the global evolutionary model parameters manually and carry out one-shot simulations, a method that is suitable for using in virtual vehicle X-Factor tests. Whereas the alternative implementation method for transient analyses and dynamic gauging studies such as the one proposed in (Allen, Perez, & Hatt, 2008) for example, is to code the mathematical functions describing the global evolutionary friction models, directly into the MBS time-stepping integration routine using Equation (5.1) in Section 5.4.4, to update the COF values as a function of time.

The variations in the local model parameters, such as the torsional stiffness and viscous damping properties of the different wear liner materials, should also be used to improve the accuracy of existing freight vehicle friction models, as well as to reduce the uncertainties associated with the modelling simplifying assumptions. From the running-in test cases, it was clear to see that stick-slip behaviour in the breakout and gross-sliding regions for example, was not present to the same extent that it was in the service test cases, mainly due to the lighter conditions. This analysis therefore, suggests that the Coulomb friction model combined with the global evolutionary friction models to describe the increases in the COF values, would be suitable for describing the contact conditions in the secondary suspension, but only for loads in the region of 0.5 kN in the case of the 1:7 scale model components, or 24.5 kN for the full size components.

Several of wear liner samples that were tested, were also observed to exhibited viscoelastic material behaviour in the breakout and transition regions of the hysteresis responses. The viscoelastic behaviour was common to all three wear liner materials and in the test cases where this was clearly evident (Sections 5.3.4 – 5.3.6), the friction surfaces started to breakout of the stiction regions when the torque responses were 100 – 200% lower, than the responses of the wear liner samples that had no viscoelastic characteristics. The torque responses in the viscoelastic samples obviously increase in proportion to the centre plate velocity, so the friction damping is clearly progressive until the responses start to transition into the gross-sliding regimes. From this analysis, it can be concluded that the secondary suspension friction models should also include a viscous damping element to take these effects into account.

For the wear liner samples that have stiff characteristics, the material behaviour is highly elastic in the stiction regions so the friction damping is minimal. However, the higher breakout torque in these samples, and in the context of a full size vehicle, could potentially lead to an increase in the rates of wheel/rail wear over time, as well as greater levels of noise emissions on routes with tight curve radii. Due to the increases in the wheel/rail contact forces as a result of the increases in the bogie rotational resistance. On network work routes that have large curve radii as well as low curve densities on the other hand, then the stiffer characteristic may be more desirable than the viscoelastic one, as this would improve the high speed running stability of the vehicle on straight sections of track. Whereas the viscoelastic response would obviously lead to a reduction in the steering forces.

The friction modelling methodology developed in this thesis still has its limitations due to the fact that the Stick-slip 2120 friction model, does not currently have the capabilities to describe the non-symmetric torque responses of the centre plate/wear liner components. This aspect of the Stick-slip 2120 friction model will be developed in the further research work. The alternative option available to describe the non-symmetric characteristics of the friction surfaces however, is to use the non-smooth Substitute friction model that was developed in (Piotrowski, 2012), as this is well suited for implementing in railway vehicle MBS, but more importantly, also takes anisotropic friction into account, meaning that it is capable of modelling the non-symmetric friction characteristics of the secondary suspension system.

The Stribeck effect/stick-slip response however, is not included in the Substitute model, but under the lighter loading conditions (0.5 kN or 24.5 kN), these effects were seen to be negligible. A Coulomb friction element connected in series with a spring and viscous damping element therefore, would be adequately sufficient for modelling the nominal behaviour of each wear liner material during the running-in test cases.

7.2. Service test results

For contact cases where the number of running cycles are 3 – 4 higher than the running-in test cases and the secondary suspension loading conditions are in the region of 147, 294 and 441 kN, which are the full scale equivalents of the 3, 6 and 9 kN scale model centre plate loads. The friction model parameters should then be reconfigured to reflect these changes.

During the service test cases it was clear to see the differences developing between stick and slip torque responses in the breakout and gross-sliding regions. The stick and slip torque responses using material A for example, ranged between 6.2 – 44.6 Nm and 5.4 – 37.6 Nm respectively, which is a difference of 14 – 18% between these two parameters. These responses for material B however, were the highest overall during the service tests, ranging between 8.5 – 93.3 Nm and 5.5 – 71.7 Nm respectively. The differences between the stick and slip torque parameters in this material therefore, are in the region of 30 – 54%, which is three times higher than material A. For material C however, the stick torque responses ranged between 14.3 – 38.1 Nm and the slip responses between 8 – 30.1 Nm which is the highest difference overall at 26 – 79% (Appendix R).

From this analyses it is clear to see that the Coulomb friction model would not provide the most accurate solution under the service test loading conditions. As a result of increasing the centre plate loading conditions relative to the running-in loading conditions by factors of 6, 12 and 18, the wear liner materials start to exhibit stick-slip behaviour in the breakout regions, but not in the gross-sliding regions of the hysteresis responses. This behaviour however, which is common to all of the wear liner samples, only applies during the initial stages of the service tests.

The Coulomb model can only describe the extremes of the stick and slip torque responses, or the nominal behaviour. Whereas the Stick-slip 2120 friction model on the other hand, does included the stick-slip behaviour as well as the viscoelastic effects taking place in the materials during the transition events and gross-sliding regimes. This model therefore, is clearly more suitable for describing the full range of materials behaviours in the centre plate system as well as the CCSB components.

The mean COF values during the 3, 6 and 9 kN loading cases also increased relative to running-in test cases and were shown to be 0.18, 0.18 and 0.21 respectively. Whereas after the running-in tests, the mean COF value for the complete data set was 0.14 (Appendix N). The SD of these parameters, were shown to be 20, 31.9 and 48.2% in the service tests and 36.2% in the running-in tests. This analysis suggests that the torque responses become more widely dispersed about the mean values as the centre plate load and number of cycles increases.

The SD of the COF values during the 9 kN loading cases however (48.2%), are in close agreement with the SD of the pre/post-test Ra-slope measurements on the centre plate components, which were shown to be 41.2 and 54% (Appendix I). From this analysis, it can be concluded that the variations observed in the torque responses during the service tests are closely related to the SD of the Ra-slope measurements on these components.

The increases in the torque responses/COF values during the vehicle life-cycle of the centre plate/wear liner components also need to be considered. The increases seen for material A were in the range of 13.8 – 251.8%, whereas for materials B and C, they ranged between 78.9 – 270% and 77.7 – 106.6% respectively. The analyses of the running-in and service test results shows that the increases in the torque responses are common to all of the wear liner materials. These parameters therefore, should be taken into account in freight vehicle MBS, as the changes in the suspension parameters over time for example, are bound to have a significant influence on the vehicle performance.

The increased number of running cycles during the service test cases were also shown to have a significant influence on the torque responses of the centre plate/wear liner components. During the first 25 cycles of these test cases for example (Appendix R), the torque responses for material A ranged between 5.4 – 22.3 Nm, whereas for materials B and C the responses ranged between 5.5 – 36 Nm and 9.7 – 30.7 Nm respectively. The peak torque response for material B was 63% higher than the peak torque for material A.

Halfway through the service test cases, it was clear to see that there had been a number of significant developments taking place in the torque responses at the local level (Sections 5.4.6.1 – 5.4.6.3). From the analyses of the hysteresis responses for material A, it could be seen that the peak torque responses during the 6 kN loading case running at 0.042 Hertz (Hz) for example, were in the region of 29.4 Nm, whereas the peak torque during the 9 kN case was slightly lower at 25.9 Nm, which was not expected. This finding clearly suggested that there was an issue with surface geometry of the centre plate or wear liner component that was used in this particular test case.

This suggestion was also supported by the fact that the even with the contaminated wear liner sample, that was used in test case 5 for example (material A), responded as expected under the 3 kN service test loading condition, i.e. the torque responses in this test case were seen to be the lowest overall, which they should be due to the relatively low contact pressure. Whereas during the running-in test cases, which were carried out under the 0.5 kN loading conditions, the torque responses during test case 5 were seen to be the highest overall due to the viscoelastic behaviour in the breakout and gross-sliding events as a result of the hydraulic oil contamination.

The torque responses for material B were the highest overall at the halfway stage of the service tests (Appendix R). The stick-slip behaviour that was developing in the breakout regions during the first 25 cycles for example, was starting to dominate the gross-sliding regimes as well, especially in the 6 and 9 kN loading cases. However, during the 9 kN loading case the torque responses were seen to be relatively smooth in CW direction, whilst in the CCW direction, stick-slip behaviour was evident throughout the gross sliding regimes (Figure 5.55 in Section 5.4.6.2). These friction characteristics in the context of the full size vehicle however, would have a negative impact on the high speed running stability of the vehicle as well as its ability to negotiate curves, switches and crossings safely and effectively without causing excessive damage to either the vehicle or track components.

During the last 25 cycles of the 6 kN service test on material A that was running at 0.042 Hz, the stick and slip torque responses were shown to be the highest overall for this material at 44.6 and 37.6 Nm respectively (Figure 5.51 in Section 5.4.6.1). These responses also had two distinctive breakout events which strongly suggested that some form of severe wear mechanism was developing in the friction surfaces. However, after analysing the post-test mass property results for this sample (Test case 2 in Figure 5.15, Section 5.2.3), it was clear to see that the wear rate of this sample was in line with the expected behaviour i.e. the mass reduction in this sample was higher than the reduction in the 3 kN loading case (Test case 1), but lower than the mass reduction in the 9 kN loading case (Test case 3). This analysis was inconclusive and requires further research to establish the root causes of the diverging torque responses as well as to better understand the causal factors leading to these developments.

The stick and slip torque responses during the last 25 cycles of the 9 kN service test cases using material B were the highest overall out of the three wear liner materials that were tested. The stick and slip torque during the test that was running at 0.042 Hz, were seen to 91.4 and 71.7 Nm, whereas during the 0.084 Hz test case, the stick and slip responses were shown to be 93.3 and 69.3 Nm (Figure

5.57 in Section 5.4.6.2). From this analysis it is clear to see that the differences between the stick and slip torque under the 9 kN loading conditions, range between 27 – 34%.

The maximum difference between the stick and slip torque responses for material B however, was observed during test case 9, which was running under the 6 kN loading condition and at the 0.042 Hz forcing frequency (Top plot in Figure 5.57). The stick and slip torque in this particular test case were shown to be 40.1 and 26.5 Nm, which is a difference of 51% (Appendix R). The test cases that were carried out on materials A, B and C under the 3 kN loading conditions on the other hand, did not exhibit any form of stick-slip behaviour during the gross-sliding regimes. From this analysis we can conclude that the levels of elastic potential energy in centre plate/wear liner materials under the 0.5 and 3 kN loading cases, are significantly lower than the energies of the centre plate system during the 6 and 9 kN loading cases.

The local analysis results for material C also revealed several interesting findings that were not mentioned in the literature review. The torque responses in this wear liner material followed the exact same pattern of behaviour regardless of the loading conditions i.e. increasing rapidly during the first 3 – 5 hours of testing, then decreasing again for the remaining part of the service tests, back towards the initial values that were measured at the start.

From the global COF results for material C (Figure 5.45 in Section 5.4.4), it was shown that the COF values increased rapidly towards the peak values of 0.21 – 0.27 during the first 3 – 5 hours of these test cases (First 907 – 1512 cycles). However, after reaching these limits, the torque responses then started to gradually decrease in proportion to the number of running cycles and after 20-hours of continuous running, were seen to converge to the exact same region of COF values, 0.18 – 0.22, which is a 15 – 19% decrease in the peak COF values. The COF values in this material then continued to decrease for the remaining part of the service tests where the final values were seen to be in the region of 0.14 – 0.17, which is another 22% decrease. The total decreases in the COF values therefore, range between 37 – 41% and were seen to be the highest overall during the 3 kN loading case (Test case 15, Appendix Q).

Also, from the hysteresis responses during the first 25 cycles of the service test cases using material C (Figure 5.58 in Section 5.4.6.3), it was clear to see that the torque responses under the 3 and 6 kN loading conditions were evenly matched, which is similar to the behaviour that was observed in material A. The torque responses during the 6 and 9 kN loading cases using this material, were also seen to be approximately the same (Figure 5.50 in Section 5.4.6.1).

This analyses clearly shows that the magnitudes of the torque responses are more sensitive to the changes in the surface roughness characteristics and wear regimes developing in the centre plate/wear liner components over time, than they are to the changes in the loading conditions. This is a significant finding and could help to explain part of the reasoning why the derailment resistance of some empty and part-laden freight vehicles for example, are lower than their laden counterparts when exposed to track-twist defaults and crossovers (RAIB, 2007) and (RAIB, 2016).

The spectral analysis results throughout the various stages of the running-in/service test cases also proved to be an essential part of this research work (Sections 5.3.7 and 5.4.7). From these responses we could identify the frequency components in the region of 224 Hz due to the hydraulic power unit on the Instron testing machine. This constant signal was used then used as a reference marker to quantify the signatures that were developing in the friction surfaces of the centre plate/wear liner components as a result of the changes that were taking place over time in the torque responses.

This dither forcing frequency however (224 Hz), is more than double the 106.8 Hz frequency that was used to analyse the centre plate friction model behaviour in Section 4.10. Therefore, it is not currently known how the dynamic centre plate model would respond to this dither frequency. However, from these simulations we could certainly see that the dither did have a measurable effect on reducing the levels of dry friction damping in the centre plate system. From the simulation results therefore, it can be suggested that the 224 Hz dither signals will also have an effect on the torque responses presented in this thesis, but this effect will be exactly the same across all of the test cases that have been studied, which obviously eliminates any form of bias between the different test cases.

Analysing the centre plate model behaviour under the 224 Hz dither forcing frequency should form part of the further work in order to quantify the smoothing effects of this signal and to establish if this parameter improves the agreement between the measurement/simulation frequency responses. The power responses of the measurements for example, were seen to be two orders of magnitude higher than the simulation responses, which clearly shows that the dynamic centre plate model has its limitations (See Sections 5.3.7, 5.4.7, 5.4.8.3, 6.4 and 6.9).

From the measurements however (Sections 5.3.7 and 5.4.7), it was clear to see a broad range of signatures developing in the responses of the running-in/service test cases as the number of running cycles increased. The changes in the frequency components of the centre plate/wear liner samples were then shown to relate back to the changes that were occurring in the hysteresis responses. The contaminated wear liner that was used in test case 5 for example (material A), had a unique frequency component developing in the region of 163 Hz that was not present in any of the wear liner samples that were tested. This particular sample also had a distinctive viscoelastic friction characteristic throughout the running-in test case which was clear to see from observing the hysteresis responses (Figures 5.24 and 5.27 in Section 5.3.4).

The developing stages of the stick-slip behaviour occurring in the centre plate/wear liner components were also relatively easy to detect using the spectral analysis method. The power responses of the frequency components for example, were shown to be proportional to the magnitude of the torque as well as the forcing frequency when there was no stick-slip behaviour present in the hysteresis responses. When stick-slip behaviour started to develop in the hysteresis responses on the other hand (Figures 5.54 and 5.57 in Section 5.4.6.2), a broad range of frequencies also started to appear in the region of 100 − 150 Hz. The stick-slip behaviour was also shown to have an even greater influence on the magnitudes of the power responses in comparison to the influence of the smoothest and highest torque responses (Figures 5.66 and 5.67 in Section 5.4.7.2).

From the spectral analyses results for the centre plate/wear liner components, it can be firmly concluded that a wide range of different wear and failure modes developing in the secondary suspension components over time for example, can be easily detected by carrying out Fast Fourier Transforms (FFT) on the measured torque signals. This analysis method therefore, could be potentially be applied in the field and used in X-Factor tests/on-track tests during vehicle acceptance procedures to identify incorrectly assembled/poorly performing bogies without having to remove the wagon body beforehand. In situations where a wagon body has been removed, only to find out that the secondary suspension components are in good working order for example, then the FFT analysis method would be more cost effective as this would reduce the downtime of the vehicle and the inherent safety risks that are associated with vehicle rebuilds and maintenance overhauls.

The variations in the surface roughness and geometric parameters of the centre plate/wear liner components also need to be considered from a friction testing/modelling perspective as these factors are suggested to exacerbate the non-symmetric friction characteristics of the centre plate system.

During the running-in tests, these parameters were seen to range between 20 – 65 % (Sections 5.3.1 – 5.3.3). The differences between the torque responses in the Clockwise (CW) and Counter Clockwise (CCW) directions during the steel-on-steel test case were also seen to be the highest overall under the 0.5 kN loading conditions, ranging between 36 – 90% (Section 5.4.8.1). During the service test cases with the wear liner samples included on the other hand, the differences between the torque/COF responses in the CW/CCW directions, were all seen to be less than 10% (Section 5.4.4). This analyses clearly shows that the friction surfaces with the wear liners included in the centre plate system, are more conformal under the service test loading conditions due to the compliancy of these components.

The torsional stiffness parameters of the centre plate/wear liner samples during the service tests were also more consistent (Appendix R), as well as 15 – 84% higher than the range of stiffness coefficients that were calculated during the running-in test cases (Appendix O). The nominal torsional stiffness during the running-in test cases, ranged between 3149 – 3215 Nm/rad, whereas during the service test cases, the stiffness parameters for materials A, B and C were shown to be range between 5883 – 5906, 5638 – 5697 and 4888 – 5039 Nm/rad respectively.

The SD`s of the service test torsional stiffnesses were also less than 6% under the full range of loading conditions. Whereas during the 17 running-in test cases, which were all carried out under the same loading conditions it should be pointed out, the SD were seen to be in the range of 23.2 – 30.1%. This range however, is seen to be in close agreement with the SD of the pre-test surface roughness measurements on the centre plate components, which were seen to range between 20.6 – 32.5%, not including the SD of the Ra-slope and Wa-slope measurements (Appendix I).

This analysis therefore, strongly suggests that there is a close cause/effect relationship between the surface roughness parameters of the centre plate components and the variations observed in the torque responses, which there definitely should be. The torsional stiffness parameters during the running-in loading cases are lower because the normal contact pressure acting on the friction surfaces for example, is supported by the tips of the surface asperities on the centre plate/wear liner components, which are much weaker than the bulk materials. The significant differences between the height of the asperities at the micron-metre level, also suggests that the distribution of the contact forces under the lightest loading conditions will be highly non-uniform, which will obviously have an influence on the non-symmetric characteristics of the centre plate system as well (See Figures 5.9 – 5.12 in Sections 5.2.1 – 5.2.2).

During the 3, 6 and 9 kN loading case on the other hand, the normal contact pressure is supported by the bulk materials of the friction surfaces, hence the reason why the system stiffness, as well as the contact area increases, due to the fact that these two parameters are inextricably linked through the constitutive equations governing Hooke`s law for elastic materials (Ashby & Jones, 1980). This change in the system parameters is also reflected in the torque responses of the X-Factor results, especially during the 9 kN loading cases for example, where the SD of the maximum values was shown to be 48.2% (Appendix S). This parameter was then shown to be in close agreement with the SD of the pre/post-test Ra-slope and Wa-slope measurements on the centre plate components as these were shown to range between 21.9 – 54% (Appendix I).

From this analyses it can be concluded that surface roughness parameters of the steel centre plate components, are the main factors to take into consideration when carrying out X-Factor tests in the laboratory as well as virtual representations of these using MBS, as these parameters dictate the levels of variation observed in the COF values of the wear liner samples, as well as in the samples of the same material under equivalent loading conditions. The SD of the wear liner roughness values

however, do still contribute to these variations, but not to the same extent due to the softness of the polymer/composite materials.

This conclusion is also supported by the torque responses during the various phases of the steel-on-steel test case. The SD of these parameters for example, were shown to be in the region of 99.2% (Table 5.9 in Section 5.4.8.2), which is double the SD of 48.2% that was observed during the 9kN/laden loading X-Factor test cases (Appendix S). These parameters therefore, should be taken into consideration in vehicle acceptance tests and railway vehicle MBS in order to reduce the uncertainties associated with these analysis techniques.

7.3. Steel-on-steel test and X-Factor results

The steel-on-steel test case also generated new knowledge in relation to the friction characteristics of the centre plate system. During this test case the torque responses were shown to be highly unstable as well as non-symmetrical, especially during the 0.5 kN loading phases. The COF values for the centre plate components without the wear liners included, were shown to be the highest overall ranging between 0.3 – 1.6 (Table 5.9 in Section 5.4.8.2).

The peak values in this range however, are 3 – 4 times higher than peak the COF values that were observed during the centre plate/wear liner test cases. This analysis clearly shows the reasons why freight operating companies have to carry out scheduled maintenance on their vehicle fleets and also, the reasons why freight vehicles with wear liner components that are worn beyond their wear limits for example, have extremely high bogie/wagon body rotational resistance which then causes these vehicles to derail (RAIB, 2016). During the 1-hour stopping period however, the torque responses decreased by 16.9%, which shows that the creepage does occur in the centre plate system under loaded conditions and also, that the steel-on-steel contact conditions are highly elastic.

The hysteresis responses of the steel-on-steel test case also provided a deeper insight into the nonlinearities that were developing in the centre plate system in the response to the changing loading conditions, as well as the number of running cycles. The non-symmetric friction characteristics that were observed through phase one of this test, also started to develop in two distinctive forms. The first is the difference between the magnitudes of the torque responses in the CW/CCW directions due to the Bauschinger effect, as well as kinematic hardening taking place in the friction surfaces. The second form, is the stick-slip response in one direction, whilst in the other, the torque responses are shown to be smooth (Figure 5.74 in Section 5.4.8.2). This behaviour however, is also suggested to be responsible for initiating the same pattern of behaviour in the hysteresis responses of material B during the latter stages of the service tests (Figure 5.55 in Section 5.4.6.2).

The spectral analysis results for the steel-on-steel test case also played an important role in better understanding the root causes of the frequency components that wear developing in the centre plate/wear liner components over time. The signatures that were developing in the region of 100 – 150 Hz during the later stages of the test cases 9, 11 and 14 using material B for example (Figures 5.65 – 5.67 in Section 5.4.7.2), were also present in the steel-on-steel frequency responses. This analyses led to the conclusion that it was the material transfer from the steel centre plates to the polymer wear liners, that was causing the stick-slip response to develop in these samples. The post-test images of the wear liner samples also showed clear evidence of material transfer as well as corrosion, which is also proof that these complex processes are taking place in the secondary suspension components (Figure 5.2 in Section 5.1).

From this analysis, it can be concluded that material transfer causes significant differences to develop between the yield strengths of the top/bottom surfaces of the wear liner components. The stationary

surfaces that are held rigid against the bogie suspension components for example, retain their `as new' mechanical properties. Whereas the opposite surfaces on the other hand, are highly dynamic due to the motion of the wagon body centre pivot/slide plates, which are obviously free to move relative to the bogie frame.

This relative motion however, causes wear and degradation, as well as different hardening and fatigue mechanisms to develop in these surfaces due to the cold-working processes that take place in the surface materials in response to the cyclic forcing frequencies. These mechanisms therefore could also be partly responsible for causing some wear liner components such as the composite type for example, to fail catastrophically in service as a result of tearing which then leads to direct steel-on-steel contact between the suspension components as well as significant increases in the bogie rotational resistance (RAIB, 2016).

From the analysis of the X-Factor results during the 3, 6 and 9 kN loading cases, which were used in the 1:7 scale model tests to represent the tare, part-laden and laden loading conditions of the full size vehicle (Sections 5.4.9.2 – 5.4.9.4). It was shown that the X-factor values for the tare loading conditions ranged between 0.044 – 0.085, whereas for the part-laden cases, these values were shown to be the lowest overall, ranging between 0.033 – 0.083. The highest X-Factor values overall however, were shown to range between 0.029 – 0.095 during the laden loading cases (Appendix S). The SD of these values was then shown to be 48.2%, which was also seen to be in closest agreement with the range of SD of the surface roughness measurements on the centre plate components (Appendix I).

By plotting the normal distributions of the X-Factor results for complete data set under each loading condition, as well as the distributions of the individual test cases. It was then clear to see that the initial X-Factor values that were measured during the first 25 cycles of the service test cases for example, formed the smallest part of the data sets due to the rapid increases that were observed in the torque responses during the first 3 – 5 hours of the service tests. The nominal increases in the X-Factor values after 10800 cycles of continuous running during the tare, part-laden and laden test cases, were shown to be 16.8, 39.2 and 58.8% respectively. The SD of these parameters however, ranged between 22.2 – 87.8% and were the highest overall in the part-laden/laden loading cases (Appendix S).

The overall conclusions that can be drawn from the analyses of the benchmark laboratory test data and simulation results, are that more test data should be made available to the rail industry/research institutions. This will enable the current testing and friction modelling methodologies to be further developed and optimised for the 21st century rail freight industry. The ultimate aim in the future however, is start replacing static gauging practices and on-track testing, as well as vehicle acceptance X-Factor tests, with virtual equivalents using data-driven MBS models to carry out these procedures (Shahidi, Maraini, Hopkins, & Seidel, 2014).

This transition would also bring significant cost benefits to the rail industry and make it more sustainable, as well as more attractive to potential new customers who are currently using other modes of freight transportation such as road sea or air for example. Based on the findings presented in this thesis, it can be seen that there is real scope for the future developments in friction modelling in general, as well as in railway freight vehicle MBS using optimised friction models in order to better understand the highly nonlinear dynamics of friction damped freight vehicles and the maintenance requirements of the suspension components.

7.4. Secondary suspension friction modelling methodology

The Stick-slip 2120 friction modelling methodology that was developed as part of this research work has proved to be successful in expending the current knowledge and understanding on dynamical contact problems with dry friction and viscous damping (Chapter 6). The basic framework of the MATLAB/SIMULINK centre plate/Constant Contact Side Bearer (CCSB) friction models, were based on the formulation of the LuGre friction model, which includes pre-sliding elastic displacements, the Stribeck effect and viscous damping.

The material behaviours that were observed throughout the running-in/service tests were modelled to an acceptable degree of accuracy using the Stick-slip 2120 friction models and the laboratory test data from various running-in/service test cases to validate the magnitudes of the torque responses, as well as the friction characteristics of the different material models. These models were shown to be capable of describing the viscoelastic characteristics of the contaminated wear liner sample, as well as the stick-slip behaviour in the breakout and gross-sling regions of the hysteresis responses (See Figures 6.6 and 6.15 in Sections 6.2 and 6.7). The measurement/simulation responses were validated in accordance with the matching error limits specified in the GM/RC 2641 standards and shown to be in good agreement and within these limits in the majority of simulation examples that were discussed.

The centre plate and CCSB 2120 friction models however, only provided a single snap-shot of the friction characteristics at any one instant in time during the life-cycle of these components. The global evolutionary friction models were then developed to describe the increases/decreases in the COF parameters as a function of the number of running cycles, which were then converted to time histories to use in railway vehicle MBS. These models can be used to update the friction model parameters at regular intervals during transient analyses as well as dynamic gauging studies.

The Stick-slip 2120 friction modelling methodology can also be used to analyse the dynamic behaviour of the centre plate/CCSB component models as isolated systems, such as in the case of a design scrutiny or parameter optimisation study for example. The component models can also be implemented into a complete freight vehicle model in SIMPACK using the co-simulation function block to make the connection between MATLAB/SIMPACK.

The intention is to use SIMPACK to calibrate the sliding distances that each wear liner sample was subjected to in the laboratory tests, to the curve densities and curve radii of different network routes. These parameters can then be used to update the global evolutionary friction models at the correct instances in time during the life-cycle of the secondary suspension components in MBS. This part of the research work however, was not completed and should be included in the further work.

The main limitations associated with the Stick-slip 2120 friction model modelling methodology are that it is not capable of describing the non-symmetric friction characteristics of the centre plate system. It is also deficient in modelling the static behaviour of the system under pre-loaded initial conditions due to the velocity threshold parameter which introduces creepage into the model responses. These aspects of the proposed Stick-slip 2120 friction models therefore, should also be refined and optimised in the further work.

8. Conclusions and further work/recommendations

8.1. Key conclusions

The key conclusions that can be drawn from the research work undertaken in this thesis are as follows;

1) The calculated Coefficient of Friction (COF) values of the centre plate/wear liner components are measurably different and vary over a wide range in response to the changes in loading conditions, the wear liner materials and the number of running cycles.

2) The Standard Deviations (SD) of the pre/post-test surface roughness measurements on the centre plate components are closely related to the variations observed in the COF values for different specimens of the same friction liner material.

3) The COF values increase rapidly during the first 2 – 3 hours of the running-in/service tests and then gradually level-off in the cases using materials A and B. In the service test cases using material C however, there is a turning point after completing between 907 – 1512 cycles, where the COF values start to decrease as the number of running cycles increases. These friction characteristics were unique to material C during the service test cases and did not start to develop during any of the running-in tests.

4) The COF values under the 0.5 kN loading conditions range between 0.05 – 0.32 and can increase by 23.5 – 154% relative to the values that were measured at the start of each test case. Under the 3, 6 and 9 kN loading conditions the COF values and percentage increases ranged between 0.09 – 0.54 and 13.8 – 270%. The COF values for the steel-on-steel contact conditions were the highest overall at 0.3 – 1.6 and can increase by 55 – 333%.

5) The nominal torsional stiffness coefficients and SD under the 0.5 kN loading conditions ranged between 3149 – 3215 Nm/rad and 27.6 – 30.1% (Running-in tests). Under the 3, 6 and 9 kN loading conditions (Service tests), the stiffness coefficients for materials A, B and C increased to 5883 – 5906, 5638 – 5697 and 4888 – 5039 Nm/rad respectively. The SD however were 5 – 6 times lower at 1 – 5.7%. The nominal torsional stiffness coefficients and SD for the steel-on-steel contact conditions were 4569 Nm/rad and 12.2% under the 0.5 loading conditions and 5636 Nm/rad and 2.5% under the 3 kN loading conditions.

6) The viscoelastic effects of the centre plate/wear liner components are common to all of the samples that were tested under the 0.5 kN loading conditions. They are also more dominant in the breakout regions of these hysteresis responses, than they are in the gross-sliding regions. These effects are also exacerbated by the levels of hydraulic oil contamination in material A.

7) Stick-slip behaviour starts to develop in a minority of the hysteresis responses under the 0.5 kN loading conditions, mainly in materials B and C. This effect however is negligible in comparison to the stick-slip behaviour observed under the 3, 6 and 9 kN loading conditions. The differences between the magnitudes of the stick and slip torque responses for material A were 14 – 18%, whereas for materials B and C they were 26 – 79%. The differences between the stick and slip torque responses during the steel-on-steel test case were in the region of 50%.

8) The non-symmetric friction characteristics of centre plate/wear liner samples under the 0.5 kN loading conditions were shown to range between 20 – 65% in the majority of the test cases. Under the 3, 6 and 9 kN loading conditions, these characteristics were all shown to be less

than 10%. However, after completing around 5400 cycles of the service test cases, stick-slip behaviour developing in one direction, combined with smooth torque responses in the other, can also start to occur in the hysteresis responses of material B under the 6 and 9 kN loading conditions.

9) The non-symmetric friction characteristics during the steel-on-steel contact case ranged between 36 – 90% and were shown to be the highest overall under the 0.5 kN loading conditions. Stick-slip behaviour combined with smooth torque responses in the CW/CCW directions also started to develop in this test case under the 0.5 kN loading condition.

10) Developing stick-slip behaviour in the centre plate/wear liner components can be detected using Discrete Fast Fourier Transforms (DFFT). This behaviour excites frequencies in the region of 100 – 150 Hz. The viscoelastic responses of the contaminated wear liner sample also cause a unique band of signatures to develop in the region of 163 Hz. The steel-on-steel contact conditions excite an even broader range of distinctive frequencies than the wear liners in the regions of 25 – 75 Hz and 100 – 150 Hz. These frequency components are all closely related to the fundamental harmonics of the centre plate system.

11) The changes in the power responses of the frequency signatures are proportional to the torque responses of the centre plate/wear liner components and the rotational velocity of the centre plate. The stick-slip behaviour however, has the most dominant influence on the power responses of the centre plate system.

12) Dither frequencies in the region of 224 Hz due to the fluid pulsations of the hydraulic power unit on the testing machine, are clear to see in the frequency responses of the 1:7 scale centre plate system. Dither frequencies thirty times higher than the natural frequency of the centre plate system also have a measurable influence on the friction model behaviour in MBS.

13) The X-Factor values for the centre plate/wear liner samples under the 3, 6 and 9 kN loading conditions (10800 running cycles), range between 0.029 – 0.095 and can increase by 5.4 – 111.1% relative to the initial values. The Standard Deviations (SD) of these parameters ranged between 22.2 – 48.2% and were the highest overall under 9 kN loading conditions.

14) The proposed Stick-slip 2120 friction modelling methodology is capable of describing pre-sliding elastic displacements and stick-slip behaviour developing in the friction surfaces of the centre plate/wear liner components, as well as the viscoelastic effects in the breakout/gross-sliding regions of the hysteresis responses. The increases/decreases in the COF parameters as a function of the number of running cycles or time, can also be described using the global evolutionary friction models.

8.2. Further work

The research findings presented in this thesis should be disseminated to the rail industry and research institutions through variety of sources. These include journal publications, presentations to rail freight conferences as well as consultations with component suppliers, freight operating companies and accident investigators. The further work in relation to improving and optimising the friction testing and modelling methodologies developed in this thesis should also focus on three key areas of research which are discussed in points 8.2.1 – 8.2.3 below:

8.2.1. Friction modelling

The optimised secondary suspension component friction models should be further developed by scaling-up the load/torque responses to the full-size equivalents following the 1:7 scaling laws derived

in Section 3.1. The full-size component models should also be validated against the scaled-up laboratory test data and then implemented, via the co-simulation function block, into a complete vehicle model developed in SIMPACK. This model should then be subjected to virtual vehicle acceptance tests using the standard friction models available in the SIMPACK to generate the benchmark simulation results.

The SIMPACK vehicle model should also be simulated using the optimised centre plate and Constant Contact Side Bearer CCSB friction models proposed in chapter 6 in order to quantify and compare the differences in the vehicle dynamics as a result of using the standard/optimised friction modelling methodologies. The global evolutionary friction models and the variations observed in the stiffness parameters and Coefficient of Friction (COF) values for each wear liner material should also be included in the vehicle simulations. The recommendation is to focus on quantifying the levels of vehicle/track damage caused by the different wear liner materials at various stages of their life-cycles. Dynamic gauging studies should also form part of this analyses with the aim of quantifying the swept envelope of the vehicle model as a result of using the standard/optimised friction modelling methodologies.

Future research work should also focus on further developing the local friction models as these still have their draws backs and limitations. The main aspects of the measured torque responses that were not taken into account in the MATLAB/SIMULINK secondary suspension models for example, were the Bauschinger effect/non-symmetric friction characteristics and the structural/fluid borne vibrations generated by the testing machine. The Bauschinger effect should be included in advanced/state-of-the-art friction models, especially in the context of freight vehicle MBS models, as this effect could be contributing towards uneven wheel/rail wear, as well as high speed running instabilities and poor curving performance.

The structural vibrations of the testing machine frame could be captured in the MATLAB/SIMULINK centre plate friction models by introducing more degrees of freedom. Whereas the fluid borne vibrations on the other hand, should be superimposed on the forcing functions that are used to excite the friction models. The velocity threshold parameter in the Stick-slip 2120 friction modelling methodology also needs to be revised in future modelling work. This parameter as was shown to be the case in the dither simulations, can lead to unrealistic effects such as creepage when the system should actually be static.

8.2.2. Further testing

The findings from the laboratory test results strongly suggest that further tests should be carried out with the aim of quantifying the dynamic response of the centre plate system due to the influence of contamination such as oil/grease. Material A was the only wear liner sample that was tested under these conditions, but from observing the torque and frequency responses, it was clearly evident that this parameter had a significant influence on the torsional stiffness and viscous damping properties of the centre plate system which require further investigating. These investigations should also aim to establish if contamination/lubrication has a detrimental/beneficial influence on the maintenance requirements of this particular material.

Further tests also need to be carried out on material C to benchmark the performance of this wear liner under the 0.042 Hertz (Hz) centre plate forcing frequency, as these results are not included in the data sets shown in Appendices Q, P and R. The laboratory tests should also be repeated on the three wear liner materials following the testing flow chart discussed in Section 5. The angular displacements in these tests however, should be set to $\pm$ 0.75 and $\pm$ 1.5 degrees in order to characterise the wear liner components over the full range of angles that are likely to be seen in service.

It should be pointed out that the angular displacement of ± 3 degrees, which is the parameter that was used in this study, is probably the maximum rotational angles that the centre plate/wear liner components are ever likely to see in service. The test cases discussed in this thesis however, were focused on quantifying the full range of friction characteristics of each wear liner material, rather than focusing on the angles that are imposed on the suspension components as a result of varying curve radii`s and vehicle geometries.

The rotational velocities that were used in the high/low speed laboratory test cases discussed in this thesis were set to 0.5 and 1 °/s. These parameters were chosen to match the range of rotational velocities that are used during vehicle acceptance X-Factor testing procedures, see the GM/RT2141 Railway Group Standards. However, to maintain similarity between the full size/scale model velocity responses, the actual rotational velocities in the scale model laboratory tests should have been set to 0.0715 and 0.143 °/s respectively. The recommendation with regards to this scaling error therefore, is to repeat several of the tests cases discussed in this thesis using the correct range of rotational velocities in order to accurately quantify the influence on the inertial effects and the wear rates of the centre plate/wear liner components.

The reliability and accuracy of the testing and surface roughness measurement methodology discussed in Sections 5 – 5.2.2, could also be improved by making a number of design changes to the centre plate components. The proposed modified centre plate design is shown in Appendix T and as can be seen, has four numbered slots machined around the circumference. These slots are for a key which is then used to accurately align the static/dynamic centre plates in the Instron machine. These slots can also be used for guidance purposes as well as to improve the repeatability of the pre/post-test surface roughness measurement methodology on the centre plates/wear liner components.

Incorporating thermocouples into the new static/dynamic centre plate designs would also be beneficial in future tests. These sensors would enable the relationships between the running temperatures of the centre plate system and the changes in the centre plate/wear liner friction characteristics, such as the decreasing friction characteristics of material C for example, to be accurately quantified. This measurement data would also help to establish if the changes in material behaviours during the running-in/service tests are caused by the changes in temperatures or alternatively, by wear due to the number of running cycles increasing over time.

8.2.3. Validation and full scale testing

To validate the scale model test results the recommendation is to manufacture a set of calibration test-piece centre plate components using precision grinding techniques after the turning process. This will help to ensure that the contact surfaces of the static/dynamic centre plates are flat and smooth. The calibration test pieces can then be used to quantify the normal force-displacement characteristics of the centre plate/wear liner samples to a good level of accuracy, as well as to establish if the Bauschinger effect/non-symmetric friction characteristics of the centre plate/wear liner samples are strongly related, as well exacerbated by the machining imperfections on the centre plate friction surfaces.

Future work should also focus on carrying out X-Factor tests on a full size freight vehicle to validate the 1:7 scale centre plate system test results. This analyses should aim to quantify the dynamic behaviour of the secondary suspension system using the spectral analysis techniques discussed in this thesis. The recommendation during these tests is to focus on the changes in the system parameters that cause the signatures in the regions of 0 – 200 Hz to develop, as the frequency components in this range were shown to be closely related to the stick-slip friction characteristics of the centre plate system.

Once the results from the full scale X-Factor tests have been validated and matched to the responses of a representative multibody simulations model. On-track ride tests should then be carried out using the 0 – 200 Hz frequency range as well as a Butterworth filter to analyse the responses of the measured vertical/lateral accelerations of the bogie/wagon body, rather than the 6 – 20 Hz low pass filters, which is the current recommendation in the GM/RT2141 standards (Issue 3). These on-track tests would be more comprehensive and cost-effective by generating additional information in relation to the dynamic performance of the secondary suspension components, rather than focusing on the lowest vibration modes of the vehicle.

8.3. Key recommendations

The level of damping provided by a steel and friction liner damper could vary significantly over the component lifetime, with variations of up to 111% calculated for equivalent X-Factor performance. Generally, the lowest damping was observed for the newest components.

1) Recommendation: Vehicle testing and model validation should consider the potential variation in damping performance over the life span of the components, where currently the practice is to consider a single condition, normally new.

The different friction liner materials tested exhibited significantly different responses in terms of nominal friction coefficient, hysteresis and stick-slip characteristics, and variation in friction coefficient over time. The 'type' or nature of the friction liner material is therefore fundamental to friction damping and dynamic performance of freight vehicles.

2) Recommendation: Friction liner materials should be specified for a given application and approval case. Materials should not be interchanged without due consideration of the different characteristics and performance responses which might result from that change.

Variability in performance was observed for different specimens of the same friction liner material. This variability was associated with the surface roughness (particularly the waviness) of the liner and centre-plate components.

3) Recommendation: Control of surface finish quality could improve the consistency of friction dampers and freight vehicle responses. However, further work is required in this area.

A friction modelling methodology was established which provided good correlations between simulation and test results for hysteresis and stick-slip responses. The methodology requires detailed parameters which were obtained from the tests conducted here.

4) Recommendation: High quality test data for representative conditions is essential in order to be able to accurately simulate the hysteresis and stick-slip response for specific friction materials, and to capture the correct variation in friction coefficient over time.

References

Adtranz. (2000). *Technical Description of a freight bogie. Y25/25T (3TNhb/04).* Wroclaw: Adtranz.

Aizpun, M., Alonso, A., & Vinolas, J. (2015). A new parameter identification methodology for the bogie rotational resistance test of a rail vehicle. *Rail and Rapid Transit*, 1-12.

Al-bender, F. (2010). *Fundementals of friction modeling.* Leuven: Department of mechanical engineering, Division PMA.

Allen, P. D. (2006). Scale Testing. In S. Iwnicki, *Handbook of railway vehicle dynamics* (pp. 507-526). Boca Raton: Taylor & Francis.

Allen, P. D., Perez, J., & Hatt, D. J. (2007). Making maximum use of the restrictive loading gauge as applied to friction damped freight vehicles. *Journal of Rail and Rapid Transit*, 255-265.

Altpeter, F. (1999). *Friction modeling, identification and compensation.* Lausanne: Ecole Polytechnique Federale De Lausanne.

Ammar, A., Mohammed, Y., & Rahim, I. (2013). Investigate stick-slip intervals with one equation of motion and analyse the effect of the friction noise. *International Journal of Science and Technology Research*, 96-111.

Amsted Rail Company. (2014, November 15). *Friction shoes.* Retrieved from www.amstedrail.com: http://www.amstedrail.com/products-services/friction-shoes

Andersson, E., Stichel, S., & Jonsson, P.-A. (2006). Influence of link suspension characteristics variation on two-axle freight wagon dynamics. *Vehicle System Dynamics*, 415-423.

Armstrong-Helouvry, B. (1990). *Stick-slip arising from Stribeck friction.* Milwaukee: Department of Electrical Engineering, University of Wisconsin.

Ashby, M. F., & Jones, D. R. (1980). *Engineering materials 1. An introduction to their properties and applications.* Oxford: Pergamon Press Ltd.

Ashtiani, I. H. (2017). Optimisation of secondary suspension of three-piece bogie with bevelled friction wedge geometry. *International Journal of Rail Transportation* , 213-228.

Bakhareva, V. E., Nikolaev, G. I., & Anisimov, A. V. (2011). Nonmetal antifriction materials for sliding friction units. *Functional materials* , 524-533.

Ballew, B., Chan, B. J., & Sandu, C. (2011). Multibody dynamics modelling of freight traing bogie system. *Vehicle System Dynamics*, 501-526.

Baraniuk, C. (2018, 8 29). *Future Now*. Retrieved from BBC-Future-The giant coal plant converting to green energy: http://www.bbc.com

Bataus, M., Maciac, A., Oprean, M., & Vasiliu, N. (2010). Utomotive Clutch models for real time simulation. *Proceedings of the Romanian Academy, Series A*, 1-8.

Benzin, Y., Jonsson, P.-A., Stichel, S., Orlova, A., & Iwnicki, S. (2015). *The Sustrail high speed freight vehicle: Simulation of novel running gear design .* Huddersfield: University of Huddersfield.

Berg, M., & Evans, G. (2009). Challenges in simulation of rail vehicle dynamics. *International Journal of Vehicle Mechanics and Mobility*, 1023-1048.

Berger, E. J. (2002). Friction modeling for dynamic system simulation. *American Society of Mechanical Engineers*, 535-578.

Bertram, A., & Gluge, R. (2013). *Solid Mechanics, Theory, modeling and problems.* Germany: Springer.

Bikerman, J. J. (1974). Sliding friction of polymers. *Journal of macromolecular science part C, Polymer reviews*, 1-44.

Bogojevic, N., & Lucanin, V. (2014). The proposal of validation metrics for the assesment of the quality of simulations of the dynamic behaviour of railway vehicles. *Journal of rail and rapid transit*, 1-13.

Boronenko, Y., & Orlova, A. (2006). The anatomy of railway vehicle running gear. In S. Iwnicki, *Handbook of railway vehicle dynamics* (pp. 39-83). Boca Raton: Taylor & Francis.

Bosso, N., Gugliotta, A., & Soma, A. (2000). Simulation of a freight bogie with friction dampers. *5th ADAMS/Rail Users`Conference, Haarlem*, 1-9.

Bowden, P., & Tabor, D. (1973). *Friction an introduction to tribology.* London: Heinemann Educational Books.

Braghin, F., Ekberg, A., Palsson, B., Sala, D., Nicklisch, D., Kabo, E., . . . Pineau, M. (2013). *Development of the Future Rail Freight System to Reduce the Occurrences and Impact of Derailment. Analysis and mitigation of derailment, assessment and commercial impact . D3.2.* London: D-RAIL Consortium.

British Standards Institute. (2002). *British Standard. Geometrical product specification (GPS)-Surface texture: Profile method - Terms, definitions and surface texture parameters (ISO 4287:1997).* London: BSI Publications.

Bruni, S., & Collina, A. (2000). Modelling the viscoelastic behaviour of elastomeric components: An application to the simulation of train-track interaction. *Vehicle System Dynamics*, 283-301.

Bruni, S., Vinolas, J., Berg, M., Polach, O., & Stichel, S. (2011). Modelling of suspension components in a rail vehicle dynamics context. *International Journal of Vehicle Mechanics and Mobility*, 1021-1072.

Canudas de wit, C., Olsson, H., Astrom, K. J., & Lischinsky, P. (1995). A new model for control of systems with friction. *IEEE Transactions on automatic control. Vol 40, No 3.*, 419-425.

Chamaret, A.-P., Dahraoui, K., Frugier, D., Henry, P., & Le Moal, E. (2016). Energy savings on traction for rolling stock, state of the art and railway rolling stock point of view for the future. *World Congress on railway research* (pp. 1-6). Milan: SNCF Rolling Stock Engineering Centre.

Chi, H., Jiang, L., Chen, G., k, Kang, P., Lin, X., & Wu, G. (2015). Dry sliding friction and wear behaviour of (TiB2 + h-BN)/2024AL composites. *Materials and Design*, 960-968.

Collina, A., & Bruni, S. (2010). Modelling the viscoelastic behaviour of elastomeric components: An application of the simualtion train-track interaction. *Vehicle System Dynamics*, 283-301.

Course Hero, Inc. (2019, January 7). *SURFACE ROUGHNESS-MARYLAND METRICS. The one stop source.* Retrieved from www.coursehero.com: https://www.coursehero.com/file/19695404/SURFACE-ROUGHNESS

Cummings, S., & Wu, H. (2016). Effects of wheel/rail profile design and maintenance on freight wagon performance. *11th World Congress on Railway Research* (pp. 1-7). Milan: Transportation Technology Centre, Inc.

Cusamano, J. P., & Gardner, J. F. (2006). *Dynamic models of friction wedge dampers.* Pennsylvania: Penn State University.

Dahl, P. R. (1968). *A solid friction model.* Los Angeles: The Aerospace Corporation.

Delta Rail. (2015). *Vampire protraining.* Derby: Delta Rail.

Dowson, D. (1997). Progress in tribology. A historical perspective. In I. Hutchings, *New directions in tribology* (pp. 3-21). London: Mechanical Engineering Publications Ltd.

Drinkwater, B., Dwyer-Joyce, R. S., & Cawley, P. (1996). A study of the interaction between ultrasound and partially contacting solid-solid interface. *Royal Society*, 2613-2628.

Eisenbahn Lauwerke Halle (ELH). (2009). *Maintenance Plan Bogie ELH2-25-UK Optitrack.* Berlin: Eisenbahn Lauwerke Halle (ELH).

Ekberg, A., Ulianov, C., Dewan, I., Mortimer, P., & Jackson, R. (2013). *D-RAIL D2.2 Future Rolling Stock Breakdown 2050.* Europe: D-RAIL.

Evans, J. R., & Rogers, P. J. (1998). Validation of dynamic simualtions of rail vehicles with friction damped Y25 bogies. *International Journal of Vehicle Mechanics and Mobility*, 219-233.

Frohling, R. D., Fergusson, S. N., & Klopper, H. (2009). Minimising wheel wear by optimising the primary suspension stiffness and centre plates friction of self-steering bogies. *Vehicle system dynamics. Vol 46*, 457 - 458.

Gough, W., Richards, J. P., & Williams, R. P. (1983). *Vibrations and waves.* Chichester: Ellis Horwood Limited.

Greenwood, D. T. (1988). *Principles of dynamics. Second edition.* New Jersey: Prentice-Hall, Inc.

Harder, R. F. (2000). Dynamic modelling and simulation of three-piece freight vehicle suspensions with non-linear frictional behaviour using ADAMS/Rail. *ASME*, 185-191.

Hawthorne, T. (1995). *Recent improvements to three-piece trucks.* Chicago: American Steel Foundaries.

Hecht, M. (2007). Wear and energy saving bogie design with rubber primary springs-Principles and experiances. *International Heavy Haul Conference* (pp. 624-628). Kiruna: IHHA.

Higgins, R. A. (1993). *Engineering Metallurgy. Applied physical metallurgy. 6th ed.* London: Edward Arnold.

Hoffman, M., & Petersen, D. E. (2003). *Dry friction and impact dynamics in railway vehicles.* Kongens Lyngby: Technical University of Denmark.

INSTRON. (2019, 1 20). *8874 Servohydraulic fatigue testing system - Instron.* Retrieved from 8874 Biaxle servohydraulic fatigue testing machine: http;//www.instron.us

Iwnicki, S. (1999). *The Manchester Benchmarks for Rail Vehicle Simulation.* Manchester: Swets & Zeitlinger.

Iwnicki, S., Stichel, S., Orlova, A., & Hecht, M. (2015). Dynamics of railway freight vehicles. *Vehicle system dynamics*, 1-39.

Izbinsky, G., Siros, G., & D`Aoust, D. (2007). Monitoring bogie performance on straight track. Part 2. Tracking error and shift. *IHHA Specialist Technical Session (STS)* (pp. 453-459). Kiruna: International Heavy Haul Association.

Jaschinski, A., Chollet, H., Iwnicki, S., Wickens, A. H., & Von Wurzen, J. (1999). The application of roller rigs to railway vehicle dynamics. *Vehicle System Dynamics*, 345-392.

Jerabek, M., Major, Z., & Lang, R. W. (2009). Uniaxial compression testing of polymeric materials. *Polymer Testing*, 302-309.

Johnson, D. M. (2006). Gauging Issues. In S. Iwnicki, *Handbook of railway vehicle dynamics* (pp. 181-207). Boca Raton: Taylor & Francis.

Johnson, K. L. (1985). *Contact mechanics.* Cambridge: Cambridge University Press.

Jonsson, P.-A. (2004). *Modelling and laboratory investigations on freight wagon link suspensions with respect to vehicle-track dynamic interaction.* Stockholm: KTH Royal Institute of Technology.

Jonsson, P.-A., & Stichel, S. (2009). Is there a future for freight wagon with link suspension? *9th International Heavy Haul Conference* (pp. 397-403). Shanghai: Royal Institute of Technology (KTH).

Kalay, S., French, P., & Tournay, H. (2011). The safety impact of wagon health monitoring in North America. *9th World Congress on Railway Research* (pp. 1-11). Lille: Transportation Technology Centre, Inc.

Karlsson, F., & Persson, A. (2003). *Modelling nonlinear dynamics of rubber bushings - Parameter identification and validation.* Sweden: Lund University.

Keyence Coporation. (2018, November 30). *Arimetical mean height (Ra, Pa, Wa) Surface roughness parameters.* Retrieved from Keyence Coporation: https://www.keyence.com/ss/products/microscope/roughness/index.jsp

Kohli, R. (2013). Design aspects to ensure rail freindly freight cars: The IR experiance. *10th International Heavy Haul Association Conference* (pp. 563-576). Pune: Research Design & Standards Organisation .

Kovalev, R., Lysikov, N., Mikheev, G., Pogorelov, D., Simonov, V., Yazykov, V., . . . Torskaya, E. (2009). Freight car models and their computer-aided dynamic analysis. *Multibody Systems dynamics*, 399-423.

Lee, W. K., & Jang, H. (2013). Moisture effet on velocity dependance of sliding friction in brake friction materials. *Wear*, 17-21.

Liu, Y. F., Zhang, Z. M., Hu, X. H., & Zhang, W. J. (2015). Experimental comparison of five friction models on the same test-bed of the micro stick-slip motion system. *Mechanical Sciences, Open Access*, 15-28.

Ma, W., Zhu, Z. C., Xu, L., & Chen, G. A. (2014). Sliding friction and wear properties of friction linings with friction-promoting grease applied. *Engineering Tribology*, 595-607.

MacMahon, P. (2014). *Control Period 4 Freight Review.* London: NetworkRail.

Meriam, J. L., & Kraige, L. G. (1998). *Engineering Mechanics. Statics 4th edition.* Canada: John Wiley & Sons, Inc.

Meriam, J. L., & Kraige, L. G. (2012). *Engineering Mechanics volume 2. Dynamics 7th Edition.* Hoboken, USA: John Wiley & Sons, Inc.

Meymand, S. Z., Keylin, A., & Ahmadian, M. (2016). A survey of wheel-rail contact models for rail vehicles. *Vehicle System Dynamics. International Journal of vehicle mechanics and mobility*, 386-428.

Miner Enterprises Inc. (2019, 2 25). *TCC-2600, 4500, 8000*. Retrieved from Constant Contact Side Bearings-Miner Enterprises Inc: https://www.minerent.com

Mitutoyo. (2016). *Quick guide to surface roughness measurement. Reference guide for laboratory and workshop. Bulletin 2229.* Boston: Mitutoyo.

Molatefi, H., Hecht, M., & Kadivar, M. H. (2006). Critical speed and limit cycles in the empty Y25-freight wagon. *Rail and Rapid Transit*, 347-359.

Montroll, E. W. (1956). Theory of the vibration of simple cubic lattices with nearest neighbour interactions. *Proceedings of the third Berkely symposium on mathematical statistics and probability* (pp. 209-246). Berkely and Los Angeles: University of California Press.

Moore, D. F. (1975). *Principles and applications of tribology.* Oxford: Pergamon Press Ltd.

Motion System Design. (2001). *Gears and drives.* Cleveland: Motion System Design.

Myshkin, N., Kovalev, A., Spaltman, D., & Woydt, M. (2012). Contact mechanics and tribology of polmer composites. *Journal of Applied Polymer Science*, 1-9.

Naumann, R., Mallwitz, C., Luck, S., & Behringer, S. (2017). *Initial experiance for the verification of vehicle models according to EN14363: 2016 Annex T.* Minden: DB BAHN.

Network Rail. (2018). *Network Rail Infrastructure. Network Statement 2018.* London: Network Rail.

NetworkRail. (2019). *Control Period 6 (CP6) Variable Usage Charge (VUC) guidance document - the calculation and approval of new rates. Version 1.* London: NetworkRail.

Nia, S. H., Stichel, S., & Jonsson, P.-A. (2014). *An investigation of the iron-ore wheel damages using vehicle dynamics simulation.* Stockholm: KTH Royal Institute of Technology. Department of Aeronautical and Vehicle Enginnering.

Nielsen, J. C., & Stensson, A. (1999). Enhancing freight railways for 30 tonne axle loads. *Journal of Rail and Rapid Transit*, 255-263.

O`Neil, H. (2007). *Research programme engineering investigation of the accumulative effect of vehicle tolerances on gauging. Effect of parameter tolerances on vehicle envelope.* London: RSSB.

Olofsson, U., & Lewis, R. (2006). Tribology of the wheel-rail contact. In S. Iwnicki, *Handbook of railway vehicle dynamics* (pp. 121-141). Boca Raton: Taylor & Francis.

Olshevskiy, A., Kim, C.-W., & Yang, H.-I. (2015). Wear simualtion for the centre plate arrangement of a freight car. *Vehicle system dynamics: International Journal of Vehicle Mechanics and Mobility*, 856-876.

Olsson, H., Astrom, K. J., Canudas de Wit, C., Gafvert, M., & Lischinsky, P. (1997). *Friction models and friction compensation.* Lund: Lund University.

Opala, M. (2018). Evaluation of bogie centre bowl friction models in the context of safety against derailment simulation predictions. *Applied Mechanics, CrossMark*, 943-953.

Orlova, A., & Boronenko, Y. (2006). The anatomy of railway vehicle running gear. In S. Iwnicki, *The handbook of railway vehicl dynamics* (pp. 39-83). Boca Raton: Taylor and Francis group.

Palo, M., Schunnesson, H., & Larsson-Kraik, P.-O. (2011). *Maintainability in extreme seasonal weather conditions.* Lulea: Lulea University of Technology.

Pearce, M. E., & Simson, S. (2006). Wheel wear losses from bogie rotation resistance, effects of cant and speed. *Joint Rail Conference* (pp. 109-104). Atlanta: Centre for Railway Engineering, Australia.

Piotrowski, J. (2010). Smoothing dry friction damping by dither generated in rolling contact of wheel and rail and its influence on ride dynamics of freight wagons. *Vehicle System Dynamics*, 675-703.

Piotrowski, J. (2012). A substitute model of two-dimensional dry friction exposed to dither generated by rolling contact of wheel and rail. *International Journal of Vehicle Mechanics and Mobility*, 1495-1514.

Piotrowski, J., & Pazdzierniak, P. (2010). Influence of dither generated by rolling contact on friction damping in freight wagons. *Vehicle system dynamics: International Journal of Vehicle Mechanics and Mobility* , 195 - 209.

Polach, O., Berg, M., & Iwnicki, S. (2006). Simualtion. In S. Iwnicki, *Hanbook of railway vehicle dynamics* (pp. 359-421). Boca Raton: Taylor & Francis.

Polach, O., Bottcher, A., Vannuci, D., Sima, J., Schelle, H., Chollet, H., . . . Mazzola, L. (2017). Validation of simualtion models in context of railway vehicle acceptance. *Rail and Rapid Transit*, 1-36.

Popov, V. (2010). *Contact mechanics and friction. Physical principles and applications.* Berlin: Springer.

Popov, V. L., Dimaki, A., Psakhie, S., & Popov, M. (2015). On the role of scales in contact mechanics and friction between elastomers and randomly rough self-afine surfaces. *Scientific Reports*, 1-7.

Prosser, I. (2014). *Recent freight derailments: The interaction of track, vehicles and freight container loads, and potential areas for improvements.* London: Office of Rail Regulation.

Qin, P., Dentel, G., & Mesh, M. (2002). Multi-leaf spring and hotchkiss suspension. *ABAQUS Users Conference*, 1-14.

RAIB. (2007). *Derailment near Waterside, East Ayeshire 21 January 2006.* Derby: Rail Accident Investigation Branch.

RAIB. (2007). *The derailment of a freight train at Washwood Heath, 8 September 2006.* Derby: Rail Accident Investigation Branch.

RAIB. (2013). *Derailment of a freight train at Shrewsbury station, 7 July 2012.* Derby: Rail Accident Investigation Branch.

RAIB. (2014). *Derailment at Primrose Hill/Camden Road West Junction, 15 October 2013.* Derby: Rail Accident Investigation Branch.

RAIB. (2014). *Freight train derailment near Gloucester, 15 October 2013.* Derby: Rail Accident Investigation Branch.

RAIB. (2016). *Derailment at Washwood Heath West Junction, Birmingham, 23 March 2015.* Derby: Rail Accident Investigation Branch.

Ren, L. H., Shen, G., & Hu, Y. S. (2007). A test-rig for measuring three-piece bogie dynamic parameters applied to a freight car application. *Vehicle Systems Dynamics: International Journal of Vehicle Mechanics and Mobility*, 853-861.

Ricciardi, V., Augsburg, K., Gramstat, S., Schreiber, V., & Ivanov, V. (2017). Survey on modelling and techniques for friction estimation in automotive brakes. *Applied Sciences*, 1-23.

RSSB. (2007). *GM/RC2641: Reccomendations for vehicle static testing.* London: Rail Safety & Standards Board.

RSSB. (2009). *GM/RT2141: Resistance of Railway Vehicles to Derailment and Roll-over.* London: Rail Safety and Standards Board.

RSSB. (2013). *Gauging. The V/S SIC Guide to british gauging practice.* London: RSSB.

RSSB. (2013). *Wheel Tread Damage (T963).* London: Rail Safety and Standards Board (RSSB).

Rubert & Co Ltd. (2018, November 30). *The Home of surface measurement.* Retrieved from Roughness parameters: http://www.rubert.co.uk/faqs/roughness-parameters/

Ruderman, M., & Bertram, T. (2011). Modified Maxwell-slip model of presliding friction. *Proceedings of the 18th world congress. The international Federation of automatic control* (pp. 10764-10769). Milano: IFAC.

Saaskilahti, K., Oksanen, J., Tulkki, J., & Volz, S. (2014). Role of anharmonic phonon scattering in the spectrally decomposed thermal conductance at planar interfaces. *Physical Review B90*, 1-8.

Schultz, C. D. (1987). *Introduction to Gear design 2nd edition.* Winfield: Beyta Gear Service.

Sextro, W. (2002). *Dynamical contact problems with friction. Models, methods, experiments and applications. Vol 3.* Berlin: Springer.

Shackleton, P. (2009). *An optimised wheel-rail contact model for vehicle dynamics simulation.* Manchester: Rail Technology Unit.

Shackleton, P. (2015). *Spectrum. Innovation and opportunities for rail freight in the 2st centuary. Suspension simulation of a rail freight vehicle for LDHV goods.* Huddersfield: Institute of Railway Research.

Shahidi, P., Maraini, D., Hopkins, B., & Seidel, A. (2014). Estimation of bogie performance criteria through on-board condition monitoring. *Annual conference of the prognistics and health management Society* (pp. 1-10). Fort Worth: Amstead Rail Company .

Shi, H.-L., Wu, P.-B., Luo, R., & Guo, J.-Y. (2013). Calculation and laboratory testing of the rotation resistance of a bogie . *Rail and Rapid Transit*, 210-219.

Simson, S. (2007). *Project 82: Bogie rotation friction management bogie design factors.* Rockhampton: Centre for Railway Engineering.

Simson, S. A., & Pearce, M. E. (2006). Wheel wear losses from bogie rotation resistance, effects of cant and speed. *Proceedings of the JRC2006 Joint Rail Conference* (pp. 109-114). Atlanta: Faculty of Engineering Central Queensland University.

Simson, S. A., & Pearce, M. E. (2006). Wheel wear losses from bogie rotation resistance, effects of cant and speed. *Porceedings of the Joint Rail Conference* (pp. 109-114). Atlanta: Queensland University.

Simson, S., & Brymer, B. (2008). Laboratory testing of bogie rotation friction with applied track twisting forces . *Conference on Railway Engineering* (pp. 395-402). Perth: Centre for Railway Engineering, Central Queensland University.

SIMULIA. (2012). *SIMPACK Multi-body Simulation.* GmbH: SIMULIA.

Spiryagin, M., George, A., Ahmad, S., Rathakrishnan, K., Sun, Y., & Cole, C. (2012). Wagon model acceptance procedure using Australian standards. *Conference on Railway Engineering* (pp. 343-350). Brisbane: RTSA.

Stichel, S., Jonsson, P.-A., & Andersson, E. (2006). Experimental and theorectical analysis of freight wagon link suspension. *Journal of Rail and Rapid Transit*, 361-372.

Stichel, S., Jonsson, P.-A., & Nia, S. H. (2014). *An investigation of the iron-ore wheel damages using vehicle dynamics simulation.* Stockholme: KTH Railway Group.

Stichel, S., Orlova, A., Hecht, M., & Iwnicki, S. (2015). Dynamics of railway freight vehicles. *Vehicle System Dynamics* , 1-39.

Stow , J., & Andersson, E. (2006). Field testing and instrumentation of railway vehicles. In S. Iwnicki, *Handbook of railway vehicle dynamics* (pp. 423-456). Boca Raton: Taylor & Francis.

Stroud, K. A. (1995). *Engineering Mathematics. Fourth edition.* London: Macmillan Press Ltd.

Sun, Y. Q., & Cole, C. (2007). Veritical dynamic behaviour of three-piece bogie suspensions with two types of friction wedge. *Multibody Systems Dynamics*, 365-382.

Sun, Y., Spiryagin, M., Cole, C., & Wu, Q. (2014). A review of dynamics modelling of friction wedge suspensions. *Vehicle system dynamics: International journal of vehicle mechanics and mobility*, 1-27.

Tanaka, T., Iida, K., Iida, T., Suzuki, M., & Watanabe, N. (2016). Evaluation of rotational resistance of bogies. *Journal of Rail and Rapid Transit*, 535-545.

Taylor Hobson . (2011). *Exploring Surface Texture. A fundamental guide to the measurement of surface finish. 7th edition. .* Leicester: Taylor Hobson.

TENMAT Ltd. (2019, 1 8). *TENMAT: Advanced materials for rail. marine, agriculture, fire protection.* Retrieved from TENMAT Advance Materials: https://www.tenmat.com

The MathWorks, Inc. (2015). *Help file documentaion. Translational/Rotational friction.* Massachusetts: The MathWorks, Inc.

Tickell, C. E., Downing, P., & Jacobsen, C. J. (2004). Rail wheel squeal - Some causes and a case study of freight-car wheel squeal reduction. *Proccedings of Acoustics*, 239 - 244.

Tottle, C. R. (1966). *The science of engineering materials.* London: Heinemann Educational Books Ltd.

Tournay, H. (2011). Integrated freight car truck design concept. *The 9th World Congress on Railway Research* (pp. 1-11). Lille: Transportation Technology Centre, Inc .

Tournay, H., & Wu, H. (2011). Investigation into the root causes of rolling contact fatigue under heavy axle loads. *The 9th World Congress on Railway Research* (pp. 1-8). Lille: Transportation Technology Centre Inc.

True, H., & Xia, F. (2004). The dynamics of the three-piece-freight truck. In M. Abe, *The dynamics of vehicles on roads and on tracks* (pp. 212-221). London : Taylor and Francis.

VESCONITE plastics. (2019, 1 8). *VESCONITE BEARINGS.* Retrieved from Vesconite Hilube-Vesconite: https://www.vesconite.com

Wang, C. (2009). Manufacturing technology of railway freight cars in China. *9th International Heavy Haul Conference* (pp. 365-370). Shanghai: MOR Railway Administration, Equipment Deprtment, Beijing.

Wickens, A. H. (2006). A History of railway vehicle dynamics. In S. Iwnicki, *Handbook of railway vehicle dynamics* (pp. 5-38). Boca Raton: Taylor & Francis Group.

Wolf, G. (2013). *Basic rail vehicle suspension system parameters.* America: WOLF Railwaay Consulting.

Wriggers, P. (2006). *Computational Contact Mechanics. Second edition.* Hannover: Springer.

Wu, H., & Robeda, J. (2004). Effects of centre plate lubrication on vehicle curving and lateral stability. In M. Abe, *The Dynamics of Vehicles on Roads and on Tracks* (pp. 292-301). Kanagawa: Taylor & Francis.

Xia, F. (2003). Modelling of two-dimensional Coulomb friction Oscillator. *Journal of Sound and Vibration*, 1063-1074.

Zaworka, B. (2012). *Introduction to optical measurment technology. Advanced Alicona.* Raaba/Graz: Alicona Imaging Gmbh.

Zaworka, C. (2012). *Optical roughness measurment basics. Alicona.* Raaba/Graz: Alicona Imaging GmbH.

Zhang, W., Dai, H., Shen, Z., & Zeng, J. (2006). Roller Rigs. In S. Iwnicki, *Handbook of Railway Vehicle Dynamics* (pp. 457-505). Boca Raton: Taylor & Francis.

Zimmermann, K., Zeidis, I., Pivovarov, M., & Abaza, K. (2006). Forced nonlinear oscillator with nonsymmetric dry friction. *Applied Mechanics*, 353-362.

Appendices

Appendix A. Iron-ore hopper dimensions and loading parameters

The design dimensions and loading parameters for an iron-ore hopper are shown in Figure A1. The four Amsted Motion Control M976 three-piece bogies, have load dependent damping in the central suspensions. The master unit in this train configuration controls the braking for both vehicles, hence the name.
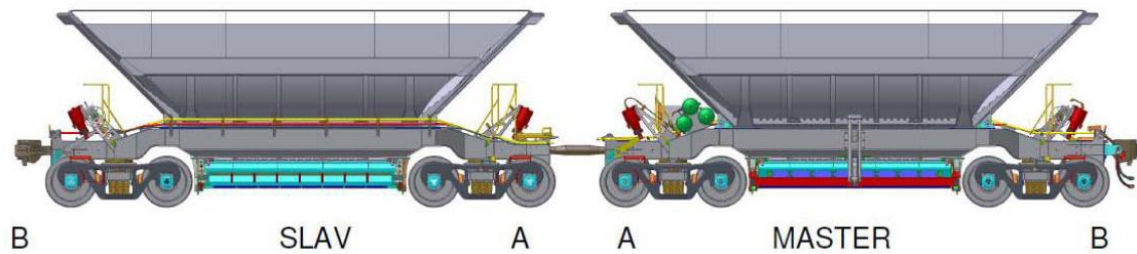
Length of wagons	10.29 (m)
Distance between centre plates	6.77 (m)
Total truck height	3.64 (m)
Basket width	3.49 (m)
Weight of empty wagon	21.6 (t)
Payload	102 (t)
Weight of loaded wagon	120 (t)
Maximum speed (empty)	70 (km/h)
Maximum speed (loaded)	60 (km/h)
Wheelbase	1778 (mm)
Track gauge	1435 (mm)
Wheel Diameter (max)	915(mm)
Wheel Diameter (min)	857 (mm)
Weight wheelset	1341 kg
Weight bogie incl. wheelsets and mechanical-braking equipment	4 650 kg

Figure A1: Iron-ore hopper dimensions and loading parameters (Stichel, Jonsson, & Nia, 2014).

Appendix B. Freight vehicle suspension system components

The secondary suspension components for the Y25 and three-piece bogies are discussed in this appendix. Picture A in Figure B1, shows the centre pivot/king pin of an HXA coal hopper and picture B, shows a reconditioned Y25 centre bowl/wear liner. Picture C also shows an example of a reconditioned UIC sprung side bearer component.

The suspension components in the worn/degraded states are shown in Figure B2, where picture A shows an example of a damaged centre bowl wear liner. Picture B also shows some evidence of corrosion and pitting marks on the steel surface of bogie centre bowl, possibly caused by the torn liner failure mode which has then led to direct steel-on-steel contact between the bogie/wagon body suspension components. Picture C shows several damaged side bearer housings and picture D, shows the tare/laden spring cap and a seriously worn connecting pin, caused by direct steel-on-steel contact between this feature and the Lenoir link.

Pictures A and B in Figure B3 show a worn wagon body centre plate component as well as a worn Constant Contact Side Bearer (CCSB) component on a three-piece bogie. The scale model centre plate components are also shown in the worn state for comparison purposes, see Figure B4. The wear and damage mechanisms on these components as can be seen, appear to be in line with those observed on the full size components, which they should be due to the fact that the contact stresses acting on the 1:7 scale/full scale components under the laden loading conditions for example, are equivalent.
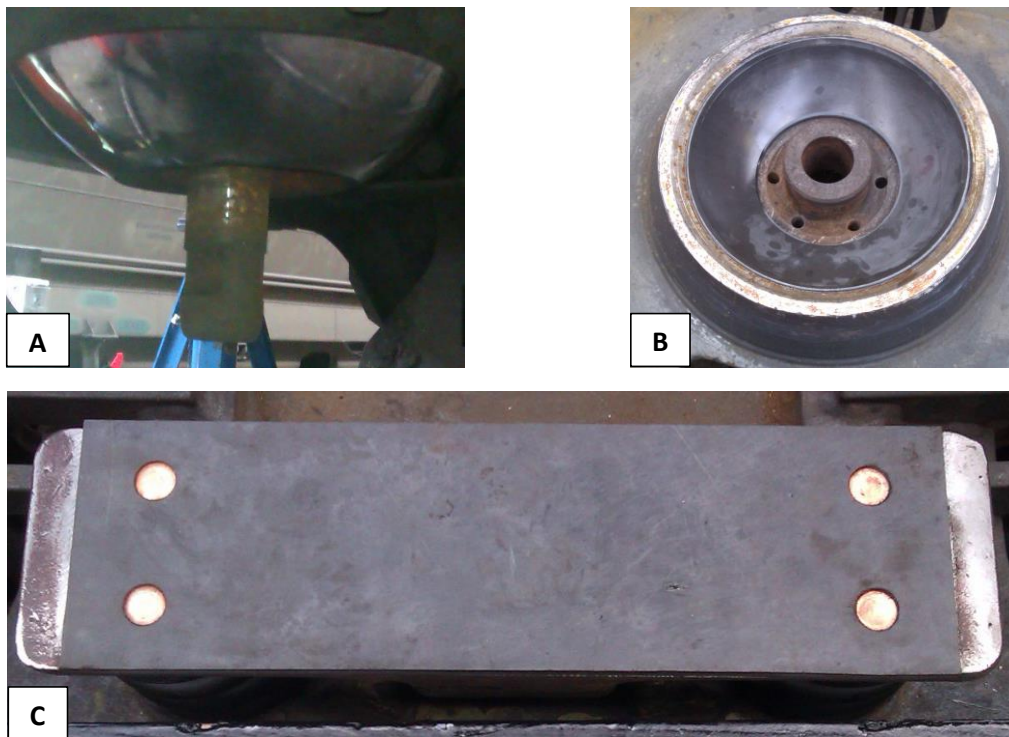
Figure B1: Secondary suspension system components (New state): (A) Wagon-body centre-pivot. (B) Y-series centre bowl/new wear liner. (C) Y-series sprung side bearer/new wear liner.
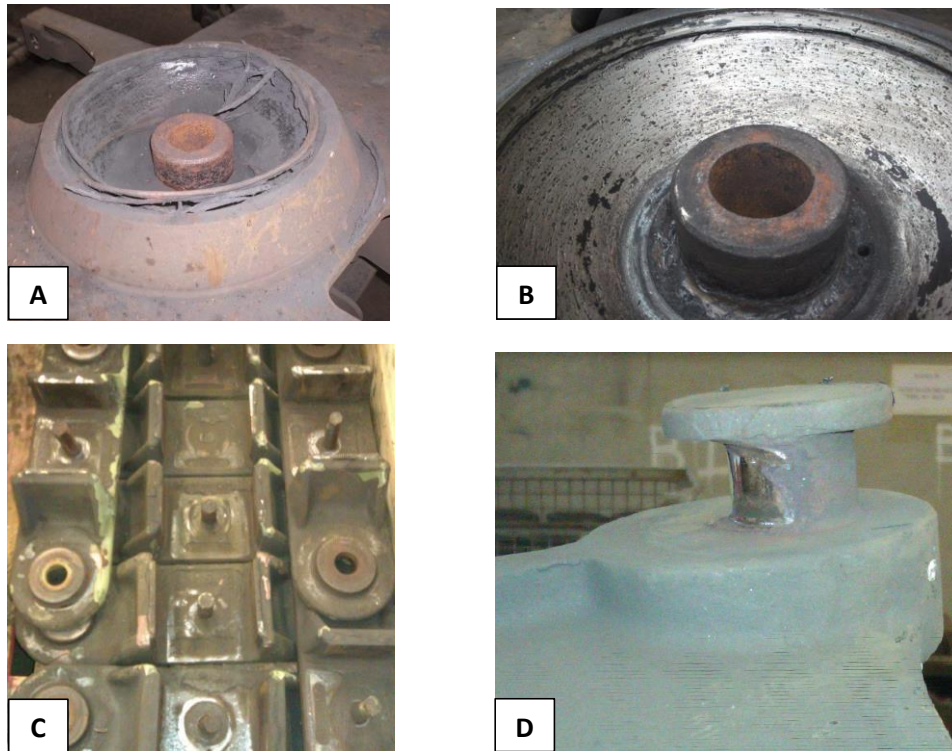
Figure B2: Secondary suspension system components (Worn state): (A) Centre bowl/damaged wear liner. (B) Pitting marks and material transfer on the centre bowl. (C) Damaged side bearer housings. (D) Worn spring cap connecting pin.
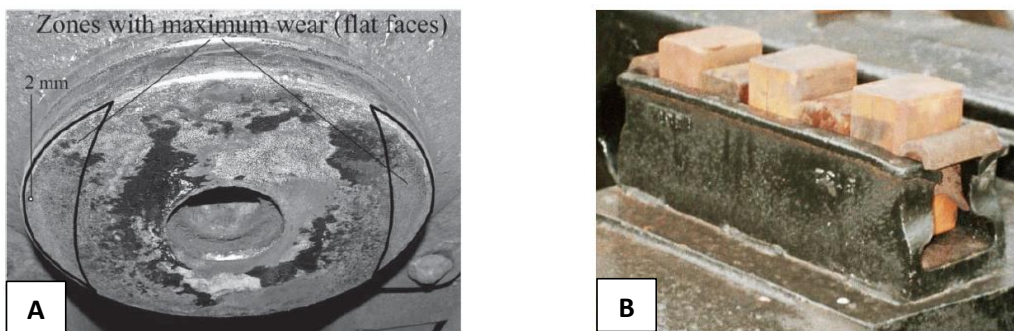
Figure B3: (A) Three-piece bogie worn centre plate (Russian 18-100) *(Olshevskiy A. , Kim, Yang, & Olshevskiy, 2015)*. (B) CCSB fitted with Stucki blocks *(Tickell, Downing, & Jacobsen, 2004)*.

Figure B4: Scale model centre plate components after preliminary testing.

Appendix C. Full size centre plate/wear liner dimensions

The design dimensions of the full size wear liner components are shown in Figure C1, whereas Figure C2 shows the dimensions of a full size centre plate component. The diameters of the Amsted Rail Hollube wear liners as can be seen, range from 354 – 405 mm, so the diameter of the scale model centre plates, were designed in accordance with the specifications for the maximum wear liner diameter of 405 mm, which scales down to approximately 58 mm following the 1:7 scaling laws.

The centre plate dimensions given in Figure C2 are for a Russian 18-100 three-piece centre plate component and are slightly smaller in comparison to wear liner dimensions shown in Figure C1, so would not be able to accommodate this particular product. The fundamental designs of the three-piece bogie centre plate mechanisms however, are basically the same regardless of the vehicle type.

Figure C1: Centre plate wear liner dimensions (Amsted Rail Company, 2014).

Figure C2: Russian 18-100 three-piece bogie centre plate dimensions (Olshevskiya, Yang, & Kima, 2015).

Appendix D. Universal testing machine specifications

The specifications for the universal testing machine that was used throughout this research work are shown in Figure D1. From these, it can be seen that the dynamic loading and torque capacities of this machine are limited to $\pm$ 10 kN and 100 Nm. The design dimensions of the machine bed and working envelope also are shown in Figure D2.

Specifications

		Standard Height Frame		Extra Height Frame	
Daylight Opening (Maximum Between Load Cell and Actuator at Midstroke)	mm	683		983	
	in	26.9		40.0	
Dynamic Load Capacity	kN	±10	±25	±10	±25
	lbf	±2250	±5620	±2250	±5620
Torque Capacity	Nm	100			
	inlb	880			
Actuator Stroke (Total)	mm	100			
	in	3.9			
Actuator Rotation	°	±130			
Configuration	-	Twin-Column High-Stiffness Load Frame with Actuator in Upper Crosshead and T-Slot Base			
Lifts and Locks	-	Hydraulically-Powered Lifts and Manual Locks			
Load Cell	-	Patented, Biaxial Dynacell™: Fatigue-Rated Load Cell with Capacity to Suit Actuators			
Load Weighing Accuracy	-	±0.5% of Indicated Load or ±0.005% of Load Cell Capacity (1-100%), Whichever is Greater			
Hydraulic Pressure Supply (Required)	bar	207			
	psi	3000			
Electrical Supply	-	Single-Phase Mains 90-132 or 180-264 VAC 45/65 Hz Power Consumption: 800 VA Max			
Operating Environment	°C	+10 to +38°C (+50 to +100°F) with 10 to 90% Humidity Non-Condensing			
Frame Stiffness	kN/mm	260			
Frame Weight	kg	287			
	lb	634			

Mechanical Interfaces

Load Cell	6 x M8 on 75 PCD
Actuator	6 x M8 on 75 mm PCD
6 x 9 mm Diameter Through Holes on 75 mm PCD
Table and Crosshead	4 × M10 Holes on a 280 mm × 90 mm for Accessory Mounting
6 x M10 x 20 Deep on 100 mm PCD (Table) with 40 mm Location Diameter
4 x M10 T-Slots Running Front to Back, Spaced 80 and 100 mm from Centerline
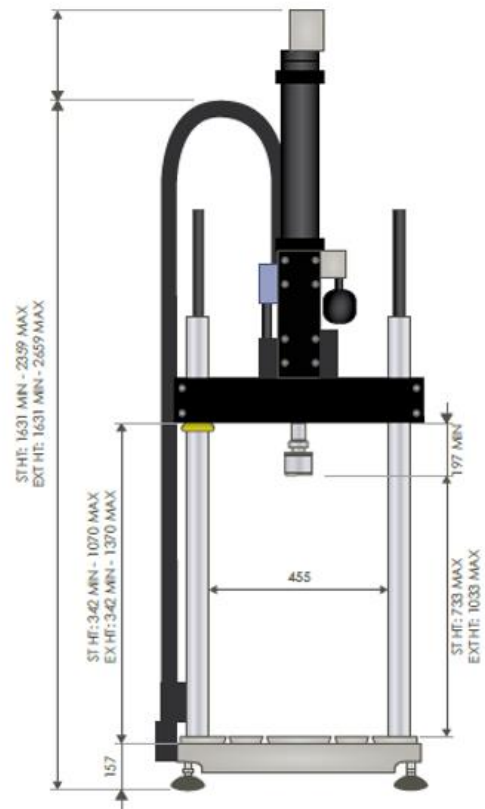
Figure D1: Instron machine specifications.

Table and Crosshead	4 × M10 Holes on a 280 mm × 90 mm for Accessory Mounting
6 x M10 x 20 Deep on 100 mm PCD (Table) with 40 mm Location Diameter
4 x M10 T-Slots Running Front to Back, Spaced 80 and 100 mm from Centerline

Accessories

Catalog Number

8260C	±25 kN / ±100 Nm Fatigue Rated Hydraulic Wedge Grips
8000-101	Attachment Kit to Provide M20 Right Hand Female Thread on 8874 Load Cell or Actuator
8000-050	Flange for 8874 Base to Provide M20 Right Hand Female Thread

1) US Patent Number 6508132
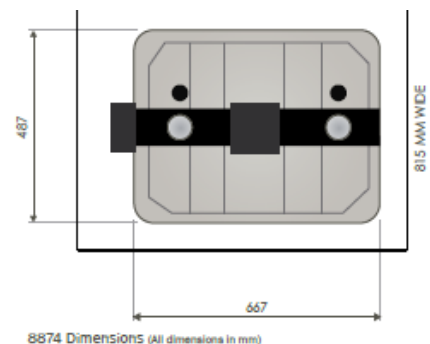
8874 Dimensions (All dimensions in mm)

Figure D2: Machine table dimensions.

Appendix E. Scaling laws for the 1:7 scale centre plate

The scaling laws that were used to design the 1:7 scale centre plate/wear liner components and the operating conditions for the laboratory tests are shown in Figure E1.

Scaling	Geometry
Length	7
Cross-section	49
Volume	343

	Material
Density	1
Mass	343
Inertia	16807
Elasticity	G,E

	Parameters
Time	1
Frequency	1
Stress	1
Strain	1
Displacement	7
Velocity	7
Acceleration	7
Stiffness	7
Viscous damping	7

	Forces
Gravitational force	1:7
Translational force	49
Torque	343

Figure E1: Scaling laws used to design the 1:7 scale centre plate/wear liner components.

Appendix F. Mechanical properties of materials A and B.

The bulk mechanical properties of materials A and B are shown in Figures F1 and F2 respectively. From these specifications, it can be seen that the Coefficient of Friction (COF) values for material A, range between 0.36 – 0.4, whereas for material B, the COF values range between 0.09 – 0.1. The manufacturers` specifications however, disagree with the range of COF values that were calculated from the laboratory tests test results.

During the running-in and service tests that were carried out on material A for example (See Appendices O and P for these results), the COF values were seen to range between 0.05 – 0.28 and between 0.09 – 0.36 respectively. The upper limit of the service test COF values as can be seen, is more in line with the manufacturers` specifications (Figure F1). The running-in and service test COF values that were calculated for material B however, were significantly higher than the specifications given in Figure F2, ranging between 0.09 – 0.32 and between 0.1 – 0.54 respectively.

The COF values that were calculated for material C were the most consistent overall, ranging between 0.06 – 0.27 during the running-in tests and between 0.1 – 0.27 during the service tests. However, it should be pointed out that only 3 test cases were carried out using material C, which reduces the statistical significance of the COF results in comparison to materials A and B.

The discrepancies between the manufacturers` COF values and the ones calculated from the scale model laboratory test results however, could be down to a number of factors. These include the testing methods used to obtain the COF values, as well as differences in the mechanical and geometrical properties of the components forming the contact interfaces. The range of normal loads, running speeds, number of running cycles and environmental conditions during the test runs, could also be contributing to the differences between the manufacturers` specifications and the ones presented in this thesis.

Therefore, further research is required to establish if this is the case as well as to better understand the dependency/relationships between the friction characteristics of the wear liner materials and the testing methodology. Rotary systems with friction damping components for example, may respond differently to translational systems, which would suggest that each friction test, should be specific to the application/system that is being analysed and quantified.

PROPERTY	UNITS	NF21/NF22
Compressive Strength	MPa	192
Compressive Yield @ 68.9 MPa	%	2.4
Normal Working Pressure	MPa	55
Shear Strength	MPa	41
Impact Strength	kJ/m^2	32
Coefficient of Friction	Dry	0.36 - 0.4
Hardness	Brinell	23
Density	g / cm^3	1.64
Coefficient of Thermal Expansion	$x10^{-6}/°C$ Normal $x10^{-6}/°C$ Parallel	43 43
Maximum Continuous Operating Temperature	°C	120
Maximum Intermittent Operating Temperature	°C	140

The information contained in this data sheet is presented in good faith. They are typical test results tested generally in accordance with BS 2782 and ASTM test methods and should not be used for specifications. **TENMAT** does not warrant the conformity of its materials to the listed properties or their suitability for any particular purpose. For further information please contact our Technical Sales Department on +44 161 872 2181.

Figure F1: Mechanical properties of material A *(TENMAT Ltd, 2019)*.

VESCONITE HILUBE TYPICAL PROPERTIES

	METRIC	IMPERIAL
Density	1.38 g.ml^{-1}	1.38
Melting point	260°C	500°F
Hardness (Shore D)	82	82
Tensile strength at yield (D-638)	66 MPa	9,500 psi
Tensile strength at break	65 MPa	9,400 psi
Tangent modulus of elasticity (D-790)	3400 MPa	493,000 psi
Flexural yield strength	113 MPa	16,400 psi
Deflection temperature at 1.85MPa / 268 psi	117°C	242°F
Modulus of elasticity under compression	2206 MPa	320,000 psi
Compression strength at yield	99 MPa	14,300 psi
Shear strength	49.4 MPa	7,163 psi
Notched impact strength charpy (D-256)	26 J.m^{-1}	0.5 ft-lb/in
Notched impact strength IZOD	30 J.m^{-1}	0.5 ft-lb/in
Heat conductivity	0.3 WK^{-1}.m^{-1}	2 Btu-in/ft^{2}/hr/^{0}F
Coefficient of linear thermal expansion	6x10^{-1}mm.mm$^{-1.o}$C^{-1}	3.3x10^{-5} in/in/ ^{0}F
Maximum moisture absorption in water at 20°C / 68°F	0.5%	0.5%
Equilibrium moisture absorption in air (50% RH, 23°C / 73°F)	0.2%	0.2%
Dynamic unlubricated friction coefficient on steel	0.10	0.10
Static friction coefficient on polished steel (no lubrication)	0.09	0.09
Dielectric strength	14kV.mm^{-1}	360kV.in^{-1}
Gamma ray resistance 50% loss of properties	100 Mrads	

The above data should be taken for indicative purposes. Physical properties may be altered to some extent by processing conditions.

Figure F2: Mechanical properties of material B *(VESCONITE plastics, 2019)*.

Appendix G. MATLAB/SIMSCAPE friction model parameters

The friction model parameters for the MATLAB/SIMSCAPE translational and rotational friction models are explained and derived below.

Translational friction model parameters:

Breakaway friction force

Breakaway friction force, which is the sum of the Coulomb and the static frictions. It must be greater than or equal to the Coulomb friction force value. The default value is `25` N.

Coulomb friction force

Coulomb friction force, which is the friction that opposes motion with a constant force at any velocity. The default value is `20` N.

Viscous friction coefficient

Proportionality coefficient between the friction force and the relative velocity. The parameter value must be greater than or equal to zero. The default value is `100` N/(m/s).

Transition approximation coefficient

The parameter sets the value of coefficient c_v, which is used for the approximation of the transition between the static and the Coulomb frictions. Its value is assigned based on the following considerations: the static friction component reaches approximately 95% of its steady-state value at velocity $3/c_v$, and 98% at velocity $4/c_v$, which makes it possible to develop an approximate relationship $c_v \sim= 4/v_{min},$ where v_{min} is the relative velocity at which friction force has its minimum value. By default, c_v is set to `10` s/m, which corresponds to a minimum friction at velocity of about `0.4` m/s.

Linear region velocity threshold

The parameter sets the small vicinity near zero velocity, within which friction force is considered to be linearly proportional to the relative velocity. MathWorks recommends that you use values in the range between `1e-6` and `1e-4` m/s. The default value is `1e-4` m/s.

Rotational friction element model parameters:

Breakaway friction torque

Breakaway friction torque, which is the sum of the Coulomb and the static frictions. It must be greater than or equal to the Coulomb friction torque value. The default value is `25` N*m.

Coulomb friction torque

Coulomb friction torque, which is the friction that opposes rotation with a constant torque at any velocity. The default value is `20` N*m.

Viscous friction coefficient

Proportionality coefficient between the friction torque and the relative angular velocity. The parameter value must be greater than or equal to zero. The default value is `0.001` N*m/(rad/s).

Transition approximation coefficient

The parameter sets the value of coefficient cv, which is used for the approximation of the transition between the static and the Coulomb frictions. Its value is assigned based on the following considerations: the static friction component reaches approximately 95% of its steady-state value at velocity $3/cv$, and 98% at velocity $4/cv$, which makes it possible to develop an approximate relationship $cv \sim= 4/\omega min,$ where ωmin is the relative velocity at which friction torque has its minimum value. By default, cv is set to `10` rad/s, which corresponds to a minimum friction at velocity of about `0.4` s/rad.

Linear region velocity threshold

The parameter sets the small vicinity near zero velocity, within which friction torque is considered to be linearly proportional to the relative velocity. MathWorks recommends that you use values in the range between `1e-5` and `1e-3` rad/s. The default value is `1e-4` rad/s.

(The MathWorks, Inc, 2015) and (Olsson, Astrom, Canudas de Wit, Gafvert, & Lischinsky, 1997)

Appendix H. Surface roughness technical specifications

The filter methods and cut-off wave lengths, λ_s, λ_c and λ_f, for the surface roughness measurements discussed in this thesis, have been carried out in accordance with the ISO 4287:1997 and ISO 11562:1996 standards, see (British Standards Institute, 2002). These cut-off parameters are illustrated in Figure H1 and the coordinate system for the surface roughness measurements is shown in Figure H2. Measurements along the x-direction for example, describe the sample length of the profile which is given as l_r in the following equations. For the surface roughness measurements discussed in Section 5.2, the sample length and evaluation length, l_n, of the stylus, were then set to 0.8 and 4 mm respectively. The height of the surface profile as can be seen in Figure H2, is measured in the z-direction.

The nine surface roughness parameters that were analysed throughout this research work, include the mean-surface roughness (Ra) and waviness (Wa) parameters, see Equation (H1). The root-mean-square roughness (Rq) and maximum profile peak height (Rp) were also measured, see Equations (H2) and (H3). The maximum valley depth (Rv) and the mean-difference between the tallest peak and deepest valley (Rz) values, which are calculated using Equations (H4) and (H5) respectively were also quantified in the pre/post-test analysis, as well as the maximum peak-valley-depth of the surface profile (R_t) and the root-mean-square-slope parameters ($R\Delta_q$ and $W\Delta_q$), see Equations (H6) and (H7a) respectively. The local slopes are then calculated using Equation (H7b). The schematic diagrams of the surface roughness parameters are also shown in Figure H3 for reference purposes.
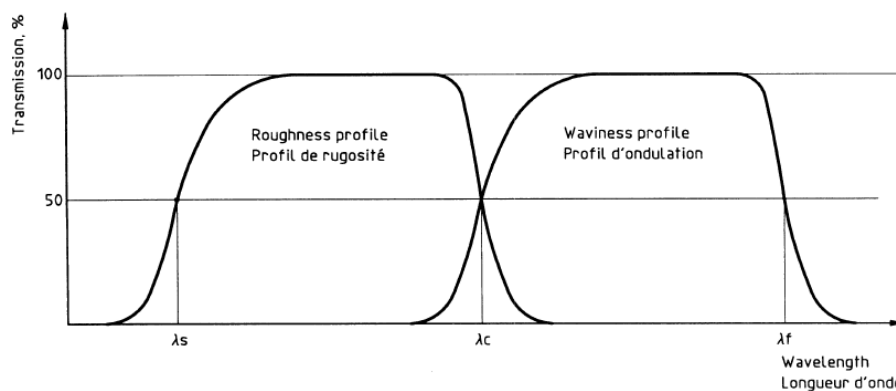
Figure H1: Transmission characteristic of the roughness and waviness profiles *(British Standards Institute, 2002)*.
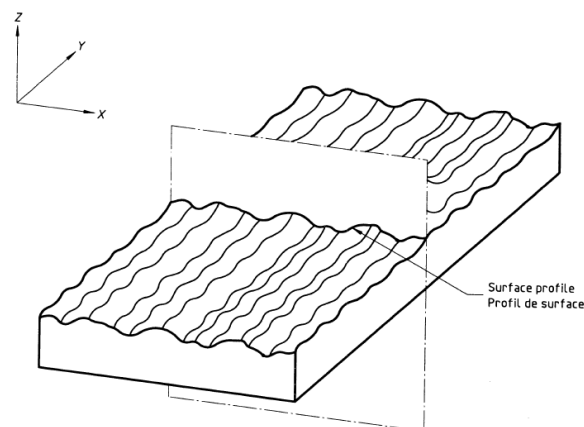
Figure H2: Coordinate system used to measure the surface roughness profile *(British Standards Institute, 2002)*.

$$R_a, Wa = \frac{1}{lr} \int_0^{lr} |Z(x)| dx \qquad \text{(H1)}$$

$$R_q = \left[\frac{1}{lr} \int_0^{lr} |Z^2(x)| dx \right]^{1/2} \qquad \text{(H2)}$$

$$R_p = \max(Z(x)) \qquad \text{(H3)}$$

$$R_v = |\min(Z(x))| \qquad \text{(H4)}$$

$$Rz = Rp + Rv \qquad \text{(H5)}$$

$$R_t = \max(Rpi) + \max(Rvi) \qquad \text{(H6)}$$

$$R\Delta_q, W\Delta_q = \sqrt{\frac{1}{lr} \int_0^{lr} \left[\frac{dZ(x)}{dx} \right]^2 dx} \qquad \text{(H7a)}$$

$$\frac{dZi}{dXi} = \frac{(Z_{i+3} - 9Z_{i+2} + 45Z_{i+1} - 45Z_{i-1} + 9Z_{i-2} - Z_{i-3})}{60x} \qquad \text{(H7b)}$$
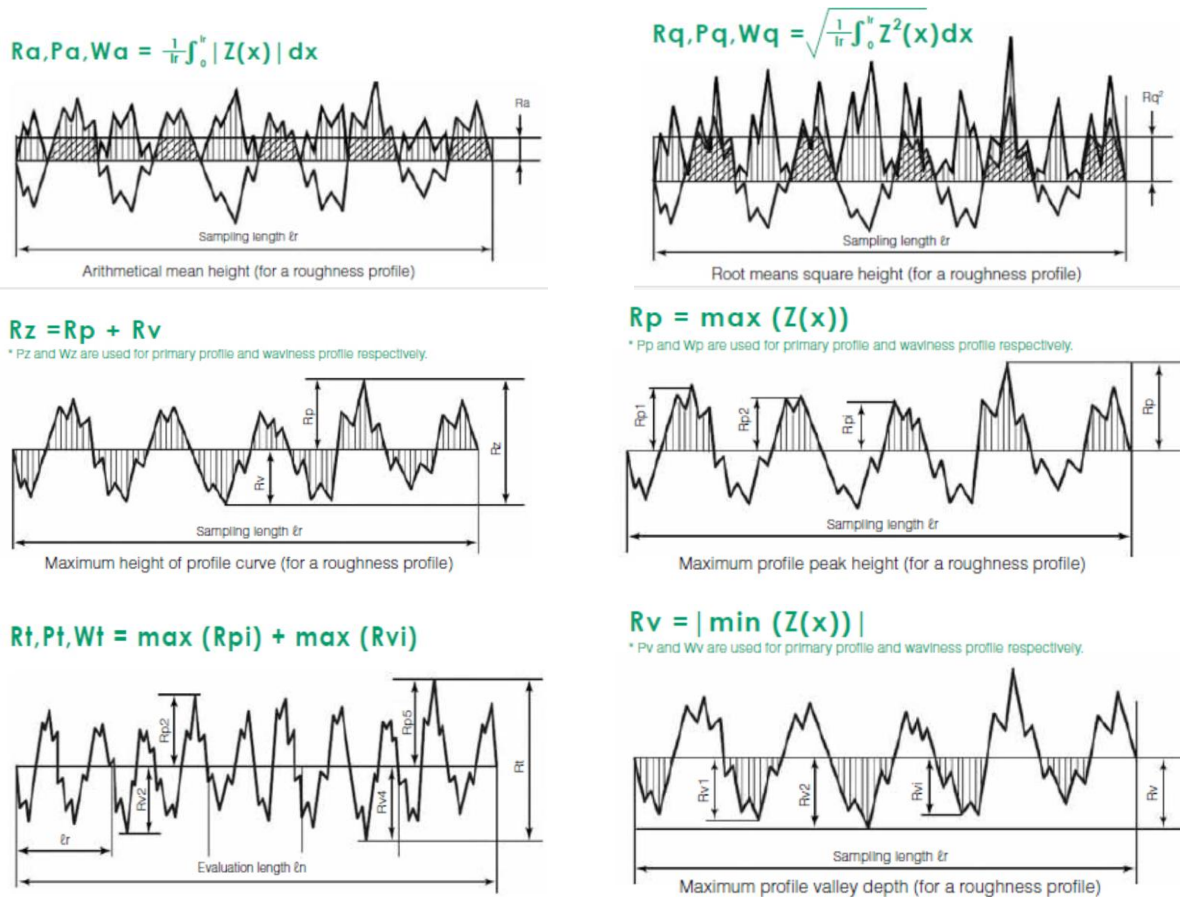
Figure H3: Schematic diagrams of the surface measurement parameters *(Keyence Coporation, 2018)*.

Appendix I. Centre plate surface roughness measurement results

The pre and post-test surface roughness measurements for the scale model centre plate components are shown in Tables I1 and I2 respectively. From these results it can be seen that the mean pre-test surface roughness (Ra) value for the complete data set is 1.757 µm (17 test cases), whereas the post-test value, is seen to be slightly lower at 1.716 µm, which is a 2.5% decrease. The maximum COF value that was calculated during the service test cases is highlighted in red and shown to be 0.54, whereas the minimum COF value of 0.05, was calculated from the running-in test results and is highlighted in green.

The percentage increases in the COF values shown in these tables therefore, take the total number of running cycles in to account that each centre plate/wear liner sample was subjected to during the running-in/service test cases, which is 13800 cycles. The maximum percentage increase in the COF value as can be seen, was 400% during test case 11 using material B, whereas the minimum was seen to be 27.8% during test case 17 using material C. The mean percentage increase for the complete data set however (17 test cases), is seen to be 178.5% with a Standard Deviation (SD) of 64.4%.

The analyses of these results shows that the pre/post-test Rt, Rq and Wa parameters are the most sensitive overall, whereas the Ra parameter on the other hand, remains fairly stable. These results were then separated into the test cases that were carried out using Centre plate number 1 and 2, to analyse the surface measurement data in greater detail, see Tables I3 and I4. These results clearly show that the centre plates were re-turned to the same specifications after each test case, as the mean values of the pre-test Ra measurements for example, are shown to range between 1.74 – 1.78 µm. The SD`s of these parameters are also closely matched at 20.8 and 21.8%, which strongly suggests that the quality and repeatability of the turning process is under control.

| | Minimum | | Maximum |

Test case	Centre plate	Liner	Material	Frequency (Hz)	Load (kN)	Ra (µm)	Rp (µm)	Rz (µm)	Rt (µm)	Rq (µm)	Rv (µm)	Wa (µm)	Slope Ra (deg)	Slope Wa (deg)	Minimum µ	Maximum µ	Mean µ	Total change in µ (%)
1	1	A	A	0.042	3	1.102	2.883	5.284	5.786	1.310	2.401	0.542	-0.122	0.620	0.05	0.16	0.11	196.3
2	2	B	A	0.042	6	1.033	2.631	5.027	6.092	1.242	2.396	0.577	-0.093	0.490	0.08	0.36	0.22	350.0
3	1	C	A	0.042	9	1.903	4.562	10.924	11.903	2.419	6.362	0.844	-0.083	1.064	0.05	0.16	0.10	210.6
4	2	D	A	0.042	6	1.919	4.995	11.326	12.253	2.458	6.332	0.792	-0.077	1.068	0.09	0.12	0.11	33.3
5	1	E	A	0.084	3	2.158	5.193	12.696	16.011	2.787	7.503	0.845	-0.012	1.218	0.10	0.22	0.16	113.6
6	2	F	A	0.084	6	2.299	5.989	13.129	15.826	3.764	7.140	1.017	-0.059	1.262	0.07	0.14	0.11	100.0
7	1	G	A	0.084	9	1.731	4.884	9.431	11.188	2.184	4.547	0.825	-0.046	0.978	0.06	0.14	0.10	129.5
8	1	AA	B	0.042	3	1.898	5.401	10.012	11.405	2.371	4.300	0.817	-0.092	1.010	0.10	0.28	0.19	171.8
9	1	II	B	0.042	6	1.860	4.986	9.244	10.552	2.261	4.258	0.918	-0.079	1.046	0.10	0.34	0.22	250.5
10	2	JJ	B	0.042	9	1.837	4.316	9.606	10.743	2.379	4.290	0.894	-0.068	1.035	N/A	N/A	N/A	N/A
11	1	KK	B	0.042	9	1.989	5.296	9.322	10.126	2.407	4.026	0.721	-0.091	1.098	0.11	0.54	0.32	400.0
12	2	BB	B	0.084	3	1.930	5.320	9.995	11.726	2.397	4.675	0.867	-0.057	1.027	0.09	0.26	0.18	188.9
13	1	GG	B	0.084	6	1.993	5.414	9.382	10.204	2.411	3.969	0.699	-0.086	1.094	0.11	0.39	0.25	251.4
14	2	HH	B	0.084	9	1.839	5.078	9.242	10.397	2.248	4.164	0.972	-0.073	1.040	0.13	0.53	0.33	320.6
15	1	A	C	0.084	3	1.110	3.474	7.070	9.220	1.416	3.596	1.279	-0.029	0.493	0.21	0.27	0.24	31.1
16	2	B	C	0.084	6	1.613	3.750	7.237	8.317	1.913	3.487	0.660	-0.053	0.815	0.12	0.21	0.16	81.0
17	1	C	C	0.084	9	1.654	3.812	7.581	9.524	1.987	3.770	0.961	-0.030	0.872	0.18	0.23	0.21	27.8
Maximum						2.299	5.989	13.129	16.011	3.764	7.503	1.279	-0.012	1.262	0.21	0.54	0.33	400.0
Minimum						1.033	2.631	5.027	5.786	1.242	2.396	0.542	-0.122	0.490	0.05	0.12	0.10	27.8
Range						1.266	3.357	8.102	10.224	2.522	5.107	0.737	0.110	0.772	0.16	0.42	0.23	372.2
Mean						1.757	4.587	9.206	10.663	2.233	4.542	0.837	-0.067	0.955	0.10	0.27	0.19	178.5
Standard deviation						0.361	0.959	2.243	2.686	0.588	1.474	0.176	0.028	0.227	0.04	0.13	0.07	115.0
Standard deviation (%)						20.6	20.9	24.4	25.2	26.3	32.5	21.0	41.2	23.8	40.7	48.2	39.9	64.4

Table I1: Summary of pre-test surface roughness measurements.

Test case	Centre plate	Liner	Material	Frequency (Hz)	Load (kN)	Ra (µm)	Rp (µm)	Rz (µm)	Rt (µm)	Rq (µm)	Rv (µm)	Wa (µm)	Slope Ra (deg)	Slope Wa (deg)	Minimum µ	Maximum µ	Mean µ	Total change in µ (%)
1	1	A	A	0.042	3	1.093	3.118	5.165	5.724	1.299	2.410	0.550	-0.089	0.608	0.05	0.16	0.11	196.3
2	2	B	A	0.042	6	1.249	3.563	6.603	13.078	1.886	3.039	2.631	-0.075	0.769	0.08	0.36	0.22	350.0
3	1	C	A	0.042	9	1.883	4.568	11.050	12.076	2.415	6.482	0.840	-0.073	1.051	0.05	0.16	0.10	210.6
4	2	D	A	0.042	6	1.886	4.896	11.312	12.250	2.438	6.416	0.772	-0.060	1.060	0.09	0.12	0.11	33.3
5	1	E	A	0.084	3	2.010	4.696	11.287	14.119	2.809	6.592	0.948	0.016	1.182	0.10	0.22	0.16	113.6
6	2	F	A	0.084	6	2.131	5.371	12.369	14.408	2.695	6.998	0.904	-0.039	1.162	0.07	0.14	0.11	100.0
7	1	G	A	0.084	9	1.687	4.677	9.181	10.740	2.131	4.506	0.873	-0.071	0.955	0.06	0.14	0.10	129.5
8	1	AA	B	0.042	3	1.896	5.435	9.617	11.198	2.366	4.182	0.791	-0.049	1.018	0.10	0.28	0.19	171.8
9	1	II	B	0.042	6	1.984	5.306	8.589	9.867	2.399	3.807	0.683	-0.111	1.098	0.10	0.34	0.22	250.5
10	2	JJ	B	0.042	9	1.897	4.921	8.702	9.474	2.338	3.941	0.637	-0.075	1.074	N/A	N/A	N/A	N/A
11	1	KK	B	0.042	9	1.310	3.315	6.352	7.044	1.570	3.037	0.659	-0.050	0.640	0.11	0.54	0.32	400.0
12	2	BB	B	0.084	3	1.912	5.375	9.778	11.424	2.365	4.402	0.871	-0.037	1.016	0.09	0.26	0.18	188.9
13	1	GG	B	0.084	6	1.997	5.328	9.244	10.134	2.415	3.916	0.722	-0.105	1.103	0.11	0.39	0.25	251.4
14	2	HH	B	0.084	9	1.854	5.036	9.036	10.048	2.255	4.000	0.827	-0.106	1.045	0.13	0.53	0.33	320.6
15	1	A	C	0.084	3	1.110	3.474	7.070	9.220	1.416	3.596	1.279	-0.029	0.493	0.21	0.27	0.24	31.1
16	2	B	C	0.084	6	1.613	3.750	7.237	8.317	1.913	3.487	0.660	-0.053	0.815	0.12	0.21	0.16	81.0
17	1	C	C	0.084	9	1.654	3.812	7.581	9.524	1.987	3.770	0.961	-0.030	0.872	0.18	0.23	0.21	27.8
Maximum						2.131	5.435	12.369	14.408	2.809	6.998	2.631	0.016	1.182	0.21	0.54	0.33	400.0
Minimum						1.093	3.118	5.165	5.724	1.299	2.410	0.550	-0.111	0.493	0.05	0.12	0.10	27.8
Range						1.038	2.317	7.205	8.684	1.510	4.588	2.082	0.127	0.688	0.16	0.42	0.23	372.2
Mean						1.716	4.508	8.834	10.508	2.159	4.387	0.918	-0.061	0.939	0.10	0.27	0.19	178.5
Standard deviation						0.330	0.818	1.989	2.316	0.426	1.381	0.472	0.033	0.206	0.04	0.13	0.07	115.0
Standard deviation (%)						19.2	18.1	22.5	22.0	19.7	31.5	51.4	54.0	21.9	40.7	48.2	39.9	64.4

Table I2: Summary of post-test surface roughness measurements.

Centre plate number 1 pre-test surface roughness measurements														
Test case	Centre plate	Liner	Material	Frequency (Hz)	Load (kN)	Ra (µm)	Rp (µm)	Rz (µm)	Rt (µm)	Rq (µm)	Rv (µm)	Wa (µm)	Slope Ra (deg)	Slope Wa (deg)
1	1	A	A	0.042	3	1.102	2.883	5.284	5.786	1.310	2.401	0.542	-0.122	0.620
3	1	C	A	0.042	9	1.903	4.562	10.924	11.903	2.419	6.362	0.844	-0.083	1.064
5	1	E	A	0.084	3	2.158	5.193	12.696	16.011	2.787	7.503	0.845	-0.012	1.218
7	1	G	A	0.084	9	1.731	4.884	9.431	11.188	2.184	4.547	0.825	-0.046	0.978
8	1	AA	B	0.042	3	1.898	5.401	10.012	11.405	2.371	4.300	0.817	-0.092	1.010
9	1	II	B	0.042	6	1.860	4.986	9.244	10.552	2.261	4.258	0.918	-0.079	1.046
11	1	KK	B	0.042	9	1.989	5.296	9.322	10.126	2.407	4.026	0.721	-0.091	1.098
13	1	GG	B	0.084	6	1.993	5.414	9.382	10.204	2.411	3.969	0.699	-0.086	1.094
15	1	A	C	0.084	3	1.110	3.474	7.070	9.220	1.416	3.596	1.279	-0.029	0.493
17	1	C	C	0.084	9	1.654	3.812	7.581	9.524	1.987	3.770	0.961	-0.030	0.872
Maximum						2.158	5.414	12.696	16.011	2.787	7.503	1.279	-0.012	1.218
Minimum						1.102	2.883	5.284	5.786	1.310	2.401	0.542	-0.122	0.493
Range						1.056	2.530	7.412	10.224	1.476	5.102	0.737	0.110	0.725
Mean						1.740	4.590	9.094	10.592	2.155	4.473	0.845	-0.067	0.949
Standard deviation						0.362	0.895	2.064	2.551	0.465	1.447	0.193	0.035	0.227
Standard deviation (%)						20.8	19.5	22.7	24.1	21.6	32.3	22.9	52.8	23.9

Centre plate number 1 post-test surface roughness measurements														
Test case	Centre plate	Liner	Material	Frequency (Hz)	Load (kN)	Ra (µm)	Rp (µm)	Rz (µm)	Rt (µm)	Rq (µm)	Rv (µm)	Wa (µm)	Slope Ra (deg)	Slope Wa (deg)
1	1	A	A	0.042	3	1.093	3.118	5.165	5.724	1.299	2.410	0.550	-0.089	0.608
3	1	C	A	0.042	9	1.883	4.568	11.050	12.076	2.415	6.482	0.840	-0.073	1.051
5	1	E	A	0.084	3	2.010	4.696	11.287	14.119	2.809	6.592	0.948	0.016	1.182
7	1	G	A	0.084	9	1.687	4.677	9.181	10.740	2.131	4.506	0.873	-0.071	0.955
8	1	AA	B	0.042	3	1.896	5.435	9.617	11.198	2.366	4.182	0.791	-0.049	1.018
9	1	II	B	0.042	6	1.984	5.306	8.589	9.867	2.399	3.807	0.683	-0.111	1.098
11	1	KK	B	0.042	9	1.310	3.315	6.352	7.044	1.570	3.037	0.659	-0.050	0.640
13	1	GG	B	0.084	6	1.997	5.328	9.244	10.134	2.415	3.916	0.722	-0.105	1.103
15	1	A	C	0.084	3	1.110	3.474	7.070	9.220	1.416	3.596	1.279	-0.029	0.493
17	1	C	C	0.084	9	1.654	3.812	7.581	9.524	1.987	3.770	0.961	-0.030	0.872
Maximum						2.010	5.435	11.287	14.119	2.809	6.592	1.279	0.016	1.182
Minimum						1.093	3.118	5.165	5.724	1.299	2.410	0.550	-0.111	0.493
Range						0.918	2.317	6.123	8.395	1.510	4.182	0.729	0.127	0.688
Mean						1.662	4.373	8.514	9.965	2.081	4.230	0.831	-0.059	0.902
Standard deviation						0.364	0.880	1.977	2.384	0.501	1.348	0.205	0.039	0.240
Standard deviation (%)						21.9	20.1	23.2	23.9	24.1	31.9	24.6	66.0	26.6

Table I3: Centre plate 1. (Top) Pre-test measurements. (Bottom) Post-test measurements.

						Centre plate number 2 pre-test surface roughness measurements								
Test case	Centre plate	Liner	Material	Frequency (Hz)	Load (kN)	Ra (µm)	Rp (µm)	Rz (µm)	Rt (µm)	Rq (µm)	Rv (µm)	Wa (µm)	Slope Ra (deg)	Slope Wa (deg)
2	2	B	A	0.042	6	1.033	2.631	5.027	6.092	1.242	2.396	0.577	-0.093	0.490
4	2	D	A	0.042	6	1.919	4.995	11.326	12.253	2.458	6.332	0.792	-0.077	1.068
6	2	F	A	0.084	6	2.299	5.989	13.129	15.826	3.764	7.140	1.017	-0.059	1.262
10	2	JJ	B	0.042	9	1.837	4.316	9.606	10.743	2.379	4.290	0.894	-0.068	1.035
12	2	BB	B	0.084	3	1.930	5.320	9.995	11.726	2.397	4.675	0.867	-0.057	1.027
14	2	HH	B	0.084	9	1.839	5.078	9.242	10.397	2.248	4.164	0.972	-0.073	1.040
16	2	B	C	0.084	6	1.613	3.750	7.237	8.317	1.913	3.487	0.660	-0.053	0.815
Maximum						2.299	5.989	13.129	15.826	3.764	7.140	1.017	-0.053	1.262
Minimum						1.033	2.631	5.027	6.092	1.242	2.396	0.577	-0.093	0.490
Range						1.266	3.357	8.102	9.734	2.522	4.745	0.441	0.040	0.772
Mean						1.781	4.583	9.366	10.765	2.343	4.640	0.825	-0.068	0.962
Standard deviation						0.388	1.119	2.640	3.074	0.757	1.624	0.161	0.014	0.245
Standard deviation (%)						21.8	24.4	28.2	28.6	32.3	35.0	19.5	20.2	25.5

						Centre plate number 2 post-test surface roughness measurements								
Test case	Centre plate	Liner	Material	Frequency (Hz)	Load (kN)	Ra (µm)	Rp (µm)	Rz (µm)	Rt (µm)	Rq (µm)	Rv (µm)	Wa (µm)	Slope Ra (deg)	Slope Wa (deg)
2	2	B	A	0.042	6	1.249	3.563	6.603	13.078	1.886	3.039	2.631	-0.075	0.769
4	2	D	A	0.042	6	1.886	4.896	11.312	12.250	2.438	6.416	0.772	-0.060	1.060
6	2	F	A	0.084	6	2.131	5.371	12.369	14.408	2.695	6.998	0.904	-0.039	1.162
10	2	JJ	B	0.042	9	1.897	4.921	8.702	9.474	2.338	3.941	0.637	-0.075	1.074
12	2	BB	B	0.084	3	1.912	5.375	9.778	11.424	2.365	4.402	0.871	-0.037	1.016
14	2	HH	B	0.084	9	1.854	5.036	9.036	10.048	2.255	4.000	0.827	-0.106	1.045
16	2	B	C	0.084	6	1.613	3.750	7.237	8.317	1.913	3.487	0.660	-0.053	0.815
Maximum						2.131	5.375	12.369	14.408	2.695	6.998	2.631	-0.037	1.162
Minimum						1.249	3.563	6.603	8.317	1.886	3.039	0.637	-0.106	0.769
Range						0.882	1.812	5.766	6.091	0.809	3.959	1.994	0.069	0.393
Mean						1.792	4.702	9.291	11.285	2.270	4.612	1.043	-0.063	0.991
Standard deviation						0.283	0.742	2.068	2.142	0.288	1.503	0.708	0.024	0.144
Standard deviation (%)						15.8	15.8	22.3	19.0	12.7	32.6	67.8	38.2	14.5

Table I4: Centre plate 2. (Top) Pre-test measurements. (Bottom) Post-test measurements.

Appendix J. Y25 centre pivot surface roughness measurements

This section discusses the surface measurements results for the new, unused, Y25 bogie centre pivot shown in Figure J1, picture A. These measurements were recorded to benchmark the surface roughness characteristics of a new centre pivot component, data which is not widely available to the rail industry. This data was also used to validate the measurements on the 1:7 scale centre plate components. However, due to the extremely large dimensions of the Y25 centre pivot, none of the working envelopes on the available measurement machines could accommodate this component, so surface replicas had to be produced using a fast drying moulding compound, as well as Blu-tack to prevent this compound from draining away from the areas of interest.

Eight surface replicas were produced using a similar measurement methodology to the one discussed in Section 5.2, but with two measurement areas at the top/bottom of the centre pivot surface to reduce the work load. The mean-roughness value (Ra), the root-mean-square roughness (Rq) and the mean-difference between the tallest peak and deepest valley (Rz) parameters, were then analysed and quantified using the Alicona Infinite Focus 3-D optical microscope. This task was carried out using a 20x lens, see picture B in Figure J1.

The results from this analysis are shown in Table J1 and as can be seen, the mean Ra value is 2.745 µm, which is also in agreement with the machining tolerances shown in Appendix K. The mean Ra value for the 17 pre-test measurements on the 1:7 scale centre plates however, is 1.757 µm, which is 1 µm lower than the mean Ra value for the full size component (2.745 µm). The main conclusion that can be drawn from this analysis, is that the Ra, Rq and Rz surface roughness values on the 1:7 scale model centre plate/full size components, are in good agreement.
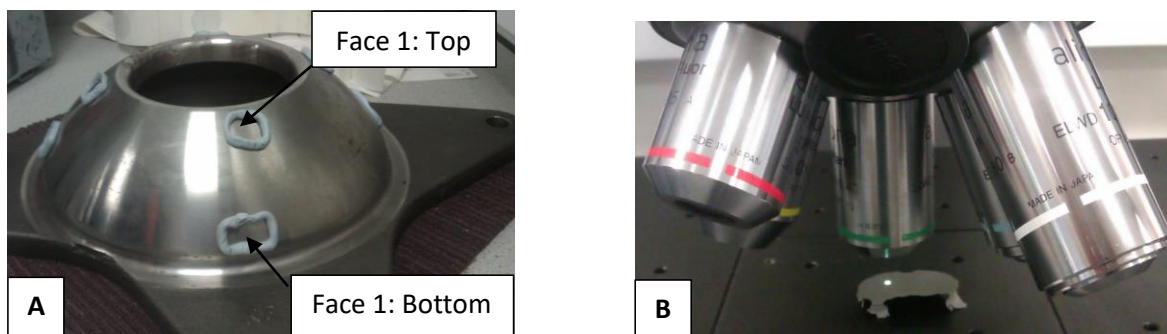
Figure J1: (Picture A) Y-series centre-pivot. (Picture B) Alicona Infinite Focus optical measurement system.

Location	Face	Ra (µm)	Rq (µm)	Rz (µm)
Top	1	2.690	3.106	10.933
Bottom	1	2.672	3.142	11.672
Top	2	2.441	2.868	10.822
Bottom	2	3.120	3.592	12.630
Top	3	2.596	3.016	10.512
Bottom	3	2.923	3.406	12.500
Top	4	2.640	3.040	10.840
Bottom	4	2.879	3.328	12.204
Mean		2.745	3.187	11.514
Maximum		3.120	3.592	12.630
Minimum		2.441	2.868	10.512
Range		0.679	0.725	2.118
Standard deviation		0.215	0.237	0.844
Standard deviation (%)		7.8	7.4	7.3

Table J1: Summary of the surface measurements on the Y25 centre pivot.

Appendix K. Roughness values for different machining methods

The achievable surface roughness (Ra) values for different machining methods are shown in Figure K1 and from this list, it can be seen that mean Ra value for the turning processes for example, should be in the region of 0.4 – 6.3 µm. The pre-test Ra measurements on the 1:7 scale centre plates/Y25 centre pivot components, are all seen to comply with the roughness specifications given below.

General guidelines for feasible roughness R_a for different processing methods

Material removing or separating operations	roughness R_a in um												
	0.012	0.025	0.05	0.1	0.2	0.4	0.8	1.6	3.2	6.3	13	25	50
flame cutting											■	●	◇
sawing								■	●	●	●	◇	
planing							■	●	●	●	◇		
punching						■	●	◇					
chemical treatment							■	●	●	◇			
spark erosion machining							■	●	●	◇			
drilling							■	●	●	◇			
boring							■	●	●	◇			
milling						■	●	●	●	◇	◇		
turning						■	●	●	●	◇			
broaching						■	●	●	◇				
reaming						■	●	●	◇				
filing						■	●	●	◇				
grinding					●	●	●	●	◇				
barreling				■	■	●	●	◇	◇				
brushing				■	●	◇							
electrolytic grinding				■	●	◇							
honing			●	●	●	◇							
polishing				●	●	◇							
lapping			●	●	●	◇							
superfinishing			●	●	◇	◇							

● AVERAGE ACHIEVABLE ROUGHNESS   ■ FINER   ◇ COARSER

Figure K1: Mean surface roughness (Ra) values for different machining methods *(Course Hero, Inc, 2019)*.

Appendix L. Wear liner surface roughness measurements

The pre and post-test surface roughness measurements results for material A are shown in Table L1. From these results, it can be seen by comparing the Standard Deviations (SD`s) of the measurements on material A against materials B and C, as well as the centre plates for example, that the contact surfaces of this material are highly nonlinear. The SD`s of the pre-test roughness measurement parameters are seen to range between 79.3 – 94%, whereas the SD`s of the Ra-slope and Wa-slope parameters are seen to range between 152.3 – 182.7%. The SD`s of the post-test roughness values on material A range between 60.7 – 108.8%, which are similar to the pre-test SD`s. The deviations of the post-test slope measurements however, are significantly higher and seen to range between 274.6 – 300.5%.

Table L2 shows the pre and post-test surface measurement results for material B and from these, it can be seen that the SD`s of the pre-test roughness values, range between 6.3 – 16.3%, whereas the post-test SD`s range between 15.2 – 21.6%. These values as can be seen, are more consistent in comparison to pre-test deviations that were measured on material A. The SD`s of the pre-test slope measurements on material B however, were seen to range between 203.5 – 308.3%, which is the highest range overall. The post-test SD`s are also fairly high, ranging between 208.6 – 263.5%.

The pre and post-test roughness measurements results for material C are shown in Table L3. From these, it can be seen that the contact surfaces of these samples are the smoothest overall, as well as most consistent. The SD`s of the pre and post-test roughness measurements for example, are seen to range between 1.2 – 4.8% and 0.5 – 13.6% respectively. Whereas the deviations of the pre and post-test slope measurements, range between 102.1 – 110.5% and 132.4 – 139.4%. The mean of the pre-test Ra values on material C is also seen to be the lowest overall at 1.49 µm, whereas the pre-test values on materials A and B, are seen to be significantly higher at 2.06 and 2.12 µm respectively, see Tables L1 and L2.

The analyses of the pre/post-test surface roughness results, strongly suggests that the slope parameters are the most sensitive overall to changes in the friction characteristics of the contact interfaces of the centre plate/wear liner components. The smoother surfaces of materials B and C it should be pointed out, are due to the manufacturing methods that were used to processes the raw materials. Material A for example, is a thermosetting composite material that is pressed and sintered to the desired wear liner shape, hence the reason why the surface texture is referred to as a particulate lay in engineering drawings. Whereas materials B and C on the other hand, are machined to shape using CNC milling machines and lathes, which is the reason why there is significantly less variation in these surface roughness measurements.

		Minimum			Maximum	

Material A pre-test surface roughness measurements																	
Test case	Centre plate	Material	Liner	Frequency (Hz)	Load (kN)	Ra (µm)	Rp (µm)	Rz (µm)	Rt (µm)	Rq (µm)	Rv (µm)	Wa (µm)	Slope-Ra (deg)	Slope-Wa (deg)	Minimum µ	Maximum µ	Mean µ	Total change in µ (%)
1	1	A	A	0.042	3	2.049	3.224	13.592	31.861	3.063	10.368	2.053	-0.004	0.017	0.05	0.16	0.11	196.3
2	2	A	B	0.042	6	0.469	1.231	3.063	6.776	0.683	2.046	0.511	-0.001	0.014	0.08	0.36	0.22	350.0
3	1	A	C	0.042	9	5.344	9.309	33.573	69.137	7.866	24.264	5.066	0.018	-0.060	0.05	0.16	0.10	210.6
4	2	A	D	0.042	6	0.649	1.311	4.891	8.501	0.995	3.413	0.534	0.000	0.004	0.09	0.12	0.11	33.3
5	1	A	E	0.084	3	0.325	1.100	2.174	3.755	0.484	1.075	0.296	0.004	-0.001	0.10	0.22	0.16	113.6
6	2	A	F	0.084	6	3.198	6.245	25.759	56.535	5.314	19.514	3.185	0.057	-0.090	0.07	0.14	0.11	100.0
7	2	A	G	0.084	9	2.417	5.111	17.014	17.350	3.659	11.903	1.368	0.084	-0.045	0.06	0.14	0.10	129.5
Maximum						5.344	9.309	33.573	69.137	7.866	24.264	5.066	0.084	0.017	0.10	0.36	0.22	350.0
Minimum						0.325	1.100	2.174	3.755	0.484	1.075	0.296	-0.004	-0.090	0.05	0.12	0.10	33.3
Range						5.019	8.209	31.398	65.381	7.382	23.189	4.770	0.088	0.106	0.05	0.24	0.12	316.7
Mean						2.064	3.933	14.295	27.702	3.152	10.369	1.859	0.023	-0.023	0.07	0.19	0.13	161.9
Standard deviation						1.814	3.118	12.058	25.989	2.739	8.973	1.748	0.034	0.042	0.02	0.08	0.05	102.2
Standard deviation (%)						87.9	79.3	84.4	93.8	86.9	86.5	94.0	152.3	182.7	26.9	45.0	35.4	63.1

Material A post-test surface roughness measurements

Test case	Centre plate	Material	Liner	Frequency (Hz)	Load (kN)	Ra (μm)	Rp (μm)	Rz (μm)	Rt (μm)	Rq (μm)	Rv (μm)	Wa (μm)	Slope-Ra (deg)	Slope-Wa (deg)	Minimum μ	Maximum μ	Mean μ	Total change in μ (%)
1	1	A	A	0.042	3	2.417	5.111	17.014	17.350	3.659	11.903	1.368	0.084	-0.045	0.05	0.16	0.11	196.3
2	2	A	B	0.042	6	1.004	3.020	5.518	11.618	1.342	2.499	3.573	-0.044	0.010	0.08	0.36	0.22	350.0
3	1	A	C	0.042	9	4.587	8.571	33.219	85.042	7.277	24.648	7.996	0.121	-0.109	0.05	0.16	0.10	210.6
4	2	A	D	0.042	6	0.890	2.348	7.622	14.408	1.432	5.274	0.721	-0.006	0.008	0.09	0.12	0.11	33.3
5	1	A	E	0.084	3	0.425	1.398	3.534	3.551	0.586	1.265	0.280	0.014	-0.016	0.10	0.22	0.16	113.6
6	2	A	F	0.084	6	3.505	6.247	20.376	20.847	4.956	14.129	1.679	0.024	-0.021	0.07	0.14	0.11	100.0
7	2	A	G	0.084	9	1.319	2.723	12.151	21.738	2.326	8.982	1.491	-0.047	0.047	0.06	0.14	0.10	129.5
Maximum						4.587	8.571	33.219	85.042	7.277	24.648	7.996	0.121	0.047	0.10	0.36	0.22	350.0
Minimum						0.425	1.398	3.534	3.551	0.586	1.265	0.280	-0.047	-0.109	0.05	0.12	0.10	33.3
Range						4.163	7.173	29.685	81.491	6.691	23.384	7.716	0.168	0.157	0.05	0.24	0.12	316.7
Mean						2.021	4.202	14.205	24.936	3.083	9.814	2.444	0.021	-0.018	0.07	0.19	0.13	161.9
Standard deviation						1.544	2.549	10.364	27.211	2.380	8.072	2.658	0.063	0.050	0.02	0.08	0.05	102.2
Standard deviation (%)						76.4	60.7	73.0	109.1	77.2	82.2	108.8	300.5	274.6	26.9	45.0	35.4	63.1

Table L1: Summary of pre and post-test surface roughness measurements on material A.

Material B pre-test surface roughness measurements

Test case	Centre plate	Material	Liner	Frequency (Hz)	Load (kN)	Ra (μm)	Rp (μm)	Rz (μm)	Rt (μm)	Rq (μm)	Rv (μm)	Wa (μm)	Slope-Ra (deg)	Slope-Wa (deg)	Minimum μ	Maximum μ	Mean μ	Total change in μ (%)
8	1	B	AA	0.042	3	2.395	7.235	14.410	20.911	3.059	7.175	1.623	0.007	-0.008	0.10	0.28	0.19	171.8
9	2	B	II	0.042	6	2.284	7.394	13.630	21.915	2.955	6.236	1.473	-0.022	0.021	0.10	0.34	0.22	250.5
10						Data error													
11	1	B	KK	0.042	9	1.871	5.764	11.702	18.086	2.347	5.938	1.177	0.000	0.000	0.11	0.54	0.32	400.0
12	1	B	BB	0.084	3	2.011	6.742	12.730	20.065	2.622	5.950	1.022	-0.005	0.039	0.09	0.26	0.18	188.9
13	1	B	GG	0.084	6	2.051	6.188	12.321	20.198	2.557	6.939	1.385	0.007	-0.008	0.11	0.39	0.25	251.4
14	2	B	HH	0.084	9	2.104	6.753	13.294	19.819	2.684	7.062	1.481	-0.008	0.010	0.13	0.53	0.33	320.6
Maximum						2.395	7.394	14.410	21.915	3.059	7.175	1.623	0.007	0.039	0.13	0.54	0.33	400.0
Minimum						1.871	5.764	11.702	18.086	2.347	5.938	1.022	-0.022	-0.008	0.09	0.26	0.18	171.8
Range						0.525	1.630	2.708	3.829	0.712	1.237	0.601	0.030	0.047	0.04	0.28	0.15	228.2
Mean						2.119	6.679	13.014	20.165	2.704	6.550	1.360	-0.004	0.009	0.11	0.39	0.25	263.9
Standard deviation						0.191	0.618	0.968	1.271	0.263	0.572	0.221	0.011	0.019	0.01	0.12	0.07	85.1
Standard deviation (%)						9.0	9.2	7.4	6.3	9.7	8.7	16.3	308.3	203.5	11.8	31.1	26.5	32.2

Material B post-test surface roughness measurements

Test case	Centre plate	Material	Liner	Frequency (Hz)	Load (kN)	Ra (μm)	Rp (μm)	Rz (μm)	Rt (μm)	Rq (μm)	Rv (μm)	Wa (μm)	Slope-Ra (deg)	Slope-Wa (deg)	Minimum μ	Maximum μ	Mean μ	Total change in μ (%)
8	1	B	AA	0.042	3	2.095	5.276	11.778	17.540	2.651	6.503	1.338	-0.007	0.008	0.10	0.28	0.19	171.8
9	2	B	II	0.042	6	1.918	4.819	10.498	17.977	2.278	5.683	1.633	0.004	-0.005	0.10	0.34	0.22	250.5
10						Data error													
11	1	B	KK	0.042	9	1.250	3.189	7.594	10.844	1.585	4.404	1.125	-0.003	0.003	0.11	0.54	0.32	400.0
12	2	B	BB	0.084	3	1.738	4.027	9.625	17.120	2.177	5.598	1.203	0.011	-0.007	0.09	0.26	0.18	188.9
13	1	B	GG	0.084	6	1.561	3.813	8.265	11.992	1.951	4.452	0.857	-0.018	0.019	0.11	0.39	0.25	251.4
14	2	B	HH	0.084	9	1.643	4.141	9.269	13.423	2.060	5.128	1.097	-0.010	0.010	0.13	0.53	0.33	320.6
Maximum						2.095	5.276	11.778	17.977	2.651	6.503	1.633	0.011	0.019	0.13	0.54	0.33	400.0
Minimum						1.250	3.189	7.594	10.844	1.585	4.404	0.857	-0.018	-0.007	0.09	0.26	0.18	171.8
Range						0.845	2.086	4.185	7.132	1.066	2.098	0.776	0.029	0.025	0.04	0.28	0.15	228.2
Mean						1.701	4.211	9.505	14.816	2.117	5.295	1.209	-0.004	0.005	0.11	0.39	0.25	263.9
Standard deviation						0.293	0.741	1.511	3.112	0.355	0.804	0.261	0.010	0.009	0.01	0.12	0.07	85.1
Standard deviation (%)						17.2	17.6	15.9	21.0	16.8	15.2	21.6	263.5	208.6	11.8	31.1	26.5	32.2

Table L2: Summary of pre and post-test surface roughness measurements on material B.

Material C pre-test surface roughness measurements

Test case	Centre plate	Material	Liner	Frequency (Hz)	Load (kN)	Ra (μm)	Rp (μm)	Rz (μm)	Rt (μm)	Rq (μm)	Rv (μm)	Wa (μm)	Slope-Ra (deg)	Slope-Wa (deg)	Minimum μ	Maximum μ	Mean μ	Total change in μ (%)
15	1	C	A	0.084	3	1.517	4.591	8.766	12.500	1.905	4.175	1.119	0.002	-0.002	0.21	0.27	0.24	31.1
16	2	C	B	0.084	6	1.467	4.270	8.590	12.400	1.862	4.166	1.215	0.002	0.000	0.12	0.21	0.16	81.0
17	1	C	C	0.084	9	1.491	4.370	8.850	13.033	1.891	4.480	1.118	0.012	-0.005	0.18	0.23	0.21	27.8
Maximum						1.517	4.591	8.850	13.033	1.905	4.480	1.215	0.012	0.000	0.21	0.27	0.24	81.0
Minimum						1.467	4.270	8.590	12.400	1.862	4.166	1.118	0.002	-0.005	0.12	0.21	0.16	27.8
Range						0.050	0.321	0.260	0.633	0.043	0.314	0.097	0.011	0.005	0.09	0.06	0.08	53.3
Mean						1.491	4.410	8.736	12.644	1.886	4.274	1.150	0.005	-0.002	0.17	0.24	0.20	46.6
Standard deviation						0.025	0.165	0.133	0.340	0.022	0.179	0.056	0.006	0.002	0.05	0.03	0.04	29.8
Standard deviation (%)						1.7	3.7	1.5	2.7	1.2	4.2	4.8	110.5	102.1	27.7	12.9	18.6	64.0

Material C post-test surface roughness measurements

Test case	Centre plate	Material	Liner	Frequency (Hz)	Load (kN)	Ra (μm)	Rp (μm)	Rz (μm)	Rt (μm)	Rq (μm)	Rv (μm)	Wa (μm)	Slope-Ra (deg)	Slope-Wa (deg)	Minimum μ	Maximum μ	Mean μ	Total change in μ (%)
15	1	C	A	0.084	3	1.231	3.576	7.579	11.061	1.594	4.003	1.318	0.005	-0.002	0.21	0.27	0.24	31.1
16	2	C	B	0.084	6	1.297	3.469	7.472	9.921	1.642	4.003	1.404	-0.002	0.001	0.12	0.21	0.16	81.0
17	1	C	C	0.084	9	1.248	3.369	7.338	12.005	1.579	3.969	1.073	0.004	-0.005	0.18	0.23	0.21	27.8
Maximum						1.297	3.576	7.579	12.005	1.642	4.003	1.404	0.005	0.001	0.21	0.27	0.24	81.0
Minimum						1.231	3.369	7.338	9.921	1.579	3.969	1.073	-0.002	-0.005	0.12	0.21	0.16	27.8
Range						0.066	0.207	0.241	2.084	0.063	0.035	0.331	0.006	0.005	0.09	0.06	0.08	53.3
Mean						1.259	3.471	7.463	10.996	1.605	3.992	1.265	0.002	-0.002	0.17	0.24	0.20	46.6
Standard deviation						0.034	0.103	0.121	1.043	0.033	0.020	0.172	0.003	0.003	0.05	0.03	0.04	29.8
Standard deviation (%)						2.7	3.0	1.6	9.5	2.1	0.5	13.6	139.4	132.4	27.7	12.9	18.6	64.0

Table L3: Summary of pre and post-test surface roughness measurements on material C.

Appendix M. Wear liner mass properties

The mass properties of the wear liner samples were measured in a pre/post-test analysis as part of the testing process in order to quantify the reduction in mass due to wear throughout the running-in/service tests. This analyses as can be seen from the results shown in Table M1, produced some unexpected, as well as interesting results that are unique to each wear liner material.

The green column in this table shows the change in mass a percentage of the initial mass. From these results, it can be seen that the mean reduction in mass for material A after 13800 cycles of testing for example, was 0.182% with a Standard Deviation (SD) of –60.8%. The mean reduction in mass for material B however, was six times lower and is seen to be 0.029% with a SD of –78.6%. Whereas the post-test measurement results for material C, suggest that there was an average increase in mass of 0.003%, which clearly shows that the wear rates of these wear liners are the lowest overall. The SD`s of these measurements as can be seen, are also the lowest overall at 23.1%, but the only one that is positive.

The SD`s of the density and pre/post-test mass measurements on the other hand, are all seen to be less than 1%, which strongly suggests that the bulk mechanical properties of the wear liner samples are consistent. These parameters can now be used to aid in the development of material dependent wear/friction models for dry friction suspension components.

Test case	Centre plate	Material	Nominal thickness (mm)	Nominal external diameter (mm)	Nominal internal diameter (mm)	Nominal dowel diameter (mm)	Nominal dowel depth (mm)	Wear liner volume (mm³)	Forcing frequency (Hz)	Centre plate load (kN)	Liner	Pre-test mass (grams)	Wear liner density (kg/cm³)	Post-test mass (grams)	Change in mass (%)	Total testing time (hours)	Number of cycles	Total angular displacement (degrees)
1	1	A	8	90	10	10	3	49794.2	0.042	3	A	83.39	1.67	83.26	-0.153	91.26	13800	165600
2	2	A	8	90	10	10	3	49794.2	0.042	6	B	83.92	1.69	83.78	-0.170	91.26	13800	165600
3	1	A	8	90	10	10	3	49794.2	0.042	9	C	83.21	1.67	83.06	-0.179	91.26	13800	165600
4	2	A	8	90	10	10	3	49794.2	0.042	6	D	83.82	1.68	83.68	-0.167	91.26	13800	165600
5	1	A	8	90	10	10	3	49794.2	0.084	3	E	84.21	1.69	84.24	0.030	45.63	13800	165600
6	2	A	8	90	10	10	3	49794.2	0.084	6	F	83.54	1.68	83.30	-0.288	45.63	13800	165600
7	1	A	8	90	10	10	3	49794.2	0.084	9	G	83.03	1.67	82.74	-0.352	45.63	13800	165600
Material A statistical analysis		Maximum (grams)										84.21	1.69	84.24	0.030			
		Minimum (grams)										83.03	1.67	82.74	-0.352			
		Mean (grams)										83.59	1.68	83.44	-0.182			
		Standard deviation (grams)										0.39	0.01	0.46	-0.111			
		Standard deviation (%)										0.5	0.5	0.6	-60.8			
8	1	B	8.6	90.25	11	10	3	53726.7	0.042	3	AA	63.87	1.19	63.87	-0.003	91.26	13800	165600
9	2	B	8.6	90.25	11	10	3	53726.7	0.042	6	II	63.85	1.19	63.81	-0.060	91.26	13800	165600
11	1	B	8.6	90.25	11	10	3	53726.7	0.042	9	KK	63.94	1.19	63.93	-0.010	91.26	13800	165600
12	2	B	8.6	90.25	11	10	3	53726.7	0.084	3	BB	63.88	1.19	63.87	-0.007	45.63	13800	165600
13	1	B	8.6	90.25	11	10	3	53726.7	0.084	6	GG	63.85	1.19	63.82	-0.048	45.63	13800	165600
14	2	B	8.6	90.25	11	10	3	53726.7	0.084	9	HH	63.84	1.19	63.81	-0.047	45.63	13800	165600
Material B statistical analysis		Maximum (grams)										63.94	1.19	63.93	-0.003			
		Minimum (grams)										63.84	1.19	63.81	-0.060			
		Mean (grams)										63.87	1.19	63.85	-0.029			
		Standard deviation (grams)										0.03	0.00	0.04	-0.023			
		Standard deviation (%)										0.0	0.0	0.1	-78.6			
15	1	C	8.5	90	11	10	3	52795.6	0.084	3	A	87.29	1.65	87.29	0.002	45.63	13800	165600
16	2	C	8.5	90	11	10	3	52795.6	0.084	6	B	87.14	1.65	87.14	0.004	45.63	13800	165600
17	1	C	8.5	90	11	10	3	52795.6	0.084	9	C	85.32	1.62	85.33	0.002	45.63	13800	165600
Material C statistical analysis		Maximum (grams)										87.29	1.65	87.29	0.004			
		Minimum (grams)										85.32	1.62	85.33	0.002			
		Mean (grams)										86.59	1.64	86.59	0.003			
		Standard deviation (grams)										0.89	0.02	0.89	0.001			
		Standard deviation (%)										1.0	1.0	1.0	23.1			

Table M1: Summary of the pre and post-test mass property results for the wear liner materials.

Appendix N. Global analysis results for the running-in tests

The torque responses and COF values that were calculated from these measurements, as well as the frictional energies and powers for materials A, B and C during the 3000 cycle running-in tests, are shown in Table N1. From these results it can be seen that the minimum and maximum torque responses during the running-in tests were ± 0.496 and ± 3.2 Nm, see test case 3 on material A and test case 14 on material B. The COF values for the complete data set under the 0.5 kN centre plate loading condition therefore, ranged between 0.05 – 0.32.

The complete data set was also broken down into the individual material groups to analyse the responses in greater detail. Table N2, N3 and N4 show the results for materials A, B and C respectively. From these it can be seen that the mean percentage increase in the COF values for materials A, B and C for example, are seen to be 71.9, 98.1 and 39.1%. Whereas the standard deviations of the measurements are seen to be 41.6, 35.6 and 20.4% respectively.

The 1:7 scale model test results shown in Tables N1 – N4, were also multiplied by the scaling factors for the external forces and moments to convert these parameters to the full scale equivalents, see Table N5. The torque responses under the full scale running-in centre plate loading condition of 24.5 kN therefore, are seen to range between ± 170.2 and ± 1097.9 Nm. These results combined with global analysis/local analysis results for the service test cases shown in Appendices P, Q and R for example, can now be used to carry out Monte-Carlo analyses in Multibody Simulations (MBS) to identify the optimum maintenance requirements and suspension parameters of the side bearer and centre plate components.

	Minimum		Maximum

Forcing frequency	Material	Test case	Liner	Effective radius (m)	Centre plate load (N)	Centre plate	Min torque (Nm)	Max torque (Nm)	Mean torque (Nm)	Min energy per cycle (Joules)	Max energy per cycle (Joules)	Mean energy per cycle (Joules)	Min Power per cycle (Watts)	Max power per cycle (Watts)	Mean power per cycle (Watts)	Min μ	Max μ	Mean μ	Percentage increase in torque
0.042	A	1	A	0.02	500	1	0.539	1.077	0.808	0.112	0.224	0.168	0.005	0.009	0.007	0.054	0.108	0.081	100.0
0.042	A	2	B	0.02	500	2	0.800	1.201	1.001	0.166	0.250	0.208	0.007	0.010	0.009	0.080	0.120	0.100	50.0
0.042	A	3	C	0.02	500	1	0.496	1.034	0.765	0.103	0.215	0.159	0.004	0.009	0.007	0.050	0.103	0.077	108.4
0.042	A	4	D	0.02	500	2	0.900	1.111	1.005	0.187	0.231	0.209	0.008	0.010	0.009	0.090	0.111	0.101	23.5
0.084	A	5	E	0.02	500	1	1.033	1.950	1.492	0.215	0.405	0.310	0.009	0.017	0.013	0.103	0.195	0.149	88.8
0.084	A	6	F	0.02	500	2	0.714	1.226	0.970	0.148	0.255	0.202	0.006	0.011	0.008	0.071	0.123	0.097	71.8
0.084	A	7	G	0.02	500	1	0.605	0.972	0.788	0.126	0.202	0.164	0.005	0.008	0.007	0.061	0.097	0.079	60.5
0.042	B	8	AA	0.02	500	1	1.029	1.729	1.379	0.214	0.359	0.287	0.009	0.015	0.012	0.103	0.173	0.138	68.0
0.042	B	9	II	0.02	500	2	0.973	1.819	1.396	0.202	0.378	0.290	0.008	0.016	0.012	0.097	0.182	0.140	86.9
0.042	B	10	JJ	0.02	500	2	0.961	2.148	1.554	0.200	0.447	0.323	0.008	0.019	0.014	0.096	0.215	0.155	123.6
0.042	B	11	KK	0.02	500	1	1.082	2.375	1.729	0.225	0.494	0.359	0.009	0.021	0.015	0.108	0.238	0.173	119.5
0.084	B	12	BB	0.02	500	2	0.897	1.416	1.157	0.187	0.294	0.240	0.016	0.025	0.020	0.090	0.142	0.116	57.8
0.084	B	13	GG	0.02	500	1	1.111	1.966	1.539	0.231	0.409	0.320	0.019	0.034	0.027	0.111	0.197	0.154	77.0
0.084	B	14	HH	0.02	500	2	1.260	3.201	2.231	0.262	0.666	0.464	0.022	0.056	0.039	0.126	0.320	0.223	154.0
0.084	C	15	A	0.02	500	1	2.062	2.829	2.446	0.429	0.588	0.508	0.036	0.049	0.043	0.206	0.283	0.245	37.2
0.084	C	16	B	0.02	500	2	1.163	1.720	1.442	0.242	0.358	0.300	0.020	0.030	0.025	0.116	0.172	0.144	47.9
0.084	C	17	C	0.02	500	1	1.797	2.377	2.087	0.374	0.494	0.434	0.031	0.042	0.036	0.180	0.238	0.209	32.3
Maximum							2.062	3.201	2.446	0.429	0.666	0.508	0.036	0.056	0.043	0.206	0.320	0.245	154.0
Minimum							0.496	0.972	0.765	0.103	0.202	0.159	0.004	0.008	0.007	0.050	0.097	0.077	23.5
Range							1.566	2.230	1.680	0.326	0.464	0.349	0.032	0.047	0.036	0.157	0.223	0.168	130.6
Mean							1.025	1.774	1.399	0.213	0.369	0.291	0.013	0.022	0.018	0.102	0.177	0.140	76.9
Standard deviation							0.406	0.660	0.506	0.084	0.137	0.105	0.010	0.015	0.012	0.041	0.066	0.051	35.7
Standard deviation (%)							39.6	37.2	36.2	39.6	37.2	36.2	72.0	66.4	67.0	39.6	37.2	36.2	46.5

Table N1: Summary of the global analysis running-in test results for the complete data set.

Forcing frequency	Material	Test case	Liner	Effective radius (m)	Centre plate load (N)	Centre plate	Min torque (Nm)	Max torque (Nm)	Mean torque (Nm)	Min energy per cycle (Joules)	Max energy per cycle (Joules)	Mean energy per cycle (Joules)	Min Power per cycle (Watts)	Max power per cycle (Watts)	Mean power per cycle (Watts)	Min μ	Max μ	Mean μ	Percentage increase in torque
0.042	A	1	A	0.02	500	1	0.539	1.077	0.808	0.112	0.224	0.168	0.005	0.009	0.007	0.054	0.108	0.081	100.0
0.042	A	2	B	0.02	500	2	0.800	1.201	1.001	0.166	0.250	0.208	0.007	0.010	0.009	0.080	0.120	0.100	50.0
0.042	A	3	C	0.02	500	1	0.496	1.034	0.765	0.103	0.215	0.159	0.004	0.009	0.007	0.050	0.103	0.077	108.4
0.042	A	4	D	0.02	500	2	0.900	1.111	1.005	0.187	0.231	0.209	0.008	0.010	0.009	0.090	0.111	0.101	23.5
0.084	A	5	E	0.02	500	1	1.033	1.950	1.492	0.215	0.405	0.310	0.009	0.017	0.013	0.103	0.195	0.149	88.8
0.084	A	6	F	0.02	500	2	0.714	1.226	0.970	0.148	0.255	0.202	0.006	0.011	0.008	0.071	0.123	0.097	71.8
0.084	A	7	G	0.02	500	1	0.605	0.972	0.788	0.126	0.202	0.164	0.005	0.008	0.007	0.061	0.097	0.079	60.5
Maximum							1.033	1.950	1.492	0.215	0.405	0.310	0.009	0.017	0.013	0.103	0.195	0.149	108.4
Minimum							0.496	0.972	0.765	0.103	0.202	0.159	0.004	0.008	0.007	0.050	0.097	0.077	23.5
Range							0.537	0.979	0.726	0.112	0.203	0.151	0.005	0.009	0.006	0.054	0.098	0.073	84.9
Mean							0.727	1.224	0.976	0.151	0.255	0.203	0.006	0.011	0.009	0.073	0.122	0.098	71.9
Standard deviation							0.197	0.332	0.250	0.041	0.069	0.052	0.002	0.003	0.002	0.020	0.033	0.025	29.9
Standard deviation (%)							27.1	27.1	25.6	27.1	27.1	25.6	27.1	27.1	25.6	27.1	27.1	25.6	41.6

Table N2: Summary of the global analysis results for material A.

Forcing frequency	Material	Test case	Liner	Effective radius (m)	Centre plate load (N)	Centre plate	Min torque (Nm)	Max torque (Nm)	Mean torque (Nm)	Min energy per cycle (Joules)	Max energy per cycle (Joules)	Mean energy per cycle (Joules)	Min Power per cycle (Watts)	Max power per cycle (Watts)	Mean power per cycle (Watts)	Min μ	Max μ	Mean μ	Percentage increase in torque
0.042	B	8	AA	0.02	500	1	1.029	1.729	1.379	0.214	0.359	0.287	0.009	0.015	0.012	0.103	0.173	0.138	68.0
0.042	B	9	II	0.02	500	2	0.973	1.819	1.396	0.202	0.378	0.290	0.008	0.016	0.012	0.097	0.182	0.140	86.9
0.042	B	10	JJ	0.02	500	2	0.961	2.148	1.554	0.200	0.447	0.323	0.008	0.019	0.014	0.096	0.215	0.155	123.6
0.042	B	11	KK	0.02	500	1	1.082	2.375	1.729	0.225	0.494	0.359	0.009	0.021	0.015	0.108	0.238	0.173	119.5
0.084	B	12	BB	0.02	500	2	0.897	1.416	1.157	0.187	0.294	0.240	0.016	0.025	0.020	0.090	0.142	0.116	57.8
0.084	B	13	GG	0.02	500	1	1.111	1.966	1.539	0.231	0.409	0.320	0.019	0.034	0.027	0.111	0.197	0.154	77.0
0.084	B	14	HH	0.02	500	2	1.260	3.201	2.231	0.262	0.666	0.464	0.022	0.056	0.039	0.126	0.320	0.223	154.0
Maximum							1.260	3.201	2.231	0.262	0.666	0.464	0.022	0.056	0.039	0.126	0.320	0.223	154.0
Minimum							0.897	1.416	1.157	0.187	0.294	0.240	0.008	0.015	0.012	0.090	0.142	0.116	57.8
Range							0.363	1.785	1.074	0.075	0.371	0.223	0.014	0.041	0.027	0.036	0.179	0.107	96.2
Mean							1.045	2.093	1.569	0.217	0.435	0.326	0.013	0.026	0.020	0.104	0.209	0.157	98.1
Standard deviation							0.120	0.576	0.342	0.025	0.120	0.071	0.006	0.015	0.010	0.012	0.058	0.034	35.0
Standard deviation (%)							11.5	27.5	21.8	11.5	27.5	21.8	43.7	54.8	50.2	11.5	27.5	21.8	35.6

Table N3: Summary of the global analysis results for material B.

Forcing frequency	Material	Test case	Liner	Effective radius (m)	Centre plate load (N)	Centre plate	Min torque (Nm)	Max torque (Nm)	Mean torque (Nm)	Min energy per cycle (Joules)	Max energy per cycle (Joules)	Mean energy per cycle (Joules)	Min Power per cycle (Watts)	Max power per cycle (Watts)	Mean power per cycle (Watts)	Min μ	Max μ	Mean μ	Percentage increase in torque
0.084	C	15	A	0.02	500	1	2.062	2.829	2.446	0.429	0.588	0.508	0.036	0.049	0.043	0.206	0.283	0.245	37.2
0.084	C	16	B	0.02	500	2	1.163	1.720	1.442	0.242	0.358	0.300	0.020	0.030	0.025	0.116	0.172	0.144	47.9
0.084	C	17	C	0.02	500	1	1.797	2.377	2.087	0.374	0.494	0.434	0.031	0.042	0.036	0.180	0.238	0.209	32.3
Maximum							2.062	2.829	2.446	0.429	0.588	0.508	0.036	0.049	0.043	0.206	0.283	0.245	47.9
Minimum							1.163	1.720	1.442	0.242	0.358	0.300	0.020	0.030	0.025	0.116	0.172	0.144	32.3
Range							0.899	1.109	1.004	0.187	0.231	0.209	0.016	0.019	0.018	0.090	0.111	0.100	15.6
Mean							1.674	2.309	1.991	0.348	0.480	0.414	0.029	0.040	0.035	0.167	0.231	0.199	39.1
Standard deviation							0.462	0.558	0.509	0.096	0.116	0.106	0.008	0.010	0.009	0.046	0.056	0.051	8.0
Standard deviation (%)							27.6	24.2	25.6	27.6	24.2	25.6	27.6	24.2	25.6	27.6	24.2	25.6	20.4

Table N4: Summary of the global analysis results for material C.

Forcing frequency	Material	Test case	Liner	Effective radius (m)	Centre plate load (N)	Centre plate	Min torque (Nm)	Max torque (Nm)	Mean torque (Nm)	Min energy per cycle (Joules)	Max energy per cycle (Joules)	Mean energy per cycle (Joules)	Min Power per cycle (Watts)	Max power per cycle (Watts)	Mean power per cycle (Watts)	Min μ	Max μ	Mean μ	Percentage increase in torque
0.042	A	1	A	0.14	24500	1	184.7	369.4	277.1	38.4	76.8	57.6	1.6	3.2	2.4	0.054	0.108	0.081	100.0
0.042	A	2	B	0.14	24500	2	274.5	411.9	343.2	57.1	85.6	71.4	2.4	3.6	3.0	0.080	0.120	0.100	50.0
0.042	A	3	C	0.14	24500	1	170.2	354.7	262.4	35.4	73.7	54.6	1.5	3.1	2.3	0.050	0.103	0.077	108.4
0.042	A	4	D	0.14	24500	2	308.6	381.1	344.8	64.2	79.2	71.7	2.7	3.3	3.0	0.090	0.111	0.101	23.5
0.084	A	5	E	0.14	24500	1	354.3	668.9	511.6	73.7	139.1	106.4	3.1	5.8	4.5	0.103	0.195	0.149	88.8
0.084	A	6	F	0.14	24500	2	244.8	420.5	332.6	50.9	87.4	69.2	2.1	3.7	2.9	0.071	0.123	0.097	71.8
0.084	A	7	G	0.14	24500	1	207.6	333.2	270.4	43.2	69.3	56.2	1.8	2.9	2.4	0.061	0.097	0.079	60.5
0.042	B	8	AA	0.14	24500	1	352.9	593.0	473.0	73.4	123.3	98.3	3.1	5.2	4.1	0.103	0.173	0.138	68.0
0.042	B	9	II	0.14	24500	2	333.8	623.9	478.9	69.4	129.7	99.6	2.9	5.4	4.2	0.097	0.182	0.140	86.9
0.042	B	10	JJ	0.14	24500	2	329.5	736.8	533.1	68.5	153.2	110.8	2.9	6.4	4.7	0.096	0.215	0.155	123.6
0.042	B	11	KK	0.14	24500	1	371.1	814.6	592.9	77.2	169.4	123.3	3.2	7.1	5.2	0.108	0.238	0.173	119.5
0.084	B	12	BB	0.14	24500	2	307.7	485.7	396.7	64.0	101.0	82.5	5.4	8.5	6.9	0.090	0.142	0.116	57.8
0.084	B	13	GG	0.14	24500	1	381.1	674.3	527.7	79.2	140.2	109.7	6.7	11.8	9.2	0.111	0.197	0.154	77.0
0.084	B	14	HH	0.14	24500	2	432.2	1097.9	765.1	89.9	228.3	159.1	7.5	19.2	13.4	0.126	0.320	0.223	154.0
0.084	C	15	A	0.14	24500	1	707.3	970.3	838.8	147.0	201.7	174.4	12.4	16.9	14.6	0.206	0.283	0.245	37.2
0.084	C	16	B	0.14	24500	2	398.9	590.0	494.4	82.9	122.7	102.8	7.0	10.3	8.6	0.116	0.172	0.144	47.9
0.084	C	17	C	0.14	24500	1	616.4	815.3	715.8	128.1	169.5	148.8	10.8	14.2	12.5	0.180	0.238	0.209	32.3
Maximum							707.3	1097.9	838.8	147.0	228.3	174.4	12.4	19.2	14.6	0.206	0.320	0.245	154.0
Minimum							170.2	333.2	262.4	35.4	69.3	54.6	1.5	2.9	2.3	0.050	0.097	0.077	23.5
Range							537.1	764.7	576.4	111.7	159.0	119.8	10.9	16.3	12.4	0.157	0.223	0.168	130.6
Mean							351.5	608.3	479.9	73.1	126.5	99.8	4.5	7.7	6.1	0.102	0.177	0.140	76.9
Standard deviation							139.2	226.3	173.7	28.9	47.0	36.1	3.3	5.1	4.1	0.041	0.066	0.051	35.7
Standard deviation (%)							39.6	37.2	36.2	39.6	37.2	36.2	72.0	66.4	67.0	39.6	37.2	36.2	46.5

Table N5: Summary of the full scale equivalent global analysis results.

Appendix O. Local analysis results for the running-in tests

The local analysis results during the first 25 cycles of the running-in tests for the complete data set are shown in Table O1 (17 test cases). This table shows the minimum/maximum torque responses, the static and dynamic Coefficient of Friction (COF) values, as well as the frictional energies and powers per cycle. From these results it can be seen that the COF values during the first 25 cycles for example, range between 0.05 – 0.22. These results were also broken down into materials A, B and C as can be seen in Tables O2, O3 and O4 respectively. From these it can be seen that the lowest COF overall of 0.05, was measured during test case 4 using material A, whereas the highest value of 0.22, was measured during test case 15 using material C.

The results during cycles 1475 – 1500 of the running-in tests are shown in Table O5 and from these, it can be seen that the COF values have increased slightly and now range between 0.06 – 0.27, which is a 23% increase in the peak COF value. This value as can be seen, was measured during test case 14 using material B, whereas the lowest value was measured during test case 4 using material A. The individual results for materials A, B and C during this stage of the running-in tests, are also shown Tables O6, O7 and O8 respectively.

The local analysis results during the last 25 cycles of the running-in test cases for the complete data set are shown in Table O9. The COF values as can be seen, now range between 0.06 – 0.32, which is another 15% increase relative to the previous measurements. Test case 14 however, is still producing the highest COF value overall, whereas the lowest value is still test case 4. The results for materials A, B and C during this stage of the running-in test cases are shown in Tables O10, O11 and O12 respectively. The torque responses and centre plate loading conditions listed in the tables below can now be converted to the full size equivalents using the torque and load scaling factors shown in Appendix D, which are seen to be 343 and 49 respectively.

| | Minimum | | | Maximum |

Test case	Forcing frequency	Material	Liner	Centre plate	Mass moment of inertia (kg.m²)	Maximum torque (N.m)	Minimum torque (N.m)	Range (N.m)	Mean value ± (N.m)	Max µ	Min µ	Mean µ	Maximum energy per cycle (Joules)	Minimum energy per cycle (Joules)	Mean energy per cycle (Joules)	Mean power per cycle at 0.042 Hertz (Watts)	Mean power per cycle at 0.084 Hertz (Watts)	Torsional stiffness (Nm/rad)	Breakout angle (mrad)	Torsional natural frequency (Hertz)
1	0.042	A	A	1	0.02145	0.88	-0.76	1.65	0.82	0.09	-0.08	0.08	0.18	-0.16	0.17	0.007	-	1418	0.62	40.9
2	0.042	A	B	2	0.02145	1.00	-1.01	2.01	1.01	0.10	-0.10	0.10	0.21	-0.21	0.21	0.009	-	3605	0.28	65.2
3	0.042	A	C	1	0.02145	1.02	-1.02	2.05	1.02	0.10	-0.10	0.10	0.21	-0.21	0.21	0.009	-	2508	0.41	54.4
4	0.042	A	D	2	0.02145	0.93	-0.54	1.47	0.74	0.09	-0.05	0.07	0.19	-0.11	0.15	0.006	-	4301	0.22	71.3
5	0.084	A	E	1	0.02145	1.24	-1.17	2.40	1.20	0.12	-0.12	0.12	0.26	-0.24	0.25	0.010	0.021	1513	0.82	42.3
6	0.084	A	F	2	0.02145	0.83	-0.96	1.79	0.89	0.08	-0.10	0.09	0.17	-0.20	0.19	0.008	0.016	2973	0.28	59.3
7	0.084	A	G	1	0.02145	0.97	-0.75	1.72	0.86	0.10	-0.07	0.09	0.20	-0.16	0.18	0.008	0.015	2557	0.38	54.9
8	0.042	B	AA	1	0.02145	1.06	-1.07	2.13	1.06	0.11	-0.11	0.11	0.22	-0.22	0.22	0.009	-	3656	0.29	65.7
9	0.042	B	II	1	0.02145	0.99	-1.01	2.00	1.00	0.10	-0.10	0.10	0.21	-0.21	0.21	0.009	-	3758	0.26	66.6
10	0.042	B	JJ	2	0.02145	0.99	-1.57	2.56	1.28	0.10	-0.16	0.13	0.21	-0.33	0.27	0.011	-	3372	0.29	63.1
11	0.042	B	KK	1	0.02145	1.90	-1.28	3.18	1.59	0.19	-0.13	0.16	0.40	-0.27	0.33	0.014	-	4572	0.42	73.5
12	0.084	B	BB	2	0.02145	0.94	-1.01	1.95	0.97	0.09	-0.10	0.10	0.19	-0.21	0.20	0.008	0.017	3054	0.31	60.1
13	0.084	B	GG	1	0.02145	1.15	-1.31	2.46	1.23	0.11	-0.13	0.12	0.24	-0.27	0.26	0.011	0.021	2848	0.40	58.0
14	0.084	B	HH	2	0.02145	1.35	-1.55	2.90	1.45	0.13	-0.16	0.15	0.28	-0.32	0.30	0.013	0.025	2353	0.57	52.7
15	0.084	C	A	1	0.02145	2.24	-1.70	3.94	1.97	0.22	-0.17	0.20	0.47	-0.35	0.41	0.017	0.034	4309	0.52	71.3
16	0.084	C	B	2	0.02145	1.20	-0.63	1.83	0.92	0.12	-0.06	0.09	0.25	-0.13	0.19	0.008	0.016	2495	0.48	54.3
17	0.084	C	C	1	0.02145	1.85	-1.29	3.14	1.57	0.19	-0.13	0.16	0.39	-0.27	0.33	0.014	0.027	4240	0.44	70.8
Maximum						2.24	-1.70	3.94	1.97	0.22	-0.17	0.20	0.47	-0.35	0.41	0.017	0.034	4572	0.82	73.5
Minimum						0.83	-0.54	1.47	0.74	0.08	-0.05	0.07	0.17	-0.11	0.15	0.006	0.015	1418	0.22	40.9
Range						1.41	-1.16	2.47	1.23	0.14	-0.12	0.12	0.29	-0.24	0.26	0.011	0.019	3154	0.60	32.6
Mean						1.21	-1.10	2.30	1.15	0.12	-0.11	0.11	0.25	-0.23	0.24	0.010	0.021	3149	0.41	60.3
Standard deviation						0.41	0.33	0.66	0.33	0.04	0.03	0.03	0.08	0.07	0.07	0.003	0.007	949	0.16	9.7
Standard deviation (%)						33.6	30.0	28.6	28.6	33.6	30.0	29.1	33.6	30.0	28.6	28.6	30.5	30.1	37.9	16.0

Table O1: Summary of the local analysis results during the first 25 cycles of the running-in tests.

Table O2 (Material A):

Test case	Forcing frequency	Material	Liner	Centre plate	Mass moment of inertia (kg.m²)	Maximum torque (N.m)	Minimum torque (N.m)	Range (N.m)	Mean value ± (N.m)	Max μ	Min μ	Mean μ	Maximum energy (Joules)	Minimum energy (Joules)	Total energy (Joules)	Mean energy per cycle (Joules)	Mean power per cycle at 0.042 Hertz (Watts)	Mean power per cycle at 0.084 Hertz (Watts)	Torsional stiffness (Nm/rad)	Breakout angle (mrad)	Torsional natural frequency (Hertz)
1	0.042	A	A	1	0.02145	0.88	-0.76	1.65	0.82	0.09	-0.08	0.08	4.58	-3.98	8.56	0.34	0.014	-	1418	0.62	40.9
2	0.042	A	B	2	0.02145	1.00	-1.01	2.01	1.01	0.10	-0.10	0.10	5.21	-5.24	10.45	0.42	0.018	-	3605	0.28	65.2
3	0.042	A	C	1	0.02145	1.02	-1.02	2.05	1.02	0.10	-0.10	0.10	5.32	-5.31	10.63	0.43	0.018	-	2508	0.41	54.4
4	0.042	A	D	2	0.02145	0.93	-0.54	1.47	0.74	0.09	-0.05	0.07	4.83	-2.81	7.64	0.31	0.013	-	4301	0.22	71.3
5	0.084	A	E	1	0.02145	1.24	-1.17	2.40	1.20	0.12	-0.12	0.12	6.42	-6.07	12.50	0.50	-	0.042	1513	0.82	42.3
6	0.084	A	F	2	0.02145	0.83	-0.96	1.79	0.89	0.08	-0.10	0.09	4.30	-4.98	9.28	0.37	-	0.031	2973	0.28	59.3
7	0.084	A	G	1	0.02145	0.97	-0.75	1.72	0.86	0.10	-0.07	0.09	5.05	-3.88	8.93	0.36	-	0.030	2557	0.38	54.9
Maximum						1.24	-1.17	2.40	1.20	0.12	-0.12	0.12	6.42	-2.81	12.50	0.50	0.018	0.042	4301	0.82	71.3
Minimum						0.83	-0.54	1.47	0.74	0.08	-0.05	0.07	4.30	-6.07	7.64	0.31	0.013	0.030	1418	0.22	40.9
Range						0.41	-0.63	0.93	0.47	0.04	-0.06	0.05	2.12	3.26	4.85	0.19	0.005	0.012	2883	0.60	30.3
Mean						0.98	-0.89	1.87	0.93	0.10	-0.09	0.09	5.10	-4.61	9.71	0.39	0.016	0.034	2696	0.43	55.5
Standard deviation						0.13	0.21	0.31	0.15	0.01	0.02	0.02	0.68	1.10	1.61	0.06	0.002	0.007	1046	0.22	11.2
Standard deviation (%)						13.4	23.9	16.6	16.6	13.4	23.9	16.6	13.4	23.9	16.6	16.6	15.7	19.2	38.8	50.6	20.1

Table O2: Summary of the local analysis results during the first 25 cycles of the running-in tests (Material A).

Table O3 (Material B):

Test case	Forcing frequency (Hz)	Material	Liner	Centre plate	Mass moment of inertia (kg.m²)	Maximum torque (N.m)	Minimum torque (N.m)	Range (N.m)	Mean value ± (N.m)	Max μ	Min μ	Mean μ	Maximum energy (Joules)	Minimum energy (Joules)	Total energy (Joules)	Mean energy per cycle (Joules)	Mean power per cycle at 0.042 Hertz (Watts)	Mean power per cycle at 0.084 Hertz (Watts)	Torsional stiffness (Nm/rad)	Breakout angle (mrad)	Torsional natural frequency (Hertz)
8	0.042	B	AA	1	0.02145	1.06	-1.07	2.13	1.06	0.11	-0.11	0.11	5.49	-5.56	11.05	0.44	0.019	-	3656	0.29	65.7
9	0.042	B	II	1	0.02145	0.99	-1.01	2.00	1.00	0.10	-0.10	0.10	5.16	-5.24	10.40	0.42	0.017	-	3758	0.26	66.6
10	0.042	B	JJ	2	0.02145	0.99	-1.57	2.56	1.28	0.10	-0.16	0.13	5.14	-8.17	13.31	0.53	0.022	-	3372	0.29	63.1
11	0.042	B	KK	1	0.02145	1.90	-1.28	3.18	1.59	0.19	-0.13	0.16	9.89	-6.66	16.55	0.66	0.028	-	4572	0.42	73.5
12	0.084	B	BB	2	0.02145	0.94	-1.01	1.95	0.97	0.09	-0.10	0.10	4.87	-5.24	10.11	0.40	-	0.034	3054	0.31	60.1
13	0.084	B	GG	1	0.02145	1.15	-1.31	2.46	1.23	0.11	-0.13	0.12	5.95	-6.81	12.77	0.51	-	0.043	2848	0.40	58.0
14	0.084	B	HH	2	0.02145	1.35	-1.55	2.90	1.45	0.13	-0.16	0.15	7.01	-8.08	15.08	0.60	-	0.051	2353	0.57	52.7
Maximum						1.90	-1.57	3.18	1.59	0.19	-0.16	0.16	9.89	-5.24	16.55	0.66	0.028	0.051	4572	0.57	73.5
Minimum						0.94	-1.01	1.95	0.97	0.09	-0.10	0.10	4.87	-8.17	10.11	0.40	0.017	0.034	2353	0.26	52.7
Range						0.97	-0.56	1.24	0.62	0.10	-0.06	0.06	5.02	2.93	6.44	0.26	0.010	0.017	2219	0.31	20.8
Mean						1.20	-1.26	2.45	1.23	0.12	-0.13	0.12	6.22	-6.54	12.75	0.51	0.022	0.043	3373	0.36	62.8
Standard deviation						0.34	0.24	0.47	0.23	0.03	0.02	0.02	1.77	1.26	2.44	0.10	0.005	0.008	717	0.11	6.7
Standard deviation (%)						28.5	19.2	19.1	19.1	28.5	19.2	19.1	28.5	19.2	19.1	19.1	21.7	19.7	21.3	30.1	10.7

Table O3: Summary of the local analysis results during the first 25 cycles of the running-in tests (Material B).

Table O4 (Material C):

Test case	Forcing frequency	Material	Liner	Centre plate	Mass moment of inertia (kg.m²)	Maximum torque (N.m)	Minimum torque (N.m)	Range (N.m)	Mean value ± (N.m)	Max μ	Min μ	Mean μ	Maximum energy (Joules)	Minimum energy (Joules)	Total energy (Joules)	Mean energy per cycle (Joules)	Mean power per cycle at 0.042 Hertz (Watts)	Mean power per cycle at 0.084 Hertz (Watts)	Torsional stiffness (Nm/rad)	Breakout angle (mrad)	Torsional natural frequency (Hertz)
15	0.084	C	A	1	0.02145	2.24	-1.70	3.94	1.97	0.22	-0.17	0.20	11.63	-8.84	20.47	0.82	-	0.069	4309	0.52	71.3
16	0.084	C	B	2	0.02145	1.20	-0.63	1.83	0.92	0.12	-0.06	0.09	6.24	-3.28	9.52	0.38	-	0.032	2495	0.48	54.3
17	0.084	C	C	1	0.02145	1.85	-1.29	3.14	1.57	0.19	-0.13	0.16	9.63	-6.68	16.31	0.65	-	0.055	4240	0.44	70.8
Maximum						2.24	-1.70	3.94	1.97	0.22	-0.06	0.20	11.63	-3.28	20.47	0.82	-	0.07	4309	0.52	71.3
Minimum						1.20	-0.63	1.83	0.92	0.12	-0.17	0.09	6.24	-8.84	9.52	0.38	-	0.03	2495	0.44	54.3
Range						1.04	-1.07	2.11	1.05	0.10	0.11	0.11	5.39	5.56	10.95	0.44	-	0.04	1814	0.08	17.1
Mean						1.76	-1.21	2.97	1.48	0.18	-0.12	0.15	9.17	-6.27	15.44	0.62	-	0.05	3681	0.48	65.5
Standard deviation						0.52	0.54	1.06	0.53	0.05	0.05	0.05	2.72	2.80	5.53	0.22	-	0.02	1028	0.04	9.7
Standard deviation (%)						29.7	44.7	35.8	35.8	29.7	44.7	35.8	29.7	44.7	35.8	35.8	-	35.8	27.9	8.6	14.8

Table O4: Summary of the local analysis results during the first 25 cycles of the running-in tests (Material C).

Legend: Minimum (green) — Maximum (red)

Table O5:

Test case	Forcing frequency	Material	Liner	Centre plate	Mass moment of inertia (kg.m²)	Maximum torque (N.m)	Minimum torque (N.m)	Range (N.m)	Mean value ± (N.m)	Max μ	Min μ	Mean μ	Maximum energy per cycle (Joules)	Minimum energy per cycle (Joules)	Mean energy per cycle (Joules)	Mean power per cycle at 0.042 Hertz (Watts)	Mean power per cycle at 0.084 Hertz (Watts)	Torsional stiffness (Nm/rad)	Breakout angle (mrad)	Torsional natural frequency (Hertz)
1	0.042	A	A	1	0.02145	0.94	-0.82	1.75	0.88	0.09	-0.08	0.09	0.19	-0.17	0.18	0.008	-	2130	0.44	50.2
2	0.042	A	B	2	0.02145	1.07	-1.08	2.15	1.07	0.11	-0.11	0.11	0.22	-0.22	0.22	0.009	-	4461	0.24	72.6
3	0.042	A	C	1	0.02145	1.09	-1.07	2.16	1.08	0.11	-0.11	0.11	0.23	-0.22	0.22	0.009	-	3121	0.35	60.7
4	0.042	A	D	2	0.02145	0.98	-0.58	1.56	0.78	0.10	-0.06	0.08	0.20	-0.12	0.16	0.007	-	4819	0.20	75.4
5	0.084	A	E	1	0.02145	1.72	-1.51	3.23	1.61	0.17	-0.15	0.16	0.36	-0.31	0.34	-	0.028	1810	0.95	46.2
6	0.084	A	F	2	0.02145	0.84	-1.10	1.94	0.97	0.08	-0.11	0.10	0.17	-0.23	0.20	-	0.017	3289	0.25	62.3
7	0.084	A	G	1	0.02145	0.81	-0.81	1.62	0.81	0.08	-0.08	0.08	0.17	-0.17	0.17	-	0.014	2503	0.32	54.4
8	0.042	B	AA	1	0.02145	1.64	-1.50	3.14	1.57	0.16	-0.15	0.16	0.34	-0.31	0.33	0.014	-	2688	0.61	56.3
9	0.042	B	II	1	0.02145	1.30	-1.45	2.75	1.37	0.13	-0.14	0.14	0.27	-0.30	0.29	0.012	-	3684	0.35	66.0
10	0.042	B	JJ	2	0.02145	1.29	-1.93	3.22	1.61	0.13	-0.19	0.16	0.27	-0.40	0.33	0.014	-	3166	0.41	61.1
11	0.042	B	KK	1	0.02145	2.01	-1.46	3.47	1.74	0.20	-0.15	0.17	0.42	-0.30	0.36	0.015	-	4474	0.45	72.7
12	0.084	B	BB	2	0.02145	1.33	-1.32	2.65	1.32	0.13	-0.13	0.13	0.28	-0.27	0.27	-	0.023	2462	0.54	53.9
13	0.084	B	GG	1	0.02145	1.52	-1.81	3.33	1.66	0.15	-0.18	0.17	0.31	-0.38	0.35	-	0.029	2890	0.52	58.4
14	0.084	B	HH	2	0.02145	2.11	-2.65	4.76	2.38	0.21	-0.27	0.24	0.44	-0.55	0.50	-	0.042	2629	0.80	55.7
15	0.084	C	A	1	0.02145	2.69	-2.18	4.87	2.44	0.27	-0.22	0.24	0.56	-0.45	0.51	-	0.043	3676	0.73	65.9
16	0.084	C	B	2	0.02145	1.57	-0.93	2.50	1.25	0.16	-0.09	0.12	0.33	-0.19	0.26	-	0.022	2594	0.60	55.3
17	0.084	C	C	1	0.02145	2.00	-1.51	3.51	1.75	0.20	-0.15	0.18	0.42	-0.31	0.36	-	0.031	4256	0.47	70.9
Maximum						2.69	-2.65	4.87	2.44	0.27	-0.27	0.24	0.56	-0.55	0.51	0.015	0.043	4819	0.95	75.4
Minimum						0.81	-0.58	1.56	0.78	0.08	-0.06	0.08	0.17	-0.12	0.16	0.007	0.014	1810	0.20	46.2
Range						1.89	-2.08	3.31	1.66	0.19	-0.21	0.17	0.39	-0.43	0.34	0.008	0.028	3009	0.75	29.2
Mean						1.46	-1.39	2.86	1.43	0.15	-0.14	0.14	0.30	-0.29	0.30	0.011	0.028	3215	0.49	61.1
Standard deviation						0.52	0.53	0.98	0.49	0.05	0.05	0.05	0.11	0.11	0.10	0.003	0.010	887	0.21	8.5
Standard deviation (%)						35.5	38.3	34.5	34.5	35.5	38.3	34.5	35.5	38.3	34.5	28.4	35.8	27.6	42.4	13.9

Table O5: Summary of the local analysis results during cycles 1475 – 1500 of the running-in tests.

Table O6 (Material A):

Test case	Forcing frequency	Material	Liner	Centre plate	Mass moment of inertia (kg.m²)	Maximum torque (N.m)	Minimum torque (N.m)	Range (N.m)	Mean value ± (N.m)	Max μ	Min μ	Mean μ	Maximum energy (Joules)	Minimum energy (Joules)	Total energy (Joules)	Mean energy per cycle (Joules)	Mean power per cycle at 0.042 Hertz (Watts)	Mean power per cycle at 0.084 Hertz (Watts)	Torsional stiffness (Nm/rad)	Breakout angle (mrad)	Torsional natural frequency (Hertz)
1	0.042	A	A	1	0.02145	0.94	-0.82	1.75	0.88	0.09	-0.08	0.09	4.86	-4.24	9.10	0.36	0.015	-	2130	0.44	50.2
2	0.042	A	B	2	0.02145	1.07	-1.08	2.15	1.07	0.11	-0.11	0.11	5.56	-5.61	11.17	0.45	0.019	-	4461	0.24	72.6
3	0.042	A	C	1	0.02145	1.09	-1.07	2.16	1.08	0.11	-0.11	0.11	5.69	-5.55	11.23	0.45	0.019	-	3121	0.35	60.7
4	0.042	A	D	2	0.02145	0.98	-0.58	1.56	0.78	0.10	-0.06	0.08	5.11	-3.00	8.11	0.32	0.014	-	4819	0.20	75.4
5	0.084	A	E	1	0.02145	1.72	-1.51	3.23	1.61	0.17	-0.15	0.16	8.96	-7.82	16.78	0.67	-	0.056	1810	0.95	46.2
6	0.084	A	F	2	0.02145	0.84	-1.10	1.94	0.97	0.08	-0.11	0.10	4.34	-5.74	10.08	0.40	-	0.034	3289	0.25	62.3
7	0.084	A	G	1	0.02145	0.81	-0.81	1.62	0.81	0.08	-0.08	0.08	4.20	-4.21	8.41	0.34	-	0.028	2503	0.32	54.4
Maximum						1.72	-1.51	3.23	1.61	0.17	-0.15	0.16	8.96	-7.82	16.78	0.67	0.019	0.056	4819	0.95	75.4
Minimum						0.81	-0.58	1.56	0.78	0.08	-0.06	0.08	4.20	-3.00	8.11	0.32	0.014	0.028	1810	0.20	46.2
Range						0.92	-0.93	1.67	0.83	0.09	-0.09	0.08	4.76	-4.82	8.67	0.35	0.005	0.028	3009	0.75	29.2
Mean						1.06	-0.99	2.06	1.03	0.11	-0.10	0.10	5.53	-5.17	10.70	0.43	0.017	0.040	3162	0.39	60.3
Standard deviation						0.31	0.30	0.57	0.28	0.03	0.03	0.03	1.61	1.54	2.96	0.12	0.003	0.015	1138	0.26	11.0
Standard deviation (%)						29.2	29.8	27.6	27.6	29.2	29.8	27.6	29.2	29.8	27.6	27.6	15.7	37.7	36.0	65.5	18.2

Table O6: Summary of the local analysis results during cycles 1475 – 1500 of the running-in tests (Material A).

Table O7 (Material B):

Test case	Forcing frequency	Material	Liner	Centre plate	Mass moment of inertia (kg.m²)	Maximum torque (N.m)	Minimum torque (N.m)	Range (N.m)	Mean value ± (N.m)	Max μ	Min μ	Mean μ	Maximum energy (Joules)	Minimum energy (Joules)	Total energy (Joules)	Mean energy per cycle (Joules)	Mean power per cycle at 0.042 Hertz (Watts)	Mean power per cycle at 0.084 Hertz (Watts)	Torsional stiffness (Nm/rad)	Breakout angle (mrad)	Torsional natural frequency (Hertz)
8	0.042	B	AA	1	0.02145	1.64	-1.50	3.14	1.57	0.16	-0.15	0.16	8.53	-7.78	16.31	0.65	0.027	-	2688	0.61	56.3
9	0.042	B	II	1	0.02145	1.30	-1.45	2.75	1.37	0.13	-0.14	0.14	6.74	-7.53	14.27	0.57	0.024	-	3684	0.35	66.0
10	0.042	B	JJ	2	0.02145	1.29	-1.93	3.22	1.61	0.13	-0.19	0.16	6.69	-10.05	16.75	0.67	0.028	-	3166	0.41	61.1
11	0.042	B	KK	1	0.02145	2.01	-1.46	3.47	1.74	0.20	-0.15	0.17	10.46	-7.59	18.05	0.72	0.030	-	4474	0.45	72.7
12	0.084	B	BB	2	0.02145	1.33	-1.32	2.65	1.32	0.13	-0.13	0.13	6.89	-6.86	13.75	0.55	-	0.046	2462	0.54	53.9
13	0.084	B	GG	1	0.02145	1.52	-1.81	3.33	1.66	0.15	-0.18	0.17	7.87	-9.42	17.30	0.69	-	0.058	2890	0.52	58.4
14	0.084	B	HH	2	0.02145	2.11	-2.65	4.76	2.38	0.21	-0.27	0.24	10.96	-13.79	24.76	0.99	-	0.083	2629	0.80	55.7
Maximum						2.11	-2.65	4.76	2.38	0.21	-0.27	0.24	10.96	-13.79	24.76	0.99	0.030	0.083	4474	0.80	72.7
Minimum						1.29	-1.32	2.65	1.32	0.13	-0.13	0.13	6.69	-6.86	13.75	0.55	0.024	0.046	2462	0.35	53.9
Range						0.82	-1.33	2.12	1.06	0.08	-0.13	0.11	4.27	-6.93	11.01	0.44	0.006	0.037	2012	0.45	18.8
Mean						1.60	-1.73	3.33	1.67	0.16	-0.17	0.17	8.31	-9.00	17.31	0.69	0.027	0.063	3142	0.53	60.6
Standard deviation						0.34	0.46	0.70	0.35	0.03	0.05	0.03	1.78	2.40	3.63	0.15	0.003	0.019	715	0.15	6.7
Standard deviation (%)						21.4	26.6	21.0	21.0	21.4	26.6	21.0	21.4	26.6	21.0	21.0	9.6	30.2	22.7	28.4	11.0

Table O7: Summary of the local analysis results during cycles 1475 – 1500 of the running-in tests (Material B).

Table O8 (Material C):

Test case	Forcing frequency	Material	Liner	Centre plate	Mass moment of inertia (kg.m²)	Maximum torque (N.m)	Minimum torque (N.m)	Range (N.m)	Mean value ± (N.m)	Max μ	Min μ	Mean μ	Maximum energy (Joules)	Minimum energy (Joules)	Total energy (Joules)	Mean energy per cycle (Joules)	Mean power per cycle at 0.042 Hertz (Watts)	Mean power per cycle at 0.084 Hertz (Watts)	Torsional stiffness (Nm/rad)	Breakout angle (mrad)	Torsional natural frequency (Hertz)
15	0.084	C	A	1	0.02145	2.69	-2.18	4.87	2.44	0.27	-0.22	0.24	14.00	-11.32	25.32	1.01	-	0.085	3907	0.69	67.9
16	0.084	C	B	2	0.02145	1.57	-0.93	2.50	1.25	0.16	-0.09	0.12	8.14	-4.84	12.99	0.52	-	0.044	2300	0.68	52.1
17	0.084	C	C	1	0.02145	2.00	-1.51	3.51	1.75	0.20	-0.15	0.18	10.40	-7.83	18.23	0.73	-	0.061	3626	0.55	65.4
Maximum						2.69	-2.18	4.87	2.44	0.27	-0.09	0.24	14.00	-4.84	25.32	1.01	-	0.09	3907	0.69	67.9
Minimum						1.57	-0.93	2.50	1.25	0.16	-0.22	0.12	8.14	-11.32	12.99	0.52	-	0.04	2300	0.55	52.1
Range						1.13	-1.25	2.37	1.19	0.11	0.12	0.12	5.86	6.48	12.34	0.49	-	0.04	1607	0.14	15.8
Mean						2.09	-1.54	3.63	1.81	0.21	-0.15	0.18	10.85	-8.00	18.85	0.75	-	0.06	3278	0.64	61.8
Standard deviation						0.57	0.62	1.19	0.60	0.06	0.06	0.06	2.96	3.24	6.19	0.25	-	0.02	858	0.08	8.5
Standard deviation (%)						27.2	40.5	32.9	32.9	27.2	40.5	32.9	27.2	40.5	32.9	32.9	-	32.9	26.2	12.1	13.7

Table O8: Summary of the local analysis results during cycles 1475 – 1500 of the running-in tests (Material C).

Minimum — Maximum

Test case	Forcing frequency (Hz)	Material	Liner	Centre plate	Mass moment of inertia (kg.m²)	Maximum torque (N.m)	Minimum torque (N.m)	Range (N.m)	Mean value (N.m)	Max μ	Min μ	Mean μ	Maximum energy per cycle (Joules)	Minimum energy per cycle (Joules)	Mean energy per cycle (Joules)	Mean power per cycle at 0.042 Hertz (Watts)	Mean power per cycle at 0.084 Hertz (Watts)	Torsional stiffness (Nm/rad)	Breakout angle (mrad)	Torsional natural frequency (Hertz)
1	0.042	A	A	1	0.02145	1.05	-0.88	1.93	0.97	0.11	-0.09	0.10	0.22	-0.18	0.20	0.008	-	2365	0.44	52.8
2	0.042	A	B	2	0.02145	1.11	-1.13	2.24	1.12	0.11	-0.11	0.11	0.23	-0.24	0.23	0.010	-	3695	0.30	66.1
3	0.042	A	C	1	0.02145	1.10	-1.11	2.22	1.11	0.11	-0.11	0.11	0.23	-0.23	0.23	0.010	-	2515	0.44	54.5
4	0.042	A	D	2	0.02145	1.03	-0.62	1.65	0.83	0.10	-0.06	0.08	0.21	-0.13	0.17	0.007	-	4560	0.23	73.4
5	0.084	A	E	1	0.02145	1.94	-1.64	3.58	1.79	0.19	-0.16	0.18	0.40	-0.34	0.37	-	0.031	1705	1.14	44.9
6	0.084	A	F	2	0.02145	0.83	-1.16	1.99	0.99	0.08	-0.12	0.10	0.17	-0.24	0.21	-	0.017	3745	0.22	66.5
7	0.084	A	G	1	0.02145	0.81	-0.81	1.62	0.81	0.08	-0.08	0.08	0.17	-0.17	0.17	-	0.014	2616	0.31	55.6
8	0.042	B	AA	1	0.02145	1.72	-1.60	3.32	1.66	0.17	-0.16	0.17	0.36	-0.33	0.35	0.014	-	3190	0.54	61.4
9	0.042	B	II	1	0.02145	1.43	-1.61	3.03	1.52	0.14	-0.16	0.15	0.30	-0.33	0.32	0.013	-	3667	0.39	65.8
10	0.042	B	JJ	2	0.02145	1.41	-2.11	3.51	1.76	0.14	-0.21	0.18	0.29	-0.44	0.36	0.015	-	3190	0.44	61.4
11	0.042	B	KK	1	0.02145	2.26	-1.86	4.13	2.06	0.23	-0.19	0.21	0.47	-0.39	0.43	0.018	-	4047	0.56	69.1
12	0.084	B	BB	2	0.02145	1.42	-1.40	2.82	1.41	0.14	-0.14	0.14	0.29	-0.29	0.29	-	0.025	2763	0.51	57.1
13	0.084	B	GG	1	0.02145	1.62	-1.95	3.57	1.78	0.16	-0.19	0.18	0.34	-0.41	0.37	-	0.031	2961	0.55	59.1
14	0.084	B	HH	2	0.02145	2.38	-3.10	5.48	2.74	0.24	-0.32	0.28	0.49	-0.64	0.57	-	0.048	2695	0.88	56.4
15	0.084	C	A	1	0.02145	2.73	-2.17	4.90	2.45	0.27	-0.22	0.24	0.57	-0.45	0.51	-	0.043	4104	0.66	69.6
16	0.084	C	B	2	0.02145	1.66	-1.04	2.70	1.35	0.17	-0.10	0.14	0.35	-0.22	0.28	-	0.024	2676	0.62	56.2
17	0.084	C	C	1	0.02145	2.01	-1.51	3.52	1.76	0.20	-0.15	0.18	0.42	-0.31	0.37	-	0.031	3335	0.60	62.8
Maximum						2.73	-3.10	5.48	2.74	0.27	-0.32	0.28	0.57	-0.64	0.57	0.018	0.048	4560	1.14	73.4
Minimum						0.81	-0.62	1.62	0.81	0.08	-0.06	0.08	0.17	-0.13	0.17	0.007	0.014	1705	0.22	44.9
Range						1.92	-2.47	3.86	1.93	0.19	-0.26	0.20	0.40	-0.51	0.40	0.011	0.034	2855	0.92	28.5
Mean						1.56	-1.51	3.07	1.53	0.16	-0.15	0.15	0.32	-0.31	0.32	0.012	0.029	3166	0.52	60.7
Standard deviation						0.56	0.61	1.10	0.55	0.06	0.06	0.06	0.12	0.13	0.11	0.004	0.011	736	0.23	7.2
Standard deviation (%)						36.0	40.5	35.9	35.9	36.0	41.5	36.3	36.0	40.5	35.9	31.6	37.5	23.2	44.6	11.9

Table O9: Summary of the local analysis results during the last 25 cycles of the running-in tests.

Test case	Forcing frequency (Hz)	Material	Liner	Centre plate	Mass moment of inertia (kg.m²)	Maximum torque (N.m)	Minimum torque (N.m)	Range (N.m)	Mean value (N.m)	Standard deviation (N.m)	Max μ	Min μ	Mean μ	Maximum energy (Joules)	Minimum energy (Joules)	Total energy (Joules)	Mean energy per cycle (Joules)	Mean power per cycle at 0.042 Hertz (Watts)	Mean power per cycle at 0.084 Hertz (Watts)	Torsional stiffness (Nm/rad)	Breakout angle (mrad)	Torsional natural frequency (Hertz)
1	0.042	A	A	1	0.02145	1.05	-0.88	1.93	0.97	0.76	0.11	-0.09	0.10	5.46	-4.58	10.05	0.40	0.017	-	2365	0.44	52.8
2	0.042	A	B	2	0.02145	1.11	-1.13	2.24	1.12	1.02	0.11	-0.11	0.11	5.77	-5.89	11.66	0.47	0.020	-	3695	0.30	66.1
3	0.042	A	C	1	0.02145	1.10	-1.11	2.22	1.11	1.00	0.11	-0.11	0.11	5.74	-5.77	11.51	0.46	0.019	-	2515	0.44	54.5
4	0.042	A	D	2	0.02145	1.03	-0.62	1.65	0.83	0.70	0.10	-0.06	0.08	5.35	-3.23	8.58	0.34	0.014	-	4560	0.23	73.4
5	0.084	A	E	1	0.02145	1.94	-1.64	3.58	1.79	1.44	0.19	-0.16	0.18	10.10	-8.50	18.60	0.74	-	0.062	1705	1.14	44.9
6	0.084	A	F	2	0.02145	0.83	-1.16	1.99	0.99	0.91	0.08	-0.12	0.10	4.31	-6.02	10.33	0.41	-	0.035	3745	0.22	66.5
7	0.084	A	G	1	0.02145	0.81	-0.81	1.62	0.81	0.74	0.08	-0.08	0.08	4.21	-4.19	8.40	0.34	-	0.028	2616	0.31	55.6
Maximum						1.94	-1.64	3.58	1.79	1.44	0.19	-0.16	0.18	10.10	-3.23	18.60	0.74	0.020	0.062	4560	1.14	73.4
Minimum						0.81	-0.62	1.62	0.81	0.70	0.08	-0.06	0.08	4.21	-8.50	8.40	0.34	0.014	0.028	1705	0.22	44.9
Range						1.13	-1.01	1.96	0.98	0.74	0.11	-0.10	0.10	5.89	-5.27	10.20	0.41	0.005	0.034	2855	0.92	28.5
Mean						1.13	-1.05	2.17	1.09	0.94	0.11	-0.10	0.11	5.85	-5.45	11.30	0.45	0.018	0.042	3029	0.44	59.1
Standard deviation						0.38	0.33	0.67	0.33	0.25	0.04	0.03	0.03	1.98	1.69	3.46	0.14	0.002	0.018	994	0.32	9.9
Standard deviation (%)						33.9	31.0	30.6	30.6	27.1	33.9	31.0	30.6	33.9	31.0	30.6	30.6	13.8	43.6	32.8	73.0	16.7

Table O10: Summary of the local analysis results during the last 25 cycles of the running-in tests (Material A).

Test case	Forcing frequency (Hz)	Material	Liner	Centre plate	Mass moment of inertia (kg.m²)	Maximum torque (N.m)	Minimum torque (N.m)	Range (N.m)	Mean value (N.m)	Standard deviation (N.m)	Max μ	Min μ	Mean μ	Maximum energy (Joules)	Minimum energy (Joules)	Total energy (Joules)	Mean energy per cycle (Joules)	Mean power per cycle at 0.042 Hertz (Watts)	Mean power per cycle at 0.084 Hertz (Watts)	Torsional stiffness (Nm/rad)	Breakout angle (mrad)	Torsional natural frequency (Hertz)
8	0.042	B	AA	1	0.02145	1.72	-1.60	3.32	1.66	1.26	0.17	-0.16	0.17	8.96	-8.29	17.25	0.69	0.029	-	3190	0.54	61.4
9	0.042	B	II	1	0.02145	1.43	-1.61	3.03	1.52	1.25	0.14	-0.16	0.15	7.41	-8.35	15.76	0.63	0.026	-	3667	0.39	65.8
10	0.042	B	JJ	2	0.02145	1.41	-2.11	3.51	1.76	1.38	0.14	-0.21	0.18	7.30	-10.94	18.24	0.73	0.031	-	3190	0.44	61.4
11	0.042	B	KK	1	0.02145	2.26	-1.86	4.13	2.06	1.48	0.23	-0.19	0.21	11.75	-9.69	21.44	0.86	0.036	-	4047	0.56	69.1
12	0.084	B	BB	2	0.02145	1.42	-1.40	2.82	1.41	1.13	0.14	-0.14	0.14	7.36	-7.29	14.65	0.59	-	0.049	2763	0.51	57.1
13	0.084	B	GG	1	0.02145	1.62	-1.95	3.57	1.78	1.42	0.16	-0.19	0.18	8.41	-10.13	18.54	0.74	-	0.062	2961	0.55	59.1
14	0.084	B	HH	2	0.02145	2.38	-3.10	5.48	2.74	2.07	0.24	-0.32	0.28	12.37	-16.09	28.46	1.14	-	0.096	2695	0.88	56.4
Maximum						2.38	-3.10	5.48	2.74	2.07	0.24	-0.32	0.28	12.37	-16.09	28.46	1.14	0.036	0.096	4047	0.88	69.1
Minimum						1.41	-1.40	2.82	1.41	1.13	0.14	-0.14	0.14	7.30	-7.29	14.65	0.59	0.026	0.049	2695	0.39	56.4
Range						0.98	-1.69	2.66	1.33	0.93	0.10	-0.18	0.14	5.07	-8.80	13.81	0.55	0.010	0.046	1352	0.49	12.7
Mean						1.75	-1.95	3.69	1.85	1.43	0.17	-0.20	0.19	9.08	-10.11	19.19	0.77	0.031	0.069	3216	0.55	61.5
Standard deviation						0.41	0.56	0.89	0.45	0.30	0.04	0.06	0.05	2.13	2.91	4.63	0.19	0.004	0.024	489	0.16	4.6
Standard deviation (%)						23.5	28.8	24.1	24.1	21.4	23.5	30.4	25.0	23.5	28.8	24.1	24.1	13.2	34.7	15.2	28.6	7.5

Table O11: Summary of the local analysis results during the last 25 cycles of the running-in tests (Material B).

Test case	Forcing frequency (Hz)	Material	Liner	Centre plate	Mass moment of inertia (kg.m²)	Maximum torque (N.m)	Minimum torque (N.m)	Range (N.m)	Mean value (N.m)	Standard deviation (N.m)	Max μ	Min μ	Mean μ	Maximum energy (Joules)	Minimum energy (Joules)	Total energy (Joules)	Mean energy per cycle (Joules)	Mean power per cycle at 0.042 Hertz (Watts)	Mean power per cycle at 0.084 Hertz (Watts)	Torsional stiffness (Nm/rad)	Breakout angle (mrad)	Torsional natural frequency (Hertz)
15	0.084	C	A	1	0.02145	2.73	-2.17	4.90	2.45	1.85	0.27	-0.22	0.24	14.18	-11.26	25.44	1.02	-	0.085	4104	0.66	69.6
16	0.084	C	B	2	0.02145	1.66	-1.04	2.70	1.35	1.04	0.17	-0.10	0.14	8.63	-5.41	14.04	0.56	-	0.047	2676	0.62	56.2
17	0.084	C	C	1	0.02145	2.01	-1.51	3.52	1.76	1.53	0.20	-0.15	0.18	10.46	-7.83	18.30	0.73	-	0.061	3335	0.60	62.8
Maximum						2.73	-2.17	4.90	2.45	1.85	0.27	-0.10	0.24	14.18	-5.41	25.44	1.02	-	0.09	4104	0.66	69.6
Minimum						1.66	-1.04	2.70	1.35	1.04	0.17	-0.22	0.14	8.63	-11.26	14.04	0.56	-	0.05	2676	0.60	56.2
Range						1.07	-1.13	2.19	1.10	0.80	0.11	0.11	0.11	5.55	5.85	11.40	0.46	-	0.04	1428	0.06	13.4
Mean						2.13	-1.57	3.71	1.85	1.47	0.21	-0.16	0.19	11.09	-8.17	19.26	0.77	-	0.06	3372	0.63	62.9
Standard deviation						0.54	0.57	1.11	0.55	0.40	0.05	0.06	0.06	2.83	2.94	5.76	0.23	-	0.02	715	0.03	6.7
Standard deviation (%)						25.5	36.0	29.9	29.9	27.5	25.5	36.0	29.9	25.5	36.0	29.9	29.9	-	29.9	21.2	5.0	10.7

Table O12: Summary of the local analysis results during the last 25 cycles of the running-in tests (Material C).

Appendix P. Global analysis results for the service tests

The torque responses, frictional energies and the increases in these parameters under the 3 kN loading conditions for materials A, B and C are shown in Table P1. The torque responses under this loading condition as can be seen, range between 5.25 – 17.5 Nm. Whereas the responses that were during the running-in test cases (0.5 kN loading conditions)0, were 5 – 10 times lower and seen to range between 0.496 – 3.2 Nm.

The percentage increase in torque responses for the complete data set as can be seen (5 tests), range between 78.9 – 105.9%. Whereas the mean value is seen to be 90.4% with a Standard Deviation (SD) of 11.6%. The mean value during the 17 running-in test cases however, was slightly lower at 76.9%, but the SD of this parameter as can be seen from the results shown in Appendix N, is significantly higher at 46.5%.

From the results shown in Table P1, it can also be seen that the frictional energies and powers of material A during test case 1 for example, are the lowest overall at 1.1 Joules (J) and 0.05 Watts (W) per cycle. Whereas the energies and powers of material C are seen to be the highest overall at 3.66 J and 0.31 W per cycle, but only during the first 3 – 5 hours of testing due to the decreasing friction characteristics. Whereas the frictional energies for material B during test cases 8 and 12, are then seen to be the highest overall after 15 hours of testing, ranging between 3.27 – 3.56 J per cycle.

Minimum value											Maximum value			

Forcing frequency (Hz)	Material	Test case	Liner	Centre plate load (kN)	Centre plate	Min torque (Nm)	Max torque (Nm)	Mean torque (Nm)	Min energy per cycle (Joules)	Max energy per cycle (Joules)	Mean energy per cycle (Joules)	Min power per cycle (Watts)	Max power per cycle (Watts)	Mean power per cycle (Watts)	Percentage increase in torque
0.042	A	1	A	3	1	5.25	9.65	7.45	1.10	2.02	1.56	0.05	0.08	0.07	83.9
	B	8	AA	3	1	9.50	17.00	13.25	1.99	3.56	2.77	0.08	0.15	0.12	78.9
0.084	A	5	E	3	1	6.90	13.00	9.95	1.44	2.72	2.08	0.12	0.23	0.17	88.4
	B	12	BB	3	2	8.00	15.60	11.80	1.67	3.27	2.47	0.14	0.27	0.21	95.0
	C	15	A	3	1	8.50	17.50	13.00	1.78	3.66	2.72	0.15	0.31	0.23	105.9
Maximum						9.50	17.50	13.25	1.99	3.66	2.77	0.15	0.31	0.23	105.9
Minimum						5.25	9.65	7.45	1.10	2.02	1.56	0.05	0.08	0.07	78.9
Mean						7.63	14.55	11.09	1.60	3.05	2.32	0.11	0.21	0.16	90.4
Range						4.25	7.85	5.80	0.89	1.64	1.21	0.10	0.22	0.16	26.9
Standard deviation						1.63	3.25	2.42	0.34	0.68	0.51	0.04	0.09	0.07	10.5
Standard deviation (%)						21.3	22.3	21.8	21.3	22.3	21.8	39.7	43.7	42.3	11.6

Table P1: Summary of the global torque, energy and power responses for the 3 kN loading cases.

From the summary of results shown in Table P2 for the 6 kN loading cases, it can be seen that the torque responses now range between 11.59 – 47.43 Nm, which is a 171% increase in the peak torque responses relative to the responses during the 3 kN loading cases. The mean torque value and SD of this parameter for the complete data set (6 tests), have also increased from 11.1 to 23.2 Nm from 21.8 to 33.4% in the 6 kN loading cases. The SD of the maximum torque values however, has doubled with respect to the previous analysis, from 22.3 to 45.2%.

The percentage increases in the torque responses have also increased and now range between 13.8 – 251.8%, whereas the mean increase for the complete data set is seen to be in the region of 115% with an SD of 81.2% (Table P2). Whereas under the 3 kN centre plate load, the mean percentage increase and SD parameters, were seen to be slightly lower at 90.4 and 11.6% respectively. The mean percentage increase during the running-in test cases however, was seen to be in the lowest overall at 76.9% out of all the loading cases that were analysed in this research work.

The lowest frictional energies and powers under the 6 kN centre plate loading condition are seen to be 2.43 J and 0.1 W per cycle, which were calculated during test case 4 using material A. The highest

values overall however, are seen to be 9.93 J and 0.83 W per cycle, which were calculated during test case 13 using material B. The mean frictional energy for the complete data set (6 test cases), has also increased to 4.85 J per cycle, whereas during the 3 kN loading cases, this parameter was seen to be 2.32 J. The mean frictional energy as expected, has doubled in 6 kN loading cases.

From this analyses it can be suggested that the friction characteristics of the centre plate/wear liner components are more sensitive to changes in the centre plate loading conditions, than they are to changes in the angular velocity. This conclusion can be drawn because the only parameter that has changed since the previous analysis for example (3 kN loading cases), is the centre plate load. The analysis of the service test results so far, also suggests that the mean frictional torque is directly proportional to the centre plate load.

Forcing frequency (Hz)	Material	Test case	Liner	Centre plate load (kN)	Centre plate	Min torque (Nm)	Max torque (Nm)	Mean torque (Nm)	Min energy per cycle (Joules)	Max energy per cycle (Joules)	Mean energy per cycle (Joules)	Min power per cycle (Watts)	Max power per cycle (Watts)	Mean power per cycle (Watts)	Percentage increase in torque
0.042	A	2	B	6	2	12.74	44.82	28.78	2.67	9.38	6.02	0.11	0.39	0.25	251.8
	A	4	D	6	2	11.59	14.79	13.19	2.43	3.10	2.76	0.10	0.13	0.12	27.6
	B	9	II	6	2	17.48	40.35	28.92	3.66	8.45	6.05	0.15	0.35	0.25	130.8
0.084	A	6	F	6	2	15.35	17.47	16.41	3.21	3.66	3.44	0.27	0.31	0.29	13.8
	B	13	GG	6	1	16.47	47.43	31.95	3.45	9.93	6.69	0.29	0.83	0.56	188.0
	C	16	A	6	2	14.16	25.16	19.66	2.96	5.27	4.12	0.25	0.44	0.35	77.7
Maximum						17.48	47.43	31.95	3.66	9.93	6.69	0.29	0.83	0.56	251.8
Minimum						11.59	14.79	13.19	2.43	3.10	2.76	0.10	0.13	0.12	13.8
Mean						14.63	31.67	23.15	3.06	6.63	4.85	0.20	0.41	0.30	115.0
Range						5.89	32.64	18.76	1.23	6.83	3.93	0.19	0.70	0.45	238.0
Standard deviation						2.24	14.32	7.74	0.47	3.00	1.62	0.08	0.23	0.15	93.3
Standard deviation (%)						15.3	45.2	33.4	15.3	45.2	33.4	42.5	56.9	48.7	81.2

Table P2: Summary of the torque, energy and power responses for the 6 kN loading cases.

The summary of results for the 9 kN loading cases are shown in Table P2 and from these it can be seen that the torque responses for the complete data set (5 test cases), now range between 17.5 – 96.2 Nm. The peak torque response under this loading condition however, has increased by 100% relative to the peak torque during the 6 kN loading cases. The mean torque response under the 9 kN loading condition as can be seen, is 39.6 Nm, whereas under the 6 and 3 kN loading conditions, the mean torque responses are seen to be 23.2 and Nm 11.1 Nm respectively, which clearly shows that the torque responses are proportional to the centre plate loading conditions.

The percentage increases in the torque responses under the 9 kN loading conditions are also seen to be the highest overall, ranging between 31.8 – 270%. The highest value of 270% was measured during test case 11 using material B. These increases however, are similar to those that were measured during the 6 kN loading cases, see test case 2 for example (Material A), where the increase in the torque response as a function of the number of running cycles is seen to be 252%.

The mean frictional energy and power for the complete data set has also increased by another 71 - 83% relative to the 6 kN loading cases. The energy as can be seen has increased from 4.85 to 8.3 J per cycle and the power, from 0.3 to 0.55 W. The SD`s of these parameters are seen to be slightly higher for the 9 kN loading cases as well, ranging between 41.2 – 68.2%, whereas for the 6 and 3 kN cases, the SD`s of the energy and power responses were seen to range between 15.3 – 56.9% and 21.3 – 43.7% respectively. This analyses clearly shows that the maximum torque responses become more widely dispersed about the mean values as the centre plate load increases.

Forcing frequency (Hz)	Material	Test case	Liner	Centre plate load (kN)	Centre plate	Min torque (Nm)	Max torque (Nm)	Mean torque (Nm)	Min energy per cycle (Joules)	Max energy per cycle (Joules)	Mean energy per cycle (Joules)	Min power per cycle (Watts)	Max power per cycle (Watts)	Mean power per cycle (Watts)	Percentage increase in torque
0.042	A	3	C	9	1	17.50	28.54	23.02	3.66	5.97	4.82	0.15	0.25	0.20	63.1
	B	11	KK	9	1	26.00	96.20	61.10	5.44	20.14	12.79	0.23	0.85	0.54	270.0
0.084	A	7	G	9	1	19.23	25.34	22.29	4.03	5.30	4.67	0.34	0.45	0.39	31.8
	B	14	HH	9	2	27.97	93.37	60.67	5.86	19.55	12.70	0.49	1.64	1.07	233.8
	C	17	C	9	1	20.13	41.59	30.86	4.21	8.71	6.46	0.35	0.73	0.54	106.6
Maximum						27.97	96.20	61.10	5.86	20.14	12.79	0.49	1.64	1.07	270.0
Minimum						17.50	25.34	22.29	3.66	5.30	4.67	0.15	0.25	0.20	31.8
Mean						22.17	57.01	39.59	4.64	11.93	8.29	0.31	0.78	0.55	141.1
Range						10.47	70.86	38.82	2.19	14.83	8.13	0.34	1.39	0.86	238.2
Standard deviation						4.55	35.03	19.73	0.95	7.33	4.13	0.13	0.53	0.32	105.4
Standard deviation (%)						20.5	61.5	49.8	20.5	61.5	49.8	41.2	68.2	58.6	74.7

Table P3: Summary of the torque, energy and power responses for the 9 kN loading cases.

Appendix Q. Coefficient of friction values

The Coefficient of Friction (COF) values that were calculated from the measured torque responses on materials A, B and C during the 3, 6 and 9 kN loading cases are summarised in Tables Q1, Q2 and Q3 respectively. The elements that are highlighted in green show the minimum COF values, whereas the ones that are highlighted in red, show the maximum values.

The maximum COF value overall that was calculated under the 3 kN loading condition as can be seen, was 0.28 during test case 8 using material B, whereas the lowest value was 0.09 during test case 1 using material A, see Table Q1. The mean COF value for the five test cases that were carried out under the 3 kN centre plate load, is seen to be 0.18 with a Standard Deviation (SD) of 20%. The mean COF value for the complete data set during the running-in tests however (17 test cases, Appendix N), was slightly lower at 0.14, whereas the SD was 36.4%.

The maximum and minimum COF values under the 6 kN load were also calculated for materials A and B during test cases 4 and 13 respectively, see Table Q2. The mean COF value for the complete data as can be seen, is 0.18 and also the same as the 3 kN loading condition mean COF value, whereas the SD has increased from 20 to 31.9%.

The COF values under the 9 kN centre plate loading condition are shown in Table Q3 and from these, it can be seen the maximum values during test cases 11 and 14 using material B, are closely matched and shown to be 0.54 and 0.53 respectively, which are the highest COF values overall. The mean COF value for the complete data set and the SD of this values are also seen to be the highest overall at 0.21 and 48.2%. This analyses clearly shows that the torque responses of the centre plate/wear liner components start to become more widely dispersed about the mean values as centre plate load increases.

The mean COF values that were calculated for materials A, B and C after the running-in/service test cases were also combined together to identify the running conditions that produced the minimum and maximum COF values overall, see Table Q4. From this table, it can be seen that the 9 kN loading cases using material B produced the maximum mean COF values overall at 0.33 during the 0.042 Hertz (Hz) as well as the 0.084 Hz forcing frequency tests cases. This analysis shows that the friction characteristics of the centre plate/wear liner components are more sensitive to changes in the loading conditions, than they are to changes in the rotational velocity.

The lowest mean COF value overall for example, is seen to be 0.075 using material A which was running at 0.042 Hz and under the 0.5 kN/running-in centre plate loading condition. The next lowest COF value in the data set, is seen to be 0.08, which was also produced during the running-in test cases using material A. From these results it can also be seen that the SD`s of the COF values that were calculated for the 0.42 and 0.84 Hz test cases, are closely matched at 43% and 35.2% respectively.

The deviations of the four different loading conditions on the other hand, are seen to range between 18.8% – 49%. This analyses therefore, also shows that the influence of the angular velocity on the friction characteristics of the centre plate/wear liner components, is relatively weak in comparison to the sensitivities associated with the changes in centre plate loading conditions.

	Minimum		Maximum

Forcing frequency (Hertz)	Material	Test case	Liner	Centre plate load (kN)	Centre plate	Min μ	Max μ	Mean μ
0.042	A	1	A	3	1	0.09	0.16	0.13
	B	8	AA	3	1	0.11	0.28	0.20
0.084	A	5	E	3	1	0.11	0.22	0.17
	B	12	BB	3	2	0.10	0.26	0.18
	C	15	A	3	1	0.17	0.27	0.22
Maximum						0.17	0.28	0.22
Minimum						0.09	0.16	0.13
Mean						0.12	0.24	0.18
Range						0.08	0.12	0.10
Standard deviation						0.031	0.049	0.035
Standard deviation (%)						27.0	20.7	20.0

Table Q1: Summary of the COF values under the 3 kN centre plate load.

Forcing frequency (Hertz)	Material	Test case	Liner	Centre plate load (kN)	Centre plate	Min μ	Max μ	Mean μ
0.042	A	2	B	6	2	0.10	0.36	0.23
	A	4	D	6	2	0.09	0.12	0.11
	B	9	II	6	2	0.11	0.34	0.23
0.084	A	6	F	6	2	0.13	0.14	0.14
	B	13	GG	6	1	0.10	0.39	0.25
	C	16	B	6	2	0.10	0.21	0.16
Maximum						0.13	0.39	0.25
Minimum						0.09	0.12	0.11
Mean						0.11	0.26	0.18
Range						0.04	0.27	0.14
Standard deviation						0.014	0.118	0.058
Standard deviation (%)						13.1	45.4	31.9

Table Q2: Summary of the COF values under the 6 kN centre plate load.

Forcing frequency (Hertz)	Material	Test case	Liner	Centre plate load (kN)	Centre plate	Min μ	Max μ	Mean μ
0.042	A	3	C	9	1	0.10	0.16	0.13
	B	11	KK	9	1	0.11	0.54	0.33
0.084	A	7	G	9	1	0.10	0.14	0.12
	B	14	HH	9	2	0.12	0.53	0.33
	C	17	C	9	1	0.11	0.23	0.17
Maximum						0.12	0.54	0.33
Minimum						0.10	0.14	0.12
Mean						0.11	0.32	0.21
Range						0.02	0.40	0.21
Standard deviation						0.008	0.199	0.103
Standard deviation (%)						7.7	62.2	48.2

Table Q3: Summary of the COF values under the 9 kN centre plate load.

Material/liner	0.042 Hertz	0.084 Hertz	0.5 kN	3 kN	6 kN	9 kN
A	0.13	0.17	0.08	0.13	0.23	0.13
	0.23	0.14	0.1	0.17	0.11	0.12
	0.23	0.12	0.075	-	0.14	-
	0.13	0.15	0.1	-	-	-
	0.08	0.1	0.15	-	-	-
	0.1	0.08	0.1	-	-	-
	0.075	-	0.08	-	-	-
	0.1	-	-	-	-	-
B	0.2	0.18	0.14	0.2	0.23	0.33
	0.23	0.25	0.14	0.18	0.25	0.33
	0.33	0.33	0.155	-	-	-
	0.14	0.12	0.175	-	-	-
	0.14	0.155	0.12	-	-	-
	0.155	0.22	0.155	-	-	-
	0.175	-	0.22	-	-	-
C	-	0.22	0.25	0.22	0.16	0.17
	-	0.16	0.14	-	-	-
	-	0.17	0.21	-	-	-
	-	0.25	-	-	-	-
	-	0.14	-	-	-	-
	-	0.21	-	-	-	-
Maximum	0.33	0.33	0.25	0.22	0.25	0.33
Minimum	0.075	0.08	0.075	0.13	0.11	0.12
Range	0.255	0.25	0.175	0.09	0.14	0.21
Mean	0.16	0.18	0.14	0.18	0.19	0.22
Standard deviation	0.07	0.06	0.05	0.03	0.06	0.11
Standard deviation (%)	43.0	35.2	36.4	18.8	30.8	49.0

Table Q4: Summary of the running-in and service test mean COF values.

Appendix R. Local analysis results for the service tests

The summary of the local analysis results for material A during the 10800 cycle service test cases are shown in Table R1. The top and middle tables show the results during the first 25 cycles and during cycles 1475 – 1500, whereas the bottom table shows the results during the last 25 cycles of the service test cases. These tables also show the stick and slip torque responses and the torsional stiffness coefficients as well as the breakout angles for each centre plate/wear liner sample. The contact stresses, moduli`s of elasticity and the stick/slip COF values are also shown and finally, the frictional energies per cycle, which are the parameters that are used to validate the responses of the optimised friction models.

From the results shown in Table R1, it can be that the mean values for stick torque responses using material A are seen to be 15.1, 18.4 and 21.3 Nm during the three different stages of the service test cases. Whereas the slip values on the other hand, are seen to be 12.9, 15.9 and 18.4 Nm which clearly shows that the slip responses in this material are around 15 – 17% lower than the stick responses. The SD`s of these parameters as can be seen, range between 39.1 – 57.6%.

The mean value of the torsional stiffness coefficients that were calculated for material A under the 3, 6 and 9 kN centre plate loading conditions, range between 5883 – 5906 Nm/rad. The SD`s of these parameters however, are seen to be the lowest overall, ranging between 3.2 – 5.7%, which suggests that these stiffness coefficients as well as the moduli`s of elasticity, have a relatively low influence on the variations observed in the torque/COF responses.

The SD`s in pre-test surface roughness measurements on the centre plate components on the other hand, have the most significant influence on the variations. The normal and shear stresses are also seen to have a fairly strong influence on the variations observed in the in the torque/COF responses of the same materials, as well as the breakout angles and the energy responses, as these SD`s for example, are also seen to be relatively high, ranging between 39.1 – 57.6%.

Minimum value (green)   **Maximum value** (red)

Test case	Material	Centre plate	Liner	Centre plate load (kN)	Centre plate radius (m)	Mass moment of Inertia (kg.m²)	Equivalent mass (kg)	Forcing frequency (Hz)	Stick torque (Nm)	Slip torque (Nm)	Torsional stiffness (Nm/rad)	Breakout angle (mrads)	Torsional natural frequency (Hertz)	Stick shear stress (kN/m²)	Slip shear stress (kN/m²)	Normal stress (kN/m²)	Stick shear modulus (MN/m²)	Slip shear modulus (MN/m²)	Stick µ	Slip µ	Mean µ	Maximum energy per cycle (Joules)	Minimum energy per cycle (Joules)	Mean energy per cycle (Joules)
1	A	1	A	3	0.029	0.13	305.8	0.042	6.2	5.4	5188	1.19	32.0	120.5	106.7	1135.5	101.6	89.9	0.11	0.09	0.10	1.28	1.13	1.21
2	A	2	B	6	0.029	0.26	611.6	0.042	16.3	13.3	6031	2.70	24.4	318.9	260.4	2270.9	118.1	96.4	0.14	0.11	0.13	3.39	2.77	3.08
3	A	1	C	9	0.029	0.39	917.4	0.042	22.0	18.9	5895	3.73	19.7	430.7	369.0	3406.4	115.4	98.9	0.13	0.11	0.12	4.57	3.92	4.25
4	A	2	D	6	0.029	0.26	611.6	0.042	13.7	12.0	5978	2.29	24.3	267.6	235.1	2270.9	117.0	102.8	0.12	0.10	0.11	2.84	2.50	2.67
5	A	1	E	3	0.029	0.13	305.8	0.084	9.1	8.1	5940	1.53	34.2	177.6	157.8	1135.5	116.3	103.3	0.16	0.14	0.15	1.89	1.68	1.78
6	A	2	F	6	0.029	0.26	611.6	0.084	16.0	13.8	6081	2.63	24.5	312.8	270.4	2270.9	119.0	102.9	0.14	0.12	0.13	3.32	2.87	3.10
7	A	1	G	9	0.029	0.39	917.4	0.084	22.3	19.0	6226	3.58	20.2	435.8	372.2	3406.4	121.9	104.1	0.13	0.11	0.12	4.63	3.95	4.29
Maximum									22.3	19.0	6226	3.73	34.2	435.8	372.2	3406.4	121.9	104.1	0.16	0.14	0.15	4.63	3.95	4.29
Minimum									6.2	5.4	5188	1.19	19.7	120.5	106.7	1135.5	101.6	89.9	0.11	0.09	0.10	1.28	1.13	1.21
Range									16.1	13.6	1038	2.55	14.5	315.3	265.5	2270.9	20.3	14.2	0.05	0.05	0.05	3.35	2.82	3.08
Mean									15.1	12.9	5906	2.52	25.6	294.8	253.1	2270.9	115.6	99.8	0.13	0.11	0.12	3.13	2.69	2.91
Standard deviation									6.0	5.1	334	0.95	5.5	118.4	99.0	927.1	6.5	5.2	0.02	0.01	0.02	1.26	1.05	1.15
Standard deviation (%)									40.2	39.1	5.7	37.8	21.6	40.2	39.1	40.8	5.7	5.2	12.5	12.6	12.5	40.2	39.1	39.7

Test case	Material	Centre plate	Liner	Centre plate load (kN)	Centre plate radius (m)	Mass moment of Inertia (kg.m²)	Equivalent mass (kg)	Forcing frequency (Hz)	Stick torque (Nm)	Slip torque (Nm)	Torsional stiffness (Nm/rad)	Breakout angle (mrads)	Torsional natural frequency (Hertz)	Stick shear stress (kN/m²)	Slip shear stress (kN/m²)	Normal stress (kN/m²)	Stick shear modulus (MN/m²)	Slip shear modulus (MN/m²)	Stick µ	Slip µ	Mean µ	Maximum energy per cycle (Joules)	Minimum energy per cycle (Joules)	Mean energy per cycle (Joules)
1	A	1	A	3	0.029	0.13	305.8	0.042	9.1	7.9	5612	1.63	33.2	178.7	154.2	1135.5	109.9	94.8	0.16	0.14	0.15	1.90	1.64	1.77
2	A	2	B	6	0.029	0.26	611.6	0.042	29.4	24.4	5662	5.20	23.6	576.2	478.1	2270.9	110.8	92.0	0.25	0.21	0.23	6.12	5.08	5.60
3	A	1	C	9	0.029	0.39	917.4	0.042	25.9	22.5	5867	4.42	19.6	507.8	441.3	3406.4	114.9	99.8	0.15	0.13	0.14	5.39	4.69	5.04
4	A	2	D	6	0.029	0.26	611.6	0.042	14.4	12.6	5741	2.51	23.8	281.9	247.3	2270.9	112.4	98.6	0.12	0.11	0.12	2.99	2.63	2.81
5	A	1	E	3	0.029	0.13	305.8	0.084	10.8	9.9	5811	1.86	33.8	211.2	193.1	1135.5	113.8	104.0	0.19	0.17	0.18	2.24	2.05	2.15
6	A	2	F	6	0.029	0.26	611.6	0.084	15.6	13.8	6223	2.51	24.8	305.4	269.6	2270.9	121.8	107.5	0.13	0.12	0.13	3.24	2.86	3.05
7	A	1	G	9	0.029	0.39	917.4	0.084	23.6	20.4	6263	3.76	20.3	461.2	399.8	3406.4	122.8	106.3	0.14	0.12	0.13	4.90	4.25	4.57
Maximum									29.4	24.4	6263	5.20	33.8	576.2	478.1	3406.4	122.6	107.5	0.25	0.21	0.23	6.12	5.08	5.60
Minimum									9.1	7.9	5612	1.63	19.6	178.7	154.2	1135.5	109.9	92.0	0.12	0.11	0.12	1.90	1.64	1.77
Range									20.3	16.5	651	3.57	14.2	397.4	323.8	2270.9	12.7	15.6	0.13	0.10	0.12	4.22	3.44	3.83
Mean									18.4	15.9	5883	3.13	25.6	360.4	311.9	2270.9	115.2	100.4	0.16	0.14	0.15	3.83	3.31	3.57
Standard deviation									7.9	6.5	261	1.35	5.7	154.3	127.2	927.1	5.1	5.8	0.04	0.04	0.04	1.64	1.35	1.49
Standard deviation (%)									42.8	40.8	4.4	43.3	22.5	42.8	40.8	40.8	4.4	5.8	27.5	25.7	26.6	42.8	40.8	41.9

Table R1:

Test case	Material	Centre plate	Liner	Centre plate load (kN)	Centre plate radius (m)	Mass moment of Inertia (kg.m²)	Equivalent mass (kg)	Forcing frequency (Hz)	Stick torque (Nm)	Slip torque (Nm)	Torsional stiffness (Nm/rad)	Breakout angle (mrads)	Torsional natural frequency (Hertz)	Stick shear stress (kN/m²)	Slip shear stress (kN/m²)	Normal stress (kN/m²)	Stick shear modulus (MN/m²)	Slip shear modulus (MN/m²)	Stick μ	Slip μ	Mean μ	Maximum energy per cycle (Joules)	Minimum energy per cycle (Joules)	Mean energy per cycle (Joules)
1	A	1	A	3	0.029	0.13	305.8	0.042	9.8	8.2	5760	1.71	33.7	192.6	160.3	1135.5	112.8	93.9	0.17	0.14	0.16	2.05	1.70	1.87
2	A	2	B	6	0.029	0.26	611.6	0.042	44.6	37.6	5787	7.71	23.9	872.9	736.1	2270.9	113.3	95.5	0.36	0.31	0.34	9.27	7.82	8.54
3	A	1	C	9	0.029	0.39	917.4	0.042	27.6	24.2	5970	4.63	19.8	540.7	473.8	3406.4	116.9	102.4	0.16	0.14	0.15	5.74	5.03	5.39
4	A	2	D	6	0.029	0.26	611.6	0.042	14.8	12.7	5875	2.51	24.1	288.8	248.8	2270.9	115.0	99.1	0.13	0.11	0.12	3.07	2.64	2.85
5	A	1	E	3	0.029	0.13	305.8	0.084	10.9	10.2	5737	1.90	33.6	213.8	198.7	1135.5	112.3	104.4	0.19	0.18	0.18	2.27	2.11	2.19
6	A	2	F	6	0.029	0.26	611.6	0.084	16.2	14.4	5867	2.77	24.0	317.9	281.1	2270.9	114.9	101.6	0.14	0.12	0.13	3.38	2.99	3.18
7	A	1	G	9	0.029	0.39	917.4	0.084	25.2	21.8	6283	4.01	20.3	493.1	426.4	3406.4	123.0	106.4	0.14	0.13	0.13	5.24	4.53	4.88
Maximum									44.6	37.6	6283	7.71	33.7	872.9	736.1	3406.4	123.0	106.4	0.36	0.31	0.34	9.27	7.82	8.54
Minimum									9.8	8.2	5737	1.71	19.8	192.6	160.3	1135.5	112.3	93.9	0.13	0.11	0.12	2.05	1.70	1.87
Range									34.8	29.4	546	6.00	13.9	680.4	575.8	2270.9	10.7	12.5	0.23	0.20	0.22	7.23	6.11	6.67
Mean									21.3	18.4	5897	3.60	25.6	417.1	360.7	2270.9	115.4	100.5	0.18	0.16	0.17	4.43	3.83	4.13
Standard deviation									12.3	10.3	188	2.10	5.8	240.5	201.4	927.1	3.7	4.6	0.08	0.07	0.07	2.55	2.14	2.35
Standard deviation (%)									57.6	55.8	3.2	58.2	22.5	57.6	55.8	40.8	3.2	4.5	43.5	43.0	43.3	57.6	55.8	56.8

Table R1: Summary of the local analysis results for material A during the 10800 cycle service tests. (Top) First 25 cycles. (Middle) Cycles 1475 – 1500. (Bottom) Last 25 cycles.

Table R2 shows a summary of the service test results for material B and from these it can be that the mean value for stick torque responses during the three stages of the service tests, are seen to be 20.8, 44.8 and 50.4 Nm, whereas the slip values are seen to be 12.9, 35.3 and 38.6 Nm. This analyses shows that the slip responses are 22 – 38% lower than the stick responses. The SD`s of these responses however, range between 50.8 – 69.3% which are around 10% higher than the deviations that were measured on material A.

The mean value of the torsional stiffness coefficients that were calculated for material B under the 3, 6 and 9 kN centre plate loading conditions, are slightly lower than the range of values that were calculated for material A, ranging between 5638 – 5697 Nm/rad. The SD`s of these values however, are seen to range between 4.5 – 5.3%, which are very similar to the SD`s that were calculated for material A (3.2 – 5.7%).

Table R2 (Top) First 25 cycles:

Test case	Material	Centre plate	Liner	Centre plate load (kN)	Centre plate radius (m)	Mass moment of Inertia (kg.m²)	Equivalent mass (kg)	Forcing frequency (Hz)	Stick torque (Nm)	Slip torque (Nm)	Torsional stiffness (Nm/rad)	Breakout angle (mrads)	Torsional natural frequency (Hertz)	Stick shear stress (kN/m²)	Slip shear stress (kN/m²)	Normal stress (kN/m²)	Stick shear modulus (MN/m²)	Slip shear modulus (MN/m²)	Stick μ	Slip μ	Mean μ	Maximum energy per cycle (Joules)	Minimum energy per cycle (Joules)	Mean energy per cycle (Joules)
8	B	1	AA	3	0.029	0.13	305.8	0.042	10.0	6.4	5700	1.75	33.5	195.6	125.8	1135.5	111.6	71.8	0.17	0.11	0.14	2.08	1.34	1.71
9	B	2	II	6	0.029	0.26	611.6	0.042	18.8	12.5	5747	3.27	23.8	368.4	244.3	2270.9	112.5	74.6	0.16	0.11	0.13	3.91	2.59	3.25
11	B	1	KK	9	0.029	0.39	917.4	0.042	31.9	19.5	5192	6.14	18.5	623.7	381.9	3406.4	101.6	62.2	0.18	0.11	0.15	6.62	4.06	5.34
12	B	3	BB	3	0.029	0.13	305.8	0.084	8.5	5.5	5458	1.55	32.8	166.1	108.3	1135.5	106.9	69.7	0.15	0.10	0.12	1.76	1.15	1.46
13	B	1	GG	6	0.029	0.26	611.6	0.084	19.6	12.0	5872	3.33	24.0	382.9	235.7	2270.9	115.0	70.8	0.17	0.10	0.14	4.07	2.50	3.28
14	B	2	HH	9	0.029	0.39	917.4	0.084	36.0	21.6	5858	6.15	19.6	705.2	422.1	3406.4	114.7	68.6	0.21	0.12	0.17	7.49	4.48	5.99
Maximum									36.0	21.6	5872	6.15	33.5	705.2	422.1	3406.4	115.0	74.6	0.21	0.12	0.17	7.49	4.48	5.99
Minimum									8.5	5.5	5192	1.55	18.5	166.1	108.3	1135.5	101.6	62.2	0.15	0.10	0.12	1.76	1.15	1.46
Range									27.5	16.0	680	4.59	15.0	539.1	313.8	2270.9	13.3	12.4	0.06	0.03	0.04	5.72	3.33	4.53
Mean									20.8	12.9	5638	3.70	25.4	407.0	253.0	2270.9	110.4	69.6	0.17	0.11	0.14	4.32	2.69	3.50
Standard deviation									11.2	6.6	265	2.03	6.4	219.4	128.6	1015.6	5.2	4.2	0.02	0.01	0.01	2.33	1.37	1.85
Standard deviation (%)									53.9	50.8	4.7	54.9	25.3	53.9	50.8	44.7	4.7	6.0	11.9	8.7	10.6	53.9	50.8	52.7

Table R2 (Middle) Cycles 1475 – 1500:

Test case	Material	Centre plate	Liner	Centre plate load (kN)	Centre plate radius (m)	Mass moment of Inertia (kg.m²)	Equivalent mass (kg)	Forcing frequency (Hz)	Stick torque (Nm)	Slip torque (Nm)	Torsional stiffness (Nm/rad)	Breakout angle (mrads)	Torsional natural frequency (Hertz)	Stick shear stress (kN/m²)	Slip shear stress (kN/m²)	Normal stress (kN/m²)	Stick shear modulus (MN/m²)	Slip shear modulus (MN/m²)	Stick μ	Slip μ	Mean μ	Maximum energy per cycle (Joules)	Minimum energy per cycle (Joules)	Mean energy per cycle (Joules)
8	B	1	AA	3	0.029	0.13	305.8	0.042	14.0	11.4	5614	2.49	33.3	274.1	223.4	1135.5	109.9	89.6	0.24	0.20	0.22	2.91	2.37	2.64
9	B	2	II	6	0.029	0.26	611.6	0.042	35.6	25.5	5883	6.04	24.1	696.0	498.4	2270.9	115.2	82.5	0.31	0.22	0.26	7.39	5.29	6.34
11	B	1	KK	9	0.029	0.39	917.4	0.042	74.0	56.5	5210	14.21	18.5	1449.3	1106.3	3406.4	102.0	77.9	0.43	0.32	0.38	15.39	11.75	13.57
12	B	3	BB	3	0.029	0.13	305.8	0.084	14.7	11.4	5568	2.63	33.1	287.0	223.6	1135.5	109.0	84.9	0.25	0.20	0.22	3.05	2.37	2.71
13	B	1	GG	6	0.029	0.26	611.6	0.084	43.7	35.9	5885	7.42	24.1	854.5	702.0	2270.9	115.2	94.6	0.38	0.31	0.34	9.07	7.46	8.27
14	B	2	HH	9	0.029	0.39	917.4	0.084	86.7	71.3	5733	15.11	19.4	1696.4	1396.4	3406.4	112.2	92.4	0.50	0.41	0.45	18.01	14.83	16.42
Maximum									86.7	71.3	5885	15.11	33.3	1696.4	1396.4	3406.4	115.2	94.6	0.50	0.41	0.45	18.01	14.83	16.42
Minimum									14.0	11.4	5210	2.49	18.5	274.1	223.4	1135.5	102.0	77.9	0.24	0.20	0.22	2.91	2.37	2.64
Range									72.7	59.9	675	12.62	14.8	1422.3	1173.1	2270.9	13.2	16.8	0.26	0.21	0.23	15.10	12.46	13.78
Mean									44.8	35.3	5649	7.99	25.4	876.2	691.7	2270.9	110.6	87.0	0.35	0.28	0.31	9.30	7.35	8.33
Standard deviation									30.2	24.4	252	5.52	6.5	590.5	478.4	1015.6	4.9	6.4	0.10	0.09	0.09	6.27	5.08	5.67
Standard deviation (%)									67.4	69.2	4.5	69.2	25.4	67.4	69.2	44.7	4.5	7.3	29.0	31.2	29.9	67.4	69.2	68.1

Table R2 (Bottom) Last 25 cycles:

Test case	Material	Centre plate	Liner	Centre plate load (kN)	Centre plate radius (m)	Mass moment of Inertia (kg.m²)	Equivalent mass (kg)	Forcing frequency (Hz)	Stick torque (Nm)	Slip torque (Nm)	Torsional stiffness (Nm/rad)	Breakout angle (mrads)	Torsional natural frequency (Hertz)	Stick shear stress (kN/m²)	Slip shear stress (kN/m²)	Normal stress (kN/m²)	Stick shear modulus (MN/m²)	Slip shear modulus (MN/m²)	Stick μ	Slip μ	Mean μ	Maximum energy per cycle (Joules)	Minimum energy per cycle (Joules)	Mean energy per cycle (Joules)
8	B	1	AA	3	0.029	0.13	305.8	0.042	17.0	13.6	5837	2.91	33.9	332.2	266.4	1135.5	114.3	91.6	0.29	0.23	0.26	3.53	2.83	3.18
9	B	2	II	6	0.029	0.26	611.6	0.042	40.1	26.5	5880	6.82	24.1	784.6	518.0	2270.9	115.1	76.0	0.35	0.23	0.29	8.33	5.50	6.92
11	B	1	KK	9	0.029	0.39	917.4	0.042	91.4	71.7	5158	17.77	18.4	1789.3	1402.9	3406.4	101.0	79.2	0.53	0.41	0.47	19.00	14.90	16.95
12	B	3	BB	3	0.029	0.13	305.8	0.084	13.6	11.2	5602	2.42	33.2	265.7	219.1	1135.5	109.7	90.4	0.23	0.19	0.21	2.82	2.33	2.57
13	B	1	GG	6	0.029	0.26	611.6	0.084	47.3	39.2	5678	8.32	23.6	925.0	767.0	2270.9	111.2	92.2	0.41	0.34	0.37	9.82	8.15	8.98
14	B	2	HH	9	0.029	0.39	917.4	0.084	93.3	69.3	6027	15.48	19.9	1826.1	1357.3	3406.4	118.0	87.7	0.54	0.40	0.47	19.39	14.41	16.90
Maximum									93.3	71.7	6027	17.77	33.9	1826.1	1402.9	3406.4	118.0	92.2	0.54	0.41	0.47	19.39	14.90	16.95
Minimum									13.6	11.2	5158	2.42	18.4	265.7	219.1	1135.5	101.0	76.0	0.23	0.19	0.21	2.82	2.33	2.57
Range									79.7	60.5	869	15.30	15.5	1560.5	1183.8	2270.9	17.0	16.2	0.30	0.22	0.26	16.57	12.57	14.38
Mean									50.4	38.6	5697	8.94	25.5	987.2	755.1	2270.9	111.5	86.2	0.39	0.30	0.35	10.48	8.02	9.25
Standard deviation									35.0	26.7	304	6.38	6.6	684.4	522.4	1015.6	6.0	6.9	0.12	0.09	0.11	7.27	5.55	6.40
Standard deviation (%)									69.3	69.2	5.3	71.3	25.8	69.3	69.2	44.7	5.3	8.0	31.6	31.4	31.3	69.3	69.2	69.2

Table R2: Summary of the local analysis results for material B during the 10800 cycle service tests. (Top) First 25 cycles. (Middle) Cycles 1475 – 1500. (Bottom) Last 25 cycles.

The service test results for material C are shown in Table R3 and from these, it can be that the mean values for stick torque responses are seen to be 20.6, 25.2 and 19.8 Nm, whereas the slip values during these test cases are seen to be 13.7, 19.8 and 16.3 Nm. This analyses shows that the slip torque responses are in the region of 18 – 33% lower than the stick responses. The SD`s of these parameters as can be seen, range between 38.3 – 54%, which are almost the same as the deviations that were measured on material A (39.1 – 57.6%).

The mean value of the torsional stiffness coefficients that were calculated for material C under the 3, 6 and 9 kN centre plate loading conditions as can be seen, are the lowest overall out of the three materials that were tested, ranging between 4888 – 5039 Nm/rad. The deviations of these parameters range between 1 – 3.4%, which are also the lowest range of SD`s overall.

The mean values of the torsional stiffness coefficients that were calculated for materials A, B and C during the running-in tests cases (Appendix O), ranged between 2696 – 4819, 3142 – 3373 and 3278 – 3681 Nm/rad respectively, which are slightly lower than the range of values that were calculated during the service tests. The SD`s of running-in test mean stiffness values however, are significantly higher than the service test deviations, ranging between 15.2 – 38.8%.

The mean values of the breakout angles during the service tests as can be seen from the results shown in Tables R1 – R3, range between 2.5 – 3.6, 3.7 – 8.94 and 3.9 – 5 mrad for materials A, B and C respectively. Whereas the SD`s of these parameters are seen to range between 37.8 – 71.3%, which are relatively high in comparison to the SD`s of the torsional stiffness parameters. During the running-in test cases, the mean values for the breakout angles were 6 – 9 times smaller and seen to range between 0.41 – 0.52 mrad (Appendix O). The SD`s of these parameters during the various stages of the running-in test cases however, were seen to range between 37.9 – 44.6% which are more consistent due to the loading conditions being exactly the same in each test case. Whereas in the service test cases on the other hand, the centre plate load was either 3, 6 or 9 kN and these changes therefore, are obviously reflected in the SD values of these system parameters.

This analyses clearly shows that the stiffness parameters of the centre plate/wear liner components become more stable as the centre plate load increases, whereas the breakout angle become more unstable. Also, during the breakout as well as the gross-sliding events throughout the running-in test cases, the stick and slip torque responses on materials A, B and C for example, were seen to be approximately the same in the majority of test cases. During the service test cases however, there was a measurable difference between these two system parameters, which clearly shows these material behaviours are strongly dependent on the loading conditions, as well as the mechanical properties of the centre plate/wear liner components.

Test case	Material	Centre plate	Liner	Centre plate load (kN)	Centre plate radius (m)	Mass moment of Inertia (kg.m²)	Equivalent mass (kg)	Forcing frequency (Hz)	Stick torque (Nm)	Slip torque (Nm)	Torsional stiffness (Nm/rad)	Breakout angle (mrads)	Torsional natural frequency (Hertz)	Stick shear stress (kN/m²)	Slip shear stress (kN/m²)	Normal stress (kN/m²)	Stick shear modulus (MN/m²)	Slip shear modulus (MN/m²)	Stick μ	Slip μ	Mean μ	Maximum energy per cycle (Joules)	Minimum energy per cycle (Joules)	Mean energy per cycle (Joules)
15	C	1	A	3	0.029	0.13	305.8	0.084	14.3	9.7	4709	3.03	30.5	279.2	189.5	1135.5	92.2	62.6	0.25	0.17	0.21	2.96	2.01	2.49
16	C	2	B	6	0.029	0.26	611.6	0.084	17.0	11.8	5038	3.37	22.3	332.0	230.8	2270.9	98.6	68.6	0.15	0.10	0.12	3.53	2.45	2.99
17	C	1	C	9	0.029	0.39	917.4	0.084	30.7	19.7	4916	6.25	18.0	601.4	384.7	3406.4	96.2	61.6	0.18	0.11	0.14	6.39	4.09	5.24
Maximum									30.7	19.7	5038	6.25	30.5	601.4	384.7	3406.4	98.6	68.6	0.25	0.17	0.21	6.39	4.09	5.24
Minimum									14.3	9.7	4709	3.03	18.0	279.2	189.5	1135.5	92.2	61.6	0.15	0.10	0.12	2.96	2.01	2.49
Range									16.5	10.0	329	3.22	12.5	322.2	195.2	2270.9	6.4	7.0	0.10	0.07	0.08	3.42	2.07	2.75
Mean									20.6	13.7	4888	4.21	23.6	404.2	268.3	2270.9	95.7	64.2	0.19	0.13	0.16	4.29	2.85	3.57
Standard deviation									8.8	5.3	166	1.77	6.3	172.8	102.9	1135.5	3.3	3.8	0.05	0.03	0.04	1.84	1.09	1.46
Standard deviation (%)									42.8	38.3	3.4	42.0	26.9	42.8	38.3	50.0	3.4	5.9	27.0	27.4	27.1	42.8	38.3	41.0

Test case	Material	Centre plate	Liner	Centre plate load (kN)	Centre plate radius (m)	Mass moment of Inertia (kg.m²)	Equivalent mass (kg)	Forcing frequency (Hz)	Stick torque (Nm)	Slip torque (Nm)	Torsional stiffness (Nm/rad)	Breakout angle (mrads)	Torsional natural frequency (Hertz)	Stick shear stress (kN/m²)	Slip shear stress (kN/m²)	Normal stress (kN/m²)	Stick shear modulus (MN/m²)	Slip shear modulus (MN/m²)	Stick μ	Slip μ	Mean μ	Maximum energy per cycle (Joules)	Minimum energy per cycle (Joules)	Mean energy per cycle (Joules)
15	C	1	A	3	0.029	0.13	305.8	0.084	13.4	10.5	4979	2.69	31.3	262.3	206.3	1135.5	97.5	76.7	0.23	0.18	0.21	2.79	2.19	2.49
16	C	2	B	6	0.029	0.26	611.6	0.084	24.1	18.9	5062	4.77	22.3	472.4	369.4	2270.9	99.1	77.5	0.21	0.16	0.19	5.02	3.92	4.47
17	C	1	C	9	0.029	0.39	917.4	0.084	38.1	30.1	5063	7.53	18.2	746.7	589.3	3406.4	99.1	78.2	0.22	0.17	0.20	7.93	6.26	7.09
Maximum									38.1	30.1	5063	7.53	31.3	746.7	589.3	3406.4	99.1	78.2	0.23	0.18	0.21	7.93	6.26	7.09
Minimum									13.4	10.5	4979	2.69	18.2	262.3	206.3	1135.5	97.5	76.7	0.21	0.16	0.19	2.79	2.19	2.49
Range									24.7	19.6	84	4.84	13.1	484.3	382.9	2270.9	1.6	1.6	0.02	0.02	0.02	5.14	4.07	4.60
Mean									25.2	19.8	5035	5.00	24.0	493.8	388.3	2270.9	98.6	77.5	0.22	0.17	0.20	5.24	4.12	4.68
Standard deviation									12.4	9.8	48	2.43	6.7	242.9	192.2	1135.5	0.9	0.8	0.01	0.01	0.01	2.58	2.04	2.31
Standard deviation (%)									49.2	49.5	1.0	48.6	27.9	49.2	49.5	50.0	1.0	1.0	5.2	5.5	5.4	49.2	49.5	49.3

Test case	Material	Centre plate	Liner	Centre plate load (kN)	Centre plate radius (m)	Mass moment of Inertia (kg.m²)	Equivalent mass (kg)	Forcing frequency (Hz)	Stick torque (Nm)	Slip torque (Nm)	Torsional stiffness (Nm/rad)	Breakout angle (mrads)	Torsional natural frequency (Hertz)	Stick shear stress (kN/m²)	Slip shear stress (kN/m²)	Normal stress (kN/m²)	Stick shear modulus (MN/m²)	Slip shear modulus (MN/m²)	Stick μ	Slip μ	Mean μ	Maximum energy per cycle (Joules)	Minimum energy per cycle (Joules)	Mean energy per cycle (Joules)
15	C	1	A	3	0.029	0.13	305.8	0.084	9.5	8.0	4872	1.94	31.0	185.1	156.0	1135.5	95.4	80.4	0.16	0.14	0.15	1.97	1.66	1.81
16	C	2	B	6	0.029	0.26	611.6	0.084	19.2	15.6	5110	3.76	22.4	375.9	305.6	2270.9	100.0	81.3	0.17	0.13	0.15	3.99	3.25	3.62
17	C	1	C	9	0.029	0.39	917.4	0.084	30.8	25.3	5135	6.01	18.4	603.8	495.3	3406.4	100.5	82.5	0.18	0.15	0.16	6.41	5.26	5.84
Maximum									30.8	25.3	5135	6.01	31.0	603.8	495.3	3406.4	100.5	82.5	0.18	0.15	0.16	6.41	5.26	5.84
Minimum									9.5	8.0	4872	1.94	18.4	185.1	156.0	1135.5	95.4	80.4	0.16	0.13	0.15	1.97	1.66	1.81
Range									21.4	17.3	263	4.06	12.6	418.6	339.3	2270.9	5.1	2.1	0.01	0.01	0.01	4.45	3.60	4.02
Mean									19.8	16.3	5039	3.90	23.9	388.3	319.0	2270.9	98.6	81.4	0.17	0.14	0.15	4.12	3.39	3.76
Standard deviation									10.7	8.7	145	2.04	6.4	209.6	170.0	1135.5	2.8	1.1	0.01	0.01	0.01	2.23	1.81	2.02
Standard deviation (%)									54.0	53.3	2.9	52.2	26.9	54.0	53.3	50.0	2.9	1.3	4.5	4.0	4.2	54.0	53.3	53.7

Table R3: Summary of the local analysis results for material C during the 10800 cycle service tests. (Top) First 25 cycles. (Middle) Cycles 1475 – 1500. (Bottom) Last 25 cycles.

Appendix S. X-Factor and COF results for the centre plate/wear liners

The X-Factor results that were calculated from the 1:7 scale centre plate/wear liner torque and Coefficient of Friction (COF) responses are discussed in this appendix. For the X-Factor calculations presented in this thesis, the COF values for the Constant Contact Side Bearer (CCSB) model for example, were set to the highest values that were calculated for materials A, B and C after the running-in test cases, which were seen to be 0.19, 0.32 and 0.27 respectively. These parameters were then set as constant values in the X-Factor calculations, see Appendices N and O.

The COF values for the centre plate/wear liner components on the other hand, were obtained from the service test cases and have been modelled as dynamic values in the X-Factor calculations. This means that these parameters can increases/decrease as a function of the number of running cycles, see Appendices Q and R. Table S1 shows the X-Factor results for the 3 kN/tare loading cases and from these it can be seen that values for the complete data set (5 test cases), range between 0.044 – 0.085. The lowest and highest and values overall under this loading condition as can be seen, were calculated for materials A and B. However, the X-Factor value during test case 15 on material C, was also seen to be in the region 0.083 after completing the 10800 cycle service test.

The X-Factor values for the complete data set under 6 kN/part-laden loading conditions as can be seen in Table S2 (6 test cases), have decreased slightly in comparison to the tare loading cases and are now seen to range between 0.033 – 0.083. It can also be seen that materials A and B produced the lowest and highest X-Factor values under the part-laden loading conditions as well. The percentage increases in the X-Factor values for the part-laden loading cases however, are significantly higher, ranging between 5.4 – 97.1%. Whereas for the tare loading cases, these parameters were shown to be in the region of 12.2 – 21.3%. The range of Standard Deviations (SD`s) of these values have also increased from 22.2 – 23.3%, to 22 – 87.8% during the part-laden loading cases.

The X-Factors results for the 9 kN/laden loading cases are seen to be the highest values overall, ranging between 0.029 – 0.095, see Table S3 (5 test cases). Materials A and B also recorded the lowest and highest values under this loading condition as well. The percentage increases in the X-Factor values are seen to range between 16.1 – 111.1%, which is similar to the range of increases that were calculated for the part-laden loading conditions. The SD`s of the X-Factor values for the laden loading conditions however, are the highest overall, ranging between 20.9 – 48.2%.

This analyses clearly shows that the X-Factor values of the centre plate/wear liner components tend to increase in proportion to the number of running-in cycles. However, this only applies to materials A and B, whereas for material C on the other hand, the X-Factor values are seen to increase during the first 3 – 5 hours of the service tests and then decrease and reaching the peak value as the number of cycles increases which is a pattern of behaviour that is unique to this particular wear liner material.

Material	Test case	Centre plate load (kN)	Side bearer load (kN)	Yaw velocity (deg/s)	Minimum X-Factor value	Maximum X-Factor value	Increase (%)
A	1	147	49	0.5	0.044	0.051	15.9
	5	147	49	1	0.047	0.057	21.3
B	8	147	49	0.5	0.071	0.085	19.7
	12	147	49	1	0.074	0.083	12.2
C	15	147	49	1	0.068	0.078	14.7
Maximum					0.074	0.085	21.3
Minimum					0.044	0.051	12.2
Range					0.030	0.034	9.1
Mean					0.061	0.071	16.8
Standard deviation					0.014	0.016	3.7
Standard deviation (%)					23.3	22.2	22.2

Table S1: Summary of the X-Factor results for the tare loading conditions.

Material	Test case	Centre plate load (kN)	Side bearer load (kN)	Yaw velocity (deg/s)	Minimum X-Factor value	Maximum X-Factor value	Increase (%)
A	2	294	49	0.5	0.034	0.067	97.1
	6	294	49	1	0.037	0.039	5.4
	4	294	49	0.5	0.033	0.036	9.1
B	9	294	49	0.5	0.054	0.077	42.6
	13	294	49	1	0.053	0.083	56.6
C	16	294	49	1	0.045	0.056	24.4
Maximum					0.054	0.083	97.1
Minimum					0.033	0.036	5.4
Range					0.021	0.047	91.7
Mean					0.043	0.060	39.2
Standard deviation					0.009	0.019	34.4
Standard deviation (%)					22.0	32.7	87.8

Table S2: Summary of the X-Factor results for the part-laden loading conditions.

Material	Test case	Centre plate load (kN)	Side bearer load (kN)	Yaw velocity (deg/s)	Minimum X-Factor value	Maximum X-Factor value	Increase (%)
A	3	441	49	0.5	0.031	0.036	16.1
	7	441	49	1	0.029	0.034	17.2
B	11	441	49	0.5	0.045	0.095	111.1
	14	441	49	1	0.046	0.093	102.2
C	17	441	49	1	0.036	0.053	47.2
Maximum					0.046	0.095	111.1
Minimum					0.029	0.034	16.1
Range					0.017	0.061	95.0
Mean					0.037	0.062	58.8
Standard deviation					0.008	0.030	45.6
Standard deviation (%)					20.9	48.2	77.5

Table S3: Summary of the X-Factor results for the laden loading conditions.

The normal distributions of the COF values that were calculated for materials A, B and C during the first 25 cycles of the running-in test cases are shown in Figures S1 – S3. The distributions of the COF values for material A are shown by the green line and from this, it can be seen that the mean value of 0.09 is the lowest overall. The mean COF value for material B as can be seen by the blue line in Figure S1, is 0.12, whereas the SD`s and Standard Errors of the Mean (SEM`s) are seen to be exactly the same for materials A and B. The mean COF value and SD parameter for material C as can be seen (Red line), are the highest overall at 0.15 and 0.05.

The distributions of the COF values during cycles 1475 – 1500 are shown in Figure S4. From these it can be seen that the mean value for material A has increased by 11%. The mean values for materials B and C however, have increased by 42 and 20% respectively. The SD`s have also increased slightly in comparison to the first 25 cycles.

Figure S3 shows the normal distributions of the COF values during the last 25 cycles of the running-in test cases. From these distributions, it can be seen that the mean value for material A is the lowest, as well as the most consistent overall, at 0.11. The mean COF values for materials B and C however, are exactly the same at 0.19, but 73% higher than the mean value for material A. The SD`s and SEM`s for materials B and C are also considerably higher, which shows that these COF values are more widely dispersed around the mean values. These variations however, are mainly due to the non-symmetric friction characteristics of the centre plate/wear liner components, which were seen to be the highest overall during the running-in test cases, ranging between 20 – 65%.
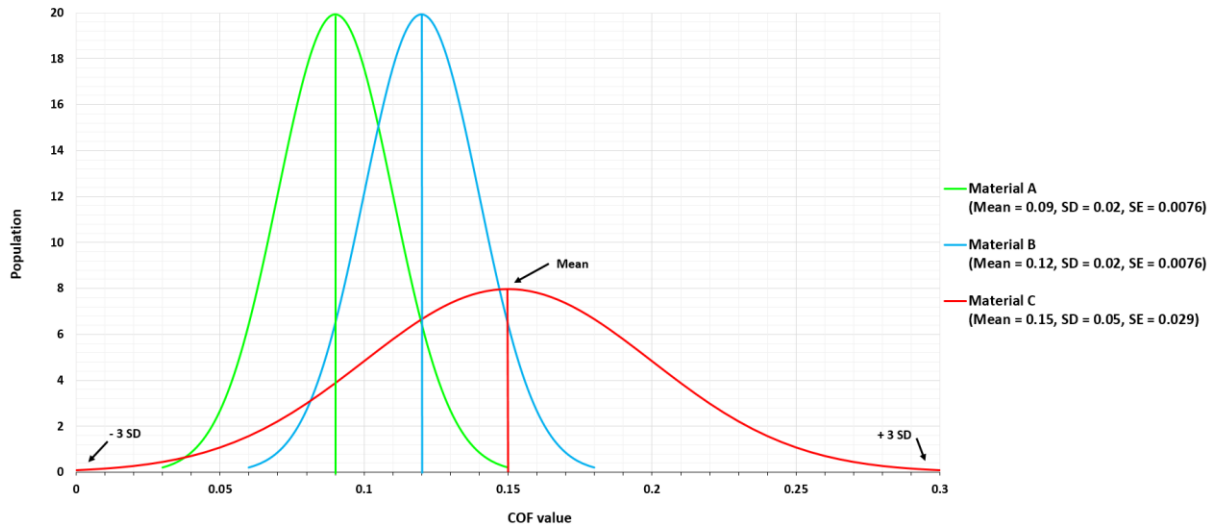
Figure S1: COF values for materials A, B and C during the first 25 cycles of the running-in tests.
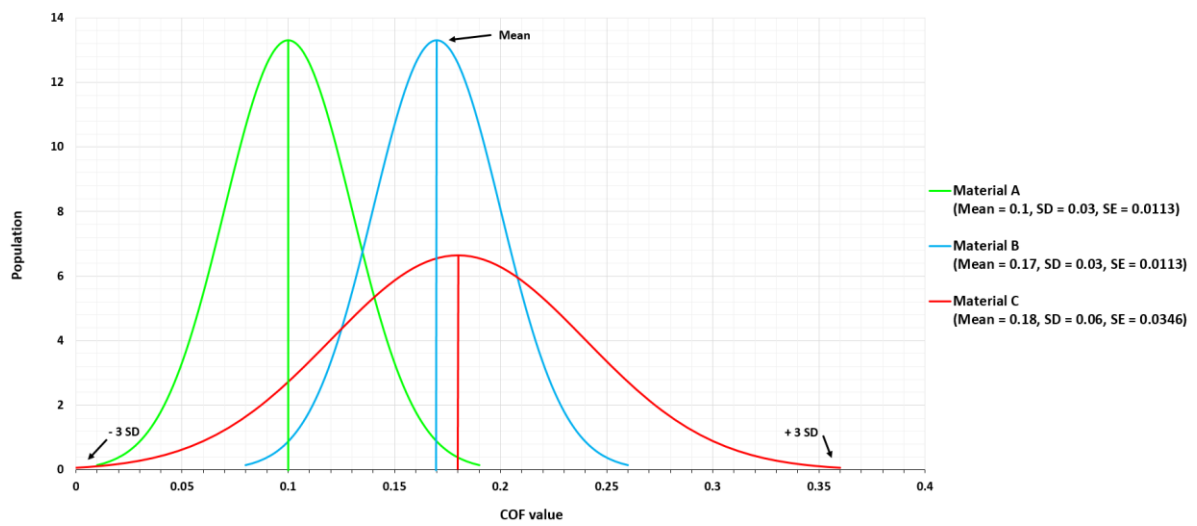

Figure S2: COF values for materials A, B and C during cycles 1475 – 1500 of the running-in tests.
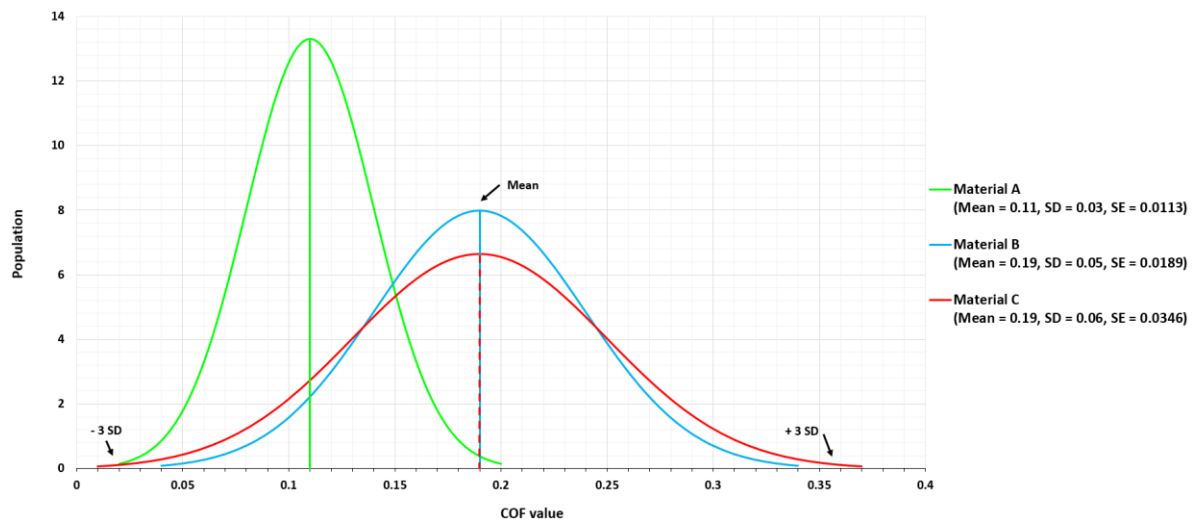

Figure S3: COF values for materials A, B and C during the last 25 cycles of the running-in tests.

The normal distributions of the COF values that were calculated for materials A, B and C after the 3, 6 and 9 kN service test cases are shown in Figures S4 – S6. The distributions of the COF values for material A during the first 25 cycles, cycles 5375 – 5400 and the last 25 cycles of these test cases are shown in Figure S4 by the green, blue and red lines respectively. From these results, it can be seen that the mean COF value during the first 25 cycles for example, starts off in the region of 0.12 and then increases to 0.15 during cycles 5375 – 5400, which is a 25% increase in the mean COF value for the complete data set (7 test cases). The mean COF value during the last 25 cycles as can be seen, is 0.17 which is only a 13% increase and suggests that the COF values are starting to settle in this region. The COF values as can be seen by the increases in the SD`s, are also becoming more widely dispersed about the mean values under the heavier loading conditions.

Figure S5 shows the distributions of the COF values for material B during the various stages of the service tests (6 test cases). From these results it can be seen that mean COF value during the first 25 cycles for example (Green lines), is 0.14 which is 17% higher than the mean value for material A during this stage of the test. Whereas the mean COF value for material B during cycles 5375 – 5400, is seen to be 0.31, which is a 121% increase relative to the COF value during the first 25 cycles, as well as double the mean COF value that was calculated for material A.

The mean COF value for material B during the last 25 cycles of the service tests is seen to be 0.35, which is a percentage increase of 13% and also, exactly the same percentage increase that was calculated for material A at this stage of the service test. The SD and SEM parameters however, are considerably higher during the latter stages of the service tests on material B, which clearly suggests that these results are much more widely dispersed about the mean values. This finding strongly suggests that it would be more difficult for example, to determine accurate maintenance schedules for this material in comparison to material A.

The normal distributions of the COF values for material C during the three service test that were carried out using this material are shown in Figure S6. From these distributions, it can be seen that the mean COF during the first 25 cycles is 0.16, which is the highest value overall. The SD of these results are also seen to be the highest overall during this stage of the service tests at 0.04. During cycles 5375 – 5400, the mean COF value for material C is seen to be 0.2, which is a 25% increase relative to the first 25 cycles and exactly the same percentage increase that was measured on material A at this stage of the service tests. Whereas during the last 25 cycles, the mean COF value for material C is seen to be 0.15 which is the lowest value overall as well as 25% decrease relative to the mean COF value during cycles 5375 – 5400.

The SD`s and SEM`s for material C are also seen to be the lowest overall during cycles 5375 – 5400 (Figure S6), as well as during the last 25 cycles of the service test cases, which is surprising considering the limited amount of test cases that were carried out using this material (3 test cases). Material C however, is the only wear liner material that has a decreasing COF value as the number of cycles increases. The COF values for materials A and B on the other hand, are seen to increase in proportion to the number of running cycles (Figures S4 and S5).

The normal distributions of the COF values that were calculated from the steel-on-steel test case responses are also shown in Figure S7. The green and red lines show the distributions of the minimum and maximum COF values and the blue line shows the mean COF values. From these distributions, it can be seen that mean of the minimum and maximum COF values are 0.6 and 1.2, whereas the mean of the mean values that were measured during the various phases of the steel-on-steel test case, is seen to be 0.9 with a SD of 0.1. The SD`s of the maximum/minimum values however, are significantly higher and seen to be 0.3 and 0.2.

The distribution curve of the mean COF values as can be seen, is located in between the minimum/maximum values. From the results shown in Table 5.10 (Section 5.4.8), it can also be seen

that this distribution provides the best representation of the full range of COF values for the steel-on-steel test case. The maximum and minimum values for example, only occur during sporadic events, hence the reason why these distribution curves are wider and lower in height. However, after evaluating the height of the mean distribution curve in Figure S7, it can be seen that this is a factor of 5 – 10 times, smaller than the heights of the distribution curves for the wear liner materials (Figures S4 – S6). This analyses clearly shows that the probabilities associated with the steel-on-steel COF values are relatively low. This analysis also suggests that it would be extremely difficult to predict accurate maintenance schedules for this material due to the instabilities in the COF values.

The normally distributed COF values presented in this Appendix can now be used in X-Factor test calculations, railway vehicle Multibody Simulations, Design of Experiments and Monte-Carlo simulations to improve the confidence levels in the friction testing/modelling methodologies that are currently used by the rail industry/research institutions. The ranges of COF values for similar as well as different wear liner materials, will also help rail engineers to better understand the safety risks, as well as the vehicle/track maintenance requirements in response to changing the wear liner materials in the secondary suspension system.
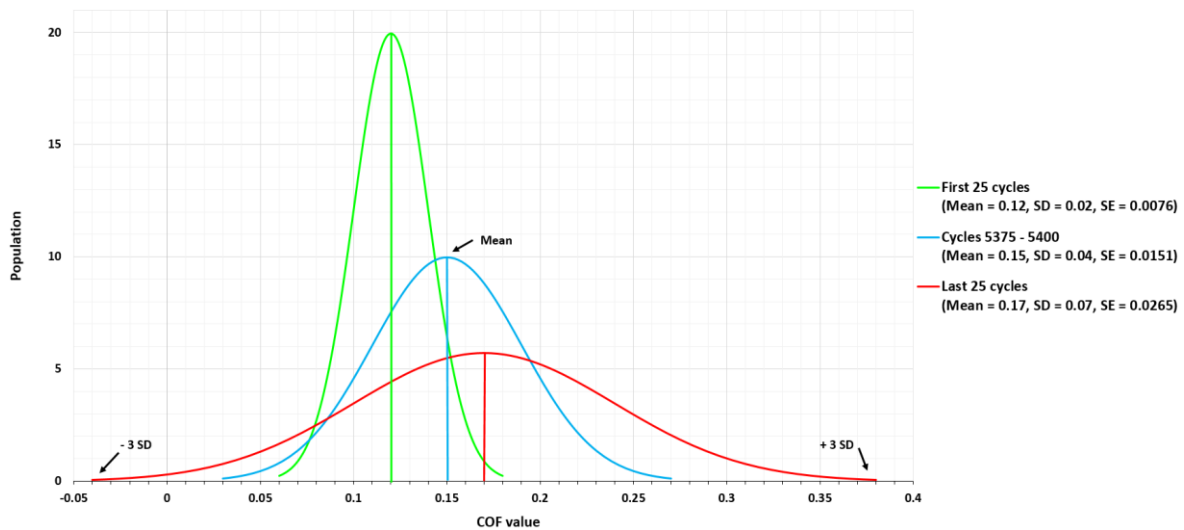

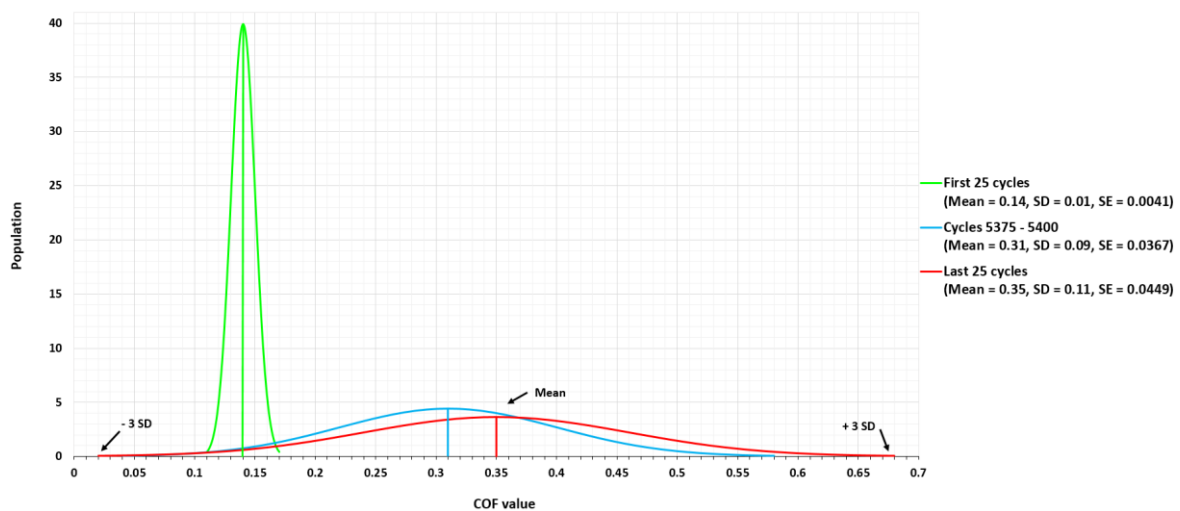Figure S4: COF values for material A during the service tests.

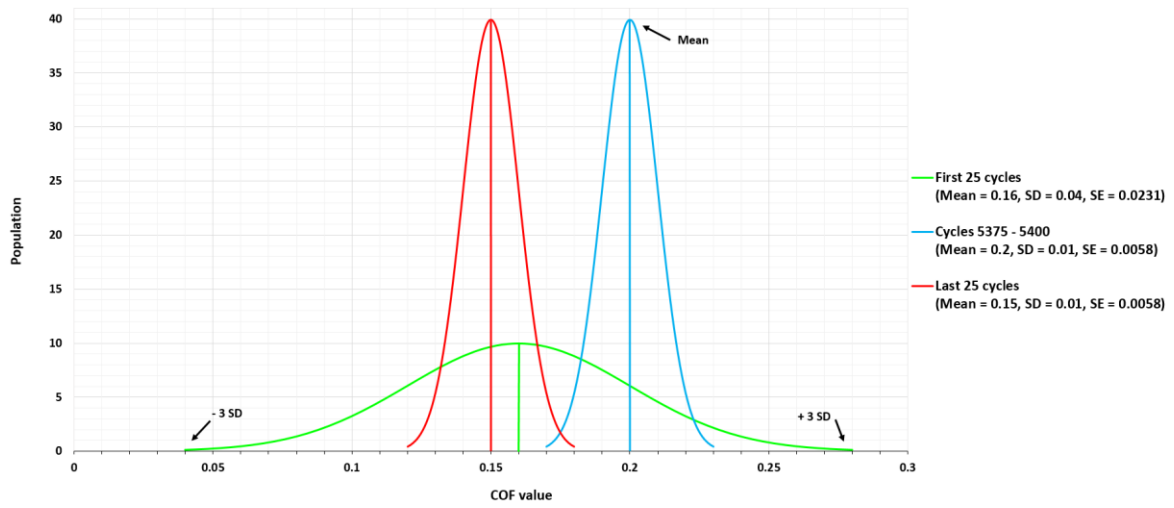Figure S5: COF values for material B during the service tests.

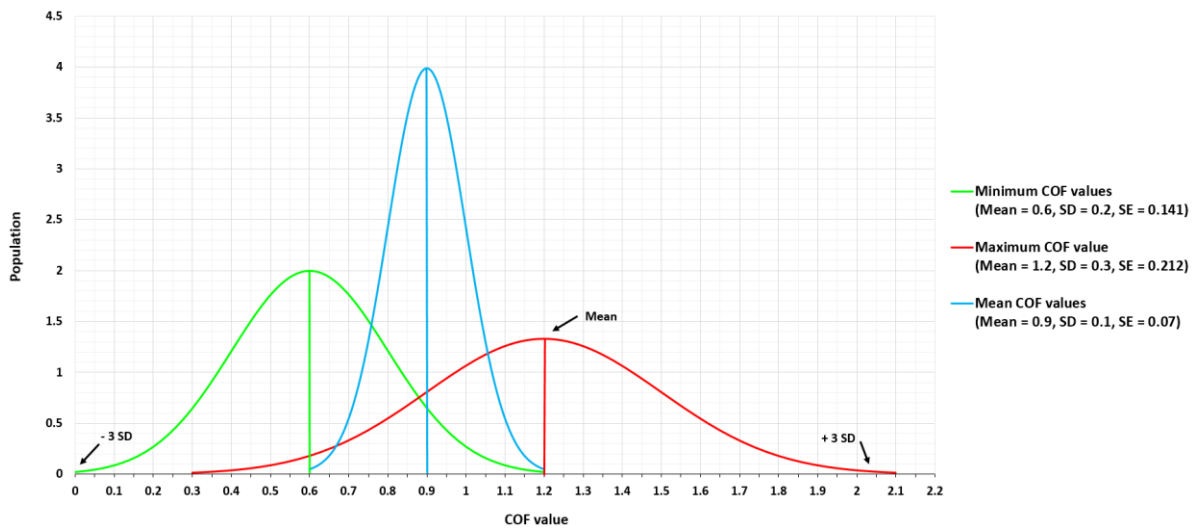Figure S6: COF values for material C during the service tests.

Figure S7: COF values during the steel-on-steel test case.

Appendix T. Modified scale model centre plate design

The modified 1:7 scale centre plate design is shown in Figure T1 which as can be seen, now has 4-slots machined around the circumference. These slots enable the static/dynamic centre plates to be accurately aligned relative to each other in the Instron machine jaws using a key. They have also been included to improve the accuracy and repeatability of the surface roughness methodology as well. This centre plate design also has the option to incorporate thermocouples in the holes for locating the dowel pins so that the temperature changes in the centre plate/wear liner components can then be measured as the number of running cycles increases.
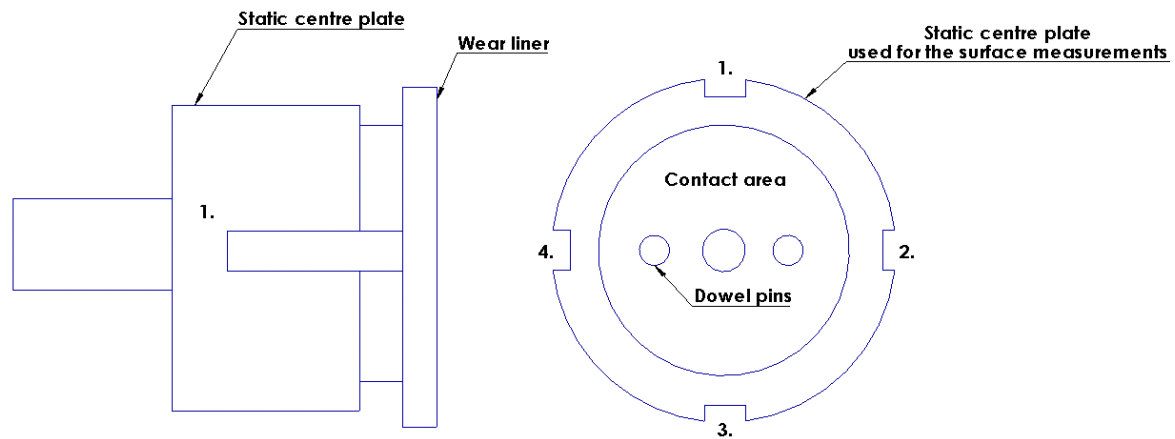

Figure T1: Modified centre plate design.